Dissertation Submitted to
Graduate School of Science of Osaka University
for the Degree of Doctor of Physics

Exotics in meson-baryon dynamics with chiral symmetry

Tetsuo Hyodo [A)]

∼ 2006 ∼

Research Center for Nuclear Physics (RCNP), Osaka University
Mihogaoka 10-1, Ibaraki, Osaka 567-0047, Japan

[A)] Email address: hyodo@rcnp.osaka-u.ac.jp

Acknowledgement

First of all, I would like to sincerely express my gratitude to the supervisor, Professor Atsushi Hosaka for enlightening discussions, helpful suggestions and continuous encouragements over the past five years. I have been instructed about plenty of things in hadron physics from fundamental facts to recent developments, which are reflected throughout this dissertation. I wish to thank Professor Eulogio Oset (IFIC, Valencia Univ.) for providing many exciting ideas and stimulating discussions. He has been giving me a lot of interesting subjects and beautiful hand-writing notes on them. Doctor Daisuke Jido (YITP) is acknowledged for collaboration and help from the beginning of the master course, which have provided fundamental tools for researches. I appreciate Doctor Seung-il Nam (Pusan National Univ.) for his friendship and interesting discussions. Without their affectionate support, I would never complete this dissertation.

The work presented in this thesis has been done with my collaborators, Professor Hyun Chul Kim (Pusan National Univ.), Doctor Felipe J. Llanes-Estrada (Madrid Univ.), Professor Jose R. Peláez (Madrid Univ.), Professor Angels Ramos (Barcelona Univ.), Doctor Sourav Sarkar (IFIC, Valencia Univ.), and Professor Manolo J. Vicente Vacas (IFIC, Valencia Univ.). I would like to thank them all again for the fruitful collaborations.

I am very grateful to Professor Takashi Nakano (RCNP), Mister Koji Miwa (Kyoto Univ.), and people of LEPS collaboration for letting me know the latest experimental situation and suggestions for the theoretical studies from experimental point of view. It is my great pleasure to visit Valencia, where many collaborators and friends of mine are studying. I thank them for their kind hospitality during my stays. I express my thankfulness to my wife Kana for generous understanding of my study and support for healthy life. The work presented here is supported in part by the Japan Society for the Promotion of Science (JSPS) the Grant for Scientific Research ((C) No.17959600).

I would like to thank all the members of theory group of Research Center for Nuclear Physics (RCNP) for their kind helps. I am very happy to study at RCNP where I have had exciting discussions with experimentalists and many opportunities to visit foreign countries. Finally, I wish to acknowledge Professor Hiroshi Toki for providing such a comfortable environment, collaborators and colleagues.

Abstract

Quantum chromodynamics (QCD) governs the strong interaction among quarks and gluons, which compose hadrons in the non-perturbative vacuum. Since hadrons are elementary excitations of the QCD vacuum, it is important to study their properties in order to understand the whole dynamics of QCD. The field of the hadron spectroscopy is being stimulated by recent experimental results, namely, evidences of new states and observation of various quantities to extract properties of excited states.

In this thesis, we study the exotics appearing in the meson-baryon dynamics. We consider not only the manifestly exotic states such as pentaquarks, but also the states which are considered to contain a large amount of $\bar{q}q$ components in addition to the valence quarks. We study the properties of these exotics in effective models with hadronic degrees of freedom. These models are constructed based on the chiral and flavor symmetries of QCD, and the results are compared with experimental data. There are two main subjects to be pursued in this thesis. One is the study of baryon resonances using the chiral unitary model, and the other is the study of pentaquarks. A key issue common for both subjects is the investigation of multi-quark components.

We adopt a model which utilizes the meson-baryon interaction derived from the chiral perturbation theory. Imposing the unitarity condition, the model describes the baryon resonances as meson-baryon molecule states. Hence, the resonances may be regarded as five-quark states in contrast to conventional approaches with three quarks. The model has been referred to as the chiral unitary model. Within this model, we study the flavor SU(3) breaking effect at the interaction level. An interesting two-pole structure of the $\Lambda(1405)$ resonance is studied through the production reactions in order to clarify the structure in experiments. The amplitude of the chiral unitary model enables us to extract various coupling constants of the generated resonance. Using this method, we calculate the magnetic moments of the $N(1535)$ resonance and K^* vector meson coupling to the $\Lambda(1520)$ resonance.

The Θ^+ baryon has strangeness $S = +1$. Therefore the minimal number of quarks to construct the Θ^+ is five, which is manifestly exotic. We study a K induced reaction to determine the Θ^+ quantum numbers in experiments. Inspired by the πKN molecule picture, we estimate the two-meson clouds around antidecuplet baryons using phenomenological interaction Lagrangians based on flavor SU(3) symmetry. A possibility of spin 3/2 for the Θ^+ is examined in the **8**-$\overline{\mathbf{10}}$ representation mixing scheme, analyzing the SU(3) relations for the mass spectra and the decay widths of known baryon resonances. This scheme is extended to determine two-meson couplings of the Θ^+. The resulting interactions are applied to the meson-induced productions of the Θ^+.

Contents

Part I

Introduction and review

Chapter 1

Introduction

1.1 Hadronic description of exotics

Strong interaction is described by quantum chromodynamics (QCD), which is color SU(3) gauge theory with quarks as fundamental fields of matter and gluons as gauge fields. Because QCD has non-Abelian gauge symmetry, gluons interact with themselves, so that the running coupling constant of QCD behaves asymptotically free. Inversely, the coupling constant becomes large in low energy regions, where perturbative calculations break down. In this non-perturbative region, *color confinement* and *chiral symmetry breaking* take place, and provide a variety of phenomena. The color confinement allows only color singlet states to exist, and the effective degrees of freedom become mesons and baryons that we refer to as hadrons. The hadrons acquire masses significantly larger than the current masses of quarks, due to the spontaneous chiral symmetry breaking. We would like to study these interesting but complicated physics of hadrons.

In recent years, there has been a remarkable development in hadron physics. From the experimental side, several evidences for manifestly exotic states have been reported, and various quantities such as spin observables and angular distributions to extract properties of excited states are becoming available. Stimulated by the observation of the exotic states, a tremendous amount of theoretical works have been devoted to study these states, which shed light on the properties of exotic states, but also reveal insufficiencies in our conventional understanding. For instance, constituent quark models provide an overall description for hadrons made from $\bar{q}q$ and qqq with simple Hamiltonians. However, for instance, pentaquarks include both quark-quark and quark-antiquark correlations in one system, in contrast to the conventional mesons and baryons. On the other hand, among conventional hadrons there are also several exceptions which have not been well described in the simple quark picture, such as the $\Lambda(1405)$ resonance, the Roper resonance, light scalar mesons, and so on. These states are considered to have other nature than the quark picture, and rather described as hadronic molecules or multi-quark states. Since the manifestly exotic states and the non-conventional states are closely related to each other, we shall call all of them as "exotics", which are investigated in this thesis.

A powerful method for the non-perturbative QCD is the simulation on the lattice. Recent

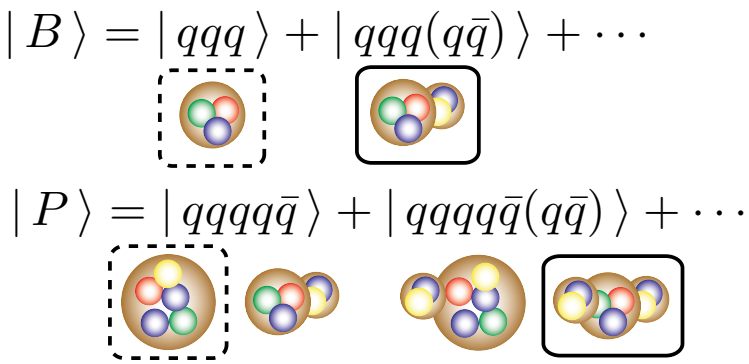

Figure 1.1: Schematic view of the multi-quark components in baryons $|B\rangle$ and pentaquarks $|P\rangle$. Those enclosed by dashed lines correspond to the conventional pictures in quark models, while there are many other structures with $\bar{q}q$ excitations. Among them, we study those enclosed by solid lines.

progress in lattice QCD researches increases the applicability of simulations, as including the spectrum of excited states. Here, however, we shall adopt effective models to study hadrons. If one wants to *understand* a phenomenon *physically*, it is important to have an intuitive picture which captures the essence of the physics there. Thus, the role of effective models is to provide intuitive pictures of hadrons. With one specific model, the picture may be too naive to reproduce all the properties, and the reality will be much more complicated. Therefore, by comparing the experimental observables predicted by two or more models with different pictures, we can extract the information of the structure of hadrons. Since we know that the dynamics of hadrons are governed by QCD, we require the models to be connected with underlying QCD. In order to construct models that share common features with QCD, we follow the symmetry principle as a guidance.

There are various symmetries in QCD Lagrangian. In physical world, some of them are approximate symmetries, but they become exact by taking a proper limit of the parameters. For instance, when the masses of quarks are small compared with the mass of hadrons—this is the case for the light quarks u and d—chiral symmetry and its spontaneous breaking govern the dynamics. If the mass difference among N_f current quarks is sufficiently small, flavor symmetry SU(N_f) becomes exact. Symmetries give strong constraints in the masses and interactions of particles, which are realized as model-independent relations. Results under exact symmetry can be perturbed by taking into account symmetry breaking corrections appropriately. Thus, we can perform a systematic expansion to obtain physical observables.

In this thesis, we investigate the hadron dynamics at low energies, using effective field theories with hadronic degrees of freedom. We focus on two subjects, baryon resonances of s-wave meson-baryon scatterings in the chiral unitary model (part II) and pentaquarks in hadronic description with flavor symmetry (part III). Both subjects are related to each other, in the sense that multi-quark states are dealt with in one way or another. The resonances in the chiral unitary model are described by the meson-baryon quasi-bound states, which have five quarks in their configuration. The pentaquarks contain minimally five quarks by construction, but we can also study seven-quark components. Schematically, this viewpoint

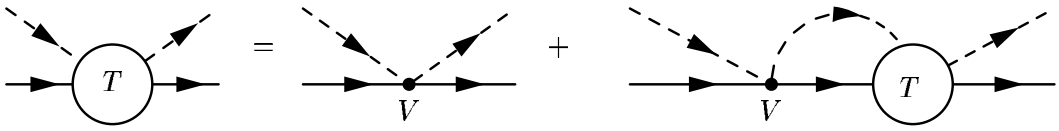

Figure 1.2: Diagrammatic representation of the Bethe-Salpeter equation for the chiral unitary model. T is the scattering amplitude and V is the kernel interaction derived from the chiral perturbation theory. Solid and dashed lines represent the baryon and meson fields, respectively.

can be depicted in Fig. 1.1. These studies eventually reveal the rich structure of quark and hadronic matter. Through the study of these exotics, we would like to emphasize the connection of theories to experiments. It is important to extract the hadron structure from existing experimental data, and to predict observables which reflect the properties of hadrons.

1.2 Baryon resonances in chiral unitary model

Chiral symmetry of QCD plays an important role in low energy hadron physics [1]. Various low energy theorems are derived from chiral symmetry and its spontaneous breaking, which have been known to dominate the low energy phenomena. Based on the nonlinear realization of chiral symmetry, chiral perturbation theory [2, 3] was developed with a systematic expansion in terms of small momenta of pseudoscalar mesons. Low energy behavior of hadrons is successfully described by the chiral perturbation theory. However, the unitarity bound restricts the applicability of the theory to the low energy region, and resonances are not described unless they are introduced as elementary fields.

On the other hand, some resonances were found to be described by introducing the unitarity condition for the scattering amplitude [4, 5], where the resonances were dynamically generated in the non-perturbative resummation. The amplitude of the chiral unitary model can be expressed as in Fig. 1.2, where the kernel interaction V is iterated infinitely to produce the total scattering amplitude T. Baryon resonances are dynamically generated in the resulting amplitude, and they are interpreted as quasi-bound states of mesons and baryons. This picture works well especially for the non-conventional states in quark models, such as the $\Lambda(1405)$ resonance.

Utilizing the amplitude obtained in the chiral unitary model, we perform the following studies. First, motivated by a large SU(3) breaking in the subtraction constants, we study the flavor SU(3) breaking effect in the chiral unitary model [6, 7]. The SU(3) breaking interaction is introduced based on chiral perturbation theory, and we study the effects of this term to the observables. This subject will be discussed in chapter 4, together with the basic formulation of the chiral unitary model and resonance structures.

The $\Lambda(1405)$ resonance has kept the attention of researchers for a long time. As is well known, it is difficult to reproduce the properties of this resonance in a constituent quark model due to its light mass, while the resonance is naturally obtained in the coupled channel scattering. As in the latter, the chiral unitary model also provides the $\Lambda(1405)$ properly. An

interesting observation is that two poles exist around the $\Lambda(1405)$ resonance energy region with the same quantum numbers. It is important to verify this structure experimentally. To do that, we study the $\pi^- p \to K^0 \pi\Sigma$ reaction [8, 9, 10] and the $\gamma p \to K^* B^* \to K\pi MB$ reaction [11, 12] that lead to the $\Lambda(1405)$ production. Each reaction turns out to enhance one of the poles, leading to very different shapes for the invariant mass distribution of the $\pi\Sigma$ state. The result will be given in chapter 5.

By attaching one external current to a meson-baryon scattering amplitude in the chiral unitary model, we can extract a coupling constant of the current to the dynamically generated resonance. Some of these couplings may not be directly measurable. For instance, the magnetic moments of a particle which decays *via* strong interaction is difficult to measure. The coupling constants of a resonance to kinematically forbidden channels cannot be observed through the particle decay. However, these quantity may be important either for the understanding of the internal structure of resonances, or in applications to various reaction processes. We calculate the magnetic moments of the $N(1535)$ resonance [13] which will be discussed in chapter 6. The coupling constant of the $\Lambda(1520)$ to the $\bar{K}^* N$ channel [14] is evaluated in chapter 7.

1.3 Pentaquarks

The evidence for the strangeness $S = +1$ baryon Θ^+ by the LEPS collaboration [15, 16] has given a great impact on hadron physics. The $S = +1$ baryon cannot be constructed by three valence quarks and the minimal quark content for the Θ^+ is $uudd\bar{s}$, therefore it is dubbed "pentaquark". In the hadron spectroscopy, the Θ^+ baryon is the first example which is manifestly exotic. Let us briefly describe the basic properties of this particle. For more detailed and comprehensive review, see chapter 3.

Apparently, there is no verification to forbid the existence of pentaquarks from the first principle of QCD, although the searches for exotic states have not observed positive evidences for a long time. A pentaquark state contains both qq and $q\bar{q}$ in one system, which provides a good test for effective interactions among quarks, since the conventional meson $q\bar{q}$ and baryon qqq only contain either qq or $q\bar{q}$ interactions in one system. Moreover, qq pair in three-quark state must be in $\bar{\mathbf{3}}$ representation of color SU(3), in order to make color singlet for qqq system. On the other hand, qq pair in five-quark system can be combined into color $\mathbf{6}$ state, which is absent in pure qqq system. In this way, the study of exotic states provides deeper understanding of hadron dynamics.

Concerning the Θ^+ state, the observed mass $M_\Theta \sim 1540$ MeV is very low compared with a naive estimation in a constituent quark model. The narrow width $\Gamma_\Theta < 1$ MeV appears difficult to understand in our present knowledge of hadron physics. In experiments, negative results of the Θ^+ search with high statistics are also reported. However, it is worth noting that any of the negative results *cannot exclude* the existence of exotic states at all. They simply indicate the contradiction with the previous positive results claiming a narrow state at low energies. For instance, they cannot exclude any broad resonances in exotic channels from the invariant mass spectrum. Even narrow states may escape the detection when the states have strong coupling to the other decay channels than the detecting one. Once again, QCD

itself does not forbid the existence of exotic states, and absence of evidence is not evidence of absence. Therefore, in spite of the controversial situation in experiments, the study of the exotic states can bring us plenty of knowledge of the hadron physics and the subject is still interesting to be studied.

In order to understand the properties and dynamics of the Θ^+ state, we perform the following studies. First, we calculate the reaction mechanism of $K^+p \to \pi^+KN$ based on the effective interactions derived from the chiral perturbation theory, assuming the s- or p-wave KN resonance at 1540 MeV [17, 18, 19, 20]. Comparing the results with different spin-parity assignment, we extract the observable which can be used as the experimental determination of the pentaquark Θ^+. We find that when we polarize the target and measure the polarization of the recoiled nucleon, we can distinguish the $J^P = 1/2^+$ case from the others. This is the topic in chapter 8.

Next we evaluate self-energies of the two-meson cloud in the Θ^+ and antidecuplet baryons as shown schematically in Fig. 1.1, using interaction Lagrangians constructed by the SU(3) symmetry [21, 22, 23]. The study is motivated by the πKN bound state conjecture for the Θ^+, and the large $\pi\pi N$ branching ratio of the $N(1710)$ resonance, which is considered to belong to the antidecuplet representation together with the Θ^+. The interaction Lagrangians are the four-point contact interaction of two mesons, one ground state baryon, and one antidecuplet baryon, being constrained by the flavor SU(3) symmetry. We observe that the two-meson cloud provides the attractive self-energy and provide about 20% of the empirical mass splitting in the antidecuplet baryons. This will be discussed in chapter 9.

The assignment of pure antidecuplet nature for $N(1710)$ and the Θ^+ is no more than an assumption. This point is clarified in more general framework including representation mixing of antidecuplet $\overline{\mathbf{10}}$ with an octet $\mathbf{8}$, for the possible spin parity assignments $J^P = 1/2^\pm, 3/2^\pm$ [24]. We derive flavor SU(3) relations for the masses and coupling constants, which are examined by fitting the properties of experimentally known resonances with proper quantum numbers. We obtain good descriptions of the mass spectra with $J^P = 1/2^+$ and $J^P = 3/2^-$ in $\mathbf{8}$-$\overline{\mathbf{10}}$ scheme. Using the SU(3) relation in coupling constants, we determine the width of the Θ^+ from the experimental width of the flavor partners of N^* resonances. A narrow decay width of the Θ^+ is naturally obtained for the $J^P = 3/2^-$ case, whereas the width is somehow larger for the $J^P = 1/2^+$ assignment. The results are shown in chapter 10.

We then study the two-meson couplings for the Θ^+ with the $J^P = 1/2^+$ and $J^P = 3/2^-$ assignments for the Θ^+ in this mixing scheme [25]. Based on the study in Ref. [21], we include two dominant interaction Lagrangians. The coupling constants are determined by the decay widths of the corresponding nucleon resonances and further constrained by the evaluation of the self-energy. We calculate the meson-induced reactions for the Θ^+ production and compare the results with experiments (chapter 11).

Chapter 2

Effective field theory and symmetries

In this chapter, we present a framework to construct effective theories of QCD. Strong interaction is described by QCD. However, at low energy, it is not easy to study the dynamics of strong interaction directly from QCD. In such a situation, it is useful to construct a field theory with effective degrees of freedom, respecting the symmetries of underlying theories. We show the symmetries of QCD and the methods to incorporate the virtue of the symmetries into effective Lagrangians.

2.1 Quantum chromodynamics

Quantum chromodynamics (QCD) is color SU(3) gauge theory of quarks and gluons. The N_f flavor (massless) QCD Lagrangian is given by

$$\mathcal{L}^0_{\rm QCD} = -\frac{1}{2}{\rm tr}[G_{\mu\nu}G^{\mu\nu}] + \bar{q}i\gamma^\mu D_\mu q, \tag{2.1.1}$$
$$G_{\mu\nu} = \partial_\mu A_\mu - \partial_\nu A_\mu - ig[A_\mu, A_\nu], \quad D_\mu = \partial_\mu - igA_\mu, \quad A_\mu = \sum_a T^a A^a_\mu,$$

where q is the quark field, $A^a_\mu (a = 1 \sim 8)$ are the gluon fields, $T^a = \lambda^a/2$ are the generators of the color SU(3) group with Gell-Mann matrices λ^a, and g is the gauge coupling constant. The quark field is represented as a three-component column vector in color space, with N_f components in flavor space.

It has been known that this theory is asymptotically free [26, 27], and it has been successful to describe high energy (short distance) phenomena of strong interaction through the perturbative calculation. On the other hand, it is formidable to apply QCD to the low energy phenomena, namely hadron physics, because of the color confinement and chiral symmetry breaking. A lot of approaches to study the hadron physics have been developed, and they have been fairly reproducing the observed phenomena. Through these phenomenological studies, we have been observing various evidences that QCD controls the dynamics of the strong interaction. Combining the direct comparison with high energy phenomena and

indirect evidences in low energy physics, it is now accepted as being beyond doubt that QCD is the theory of strong interaction. Therefore, the study of hadron physics at low energy is in some sense strange; although we know the correct theory of strong interaction, *i.e.* QCD, we can not apply it to the phenomena that we are interested in. This is in contrast to, for instance, the quantum electrodynamics (QED); we know that QED is the correct theory of the electromagnetic interaction, and it is applicable to calculate the cross section of Compton scattering. The aim of the study of hadron physics is to provide the understanding of the low energy dynamics of strong interaction in connection to QCD, as close as possible. To do that, we shall employ the effective field theory, guided by the symmetry principle of QCD.

2.2 Introduction to effective field theory

An effective field theory is a way to describe the low energy dynamics, using phenomenological Lagrangians restricted by symmetries of the underlying theory. Asymptotic fields in the effective Lagrangian can be different from those of the fundamental theory, when we integrate out the original degrees of freedom using the path integral formulation. Schematically, for the QCD case, this procedure can be expressed as

$$\exp\{iZ\} = \int \mathcal{D}q\mathcal{D}\bar{q}\mathcal{D}A_\mu \exp\left\{i\int d^4x \mathcal{L}_{\rm QCD}\right\} = \int \mathcal{D}U \exp\left\{i\int d^4x \mathcal{L}_{\rm eff}\right\},$$

where $\mathcal{L}_{\rm eff}$ is the Lagrangian of the effective theory with effective degrees of freedom U. Notice, however, that this procedure is only *schematic*, and no theory has been derived from QCD in the path integral method without introducing approximations. Instead, we follow the guiding principle introduced by Weinberg [2] to construct the effective Lagrangian;

> *If one writes down the most general possible Lagrangian, including all terms consistent with assumed symmetry principles, and then calculates matrix elements with this Lagrangian to any given order of perturbation theory, the result will simply be the most general possible S-matrix consistent with analyticity, perturbative unitarity, cluster decomposition and the assumed symmetry principles.*

This is a "theorem" which has not been proved so far. In practice, it works, as we can see, for instance, the success of the chiral perturbation theory, which was constructed following this principle. In $\mathcal{L}_{\rm eff}$, the effects from the original fields in the underlying theory are assumed to be included in the low energy constants of the effective Lagrangian, that are not determined by the symmetries.

In what follows, we construct the effective theory of QCD based on chiral symmetry. We also assume the trivial symmetries such as Lorentz invariance and CPT invariance, that the QCD Lagrangian (2.1.1) has. In principle, infinite number of terms are allowed by the symmetry. There are several ways to restrict the number of terms. One way is to make the theory renormalizable, and the other way is to introduce expansion parameters. The former corresponds to the concept of linear sigma model, while the latter will be used for the chiral perturbation theory, in the following.

2.3 Symmetries of QCD Lagrangian

In this section we consider the symmetries of QCD. First we review the chiral symmetry of N_f flavor QCD and its spontaneous breakdown. For massless quarks, the QCD Lagrangian (2.1.1) is invariant under a global transformation, which is called chiral symmetry. In real world, due to the non-perturbative vacuum, chiral symmetry is spontaneously broken, accompanied by the appearance of the Nambu-Goldstone (NG) bosons [28, 29, 30], such as pions. Because quarks have small but nonzero masses, chiral symmetry also breaks explicitly. Nevertheless, it is important to discuss the low energy hadron physics respecting chiral symmetry, because the explicit breaking effects are small, and we can neglect them at leading order and including their effects as perturbative corrections. Phenomenological successes of the low energy theorems and the current algebra also indicate the importance of the chiral symmetry in low energy hadron physics [1, 31].

2.3.1 Chiral symmetry

Historically, before the establishment of QCD, the notion of the chiral symmetry has been developed in current algebra [31, 32]. Being started with the Goldberger-Treiman relation [33], an idea of partially conserved axial current (PCAC) was introduced. PCAC was later understood by the spontaneous breaking of chiral symmetry, where pions were interpreted as the NG bosons of the broken generators. Considering the process with more than one pion, such as πN scatterings, commutation relations of the broken generators were determined, so that the broken symmetry group was specified as $\mathrm{SU}(2) \times \mathrm{SU}(2)$. One of the reasons that QCD had been accepted was that $\mathrm{SU}(2) \times \mathrm{SU}(2)$ could be understood by the results of small masses of u and d quarks.

In general,a field theory with massless fermions has a global symmetry. To see this for the case of QCD (2.1.1), it is useful to define the left-handed and right-handed quarks as

$$q_L = P_L q, \quad P_L = \frac{1}{2}(1 - \gamma_5),$$
$$q_R = P_R q, \quad P_R = \frac{1}{2}(1 + \gamma_5),$$

where the projection operators $P_{L,R}$ have the properties

$$P_{L,R}^2 = P_{L,R}, \quad P_L P_R = 0, \quad P_L + P_R = 1.$$

The last equation indicates that $q = q_L + q_R$. For the antiquark,

$$\bar{q}_L = (P_L q)^\dagger \gamma^0 = \bar{q} P_R, \quad \bar{q}_R = \bar{q} P_L.$$

Using left- and right-handed fields, the Lagrangian (2.1.1) can be expressed as

$$\mathcal{L}_{\mathrm{QCD}}^0 = -\frac{1}{2}\mathrm{tr}[G_{\mu\nu} G^{\mu\nu}] + \bar{q}_L i\gamma^\mu D_\mu q_L + \bar{q}_R i\gamma^\mu D_\mu q_R.$$

Here q_L and q_R are separated each other, and the Lagrangian is invariant under unitary transformation of quark fields. Hence the theory has a global symmetry $\mathrm{U}(N_f)_L \times \mathrm{U}(N_f)_R$.

Among this symmetry, $\mathrm{U}(1)_A$ is broken by axial anomaly by quantum correction [34], while $\mathrm{U}(1)_V$ holds trivially as the quark number conservation in strong interaction. Removing these U(1) subgroups, the global $\mathrm{SU}(N_f)_L \times \mathrm{SU}(N_f)_R$ remains, that we refer to as chiral symmetry of QCD. Under chiral transformations, the quark fields transform as

$$\begin{aligned} &q_L \to Lq_L, \quad L = e^{i\theta_L^a t^a} \in SU(N_f)_L \\ &q_R \to Rq_R, \quad R = e^{i\theta_R^a t^a} \in SU(N_f)_R \end{aligned} \quad (a = 1 \sim N_f^2 - 1),$$

where $\theta_{L,R}^a$ are arbitrary real parameters and t^a are the generators of $\mathrm{SU}(N_f)$. When we consider the group $G = \mathrm{SU}(N_f)_L \times \mathrm{SU}(N_f)_R$, it is convenient to write an element of G in two component form as

$$g = (R, L), \quad g_R = (R, 1), \quad g_L = (1, L),$$

where we follow the notation in Ref. [1]. Note that R is an element of $\mathrm{SU}(N_f)_R$, while g_R is an element of $G = \mathrm{SU}(N_f)_L \times \mathrm{SU}(N_f)_R$. Then we define generators of G as

$$t_R^a = (t^a, 0), \quad t_L^a = (0, t^a),$$

with t^a being the generators of $\mathrm{SU}(N_f)$. The commutation relations among t_L^a and t_R^a are given by

$$\begin{aligned} &[t_L^a, t_L^b] = if^{ab}{}_c t_L^c, \\ &[t_R^a, t_R^b] = if^{ab}{}_c t_R^c, \\ &[t_L^a, t_R^b] = 0, \end{aligned}$$

where $f^{ab}{}_c$ are the structure constants of $\mathrm{SU}(N_f)$.

2.3.2 Spontaneous chiral symmetry breaking

In the previous subsection, the chiral symmetry is manifested among the field operators in the Lagrangian (2.1.1). If an operator has a finite vacuum expectation value, which is not invariant under chiral transformations, then the symmetry is spontaneously broken. In the case of QCD, quark condensate $\bar{q}q = \bar{q}_R q_L + \bar{q}_L q_R$ has a finite vacuum expectation value v

$$\langle 0|\bar{q}_R q_L + \bar{q}_L q_R|0\rangle = v. \tag{2.3.1}$$

Under $g = (R, L) \in \mathrm{SU}(N_f)_L \times \mathrm{SU}(N_f)_R$, the expectation value transforms

$$\langle 0|\bar{q}_R q_L + \bar{q}_L q_R|0\rangle \xrightarrow{g} \langle 0|\bar{q}_R R^\dagger L q_L + \bar{q}_L L^\dagger R q_R|0\rangle,$$

which is not invariant, because the parameters $\theta_{L,R}^a$ in L and R are arbitrary.

In order to consider the transformation which makes the expectation value invariant, we define the generators t_V^a and t_A^a as

$$t_V^a \equiv t_R^a + t_L^a = (t^a, t^a), \quad t_A^a \equiv t_R^a - t_L^a = (t^a, -t^a). \tag{2.3.2}$$

It is clear that the $\{t_V^a, t_A^a\}$ is the basis of the same Lie algebra as $\{t_L^a, t_R^a\}$, both of which generate the chiral group G. From Eq. (2.3.2), it is clear that the commutation relations among t_V^a and t_A^a are given by

$$
\begin{aligned}
[t_V^a, t_V^b] &= i f^{ab}{}_c t_V^c, \\
[t_V^a, t_A^b] &= i f^{ab}{}_c t_A^c, \\
[t_A^a, t_A^b] &= i f^{ab}{}_c t_V^c.
\end{aligned}
$$

It is seen that t_V^a forms a closed algebra. In this case, the subspace of G generated by t_V^a, namely, $\{(e^{i\theta_V^a t^a}, e^{i\theta_V^a t^a})\} \subset G$ forms a group. Under the transformation in this subgroup, the condensate (2.3.1) is invariant, as we see

$$
\langle 0|\bar{q}_R q_L + \bar{q}_L q_R|0\rangle \to \langle 0|\bar{q}_R e^{-i\theta_V^a t^a} e^{i\theta_V^a t^a} q_L + \bar{q}_L e^{-i\theta_V^a t^a} e^{i\theta_V^a t^a} q_R|0\rangle = v.
$$

In this way we see that the $\mathrm{SU}(N_f)_L \times \mathrm{SU}(N_f)_R$ symmetry is broken to the subgroup $\mathrm{SU}(N_f)_V$. This is called spontaneous breaking of chiral symmetry, where the vacuum expectation value breaks the symmetry of the Lagrangian.

When the symmetry is spontaneously broken, Nambu-Goldstone theorem ensures that the spectrum of physical particles must contain one particle of zero mass and spin for each broken symmetry. These bosons are called the Nambu-Goldstone (NG) bosons. In the case of QCD with two flavors (u and d), the NG bosons are three pions, while in the case of QCD with three flavors (u, d and s), pions, kaons, and eta are generated as the NG bosons.

2.3.3 Flavor symmetry and explicit symmetry breaking

After spontaneous chiral symmetry breaking, only vector symmetry $\mathrm{SU}(N_f)_V$ remains, which is called flavor symmetry. The origin of the flavor symmetry is much older than the chiral symmetry, as the isospin SU(2) symmetry was the symmetry of proton and neutron in nuclear physics. The flavor SU(3) was introduced as an extension of the isospin SU(2) in order to classify the particles [35, 36, 37]. A great success was the prediction of the Ω baryon and the η meson, which were subsequently observed in experiments.

In reality, the quarks have masses, and QCD Lagrangian can be written as

$$
\mathcal{L}_{\mathrm{QCD}}^{\mathrm{mass}} = \mathcal{L}_{\mathrm{QCD}}^{0} - \bar{q}\boldsymbol{m}q, \quad \boldsymbol{m} = \begin{pmatrix} m_u & & \\ & m_d & \\ & & m_s \end{pmatrix}, \tag{2.3.3}
$$

where the mass matrix is defined in flavor space, and we neglect the heavy flavor quarks, c, b, and t. The mass term breaks the chiral symmetry explicitly. However, note that the flavor symmetry $\mathrm{SU}(3)_V$ holds when $m_u = m_d = m_s$. In practice, this symmetry is broken. The masses of the u and d quarks are as light as several MeV, while the mass of the s quark is about 150 MeV. This indicates that the flavor symmetry breaking is important for the SU(3) case.

The explicit chiral symmetry breaking gives the small masses for the NG bosons, and flavor symmetry breaking induces the mass difference among hadrons. These effects will be incorporated in the chiral Lagrangian, introducing the mass term as in the same way with QCD.

2.4 Chiral perturbation theory

Chiral perturbation theory is based on the nonlinear realization of chiral symmetry [32, 38, 39, 40]. The nonlinear realization provides a representation for a system with a global symmetry G—in the present case, chiral symmetry $\mathrm{SU}(3)_L \times \mathrm{SU}(3)_R$—which breaks spontaneously down into a subgroup $H \subset G$—in the present case, $\mathrm{SU}(3)_V$. It is important that spontaneous symmetry breaking of the system is already assumed from the beginning. In other words, symmetry breaking is incorporated at the Lagrangian level.

2.4.1 Meson system

Following the constructions in Ref. [38, 39], we write the octet pseudoscalar mesons in the SU(3) matrix form as [3, 41, 42]

$$\Phi = \begin{pmatrix} \frac{1}{\sqrt{2}}\pi^0 + \frac{1}{\sqrt{6}}\eta & \pi^+ & K^+ \\ \pi^- & -\frac{1}{\sqrt{2}}\pi^0 + \frac{1}{\sqrt{6}}\eta & K^0 \\ K^- & \bar{K}^0 & -\frac{2}{\sqrt{6}}\eta \end{pmatrix},$$

and the chiral fields U and ξ are defined by

$$U(\Phi) = \exp\left\{\frac{i\sqrt{2}\Phi}{f}\right\}, \quad \xi(\Phi) = \exp\left\{\frac{i\Phi}{\sqrt{2}f}\right\}, \quad U(\Phi) = \xi^2(\Phi),$$

where f is a quantity of mass dimension, and will be identified with the meson decay constant. The transformation lows of these fields under chiral transformation $g \in \mathrm{SU}(3)_L \times \mathrm{SU}(3)_R$ are given by [38, 39]

$$U \xrightarrow{g} RUL^\dagger, \quad U^\dagger \xrightarrow{g} LU^\dagger R^\dagger,$$
$$\xi \xrightarrow{g} R\xi h^\dagger = h\xi L^\dagger, \quad \xi^\dagger \xrightarrow{g} L\xi^\dagger h^\dagger = h\xi^\dagger R^\dagger,$$

where $L \in \mathrm{SU}(3)_L$, $R \in \mathrm{SU}(3)_R$, and $h(\Phi, g_0) \in \mathrm{SU}(3)_V$, all of which are determined according to g.

In order to construct an effective field theory, we organize the most general Lagrangians using these fields, following the principle presented in section 2.2. For the systematic expansion, we define a chiral counting rule, as introduced in Refs. [3, 41, 42]. Since the octet mesons are the NG bosons, their masses are zero in the chiral limit, and small even if the explicit breaking effect is included. This means that if the spatial momentum of a meson $\boldsymbol{p}$ is small, we can also regard the four momentum p^μ as small.

In this way, possible structures are classified in powers of momenta, which is expressed by derivatives acting on meson fields in the effective Lagrangian. In a low energy region, where the momentum of each particle is small, lower order terms should be dominant and we can neglect the higher order terms. Chiral Lagrangian should be invariant under chiral transformation $\mathrm{SU}(3)_L \times \mathrm{SU}(3)_R$, Lorentz transformation, charge conjugation, parity, and time reversal. Due to the Lorentz invariance, the Lagrangian contains even number of derivatives

$$\mathcal{L}_{\text{eff}}(U) = \sum_n \mathcal{L}^M_{2n}(U), \tag{2.4.1}$$

where $2n$ denotes the number of derivatives. Defining U as a quantity of order $\mathcal{O}(1)$, a term with n derivative is counted as $\mathcal{O}(p^n)$. In Eq. (2.4.1), the terms with $n = 0$ provide unity, because of the unitarity of the field U. Therefore the lowest order Lagrangian consists of two derivatives of U field and is uniquely given as

$$\mathcal{L}_2^M = \frac{f^2}{4}\mathrm{Tr}(\partial_\mu U^\dagger \partial^\mu U), \tag{2.4.2}$$

which is of order $\mathcal{O}(p^2)$. In the same way, we can construct a series of the effective Lagrangians $\mathcal{L}_{2n}^M(U)$ up to desired chiral order. For the low energy problem, the leading order term (2.4.2) becomes dominant, thanks to the chiral counting rule.

In general, the factors in front of the effective Lagrangian are called as the low energy constants, which can not be determined by the symmetry itself. However, the constant for the leading order term (2.4.2) has been determined by the normalization of the kinetic term. Since the Φ field is included in the exponential, by expanding the U field in Eq. (2.4.2), we obtain the terms including two Φ fields, four Φ fields, and so on:

$$\mathcal{L}_2^M = \frac{1}{2}\mathrm{Tr}(\partial_\mu \Phi \partial^\mu \Phi) + \frac{1}{12f^2}\mathrm{Tr}\left((\Phi\partial_\mu\Phi - \partial_\mu\Phi\Phi)^2\right) + \cdots .$$

The first term with two Φ fields represents the kinetic term of mesons, while the second term is responsible for the meson four-point interaction. This means that we can relate the strength of the meson-meson interaction to the normalization of the kinetic term. This is an advantage of the chiral Lagrangian, that is, the relation between the terms with different number of mesons is determined by the symmetry. Indeed, the factor $f^2/4$ in Eq. (2.4.2) has been chosen such that the kinetic term appears with correct normalization, which determines the strength of the meson-meson interaction.

Another virtue of the chiral Lagrangian is the renormalizability at given chiral order. Apparently, since the lowest order Lagrangian contains terms with any number of meson field, the theory is non-renormalizable. However, we can define the chiral counting rule for the amplitude. It is shown that the divergence that arises from the loop diagram can be tamed by the counter term in the higher order Lagrangians, namely, the renormalization can be performed order by order.

Since we are considering the flavor SU(3) case, it is important to introduce the SU(3) breaking term as in Eq. (2.3.3). This procedure can be interpreted as the introduction of scalar external field into the Lagrangian (2.1.1), which can be generalized for arbitrary external fields as

$$\mathcal{L}_{\mathrm{QCD}}^{\mathrm{ext}} = \mathcal{L}_{\mathrm{QCD}}^0 + \bar{q}\gamma^\mu(v_\mu + \gamma^5 a_\mu)q - \bar{q}(s - i\gamma_5 p)q, \tag{2.4.3}$$

where the external fields v_μ, a_μ, s and p are vector current, axial vector current, scalar and pseudo scalar field, respectively. Using q_L and q_R, this can be written as

$$\mathcal{L}_{\mathrm{QCD}}^{\mathrm{ext}} = \mathcal{L}_{\mathrm{QCD}}^0 + \bar{q}_L\gamma^\mu(v_\mu - a_\mu)q_L + \bar{q}_R\gamma^\mu(v_\mu + a_\mu)q_R - \bar{q}_R(s + ip)q_L - \bar{q}_L(s - ip)q_R.$$

Defining l_μ and r_μ as

$$l_\mu \equiv v_\mu - a_\mu, \quad r_\mu \equiv v_\mu + a_\mu, \tag{2.4.4}$$

it is easy to derive the transformation lows for the external fields:

$$\begin{aligned} &s+ip \xrightarrow{g} R(s+ip)L^\dagger, \quad s-ip \xrightarrow{g} L(s-ip)R^\dagger, \\ &l_\mu \xrightarrow{g} Ll_\mu L^\dagger + iL\partial_\mu L^\dagger, \\ &r_\mu \xrightarrow{g} Rr_\mu R^\dagger + iR\partial_\mu R^\dagger. \end{aligned} \tag{2.4.5}$$

In this case, the Lagrangian (2.4.3) is invariant under $\mathrm{SU}(3)_L \times \mathrm{SU}(3)_R$. Note that the transformation lows are local because they contain derivatives. We then incorporate the external fields and their transformation laws with the effective chiral Lagrangian (2.4.1). As a consequence of the local transformation, derivatives of the field $U(\Phi)$ should be replaced by covariant derivatives, which are given by [3, 41, 42]

$$D_\mu U = \partial_\mu U - ir_\mu U + iUl_\mu, \quad D_\mu U^\dagger = \partial_\mu U^\dagger + iU^\dagger r_\mu - il_\mu U^\dagger.$$

For convenience, we define χ and field strength tensors as

$$\begin{aligned} &\chi = 2B_0(s+ip), \quad \chi^\dagger = 2B_0(s-ip), \\ &L^{\mu\nu} = \partial^\mu l^\nu - \partial^\nu l^\mu - i[l^\mu, l^\nu], \quad R^{\mu\nu} = \partial^\mu r^\nu - \partial^\nu r^\mu - i[r^\mu, r^\nu] \end{aligned} \tag{2.4.6}$$

with a constant B_0, which will be determined later. Their transformation lows are given by

$$\chi \xrightarrow{g} R\chi L^\dagger, \quad \chi^\dagger \xrightarrow{g} L\chi^\dagger R^\dagger, \quad L^{\mu\nu} \xrightarrow{g} LL^{\mu\nu}L^\dagger, \quad R^{\mu\nu} \xrightarrow{g} RR^{\mu\nu}R^\dagger.$$

Using these external fields, we can introduce SU(3) breaking effects and photon couplings. For example, in order to include the quark mass term, we choose

$$s = \boldsymbol{m}, \quad \boldsymbol{m} = \begin{pmatrix} m_u & & \\ & m_d & \\ & & m_s \end{pmatrix}. \tag{2.4.7}$$

The photon field A_μ can be introduced as

$$l_\mu = r_\mu = eQA_\mu, \quad Q = \frac{1}{3}\begin{pmatrix} 2 & & \\ & -1 & \\ & & -1 \end{pmatrix}, \tag{2.4.8}$$

where e is the unit electric charge. Substituting this current into Eq. (2.4.3), we see that the kinetic term is properly gauged as $\partial_\mu \to \partial_\mu - ieA_\mu$. It is worth noting that once specific directions in flavor space are selected in this way, chiral symmetry is explicitly broken. Indeed, the expressions (2.4.7) and (2.4.8) do not satisfy the transformation laws (2.4.5). However, when we construct the effective Lagrangian invariant under the transformation laws (2.4.5), it is ensured that the way we break the symmetry is exactly the same as that in the underlying QCD Lagrangian (2.4.3).

The chiral order of the external fields is assigned as

$$U, \xi : \mathcal{O}(1), \quad a_\mu, v_\mu, l_\mu, r_\mu, : \mathcal{O}(p), \quad s, p, \chi : \mathcal{O}(p^2). \tag{2.4.9}$$

Let us remark that there is no *a priori* reason to assign the chiral order of the external fields in this way. There are some indirect reasons. For instance, in order to construct Lorentz vectors from the combination of meson field Φ, a derivative is necessary, which introduces $\mathcal{O}(p)$ in the currents v_μ and a_μ. The scalar quantity s is identified as the quark mass term $\boldsymbol{m}$ as in Eq. (2.4.7), and the Gell-Mann–Oakes–Renner (GMOR) relation [43] requires that this quantity should be $\mathcal{O}(p^2)$, as we will see below.

Once the counting rule (2.4.9) is accepted, it is straightforward to write down the effective Lagrangian at leading order as

$$\mathcal{L}_2^M = \frac{f^2}{4}\mathrm{Tr}(D_\mu U^\dagger D^\mu U + U^\dagger\chi + \chi^\dagger U). \tag{2.4.10}$$

In this Lagrangian, there are two low energy constants f and B_0. By taking the derivatives with respect to the external field for the classical action $S_2^M = \int d^4x \mathcal{L}_2^M$, we can read the physical meanings of the low energy constants.

$$\frac{\delta S_2^M}{\delta a_\mu} = -\sqrt{2} f D^\mu \Phi + \cdots,$$
$$\frac{\delta S_2^M}{\delta s} = -f^2 B_0 + \cdots.$$

Taking the matrix elements, we can identify f as the pion decay constant f_π and B_0 is related with quark condensate $\langle\, 0\,|\bar{q}q|\,0\,\rangle = -f^2 B_0$. Expanding the chiral field in Eq. (2.4.10), we obtain the kinetic terms and mass terms for mesons:

$$\mathcal{L}_2^M = \frac{1}{2}\mathrm{Tr}(\partial_\mu\Phi\partial^\mu\Phi) - B_0\mathrm{Tr}\left(\boldsymbol{m}\Phi^2\right) + \cdots.$$

The second term appears when we include the explicit symmetry breaking effect (2.4.7). From this term, we can read the meson masses as

$$\begin{aligned} M_{\pi^\pm}^2 =& 2\hat{m}B_0, \quad M_{\pi^0}^2 = 2\hat{m}B_0 - \epsilon + \mathcal{O}(\epsilon^2), \quad M_\eta^2 = \frac{3}{2}(\hat{m}+2m_s)B_0 + \epsilon + \mathcal{O}(\epsilon^2), \\ M_{K^\pm}^2 =& (m_u+m_s)B_0, \quad M_{K^0}^2 = (m_d+m_s)B_0, \end{aligned}$$

where $\hat{m} = (m_u+m_d)/2$ and $\epsilon = B_0(m_u-m_d)^2/4(m_s-\hat{m})$, which originate in the small mixing between π^0 and η. Ignoring the isospin breaking effect ($m_u = m_d = \hat{m}$) and higher order corrections, the meson masses are given by

$$M_\pi^2 = 2\hat{m}B_0, \quad M_K^2 = (\hat{m}+m_s)B_0, \quad M_\eta^2 = \frac{3}{2}(\hat{m}+2m_s)B_0. \tag{2.4.11}$$

From these equations, we obtain the Gell-Mann–Okubo mass relation for mesons

$$3M_\eta^2 = 4M_K^2 - M_\pi^2.$$

Eq. (2.4.11) also suggests that

$$\chi = 2B_0\boldsymbol{m} = \begin{pmatrix} m_\pi^2 & & \\ & m_\pi^2 & \\ & & 2m_K^2 - m_\pi^2 \end{pmatrix}.$$

For completeness, we also present the $\mathcal{O}(p^4)$ Lagrangian in Appendix B.1, together with the summary of definition of fields and their transformation lows.

2.4.2 Meson-baryon system

In this subsection, we introduce SU(3) octet baryon fields in the chiral Lagrangian [44]. From the viewpoint of the nonlinear realization, it is possible to introduce the matter fields, which transforms under $h \in \mathrm{SU}(3)_V$ [38, 39]. Let us introduce the octet baryon fields, as the adjoint representation of SU(3),

$$B \equiv \sum_{a=1}^{8} \lambda^a B^a = \begin{pmatrix} \frac{1}{\sqrt{2}}\Sigma^0 + \frac{1}{\sqrt{6}}\Lambda & \Sigma^+ & p \\ \Sigma^- & -\frac{1}{\sqrt{2}}\Sigma^0 + \frac{1}{\sqrt{6}}\Lambda & n \\ \Xi^- & \Xi^0 & -\frac{2}{\sqrt{6}}\Lambda \end{pmatrix}, \quad \bar{B} = B^\dagger \gamma^0.$$

Because B and $\bar{B}$ are adjoint representations, they transform under $\mathrm{SU}(3)_L \times \mathrm{SU}(3)_R$ as

$$B \xrightarrow{g} hBh^\dagger, \quad \bar{B} \xrightarrow{g} (hBh^\dagger)^\dagger \gamma^0 = h\bar{B}h^\dagger. \tag{2.4.12}$$

When we introduce the baryon fields, a problem arises concerning the chiral counting rule. As a consequence of the transformation law (2.4.12), a chiral invariant mass term $M_0 \mathrm{Tr}(\bar{B}B)$ can exist, even if the quark mass is absent:

$$M_0 \mathrm{Tr}(\bar{B}B) \xrightarrow{g} M_0 \mathrm{Tr}(h\bar{B}h^\dagger hBh^\dagger) = M_0 \mathrm{Tr}(\bar{B}B).$$

The presence of the mass term in baryon sector can be understood by the spontaneous breaking of chiral symmetry, but this is an important difference from the pseudoscalar meson case. In the pseudoscalar meson sector, we define chiral counting rule using the fact that the meson mass is zero or very small. However, we see that in the baryon sector a large mass can exist, of the order of 1 GeV, in practice. This means that the energy of the baryon $p^0 = \sqrt{M_0^2 + \boldsymbol{p}^2}$ is not small even if $|\boldsymbol{p}|$ is small. Hence we cannot treat the four-momentum of the baryons as a small quantity any more. This fact also causes the complicated counting for loops. In the meson sector, there is a one-to-one correspondence between the diverging amplitude and the counter terms in Lagrangian. However, in the baryon sector, the baryon propagator gives a contribution of the baryon mass instead of typical low momenta, since the baryon mass is not small.

Actually there is a method which allows us to perform power counting in a consistent way [44]. In that case the counting rule becomes more complicated and many terms appear even in the next-to-leading order. Another way to avoid this difficulty is to adopt the heavy baryon chiral perturbation theory [45, 46, 47], taking the limit $p/M_0 \ll 1$. In this limit, the number of terms is suppressed and counting rule becomes much simpler. Here we however take the approaches in Ref. [44] for the counting rule for baryons. In practice, two approaches give the same terms for the leading order, that we are going to use.

In order to introduce the coupling with external fields with matter fields, it is convenient to use the quantities, which transforms

$$O \xrightarrow{g} hOh^\dagger, \tag{2.4.13}$$

because of the transformation lows of B and $\bar{B}$ (2.4.12). Using χ field, we construct scalar (σ) and pseudoscalar (ρ) quantities defined as

$$\sigma \equiv \xi\chi^\dagger\xi + \xi^\dagger\chi\xi^\dagger, \quad \rho \equiv \xi\chi^\dagger\xi - \xi^\dagger\chi\xi^\dagger.$$

Vector (V_μ) and axial vector (A_μ) currents are given by

$$V_\mu = -\frac{i}{2}(\xi^\dagger\partial_\mu\xi + \xi\partial_\mu\xi^\dagger) - \frac{1}{2}(\xi^\dagger r_\mu\xi + \xi l_\mu\xi^\dagger),$$
$$A_\mu = -\frac{i}{2}(\xi^\dagger\partial_\mu\xi - \xi\partial_\mu\xi^\dagger) - \frac{1}{2}(\xi^\dagger r_\mu\xi - \xi l_\mu\xi^\dagger).$$

Using the field strength tensors (2.4.6), we define

$$F_R^{\mu\nu} = \xi^\dagger R^{\mu\nu}\xi, \quad F_L^{\mu\nu} = \xi L^{\mu\nu}\xi^\dagger.$$

From the chiral transformation lows of ξ fields, it is straightforward to show that σ, ρ, A_μ, $F_R^{\mu\nu}$, and $F_L^{\mu\nu}$ satisfy the transformation (2.4.13). The vector current transforms as

$$V_\mu \xrightarrow{g} hV_\mu h^\dagger - ih\partial_\mu h^\dagger.$$

Thanks to this properties, covariant derivatives can be defined for the octet matter fields as

$$\mathcal{D}_\mu B = \partial_\mu B + i[V_\mu, B], \tag{2.4.14}$$

which transform as

$$\mathcal{D}_\mu B \xrightarrow{g} h\mathcal{D}_\mu B h^\dagger.$$

According to the detailed discussion of chiral power counting for the baryons in Ref. [44], the quantities we defined above are counted as

$$\sigma, \rho : \mathcal{O}(p^2), \quad A_\mu, V_\mu : \mathcal{O}(p), \quad F_R^{\mu\nu}, F_L^{\mu\nu} : \mathcal{O}(p^2),$$

and baryon fields are

$$B, \bar{B} : \mathcal{O}(1), \quad \mathcal{D}_\mu B : \mathcal{O}(1), \quad i\gamma^\mu\mathcal{D}_\mu B - M_0 B : \mathcal{O}(p).$$

With these counting rules, we can construct the most general effective Lagrangian as in the meson sector. Couplings between mesons and baryons are introduced in the expansion of the ξ field, which is governed by the chiral symmetry.

In baryon case, an effective Lagrangian can contain the terms of order odd number of momentum,

$$\mathcal{L}_{\text{eff}}(B, \Phi) = \sum_n \mathcal{L}_n^B(B, \Phi).$$

Considering the Lorentz structure of the currents, the most general Lagrangian with baryons in the lowest order of the chiral expansion is given by

$$\mathcal{L}_1^B = \mathrm{Tr}\Big(\bar{B}(i\not{\mathcal{D}} - M_0)B - D(\bar{B}\gamma^\mu\gamma_5\{A_\mu, B\}) - F(\bar{B}\gamma^\mu\gamma_5[A_\mu, B])\Big),$$

where D and F are low energy constants and M_0 denotes a common mass of the octet baryons. Here we follow the notation in Ref. [48].

In next-to-leading order $\mathcal{O}(p^2)$, we have twenty one terms in the most general effective Lagrangian [44]. Among them, here we show the terms that we will use in later chapters. Flavor SU(3) breaking terms are given by

$$\mathcal{L}^B_{SB} = b_0 \mathrm{Tr}(\bar{B}B)\mathrm{Tr}(\sigma) + b_d \mathrm{Tr}\big(\bar{B}\{\sigma, B\}\big) + b_f \mathrm{Tr}\big(\bar{B}[\sigma, B]\big), \tag{2.4.15}$$

and photon coupling terms by

$$\mathcal{L}^B_{(\gamma)} = \frac{b_6^D}{8M_p}\mathrm{Tr}\big(\bar{B}\sigma^{\mu\nu}\{F^+_{\mu\nu}, B\}\big) + \frac{b_6^F}{8M_p}\mathrm{Tr}\big(\bar{B}\sigma^{\mu\nu}[F^+_{\mu\nu}, B]\big), \tag{2.4.16}$$

where M_p is the mass of proton and we have defined

$$F^{\mu\nu}_+ = F^{\mu\nu}_L + F^{\mu\nu}_R, \quad \sigma^{\mu\nu} = \frac{i}{2}[\gamma^\mu, \gamma^\nu].$$

In practical calculations, we will use slightly modified forms from Eqs. (2.4.15) and (2.4.16). Details on the convention of chiral Lagrangian are summarized in Appendix B.1.

Chapter 3

Overview of pentaquarks

It has been three years since the evidence for the Θ^+ resonance was reported [16]. Since then, the studies of exotic baryons have been continuously excited by new results from experiments and new ideas from theory side. There are more than 500 papers on the web concerning the exotic states so far.

In this chapter, the studies devoted to the exotic baryons are reviewed. These studies are usually based on the models and approaches which have been developed for the description of hadrons and applied to the studies of their properties. Therefore, reviewing the studies on exotic baryons will provide a guidance for various techniques in hadron physics. On the other hand, through the intensive studies of five-quark states, we have encountered several problems and questions which have not been appeared in the case of three-quark baryons. These lessons urge us to revisit the studies for the non-exotic states and basis of our model constructions.

Because there are already many review articles available, we list some of them in the following. Ref. [49] gives a detail and comprehensive review of existing studies up to the time of publication. It also surveys the old searches of Z^* resonances. A review by the one of the authors of the prediction of the Θ^+ can be found in Ref. [50], where the basis of the chiral soliton models and connection to QCD were discussed. A discussion on constituent quark models can be found in Ref. [51]. Ref. [52] is a review of pentaquarks and various related topics, emphasizing the diquark correlation in hadrons. Summary of experimental status can be found in Ref. [53].

3.1 Researches before the first evidence

Before the first experimental evidence for the Θ^+ was announced in Ref. [16], there were several studies of possible exotic states in quark models and chiral soliton models, as well as the experimental searches for them. In this section, we summarize the researches which were performed before the first evidence. One may also refer to recent review articles [49, 54, 55].

Experimental searches for $S = +1$ states (called Z^* resonances at that time) were performed in K^+ beam experiments. Relevant data and references are summarized in the KN phase shift analyses in Refs. [56, 57]. In these studies, the authors could find some "resonance

Table 3.1: Summary of the Z^* search in Ref. [57]. Masses and widths are extracted from the positions of poles found in the partial wave analysis of the KN scattering.

Amplitude (J^P)	Mass [MeV]	Width [MeV]
D_{03} $(3/2^-)$	1788	340
P_{13} $(3/2^+)$	1811	236
P_{01} $(1/2^+)$	1831	190
D_{15} $(5/2^+)$	2074	506

like structures", which had large widths, but the phase motions were not very convincing. The pole positions found in the latest analysis [57] are summarized in Table 3.1. Note, however, that in these old searches in KN scattering, data of the energy region around 1540 MeV were rather sparse, and there was inconsistency between different measurements at the same energies. These may be caused by the difficulty of producing the low energy kaon beam in experiments [53]. The experimental Ξ^* searches including exotic channels were summarized in Ref. [58], where no prominent structure has been observed. Motivated by the quark model prediction, an experimental search for heavy pentaquark $uuds\bar{c}$ was performed in $\phi\pi p$ [59] and $K^{*0}K^-p$ [60] decay modes, but the results were negative.

Theoretical studies for the exotic baryons have been started in the scattering theory, even before the establishment of QCD. The existence of a baryon with exotic flavor quantum numbers was first argued in the context of a general assumption of the duality of Regge trajectory and s-channel resonance contributions [61]. The existence of baryon antidecuplet was discussed by analyzing the KN scattering data in 60's [62], where the Z^* candidate was studied in connection with corresponding N^* partner, with $J^P = 1/2^+$. Flavor SU(3) selection rules such as $N_{\overline{\mathbf{10}}} \nrightarrow \pi\Delta$ were already mentioned there.

Explicit five-quark states were studied within the constituent quark models [63, 64, 65], although the existence of such states was already "mentioned" by Gell-Mann much earlier [66]. In the models of Refs. [63, 64, 65], negative parity pentaquarks were considered, since all quarks were in s orbit, and therefore, naively expected to be the lightest. Non-triviality of the color configuration in $qqqq\bar{q}$ system was pointed out in Ref. [64], together with the possibility of having a narrow width into meson-baryon channel due to the color configurations. In Ref. [65], a systematic calculation for the pentaquarks and seven-quark states $qqqqq\bar{q}\bar{q}$ was performed, assigning the known negative parity resonances as these multi-quark states in the MIT bag model.

In Refs. [67, 68] pentaquark states including one heavy quark were studied based on quark models with color-magnetic interaction. In these studies, $uuds\bar{Q}$ states with $Q = c$ or b, were found to be stable against the strong decay. Subsequent studies and experimental efforts [59, 60] were summarized in Ref. [69].

The heavy pentaquarks were also studied in the constituent quark model with Goldstone boson exchange interaction [70]. In this model, ground state was found to be positive parity with one quark in p state, in contrast to the previous studies with one gluon exchange model. Non-strange (but heavy) pentaquarks like $uudd\bar{c}$ were predicted to be stable, while the states with strange quarks $uuds\bar{c}$ were unbound. The reversal of the level ordering of $(0s)^5$ states

and states with one orbital excitation was observed for the light quark sector as well, when the Goldstone boson exchange was used as the hyperfine interaction [71]. This observation was reconsidered again in recent studies.

In the chiral soliton models, the appearance of the $\overline{\mathbf{10}}$ (and $\mathbf{27}$) was sometimes mentioned soon after the generalization of the model to the SU(3) sector [72, 73], but the exotic states were not studied in detail, probably because of the lack of experimental evidences and very the exotic nature of the states. In Ref. [74], meson-baryon scattering was studied based on the Skyrmion model, including the KN scattering. Some structures were observed in the KN amplitude, being consistent with the experimental observation, but no prominent state was found.

Explicit calculation of the exotic state in the chiral soliton models was performed in Ref. [75], which was not published at that time and the essential argument can be found in Ref. [76]. In this work, the mass of the baryon antidecuplet was estimated in the Skyrme model, providing the light value of 1530 MeV for the $S = +1$ particle. More striking result was obtained by Diakonov *et al.* [77], namely the narrow width of $\Gamma < 15$ MeV and a light mass of 1540 MeV. The prediction of the light and narrow state partly motivated the recent experimental searches for the Θ^+. We will discuss these predictions in section 3.5.

Heavy pentaquarks were also studied in the bound state approach of the Skyrmion [78], predicting several stable states against strong decay. In the quark language, the states corresponded to $uudd\bar{Q}$, which were not accompanied by the strange quark in contrast to the states predicted in the quark models with one gluon exchange [67, 68].

Within the chiral soliton model, the effect of the collective radial excitations was studied in addition to the flavor rotation mode of rigid rotor quantization [79, 80]. Coupling between two modes was deduced by flavor symmetry breaking. In this approach, several radial excitations of the ground states were predicted. For the Θ^+, state mixing with higher dimensional representations and radially excited states was found to be important, and the mass and width of the lowest state were obtained as 1580 MeV and 100 MeV, respectively.

Based on the model predictions of mass and width of the $S = +1$ state, several production reactions were proposed in order to detect it experimentally. In Ref. [81], the $pp \to n\Sigma^+K^+$ reaction was studied. The possibility to observe an $S = +1$ baryon as predicted in the chiral soliton model [77] was demonstrated in this reaction close to the production threshold. Electroproduction of K^- off proton target was proposed in Ref. [82].

3.2 Experiments

In this section, we summarize the current status of the experiments. The evidences for the $\Theta^+(uudd\bar{s})$ state are shown first, followed by the studies imposing the upper limit of the decay width based on the old KN scattering data. We then mention the status of searches for other pentaquark candidates, $\Xi^{--}(ddss\bar{u})$, $\Theta_c(uudd\bar{c})$, and $\Theta^{++}(uuud\bar{s})$. The negative results for the pentaquarks are also reviewed, with the discussions trying to explain the positive/negative results by theoretical speculations. For an review of this subject, one may refer to Ref. [53].

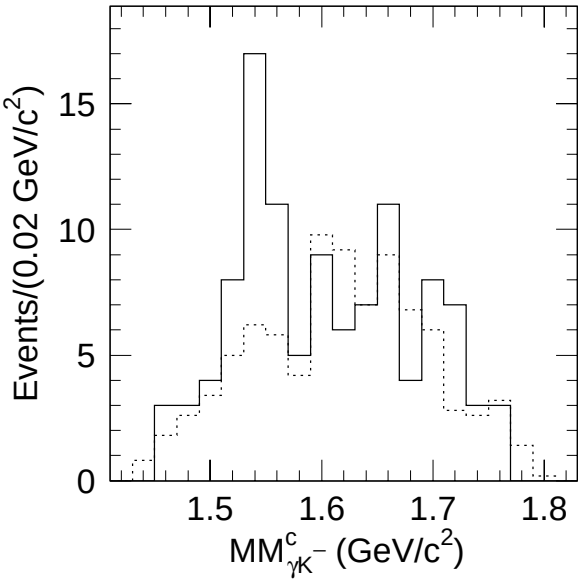

Figure 3.1: The result by LEPS collaboration taken from Ref. [16]. Solid histogram shows the fermi motion corrected missing mass spectrum $MM^c_{\gamma K^-}$, explained in the text. Dotted histogram represents the normalized spectrum for events from LH_2 target.

3.2.1 Evidences for the $\Theta(uudd\bar{s})$ state

Here the experimental evidences for the Θ^+ state are reviewed. Searches for the possible Θ^{++} state will be given later. As a summary of the positive results, the reaction, obtained mass, and width for each experiment are shown in Table 3.2.

The first experimental evidence for the Θ^+ was reported by LEPS collaboration [16]. The reaction $\gamma n \to K^+K^-n$ was carried out at SPring-8 on ^{12}C target. Events for the $\phi(1020)$ production in K^+K^- system were removed, as they were the background processes. Since the target neutron was bound in ^{12}C, Fermi motion of the initial neutron should be corrected for the accurate missing mass spectrum. Using the correlation between the missing mass of K^+K^- system $MM_{\gamma K^+K^-}$ and the $K^\pm$ missing mass $MM_{\gamma K^\pm}$, the Fermi motion corrected missing mass $MM^c_{\gamma K^\pm}$ was obtained as

$$MM^c_{\gamma K^\pm} = MM_{\gamma K^\pm} - MM_{\gamma K^+K^-} + M_N,$$

with M_N being the nucleon mass. In the $MM^c_{\gamma K^\pm}$ spectrum, a sharp peak was observed at 1540 ± 10 MeV as shown in Fig. 3.1. The width of the resonance was estimated to be smaller than 25 MeV, being consistent with the experimental resolution. Notice that the LEPS detector covers forward angle and acceptance is symmetric for positive and negative particles. The result was reported first at PANIC02 conference [15], and also given in Refs. [83, 84, 85]. New preliminary results on deuteron target from LEPS can be found in Refs. [86, 87, 88].

DIANA collaboration studied the K^+Xe collisions in Xenon bubble chamber [89]. A peak of K^0p invariant mass spectrum was observed in $K^+\mathrm{Xe} \to K^0pX$ reaction, where K^0 was detected *via* K^0_s decays into $\pi^+\pi^-$. Background shape was estimated by mixed-event technique. In order to make the signal clean, they applied two event selections: $\theta_p < 100^\circ$ and

$\theta_{K^0} < 100^\circ$ with respect to beam direction, and $\cos\Phi_{pK} < 0$ for the azimuthal angle between p and K^0 in Laboratory frame. These event cuts reduced the K^0p rescattering, and signal became more prominent with the cuts. Validity of these cuts were verified theoretically by meson-exchange model calculation [90]. The mass and the width of the resonance were reported as $M = 1539 \pm 2$ MeV and $\Gamma < 9$ MeV.

An experiment on deuteron target was reported by CLAS collaboration [91]. which was an exclusive reaction $\gamma d \to K^+K^-pn$ with all the charged particles being detected, so that the Fermi motion correction of the initial nucleon was not necessary. After applying several cuts, the nK^+ invariant mass spectrum showed a peak at 1542 ± 5 MeV, with a width of 21 MeV, consistent with the instrumental resolution. The result was also reported in Refs. [92, 93, 94, 95]. However, new result with high statistics by the same collaboration [96] was in contradiction to the result in Ref. [91], finding no peak.

In Ref. [97], SAPHIR collaboration studied the $\gamma p \to \bar{K}^0K^+(n)$ reaction, where $\bar{K}^0$ was detected as $K^0_s \to \pi^+\pi^-$ and the neutron momentum was reconstructed from kinematics. This is the simplest reaction for the Θ^+ production, free from the Fermi motion of initial state and complicated kinematical mechanism. A peak for the Θ^+ was found in the invariant mass spectrum of nK^+ system at 1540 ± 6 MeV. However, the same reaction was tested by CLAS collaboration with high statistics [98], which found no structure for the Θ^+.

Ref. [99] reported the evidence in neutrino interactions. They combined data of neutrino and antineutrino collisions with hydrogen, deuterium and neon in bubble chambers. In an inclusive experiment of this kind, where a signal is searched for in the K^0_sp spectrum, the strangeness of the final state can not be tagged, and both $S = +1$ and $S = -1$ particles can contribute, namely, Θ^+ and Σ^{*+}. Background shape was estimated by the events of the same final states randomly, which were normalized at the non-resonant region $m(K^0_sp) > 2$ GeV. A narrow enhancement was observed at 1533 ± 5 MeV, whose width was consistent with experimental resolution, estimated as < 20 MeV. A broad excess was also found in $1650 < m(K^0_sp) < 1850$ MeV, which was interpreted as the contribution from Σ^* resonances. In Ref. [100], the result of further analysis was reported. The state observed above was still there, and its mass and width were given by $M = 1532.2 \pm 1.3$ MeV and $\Gamma < 12$ MeV.

The reaction $\gamma p \to \pi^+K^-K^+n$ was studied by CLAS collaboration [101]. This is considered as the one of the best positive results [53], since the reaction is exclusive and the significance of the peak is above 7σ. First they excluded the ϕ production in K^+K^- channel, removing the invariant mass less than 1.06 GeV. With this cut only, no obvious peak was found in the K^+n spectrum. In order to remove the background events, the angle cuts were applied as $\cos\theta^*_{\pi^+} > 0.8$ and $\cos\theta^*_{K^+} < 0.6$, namely the selection of the forward going π^+ and backward K^+. Then the spectrum showed a clear peak at $M = 1555 \pm 10$ MeV and $\Gamma < 26$ MeV, as shown in Fig. 3.2. Further structure was found in the Θ^+K^- channel, where $S = 0$ baryon resonance can be seen. An excess of events near 2.4 GeV was observed, although the statistics was very low. The result was first reported in Ref. [93], and also presented in Refs. [95, 102]. After the above two published works by CLAS, the up-to-date status of the analysis and future perspective were presented in Refs. [95, 103, 104, 105, 106, 107].

The evidence for an $|S| = 1$ narrow resonance in quasi-real photoproduction was reported by HERMES collaboration [108]. With 27.6 GeV positron beam on deuterium target, a

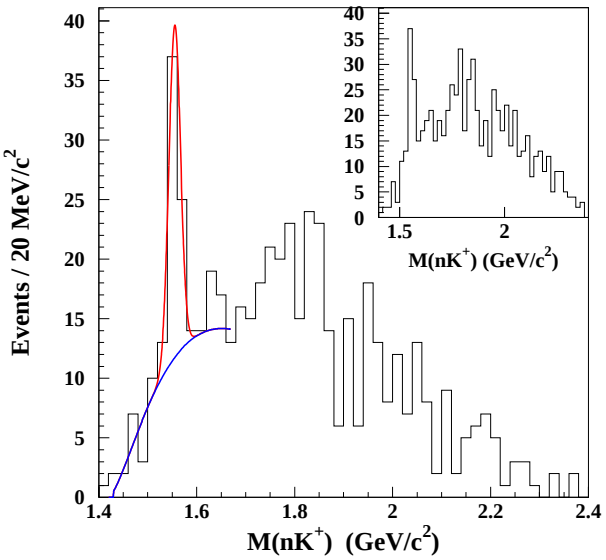

Figure 3.2: The result by CLAS collaboration taken from Ref. [101]. The nK^+ invariant mass spectrum in the reaction $\gamma p \to \pi^+ K^- K^+(n)$ with the cut $\cos\theta^*_{\pi^+} > 0.8$ and $\cos\theta^*_{K^+} < 0.6$. $\theta^*_{\pi^+}$ and $\theta^*_{K^+}$ are the angles between the π^+ and K^+ mesons and photon beam in the center-of-mass system. The background function we used in the fit was obtained from the simulation. The inset shows the nK^+ invariant mass spectrum with only the $\cos\theta^*_{\pi^+} > 0.8$ cut.

signal was searched for in the invariant mass of $K^0_s p$ channel. To study the peak structure, three different methods for the background estimation were used: (i) known Σ^* resonances on top of the Monte Carlo simulation, (ii) known Σ^* resonances on top of the background by mixed event technique, and (iii) polynomial. Mass and width of the state were estimated as $M = 1528 \pm 2.6 \pm 2.1$ MeV and $\Gamma = 17 \pm 9 \pm 3$ MeV. The cross section of $\gamma^* D \to \Theta^+ X$ was estimated as 100-220 nb $\pm 25\%$, while that for the $\Lambda(1520)$ production was 62 ± 11 nb. The result was also reported in Ref. [109], where the $\Lambda\pi^+$ spectrum was further studied, which suggested that the observed signal was not a Σ^* resonance. $K^0 p$ spectrum with additional pion detection was also shown, in which the signal to noise ratio was improved. One may find results in Refs. [110, 111].

In Ref. [112], the reaction $pA \to pK^0_s X$ was studied with 70 GeV proton beam by SVD collaboration. Applying event selection of the pK^0 system to be forward of 90° in the center of mass frame, a narrow structure was observed. Above the background estimated by simulation, the peak was found at $1526 \pm 3 \pm 3$ MeV with the width of < 24 MeV. The result was also reported in Ref. [113]. A further analysis with new data sample [114] confirmed the peak, giving the mass and width of $1523 \pm 2 \pm 3$ MeV and < 14 MeV, respectively.

An evidence in low-energy proton-proton collision was reported by COSY-TOF collaboration [115]. The experiment of $pp \to \Sigma^+ K^0 p$ was performed with the 2.95 GeV proton beam, and a clear signal was seen in the $K^0 p$ invariant mass spectrum. In this case, the strangeness of the signal was tagged by the simultaneous detection of the Σ^+. By applying the efficiency correction, the observed spectrum was fitted by the gaussian for the peak on top of polyno-

mial background. The mass and width of the peak were extracted as $M = 1530 \pm 5$ MeV and $\Gamma < 18 \pm 4$ MeV. Cross section for the Θ^+ production was estimated as $0.4 \pm 0.1 \pm 0.1 \mu$b, by comparing the number of events with those of the elastic reaction whose total cross section was known. The result was also reported in Ref. [116], where the improved results with further measurement with 3.05 GeV beam was briefly described.

A study of the reaction $pA \to K^0 pX$ was reported in Ref. [117]. The experiment was performed with 10 GeV proton beam on C_3H_8 target in bubble chamber, and a signal was searched for in the $K^0_s p$ invariant mass spectrum. A peak was found at 1540 ± 8 MeV with the width of 9.2 ± 1.8 MeV. Result can be found in Ref. [118].

ZEUS collaboration at HERA reported an evidence for the Θ^+ in e^+p deep inelastic scattering at center-of-mass energy of 300-318 GeV with the virtual photon of $Q^2 > 1$ GeV^2 [119]. In $K^0_s p$ and $K^0_s \bar{p}$ spectra, they observed a peak around the mass of 1522 ± 3 MeV, which was more clearly seen in higher Q^2 region. The fitting was improved when another gaussian was included for lower energy region, which would be identified as the $\Sigma(1480)$ bump. Applying several background estimation, the width was estimated to be 8 ± 4 MeV. Based on the Monte Carlo simulation, they also investigate the probability of having a fake signal due to statistical fluctuation, which was turned out to be 6×10^{-5}. The result was also reported in Refs. [120, 121, 122, 123, 124, 125, 126, 127, 128, 129, 130].

In Ref. [131], the hadronic reaction $\pi^- p \to K^- X$ was studied at KEK. Using the 1.87 and 1.92 GeV π^- beam, the Θ^+ signal was searched for in the missing mass of the K^-. A bump structure was found at 1530 MeV, although the statistical significance is low. The upper limit of the cross section of this reaction was estimated as 4.3 μb for 1.92 GeV, by comparing the number of events of signal with that of background.

In addition to the above evidences, yet preliminary, but positive results were reported. As we mentioned before, new results on deuteron target from LEPS can be found in Refs. [86, 87, 88]. The Θ^+ search from NA49 was reported in Ref. [132], where a peak structure was observed at 1526 MeV in pp collisions at $\sqrt{s} = 17.2$ GeV. NOMAD collaboration reconstructed the $K^0_s p$ spectrum in neutrino experiment [133], finding a peak at 1528.7 ± 2.5 MeV with the width of a few MeV. These experiments may provide further evidences in near future.

In summary, we have seen many experimental evidences for the existence of the Θ^+, as listed in Table 3.2. The evidences were found in a variety of experiments with different beams, different reactions, different energy region, and different collaborations. Therefore, it is hard to believe that all the signals in these experiments were produced due to statistical fluctuations or improper analyses. In order to claim the absence of the Θ^+, we should explain the observed structures in all these positive results. On the other hand, from a critical point of view, these evidences have common problems: relatively low statistics, deviations in masses beyond the uncertainties, and ambiguities in background estimation. Indeed, we have seen that two of positive evidences [91, 97] were denied by the new experiments with higher statistics. Therefore, in order to establish the Θ^+ state, it is necessary to confirm the existence in experiments with higher statistics, which will be brought by some of the above experiments.

Table 3.2: Summary of experimental evidences for the Θ^+ resonance. Two of them, CLAS [91]* and SAPHIR [97]* are challenged by the high statistics experiments by CLAS in Refs. [96] and [98], respectively.

Collaboration [Ref.]	reaction	mass [MeV]	width [MeV]
LEPS [16]	$\gamma C \to K^+K^-X$	1540 ± 10	< 25
DIANA [89]	$K^+\mathrm{Xe} \to K^0pX$	1539 ± 2	< 9
CLAS [91]*	$\gamma d \to K^+K^-p(n)$	1542 ± 5	< 21
SAPHIR [97]*	$\gamma p \to \bar{K}^0K^+(n)$	1540 ± 6	< 25
ITEP [99]	$\nu(\bar{\nu})A \to K^0pX$	1533 ± 5	< 20
CLAS [101]	$\gamma p \to \pi^+K^-K^+(n)$	1555 ± 10	< 26
HERMES [108]	$e^+d \to K^0pX$	$1528 \pm 2.6 \pm 2.1$	$17 \pm 9 \pm 3$
SVD [112]	$pA \to pK^0X$	$1526 \pm 3 \pm 3$	< 24
COSY-TOF [115]	$pp \to \Sigma^+K^0p$	1530 ± 5	$< 18 \pm 4$
JINR [117]	$pA \to pK^0X$	1540 ± 8	9.2 ± 1.8
ZEUS [119]	$e^+p \to K^0p(\bar{p})X$	1522 ± 3	8 ± 4
SVD(2) [114]	$pA \to pK^0X$	$1523 \pm 2 \pm 3$	< 14
KEK [131]	$\pi^-p \to K^-X$	$1530.6\ ^{+2.2+1.9}_{-1.9-1.3}$	$9.8^{+7.1}_{-3.4}$

3.2.2 Restriction on the decay width

The existence of the Θ^+ should have implication in the experimental data of the KN scattering, where no indication of the narrow state has been found around 1540 MeV. The reason for the non-observation may be understood by the coarseness of data points, momentum spread of the low energy K^+ beam, and too narrow decay width of the Θ^+. The last point provides a way to impose an upper limit for the width Γ_Θ, by analyzing the KN scattering data carefully.

An analysis of the KN scattering data in this direction was done by Nussinov [134] for the first time. Analyzing the K^+d total cross section at resonance energy, and the upper limit of $\Gamma_\Theta < 6$ MeV was obtained for the $J^P = 1/2^+$ and $I = 0$ state.

Partial wave analysis of the K^+-nucleon elastic scattering process was performed in Refs. [135, 136]. The previous analysis [57] was modified by including a Breit-Wigner amplitude for possible narrow resonance in s, p, and d waves. A tighter limit of $\Gamma_\Theta <$ 1-2 MeV for the Θ^+ width was obtained.

The total cross section of KN elastic scattering and KN phase shift in the P_{01} partial wave were studied by using Jülich potential [137]. In order to be compatible with experiments, it was concluded that the width should be less than 5 MeV or the resonance should lie at much lower energy. A similar method was applied to the $K^+d \to K^0pp$ reaction [138] and $K^+\mathrm{Xe} \to K^0pX$ reaction of DIANA experiment [90]. The former analysis gave an upper limit for the width of $\Gamma_\Theta < 1$ MeV , while the latter provided the comparable descriptions with and without the Θ^+.

In Ref. [139], the total cross section of the K^+d scattering and result of DIANA experiment [89] were analyzed. By counting the number of events of the signal and background in DIANA experiment, the width of the Θ^+ was estimated as $\Gamma_\Theta = 0.9 \pm 0.3$ MeV. K^+d

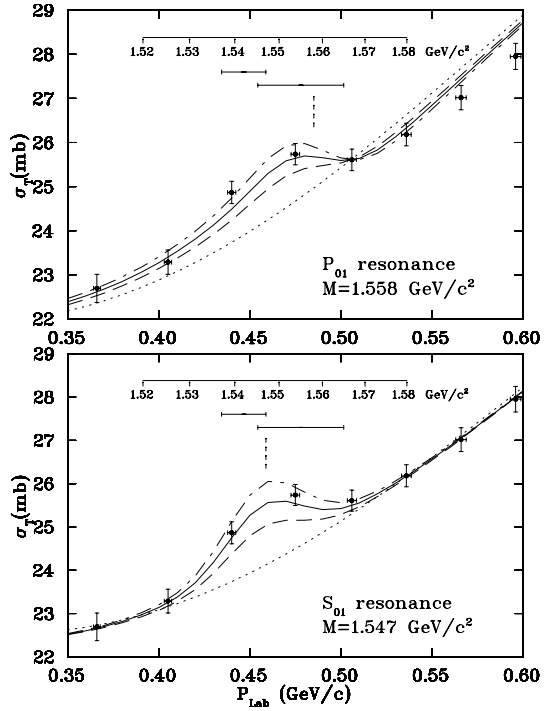

Figure 3.3: Total cross sections of K^+d reaction, taken from Ref. [142]. The dash-dotted, solid and dashed curves correspond to widths of 1.2, 0.9, and 0.6 MeV, respectively.

experiment was analyzed with proper Fermi motion correction, leading to the upper limit of 1-4 MeV for the Γ_Θ.

From a different point of view, total cross section of the K^0_Lp scattering was analyzed in Ref. [140], which can be obtained by analyzing the $\bar{K}N$ and KN data. In the K^0_Lp scattering, we can avoid the problem of Fermi motion correction, unlike in the K^+ beam experiments. However, the present data set was not sufficient to provide a quantitative conclusions. In the same way, total cross sections of K^+p and K^0_Lp scatterings were analyzed to restrict the width of the Θ^+ and Θ^{++} [141].

An interesting observation was reported in Ref. [142] that the resonance structure of the Θ^+ was indeed seen in the K^+d total cross section data. Based on a weak scattering approximation, and taking into account the Fermi motions in the deuteron, total cross section was calculated with a resonances with assumed width and mass. Experimental bump structure was well reproduced by the assumption of a resonance, as shown in Fig. 3.3. The extracted masses were 1559 ± 3 MeV for $J^P = 1/2^+$ resonance and 1547 ± 2 MeV for $1/2^-$ resonance. In both cases, the width should be $\Gamma = 0.9 \pm 0.3$ MeV.

In summary, the KN database provides a strict upper limit for the Γ_Θ of the order of 1 MeV or less. A possible structure at 1540 MeV may be found even in these data. On the other hand, it was also pointed out that a too small width was not consistent with the observed peak of photoproductions, when the t-channel exchange diagrams were dominant mechanisms [143]. In general, one should keep in mind that the KN scattering data at low energy are not of good quality, because of the experimental difficulties. Therefore, precise

measurements for the low energy KN scattering in modern technique are strongly desired.

3.2.3 Searches for other exotic candidates

Here we review the searches for other candidates for pentaquarks, Ξ^{--}[A], Θ_c, and Θ^{++}, which are described by the minimal quark contents $ddss\bar{u}$, $uudd\bar{c}$, and $uuud\bar{s}$, respectively. Unfortunately, so far only one experiment for each state claimed the existence, while no other experiments could confirm the evidence. Of course, cross section for a state generally depends on the production reaction and energy, therefore the sensitivity for the observation should be different in each experiment.

If the Θ^+ belongs to the flavor antidecuplet representation, we naively expect the flavor partner with $S = -2$ and $I = 3/2$, which contains manifestly exotic states of Ξ^{--} and Ξ^+. An evidence for the exotic cascade $\Xi_{3/2}(1860)$ was reported by NA49 collaboration [145]. In proton-proton collisions at $\sqrt{s} = 17.2$ GeV, a signal was searched for in the $\Xi^-\pi^-$, $\Xi^-\pi^+$, $\overline{\Xi}^+\pi^-$, and $\overline{\Xi}^+\pi^+$ spectra, followed by subsequent decays $\Xi \to \Lambda\pi$ and $\Lambda \to p\pi^-$. An angle cut was applied as $\theta > 4.5^\circ$ with θ being the opening angle between the Ξ and the π in laboratory frame. A peak was observed at 1862 ± 2 MeV, the width being below the detector resolution of about 18 MeV. The result can be found in Refs. [146, 132].

In Ref. [58], however, the existence of $\Xi^{--}(1860)$ was critically argued. The authors summarized data on Ξ^* searches in previous experiments, mostly with K^- beam of energies $2 \sim 6$ GeV. In these experiments, the peak structure at 1860 MeV was absent both in $\Xi^-\pi^+$ and $\Xi^-\pi^-$ channels, in spite of the fact that some of them had higher statistics than NA49. Subsequently, several searches for the signal around 1860 MeV were performed, but none of them could confirm the peak reported by NA49. Negative results were reported by WA89 (Σ^--nucleus collisions at 340 GeV) [147], HERA-B (920 GeV ($\sqrt{s} = 41.6$ GeV) pA collisions) [148], ALEPH (Z decay in e^+e^-) [149], CDF ($p\bar{p}$ at $\sqrt{s} = 1.96$ TeV) [150], FOCUS (γBeO) [151], HERMES (quasi-real photoproduction) [152], ZEUS (300 GeV e^+p collisions) [153], BABAR ($\Upsilon(4S)$ decay in e^+e^-) [154], COMPASS (μ^6LiD at 160 GeV) [155], and Fermilab (800 GeV pp) [156].

The evidence of the anti-charmed pentaquark Θ_c was reported in Ref. [157] by H1 collaboration. The search was performed in the electron proton scattering with center-of-mass energy of 300 and 320 GeV, both in deep inelastic scattering ($1 < Q^2 < 100$ GeV^2) and quasi-real photoproduction ($Q^2 \lesssim 1$ GeV^2). A narrow state was observed in $D^{*-}p$ and $D^{*+}\bar{p}$ spectra at $3099 \pm 3 \pm 5$ MeV with width of 12 ± 3 MeV, compatible with the experimental resolution. The result was also reported in Refs. [158, 126, 127, 128, 159]. On the other hand, no evidence was found by ZEUS (300 GeV e^+p collisions) [160], ALEPH (Z decay in e^+e^-) [149], CDF ($p\bar{p}$ at $\sqrt{s} = 1.96$ TeV) [150], FOCUS (γBeO) [161], and BABAR ($\Upsilon(4S)$ decay in e^+e^-) [162].

Doubly charged Θ^{++} can be searched for in the pK^+ spectrum, which has an advantage for detection since the final states are all charged particles. If the Θ^+ has $I = 1$ or $I = 2$, there must be the isospin partner in this channel at the same energy with the Θ^+. Several

[A] The exotic state with $S = -2$ and $I = 3/2$ is denoted as $\Phi(1860)$ in PDG [144], but we call it $\Xi_{3/2}$ or Ξ^{--} in this thesis, because these symbols are more informative.

groups that reported the evidence for the Θ^+ also investigated the pK^+ channel in order to determine the isospin. For instance, CLAS collaboration looked at the pK^+ system both in deuteron target [91] and in proton target [101], finding no peak. A detailed discussion on the Θ^{++} search at CLAS can be found in Ref. [163]. In the pK^+ spectrum of $\gamma p \to K^- K^+ p$ reaction. Some structure was seen around 1590 MeV, but it turned out to be mainly due to reflection of ϕ production in K^+K^- system. Another search was performed by HERMES collaboration [108]. The pK^+ spectrum showed no structure for the Θ^{++}, which ruled out the $I = 2$ candidate based on the isospin analysis. On the other hand, isospin symmetry can not relate the strength of Θ^+ and Θ^{++} production for the $I = 1$ assignment, and therefore the cancellation of the amplitudes might occur, although unlikely. In addition, BABAR found no evidence for this state [164].

However, a positive evidence was reported by STAR at RHIC [165]. In d+Au collision at $\sqrt{s_{NN}} = 200$ GeV, about 20,000 of pK^+ and $\bar{p}K^-$ events were summarized. After subtracting the background contribution estimated by the mixed-event technique, they found a signal at $1528 \pm 2 \pm 5$ MeV with the width less than 15 MeV in the spectra, which still contained several hundreds of events. A weak signal was also found in Au+Au at 62.4 GeV.

3.2.4 Negative results for the Θ^+ and interpretation of experimental results

Let us describe the experiments that could not see the peak for the Θ^+. These are mostly high energy experiments with huge number of events. Among them, we will address two typical experiments of e^+e^- collision by BES [166] and pA collision by HERA-B [148]. We also list the works which explain possible reasons for the non-observations in these experiments. Then we present discussions which regard the observed peak in positive results as kinematical artifacts.

BES collaboration searched for the the Θ^+ signal in the $K^0_s p K^- \bar{n}$ and $K^0_s \bar{p} K^+ n$ spectra in hadronic decay of charmonia produced by e^+e^- collision [166]. Among the total $10 \sim 20$ events, no clear signal for the Θ^+ was observed. The upper limit of the branching ratio was estimated by the number of events and detector efficiencies, leading to $B(J/\psi \to \Theta\overline{\Theta} < 1.1 \times 10^{-5})$. Decay from $\psi(2S)$ gave a result with the same order. In proton induced reactions on C, Ti, W targets at midrapidity and $\sqrt{s} = 41.6$ GeV, a null result for the Θ^+ was reported by HERA-B collaboration [148]. No clear signal for the $\Theta(1540)$ candidate was found in $pK^0_s \to p\pi^+\pi^-$ mass spectrum. On the other hand, they observed the $\Lambda(1520)$ clearly in K^-p spectrum. Since the acceptance for $K^0_s p$ and K^-p combinations was expected to be similar at mid-rapidity ($\sim$4%), the yield ratio was estimated as $\Theta^+/\Lambda(1520) <$ (3-12)%, which was significantly lower than theoretical model predictions.

Subsequently, negative results were reported by PHENIX (Au+Au, $\sqrt{s_{NN}} = 200$ GeV) [167], SPHINX (pC at 70 GeV) [168], BELLE ($\bar{B}^0 B^0$ decay in e^+e^-) [149], ALEPH (Z decay in e^+e^-) [149], CDF ($p\bar{p}$ at $\sqrt{s} = 1.96$ TeV) [150], HyperCP (pCu at 800 GeV) [169], FOCUS (γBeO) [151], LASS ($K^+p \to K^+n\pi^+$) [170], BABAR ($\Upsilon(4S)$ decay in e^+e^-) [154], BELLE (secondary interaction) [171], COMPASS (μ^6LiD at 160 GeV) [172], and WA89 (Σ^--nucleus at 340GeV) [173].

All these experiments showed no structure for the Θ^+ in the spectra, giving upper limits

on the production rates. However, in these high statistics experiments, the spectra of $K_s^0 p$ were extremely flat, where the Σ^* resonances could in principle contribute [53]. The same argument can be applied to the $K^- p$ spectra, where no evidence for the Λ^* resonances was seen other than an excellent $\Lambda(1520)$ (and sometimes Λ_c) peak. Strictly speaking, the production mechanism of the particles, especially for the excited states in high energy experiment is not well known yet. For instance, the production rate of anti-deuteron in LEP experiments is significantly lower than expected [174]. Therefore, before concluding the absence of the Θ^+ by these null results, we should understand the production mechanism for the Θ^+ in high energy experiments.

Of course, as the proof of the absence of the Θ^+ requires the explanation of positive evidences, in order to establish the presence of the Θ^+, one should explain why the negative experiments could not find the signal. There were several attempts, for instance, a possible explanation of the non-observations was presented in Ref. [174] by assuming the crypto-exotic $N(2400)$ resonance which decayed into $\Theta^+ K^-$. The BES experiment was analyzed in Ref. [175], and the sensitivity turned out not to be so good for the Θ^+ search. The decrease of the production ratio of the Θ^+ with reaction energy was found in Ref. [176], which indicated that the high energy experiments were not suitable to produce the Θ^+ (or five-quark) states. The estimation was consistent with the null result by, for instance, HERA-B [148]. A similar idea can be found in Ref. [177]. In Ref. [178], there was a discussion on the ZEUS result, which was a high energy experiment with positive evidence. The best condition to observe the Θ^+ in $e^+ p$ experiment was found to be in the forward region of pseudorapidity, at low p_T and at medium or high Q^2 regions. An explanation for the systematic lowering in mass in pK^0 channel was suggested in Ref. [179] by association of another Σ^* resonance.

A recent CLAS experiment [98] imposed a very small upper limit for the cross section of the $\gamma p \to \bar{K}^0 \Theta^+$ reaction. In order to explain this result and the positive evidence on neutron target simultaneously, there must be a large difference between cross section for $\gamma p \to \bar{K}^0 \Theta^+$ and that of $\gamma n \to K^- \Theta^+$. A solution was reported in Ref. [180]. It was found that the cross section for the proton target case was strongly suppressed, when the spin of the Θ^+ was 3/2. This was because a large cross section was produced by the Kroll-Ruderman contact term, which was present for the proton target case, but was absent for the neutron target. For the $J^P = 3/2^+$ case, the ratio of the cross sections was about 25, while for the $3/2^-$ case, it was about 50. From a different point of view, p/n asymmetry was explained in Ref. [181]. Since the argument is based on the isospin analysis, it can be applied to the Θ^+ with arbitrary spin and parity.

On the other hand, there are some arguments that the observed peak in the positive experiments could be explained as an artifact which has kinematical origin. Ref. [182] discuss the possibilities of the Θ^+ signal as kinematic reflections resulting from the decay of mesons in $\bar{K}K$ system, by taking an example of CLAS data [91]. For a given three-body system (for instance, $N\bar{K}K$), an enhancement of the invariant mass of a two-body system (NK) can be influenced by the decay of a resonance in another two-body system ($\bar{K}K$), due to the decay angular distribution. This is called the kinematic reflection. It is worth noting that if a peak is generated by the reflection, the position of the peak changes with changing the initial energy of the beam. For the Θ^+ in NK channel, reflection of $f_2(1275)$, $a_2(1320)$, and

$\rho_3(1690)$ in $\bar{K}K$ system could play a role. Similar argument of the kinematic reflection can be found in Ref. [183]. Ref. [184] discussed the kinematic reflection on charmed pentaquark. However, the kinematical reflection can not account for the very narrow resonance, and the analysis in Ref. [182] was criticized by the model dependence, neglect of detector acceptance, determination of parameters, and so on [185]. Despite the quantitative uncertainties in the analysis, however, presence of a resonance in $\bar{K}K$ system could affect the invariant mass distribution of KN system [186]. In Ref. [187], the author argued that the narrow signal of $\Xi(1860)$ was due to a threshold cusp in $\Sigma(1385)\bar{K}$ coupled to $\Xi\pi$ and $\Sigma\bar{K}$ channels. In general, scattering amplitude has a cusp singularity at threshold of a channel, induced by the step of imaginary part. In any event, estimation of background effects for the production experiments is important, though hard to control.

3.3 Theoretical studies on reaction mechanism

Here we summarize the theoretical studies on reaction mechanism for the Θ^+ production and possible method to determine the quantum numbers in experiments. Adopting the effective models, total and differential cross sections can be estimated. The spin and parity of the Θ^+ can be extracted from qualitative differences in the results, which may be implemented by the use of the polarization of initial and final states. These studies are important in connection with interpretation of existing data and future plans for experiments, but we should keep in mind the model dependence in these analyses. There are several unknown parameters such as $\Theta K^* N$ coupling constant and cutoff value of form factor, so that the results can be different depending on details of the model employed. Nevertheless, qualitative understanding of the experiments is important and model-independent selection rules can be obtained, by taking certain limits.

3.3.1 Photoproduction

There are many studies for photoproduction of Θ^+, since the first evidence for the Θ^+ was observed in a photoproduction experiment, and it has been confirmed in other experiments with photon beam. In general, at low energies, effective Lagrangian approaches with Born approximation are applicable to describe the reaction, while the Regge formulation will be needed to reproduce the higher energy behavior.

The basic reaction of $\gamma N \to \bar{K}\Theta$ was first studied in Refs. [188, 189, 190], where the Born diagrams shown in Fig. 3.4 were calculated by the effective hadronic Lagrangians. In Ref. [188], pseudoscalar (PS) type coupling was adopted for the $KN\Theta$ vertex, which is schematically written as

$$\mathcal{L}_{\rm PS} = -ig\bar{B}\gamma_5 MB, \tag{3.3.1}$$

where B and M are the baryon and meson fields, and g is the coupling constant. The PS coupling is based on the linear representation of the chiral symmetry. Note that the diagram (d) in Fig. 3.4 is absent for the PS scheme. In Ref. [188] only the positive parity state with spin 1/2 was considered with s- and u-channel diagrams, and the calculation was later

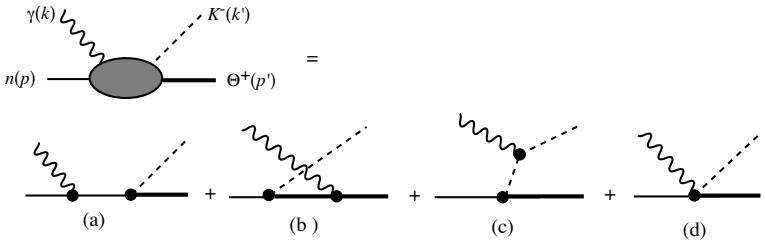

Figure 3.4: The tree diagrams for the $\gamma n \to K^- \Theta^+$ taken from Ref. [189]. (a) the direct Born Diagram (s-channel), (b) the exchange Born diagram (u-channel), (c) the meson exchange diagram (t-channel), and (d) the contact (Kroll-Ruderman $\equiv$ KR) term.

extended for more general cases [191]. A systematic study for this reaction with the Born approximation was performed in Ref. [189], with both the $J^P = 1/2^{\pm}$ cases on the neutron target. For the $KN\Theta$ coupling, pseudovector (PV) scheme was also considered

$$\mathcal{L}_{\rm PV} = g\bar{B}\gamma_\mu\gamma_5\partial^\mu MB. \tag{3.3.2}$$

This is related to the nonlinear realization of the chiral symmetry, as we have seen in chapter 2. The authors of Ref. [189] studied not only the PS and PV schemes, but also the hybrid model using the gauge invariant form factor. In Ref. [190] the K^* vector meson exchange was introduced in addition to the pseudoscalar K exchange in t-channel. A similar study based on the prescription for the gauge invariance was performed in Ref. [192] where the axial vector K_1 meson exchange was also introduced. In these studies, total cross sections and angular distributions were calculated. In spite of the quantitative differences depending on the uncertainties and model parameters, it was commonly confirmed [189, 190, 191, 192] that the positive parity assignment predicts about ten times larger cross section than the negative parity does. More comprehensive calculations can be found in Refs. [193, 194], where $\gamma N \to K\bar{K}N$ reaction was studied with hyperon resonances in the intermediate state as well as the nonresonant background processes. In Ref. [193], spin $3/2^{\pm}$ cases were also considered.

Regge treatment was introduced in the t-channel K and K^* exchange terms in Refs. [195, 196]. In Ref. [195], the effect of the hadronic form factor in the Born approximation was estimated by comparing with the Regge model. It was found that the soft form factor $0.6 \leq \Lambda \leq 0.8$ GeV was favorable for the consistency with the Regge amplitude. A comprehensive calculation can be found in Ref. [196], including the spin 3/2 cases and polarization observables.

Several attempts were proposed in order to determine the spin and parity using the polarization of beam and target in photoproduction. The determination of spin and parity using polarized photon beam asymmetry was suggested [197]. The polarized photon beam asymmetry is defined by

$$\Sigma_A \equiv \frac{\sigma_\parallel - \sigma_\perp}{\sigma_\parallel + \sigma_\perp}, \tag{3.3.3}$$

where $\sigma_\parallel(\sigma_\perp)$ are the cross sections of the linearly polarized photon beam with polarization

vector lying in (perpendicular to) the reaction plane. Photoproduction of the Θ^+ states with $J^P = 1/2^{\pm}$, $3/2^+$ states was examined by the Born approximation in Ref. [197]. It was found that the quantity could be used to distinguish the parity of the spin $1/2$ states, but the result was sensitive to the K^* exchange contribution, which contained an unknown $\Theta N K^*$ coupling constant. The photon asymmetry in Eq. (3.3.3) was also proposed in Ref. [198], taking into account the background processes as well. The effect of the background contributions appeared to mask the possible signal for the parity determination. Beam-Target double polarization asymmetry was then proposed to determine the parity of the Θ^+ with $J = 1/2$ [199]. Near the threshold, this quantity was less ambiguous than the single asymmetry studied in Ref. [197], and would be useful to filter the parity of the Θ^+ state.

However, a model-independent analysis for the determination of the Θ^+ parity in K photoproduction process was performed in Ref. [200]. It was found that *the parity of the* Θ^+ *can be determined model independently, only when we measure the polarization of the produced* Θ^+ *(and hence, that of the nucleon in decay channel).* The detection of the polarization of the particle in the final state is experimentally difficult. The spin observable was further considered in Ref. [201], confirming the above conclusion. The polarization observables were evaluated in a detailed model calculation [202], including several background processes.

In Ref. [203], the photon induced reaction with K^* production $\gamma N \to K^* \Theta^+$ was analyzed. This is the reaction of CLAS experiment [101]. The cross section for the negative parity case was turned out to be smaller than the positive parity case. Spin asymmetries in K^* photoproduction case were extensively studied in Ref. [204]. Target-recoil double asymmetries were found to be sensitive to the parity of the Θ^+, although the measurement would be difficult. Extension to the spin $3/2$ cases and inclusion of the scalar kaon exchange for the K^* photoproduction were performed in Ref. [205].

As we have described before, explanations for the recent negative result by CLAS collaboration [98] were proposed in Refs. [180, 181]. One is based on the dominance of the Kroll-Ruderman term [180], while the other is derived from the isospin of photon [181].

Let us mention the case with the deuteron target. Photoproduction of Θ^+ from the deuteron was studied in Ref. [206], through Λ and Σ associate reactions with neutron spectator background processes. The reaction was described by combining the measured amplitudes of photoproduction of Λ and Σ off proton, phenomenologically parametrized amplitudes of photoproduction off neutron, and the deuteron wave function. The cross sections of the Λ and Σ associated reactions turned out to be sensitive to the isospin of the Θ^+, so the isospin of Θ^+ could be identified by comparing these reactions. Coherent Θ^+ and $\Lambda(1520)$ photoproduction off the deuteron was studied in Ref. [207], where productions of either of the resonances as well as the non-resonant background processes were analyzed in the same framework. It was found that the coherent Θ and $\Lambda(1520)$ photoproduction was enhanced relative to the background processes in the forward hemisphere of pK^- pair photoproduction. The result did not depend on the photoproduction amplitude of Θ^+ subprocess, since the Θ^+ was produced *via* hadronic subprocess when the $\Lambda(1520)$ came forward. This observation seems compatible with the recent LEPS result.

3.3.2 Hadron-induced reactions

Hadron-induced production has an advantage of relatively large cross section, because all the vertices are described by the strong interaction. For the meson-induced case, in addition, the momentum transfer of the reaction is relatively small, compared with the photoproduction. On the other hand, in general, quality of the beam is not very good, especially for the low energy region, and the non-resonant background terms also have large cross sections. However, since the confirmation by various reactions is crucial to establish a new state, it is important to study the meson-induced reactions from theoretical point of view.

The first study for the meson-induced reaction was performed in Ref. [17] in order to determine the spin and parity of the Θ^+. The production of Θ^+ with $J^P = 1/2^{\pm}, 3/2^+$ in the $K^+p \to \pi^+KN$ reaction was calculated based on the chiral Lagrangians, assuming the momentum of π^+ as small. It was found that the combined examination of the peak strength with polarization observation could help to determine the J^P of the state. Details of this study will be discussed in chapter 8.

Effective Lagrangian approaches for the meson-induced reactions with Born approximation were performed in Refs. [188, 190, 208]. In Ref. [188] several reactions were calculated for positive parity Θ^+, but only baryon pole terms were included. Adopting the PS coupling (3.3.1) the cross sections close to the threshold were estimated as 1.5 mb for $KN \to \pi\Theta$, 0.05 mb for $\pi N \to \bar{K}\Theta$, and 0.1 mb for $\rho N \to \bar{K}\Theta$. Oh *et al.*, calculated the pion-induced reaction [190] and the kaon-induced reaction [208]. They evaluated the t-channel K^* meson exchange in addition to the s- or u-channel baryon pole terms. PS coupling was used for $KN\Theta$, while PV scheme (3.3.2) was adopted for πNN. They found that the cross section was sensitive to the choice of the form factor and the K^* exchange diagram, which contained an unknown coupling constant of ΘK^*N vertex. For $\pi^-p \to K^-\Theta^+$ reaction, both positive and negative parity cases were examined, finding that the cross section was suppressed in the negative parity case. This is a similar tendency as in the photoproduction case.

In Ref. [25], the $\pi^-p \to K^-\Theta^+$ and $K^+p \to \pi^+\Theta^+$ reactions were studied based on the two-meson coupling of the Θ^+ with $J^P = 1/2^+$ and $3/2^-$. Since the two reactions were treated on the same footing, the ratio of the cross sections could be estimated. For the $J^P = 1/2^+$ case, the difference between two reactions was large, while the $3/2^-$ case it was rather moderate. We will discuss this subject in chapter 11. The $\pi D \to \Theta^+\Sigma$ reaction was studied in Ref. [209] focusing on the spin correlation observables. The spin-transfer coefficients and the deuteron spin anisotropy were found to be sensitive to the parity of the Θ^+, in a model-independent manner.

Low energy NN collision is one of the most interesting reactions for the Θ^+ production, since it is possible to determine the parity of the Θ^+ using experimentally feasible method with polarized beam and target. As we mentioned above, the $pp \to n\Sigma^+K^+$ reaction was already studied in Ref. [81]. In the following, we list studies after LEPS experiment.

The pp collisions with two- and three-body final states were studied in Ref. [188] by the effective Lagrangian approach with K exchange diagrams. For the positive parity Θ^+ with the width 20 MeV, the cross sections were estimated as 2 μb for $pp \to \Sigma^+\Theta^+$, 3 μb for $pp \to \pi^+\Lambda\Theta^+$, and 13 μb for $pp \to \bar{K}^0p\Theta^+$. In Ref. [208], $np \to \Lambda\Theta^+$ was studied in addition

to $np \to \Sigma^0\Theta^+$ with taking into account the K^* exchange diagrams. It was found that the cross section for the $np \to \Lambda\Theta^+$ was about 5 times larger than that of the Σ^0 production. The np collision was studied in Ref. [210] for both positive and negative parities.

A model-independent method to determine the parity of Θ^+ in pp collision was presented in Ref. [211]. At the threshold of the production reaction $pp \to \Sigma^+\Theta^+$ where $l = 0$ component is dominant, one obtains a selection rule which depends on the spin of the initial pp state and the parity of the Θ^+. Therefore, clear distinction of parity would be possible by the cross sections with different initial pp states, which could be achieved by polarizing the beam and target. The same idea of polarized pp collision for the determination of the parity of Θ^+ was given in Ref. [212], where the spin correlation coefficient A_{xx} was proposed for a suited observable for this method. In addition to the method proposed in Refs. [211, 212], polarization transfer coefficient D_{xx} was also suggested as another measurable quantity [213, 214]. This can be obtained by the single polarization of the initial state and it is possible to perform in the $np \to \Lambda\Theta^+$ reaction. The spin observables in NN collisions were extensively summarized in Ref. [215]. The above arguments were essentially based on the conservation lows and Pauli exclusion principle, and therefore the results were model independent.

These selection rules were then numerically examined. The spin correlation A_{xx} was evaluated in Ref. [216], as well as the total cross section of the $pp \to \Sigma^+\Theta^+$ reaction with K and K^* exchanges. The total cross section was of the order of 0.1-1 mb, which was accessible by experiment. Up to center-of-mass energy $\sqrt{s} < 2750$ MeV, s-wave dominance was observed so that the $l = 0$ assumption could be valid. It was numerically shown that A_{xx} indeed reflected the selection rule close to threshold. Numerical estimation of the spin transfer D_{xx} was performed in Ref. [217] as well as A_{xx}. Energy dependences of these quantities were also evaluated. Angular distribution and azimuthal asymmetry in the $pp \to \Sigma^+\Theta^+$ reaction were evaluated in Ref. [218] where the spin 3/2 cases were taken into account.

3.3.3 High energy reaction

Apart from the above low-energy reactions, Θ^+ production in high energy inclusive processes has also been studied. As we mentioned in section 3.2, the Θ^+ may be observed in the $K^0_s p$ mass spectrum in this kind of reactions.

In Ref. [219], production rate of the Θ^+ in relativistic heavy ion collision was studied at midrapidity region in central Au + Au collisions. Based on the statistical considerations, production abundance ratios of the Θ^+ to Λ, p, K^+, and π^+ were estimated. The production and absorption in subsequent hadronic matter were included in Ref. [220]. It was found that the effect of the interaction was small, and therefore, the yield of the Θ^+ was determined by the initial number produced in the Quark-Gluon plasma. The statistical hadronization model was applied to the Θ^+ [221] and Ξ^{--} [222] productions in heavy ion collisions. It was shown that the production yields depend on the collision energy, and the detection for Θ^+ was promising at lower energy. The detection of the other pentaquarks was found to be difficult. Subsequently, estimation of the production yield in pp collision such as SPS and RHIC was also performed using the Gribov-Regge theory [223], microcanonical statistical approach [224], quark combination model [225], and quark molecular dynamics model [226].

Possible exotics searches in high energy e^+e^- and $\gamma\gamma$ collisions were discussed in Refs. [227, 228, 229]. Decay mechanism from B mesons into exotics was discussed in Ref. [227], and several decay channels from exotic candidates were listed in Ref. [228]. The pentaquark production in charmed and bottomed hadrons was discussed in Ref. [229], including the possibilities of $I = 3/2$ isovector pentaquarks state. The probability of finding Θ_c signal in the decay of bottom hadrons was also discussed. These works would be compared with the inclusive production experiment of the high energy e^+e^- collisions.

Production of the heavy pentaquarks was studied in fragmentation model [230]. Θ_c production was also studied in coalescence model [231]. Based on the observation at H1 experiment, the number of events at LEP and the Tevatron ware estimated.

3.3.4 Other studies on reaction mechanisms

The time delay and speed plot of the KN scattering was studied in Ref. [232], in order to search for the resonance signal in the KN scattering data. The time delay and the speed plot are essentially the energy derivative of the T-matrix, which shows a peak when there is a resonance. Using a model-dependent T-matrix amplitude of KN scattering, a possible signal of the $\Theta(1540)$ was searched for, as well as the resonances previously found in the partial wave analysis [57]. The signal was further purchased in Ref. [233] by using the phase shift of the KN scattering, where the signal was found in D_{03} partial wave, indicating the existence of a $3/2^-$ resonance around 1540 MeV.

Exclusive electroproduction of Θ^+ was studied in Ref. [234], which was useful to extract the information of internal structure of the Θ^+. A modest value for Q^2 was found to be appropriate to have large cross section. Parity determination within the electroproduction was discussed in Ref. [235].

An nucleon partner suggested in Ref. [236] was searched for by the partial wave analysis [237]. In addition to the nominal $N(1710)$, two candidates with $J^P = 1/2^+$ were found at 1680 MeV and/or 1730 MeV, both of which were narrow and highly inelastic. However, see also Ref. [238].

Exotic Ξ production in exclusive processes has been studied in photon-induced reaction [239] and kaon-induced reaction [240, 241]. These studies have been performed after the report by NA49 [145], so the mass of Ξ was fixed at 1860 MeV. Using effective Lagrangians, total cross sections and angular distributions for these exclusive experiments were estimated.

Kinematics of two-body decay in high energy reactions were studied in Ref. [242]. Several method to increase the efficiency of the detection were suggested. In Ref. [243], a method was suggested in order to distinguish a resonance from the nonresonant terms by choosing proper kinematics.

An attempt to relate the cross sections of different processes were performed in Ref. [244]. Using the five-quark wave functions of positive parity pentaquarks, relations between Θ production with Σ_5, Λ_5, and N_5 were derived. Importance to measure the cross section for these non-exotic pentaquark productions were emphasized. In the same direction, in Ref. [245], γp, πp, and pp reactions for the Θ^+ production were studied as well as the other hyperon

productions, based on the regge analysis. The hyperon productions showed a universality in these reactions, due to the formulation of the Regge model. On the other hand, the Θ^+ production does not follow the universality, which indicate the different structure and production mechanism of the Θ^+ from the ordinary hyperons.

3.4 Analysis based on the symmetry principle

As we have emphasized in chapter 2, symmetries can restrict the properties of hadrons in certain limits. Here we summarize the studies based on the symmetries of QCD.

3.4.1 Flavor symmetry

Using the flavor symmetry, we can derive several relations between masses and coupling constants. For instance, a formula of the ratio between two decay modes K^+n and K^0p was derived for general isospin (and spin) states of the Θ^+ in Ref. [246].

Properties of the baryon antidecuplet were systematically studied in Ref. [247] for the cases without representation mixing and with ideal mixing with an octet. Mass formulae up to linear order in m_s were derived. For the pure antidecuplet, it leads the equal-spacing formula

$$M(\overline{\mathbf{10}}; Y) = M_{\overline{\mathbf{10}}} - aY, \tag{3.4.1}$$

where Y is the hypercharge of the state, $M_{\overline{\mathbf{10}}}$ and a are the masses parameters that can not be determined from the symmetry. In addition, the SU(3) symmetric Lagrangian of the coupling of antidecuplet to octet meson and octet baryon was presented. The decay of antidecuplet baryon to the octet meson and decuplet baryon was shown to be forbidden. The identification of $N(1710)$ as in pure antidecuplet seemed to be ruled out, since the $N(1710)$ has empirical decay width into $\pi\Delta$.

Along the same line with Ref. [247], classification of the five quark states and their effective interaction Lagrangians was performed in Ref. [248] for the ideal mixing case and in Ref. [249] for the complete set including **27** and **35** representations. Flavor symmetry relations and various selection rules were obtained. The same tables for the decays were given in Ref. [250], but with including the SU(3) breaking interactions. Tables for the couplings with decuplet baryons can be found in Ref. [251].

Following the formula (3.4.1), it is possible to argue that the nucleon partner of the Θ^+. For instance, a putative low-lying nucleon state around 1200 MeV was suggested as a flavor partner of the Θ^+ [252], in order to explain the narrow width of the Θ^+. In Ref. [236], using Eq. (3.4.1) and the mass of exotic Ξ^{--}, a nucleon state was predicted around 1650-1690 MeV. The decay of exotic $\Xi(1860)$ was studied using flavor SU(3) argument [253]. Several selection rules and branching ratio was provided by the symmetry consideration, which were compared with the observation in NA49 experiment. An absence of the decay of $\Xi^+(1860) \to \Xi^0(1530)\pi^+$ would support the interpretation of $\Xi(1860)$ as a member of flavor antidecuplet. A similar argument can be found in Ref. [254]. Various decays of the heavy pentaquarks were studied using effective Lagrangians based on flavor SU(3) symmetry [255]. The B meson decays into pentaquarks were also evaluated.

3.4.2 Chiral symmetry

A simple way to incorporate the chiral symmetry for exotic state is to write down the Lagrangian in chiral perturbation theory. In this direction, chiral Lagrangian was introduced first in Ref. [256], by assuming the Θ^+ belongs to the antidecuplet. They gave the lowest order Lagrangians for $J^P = 1/2^{\pm}$, which were applied to the $\pi^- p \to K^- \Theta^+$ and $\gamma n \to K^- \Theta^+$ reactions. Extension to the $J^P = 3/2^{\pm}$ cases was done in Ref. [254], and strong decay widths of the Ξ^{--} were estimated as functions of the width of the Θ^+. Photoproduction and radiative decay were studied in Ref. [257]. Chiral Lagrangian for the heavy-light pentaquarks were introduced in Ref. [258].

A systematic evaluation of the mass in heavy baryon chiral perturbation theory was given in Ref. [259]. The masses of the members of baryon antidecuplet was calculated up to next-to-next-to leading order for $J^P = 1/2\pm$ states. The coupling constants between antidecuplet pentaquarks and nonexotic octet baryons were used as expansion parameters. Corrections to the Gell-Mann–Okubo rule at NNLO turned out to be negligible. The representation mixing was also considered later in Ref. [260].

In Ref. [261], chiral doubling scenario was applied to the Θ_c found by H1 collaboration, predicting the lighter Θ_c state as a doubling partner. Size of the mass splitting in the doublets were estimated by the D meson spectrum, and the doubling partner of the Θ_c was predicted to appear around 2700 MeV.

There are discussions on the narrow width of the Θ^+ using chiral symmetry. The chiral multiplet for the Θ^+ was considered in Ref. [262]. It was found that the $\mathbf{8}$ and $\overline{\mathbf{10}}$ multiplets of SU(3) degenerated in the chiral limit, when the multiplets were constructed as in the Jaffe-Wilczek model. As consequences, the ideal mixing is manifested in the chiral limit, and the axial current coupling to the other multiplets vanishes, which indicates the narrow width for the Θ^+.

In Ref. [263], a suppression mechanisms was suggested for the decay width of a local operator of Θ^+ into KN state, by chiral symmetry. Its decay width vanishes at chiral limit, and spontaneous chiral symmetry breaking may provide the width proportional to the quark condensate. Therefore, the decay of a local five-quark field is in general suppressed by the chiral symmetry. The decay width of the Θ^+ in chiral symmetric limit was further discussed in Ref. [264]. It was confirmed that a local operator with two chirally different diquarks was shown not to decay into KN state at chiral limit, but the effect of quark condensate was large enough to make a wide width. In addition, a p-wave positive parity state was also examined, and its coupling to KN can be constructed in chirally invariant way. Hence, the conclusion was that chiral symmetry should not be an origin of the small decay width for these cases, once the spontaneous symmetry breaking happened.

3.4.3 Large N_c analysis

The idea of the large N_c was introduced by 't Hooft in Ref. [265] which have been extensively applied to the baryon sector [266]. The large N_c argument is closely related to the soliton picture of the baryons. Indeed, through the consistency condition of the meson-baryon scattering, it was found that baryons have an exact contracted spin-flavor SU($2N_F$) symmetry

in the large N_c limit [267, 268, 269], where N_F is the number of the flavor. The SU($2N_F$) symmetry is the same with that of the Skyrmion, but also the same with that in constituent quark models. In general, taking the large N_c limit, simple relations can be derived, which is exact in this limit and physical world of $N_c = 3$ can be approached by including the $1/N_c$ corrections systematically.

The existence of $S = +1$ states with different spin and isospin were discussed by assuming the existence of Θ^+ [270]. In large N_c limit, several scattering amplitudes of meson and baryon are related with one reduced matrix element, and therefore, the resonances appearing in the different amplitudes become degenerate. This means that the existence of a resonance in one particular channel implies the existence of other poles in different partial waves and isospin. Assuming quantum numbers of Θ^+, several possible partners were discussed, which would have similar masses as Θ^+ within ~ 100 MeV, due to $1/N_c$ corrections. The existence of the SU(2) rotational partner of Θ^+ was also discussed in a similar way in Ref. [271]. The mass splitting among these partners were determined by the SU(2) moment of inertia, which was constrained by the N-Δ splitting.

Quantum numbers of baryon exotics in constituent quark models and the Skyrme models were studied in Ref. [272, 273]. It was shown that the exotic states in two approaches should have the same quantum number. The equivalence was shown to hold in arbitrary numbers of color and flavor. This is an extension of the conclusion in Refs. [267, 268, 269], where the common symmetry SU($2N_F$) appears in the large N_c limit. Quantum numbers for the allowed state for three flavor case were derived.

Large N_c analyses for the pentaquarks including heavy states based on the quark operator method [274] were performed in Ref. [275] for the positive parity pentaquarks and in Refs. [276, 277] for the negative parity cases. Properties of the exotic states such as mass spectrum and coupling constants were derived in $1/N_c$ expansion.

A particularly interesting result was obtained in Ref. [278]. It was shown that the heavy pentaquark $uudd\bar{Q}$ should exist in the large N_c and heavy quark $m_Q \to \infty$ limits. The proof is exact in the limits, but the $1/N_c$ and $1/m_Q$ corrections should be included in reality. Utilizing effective models, such corrections were studied, and it was found that the existence of the pentaquark state depended strongly on the model details, indicating the real world was not so close to the both heavy quark and large N_c limits.

3.5 Chiral soliton models

Here the studies based on chiral soliton models are summarized. We use the word "chiral soliton models" for those regard the nucleons as solitons of the chiral field, namely, Skyrme models, chiral quark soliton models, and other variants. The idea itself is rather old [279], but it has been developed in connection with the QCD *via* large N_c and chiral symmetry [280, 281].

3.5.1 Rigid rotator quantization in flavor SU(3)

The Skyrmion model was developed in the SU(2) sector. It was generalized to the SU(3) sector [282] as a natural extension of the collective quantization of SU(2) Skyrmion [280]. The

quantization method is called as rigid-rotator quantization. Since the rigid-rotator quantization was employed in the prediction and has been discussed later extensively, let us review the essential point here.

The classical soliton field of SU(2) hedgehog was embedded in the SU(3) space as

$$U_0 = \begin{pmatrix} e^{i\boldsymbol{n}\cdot\boldsymbol{\tau}P(r)} & 0 \\ 0 & 1 \end{pmatrix}, \tag{3.5.1}$$

where $P(r)$ is the profile function of the soliton, $\boldsymbol{\tau}$ are the Pauli matrices in flavor space and $\boldsymbol{n}$ is the unit vector in coordinate space. This field is rotated in SU(3) space by $U = AU_0A^\dagger$ with SU(3) matrices A. This rotation is quantized, leading to the rotational Hamiltonian

$$H^{\rm rot} = \frac{1}{2I_1}\sum_{A=1}^{3} J_A^2 + \frac{1}{2I_2}\sum_{A=4}^{7} J_A^2, \tag{3.5.2}$$

where $I_1(I_2)$ is the moment of inertia within (out of) the SU(2) subspace. These moments can be calculated numerically when the model is specified, while the result becomes "model independent" when we treat them as free parameters. Notice that in Eq. (3.5.2), there are only seven axes of the rotation, since λ^8 commute with U_0 in Eq. (3.5.1). Instead, there is an additional quantization prescription,

$$J_8 = -\frac{N_cB}{2\sqrt{3}} = -\frac{\sqrt{3}}{2}, \quad Y' = -\frac{2}{\sqrt{3}}J_8 = 1, \tag{3.5.3}$$

where B is the baryon number, $B = 1$. This quantization was derived from the Wess-Zumino-Witten term in Skyrmion model to incorporate the anomaly, or originated in "valence" quarks in chiral quark soliton model [283]. Then the excitation spectrum of this rotation can be written as

$$E^J_{(p,q)} = M_{cl} + \frac{1}{6I_2}[p^2+q^2+pq+3(p+q)] + \left(\frac{1}{2I_1} - \frac{1}{2I_2}\right)J(J+1) - \frac{(N_cB)^2}{24I_2}, \tag{3.5.4}$$

where J is the spin and (p,q) denotes the SU(3) representation and we have explicitly written the quadratic Casimir by p and q. This provides the mass splittings of SU(3) multiplets as

$$\Delta_{\mathbf{10}-\mathbf{8}} = \frac{3}{2I_1}, \quad \Delta_{\overline{\mathbf{10}}-\mathbf{8}} = \frac{3}{2I_2}. \tag{3.5.5}$$

The flavor SU(3) breaking effect can be incorporated with the Hamiltonian

$$\Delta H_m = \alpha D^{(8)}_{88} + \beta Y + \frac{\gamma}{\sqrt{3}}\sum_{i=1}^{3} D^{(8)}_{8i}J_i, \tag{3.5.6}$$

where the first term is of the order of N_c while the rest terms are of N_c^0. This provides the mass splittings among the SU(3) multiplet, leading to the Gell-Mann–Okubo mass formulae, which take the form of Eq. (3.4.1) for the antidecuplet. In addition, thanks to Eq. (3.5.4), there is a relation between two masses of the different flavor multiplet. A famous example is obtained for the

$$8(m_{\Xi^*} + m_N) + 3m_\Sigma = 11m_\Lambda + 8m_{\Sigma^*}, \tag{3.5.7}$$

which is known as Guadagnini relation, and well satisfied up to 1% level.

3.5.2 Predictions and related studies

Among many studies of the exotic baryons, the paper by Diakonov *et al.* in 1997 [77] gave a strong influence on the later researches. They calculated the mass and width of the baryon antidecuplet in the chiral quark soliton model. The Θ^+ baryon (called Z^+ baryon at that time) was predicted with light mass (1540 MeV) and narrow width (less than 15 MeV), which partly motivated the experimental search by LEPS [16]. The important features in Ref. [77] are

(i) $N(1710)$ as an anchor,

(ii) Rigid rotator quantization, and

(iii) narrow width.

In the following, we consider these issues listing the related studies.

(i) In the rigid rotator approach the decuplet baryons are identified as the rotational excitation of the classical soliton. Therefore, it is natural to consider the next rotational excitation states. In flavor SU(3) case, this is the antidecuplet with $J^P = 1/2^+$. Whether this excitation really exists or not is the issue of (ii) and let us agree with the existence here. Then the mass of the antidecuplet is related with that of the octet by Eq. (3.5.5). The moment of inertia I_2 can be calculated by specifying a model, but it depends on the dynamics. In Ref. [77], it was *assumed* that the $N(1710)$ belongs to the antidecuplet representation, in order to determine the $\Delta_{\overline{\mathbf{10}}-\mathbf{8}}$.

Once we accept this point, the mass of the Θ^+ can be derived automatically by the Gell-Mann–Okubo rule. The mass splitting among the antidecuplet was determined by setting the SU(3) breaking parameters so as to reproduce the phenomenological inputs. As we see in Eq. (3.5.6), there are three parameters, α, β, and γ. Two constraints came from the empirical splitting of baryon octet and decuplet. The last constraint was fixed by the knowledge of the nucleon sigma term and the ratio of current quark masses. Using $\Sigma_{\pi N} = 45$ MeV, the mass of the Θ^+ appeared at 1530 MeV, accompanied by the other exotic cascade at 2070 MeV.

After the exotic Ξ was observed by NA49, the masses and widths of baryons were examined including $\Xi^{--}(1860)$ in the antidecuplet [236]. Following the general mass formulae for the antidecuplet as in Ref. [247], experimentally known resonances of $J^P = 1/2^+$ were examined, but no satisfactory identification was obtained. Based on this fact, to complete the antidecuplet, they concluded that the N and Σ partners of exotic states should be in the mass range of 1650-1690 and 1760-1810 MeV, respectively.

Instead of assigning the nucleon partner, more general result in the chiral soliton model was analyzed in Ref. [284]. With the moment of inertia I_2 calculated in the chiral soliton model and the recent determinations of nucleon sigma term $\Sigma_{\pi N} = 64 \pm 8 (79 \pm 7)$ MeV, the masses of the exotic states were found to be 1430 MeV $< m_\Theta <$ 1660 MeV and 1790 MeV $< m_{\Xi_{3/2}} <$ 1970 MeV, which were consistent with the experimental observations, but more precise determination required the additional assumptions. Representation mixing due to the SU(3) breaking effects was also studied. The effect found to suppress the Θ^+ decay width, while the width of the $\Xi_{3/2}$ was enhanced.

(ii) There are extensive discussion on the validity of the rigid rotator quantization in flavor SU(3) sector. It was argued in the context of the consistency with large N_c expansion [285]. The point was that the excitation energy of the Θ^+ due to the collective rotation is of the order of N_c^0, while the collective quantization of the classical soliton is valid for the excitation of N_c^{-1}. Indeed, in the large N_c limit, the mass difference between "$\overline{\mathbf{10}}$" (which coincides with the antidecuplet in $N_c = 3$) and "$\mathbf{8}$" (coincides with octet) is

$$\Delta_{\text{“}\overline{\mathbf{10}}\text{”}-\text{“}\mathbf{8}\text{”}} = \frac{3 + N_c}{4I_2}, \tag{3.5.8}$$

which reduces to Eq. (3.5.5) when $N_c = 3$. The rotational excitation energy of order N_c is outside regime of validity of the collective quantization. More detailed discussion can be found in Ref. [286]. This problem was further discussed in Ref. [287]. They introduced the label "exoticness" X[B)], the number of extra $\bar{q}q$ pair needed to construct the multiplet. The splitting among multiplets with same X was of the order of $\mathcal{O}(1/N_c)$, while that for the different X was $\mathcal{O}(1)$. Actually, the mass difference agrees with Eq. (3.5.8), and it was systematically generalized to the higher multiplets. However, the rotational angular velocities for exotic multiplets were of the order of $1/\sqrt{N_c}$, and the mixing of the rotational mode with the other degrees of freedom goes $1/N_c$, then they concluded that the description of the exotic multiplet was possible by the rotational quantization.

The validity of the rigid rotor quantization was studied in connection with the Skyrmion bound state approach [271], which is another quantization scheme of SU(3) Skyrmion [288]. These two approaches should coincide with each other when $m_K \to 0$. It was found that for small m_K, there was no bond state or resonance with $S = +1$, which might indicate the exotic state was an artifact of the rigid rotor quantization, at least for large N_c and small m_K. In this approach, the Θ^+ could be accommodated only when the large SU(3) breaking effect was introduced. On the other hand, the bound state approach was further extended in the vector manifestation scenario in the hidden local symmetry [289]. It was shown that the $S = +1$ bound state could be formed in the vector manifestation due to the vector K^* meson effect.

Using toy models [290, 291], the rigid rotator quantization scheme has been further tested. In Ref. [290] several toy models were examined, which had exact solutions and shared main symmetries with QCD. The rigid rotator approximation was then compared with the systematic large N_c expansion. The analysis raised doubts on the relevance of the rigid rotator approximation and existence of exotic states, at least within toy models used there. Comparison of the rigid rotor quantization with the bound state approach was made in Ref. [291] using a toy model. It was found that the Callan-Klebanov bound state approach was consistent with the numerical solution, while the rigid rotor approach was not.

On the other hand, there were studies to construct a correct quantization scheme along the same line with the rigid-rotator approach. In Ref. [292], collective quantization scheme in Skyrmion model was examined, focusing on the zero-modes of rotations. It was shown that four zero-mods out of seven in Eq. (3.5.2) would be eliminated by the Wess-Zumino term. This led to the absence of the $S > 0$ states in the rotational spectrum, and hence the Θ^+ did

[B)] The definition of the Exoticness was later corrected in Ref. [272].

not arise as a collective excitation in this approach. In Ref. [293] (see also Refs. [294, 295]), it was shown that once the modification of the rotational-vibrational approach was included, the rigid rotator quantization agreed with the bound state approach in the large N_c limit. Within this approach, the mass and width of the Θ^+ were calculated.

(iii) One of the influential results in Ref. [77] was the narrow width of the Θ^+. This was calculated including the $1/N_c$ correction. The narrow width was obtained by the cancellation of the two coupling constant

$$G_{\bar{10}} \sim G_0 - G_1 \sim 9.5. \tag{3.5.9}$$

This value actually vanishes in the nonrelativistic quark model limit of the chiral quark soliton model.

Notice, however, that the coupling constants are leading (G_0) and next to leading (G_1) orders of $1/N_c$ expansion. In Ref. [296], it was shown that the small width of the due to cancellation (3.5.9) could be valid when the flavor structure was properly taken into account. The narrowness of the width of the Θ^+ relative to the Δ was shown by estimating the N_c counting of the phase space factors.

There was a discussion on the arithmetic in Ref. [77]. Ref. [297] argued that the width of the Θ^+ predicted in Ref. [77] should be less than 30 MeV, not 15 MeV as written in the original paper. One can trace the subsequent discussions in Refs. [298, 299]. In any event, 30 MeV is still small compared with the ordinal resonances, and the conclusion of a narrow width in soliton model of Ref. [77] would not be changed.

In Ref. [300], wave functions for baryons were derived in the chiral quark soliton model. The presence of higher Fock components in baryons were discussed in both exotic and nonexotic baryons. The approach was further extended in Ref. [301], where the width of the Θ^+ was estimated as very small.

3.5.3 Skyrmion model

The Skyrmion model is one of the simplest approaches in the chiral soliton models. Here we show the results with this scheme. The mass of the Θ^+ was studied in the Skyrme model in Ref. [76], which was based on the results presented in 1987. [75]. The mass of the antidecuplet was calculated up to m_s^2 order, with which the absolute mass of the Θ^+ could be calculated without using the phenomenological input such as the $N(1710)$. In the Skyrme model, the SU(3) breaking effect was encoded by the first term of Eq. (3.5.6), and perturbation was performed up to the second order. Then the masses of the particles in octet and decuplet were expressed in terms of 4 parameters, and the mass of the Θ^+ could be calculated by the same parameters. Taking $\Sigma_{\pi N} = 60$ MeV and $m_s = 200$ MeV, the mass of the Θ^+ was obtained as 1534 MeV. Although the result was sensitive to the values of $\Sigma_{\pi N}$ and m_s, the light exotic state was naturally obtained in the Skyrme model framework.

Bound state approach for the Skyrmion was discussed in Ref. [271]. It was found that the Θ^+ could be accommodated only when the large SU(3) breaking effect was introduced. It s extension to the theory with vector meson in the hidden local symmetry was studied in Ref. [289], where the Θ^+ could be formed in the vector manifestation scenario.

Systematic calculations based on the minimal extension of the Skyrme model to SU(3) sector were performed in Refs. [302, 303, 304]. Mass spectra and splittings among different multiplets were evaluated with exotic sectors $\overline{\mathbf{10}}$ [302] and **27** [303] in addition to **8** and **10**. Moments of inertia, nucleon axial coupling were also calculated in Ref. [304].

Skyrmion model was applied to charmed states in Ref. [305] using flavor SU(4) collective quantization and the bound state approach for the heavy quark. Several charmed pentaquarks were predicted within this model.

The Skyrmion was studied in the context of the quark-hadron continuity [306]. It was shown that both the chiral soliton and Nambu-Goldstone bosons can exist in the region between the color-flavor-locking phase and the hypernuclear phase.

Representation mixing effect due to the flavor symmetry breaking was studied in the Skyrmion [307]. The masses and the decay widths of the **8**, **10**, and $\overline{\mathbf{10}}$ were evaluated in the second order perturbation. The mixing with the **27** representation was found to be important for the states in $\overline{\mathbf{10}}$.

In Ref. [308], the Lagrangian of the Skyrmion model was generalized to include more terms. The coefficients were fitted to reproduce the spectrum of the low-lying baryons, and the model was applied to the antidecuplet baryons.

3.5.4 Other calculations

Using the mass of $\Theta(1540)$, the spectrum of other states in higher dimensional representation (exotic and nonexotic) were estimated in chiral soliton model [309]. In this scheme, not only the symmetry breaking term of leading order in m_s, next to leading order operator were tested. It was found that the next to leading order term might not be negligible.

The mass spectrum of 27-plet was studied by fitting the parameters α, β, γ, I_1 and I_2 to experimental data [310]. To fix the parameters, in addition to the masses of octet and decuplet, masses of $\Theta^+(1540)$ and $\Xi^{--}(1860)$ were adopted. The obtained masses agree well with the experimentally known non-exotic resonances of spin $3/2^+$, including $\Xi(1950)$, whose spin and parity are not yet known. The width of the 27-plet was then studied in the same framework [311], up to linear order in m_s and $1/N_c$. The width of the Θ^* with spin $3/2^+$ and isospin $I = 1$ turned out to be less than 43 MeV. The 35-plet was also studied along the same line in Ref. [312].

In the same way as that in Ref. [236], the properties of the antidecuplet was studied, but with negative parity as well [313]. Since the symmetry relation was free form the parity, the negative parity states are assigned to the antidecuplet with $\Theta^+(1540)$ and $\Xi^{--}(1860)$. The masses of $N(1650)$ and $\Sigma(1450)$ were well reproduced with these exotic states. The widths of the $N(1650)$ was too wide to be a partner with the Θ^+, while the widths of the $\Sigma(1750)$ agree with the experiment. Therefore, if the scheme was correct, there should be a new negative parity resonance around 1.65 GeV, or the large SU(3) breaking effect takes place. Note however that the determination of the parameters in soliton model was based on the properties of the octet and decuplet baryons with *p*ositive parity.

In the chiral quark soliton model, the masses of flavor **27** states were calculated with the parameters determined in the paper by Diakonov *et al.* [314]. The mass and width of the

$I = 1$ Θ^* state in **27** was found to be 1595 MeV and 80 MeV, respectively. This scheme was further extended to calculate the **35** states as well [315], where the masses of $\Theta(1540)$ and $\Xi(1860)$ were used to determine the parameters. In this case, the $I = 1$ Θ^* state had a mass of 1599 MeV and became somewhat broad. A similar approach for the estimation of **27** but with the parameters in updated version of Diakonov *et al.* [236] can be found in Ref. [49].

In Ref. [316], using the observed mass of Θ^+, the pion-nucleon sigma term was extracted in the chiral quark soliton model. The masses of the Θ^+ and Ξ^{--} determined the value $\sigma_{\pi N} = (74 \pm 12)$ MeV which was consistent with the recent determination from the pion nucleon scattering data as well as the lattice QCD simulation.

Decay widths of decuplet and antidecuplet with representation mixing introduced by the SU(3) breaking effect were discussed in Ref. [317]. The importance of the mixing with 27-plet in the antidecuplet baryons was emphasized. The $\mathcal{O}(m_s)$ correction to the decay widths of baryon decuplet was found to be a factor 3 or more. Furthermore, $\mathcal{O}(m_s)$ correction was found to suppress the decay width of Θ by factor 0.17, relative to the width of Δ.

Corrections to the Gell-Mann–Okubo mass splitting for the ground state octet and decuplet were studied in the Skyrme model up to next to leading order of m_s [318]. The small experimental deviations from the GMO rule in these multiplets could be complemented by the correction terms with the mixture of the higher dimensional multiplets. This could be interpreted as an evidence for the existence of higher multiplets.

Radial excitations of the chiral soliton and their interplay with the rotational excitations were studied in Ref. [319]. The flavor SU(3) symmetry breaking was introduced, which led to the **8**-$\overline{\mathbf{10}}$ mixing as suggested by the Jaffe-Wilczek model. The predicted masses were in good agreement with observed spectrum.

Multi-baryon state was studied in the soliton model in Ref. [320]. Properties of possible Θ^+ hypernuclei were evaluated, as well as the anti-charmed and anti-bottomed states.

In Ref. [321], the soliton model was examined in the two-dimensional QCD, where the rotational and vibrational excitations were absent in the strong-coupling regime. Because of the absence of these modes, the analysis would be free from the controversial arguments on the quantization method in soliton models. The mass of the classical soliton and leading quantum corrections were evaluated.

Electromagnetic properties were also studied in the soliton models. Transition magnetic moments of the antidecuplet baryons to the octet baryons were evaluated in Ref. [322]. It was found that the transition of $n^* \to n$ and $\Sigma^* \to \Sigma$ were forbidden in the chiral limit, and would be small when the symmetry breaking effects were taken into account. This property was suggested to distinguish the nucleon resonance of the antidecuplet from others.

The magnetic moments of the Θ^+ and antidecuplet baryons were calculated in Ref. [323], in the context of the chiral quark soliton model in the chiral limit. Model-independent relations between magnetic moments were derived. By calculating the unknown parameter by the chiral quark soliton model, the magnetic moment of the Θ^+ was estimated as $\mu_{\Theta^+} = 0.2$-$0.3\mu_N$. The calculation was later extended to include the symmetry breaking correction [324] and in the context of recent measurements of baryon resonance [325] by SELEX [326] and GRAAL [327].

3.6 Constituent quark models

3.6.1 General features and interactions

Here we summarize the studies based on constituent quark models, in which the hadrons are constructed by the valence quarks with the constituent mass. Started in Ref. [328], the quark models have been providing a good description for overall spectra of mesons and baryons including excited states [329, 330, 331]. On the other hand, there are several problems in quark models. Several states such as pseudoscalar mesons, Roper resonance, $\Lambda(1405)$, etc. are not well reproduced in naive treatment. These states are considered to have other origin, say, goldstone bosons of symmetry breaking and chiral dynamics. The models predict many states which are not yet observed in experiments. There is no clear justification of the non-relativistic treatment of the quarks with schematic hyperfine interaction. Nevertheless, a great advantage of the quark model is that one can extract an intuitive information of hadrons.

In general, quarks are confined in a potential, and interacting each other *via* hyperfine interactions. The mass of a state in the constituent quark model is given by

$$M = \sum_i m_i + \delta M_k + \delta M_c + \delta M_{hf} \tag{3.6.1}$$

where m_i is the mass of the constituent quark i, δM_k is the contribution coming from the kinetic energy of quarks, δM_c is the contribution from the confining force, and δM_{hf} is the contribution from the hyperfine interactions. These δM contributions are calculated by taking the matrix element of the interaction Hamiltonian with the wave function of the state, which is constructed based on color-flavor-spin-orbital symmetry. A typical hyperfine interaction is the Color-Spin (CS) interaction, which originates in the one-gluon exchange between quarks. The effective hamiltonian for the CS interaction can be written as

$$H_{\rm CS} = -\frac{f_{\rm CS}(r)}{m_i m_j}(\lambda_i^c \cdot \lambda_j^c)(\boldsymbol{\sigma}_i \cdot \boldsymbol{\sigma}_j), \tag{3.6.2}$$

where λ_i^c ($-(\lambda_i^c)^*$) is the Gell-Mann matrix in color SU(3) space for quark (antiquark) labeled i, and $\boldsymbol{\sigma}_i$ are the Pauli spin matrix, and m_i is the constituent mass. $f_{\rm CS}(r)$ governs the interaction range and strength. Another choice is the Flavor-Spin (FS) interaction [330], which is generated by effective Goldstone boson exchange between quarks:

$$H_{\rm FS} = -\frac{f_{\rm FS}(r)}{m_i m_j}(\lambda_i^F \cdot \lambda_j^F)(\boldsymbol{\sigma}_i \cdot \boldsymbol{\sigma}_j), \tag{3.6.3}$$

where λ_i^F is the Gell-Mann matrix of flavor SU(3).

Concerning the pentaquark $uudd\bar{s}$ state, the sum of the masses of the five quarks are $\sum_i m_i \sim 1800$ MeV, when we choose $m_{u,d} \sim 300$ MeV and $m_s \sim 500$ MeV. This is rather high compared with the observed mass of the Θ^+ of 1540 MeV. In order to achieve the experimental value, we should expect the large attraction from the rest terms in Eq. (3.6.1). Since the quarks have parity $P = +$ and antiquarks have $P = -$, five-quark system without orbital excitation would have negative parity. For the state with angular momentum l, we will have $P = (-)^{l+1}$.

3.6.2 Hyperfine interactions in five-quark system

In Ref. [332], the mass of the $uudd\bar{s}$ state was studied with FS interaction in Eq. (3.6.3). It was found that the energy of the $l = 1$ state with totally symmetric four quarks in flavor-spin space becomes lower than that of $l = 0$ state, overcoming the kinetic energy. This led to the $J^P = 1/2^+$ for the ground state for $uudd\bar{s}$ pentaquark. Hence the ground state was the positive parity.

Comparison between CS and FS interactions for negative parity pentaquarks was made in Ref. [333], using the MIT bag model. For the mass splitting among the antidecuplet members, CS interaction provided the small value of 52 MeV, while the CS model gave rather large splitting of 155 MeV. The authors constructed general expression of wave functions of five-quark states in flavor antidecuplet. It was found that because of hidden $s\bar{s}$ component, the nucleon state was heavier than the Θ^+, in accordance with the GMO rule for the antidecuplet (3.4.1). The positive parity case was also considered by the same authors, utilizing the FS interaction [334]. Calculating the hyperfine interaction, mass splitting of ~ 120 MeV was obtained for the antidecuplet.

In Ref. [335], pentaquark states with $J^P = 1/2^{\pm}$ and $I = 0$, 1, and 2 were studied with both FS and CS interactions as well as the quark-antiquark interaction. It was found that the $I = 0$ state becomes the lowest one for both parities. In contrast to the results in Ref. [332], the negative parity state became lower than the positive parity state, when the quark-antiquark interaction through annihilation terms were included. The mass of the lowest $J^P = 1/2^-$ state was about 200-300 MeV higher than the experimental value of 1540 MeV. Further modifications were performed in Ref. [336], however the mass appeared still 200 MeV higher than the observed one. This might indicate the necessity of the dynamical calculation. In this direction, KN scattering state was studied by resonating group method based on the same model for s- and p-waves [337], and later for d- and f-waves as well [338], providing a good agreement with experimental data.

Excited states of heavy pentaquarks with positive parity were studied in Ref. [339] using CS and FS interactions. It was found that a denser level structure appeared above the ground state than the non-exotic baryons, because of the larger number of Pauli-allowed states in five-quark channels. Pattern of the excitations showed difference between CS and FS interactions.

In Ref. [340], the effect of the instanton induced ('t Hooft) interaction [341] was discussed using the MIT bag model. A strong attraction was obtained from the two-body part of the interaction, while the three-body force was repulsive. The mass of the $J^P = 1/2^-$ state was lowered about 100 MeV when the instanton induced interaction was introduced. Along the same line, $J^P = 1/2^+$ states were also studied in Ref. [342].

In the quark model study for the pentaquarks, importance of the quark-antiquark interaction and the role of the 't Hooft interaction were discussed in Ref. [343]. Reviewing the previous analyses, it was pointed out that the FS interaction did not affect very much the exotic states, once the $\bar{q}q$ interaction was taken into account.

Table 3.3: Quark correlations for the Θ^+ in Jaffe-Wilczek (JW), Karliner-Lipkin (KL), and Shuryak-Zahed (SZ) models.

model	Ref.	structure	orbital excitation	total J^P
JW	[344]	$[ud]_{\bar{\mathbf{3}}_c\bar{\mathbf{3}}_f\mathbf{0}_s} \otimes [ud]_{\bar{\mathbf{3}}_c\bar{\mathbf{3}}_f\mathbf{0}_s} \otimes \bar{s}$	$l = 1$ between diquarks	$1/2^+$
KL	[345]	$[ud]_{\bar{\mathbf{3}}_c\bar{\mathbf{3}}_f\mathbf{0}_s} \otimes [ud\bar{s}]_{\mathbf{3}_c\bar{\mathbf{6}}_f\mathbf{1/2}_s}$	$l = 1$ between clusters	$1/2^+$
SZ	[346]	$[ud]_{\bar{\mathbf{3}}_c\mathbf{6}_f\mathbf{1}_s} \otimes [ud]_{\bar{\mathbf{3}}_c\bar{\mathbf{3}}_f\mathbf{0}_s} \otimes \bar{s}$	$l = 1$ in tensor diquark	$1/2^+$

3.6.3 Quark correlations

The problem of the light mass and the narrow width may be resolved by introducing specific inter-quark correlations. Various effective quark interactions as well as phenomenological analysis predicts the strong correlation between quarks [52]. In the following, we show typical models of this kind, namely Jaffe-Wilczek (JW) model [344], Karliner-Lipkin (KL) model [345], and Shuryak-Zahed (SZ) model [346]. The structures of these models are summarized in Table 3.3.

JW model was proposed in Ref. [344]. An essential ingredient of this model was the strong quark-quark correlation in spin 0, color $\bar{\mathbf{3}}$ and flavor $\bar{\mathbf{3}}$ channel, which formed the diquark $\mathbb{Q}$[C)]. This channel is attractive either CS or FS interactions, as well as the instanton induced interaction [341]. In the JW model, the ud pair in $uudd\bar{s}$ state were correlated to construct two $\mathbb{Q}$s. Two diquarks should be combined in $l = 1$ state, because color should be $\mathbf{3}$ for two-diquark system in order to make color singlet with antiquark. This led to the $J^P = 1/2^+$ for the Θ^+. In this case, this state differs from the KN state in color, spin and spatial wave functions, so that the decay width is expected to be small. A similar idea for this configuration was also presented in Ref. [134].

Another important point introduced here is the representation mixing of flavor octet and antidecuplet, which naturally appears in the diquark model with flavor SU(3) breaking, since the four-quark state in this picture is in flavor $\mathbf{6}$, which produces $\mathbf{8}$ and $\overline{\mathbf{10}}$ by combining with the $\bar{\mathbf{3}}$ antiquark. These $\mathbf{8}$ and $\overline{\mathbf{10}}$ are degenerate in the SU(3) limit. If the SU(3) breaking is introduced by the schematic Hamiltonian

$$H_s = M_0 + (n_s + n_{\bar{s}})m_s + n_s\alpha, \tag{3.6.4}$$

the ideal mixing takes place where the $s\bar{s}$ component is diagonalized. Thus the $N(1440)$ and $N(1710)$ resonances were well fit in this simple scheme, and exotic Ξ state appeared at 1750 MeV, which was significantly lower than the prediction by chiral soliton model [77]. By assuming the same structure for the heavy pentaquarks Θ_c and Θ_b, the states were predicted to appear below thresholds for the strong decay and become bound states.

This scenario looks attractive, since it explains not only the low mass of the Θ^+, but also the Roper resonance, whose interpretation is still controversial. However, the inclusion of the $N(1440)$ in this scheme contain a difficulty to reproduce the large decay width of the $N(1440)$. It was pointed out in qualitative manner in a comment [347] to the original paper, and studied more quantitatively in Refs. [348, 349, 350]. In Ref. [348], An inequality was derived for the

[C)] The symbol $\mathbb{Q}$ will be used for the diquark in spin 0, color $\bar{\mathbf{3}}$ and flavor $\bar{\mathbf{3}}$ channel.

widths of the nucleon resonances and the Θ^+ under the ideal mixing. This inequality was badly broken by the experimental decay widths of $N(1440)$ and $N(1710)$ together with the width of Θ^+, if it is less than 1 MeV. It was also found that the wave functions of octet and antidecuplet should be identical (except for the flavor) for the ideal mixing. Assignment of the experimentally observed $J^P = 1/2^+$ resonances to the **8**-$\overline{\mathbf{10}}$ mixing scheme was done in Ref. [349] for general mixing angle. They found an inconsistency between the mixing angle obtained from the mass spectrum and that from the decay widths. More comprehensive study including the mixing with ground state octet and another octet at higher energy can be found in Ref. [351]. Application to the spin 3/2 particles was performed in Ref. [24], which we will explain later in chapter 10.

For the JW model with point like $\mathbb{Q}$ diquarks, QCD inequality was derived [352], which gave the lower limit for the mass of the Θ^+. In Ref. [353], $J^P = 1/2^-$ pentaquarks were studied in the JW model without orbital excitation. Two $\mathbb{Q}$s were combined in relative $l = 0$, then the flavor of four quark system became **3**, which was combined with $\bar{\mathbf{3}}$ of the antiquark to construct the **1** and **8**. As a result, several low lying pentaquark states with $J^P = 1/2^-$ were predicted. Mixing between the same charge members of exotic $\Xi_{3/2}$ and ordinary Ξ was discussed in Ref. [354]. A comparison of the quark model and soliton model was made in Ref. [355]. It was found that the quark model preferred large representation mixing, while the soliton model favored a small mixing.

KL model was given in Ref. [345], which was based on an unpublished paper [356]. This model describes the Θ^+ as a molecule of two clusters, a ud diquark and a $ud\bar{s}$ triquark, which are in relative p wave and are separated by a distance larger than the range of the color-magnetic force. The ud in the triquark is color **6**, flavor $\bar{\mathbf{3}}$ and spin 1, which is combined with an antiquark to form the triquark of color **3**, flavor $\bar{\mathbf{6}}$ and spin 1/2. Then the triquark is bound with another diquark with color $\bar{\mathbf{3}}$, flavor $\bar{\mathbf{3}}$ and spin 0, *via* the color-electric force. Naive mass estimation in Ref. [345] was about 1592 MeV. The study of the heavy flavored pentaquarks in this model was performed in Ref [357].

The masses of Θ^+ in JW and KL models were compared with the CS interaction [358]. It was found that the JW model gives a smaller mass than the KL model does. In KL model, the hyperfine interaction between diquark and triquark was shown to lower the energy further, which was not considered in the original KL treatment. The mass of charmed and bottomed pentaquark was also estimated in the JW framework.

This idea of KL model was examined with the instanton-induced interaction in Ref. [359]. The masses of the ud diquark and the $ud\bar{s}$ triquark were estimated as 440 and 750 MeV, respectively, which was reasonable to construct the Θ^+ in a relative $l = 1$ state. The triquark was also examined with the color-magnetic interaction in Ref. [360].

In quark cluster model with CS interaction, the favored configuration was found to be KL model [361]. Within the same model, masses and magnetic moments of the antidecuplet baryons were estimated. In Ref. [362] the triquark correlation was also investigated in the QCD sum rule approach including the direct instanton contributions.

A relativistic calculation for the width of the Θ^+ was performed in Ref. [363] based on the KL model. Varying a parameter for the size of the state, width was found to be very small. The method was applied to other pentaquarks [364] and also the structure of the

triquark [365].

Another description of the Θ^+ was proposed by Shuryak and Zahed in Ref. [346]. The diquark correlation was estimated based on the instanton liquid model. It was found that the Jaffe-Wilczek model has a large p-wave excitation energy, leading to $m_\Theta \sim 1880$ MeV. On the other hand, it was more reasonable to construct the Θ^+ state with one scalar diquark and one tensor diquark in relative s wave, where the tensor diquark is color $\bar{\mathbf{3}}$, flavor $\mathbf{6}$ and spin 1. The mass of this state was found to be 1550 MeV, closer to experimental value. This is because the absence of the relative angular momentum among clusters.

This idea was studied in the semi-relativistic effective QCD Hamiltonian approach assuming the diquark clustering [366]. It was shown that the SZ model indeed gave the lower mass than the JW model, when the mass of the tensor diquark was as small as that of the scalar diquark.

3.6.4 Diquark effective models

There are models which treat the diquarks as effective degrees of freedom in the field theory. In Ref. [367], diquark chiral effective theory was applied to the pentaquarks. The parameters in the model was fixed by the chiral symmetry and random instanton model. The model predicted the decay widths of the Θ^+ and Ξ^{--} to be very narrow, due to a large tunneling suppression of a quark between a pair of diquarks. Strong and radiative decays of the members of the octet-antidecuplet mixing scheme was studied in Ref. [368].

In Ref. [369], an estimate for the heavy pentaquarks based on diquark picture was performed. The mass of heavy pentaquarks with two diquarks of flavor SU(3) in relative s wave could be lower than the strong decay threshold. Possible weak decay modes of these states were discussed.

Treating the diquark as a point like particle, the form factors and magnetic moments were evaluated for the Θ^+ and Θ_c by solving the three-body problem in Ref. [370]. The valence antiquark was found to be embedded in the four-quark core, in contrast to the nucleon case.

Group theoretical point of view, the diquark $\mathbb{Q}$ is something similar to the antiquark. In this sense, it is possible to discuss the other related exotics by the replacement of $\mathbb{Q} \leftrightarrow \bar{q}$ in the diquark model for the pentaquarks.

Pentaquark states were discussed in connection with dibaryon, replacing an antiquark by a diquark [371]. Based on the diquark clustering, mass of a pentaquark state was estimated by the energy coming from orbital excitation, from Pauli blocking effect between quarks, and from pair annihilation effect of $q\bar{q}$, in addition to the sum of constituent quark and diquark masses. In this framework, pentaquarks with parity $P = -$ and flavor $F = \mathbf{8}$ and $\overline{\mathbf{10}}$ were related with dibaryons with $P = +$ and $F = \mathbf{8}$. In the same way, pentaquarks with parity $P = +$ and flavor $F = \mathbf{8}$ and $\mathbf{1}$ were related with dibaryons with $P = -$ and $F = 1$.

Possible exotic tetraquark state $ud\bar{s}\bar{s}$ was considered by replacing ud in the Θ^+ by $\bar{s}$. In Ref. [372], based on the KL model of triquark-diquark, a bound state of $ud\bar{s}$ and $\bar{s}$ was suggested as a candidate. A similar idea can be found in Ref. [373]. Other members of flavor multiplet was also studied. A dynamical calculation was performed in Ref. [374] for this state, and the mass was predicted as 1.4 GeV.

3.6.5 Calculations in quark models

The Θ^+ was interpreted as an isotensor $I = 2$ state in Ref. [375]. In this case, the decay of $\Theta^+(I = 2)$ into $KN(I = 0, 1)$ is isospin breaking, which is naturally suppressed down to a fraction of MeV. By constructing the $I = 2$ pentaquark state from quark model, possible assignment of spin and parity was found to be $J^P = 1/2^-$ or $3/2^-$. The result was further discussed in Ref. [376], in connection with the SAPHIR experiment[97], which did not see the Θ^{++}, possible production mechanisms, and Ξ^{--} decays in **35**-plet.

In Ref. [377], it was found that the parity of the ground state of $uudd\bar{s}$ system depends on the strength of the pion field in the chiral bag model [378]. The single particle energy of quarks in chiral bag was affected by the strength of the pion coupling at the bag surface. When the strength is small, which was close to the constituent quark model picture, the ground state was negative parity, while for the strong pion interaction, which was close to the Skyrmion, positive parity state becomes the lowest.

Magnetic moments of Θ^+ and exotic Ξ were studied in quark models [379]. They assume several inter-quark correlations such as Jaffe-Wilczek type, Karliner-Lipkin type, and Shuryak-Zahed type, in addition to the calculation based on MIT bag model. Comparison with several other approaches were also tabulated. Extension to the $J^P = 3/2^+$ states was performed in Ref. [380]. The similar calculation for the heavy pentaquarks were performed in Ref. [381].

In Ref. [382], the Θ^+ state was studied with FS interaction, which made the $J^P = 1/2^+$ lower than the negative parity state, as shown in Ref. [332]. A list of interpolating fields for Θ^+ was presented. The existence of spin-orbit partner with $J = 3/2$ was proposed, which was an inherent feature of the five-quark picture, and it made the difference from the chiral soliton models.

A complete classification of the five-quark wave functions was constructed in Ref. [383] based on the spin-flavor SU(6) symmetry. The lowest state was found to be isosinglet in antidecuplet representation. The magnetic moments of the antidecuplet baryons for the $J^P = 1/2^\pm$ and $3/2^+$ cases were calculated in this model [384]. A similar calculation but with the $3/2^-$ case can be found in Ref. [385].

A spin-orbit partner of Θ^+ with $J^P = 1/2^+$ was discussed in Ref. [386]. It was shown that the Θ^+ described by five-quark with $J^P = 1/2^+$ should imply the Θ^* state with $J^P = 3/2^+$, as mentioned in Ref. [382]. The mass of the Θ^* was estimated to be 100 MeV above the Θ state, and width was at least three times larger than that of the Θ.

In constituent quark models, the decay width of the Θ^+ into KN channel can be estimated, when the wave function of the initial state is known. In Ref. [387], width was calculated for the lightest configuration with the FS interaction [334], which was the positive parity state with spin 1/2. The overlap of the Θ^+ wave function with the KN state was found to be 5/96. Estimated width for this state was about 4.4 MeV, while the width of the negative parity state was about 1 GeV order. The decay width of $J^P = 1/2^+$ pentaquark with Jaffe-Wilczek type was studied in Ref. [388]. It was found that the spatial structure was essential for the decay width. When the size of pentaquark was similar to the usual hadrons, the decay width becomes of the order of 100 MeV, while an distorted "peanut" structure could lead to

the narrow width of ~ 1 MeV. In Ref. [389], decay of the Θ^+ was studied in quark model. Results for the $J^P = 1/2^\pm$ were qualitatively consistent with previous works, while a strong suppression of the Θ^+ decay for the $J^P = 3/2^-$ was pointed out.

Selection rules based on the SU(6) spin-flavor symmetry were derived in Ref. [390] for the $l = 1$ five-quark states. Observed Θ^+ and Ξ^{--} were assigned in the antidecuplet representation. Based on the wave functions of five-quark states in antidecuplet and octet, selection rules and relations between coupling constants were derived in Ref. [391]. Mass difference between Θ and Ξ was estimated in Ref. [392] using the phenomenological inputs.

The pentaquark states in antidecuplet representation were studied in the perturbative chiral quark model [393] for $J^P = 1/2^-$ and $3/2^-$ cases. The mass splitting of the states were evaluated by the sum of the contributions from quark masses, meson loops, and gluon loops. It was found that the spin $3/2^-$ state appeared about 185 MeV above the $1/2^-$ state, due to the gluon effects.

In Ref. [394] the width of the Θ^+ was investigated using the color molecular dynamics simulation. It was found that the probability of forming color singlet N and K was small, so that the width of the Θ^+ was suppressed.

The Θ^+ state was studied in Ref. [395], utilizing the Fock space expansion model, quark delocalization color screening model, and Jaffe-Wilczek inspired model. All the models were based on the constituent quark model with variational calculation, and the minimum of the Θ^+ mass was found at 1620 MeV, for the $J^P = 1/2^\pm$ states.

In Ref. [396], the magnetic moment of the strange quark was discussed in the JW, KL, and SZ models.

Dynamical study based on the flavor-spin interaction was performed in Ref. [397]. The mass of the antidecuplet including Θ^+ was studied by the interaction given in Ref. [332], and the mass of Θ^+ was adjusted by flavor-independent attraction, which was induced by the η meson exchange between $\bar{s}$ and light quarks. Then the mass of the Ξ^{--} appeared at 1962 MeV. The representation mixing with $\mathbf{8}$ was also introduce in this framework, in which the mixing could be induced by the hyperfine interaction as well as the mass term. The resulting mixing angle showed the value close to the ideal one.

In Ref. [398], the Θ^+ state was studied in the antisymmetrized molecular dynamics technique. They used the one-gluon exchange potential and linear confining potential, and calculated the masses of $J^P = 1/2^\pm$, $3/2^\pm$, and $5/2^\pm$ states. The masses of the $J^P = 1/2^\pm$ and $3/2^\pm$ states appeared nearly degenerated. The widths of the $J^P = 1/2^+$ and $3/2^+$ states were predicted to be narrow, and interpreted as the candidate for the observed Θ^+.

In Ref. [399], mass of the $uudd\bar{s}$ state was calculated for $TJ^P = 0\frac{1}{2}^-$, $0\frac{3}{2}^-$ and $1\frac{1}{2}^-$, which were considered to be the three lowest states from the group theoretical point of view. With the exchange of the gluon and chiral mesons, parameters were set to reproduce the observed masses of baryon octet, decuplet and vector mesons. The zero-point energy of the pentaquark was taken to be twice as large as that of the three-quark states. Among three states, the $J^P = 3/2^-$ state could have a very narrow width, so the authors identified this state as the Θ^+. The mass was about ~ 1680 MeV, which was 80 MeV higher than the mass of the $J^P = 1/2^-$ state. The qq correlation was also investigated, and the effect was important to reduce the mass up to 1680 MeV. The result was also presented in Ref. [400], with the result

of $1/2^+$ states.

The KN scattering state was also included in the dynamical calculation for the Θ^+ with color magnetic interaction in Ref. [401]. The mass was obtained around 2 GeV for the $J^P = 1/2^\pm$ states. The widths of the states were evaluated in the phase shift, and the $1/2^-$ state had a very narrow width of 0.12 MeV, in spite of the large phase space.

The Θ^+ with $J^P = 1/2^\pm$ were studied in Ref. [402] with FS and CS interactions. A dynamical study with one-gluon exchange can be found in Ref. [403]. In view of these dynamical calculations, the light mass of 1540 MeV for the $uudd\bar{s}$ system seems to be difficult.

3.7 Other models and approaches

3.7.1 Hadronic molecule

The interactions among hadrons have been studied for long time. Chiral perturbation theory allows us to calculate the interactions systematically. It is possible to observe, for instance, the scattering lengths directly in experiments. This is an advantage compared with the quark pictures, where the effective interaction of quarks is not directly tested. Therefore, it is natural to expect that the Θ^+ can also be described in terms of hadronic degrees of freedom.

The simplest way to describe Θ^+ in hadronic molecule is the resonance of K and N. A resonance state of KN system was discussed in non-relativistic potential model [404]. It was shown that the centrifugal barrier in $l = 1$ state was not enough to reproduce the width of Θ^+. Possibilities of resonances in higher partial waves were discussed. The decay width of Θ^+ was studied by low energy scattering theory of K and N [405]. It was found that the orbital angular momentum should be two or greater in order to have very narrow width < 1 MeV. A qualitative discussion on this issue was already presented in Ref. [344].

Mixing of the five-quark state and meson-baryon molecule state was discussed in Ref. [406] using an effective potential. In this scheme, the narrow width can be naturally explained by the destructive interference effect.

As we have seen, by considering the interaction at hadron level, it is hard to construct the Θ^+ by K and N, unless they are in relatively higher partial waves. On the other hand, there is a possibility of constructing πKN three-body bound state, since the mass of Θ^+ is only 30 MeV below the πKN energy. In addition, the decay width is suppressed because of the absorption of π, which requires the $l = 1$ excitation.

This idea of the πKN bound state was first explored by resonating group method in Ref. [407]. It was found that the repulsive interaction between K and N in s wave was compensated by the attraction in other channels of $\pi N(I = 1/2)$ and $\pi K(I = 1/2)$. This combination leads to the $I = 0$ and $J^P = 1/2^+$ state for the Θ^+, which coincides with the prediction by the chiral soliton models. However, the strength of the attraction was not enough to bind the total three-body system. The model was applied for the exotic cascade $\Xi^{--}(1860)$ [408] and for the heavy quark sectors [409].

The πKN bound state was studied in detail by chiral unitary model [410]. Two-body interactions of meson-meson and meson-baryon, as well as the three-body forces were derived

from the chiral Lagrangians, and the amplitude was iterated infinitely by the Bethe-Salpeter equation. An attraction was found in $I = 0$ and $J^P = 1/2^+$ channel, but the interaction was not enough to provide the binding energy observed in experiment, if the Θ^+ were the three body bound state.

In Ref. [411] $K\pi N$ bound state conjecture was studied with hypothetical $K\pi$ bound state X, which had not been detected experimentally. The $K\pi$ interaction was assumed to be so strong that there was the bound state. Then the properties of the Θ^+ could be naturally explained.

The similar idea for the $K\pi N$ bound state but with $I = 1$ and $J^P = 3/2^-$ was examined in Ref. [412] based on the resonating group method. Possible configuration mixing with ΔK state was introduced. The energy of this state appeared close to the threshold of the $K\pi N$ system.

Based on the three-body bound state picture, the effect of two-meson cloud for the Θ^+ [413] with $J^P = 1/2^+$ and for the antidecuplet baryons [21] were studied, by estimating the self-energies for two-meson loop. The self-energies turned out to be attractive, with the strengths compatible with the previous attempt in a different point of view [410]. We will discuss this topic in chapter 9. The two-meson couplings were studied in the $J^P = 3/2^-$ case and with the representation mixing in Ref. [23], which were applied to the reaction processes of the Θ^+ productions. The topic will be discussed in chapter 11.

In the chiral unitary model of the scattering of an octet meson and a decuplet baryon, the $S = +1$ state with $I = 1$ and $J^P = 3/2^-$ was studied in Ref. [414], which was later extended to more general cases [415]. Based on the chiral Lagrangians, an attraction was found in ΔK channel, which led to the generation of a pole dynamically. However, the existence of the pole was found to be sensitive to the input parameters. The attraction in ΔK channel was consistent with that found by resonating group method based on the chiral quark model [338, 416], which also led to the formation of bound state in this channel.

Molecule state of a vector meson with a baryon was considered in Ref. [417], as in the similar approach with the chiral unitary model. The Weinberg-Tomozawa interaction was extended to the interaction between vector mesons and baryons, and iterated using the Bethe-Salpeter equation. A bound state of K^*N was found around 1.7-1.8 GeV, which had $J^P = 2/3^-$.

The meson-baryon molecule picture for the charm sector was studied in Ref. [418]. An exotic state was found at 2.78 GeV, below the DN threshold.

3.7.2 Flux tube picture

Hadronic flux tube picture of the Jaffe-Wilczek model was first mentioned in Refs. [252, 143] as a possible structure of the Θ^+. This picture was examined by effective Hamiltonian approach to QCD [419, 420]. Assuming the ud diquark clustering, they solved a three-body problem using string tension and strong coupling constants [419] or instanton-induced force [420]. The mass for Θ^+ was obtained above 2 GeV for both parities. Non-exotic $uudd\bar{d}$ state was predicted also above 2 GeV, which was too high to be assigned for $N(1440)$. The model was also applied to the heavy quark sectors [421]. On the other hand, the mass of the Θ^+ can be lower than 1.7 GeV with color $\bar{\mathbf{3}}$ and $\mathbf{6}$ diquarks, when the masses of two diquarks are

similar [366].

Pentaquark states were studied in the dual gravity theory of QCD based on the AdS/CFT correspondence in the string theory [422]. The masses of pentaquarks were calculated by the length of the string between quarks in the theories dual to the supersymmetric and ordinal QCD. The narrow decay width of the Θ^+ was explained by the cost to make a flux loop in the recombination from Θ state to the NK state.

An explanation of the narrow width of the Θ^+ was made in Ref. [423] based on the string picture of the hadrons. In this picture, the decay of the pentaquark state required the creation of a pair of Y-shaped junctions. A large excitation energy was needed for such gluonic excitation processes and therefore the decay width should be suppressed.

The Θ^+ was discussed in the hadron string model [424]. Assuming the Jaffe-Wilczek type structure, the mass of the Θ^+ appeared 290 MeV above the observed mass. A structure in which the $\bar{s}$ was not at the end of the string was suggested to reproduce the low mass of the Θ^+.

3.7.3 Miscellaneous studies

There was a discussion on the narrow width of the Θ^+. In Ref. [425], super-radiance mechanism was proposed for a possible explanation of the narrow width. When two overlapping resonances exist and interact each other through the coupling to the continuum, a narrow state (and a broad state) can be produced. A similar idea was proposed in Ref. [426].

Relativistic five-body equations were studied for the Θ^+ states with spin $1/2^{\pm}$ and $3/2^{\pm}$ [427] and for $5/2^-$ [428]. The formulation was also applied to the widths of the Θ^+ [429].

In the context of duality between Regge pole and s-channel resonance contribution, the existence of exotic baryons was argued [54], based on the study in Ref. [61]. A consistent description of baryon-antibaryon scattering required the presence of mesons with exotic flavor quantum numbers, which had a small decay width due to the generalized OZI rule. In the same way, consistent description of the scattering of these exotic mesons with baryons demanded the existence of exotic baryons. The generalized OZI rule indicated the small coupling of the exotic baryon to ordinary meson and baryon, while it gave large coupling to the two mesons and one baryon state. A similar argumentation can be found in Ref. [430].

Non-leptonic decay of heavy pentaquarks was discussed in Ref. [431] by soft-collinear effective theory. Possible decay channels such as $\Theta_b^+ \to \Theta_c^0 \pi^+$ and $\Theta_c^0 \to \Theta^+ \pi^-$ preserve the diquark structure of these states. Since the decays were Cabibbo-allowed and the all final states were charged particles, search for these states were promising.

The five-quark state can have spatially non-planar structure, which was absent for two- or three-quark states. A diamond structure for the Θ^+ was investigated [432], where the $\bar{s}$ was in the center of the regular tetrahedron and the u and d quarks are at the corners of the tetrahedron.

The decays of the pentaquarks were studied in the light-front quark model. The week decays of heavy pentaquarks [433] and strong decays for light and heavy pentaquarks [434] were evaluated, based on the Jaffe-Wilczek model.

The calculation based on a schematic model [435] was performed for the pentaquark [436].

In the model, the constituent quarks and gluons interact *via* phenomenological interaction, which is fixed by the observed states. The $uudd\bar{s}$ state with $J^P = 1/2^-$ was predicted to be 1.5 GeV, which was assigned to the Θ^+.

3.8 In-medium properties and Θ^+ hypernuclei

At finite temperature and density, properties of hadrons such as masses, widths, and coupling constants can change from the values in vacuum, due to medium effects. In this section, we discuss the in-medium properties of the Θ^+ and possible formation of Θ^+ hypernuclei based on the medium effects.

In Ref. [437], medium effects on Θ^+ were investigated for negative and positive parity states. The authors estimated the in-medium self-energy of Θ^+ into KN channel, with Pauli blocking on nucleon propagator and mass modification of the nucleon. The mass modification of Θ^+ depending on the density was observed. Obtained potential was not strong enough to make bound states at normal nucleon density, but relatively large binding energy was observed at higher density region.

A schematic model for nucleon with $q\bar{q}$ pair excitation was developed to describe the Θ^+ with positive parity [438]. Collective excitation of $q\bar{q}$ pair led to the low mass of Θ^+, and accounted for the small decay width into the KN channel. Virtual coupling to K^*N was found to be large compared with the KN mode. Within this model, it was found that ΘN interaction could be strongly attractive, and the Θ^+ hypernuclei became stable against the strong decay.

Cabrera *et al.* [413] calculated the medium effects due to the πKN intermediate state, in addition to KN channel studied previously [437]. The coupling constants for the new channel were determined by assuming that the $N(1710)$ was an SU(3) partner of Θ^+. This new channel gave appreciable attractive potential, indicating the appearance of well separated bound states of Θ^+ in nuclei. On the other hand, the KN channel gave only tiny effect, consistent with the previous works qualitatively, reflecting the small decay width of Θ^+ in vacuum. The Θ^+ potential at normal nuclear density was obtained as -60 to -120 MeV, where uncertainty came from those in cutoff parameter and inputs. Solving the Schrödinger equation with obtained potential, many bound states were found in ^{12}C and ^{40}Ca.

With the model developed in Ref. [413], the production of Θ^+ hypernuclei was studied in Ref. [439]. The reaction was (K^+, π^+) on the ^{12}C target, with the initial kaon kinetic energy $T_K = 300$ MeV in Laboratory frame. This reaction was suitable for the Θ^+ hypernuclei, since the momentum transfer was small compared with the (γ, K^-) and (π^-, K^-) reactions. In the obtained spectrum, reasonably large separation between states was observed, which could be detected in experiments. Several recoilless productions for the Θ^+ hypernuclei were suggested in Ref. [440].

In Ref. [441], the Θ^+ hypernuclei was studied within relativistic mean field (RMF) formulation [442], as in the same way with usual Λ hypernuclei. Lagrangian for Θ was introduced with the similar structure as that of nucleons. The coupling constants of σ- and ω-Θ were

deduced from the quark meson coupling model as

$$g_\sigma^\Theta = \frac{4}{3} g_\sigma^N, \quad g_\omega^\Theta = \frac{4}{3} g_\omega^N, \tag{3.8.1}$$

essentially reflecting the number of u and d quarks. Several quantities were calculated for Θ in ^{6}Li, ^{12}C, ^{16}O, ^{40}Ca, and ^{208}Pb. Large separation between two deepest bound states were observed, which makes the experimental detection easier. The shrinking effect was found for light nuclei, as in the Λ hypernuclei. Although the result was depending on the unknown parameters, such as the ratio of the nucleon mass in the medium and the coupling constants, the Θ potential was estimated as -50 to -90 MeV at normal nuclear density. In the same framework, the πKN structure was also studied in Ref. [443]. It was found that a shallower potential than the point like treatment was obtained for this structure.

The medium effect of the Θ^+ in the QCD sum rule framework was studied in Ref. [444]. The scalar and vector self-energies were estimated by the sum rule with the medium effect included in the condensates [445]. The interpolating current was the same as that in Ref. [446], and the sharp pole hypothesis was adopted in the medium. They found that the scalar self-energy was positive and vector one was negative, which was originated from the existence of the antiquark in the Θ^+ interpolating field. The cancellation of scalar and vector terms led to the moderate size attraction of the Θ^+ in the medium.

Modification of Θ^+ mass and width with respect to temperature was studied as well as the density dependence [447]. They evaluated the self-energy at KN one loop level as in Ref. [437], but with the modification of nucleon mass based on the NJL model. With ΘKN coupling, pseudoscalar and pseudovector were used. In general, the modification was prominent in positive parity case, and the density dependence of the width was rather large.

In Ref. [448], quark mean field model [449, 450] was applied to the Θ^+ hypernuclei. The framework was similar to the RMF approach [441], but the coupling constants of σ- and ω-Θ were calculated within the quark mean field approach, which gave the different value for $g_\sigma^\Theta = (\partial M_\Theta^*/\partial\sigma)$ from Eq. (3.8.1), reflecting the self-consistent equations. It was found in Ref. [441] that the single particle energy was sensitive to this coupling constant. Furthermore, in the QMF framework, since the Θ^+ was constructed from five quarks in the ground state, the parity of the Θ^+ was negative, while it was not fixed in RMF. The Θ^+ bound states were calculated for $^{16}_{\Theta}$O, $^{41}_{\Theta}$Ca and $^{209}_{\Theta}$Pb were calculated.

The K^+-nucleus interaction was studied in Ref. [451], where the deviation from the impulse approximation has been discussed for long time. The authors argued that the discrepancy could be resolved by the kaon absorption via $K^+nN \to \Theta^+N$. The cross section of some reactions for pentaquark production were estimated. An extended discussion can be found in Ref. [452].

Kaon optical potential was studied in Ref. [453], based on the Jülich potential and including the effect of the Θ^+. The effect of the Θ^+ due to the two-nucleon absorption $KNN \to \Theta^+N$ was found to be important, which was derived from the two-meson coupling developed in Ref. [413].

In Ref. [454] mass formula for the hypernuclei was derived from spin-flavor SU(6) symmetry. The formula was used to predict the Θ^+ hypernuclei.

Table 3.4: In-medium Θ^+ potential around $\rho \sim \rho_0$ ($k_F \sim 270$ MeV) found in several models.

	J^P	V [MeV]	model
Kim *et al.* [437]	$1/2^{\pm}$	$-$(a few)	in-medium self-energy (KN)
Miller [438]	$1/2^+$	-490	schematic $\bar{q}q$ interaction
Cabrera *et al.* [413]	$1/2^+$	-60 to -120	in-medium self-energy (KN and $K\pi N$)
Zhong *et al.* [441]	$1/2^{\pm}$	-50 to -90	Relativistic Mean Field
Navarra *et al.* [444]	$1/2^-$	-40 to -90	QCD sum rule
Shen *et al.* [448]	$1/2^-$	-50	Quark Mean Field
Zhong *et al.* [443]	$1/2^-$	-37.5	Relativistic Mean Field ($K\pi N$ structure)

In-medium properties of the Θ^+ was studied in quark meson coupling model in Ref. [455] for difference strange quark masses. The KN decay channel of the Θ^+ was considered, which gave a small correction to the width. The properties of the $\Xi_{3/2}$ state in nuclear matter was also studied in Ref. [456].

The obtained values for Θ^+ potential are summarized in Table 3.4. It is interesting to note that the potential becomes reasonably attractive when the coupling of Θ^+ to the channels other than KN are taken into account. The strength of potential is not very strong with KN channel only. Therefore, strictly speaking, the strong attractive potential can be obtained with some coupling constants that can not be determined directly from experiments. On the other hand, the experimental observation of Θ^+ hypernuclei imply the existence of the coupling of Θ^+ to various channels. Hence, the estimation of such coupling constants is important for the study of in-medium properties of Θ^+.

3.9 QCD sum rule approaches

In the QCD sum rule approach [457, 458, 459], the correlation function of an interpolating operator can be calculated using the operator product expansion (OPE) in the deeply Euclidean region, which is compared with the phenomenological parametrization. The two-point correlation function can be written as

$$\Pi(p) = i \int d^4x e^{ipx} \langle\, 0 \,|T\{\eta(x)\bar{\eta}(0)\}|\, 0 \,\rangle, \tag{3.9.1}$$

where $\eta(x)$ represents the interpolating field of the state of interest. This correlation function is evaluated in phenomenological side and OPE side. Thus the properties of hadrons are related with the QCD through vacuum condensates. The approach has been applied to the baryon sector [460, 461, 462]. It is also possible to extract the quantities such as magnetic moment and the coupling constants. One way is to introduce an external source field, and the other way is to evaluate the three-point function.

There are some subtleness in the approach, such as the choice of the interpolating operator, convergence of the OPE, value of higher dimensional condensates, dependence of the result on Borel mass and threshold energy, and so on. In principle, these problems are common with the study of the ordinary three-quark baryons. On the other hand, it has turned out to

be important that there is a problem peculiar to the five-quark state, namely, the existence of the meson-baryon continuum state in the correlator.

3.9.1 Mass of spin $1/2$ Θ^+ state

The pentaquark $\Theta(uudd\bar{s})$ state was first studied with the QCD sum rule approach in Ref. [463]. The colored NK type operator with $I = 0$ was used as interpolating field, as well as the $I = 1$ and 2 operators. Taking the chiral even terms into account, sum rule was obtained up to dimension (to be). All the masses of $I = 0, 1$, and 2 states appeared close to 1.5 GeV.

In Ref. [464], the $uudd\bar{u}$ states were examined in addition to Θ^+, with the linear combination of two interpolating currents which were products of two scalar ud diquarks and products of two pseudoscalar diquarks. Taking the chiral even terms, sum rule was derived up to linear order to m_s. The Θ^+ state appeared at 1.55 GeV, while the $uudd\bar{u}$ state appeared at 1.44 GeV. Thus, the $uudd\bar{u}$ state was interpreted as the Roper resonance $N(1440)$, as indicated by the Jaffe-Wilczek model.

In the QCD sum rule approach, the parity projection was first performed in Ref. [446] The projection is important since the two-point correlation function contains contributions from both parity states. The authors used operator of the product of scalar and pseudoscalar diquarks, and took chiral odd terms into account, in addition to the chiral even terms. The contribution from chiral odd terms had opposite sign for the negative and positive parity states, and therefore, the effect was essential for parity projection. The negative parity state appeared at around 1.5 GeV, while for the positive parity state, the spectral weight became negative.

Diquark clustering in the Θ^+ was also studied in Ref. [465], but with a different interpolating operator, which include a derivative in the field. The mass of Θ^+ was obtained at 1.64 ± 0.15 GeV, and $uudd\bar{u}$ state at about 70 ± 50 MeV below the Θ^+, which would be identified as the $N(1440)$.

The above approaches were criticized in Ref. [466], where the importance of two-hadron reducible contribution was discussed. The problem is characteristic for the study of exotic particles, such as Θ^+, whose interpolating field can be decomposed into the product of color singlet meson and singlet baryon. In this case, the correlation function contains propagation of two particles without interaction, which was called two-hadron-reducible (2HR) part. It was pointed out that the correlation functions in previous works [463, 464, 446] had included large amount of the 2HR parts. Taking the correlation function in Ref. [446] as an example, numerical calculation was performed, leading to the opposite conclusion of parity after removing the 2HR contribution.

An analysis based on QCD sum rule was performed in Ref. [263] with a new operator of KN type but with tensor diquark in N part. This operator had an advantage of not having the 2HR contribution, because the tensor diquark had $d_l d_l$ or $d_r d_r$ quark components and the nucleon operator had $d_l d_r$. With sum rule up to dimension 13 operators, the mass of Θ^+ was obtained about 1.6 ± 0.2 GeV, and parity was positive.

The problem of the KN scattering state was further considered in Refs. [467, 468]. The

soft-kaon theorem was used in order to extract the KN contribution. The contribution from KN state was found to be 10% in the sum rule, and the conclusion in Ref. [446] was again considered to be valid.

Application of the finite energy sum rule to the Θ^+ was performed in Ref. [469], where the importance of finding Borel window was emphasized.

3.9.2 Studies for other pentaquarks

Here we summarize the QCD sum rule analyses for other pentaquarks.

The anti-charmed pentaquark state Θ_c was studied in Ref. [470] using the interpolating operator used in Ref. [446] with replacement $\bar{s} \to \bar{c}$. They obtained the mass around 3.1 GeV, which was consistent with the H1 experiment [157]. The parity of the state turned out to be positive, in contrast to the Θ^+ case [446]. This was mainly due to the difference of the treatment of the charm quark mass, which was kept finite. A more comprehensive analysis can be found in Ref. [471], where the $uuds\bar{c}$ states were studied as well. After subtracting the DN continuum, a signal for stable $uudd\bar{c}$ state with positive parity was found, where OPE was convergent.

The Ξ^{--} state was also studied in the QCD sum rule approach [472], using two diquark type interpolating currents analogous to those used in Refs. [464, 446]. The mass around 1.9 GeV was obtained from both currents. Although the mass was in agreement with the experiment [145], some properties such as OPE convergence and pole dominance were different from each other.

Doubly charged Θ^{++} state was studied in Ref. [473]. It was found that the $J = 3/2$ and $I = 1$, negative parity state could exist at $1.5 \sim 1.6$ GeV. Since its decay into KN state was strongly suppressed because it was in d wave. There was a possibility of the existence of the $J^P = 3/2^+$ state, which appeared close to the $3/2^-$ signal, but its decay width might be broad, due to p-wave nature of the decay. Spin 3/2 states were further purchased in Ref. [474] for $I = 0$ state as well. In addition to the previously obtained $I = 1$ negative parity state, isoscalar state with $J^P = 3/2^-$ was also found at slightly higher mass region: 1.5-1.7 GeV. It was pointed out that the higher spin state appeared in the same energy region as the $J = 1/2$ states obtained by other groups.

In Ref. [475], finite energy sum rule was applied to the spin 3/2 pentaquarks. It was found that the OPE convergence could take place only when the threshold parameter s_0 was chosen above 10 GeV^2.

The sum rule was obtained up to dimension $d = 13$ operators in Ref. [476], including direct instantons. The sum rule converged and the evidence was found for the positive parity state.

As noted by the authors in Refs. [469, 475] an important process of the QCD sum rule is to find the Borel window, in which the sum rule is reliable.

3.9.3 Estimation of coupling constants

Using an external source field, or evaluating the three-point function, it is possible to extract the information of the coupling constants in the QCD sum rule approach.

In Ref. [477], magnetic moment of Θ^+ was calculated within the QCD sum rule approach. The interpolating field and correlator were calculated based on the mass sum rule developed in Ref. [463]. Introducing the electromagnetic vertex, magnetic moment was extracted using the light cone QCD sum rule, where the photon light cone distribution amplitude was used as an input. The result was obtained as $|\mu_{\Theta^+}| = (0.12 \pm 0.06)\mu_N$. A different approach was taken in Refs. [478, 479] to estimate the magnetic moment of the Θ^+, obtaining $|\mu_{\Theta^+}| = (0.24 \pm 0.02)\mu_N$ [478] and $|\mu_{\Theta^+}| = -(0.11 \pm 0.02)\mu_N$ [479].

The decay width of the Θ^+ was studied by evaluating the three-point function to extract the coupling constant in Ref. [480]. It was found that the width could be narrow for the positive parity state, while the narrow width was difficult to reproduce for the negative parity state. In Ref. [481], however, the width $\Gamma < 4$ MeV was obtained for the negative parity case.

3.10 Lattice QCD simulation

In this section, we overview the studies of pentaquark baryons with lattice QCD simulations. Lattice QCD [482, 483] is a powerful tool to study the non-perturbative phenomena from first principle of QCD. Discretizing the space and time, one can numerically evaluate the expectation value of given operator by path-integral method in Euclidean space. It has also been successful in the hadron spectroscopy. All the studies for the pentaquarks available so far have been done in quenched approximation, in which the pair creation and annihilation of quarks do not occur. In general, one should keep in mind that there should be some quenching errors. Although the quenched simulation has been successfully reproducing the spectrum of three-quark baryons, it is not trivial that the approximation also works for the pentaquark state.

3.10.1 Mass of the pentaquark states

In this subsection, we review the lattice calculations for the masses of the pentaquark states, which are extracted from the correlation function of some pentaquark interpolating operators. Pentaquark spectroscopy is complicated due to the presence of two-particle scattering state below the resonance energy, which can couple to any operators even in the quenched approximation. This is in contrast to the three-quark baryons on the lattice, which cannot decay. Therefore, the discrimination of the signal from the scattering state is essential in these studies. The details of the simulations in these studies are summarized in Table 3.5 for $J = 1/2$ and in Table 3.6 for $J = 3/2$.

Csikor *et al.* [484] calculated the isoscalar and isovector states in both parity channels. The interpolating operator used there was the colored NK type:

$$\eta_{0/1} = \epsilon^{abc}[u_a^T C\gamma_5 d_b]\{u_e \bar{s}_e i\gamma_5 d_c \mp (u \leftrightarrow d)\}, \tag{3.10.1}$$

which is the product of the N and K operators but with the color indices of N and K are exchanged. The parity projection was performed by applying the projection operator to the correlator, which was confirmed by independent method using periodic and antiperiodic boundary conditions. Possibilities of scattering state was investigated by checking the volume

Table 3.5: Summary of the simulation setup of lattice QCD studies for spin $J = 1/2$ pentaquark Θ^+ states. We represent "Dw" for the domain-wall fermion, "LW" for the Luscher-Weisz plaquette plus rectangle action, and "FLIC" for the fat-link irrelevant action.

Ref.	gauge	fermion	size	configs.	lowest m_π
Csikor [484]	Wilson	Wilson	$(10\text{-}20)^3 \times (24\text{-}36)$	90-726	420
Sasaki [485]	Wilson	Wilson	$32^3 \times 48$	240	600
Chiu [486]	Wilson	Dw	$20^3 \times 40$	100	440
Mathur [487]	Iwasaki	overlap	$(12,16)^3 \times 28$	80	180
Ishii [488]	Wilson	clover	$12^3 \times 96$	504	656
Lasscock [489]	LW	FLIC	$20^3 \times 40$	200-340	464
Takahashi [490]	Wilson	Wilson	$(8\text{-}12)^3 \times 24$	950-2900	440

Table 3.6: Summary of the simulation setup of lattice QCD studies for spin $J = 3/2$ pentaquark Θ^+ states.

Ref.	gauge	fermion	size	configs.	lowest m_π
Lasscock [491]	LW	FLIC	$20^3 \times 40$	290	464
Ishii [492]	Wilson	clover	$12^3 \times 96$	1000	658

dependence and 2×2 correlation matrix method with the NK type operator. Finally, they concluded that the isospin 0 and negative parity state had the lowest mass, which was close to the observed mass of Θ^+.

In Ref. [485], the diquark-diquark type operator

$$\Theta^1_+ = \varepsilon_{abc}\varepsilon_{aef}\varepsilon_{bgh}(u_e^T C d_f)(u_g^T C\gamma_5 d_h)C\bar{s}_c^T, \tag{3.10.2}$$

was introduced to calculate the $I = 0$ pentaquark states in both parity channels. Notice that the local operator with scalar and pseudoscalar diquarks was used, in contrast to the original Jaffe-Wilczek model, which was the combination of two scalar diquarks with orbital angular momentum $l = 1$. The lowest state was negative parity state, which located slightly above the NK threshold. The positive parity state had much heavier mass and the assignment for $\Theta(1540)$ was not possible. Therefore, the conclusion was that the parity of the observed state should be negative. In this work, the anti-charmed pentaquark $\Theta_c(uudd\bar{c})$ was also studied. The interpolating operator was the diquark type with replacement of $\bar{s}$ by $\bar{c}$. The lower state was the negative parity state, and it appeared above the DN threshold.

Pentaquark states were studied by using the domain-wall fermion in Ref. [486]. This action has the (extended) chiral symmetry in the continuum limit. Signals were found in both parity channels. The state in negative parity was at 1424 ± 57 MeV, being consistent with $m_K + m_N$. Therefore, it was identified as the KN scattering state. On the other hand, the signal in positive parity did not behave as any of possible scattering state, so they concluded that the pentaquark state observed in experiment had positive parity.

The study in Ref. [487] used the chiral fermion action for $I = 0, 1$ states with parity $P = \pm$. The overlap fermion preserves exact chiral symmetry on the lattice, and allows one to work at small quark masses $m_\pi \sim 180$ MeV. The operator adopted in this study was the simple

KN type operator:

$$\chi_1^{\mp} = \epsilon^{abc} \left(u^{Ta} C\gamma_5 d^b \right) \left[u^c (\bar{s}^e \gamma_5 d^e) \mp \{u \leftrightarrow d\} \right]. \tag{3.10.3}$$

The mass of lowest-lying state was extracted by using the Bayesian fitting technique. The calculation was done in two different size of lattices, and the volume dependence of the spectral weights was studied, which could be used to distinguish a resonance from scattering states. It was found that the lowest lying states in all channels showed the volume dependence of the scattering state. Therefore, they concluded the non-observation of any states in these channels.

In Ref. [488], the Θ was calculated in anisotropic lattice with diquark type operator (3.10.2). In order to discriminate the resonance state from the scattering state, the authors developed the hybrid boundary condition method, which used an artificial boundary condition in spatial direction to raise up the threshold energy of the scattering state, reflecting the minimum momenta allowed by the boundary condition. A signal in negative parity channel had lower mass, but the state was identified as the scattering state by applying the hybrid boundary condition. The positive parity state was much heavier than the observed mass of 1540 MeV. Thus they concluded that there was no signal for the $\Theta(1540)$ in these channels.

The study in Ref. [489] adopted a different strategy to search for the resonance state from others. They tried to find the lowest energy state in the pentaquark channel, and identify the signal as the resonance state if it appeared below the lowest two particle threshold. This is a sufficient condition to indicate a resonance, but the absence of binding cannot rigorously exclude the possibility of a resonance. However, the known three-quark resonances have appeared in that way, due to the large mass of pion. Whether the pentaquark signal should be bound in large quark mass region or not was later examined in Ref. [493], and it was found that the sufficiently large hyperfine interaction among quarks could bound the system in this region. The correlation matrix method was used in order to reach the ground state. They adopted the results with correlation matrix method only when the obtained mass was lower than the one in standard analysis. Resonances in $J^P = 1/2$ with both parity and isospin $I = 1$ and 0 were searched for, finding no signal of binding of quarks. A comparison of different studies were made for $I(J^P) = 0(1/2^-)$ channel. It was found that the results in Refs. [484, 485, 487, 488, 489] for this channel agreed with each other, despite the use of different interpolating fields, lattice size, lattice actions, and so on.

Takahashi *et al.* [490] performed 2×2 correlation matrix calculation of NK- and colored NK- type operators in four different sizes with good statistics. This setup enabled them to separate the lowest- and 2nd-lowest-states. Volume dependence of both the energy and spectral weight were studied in order to distinguish a resonance state from the scattering states. The spatially spread "wall" operator was used as well as the standard point like operator. It was found that the color variant point operators, NK, colored NK, and Dq, gave a similar results, while larger difference was observed when the spatial structure of operators were changed from point to wall. In the negative parity channel, the lowest-lying state was found to be the NK scattering state, while the second-lowest state was difficult to be regarded as the scattering state. In the positive parity channel, the diagonalization was unstable so that the extraction of second-lowest state was not possible. The lowest state was

identified as s-wave N^*K scattering state. Hence, the possible interpretation of low Θ^+ was the negative parity.

There are yet unpublished lattice studies in Refs. [494, 495, 496, 497, 498]. In Ref. [494], A large correlation matrix was used to extract the resonance signal from the scattering states. Detailed study of the volume dependence of the spectral weights were performed in Ref. [495]. In Ref. [496], the fixed point action was used for the pentaquark state. Complete set of 19 local operators was constructed in Ref. [497]. In Ref. [498], a chirally improved fermion was adopted. The final results from these studies will bring more information on the pentaquark search on the lattice.

All the above studies are for the spin 1/2 states. The spin 3/2 state of Θ has been investigated in Refs. [491, 492]. The study in Ref. [491] was based on the calculation in Ref. [489]. The authors used the operator of the product of vector K^* meson and a nucleon. The isospin 0 and 1 with both parity channels were calculated. They found an evidence of a bound state in isoscalar channel of positive parity $I(J)^P = 0(3/2)^+$, which would be a candidate of the Θ^+ observed experimentally. However, the signal was not found in the study with higher statistics [492], where two more operators were used in addition to that of Ref. [491]. In Ref. [492], all the measured states were either found to be scattering states by the hybrid boundary condition, or appeared at higher energy than the observed mass of the Θ^+.

In summary, the status of the pentaquark on the lattice is still controversial and inconclusive. At a glance, the conclusions of different groups are diverging. However, for instance, the effective mass plots by different groups agree with each other, in spite of the different simulation details as shown in Ref. [489]. This indicates the consistency among the lattice simulations. Therefore, the difference in the conclusions mainly comes from the interpretation of the results. As stated by some authors, it is crucial to find an operator which has maximal overlap with the desired signal and minimal overlap with competing unwanted states. For the conclusive study, clear separation of the signal from the scattering state is indispensable, using cross correlator method and investigation of the volume dependence of the energy and spectral weight.

On the other hand, it is interesting to see whether lattice QCD predicts exotic states or not, apart from the experimental evidences. For instance, the positive parity state for the Θ^+ have been not investigated very much, since it locates at higher energy than the observed mass of 1540 MeV. Apparently, there is no reason to exclude the higher energy states in QCD. Since lattice QCD is the method closest to the first principle, precise predictions for the exotic states would stimulate the experimental searches.

3.10.2 Pentaquark potential

The static pentaquark potential was studied in Ref. [499] as an extension of the two- and three-quark potentials by evaluating the Wilson loop for some geometries of five quarks. Note that there are many possibilities for the geometry of five quarks including non-planar structures. The authors studied the configurations for multi-Y shape flux tube, with spatially twisted configurations. The obtained potential was well described by the sum of one gluon

exchange Coulomb term plus minimal total length of the flux tube linking the five quarks. The universality of the string tension $\sigma_{Q\bar{Q}} \sim \sigma_{3Q} \sim \sigma_{5Q}$ was also observed.

A study for the pentaquark potential can be found in Ref. [500]. Lattice data was compared with the pentaquark potential V^{5q}_{min} and the sum of the meson and baryon potentials $V_{qqq}+V_{q\bar{q}}$. It was found that the transition from $V_{qqq}+V_{q\bar{q}}$ to $V^{5q}_{\rm min}$ occurs as the separation of two diquark cluster becomes larger.

Part II

Baryon resonances in chiral unitary model

Chapter 4

Chiral unitary model and flavor SU(3) breaking effect

In this chapter, we describe the framework of the chiral unitary model for the s-wave meson-baryon scattering, which will be used in the following chapters 5, 6, and 7 for the study of the properties of baryon resonances. We focus on the flavor SU(3) and $J^P = 1/2^-$ baryon resonances, which appear as quasi-bound states of the low lying octet mesons (π, K, η) and octet baryons $(N, \Lambda, \Sigma, \Xi)$. Since there are experimental data from $\bar{K}N$ and πN scatterings, we study the $S = -1$ and $S = 0$ channels, in which the $\Lambda(1405)$, $\Lambda(1670)$, and $N(1535)$ resonances are dynamically generated.

The model successfully reproduces the properties of the resonances, but the subtraction constants in loop integral need to be fitted. In order to clarify the meaning of the subtraction constants, we introduce the flavor SU(3) breaking interaction based on the chiral perturbation theory. It is found, however, that the observed SU(3) breaking in subtraction constants cannot be explained by the present SU(3) breaking interactions. The role and importance of the subtraction constants in the present framework are discussed. This topic is reported in Refs. [6, 7].

After an introduction, the formulation of our model is presented in section 4.2. Numerical results with a common subtraction constant as well as comparison with the results of previous works are given in section 4.3. We then introduce the flavor SU(3) breaking effects in the interaction kernel and present numerical results in section 4.5. Section 4.6 is devoted to the summary and discussion. For completeness, we review several variants of this approach and applications of the obtained amplitude to various subjects in section 4.7.

4.1 Introduction

A unified study of meson-baryon scattering in various channels is important to understand hadron dynamics in low and intermediate energy regions from the viewpoint of QCD. In particular, the properties of excited baryons observed in meson-baryon scattering as resonances have been investigated with great interest both theoretically and experimentally. At this time, there are several established approaches to describe the properties of baryon resonances. A

recent development in this field is the introduction of the chiral unitary model [4, 5], in which the s-wave baryon resonances are dynamically generated in meson-baryon scattering, while the conventional quark model approach describes the baryon resonances as three-quark states with an excitation of the quarks.

The chiral unitary model is based on chiral perturbation theory (ChPT) [2, 3], which is a low energy effective field theory based on the nonlinear realization of chiral symmetry of underlying QCD. ChPT is very successful to reproduce the hadron properties in the low energy region, because the low energy theorems of chiral symmetry are properly encoded in the theory. On the other hand, the scattering amplitude obtained by ChPT violates the unitarity of scattering theory at intermediate energy region, and the resonances appearing in the hadron scattering cannot be generated by the perturbative calculation, unless they are introduced as explicit fields.

Unitarity of scattering matrix ensures the conservation of probability, that should be maintained in physical amplitudes. There are several methods to recover the unitarity, for instance, by solving the Bethe-Salpeter (BS) equation [501, 502]. Imposing the unitarity condition, we can study the energy region higher than the region where the original perturbative calculation is applicable, and the resonances are dynamically generated by non-perturbative resummations.

The present framework is essentially based on Ref. [5], where s-wave scattering in meson-baryon system with strangeness $S = -1$ was investigated by solving the BS equation in coupled channels with interaction kernel derived from the lowest order chiral Lagrangian. With only one parameter of cutoff, the invariant mass distribution of $\Lambda(1405)$ resonance was well reproduced, as well as the total cross sections and threshold branching ratio of KN scattering. The model was systematically extended for all SU(3) sector [503, 504, 505], providing $\Lambda(1405)$, $N(1535)$, $\Lambda(1670)$, $\Sigma(1620)$, and $\Xi(1620)$.

Historically, the studies of the resonances in coupled channel approach started in 60's. For instance, the $\Lambda(1405)$ resonance was previously obtained as a quasi-bound state of $\bar{K}N$ [506, 507, 508]. In the same way, $N(1535)$ was considered as a quasi-bound state of $K\Sigma$ [509]. In these studies, phenomenological vector meson exchange was used as an interaction kernel, which corresponds to the Weinberg-Tomozawa term in the lowest order chiral Lagrangian, that we are going to employ.

Therefore, recent development of chiral unitary model provides a theoretical foundation for the earlier works, based on the modern knowledge of chiral symmetry and QCD. Moreover, it also reveals the novel structures of the resonances and complementary description to the conventional three-quark pictures.

4.2 Formulation of chiral unitary model

In this section we review the chiral unitary model. We derive the basic interaction between mesons and baryons from the lowest-order chiral Lagrangian, and we maintain the unitarity of the S-matrix. There are several methods that recover the unitarity of the S-matrix. In this work, we adopt the N/D method [510], because this method provides a general form of the T-matrix using the dispersion relation and the analyticity of the inverse of the T-matrix.

The N/D method has been applied to coupled channel meson-baryon scattering with chiral interactions [511, 512]. It was found that the final form of the T-matrix obtained in the N/D method is essentially equivalent to the result given in Ref. [5] derived from the BS equation with on-shell factorization.

4.2.1 Kernel interaction

The chiral Lagrangian for baryons [48, 40, 513, 514] in the lowest-order of the chiral expansion is given by [A)]

$$\mathcal{L}_1^B = \mathrm{Tr}\Big(\bar{B}(i\not{\mathcal{D}} - M_0)B - D(\bar{B}\gamma^\mu\gamma_5\{A_\mu, B\}) - F(\bar{B}\gamma^\mu\gamma_5[A_\mu, B])\Big). \tag{4.2.1}$$

Here D and F are coupling constants. In Eq. (4.2.1), the covariant derivative $\mathcal{D}_\mu$, the vector current V_μ, the axial vector current A_μ and the chiral field ξ are defined by

$$\begin{aligned}
\mathcal{D}_\mu B =& \partial_\mu B + i[V_\mu, B], \\
V_\mu =& -\frac{i}{2}(\xi^\dagger\partial_\mu\xi + \xi\partial_\mu\xi^\dagger), \\
A_\mu =& -\frac{i}{2}(\xi^\dagger\partial_\mu\xi - \xi\partial_\mu\xi^\dagger), \\
\xi(\Phi) =& \exp\{i\Phi/\sqrt{2}f\},
\end{aligned}$$

where f is the meson decay constant. The meson and baryon fields are expressed in SU(3) matrix form as

$$B = \begin{pmatrix} \frac{1}{\sqrt{2}}\Sigma^0 + \frac{1}{\sqrt{6}}\Lambda & \Sigma^+ & p \\ \Sigma^- & -\frac{1}{\sqrt{2}}\Sigma^0 + \frac{1}{\sqrt{6}}\Lambda & n \\ \Xi^- & \Xi^0 & -\frac{2}{\sqrt{6}}\Lambda \end{pmatrix},$$

$$\Phi = \begin{pmatrix} \frac{1}{\sqrt{2}}\pi^0 + \frac{1}{\sqrt{6}}\eta & \pi^+ & K^+ \\ \pi^- & -\frac{1}{\sqrt{2}}\pi^0 + \frac{1}{\sqrt{6}}\eta & K^0 \\ K^- & \bar{K}^0 & -\frac{2}{\sqrt{6}}\eta \end{pmatrix}.$$

In the Lagrangian (4.2.1), M_0 denotes the common mass of the octet baryons. However, we use the observed values of the baryon masses for the baryon propagator in the following calculations. The mass splitting among the octet baryons in the Lagrangian level are introduced consistently with the SU(3) breaking terms in section 4.5.

The s-wave interactions at tree level come from the Weinberg-Tomozawa (WT) interaction [515, 516], which can be found in the vector coupling term in the covariant derivative, by expanding chiral field ξ:

$$\mathcal{L}_{WT} = \mathrm{Tr}\Big(\bar{B}i\gamma^\mu\frac{1}{4f^2}\big[(\Phi\partial_\mu\Phi - \partial_\mu\Phi\Phi), B\big]\Big).$$

[A)] We summarize the notation of chiral Lagrangians and and relation to other conventions in Appendix B.

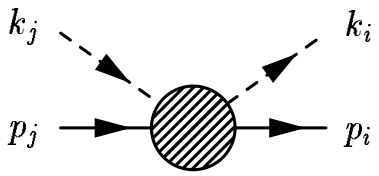

Figure 4.1: Definition of the momentum variables. The dashed and solid lines represent mesons and baryons, respectively.

From this Lagrangian, the meson-baryon scattering amplitude at tree level is given by

$$\begin{aligned} V_{ij}^{(WT)} &= -\frac{C_{ij}}{4f^2}\bar{u}(p_i)(\not{k}_i + \not{k}_j)u(p_j) \\ &= -\frac{C_{ij}}{4f^2}(2\sqrt{s} - M_i - M_j)\sqrt{\frac{E_i + M_i}{2M_i}}\sqrt{\frac{E_j + M_j}{2M_j}}, \end{aligned} \tag{4.2.2}$$

where the indices (i, j) denote the channels of the meson-baryon scattering, and M_i and E_i are the mass and the energy of the baryon in the channel i, respectively. These masses and factors come from the spinors of the baryons, which are summarized in Appendix A. The kinematics of this vertex are depicted in Fig. 4.1, and s in Eq. (4.2.2) is defined as $s = (k_i + p_i)^2$. The second line is obtained in the center of mass frame with nonrelativistic reduction, which is demonstrated in Appendix B.3.2. The channels (i, j) are shown in Table D.1 of Appendix D.1. The coefficient C_{ij} is fixed by chiral symmetry, and the explicit form of C_{ij} for relevant channels is given in Tables D.4-D.8 in Appendix D.2.

Several comments on the interaction kernel are in order. First, there are two more terms for the process at the same order in chiral counting, namely, the s- and u-channel baryon exchange Born diagrams, which are derived from the axial vector coupling in Eq. (4.2.1). Second, it seems reasonable to use the common mass M_0 in the Lagrangian. However, in the present framework, we adopt the physical masses, and Born terms are not included. The Born terms are of the higher order in non-relativistic expansion, and they contribute to the p-wave interaction dominantly. Indeed, formulation with the Born terms and common mass M_0 is studied in Ref. [512], and we have checked that the present results are qualitatively similar to those in Ref. [512]. The smallness of the Born terms is also confirmed in Ref. [517].

4.2.2 Unitarization of the amplitude by the N/D method

In the coupled channel formulation, the T-matrix takes a matrix form. The unitarity condition is guaranteed by the optical theorem, *i.e.* $-2\mathrm{Im}[T_{ii}] = T_{ik}\rho_k T^*_{ki}$, which can be written as

$$2\mathrm{Im}[T_{ii}^{-1}] = \rho_i, \tag{4.2.3}$$

where we denote the phase space ρ_i[B)]. With the condition (4.2.3) and the dispersion relation for T_{ii}^{-1}, we find a general form of the T-matrix using the N/D method. Following Ref. [512],

[B)] Note that the definition of ρ_i is twice of that in Ref. [512].

we write

$$T_{ij}^{-1}(\sqrt{s}) = \delta_{ij}\Big(\tilde{a}_i(s_0) + \frac{s-s_0}{2\pi}\int_{s_i^+}^{\infty} ds' \frac{\rho_i(s')}{(s'-s)(s'-s_0)}\Big) + \mathcal{T}_{ij}^{-1}, \tag{4.2.4}$$

where s_i^+ is the value of s at the threshold of the channel i, and s_0 denotes the subtraction point. The parameter $\tilde{a}_i(s_0)$ is the subtraction constant and is a free parameter within the N/D method. The matrix $\mathcal{T}_{ij}$ is determined by the chiral perturbation theory, as discussed below. In the derivation of Eq. (4.2.4), we have ignored the left-hand cuts, which correspond to u-channel diagrams of the crossing symmetry.

Let us assume that the intermediate states of the meson-baryon scattering are composed of one octet meson and one octet baryon. We do not consider the case of multiple mesons and excited baryons, such as $\pi\pi N$ and $\pi\Delta$. In this case, the phase space ρ_i in Eq. (4.2.3) is written as

$$\rho_i(s) = \frac{2M_i|\boldsymbol{q}_i|}{4\pi\sqrt{s}}, \tag{4.2.5}$$

where $\boldsymbol{q}_i$ is a three-momentum of the particle in the center of mass frame on the mass shell. Eq. (4.2.5) can be checked by $\rho_i = \int d\Pi_i$ with $d\Pi$ given in Appendix A.3. Let us define the G function by

$$G_i(\sqrt{s}) = -\tilde{a}_i(s_0) - \frac{s-s_0}{2\pi}\int_{s_i^+}^{\infty} ds' \frac{\rho_i(s')}{(s'-s)(s'-s_0)},$$

which takes the same form as, up to a constant, the ordinary meson-baryon loop function:

$$G_i(\sqrt{s}) = i\int \frac{d^4q}{(2\pi)^4}\frac{2M_i}{(P-q)^2 - M_i^2 + i\epsilon}\frac{1}{q^2 - m_i^2 + i\epsilon}.$$

This integral should be regularized with an appropriate regularization scheme. In the dimensional regularization, the integral is calculated as

$$\begin{aligned} G_i(\sqrt{s}) = \frac{2M_i}{(4\pi)^2}\Bigg\{ & a_i(\mu) + \ln\frac{M_i^2}{\mu^2} + \frac{m_i^2 - M_i^2 + s}{2s}\ln\frac{m_i^2}{M_i^2} \\ & + \frac{\bar{q}_i}{\sqrt{s}}\Big[\ln(s - (M_i^2 - m_i^2) + 2\sqrt{s}\bar{q}_i) + \ln(s + (M_i^2 - m_i^2) + 2\sqrt{s}\bar{q}_i) \\ & - \ln(-s + (M_i^2 - m_i^2) + 2\sqrt{s}\bar{q}_i) - \ln(-s - (M_i^2 - m_i^2) + 2\sqrt{s}\bar{q}_i)\Big]\Bigg\}, \end{aligned} \tag{4.2.6}$$

where μ is the regularization scale, $a_i = -\frac{(4\pi)^2}{2M_i}\tilde{a}_i$ is the subtraction constant, and $\bar{q}_i$ is defined by

$$\bar{q}_i(\sqrt{s}) = \frac{\sqrt{(s-(M_i-m_i)^2)(s-(M_i+m_i)^2)}}{2\sqrt{s}} = \frac{\lambda^{1/2}(s, M_i^2, m_i^2)}{2\sqrt{s}},$$

with the Källen function $\lambda^{1/2}(x,y,z) = x^2+y^2+z^2-2xy-2yz-2zx$. Above the threshold of channel i, this quantity corresponds to the magnitude of the three momentum $|\boldsymbol{q}_i|$, but this

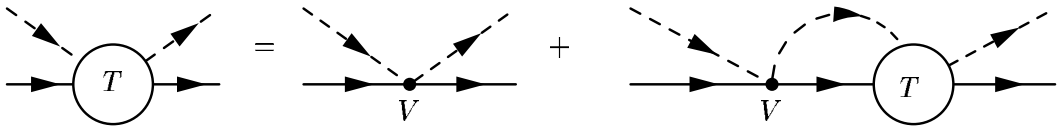

Figure 4.2: Diagrammatic interpretation of Eq. (4.2.8). Solid and dashed lines represent the baryon and meson fields, respectively.

is also defined below the threshold, where it becomes pure imaginary. Detailed discussion on the meson-baryon loop integrals can be found in Appendix C.1.2.

Now for the $\mathcal{T}_{ij}$, we adopt the matching scheme in Ref. [512]. This scheme provides $\mathcal{T}_{ij} = V_{ij}$, at the leading order $\mathcal{O}(p)$, which corresponds to the tree level approximation, where only the $\mathcal{T}_{ij}$ term survives in Eq. (4.2.4). It is shown that the identification $\mathcal{T}$ with the amplitude by ChPT $V_{\rm ChPT}$ is true up to $\mathcal{O}(p^2)$, but not valid for $\mathcal{O}(p^3)$ or higher [512]. Hence, the resulting T-matrix is written as

$$T^{-1} = -G + (V^{(WT)})^{-1}, \tag{4.2.7}$$

$$\begin{aligned} T &= V^{(WT)} + V^{(WT)}GT \\ &= V^{(WT)} + V^{(WT)}GV^{(WT)} + V^{(WT)}GV^{(WT)}GV^{(WT)} + \cdots , \end{aligned} \tag{4.2.8}$$

which can be solved by

$$T = (1 - V^{(WT)}G)^{-1}V^{(WT)}. \tag{4.2.9}$$

This is the algebraic equation for the T-matrix, which corresponds to the integral BS equation. The diagrammatic interpretation of Eq. (4.2.8) is displayed in Fig. 4.2.

The subtraction constants $a_i(\mu)$ in Eq. (4.2.6), in principle, would be related to the counter terms in the higher-order Lagrangian in the chiral perturbation theory. In previous works, the subtraction constants a_i were fitted either to the real part of the loop function in the cutoff scheme $q_{\rm max} = 630$ MeV (the $S = -1$ sector [503]), or to the experimental data for the $\pi N(S = 0)$ scatterings [504]. In Table 4.1, we list the subtraction constants used in Refs. [503] and [504]. In the table, in order to compare the channel dependence of the subtraction constants, we take the regularization scale at $\mu = 630$ MeV in the both channels. Changing the regularization scale, the subtraction constants are simply shifted by $a(\mu') = a(\mu) + 2\ln(\mu'/\mu)$. From this table, we see that the values of a_i for $S = 0$ differ significantly depending on the particle channels. It is also worth noting that the value $a = -2$ is called as "natural size" together with $\mu = 630$ MeV, since it corresponds to the $q_{\rm max} = 630$ MeV with the three momentum cutoff regularization [512]. This value is consistent with that often used in single nucleon processes [518], and well reproduces the $\bar{K}N$ scattering [5]. The constants for $S = -1$ are around this "natural size", but the values for $S = 0$ channel deviates from it. In the rest of this chapter, we refer to the parameters tabulated in Table 4.1 as "channel-dependent a_i".

Table 4.1: Channel-dependent subtraction constants a_i used in Refs. [503] and [504] with the regularization scale $\mu = 630$ MeV. For the $S = 0$ channel, although the original values of a_i are obtained with $\mu = 1200$ MeV, here we give the values of a_i corresponding to $\mu = 630$ MeV obtained using the relation $a(\mu') = a(\mu) + 2\ln(\mu'/\mu)$.

channel-dependent a_i $(S = -1)$						
channel	$\bar{K}N$	$\pi\Sigma$	$\pi\Lambda$	$\eta\Lambda$	$\eta\Sigma$	$K\Xi$
a_i	-1.84	-2.00	-1.83	-2.25	-2.38	-2.67

channel-dependent a_i $(S = 0)$				
channel	πN	ηN	$K\Lambda$	$K\Sigma$
a_i	0.711	-1.09	0.311	-4.09

4.3 Calculation with a common subtraction constant

In this section, we present calculations in which a single subtraction constant a is commonly used in the meson-baryon loop function (4.2.6) in order to investigate the role of the channel-dependent a_i in reproducing the observed cross sections and the resonance properties. The formulae to calculate the total cross section, invariant mass distribution, and T-matrix amplitude are given by

$$\sigma_{ij} = \frac{1}{4\pi s}\frac{|\boldsymbol{k}_j|}{|\boldsymbol{k}_i|} M_i M_j \bar{\Sigma}\Sigma |T_{ij}|^2, \tag{4.3.1}$$

$$\frac{d\sigma}{dM_I} \propto |\boldsymbol{k}_{\pi\Sigma}| \bar{\Sigma}\Sigma |T_{\pi\Sigma\pi\Sigma}|^2, \tag{4.3.2}$$

$$T_{ij}^{\rm plot} = -\frac{1}{8\pi\sqrt{s}}\sqrt{|\boldsymbol{k}_i||\boldsymbol{k}_j|}\sqrt{2M_i}\sqrt{2M_j}T_{ij}, \tag{4.3.3}$$

where T_{ij} is the amplitude obtained in Eq. (4.2.9), M_i and $\boldsymbol{k}_i$ are the mass of the baryon and the three momentum in the center of mass system of channel i and $\bar{\Sigma}\Sigma$ stands for the spin summation of fermions, which will be explained in Appendix A.2. A derivation of these formulae can be found in Appendix A.4.1. Note that the formula (4.3.2) will be improved in the next chapter, but the present form can be applicable for a qualitative discussion here.

4.3.1 Subtraction constants in the SU(3) limit

Let us first show that in the SU(3) limit, together with the constraint in the chiral unitary model, there should be only one subtraction constant [6, 7, 519]. Under the SU(3) symmetry, the scattering amplitudes of one octet meson and one octet baryon are composed of SU(3) irreducible representations. The amplitudes satisfy the following scattering equation in each representation:

$$T(D) = V(D) + V(D)G(D)T(D).$$

Here, D represents an SU(3) irreducible representation, $D = \mathbf{1}, \mathbf{8}, \mathbf{8}, \mathbf{10}, \overline{\mathbf{10}}$, and $\mathbf{27}$. Therefore, on one hand, the functions G, or equivalently the subtraction constants a_i, are represented by diagonal matrices in the SU(3) basis. On the other hand, because G functions are

given as loop integrals, as shown in Eq. (4.2.6), they are also diagonal in the particle basis $(\pi^- p, \eta\Lambda, \cdots)$. These observations imply that the subtraction constants are components of a diagonal matrix both in SU(3) and in particle bases, which are transformed uniquely with a unitary matrix of the SU(3) Clebsch-Gordan coefficients,

$$a(D) = \sum_k U_{Dk} a_k (U^\dagger)_{kD}, \tag{4.3.4}$$

where the explicit form of the transformation matrix U can be found in Appendix D.1. Eq. (4.3.4) is satisfied only when a_k is proportional to unit matrix. Hence, the subtraction constants are not dependent on the channel in the SU(3) limit.

In the following, we first discuss the $S = -1$ case, in which the subtraction constants a_i do not depend strongly on the channel, as shown in Table 4.1. Therefore, it is expected that a calculation with a common value for a gives a good description if we choose a suitable value. Next we study the $S = 0$ channel using a common subtraction constant. Here, we find that common value a cannot simultaneously reproduce the resonance properties and the S_{11} amplitude in the low energy region.

In order to concentrate on the role of the subtraction constants and to deduce the channel dependence, we make the following simplifications for the calculations of the $S = -1$ and $S = 0$ channels:

- We use an averaged value for the meson decay constants, $f = 1.15 f_\pi = 106.95$ MeV, while in Ref. [504], physical values were taken as $f_\pi = 93$ MeV, $f_K = 1.22 f_\pi$, $f_\eta = 1.3 f_\pi$.

- We do not include the effect of vector meson exchanges and $\pi\pi N$ channels to reproduce the $\Delta(1620)$ resonance, which were considered in Ref. [504].

With these simplifications, the calculations in the $S = -1$ and $S = 0$ channels are based on exactly the same formulation, and the differences exist in the flavor SU(3) coefficients C_{ij} in Eq. (4.2.2) and in the channel-dependent subtraction constants.

4.3.2 The $S = -1$ channel ($\bar{K}N$ scattering)

In the $S = -1$ channel, the subtraction constants a_i obtained in Ref. [503] do not depend strongly on the channel. In Ref. [512], a common value of $a \sim -2$ was "naturally" obtained from matching with the three-momentum cutoff regularization with $q_{\max} = 630$ MeV. In both works, the total cross sections of the $K^- p$ scattering and the mass distribution of the $\pi\Sigma$ channel with $I = 0$, where the $\Lambda(1405)$ resonance is seen, were reproduced very well. In Ref. [503], the $\Lambda(1670)$ resonance was also obtained with the channel-dependent subtraction constants, and its properties were investigated by analyzing the speed plots in the $I = 0$ channels.

Here we search for one common value a to be used in all channels for $S = -1$. In order to fix this common value a, we use threshold properties of the $\bar{K}N$ scattering, which are well

Table 4.2: Threshold branching ratios calculated with channel-dependent a_i, common value $a = -1.96$, and $a = -1.59$ with the SU(3) breaking interaction. The experimental values were taken from Refs. [520] and [521].

	γ	R_c	R_n
experiment	2.36 ± 0.04	0.664 ± 0.011	0.189 ± 0.015
channel-dependent a_i	1.73	0.629	0.195
common value a	1.80	0.624	0.225
SU(3) breaking	2.19	0.623	0.179

observed in the branching ratios [520, 521]:

$$\begin{aligned}
\gamma =& \frac{\Gamma(K^- p \to \pi^+ \Sigma^-)}{\Gamma(K^- p \to \pi^- \Sigma^+)} \sim 2.36 \pm 0.04 \ , \\
R_c =& \frac{\Gamma(K^- p \to \text{charged particles})}{\Gamma(K^- p \to \text{all})} \sim 0.664 \pm 0.011 \ , \\
R_n =& \frac{\Gamma(K^- p \to \pi^0 \Lambda)}{\Gamma(K^- p \to \text{neutral particles})} \sim 0.189 \pm 0.015 \ .
\end{aligned} \tag{4.3.5}$$

After fitting, we find the optimal value $a = -1.96$, with which the threshold branching ratios are obtained, as shown in Table 4.2. The result obtained using the common value $a = -1.96$ does not differ much from that obtained with channel-dependent values, and also the value $a = -1.96$ is close to the averaged value of the channel-dependent subtraction constants a_i, namely ~ -2.15. Therefore, the threshold properties are not sensitive to such a fine tuning of the subtraction constants.

Using the common value $a = -1.96$, we calculate the total cross sections of the $K^- p$ scattering (Fig. 4.3, solid curves), the T-matrix amplitude of the $\bar{K}N$ scattering with $I = 0$ ((a) and (b) in Fig. 4.4, solid curves), and the mass distributions of the $\pi\Sigma$ channel with $I = 0$ ((c) in Fig. 4.4, solid curve), which is normalized according to Eq. (4.3.3). In Fig. 4.4, experimental data indicates the $\Lambda(1620)$ structure by the behavior of the T-matrix amplitude (see subsection 4.4.1), while in t he invariant mass distributions of $\pi\Sigma$ shows the resonant peak of the $\Lambda(1405)$. For comparison, we also plot the results obtained with the channel-dependent a_i from the calculation given in Ref. [503] in Figs. 4.3 and 4.4 as the dotted curves. Both the $\Lambda(1670)$ and $\Lambda(1405)$ are well reproduced.

Here, we find that the present calculations with $a = -1.96$ give results that are slightly different from those of the calculations with the channel-dependent a_i in the total cross sections and the $\pi\Sigma$ mass distributions. Therefore, the $\Lambda(1405)$ resonance is well reproduced with the common value $a = -1.96$, which is consistent with the results in Ref. [512]. However, the resonance $\Lambda(1670)$ disappears when this common value a is used, as we see in the T-matrix amplitude of $\bar{K}N \to \bar{K}N$ with $I = 0$ in Fig. 4.4. As pointed out in Ref. [503], the $\Lambda(1670)$ resonance structure is very sensitive to the value of $a_{K\Xi}$. Indeed, we have checked that the $\Lambda(1670)$ resonance is reproduced when we choose $a_{K\Xi} \sim -2.6$ with the other a_i unchanged, *i.e.*, at -1.96. In a recent publication, it was shown that the poles of $\Lambda(1405)$ and $\Lambda(1670)$ are simultaneously reproduced by taking into account the approximate crossing symmetry

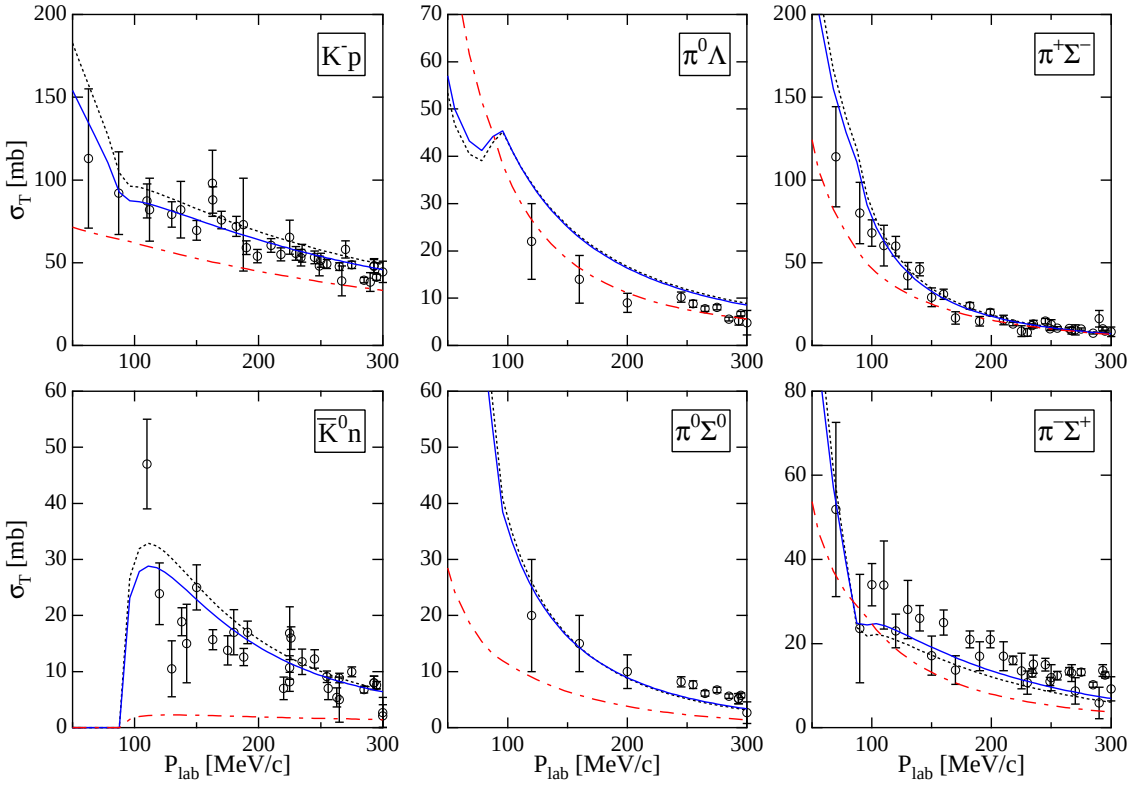

Figure 4.3: Total cross sections of $K^- p$ scattering ($S = -1$) as functions of $P_{\rm lab}$, the three-momentum of the initial K^- in the laboratory frame. The dotted curve represent the results obtained with the channel-dependent a_i, the solid curves represent the results obtained with the common value $a = -1.96$, and the dash-dotted curves represent the results obtained with the common value $a = -2.6$. The open circles with error bars are experimental data taken from Refs. [522, 523, 524, 525, 526, 527, 528, 529, 530, 531, 532, 533].

without considering explicitly the channel dependence [536]. The inclusion of the crossing symmetry is, however, beyond the scope of the present discussion.

If we choose $a = -2.6$ for all subtraction constants, the threshold branching ratios are obtained as $\gamma = 2.41$, $R_c = 0.596$ and $R_n = 0.759$, and the agreement with the experimental data of scattering observable becomes poor, as shown in Figs. 4.3 and 4.4. In particular, the $K^- p \to \bar{K}^0 n$ cross section is underestimated, and also the resonance structure of $\Lambda(1405)$ disappears in the $\pi\Sigma$ mass distribution ((c) in Fig. 4.4). As we change all subtraction constants from $a = -1.96$ to $a = -2.6$ gradually, the position of the peak of $\Lambda(1405)$ moves to the lower energy side and finally disappears under the $\pi\Sigma$ threshold. Therefore, using the common value $a \sim -2$ is essential to reproduce the resonance properties of $\Lambda(1405)$ and the total cross sections of the $K^- p$ scattering in the low energy region.

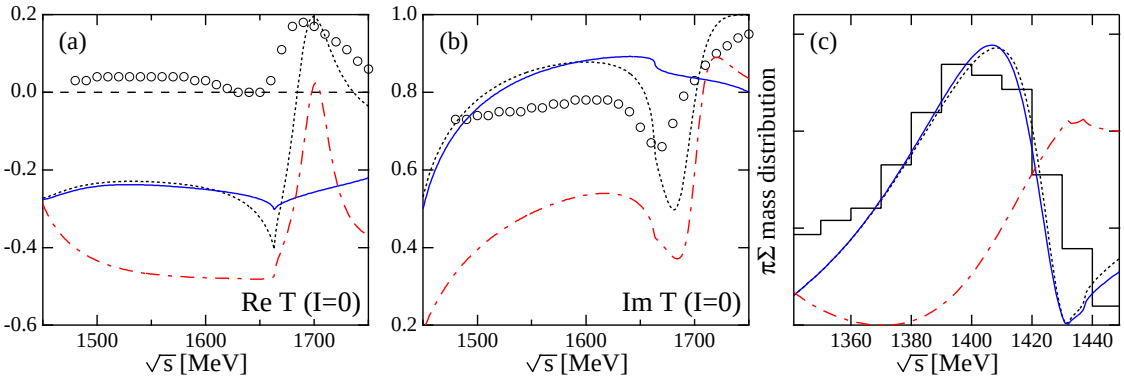

Figure 4.4: Real (a) and imaginary (b) parts of the T-matrix amplitude of $\bar{K}N \to \bar{K}N$ with $I = 0$ and the mass distributions (c) of the $\pi\Sigma$ channel with $I = 0$. The dotted curves represent the results obtained with the channel-dependent a_i, the solid curves represent the results obtained with the common value $a = -1.96$, and the dash-dotted curves represent the results obtained with the common value $a = -2.6$. The open circles in (a) and (b) are experimental data taken from Ref. [534], while the histogram in (c) represents experimental data taken from Ref. [535].

4.3.3 The $S = 0$ channel (πN scattering)

In Ref. [504], the total cross sections of the $\pi^- p$ inelastic scattering and the resonance properties of the $N(1535)$ were reproduced well by using channel-dependent a_i. After the simplification applied to f and inelastic channels, the agreement with the data is still acceptable, as shown in Fig. 4.5 by the dotted curves, as long as channel-dependent a_i are employed. In the T-matrix elements of the πN scattering in the S_{11} channel (Fig. 4.6), we see a kink structure around the energy $\sqrt{s} \sim 1500$ MeV, which corresponds to the $N(1535)$ resonance [504].

In the previous subsection, we obtained the common subtraction constant $a = -1.96$ with which the $\bar{K}N$ total cross sections and the $\Lambda(1405)$ properties are reproduced well. First, we use this common value of a for the $S = 0$ channel. Shown in Figs. 4.5 and 4.6 by the dash-dotted curves are the results with $a = -1.96$ for the total cross sections of the $\pi^- p \to \pi^0\eta$, $K^0\Lambda$ and $K^0\Sigma$ scatterings, and the S_{11} T-matrix amplitude of $\pi N \to \pi N$. As can be seen in Figs. 4.5 and 4.6, the results with $a = -1.96$ in the $S = 0$ channel are far from the experimental data. In particular, in the $\pi^- p \to \eta n$ cross section, the threshold behavior disagrees with the experiment, and a resonance structure of $N(1535)$ disappears. In addition, as shown in Fig. 4.6, the T-matrix amplitude of the S_{11} channel is overestimated, and an unexpected resonance has been generated near $\sqrt{s} \sim 1250$ MeV.

Next, we search for a single optimal subtraction constant within the $S = 0$ channel, because an unnecessary resonance is obtained with $a = -1.96$ at low energy. In order to avoid the appearance of such an unphysical resonance, we determine the common subtraction constant a so as to reproduce the observed data up to $\sqrt{s} = 1400$ MeV. The optimal value is found to be $a = 0.53$. The calculated S_{11} amplitude as well as the total cross sections are plotted in Figs. 4.5 and 4.6 by the solid curves. With this subtraction constant, the low energy behavior of the S_{11} amplitude of the πN scattering ($\sqrt{s} < 1400$ MeV) is well reproduced. Therefore,

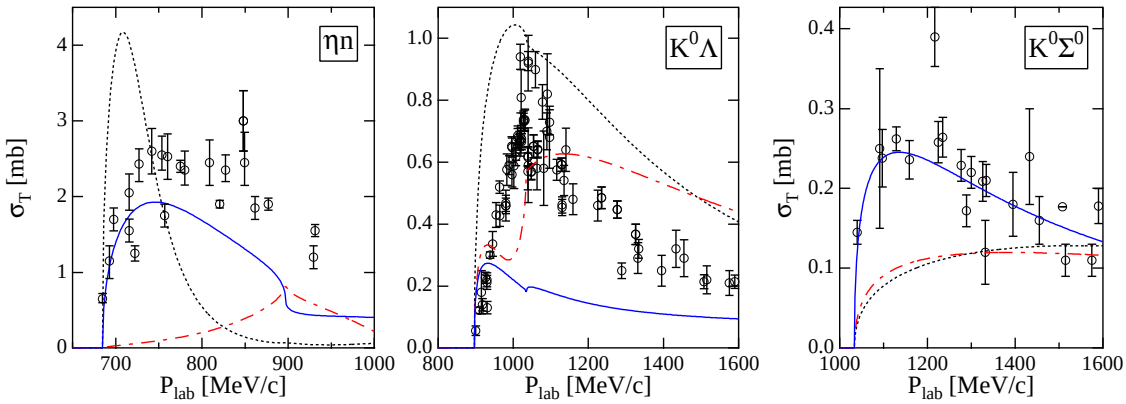

Figure 4.5: Total cross sections of $\pi^- p$ scattering ($S = 0$) as functions of $P_{\rm lab}$, the three-momentum of the initial π^- in the laboratory frame. The dotted curves represent the results obtained with channel-dependent a_i, the dash-dotted curves represent the results obtained with the common value $a = -1.96$, obtained for $S = -1$, and the solid curves represent the results obtained with the common value $a = 0.53$. The open circles with error bars are the experimental data taken from Refs. [537, 538, 539, 540, 541, 542, 543, 544, 545, 546, 547, 548, 549, 550, 551, 552, 553, 554, 555, 556].

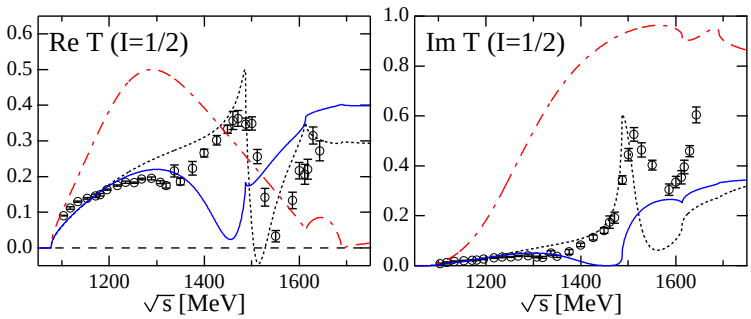

Figure 4.6: Real and imaginary parts of the S_{11} T-matrix amplitudes of $\pi N \to \pi N$. The dotted curves represent the results obtained with channel-dependent a_i, the dash-dotted curves represent the results obtained with the common value $a = -1.96$, obtained for $S = -1$, and the solid curves show the results with the common value $a = 0.53$. The open circles with error bars are experimental data taken from Ref. [557].

the scattering length is also reproduced. However, the $N(1535)$ resonance structure is not still generated. We have also checked that there is no pole in the scattering amplitudes in the second Riemann sheet. Therefore, we conclude that in the $S = 0$ channel we cannot reproduce simultaneously the $N(1535)$ resonance and the S_{11} amplitude at low energy if a single subtraction constant is used within the present approach.

4.4 Resonances in the scattering amplitude

Let us look at the structure of the amplitude near the resonance in more detail. We show the way to extract the information of the resonance from the scattering amplitude. We first study the behavior of the T-matrix around the pole on the real axis. Then we perform the analytic continuation of the variable $\sqrt{s}$, and search for poles in the complex z plane by calculating the T-matrix on the second Riemann sheet. The residues of the poles are evaluated, in order to estimate the coupling strength for each channel.

4.4.1 General behavior of the amplitude

When a baryon resonance is dynamically generated, the scattering amplitude close to the resonance energy region can be expressed in terms of the Breit-Wigner amplitude plus non-resonant background term. For an s-wave resonance with mass M_R and total width Γ_R, the T-matrix amplitude is written as

$$\begin{aligned} -iT_{ij}(\sqrt{s}) &= -ig_i \frac{i}{\sqrt{s} - M_R + i\Gamma_R/2}(-ig_j) - iT_{ij}^{BG} \\ T_{ij}(\sqrt{s}) &= \frac{g_i g_j}{\sqrt{s} - M_R + i\Gamma_R/2} + T_{ij}^{BG}, \end{aligned} \tag{4.4.1}$$

where the amplitude of the resonance R to channel i is defined by $-it_{Ri} \equiv -ig_i$, since it is in an s wave. For resonances in higher partial waves, we can replace it by appropriate structure, such as $-it_{Ri} \equiv -ig_i \boldsymbol{\sigma} \cdot \boldsymbol{q}_i/f$ for p wave, and so on. Qualitative conclusions at $\sqrt{s} = M_R$ does not change by this replacement. The non-resonant background term T_{ij}^{BG} is assumed to be slowly varying function of $\sqrt{s}$. The amplitude (4.4.1) indicates the existence of a pole in the complex energy plane at

$$z_R = M_R - i\frac{\Gamma_R}{2}.$$

In this way, through the Breit-Wigner term, the position of the pole z_R tells us the mass M_R and the decay width Γ_R of the corresponding resonance.

Let us discuss the property of the T-matrix amplitude on the real axis around the resonance energy region. Eq. (4.4.1) can be written as

$$T_{ij}(\sqrt{s}) = (\sqrt{s} - M_R - i\Gamma_R/2)\frac{g_i g_j}{(\sqrt{s} - M_R)^2 - (\Gamma_R/2)^2} + T_{ij}^{BG},$$

which imply that, if the background term T_{ij}^{BG} is negligible, the amplitude becomes pure imaginary at $\sqrt{s} = M_R$. It is instructive to differentiate $T_{ij}(\sqrt{s})$ in terms of $\sqrt{s}$, leading to

$$\begin{aligned} \frac{\partial}{\partial\sqrt{s}} T_{ij}(\sqrt{s}) &= -\frac{g_i g_j}{(\sqrt{s} - M_R + i\Gamma_R/2)^2} + \frac{\partial}{\partial\sqrt{s}} T_{ij}^{BG} \\ &= -\frac{g_i g_j}{(\sqrt{s} - M_R)^2 - (\Gamma_R/2)^2 + i\Gamma_R(\sqrt{s} - M_R)} + \frac{\partial}{\partial\sqrt{s}} T_{ij}^{BG} \\ &= -\frac{g_i g_j(\sqrt{s} - M_R)^2 - (\Gamma_R/2)^2 - i\Gamma_R(\sqrt{s} - M_R)}{[(\sqrt{s} - M_R)^2 - (\Gamma_R/2)^2]^2 - [\Gamma_R(\sqrt{s} - M_R)]^2} + \frac{\partial}{\partial\sqrt{s}} T_{ij}^{BG}, \end{aligned}$$

Table 4.3: Features of the scattering amplitude at $\sqrt{s} = M_R$. ∂ denotes the derivative in terms of the total energy.

	real	error	imaginary	error
T	0	$\mathcal{O}(T^{BG})$	extreme	$\mathcal{O}(\partial T^{BG})$
∂T	extreme	$\mathcal{O}(\partial T^{BG})$	0	$\mathcal{O}(\partial^2 T^{BG})$

which imply that $\frac{\partial}{\partial\sqrt{s}}T_{ij}(\sqrt{s})$ becomes pure real at $\sqrt{s} = M_R$, if the first derivative of the background term is negligible. This also shows that $\mathrm{Im}[T_{ij}]$ has an extreme value at $\sqrt{s} = M_R$, since its derivative is zero. Hence, if the background term and its first derivative are negligible, or in the other words, if the Breit-Wigner term is dominant, the T-matrix has the following properties;

- $\mathrm{Re}[T]$ becomes zero at $\sqrt{s} = M_R$.
- $\mathrm{Im}[T]$ has an extreme value at $\sqrt{s} = M_R$.

As an example, in Fig. 4.4, we see that zero of the real part and extreme value of imaginary part of dotted curves are around $\sqrt{s} = 1670$ MeV, which corresponds to the mass of the $\Lambda(1670)$ resonance.

Since the background term T_{ij}^{BG} is assumed to be slowly varying function of $\sqrt{s}$ compared with the Breit-Wigner term, its first derivative can be negligible. However, it is not always true that the background term itself is negligible. Therefore, in general, the zero of the real part and the extreme value of the imaginary part might not coincide, as seen in, for instance, Fig. 4.6, where the real part of the experimental amplitude is not zero although there is the $N(1535)$ resonance. This discrepancy is referred to as the background effects. In such a case, taking derivative in terms of $\sqrt{s}$ can help to determine the Breit-Wigner parameters, since the energy dependence of the background term is expected to be small, and therefore its derivative is small. It is straightforward to show the second derivative of the T_{ij} becomes pure imaginary, and therefore the real part of the $\frac{\partial}{\partial\sqrt{s}}T_{ij}$ is the extreme value. Hence, in summary, the scattering amplitude shows the features shown in Table 4.3 at $\sqrt{s} = M_R$.

4.4.2 Poles in the second Riemann sheet

As we mentioned, the Breit-Wigner amplitude (4.4.1) implies the existence of a pole at $z_R = M_R - i\Gamma_R/2$ in complex z plane. However, causality requires the absence of poles in the physical (first Riemann) sheet [558]. Therefore, the pole that corresponds to the resonance will appear in the unphysical sheet, namely the second Riemann sheet. Let us examine the existence of the pole by calculating the scattering amplitude numerically in the second Riemann sheet of the complex energy plane. Here we use the amplitude with the channel dependent subtraction constants, which gives a reasonable description of the resonances. The definition of the amplitude in the complex plane and related issues are summarized in Appendix C.1.2.

We plot the absolute value of the T-matrix amplitudes $|T|$ of $\bar{K}N \to \bar{K}N$ with $I = 0$ in Fig. 4.7 and of $\pi N \to \pi N$ with S in Fig. 4.8. In the $S = -1$ channel, around the energy

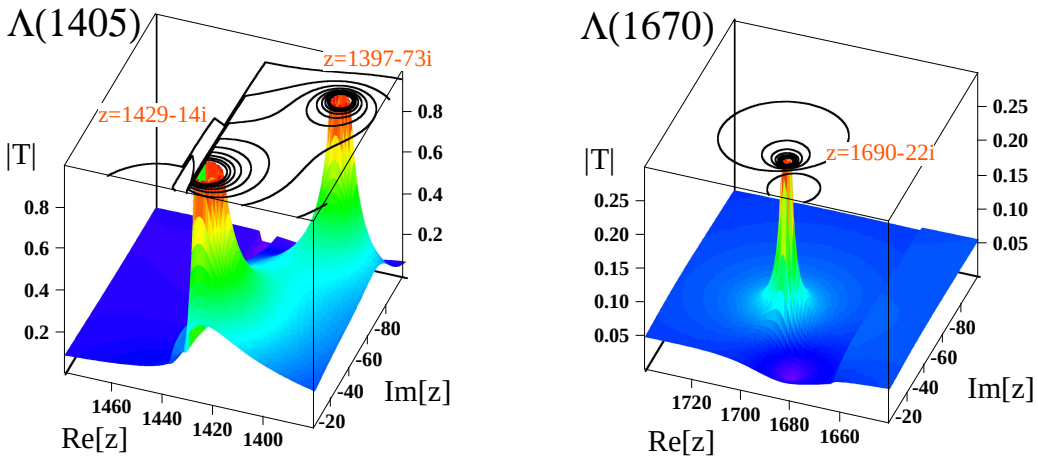

Figure 4.7: The absolute value of the scattering amplitude of $\bar{K}N \to \bar{K}N$ with $I = 0$ in the complex z plane. The amplitudes are plotted in energy region close to the $\Lambda(1405)$ resonance (left) and the $\Lambda(1670)$ resonance (right).

region of $\Lambda(1405)$, we find two poles at

$$z_1 = 1397 - 73i, \quad z_2 = 1429 - 14i. \tag{4.4.2}$$

Notice that there are two poles around this energy region, and they construct a distorted shape in the $\pi\Sigma$ mass distribution (Fig. 4.4). The two-pole structure of the $\Lambda(1405)$ will be discussed in Chapter 5 in more detail. Around the energy region of $\Lambda(1670)$, we also find a pole at

$$z = 1690 - 22i. \tag{4.4.3}$$

The values in Eqs. (4.4.2) and (4.4.3) are slightly different from the values in Ref. [503], because here we use $f = 1.15 \times 93$ MeV for the meson decay constant, while $f = 1.123 \times 93$ MeV is used in Ref. [503]. In the $S = 0$ channel, we find a pole at

$$z = 1496 - 31i,$$

as shown in Fig. 4.8. This pole corresponds to the $N(1535)$ resonance. The mass and width extracted from the pole deviates from the nominal values. The difference can be reduced by introducing vector meson exchange and $\pi\pi N$ channel [504].

Next we calculate residues of the poles,

$$\begin{aligned}\lim_{z\to z_R}[(z-z_R)T_{ij}(z)] &= \lim_{z\to z_R}\left[(z-z_R)\frac{g_i g_j}{z-z_R} + (z-z_R)T_{ij}^{BG}\right] \\ &= g_i g_j.\end{aligned}$$

where $z_R = M_R - i\Gamma_R/2$. These values determine the coupling strengths g_i and g_j of the resonance to meson-baryon states, which are well defined even if these states are closed in the decay of the resonance. The values of $|g_i|^2$ are shown in Tables 4.4 and 4.5.

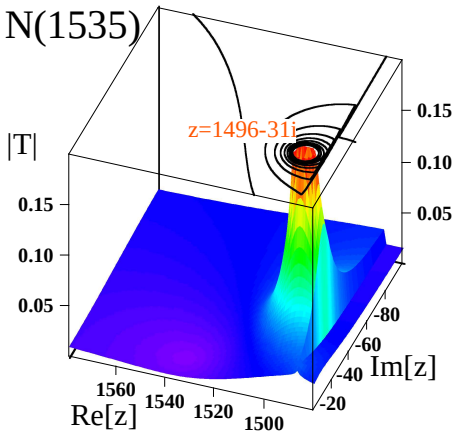

Figure 4.8: The absolute value of the scattering amplitude of $\pi N \to \pi N$ with $I = 1/2$ in the complex z plane. The amplitude is plotted in energy region close to the $N(1535)$ resonance.

Table 4.4: Coupling strengths of the $\Lambda(1405)$ and $\Lambda(1670)$ resonances to meson-baryon channels. All channels are in $I = 0$. Around the $\Lambda(1405)$ resonance, there are two poles z_1 and z_2 (4.4.2).

	z_R	$\lvert g_{\bar{K}N}\rvert^2$	$\lvert g_{\pi\Sigma}\rvert^2$	$\lvert g_{\eta\Lambda}\rvert^2$	$\lvert g_{K\Xi}\rvert^2$
$\Lambda(1405)$	$1397 - 73i$	3.83	8.20	0.497	0.383
	$1429 - 14i$	6.57	1.88	1.74	0.100
$\Lambda(1670)$	$1690 - 22i$	0.585	0.725	1.10	11.3

Table 4.5: Coupling strengths of the $N(1535)$ resonance to meson-baryon channels. All channels are in $I = 1/2$.

	z_R	$\lvert g_{\pi N}\rvert^2$	$\lvert g_{\eta n}\rvert^2$	$\lvert g_{K\Lambda}\rvert^2$	$\lvert g_{K\Sigma}\rvert^2$
$N(1535)$	$1496 - 31i$	0.895	2.65	2.11	8.61

From the Table 4.4, we see that the two poles for the $\Lambda(1405)$ have different coupling strengths. The pole at lower energy has a strong coupling to the $\pi\Sigma$ channel, while the pole at higher energy strongly couples to the $\bar{K}N$ channel. This fact will be important to study the $\Lambda(1405)$ structure in the next chapter. It is also seen that $\Lambda(1670)$ strongly couples to the $K\Xi$ channel, and this agrees with the fact that the position of the $\Lambda(1670)$ structure is dominated by $a_{K\Xi}$ parameter (Fig. 4.4). Concerning the $N(1535)$ resonance, the πN and ηN channels are open at the energy of the resonance. A large coupling constant for the ηN channel accounts for the decay branching ratio as large as that for πN channel, in spite of the small phase space ($p_{\pi N} = 468$ MeV, $p_{\eta N} = 186$ MeV). This corresponds to the experimental observation. It is worth noting that the channel which has the strongest coupling is $K\Sigma$, indicating the interpretation of $N(1535)$ as a $K\Sigma$ bound state [559, 560].

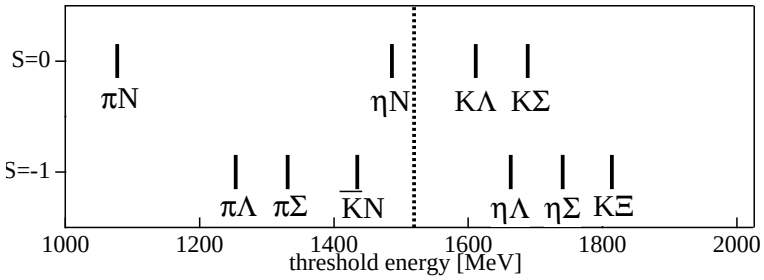

Figure 4.9: Threshold energies of meson-baryon scattering in the $S = -1$ and $S = 0$ channels. The dotted line in the middle represents the averaged energy of all the meson-baryon thresholds.

4.5 Flavor SU(3) breaking interactions

As we have seen in the previous sections, the channel-dependent subtraction constants a_i are crucial in order to reproduce important features of experimental data in Refs. [503, 504]. In this section, we consider SU(3) breaking terms of the chiral Lagrangian in order to see if the channel dependence in the subtraction constants can be absorbed into those terms. In this way, we are hoping that the number of free parameters can be reduced and that the origin of the channel dependence can be clarified.

As we have discussed in subsection 4.3.1, the subtraction constants should not depend on the scattering channel in the SU(3) limit [6, 519]. The SU(3) breaking should have a significant effect on the observed quantities. This is expected from, for instance, the large dependence of the threshold energies on the meson-baryon channels, as shown in Fig. 4.9. This is particularly true for $S = 0$, in which case the lowest threshold energy of the πN channel deviates considerably from the mean value. Furthermore, it was discussed in Ref. [561] that the number of channel-dependent subtraction constants for all SU(3) channels exceeds the number of available counter terms of chiral order p^3. The SU(3) breaking effect was partly included as the masses of particles in the previous formulation, but the kernel interaction (4.2.2) was SU(3) symmetric. Here we consider the SU(3) breaking effect at the interaction level.

In this way, we expect that the parameters in previous treatments could be controlled based on appropriate physical considerations. This would allow us to extend this method to other channels with predictive power.

4.5.1 Flavor SU(3) breaking terms in the chiral Lagrangian

Here we introduce the flavor SU(3) breaking effects in the chiral Lagrangian by the quark masses. They are obtained by assuming that the current quark mass matrix $\boldsymbol{m}$ is transformed under the chiral transformation as $\boldsymbol{m} \to R\boldsymbol{m}L^\dagger$ and $\boldsymbol{m}^\dagger = \boldsymbol{m}$. Here we maintain isospin symmetry, that is, $\boldsymbol{m} = \mathrm{diag}(\hat{m}, \hat{m}, m_s)$. Then, the SU(3) breaking terms are given uniquely

up to order $\mathcal{O}(m_q)$ as [48]

$$\begin{aligned}\mathcal{L}_{SB} =& -\frac{Z_0}{2}\mathrm{Tr}\Big(d_m\bar{B}\{\xi\boldsymbol{m}\xi+\xi^\dagger\boldsymbol{m}\xi^\dagger,B\}+f_m\bar{B}[\xi\boldsymbol{m}\xi+\xi^\dagger\boldsymbol{m}\xi^\dagger,B]\Big)\\ &-\frac{Z_1}{2}\mathrm{Tr}(\bar{B}B)\mathrm{Tr}(\boldsymbol{m}U+U^\dagger\boldsymbol{m}),\end{aligned} \tag{4.5.1}$$

where $f_m + d_m = 1$ and $U(\Phi) = \xi^2 = \exp\{i\sqrt{2}\Phi/f\}$. In this Lagrangian, there are three free parameters, $Z_0, Z_1, f_m/d_m$, which are determined by the baryon masses and the pion-nucleon sigma term, as we see below. For the quark mass, we take $m_s/\hat{m} = 26$, which is determined in ChPT from the meson masses. According to the chiral counting rule, these quark mass terms can be regarded as quantities of $\mathcal{O}(p^2)$, if we assume the Gell-Mann–Oakes–Renner (GMOR) relation [43], which implies $m_q \propto m_\pi^2$. In this work, we take into account only the terms in Eq. (4.5.1), and we do not consider other terms of order $\mathcal{O}(p^2)$. We explain the reason in the next subsection.

Expanding the Lagrangian (4.5.1) in powers of the meson fields, the zeroth order terms contribute to the baryon mass splitting, which automatically satisfy the Gell-Mann–Okubo (GMO) mass formula [562, 563]. By using the mass differences among the octet baryons, we determine the parameters Z_0 and f_m/d_m. The πN sigma term, which we take here to be $\sigma_{\pi N} = 36.4$ MeV, is used to determine the parameter Z_1. The choice of the $\sigma_{\pi N}$ would be consistent with the value in Ref. [564], taking into account the one-loop correction of about +10 MeV [565]. The resulting parameters are given as

$$Z_0 = 0.528, \quad Z_1 = 1.56, \quad f_m/d_m = -0.31,$$

and $M_0 = 759$ MeV in the Lagrangian (4.2.1), which is consistent with the recent analysis [566].

The meson-baryon interaction Lagrangian with SU(3) breaking is obtained by picking up the terms with two meson fields. We find

$$\begin{aligned}\mathcal{L}^{(2)}_{SB} =& \frac{Z_0}{4f^2}\mathrm{Tr}\Big(d_m\bar{B}\big\{(2\Phi\boldsymbol{m}\Phi+\Phi^2\boldsymbol{m}+\boldsymbol{m}\Phi^2),B\big\}+f_m\bar{B}\big[(2\Phi\boldsymbol{m}\Phi+\Phi^2\boldsymbol{m}+\boldsymbol{m}\Phi^2),B\big]\Big)\\ &+\frac{Z_1}{f^2}\mathrm{Tr}(\bar{B}B)\mathrm{Tr}(\boldsymbol{m}\Phi^2).\end{aligned}$$

From this Lagrangian, the basic interaction is given by

$$\begin{aligned}V^{(SB)}_{ij} =& -\frac{1}{f^2}\Big[Z_0\Big((A^d_{ij}d_m+A^f_{ij}f_m)\hat{m}+(B^d_{ij}d_m+B^f_{ij}f_m)m_s\Big)+Z_1\delta_{ij}D_i^{Z_1}\Big]\\ &\times\sqrt{\frac{E_i+M_i}{2M_i}}\sqrt{\frac{E_j+M_j}{2M_j}}.\end{aligned} \tag{4.5.2}$$

The explicit forms of the coefficients A_{ij}, B_{ij} and D_i are given in Tables D.9-D.14 in Appendix. These interaction terms are independent of the meson momenta, unlike the WT interaction (4.2.2).

Adding Eq. (4.5.2) to Eq. (4.2.2) and substituting them into Eq. (4.2.8), we obtain the unitarized T-matrix with the flavor SU(3) breaking effects as

$$T = \Big[1-\Big(V^{(WT)}+V^{(SB)}\Big)G\Big]^{-1}\Big(V^{(WT)}+V^{(SB)}\Big). \tag{4.5.3}$$

Because we have already fitted all parameters in the chiral Lagrangian, our parameters in the chiral unitary model with SU(3) breaking effects are only the subtraction constants.

4.5.2 Other SU(3) symmetric terms of $\mathcal{O}(p^2)$

In the chiral Lagrangian, there are other $\mathcal{O}(p^2)$ terms symmetric in the SU(3) flavor in addition to the above breaking terms, if we strictly follow the ordinary chiral counting rule in powers of the pseudoscalar meson momentum p and the quark mass m, where the GMOR relation fixes the ratio of m and p^2. Indeed, it is known in chiral perturbation theory that at $\mathcal{O}(p^2)$, the πN scattering length is correctly obtained through a large cancellation between the SU(3) breaking term and a symmetric term [567, 568], because the lowest-order, *i.e.* the Weinberg-Tomozawa term, already provides a sufficiently good result. This would imply that only the inclusion of the breaking term would be inconsistent with the cancellation.

However, in the present work, the symmetric terms are not taken into account for the following reasons. 1) These terms are not responsible for the symmetry breaking which we would like to study in this paper. 2) The purpose of the present work is to investigate baryon resonances as dynamically generated objects. The symmetric terms of $\mathcal{O}(p^2)$ may contain information regarding resonances [514], as shown for the role of the ρ meson in π-π scattering [569]. The inclusion of some of the symmetric terms would introduce intrinsic properties of genuine resonances that originate from the quarks. 3) As we will see below, the πN scattering length is qualitatively reproduced well without the $\mathcal{O}(p^2)$ symmetric terms, because the subtraction constants in the chiral unitary approach are adjustable parameters determined by the threshold branching ratio Eq. (4.3.5). Strictly speaking, as argued in Ref. [512], the subtraction constants appear as $\mathcal{O}(p^3)$ quantities in the chiral expansion of the amplitude obtained in the unitary approach, because they originate from the loop integral. Therefore, they should not cancel the quark mass terms, which are counted as $\mathcal{O}(p^2)$. Nevertheless, we have room to interpret the subtraction constants as containing some of the $\mathcal{O}(p^2)$ terms that we do not take into account explicitly, as the parameter fitting is carried out for the full amplitudes obtained in the unitarity resummation at the physical threshold, and, as we see below, the threshold ratios are qualitatively reproduced much better than ChPT at lowest-order. This implies that some partial contributions of the symmetric terms are taken into account as constant values at the threshold.

In order to demonstrate the third point above, let us introduce another set of parameters a'_i that originate in the $\mathcal{T}_{ij}^{-1}$ term in Eq. (4.2.4),

$$T_{ij}^{-1}(\sqrt{s}) = \delta_{ij}\Big(\tilde{a}_i(s_0) + \frac{s-s_0}{2\pi}\int_{s_i^+}^{\infty} ds' \frac{\rho_i(s')}{(s'-s)(s'-s_0)}\Big) + a'_i\delta_{ij} + \mathcal{T}_{ij}^{-1}. \tag{4.5.4}$$

Here, we assume that the parameters a'_i form a diagonal matrix in the channel space. Note that the parameters a'_i are introduced as quantities that are not related to the regularization of the loop integral, but they should be determined by ChPT. Now the parameters a'_i can be related to the coefficients of the $\mathcal{O}(p^2)$ symmetric Lagrangian. They are expressed as combinations of the two meson momenta

$$p_1^2, \quad p_2^2, \quad p_1 \cdot p_2, \quad \sigma_{\mu\nu} p_1^\mu p_2^\nu,$$

with subscripts 1 and 2 indicating the initial and final states, respectively. The last term does not contribute to the s-wave amplitude, and due to the symmetry under interchanges of 1 and 2 mesons, the coefficients of p_1^2 and p_2^2 should be the same. Therefore we have two independent coefficients. It is appropriate to consider the complete set of p^2 terms in the interaction kernel in order to strictly maintain consistency with ChPT and to achieve better agreement with the amplitudes. Once again, however, here we would like to study the SU(3) breaking effect on the excited baryons as dynamically generated objects. In our procedure, the SU(3) breaking is considered in the chiral perturbation theory completely, but without properties of genuine resonances.

As seen in Eq. (4.5.4), the parameters a_i' can be absorbed into the subtraction constants $\tilde{a}_i$, as $\tilde{a}_i \to \tilde{a}_i + a_i'$. Furthermore, SU(3) symmetry reduces $\tilde{a}_i$ to a single parameter, $\tilde{a}$. Hence, by adjusting $\tilde{a}$, we can use one degree of freedom of a' to fit the low energy data. The introduction of a' is equivalent to the replacement

$$G \to G + a'.$$

Now, we expand the unitarized amplitude (4.5.3) in terms of the small meson momentum p, assuming that a' is an $\mathcal{O}(p^0)$ quantity, as

$$\begin{aligned} T &= V^{(WT)} + V^{(SB)} + (V^{(WT)} + V^{(SB)})(G + a')(V^{(WT)} + V^{(SB)}) + \cdots \\ &= \underbrace{V^{(WT)}}_{p^1} + \underbrace{V^{(SB)} + V^{(WT)} a' V^{(WT)}}_{p^2} + V^{(WT)} G V^{(WT)} + \cdots . \end{aligned}$$

The third term in the second line, $V^{(WT)} a' V^{(WT)}$, can play the role of an interaction derived from the p^2 Lagrangian and may cancel the $V^{(SB)}$ contribution to the scattering length when we choose $\tilde{a} + a'$ such that the low energy amplitude is reproduced.

4.5.3 The $S = -1$ channel

Let us calculate the amplitude numerically. We follow the same procedures here as in the calculations without the SU(3) breaking terms. First, we determine the common subtraction constant a from the threshold branching ratios (4.3.5). The optimal value is found to be $a = -1.59$ and the results for the branching ratios are shown in Table 4.2. With this subtraction constant, the total cross sections of the $K^- p$ scattering, the $\pi\Sigma$ mass distribution, and the scattering amplitude of $\bar{K}N \to \bar{K}N$ with $I = 0$ are plotted in Figs. 4.10 and 4.11 by the dash-dotted curves. For comparison, we plot the results without SU(3) breaking by the dotted curves. As seen in Fig. 4.10, for all the total cross sections, the inclusion of the SU(3) breaking terms with the common value a causes the agreement with data to become worse, although the threshold branching ratios are produced much better than in the previous works.

In the $\pi\Sigma$ mass distribution shown in Fig. 4.11 (the dash-dotted curve), a sharp peak is seen, in obvious contradiction with the observed spectrum. This means that the important resonance structure of $\Lambda(1405)$ has been lost. However, we find two poles of the T-matrix amplitude at $z_1 = 1389 - 135i$ and $z_2 = 1424 - 1.6i$ in the second Riemann sheet, which should be compared with the previous results (4.4.2). These agree with the previous results

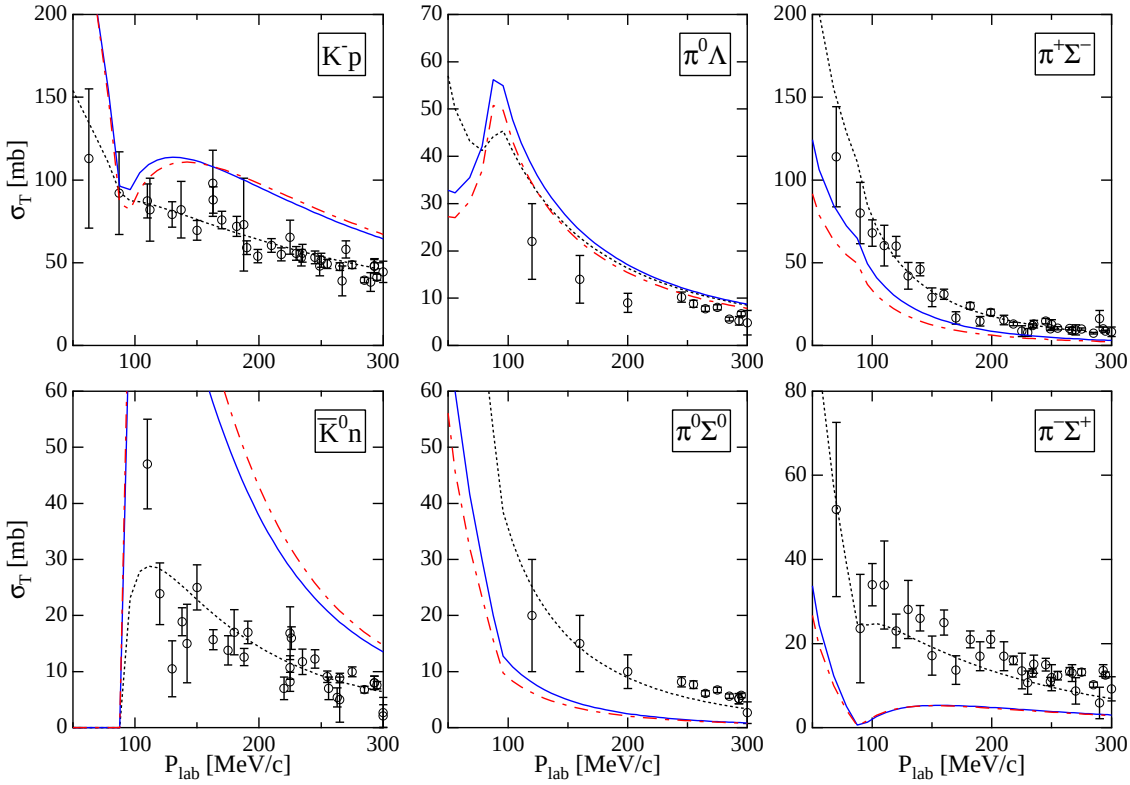

Figure 4.10: Total cross sections of $K^- p$ scattering ($S = -1$) as functions of $P_{\rm lab}$, the three-momentum of the initial K^- in the laboratory frame. The dotted curves represent the results obtained with the common value $a = -1.96$ without SU(3) breaking, the dash-dotted curves represent the results obtained including the SU(3) breaking with the common value $a = -1.59$, and the solid curves represent the results obtained including the SU(3) breaking and the physical f with the common value $a = -1.68$. The open circles with error bars are experimental data taken from Refs. [522, 523, 524, 525, 526, 527, 529, 530, 528, 531, 532, 533].

qualitatively. The inclusion of the SU(3) breaking terms does not change the conclusion of two poles, although the positions of the poles change.

We also calculate the total cross sections and the $\pi\Sigma$ mass distribution with the physical values of the meson decay constants, $f_\pi = 93$ MeV, $f_K = 1.22 f_\pi$, $f_\eta = 1.3 f_\pi$. The calculated results are represented in Figs. 4.10 and 4.11 by the solid curves. The optimal value of the subtraction constants is $a = -1.68$, and with this value, the threshold branching ratios are reproduced as $\gamma = 2.35$, $R_c = 0.626$ and $R_n = 0.172$. The SU(3) breaking effect on the meson decay constants is not so large in the total cross sections. However, the shape of the peak seen in the $\pi\Sigma$ mass distribution becomes wider than that in the calculation with the averaged meson decay constant.

Indeed, we again find two poles in the scattering amplitudes at $z_1' = 1363 - 87i$ and $z_2' = 1424 - 2.6i$ in the second Riemann sheet. Compared with the poles z_1 and z_2 obtained in the above calculation, the position of the pole z_1' moves to the lower energy side and

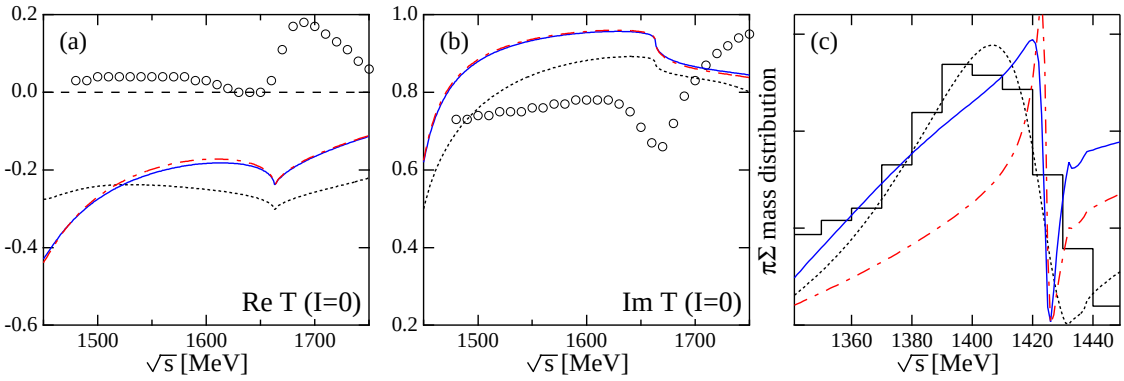

Figure 4.11: Real (a) and imaginary (b) parts of the T-matrix amplitude of $\bar{K}N \to \bar{K}N$ with $I = 0$ and the mass distributions (c) of the $\pi\Sigma$ channel with $I = 0$. The dotted curves represent the results obtained with the common value $a = -1.96$ without SU(3) breaking, the dash-dotted curves represent the results obtained including the SU(3) breaking with the common value $a = -1.59$, and the solid curves represent the results obtained including the SU(3) breaking and the physical f with the common value $a = -1.68$. The open circles in (a) and (b) are the experimental data taken from Ref. [534], while the histogram in (c) represents the experimental data taken from Ref. [535]

approaches the real axis. The reason why the position of z_1' changes can be understood as follows. Because z_1 has a large imaginary part, which implies a large width, and only the $\pi\Sigma$ channel is open in this energy region, the resonance represented by the pole z_1 has a strong coupling to the $\pi\Sigma$ channel. This fact implies that the position of the pole z_1 is sensitive to the $\pi\Sigma$ interaction. In the present calculation, the pion decay constant (93 MeV) is smaller than the averaged value (106.95 MeV) used in the above calculation, so that the attractive interaction of $\pi\Sigma$ becomes stronger. This shifts the position of the pole z_a to the lower energy side. Simultaneously, this suppresses the phase space of the decay of the resonance to the $\pi\Sigma$ channel, and hence, the position of the pole approaches the real axis.

4.5.4 The $S = 0$ channel

Here we present calculations in the $S = 0$ channel with the SU(3) breaking terms. With a common value $a \sim -1.5$, with which the threshold properties are reproduced well in the $S = -1$ channel, we still obtain a large contribution in the S_{11} πN scattering amplitude at low energy, as in the calculation without the SU(3) breaking effects. From this analysis, it is found that the low energy behavior of the πN scattering cannot be reproduced as long as we use the common value $a \sim -2$, even if we introduce the SU(3) breaking effects.

In order to search for the optimal value of the common subtraction constant within the $S = 0$ channel, we carried out a fitting of the T-matrix elements in the πN S_{11} channel in the low energy region up to 1400 MeV. We find $a = 1.33$. The results including the SU(3) breaking effects with $a = 1.33$ are represented as the dash-dotted curves in Figs. 4.12 and 4.13. The results without SU(3) breaking are plotted by the dotted curves. As seen in Fig. 4.13, the fitting is accurate up to $\sqrt{s} \sim 1400$ MeV, while, however, the resonance structure does

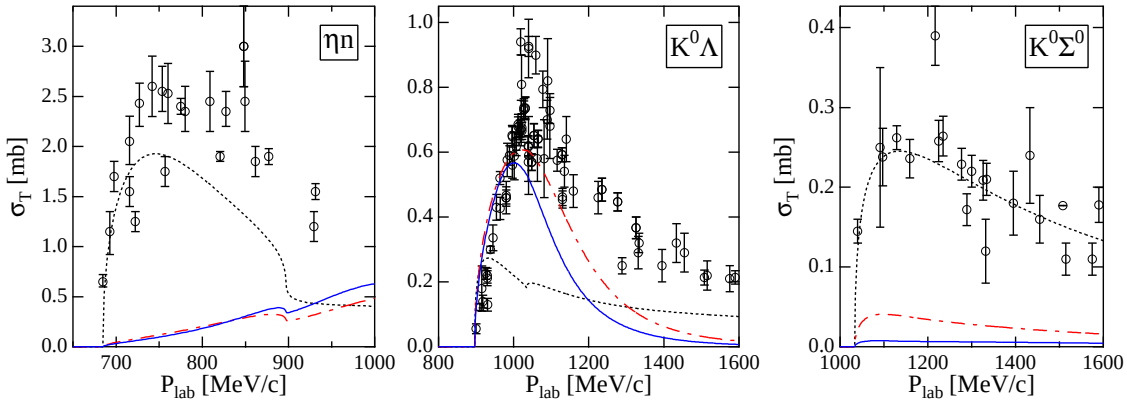

Figure 4.12: Total cross sections of $\pi^- p$ scattering ($S = 0$) as functions of $P_{\rm lab}$, the three-momentum of the initial π^- in the laboratory frame. The dotted curve represent the results obtained with the common value $a = 0.53$ without SU(3) breaking, the dash-dotted curves represent the results obtained including the SU(3) breaking interaction with the common value $a = 1.33$, and the solid curves represent the results obtained including the SU(3) breaking and the physical f with the common value $a = 2.24$. The open circles with error bars are experimental data taken from Refs. [537, 538, 539, 540, 541, 542, 543, 544, 545, 546, 547, 548, 549, 550, 551, 552, 553, 554, 555, 556].

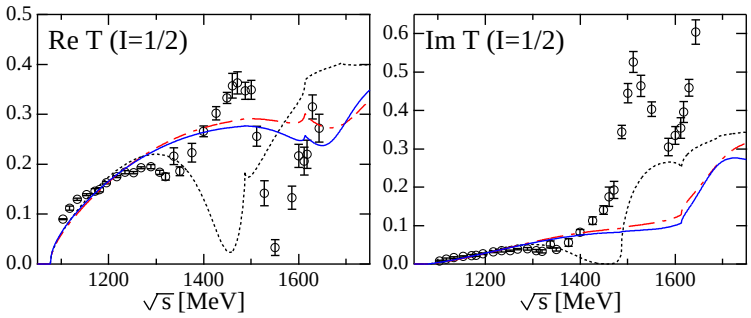

Figure 4.13: Real and imaginary parts of the S_{11} T-matrix amplitudes of $\pi N \to \pi N$. The dotted curves represent the results obtained with the common value $a = 0.53$ without SU(3) breaking, the dash-dotted curves represent the results obtained including the SU(3) breaking interaction with the common value $a = 1.33$, and the solid curves represent the results obtained including the SU(3) breaking and the physical f with the common value $a = 2.24$. The open circles with error bars are experimental data taken from Ref. [557].

not appear near energies of $N(1535)$.

Finally, we present the calculations with the physical values of the meson decay constants in Figs. 4.12 and 4.13 (solid curves). The optimal value of the common subtraction constant is found to be $a = 2.24$. The results with the physical meson decay constants and $a = 2.24$ are very similar to the results of the calculation with the averaged value of the decay constants and $a = 1.33$. In this sense, the SU(3) breaking effect of the meson decay constant f is absorbed into the change of the common subtraction constant a.

In closing this section, we conclude that even if we introduce the SU(3) breaking effects at the Lagrangian level, the SU(3) breaking in the channel-dependent subtraction constants a_i cannot be absorbed into the SU(3) breaking effects in the fundamental interactions in both the $S = -1$ and $S = 0$ channels.

4.6 Summary and discussion

In this chapter, we have presented the formulation of the chiral unitary model for meson-baryon scattering, in which baryon resonances are generated dynamically in the non-perturbative resummation. Numerical results are shown for the total cross sections and scattering amplitudes in $S = -1$ and $S = 0$ channels. Then we introduce the SU(3) breaking interaction in order to see the effect in the scattering observables.

First we have attempted to use a single common subtraction constant in order to describe meson-baryon scattering and baryon resonance in a unified way. In the $S = -1$ channel, $a \sim -2$ is fixed from the threshold branching ratios of the $K^- p$ scattering. With this parameter value, the total cross sections of the $K^- p$ scattering are reproduced well, as well as the mass distribution for the $\Lambda(1405)$. However, in this case the $\Lambda(1670)$ resonance cannot be reproduced. The subtraction constant $a \sim -2$ corresponds to $q_{\rm max} = 630$ MeV in the three-momentum cutoff regularization of the meson-baryon loop integral [512]. The elementary interaction of the $\bar{K}N$ system is sufficiently attractive, and a resummation of the coupled channel interactions causes the $\Lambda(1405)$ resonance to appear at the correct position, by imposing the unitarity condition and by using the natural value for the cutoff parameter. Hence, the wave function of $\Lambda(1405)$ is largely dominated by the meson-baryon component.

On the other hand, in the $S = 0$ channel, if one uses the natural value for the subtraction constant, as in the $S = -1$ channel, the attraction of the meson-baryon interaction becomes so strong that an unexpected resonance is generated near $\sqrt{s} \sim 1250$ MeV. Therefore, a repulsive component is necessary to reproduce the observed πN scattering. The fitted subtraction constant using the low energy πN scattering amplitude is $a \sim 0.5$. With this value, however, the $N(1535)$ resonance is not generated, while the agreement among the cross sections of $\pi^- p \to \eta n$ is rather good, due to the threshold effects.

The unitarized amplitudes are very sensitive to the attractive component of the interaction. The interaction terms of the ChPT alone do not explain all scattering amplitudes simultaneously. Rather, they must be supplemented by subtraction constants in the chiral unitary model to provide a reasonable description. For smaller a, the interaction becomes more attractive, and for larger a, less attractive. For $S = 0$, we need to choose $a \sim 0.5$ in order to suppress the attraction from the πN interaction, in contrast to the situation for

the natural value $a \sim -2$ in the $S = -1$ channel. Therefore, it is not possible to reproduce both the $\Lambda(1405)$ resonance properties and the low energy πN scattering with a common subtraction constant within the present framework.

Generally speaking, the chiral unitary approach is a powerful phenomenological method. It can reproduce cross sections and generate s-wave resonances dynamically, once the subtraction constants are determined appropriately, using experimental data. However, it is not straightforward to apply the method to channels for which there are not sufficient experimental data, because they are needed to determine the subtraction constants.

Next, we introduced the flavor SU(3) breaking Lagrangian, with the hope that the channel dependence in the subtraction constants would be absorbed into the coefficients in the chiral Lagrangian. These coefficients can be determined from other observables, and hence they are more controllable than the subtraction constants which have to be fitted to the experimental data. However, the channel dependence of the subtraction constants in each strangeness channel cannot be replaced by the SU(3) breaking Lagrangian, although we have exhausted possible breaking sources up to order $\mathcal{O}(m_q)$.

Therefore, in the present framework, where the Weinberg-Tomozawa term and symmetry breaking terms are taken into account, a suitable choice of the channel-dependent subtraction constants is essential. Theoretically, it would be very important to obtain a microscopic explanation of the origin of the channel-dependent subtraction constants. One possibility is to consider quark degrees of freedom, which can generate genuine resonance states. Another possibility to solve this problem is to employ interaction terms up to order p^3 with the channel-independent renormalization scheme [570]. Further investigations should be carried out in order to better understand the nature of baryon resonances.

4.7 Variants and applications

Before closing this chapter, let us review various approaches in chiral unitary models, focusing on the differences among their results and formulations. Since all the different approaches share the fundamental features of chiral symmetry and unitarity, qualitative results agree with each other, but quantitative differences can be observed. It is also instructive to list the applications of the chiral unitary models, for instance, to the reaction processes and to in-medium properties of hadrons.

4.7.1 Meson-baryon scattering

In the modern context, the chiral unitary model for meson-baryon scattering was first developed by Kaiser, Siegel, and Weise [4, 559]. They solved the Lippman-Schwinger equation with the interaction kernel deduced from the heavy baryon chiral Lagrangian up to $\mathcal{O}(p^2)$ terms. The low-energy constants in $\mathcal{O}(p^2)$ Lagrangians were fitted to reproduce data. Regularization of the loop integral was done by the range parameters in the kernel, which were channel dependent. The $S = -1$ [4] and $S = 0$ [559] scatterings were treated on the same basis. In both cases, the scattering data and the resonance properties of the $\Lambda(1405)$ and $N(1535)$ were well reproduced. These studies are complied in Ref. [560]. Further study with

this model was performed [571, 517] in connection with the DEAR experiment [572] and two-pole structure of the $\Lambda(1405)$.

A different approach was taken in Ref. [5] by Oset and Ramos for the $S = -1$ scattering. With the leading order Weinberg-Tomozawa (WT) term for the fundamental interaction, Bethe-Salpeter (BS) equation was solved with on-shell factorization. The loop integral was regularized by cutoff in the three-momentum, and total cross sections of the $K^- p$ scattering, threshold branching ratios, and the $\Lambda(1405)$ properties were well reproduced. They emphasized the importance of the full SU(3) channels, namely the inclusion of the channels with η or Ξ, which had not been included in the previous studies. The $S = -1$ scattering was discussed in the context of the N/D method [512], where the authors studied the relation between the dimensional regularization and cutoff scheme adopted in Ref. [5]. For the kernel interaction, they included all the terms of $\mathcal{O}(p)$, namely, the Born terms are included in addition to the dominant WT term. By solving the scattering amplitude analytically, the structure in the complex energy plane was first studied, finding two poles for the $\Lambda(1405)$ in the chiral unitary model. This approach has been extended in Ref. [573] (see also Refs. [574, 575]).

In this context, the amplitude in $S = -1$ channel was further studied in Ref. [503] with the WT term and dimensional regularization. They round the $\Lambda(1670)$ and the $\Sigma(1620)$ resonances in addition to the $\Lambda(1405)$. This framework can be applied to other strangeness sectors. For the $S = 0$ sector [504], the $N(1535)$ and $\Delta(1620)$ were observed, and for the $S = -2$ sector [505], a baryonic resonance was dynamically generated around the $\Xi(1620)$ resonance, whose spin and parity are not known. Therefore, they assigned $J^P = 1/2^-$ for the $\Xi(1620)$ resonance. The p-wave interaction for the $S = -1$ scattering was studied in Ref. [576], providing a reasonable description of the differential cross section and the $\Sigma(1385)$ resonance. In this study the pole of the $\Sigma(1385)$ was introduced as an elementary field, and it acquires the imaginary part by the non-perturbative resuumation. Scheme dependence of the renormalization was studied in Ref. [577], where the dimensional regularization and form factor scheme were compared. The dependence of the regularization scheme was found to be minimized by choosing appropriate regularization parameters. The two-pole structure of the $\Lambda(1405)$ was studied based on the SU(3) symmetry in Ref. [519]. This subject will be discussed in the next chapter.

A systematic calculation was performed in Refs. [578, 579, 570], including the chiral Lagrangians up to $\mathcal{O}(p^3)$, which was further constrained by the large N_c counting. The authors developed an renormalization scheme, which incorporated approximate crossing symmetry. Based on a similar framework, but with the lowest order WT term for the interaction, $S = 0, -1, -2$ channels were studied with quark mass dependence of the poles for the resonances [536]. In this scheme, two-pole structure for the $\Lambda(1405)$ was qualitatively confirmed. For the $S = -2$ channel, the $\Xi(1690)$ resonance was found in addition to the $\Xi(1620)$, reported in Ref. [505]. An advantage in this approach was the systematized renormalization, where no additional parameter was necessary.

Another approach was applied to S_{11} channel with $S = 0$ and reproduced the $N(1535)$ and the $N(1650)$ resonances [580]. The interaction was the lowest order WT term, and BS equation was solved relativistically. In the same formalism, $S = -1$ and $I = 0$ channel was calculated [581]. Two poles for the $\Lambda(1405)$ were found, but the lower one had a large

imaginary part ~ 250 MeV. This may have been caused by the fact that the K^-p threshold branching ratios (4.3.5) are not used for their fitting.

Apart from the above studies for the scattering of the pseudoscalar octet mesons and octet baryons of the ground states, several studies for the scattering between other mesons and baryons were performed.

The scattering between pseudoscalar **8** meson and **10** baryon with $J^P = 3/2^+$ *via* the WT interaction was studied in Ref. [561] along the same line with the model in Ref. [536]. The generated resonances were identified as experimentally known $J^P = 3/2^-$ particles. The **8**-**10** scattering was also studied [415, 414] with the same formulation in Refs. [5, 503]. This model will be used in chapter 7 and we will explain it later.

The application to the charm sector was performed [582] in the scattering of the pseudoscalar mesons with the ground state heavy baryons based on Ref. [536]. The heavy baryons were in $\overline{\mathbf{3}}$ and **6** representations of flavor SU(3), and the WT interaction was used for the kernel. Several charmed resonances were reproduced.

4.7.2 Applications

The scattering amplitudes obtained in the above studies can be applied to the production reactions, calculation for the coupling constants of the resonance, and hadron properties in nuclear matter.

In Ref. [560], coupling to the photons were introduced, and the photoproductions for η mesons and strangeness productions were studied in comparison with existing data. Based on the model [570], kaon photoproductions with the $\Lambda(1405)$ and the $\Sigma(1385)$ were studied [583]. The models in Ref. [5, 503] were applied to various reactions such as $\gamma p \to K^+\Lambda(1405)$ [584], $K^-p \to \Lambda(1405)\gamma$ [585], $\pi^-p \to K^0\Lambda(1405)$ [8], $\gamma p \to K^*\Lambda(1405)$ [11], and $K^-p \to \pi^0\Lambda(1405)$ [586]. These works can be used to study the two-pole structure of the $\Lambda(1405)$ in experiments.

Using the amplitudes obtained in the chiral unitary model, it is possible to extract the coupling constant of the resonance to various channels by attaching an external line. Based on the model in Ref. [5], coupling constants for the $N^*N^*\pi^0$ and $N^*N^*\eta$ were calculated [587]. Magnetic moments of $\Lambda(1405)$ and $\Lambda(1670)$ were evaluated in Ref. [588] based on the amplitude obtained in Ref. [503]. In the same way, the magnetic moments of the $N(1535)$ were studied in Ref. [13], which will be discussed in chapter 6.

In a recent paper, gauge invariance of the unitarized amplitude was studied [589]. It was shown that the photon field should be coupled not only to the external legs and the interaction kernel, but also to the all possible vertices in the resummation, in order to maintain the gauge invariance.

Low-energy $\bar{K}N$ interaction in nuclear matter was studied in the model of Ref. [4] with Pauli blocking, Fermi motion, and binding effects [590]. A strong in-medium modification for the $\bar{K}N$ interaction was observed and the mass of the $\Lambda(1405)$ increased as the density was increased. In further analysis for K and η in medium [591], the $N(1535)$ was predicted to survive in the nuclear matter, unlike the $\Lambda(1405)$ which dissolves. However, the importance of the self-consistent treatment was pointed out [592], which lead to the $\Lambda(1405)$ dissolved

even faster, without changing the position.

Chapter 5

Structure of $\Lambda(1405)$ and production reactions

In this chapter, we discuss the reaction mechanisms that lead to the $\Lambda(1405)$ production using the chiral unitary model. In the chiral unitary model, it is found that:

- there are two poles with $S = -1$ and $I = 0$ around the energy region of 1400 MeV, and
- they couple to the $\pi\Sigma$ and $\bar{K}N$ channels with different strengths.

These conclusions do not depend on the details of the model constructions. Here we investigate reaction processes for the $\Lambda(1405)$ production in order to provide a way to clarify the two-pole structure experimentally.

First, we study the $\pi^- p \to K^0\pi\Sigma$ reaction (section 5.2). In this reaction, we find two mechanisms which eventually filter each one of the resonances. The combination of the two mechanisms leads to a shape of the invariant mass distribution compatible with the experimental measurements. It turns out that this reaction is dominated by the contribution from the first pole, which locates at lower energy side and couples strongly to the $\pi\Sigma$ channel. This topic is reported in Refs. [8, 9, 10].

Next, the photo-induced K^* vector meson production ($\gamma p \to K^*\Lambda(1405) \to K\pi MB$) is investigated in section 5.3. From experimental point of view, this reaction has an advantage to suppress the background contribution by using the polarized photon beam. In addition, this reaction is particularly suited to the isolation of the pole at higher energy region, which strongly couples to the $\bar{K}N$ channel. We obtain the mass distribution of the $\Lambda(1405)$ peaking at 1420 MeV. Combined with the previous reaction $\pi^- p \to K^0\pi\Sigma$ which favors the other pole, this detailed study will reveal a novel structure of the $\Lambda(1405)$ state. The result is presented in Refs. [11, 12]. Finally, we summarize this chapter and recent progress in this fields in section 5.4.

5.1 Introduction : two-pole structure

There is a long-standing problem on the interpretation of the $\Lambda(1405)$ resonance. The $\Lambda(1405)$ was predicted through the analysis of the $K^- p$ scattering data [593], which was later con-

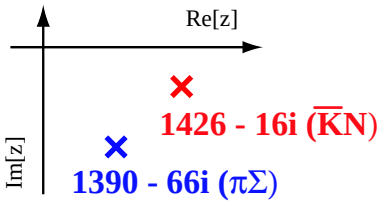

Figure 5.1: Schematic view of the two-pole structure.

firmed experimentally in Ref. [594]. It is known to be difficult to describe the Λ(1405) as a three-quark state within a naive constituent quark model [329], because of its light mass. Rather, it has been suggested to regard the Λ(1405) as a quasi-bound $\bar{K}N$ state which naturally appears in a coupled channel meson-baryon scattering close to the $\bar{K}N$ threshold [506, 507, 508]. These facts may imply that the Λ(1405) state is largely dominated by five-quark component.

In recent years, chiral unitary models which implement strong s-wave meson-baryon interactions have been showing that some of the $1/2^-$ resonances—including the Λ(1405)—are indeed well described by the coupled channel scattering approach. The use of the chiral Lagrangians has provided a systematic approach to face the meson-baryon interaction based on the chiral symmetry of QCD.

These models reveal an interesting structure of the Λ(1405) resonance; there are two poles, rather than one, in the region of the Λ(1405). The existence of two poles was first reported in the context of the cloudy bag model [595]. Recent analysis of chiral dynamics has confirmed the structure, and further investigation has been performed for the origin of these poles. Confirmation of this picture is important in order to understand better the non-perturbative dynamics of QCD.

Taking the model in Ref. [503], we find two poles at [519]

$$z_1 = 1390 - 66i \text{ MeV}, \quad z_2 = 1426 - 16i \text{ MeV}, \tag{5.1.1}$$

both of which have strangeness $S = -1$ and isospin $I = 0$. Despite two poles, one observe a single bump in the $\pi\Sigma$ mass distribution, which consists of the superposition of the two contributions. The former at lower energy and with a wider width z_1 couples dominantly to $\pi\Sigma$ channels, while the latter at higher energy with a narrower width z_2 couples dominantly to $\bar{K}N$ channels. This is schematically depicted in Fig. 5.1. Note that the positions of the poles slightly deviate from the one obtained in the previous chapter (Eq. (4.4.2)), because of the difference of the choice of the subtraction constants. Similarly, the quantitative values for the poles are different depending on the model set up, but all the model based on the chiral unitary approach agree qualitatively.

A clarification of this interesting result has been made in Ref. [519] where the two Λ(1405) states have been interpreted in the following way. They calculated the meson-baryon scattering amplitude in the SU(3) limit, and introduced gradually the SU(3) breaking effects coming from the particle masses and subtraction constants. In the SU(3) limit, the meson-baryon scattering amplitudes can be decomposed into channels in SU(3) irreducible representations. The Weinberg-Tomozawa term, which is SU(3) invariant and diagonal in SU(3) channels,

provides the strength of the interaction

$$V_{\alpha\beta} = \mathrm{diag}(6,\ 3,\ 3,\ 0,\ 0,\ -2), \tag{5.1.2}$$

for $\alpha = \mathbf{1}, \mathbf{8}_s, \mathbf{8}_a, \mathbf{10}, \overline{\mathbf{10}}$, and $\mathbf{27}$. This shows that there are attractive interactions for $\mathbf{1}, \mathbf{8}_s$, and $\mathbf{8}_a$ representations, which leads to a bound state for each channel. Two of them from $\mathbf{8}_s$ and $\mathbf{8}_a$ are degenerate, and one pole from the singlet locates at lower energy, because of the interaction strengths. On the other hand, Eq. (5.1.2) indicates the nonexistence of bound states in channels with exotic flavors $\overline{\mathbf{10}}$, and $\mathbf{27}$, at least for the s-wave meson-baryon scattering in the SU(3) limit.

In the $S = -1$ and $I = 0$ channel which consists of $\alpha = \mathbf{1}, \mathbf{8}_s, \mathbf{8}_a$, and $\mathbf{27}$, three bound states are observed in the SU(3) limit. The positions of poles change as the SU(3) breaking effects are switched on, and show trajectories in the complex energy plane [519]. The singlet pole and one of the octet poles move to the $\Lambda(1405)$ energy region, producing only one apparent bump in the spectrum. The other octet pole moves to the higher energy region, making the $\Lambda(1670)$ structure. In this sense, the appearance of two poles for the $\Lambda(1405)$ would be natural, based on attractions in three channels and two established resonances $\Lambda(1405)$ and $\Lambda(1670)$ at low energy. However, it should be noted that the SU(3) symmetry is not exact in physical world, and a state is the mixture of SU(3) representations. Some of the poles may disappear during the extrapolation to the physical world [519].

Since both the poles have the same quantum numbers, it seems difficult to confirm the two-pole structure in experiments. However, if the two resonances couple very differently to the $\pi\Sigma$ and $\bar{K}N$ (or any other) states, different reactions can give more weight to one or the other resonance leading to different shapes in the $\pi\Sigma$ mass distribution. This reopens a problem since the shape of the $\Lambda(1405)$ resonance from the $\pi\Sigma$ mass distribution was formerly assumed to be an intrinsic property of the resonance and hence independent of the reaction used to produce it. For instance, in previous works, the $\pi\Sigma$ mass distribution was calculated assuming

$$\frac{d\sigma}{dM_I} = C|t_{\pi\Sigma\to\pi\Sigma}|^2 p_{\mathrm{cm}}, \tag{5.1.3}$$

with p_{cm} the three momentum of the particle in the $\pi\Sigma$ rest frame. In practice, however, if one bears in mind that the $\Lambda(1405)$ resonance is built up from the multiple scattering of the coupled channels, $\bar{K}N$, $\pi\Sigma$, $\eta\Lambda$, $K\Xi$, one can produce the resonance first by producing any of these channels and then having final state interaction leading to the final $\pi\Sigma$ state. Hence, instead of Eq. (5.1.3), we should rather have

$$\frac{d\sigma}{dM_I} = |\sum_i C_i t_{i\to\pi\Sigma}|^2 p_{\mathrm{cm}}, \tag{5.1.4}$$

with i standing for any of the coupled channels, and the coefficients C_i will depend upon the particular reaction, when there are two poles with different coupling strengths to each channel i [519].

If there were only one state for $\Lambda(1405)$, Eqs. (5.1.4) and (5.1.3) would give the same result. This means that the peak position of a resonance seen in the invariant mass distribution does

not depends on the reaction to produce it (up to the interference effect with backgrounds). It should be noted that even if there are two poles, we obtain the same mass distribution for different reactions, when the two poles have *exactly the same coupling strengths* to the meson-baryon channels. The important thing in the present problem is not only the existence of two poles in the Λ(1405) energy region, but also the different coupling strengths of these resonances to the meson-baron channels.

Therefore, the mass distribution develops one or another shape depending on the coefficients C_i. The fact that this distribution follows Eq. (5.1.4) rather than Eq. (5.1.3), was already pointed out in Ref. [512]. However, no attempt was performed to calculate the C_i coefficients, but rather they were fitted to the data to obtain the experimental shape of the Λ(1405) resonance. However, it is possible to evaluate the C_i coefficients by calculating the reaction explicitly, as in Refs. [584, 585] and in the following studies.

In fact, the different shapes of the mass distribution were observed in the $\gamma p \to K^+\Lambda(1405)$ reaction [584] and $K^- p \to \Lambda(1405)\gamma$ reaction [585], which results in a $\pi\Sigma$ mass distribution narrower than the nominal one with the peak position shifted by about 20 MeV to higher energies.

In this chapter, we study the $\pi^- p \to K^0\pi\Sigma$ reaction and the $\gamma p \to K^*\Lambda(1405) \to K\pi MB$ reaction. The former will turn to be particularly selective of the first pole z_1, while the latter prefers the second pole z_2. Combining these two reactions, we can reveal the two poles really exist in the nominated resonance region.

5.2 The $\pi^- p \to K^0\pi\Sigma$ reaction

The aim of the present work is to study the $\pi^- p \to K^0\pi\Sigma$ reaction, from which the experimental data of the Λ(1405) resonance are usually extracted [543]. Another source of experimental information for the Λ(1405) spectrum comes from the $K^- p \to \Sigma^+(1660)\pi^-$ reaction followed by $\Sigma^+(1660) \to \Lambda(1405)\pi^+$, $\Lambda(1405) \to \pi\Sigma$ [535]. Here we would like to investigate the dynamics of the $\pi^- p \to K^0\pi\Sigma$ reaction, where the Λ(1405) is seen in the invariant mass spectrum of $\pi\Sigma$ state, and calculate the C_i coefficients entering Eq. (5.1.4) which determine the shape of the Λ(1405) resonance.

In the next subsection, we present the mechanisms of the $\pi^- p \to K^0\pi\Sigma$ reaction as an analogy of the model for the $\pi N \to \pi\pi N$ reaction based on the effective chiral Lagrangians [596]. In subsection 5.2.2, we explain the on-shell factorization, which is used to extract the momentum dependence out of the loop integral. The expressions of the resulting amplitudes are given in subsection 5.2.3 together with the correction factors. The numerical results with this model is shown in subsection 5.2.4, and in subsection 5.2.5, we introduce the contribution of a N^* resonance excited in the s channel. Combining the two mechanisms, we obtain a reasonable description for the experiments which is shown in subsection 5.2.6. Summary and conclusions are shown in the last subsection.

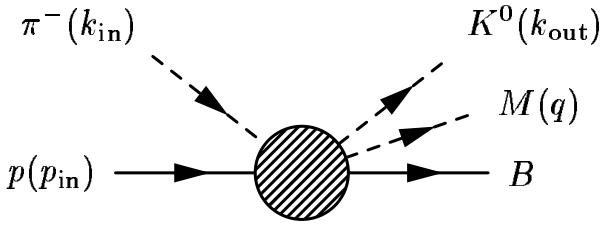

Figure 5.2: Kinematics of the $\pi^- p \to K^0 MB$ reaction. For the threshold production of K^0 and $\Lambda(1405)$, the three momentum $\boldsymbol{k}_{out}$ is negligible.

5.2.1 Construction of the chiral amplitude

Here we construct a model for the $\pi^- p \to K^0 \pi\Sigma$ reaction. Kinematics of this reaction is depicted in Fig. 5.2. We consider the reaction at energies close to threshold for the $K^0\Lambda(1405)$ production, *i.e.*, a total center of mass energy $\sqrt{s} \sim 2$ GeV, or equivalently a three momentum of the initial pion $p_\pi \sim 1.7$ GeV in the Laboratory frame. This means that the three momentum of the final kaon ($\boldsymbol{k}_{\rm out}$) is negligible. Details of this kinematics are presented in Appendix A.3.3.

We first present the interaction Lagrangians that we use in the following calculations. These terms are derived from the chiral Lagrangians, which are summarized in Appendix B together with the definition of the meson octet field Φ and baryon octet field B. The meson-meson interaction takes on the form

$$\mathcal{L}_2^{M(4)} = \frac{1}{12f^2}\mathrm{Tr}\left((\partial_\mu\Phi\Phi - \Phi\partial_\mu\Phi)^2\right) + B_0\mathrm{Tr}\left(\boldsymbol{m}\Phi^4\right), \tag{5.2.1}$$

where f is the meson decay constant and $\boldsymbol{m}$ is the quark mass matrix $\boldsymbol{m} = \mathrm{diag}(\hat{m}, \hat{m}, m_s)$. These terms are of the order of $\mathcal{O}(p^2)$. Similarly, from the lowest order meson-baryon Lagrangian, s-wave meson-baryon interaction is obtained as

$$\mathcal{L}_{WT} = \mathrm{Tr}\Big(\bar{B}i\gamma^\mu\frac{1}{4f^2}\left[(\Phi\partial_\mu\Phi - \partial_\mu\Phi\Phi), B\right]\Big), \tag{5.2.2}$$

which will provide a kernel interaction of the chiral unitary model. We derive the meson-baryon Yukawa interaction from the same Lagrangian as

$$\mathcal{L}_{\rm Yukawa} = -\frac{1}{\sqrt{2}f}\mathrm{Tr}\left(D(\bar{B}\gamma^\mu\gamma_5\{\partial_\mu\Phi, B\}) + F(\bar{B}\gamma^\mu\gamma_5[\partial_\mu\Phi, B])\right), \tag{5.2.3}$$

and the $MMMBB$ (three meson-two baryon) contact interaction as

$$\begin{aligned}\mathcal{L}_1^{B(3)} =& \frac{1}{12\sqrt{2}f^3}\mathrm{Tr}\Big(D(\bar{B}\gamma^\mu\gamma_5\{(\partial_\mu\Phi(\Phi^2) - 2\Phi\partial_\mu\Phi(\Phi) + \Phi^2\partial_\mu\Phi), B\}) \\ &+ F(\bar{B}\gamma^\mu\gamma_5[(\partial_\mu\Phi(\Phi^2) - 2\Phi\partial_\mu\Phi(\Phi) + \Phi^2\partial_\mu\Phi), B])\Big).\end{aligned} \tag{5.2.4}$$

The strengths of the F and D coupling constants are fixed as $F = 0.51$, $D = 0.75$. The Lagrangians of the chiral perturbation theory are summarized in Appendix B.1.

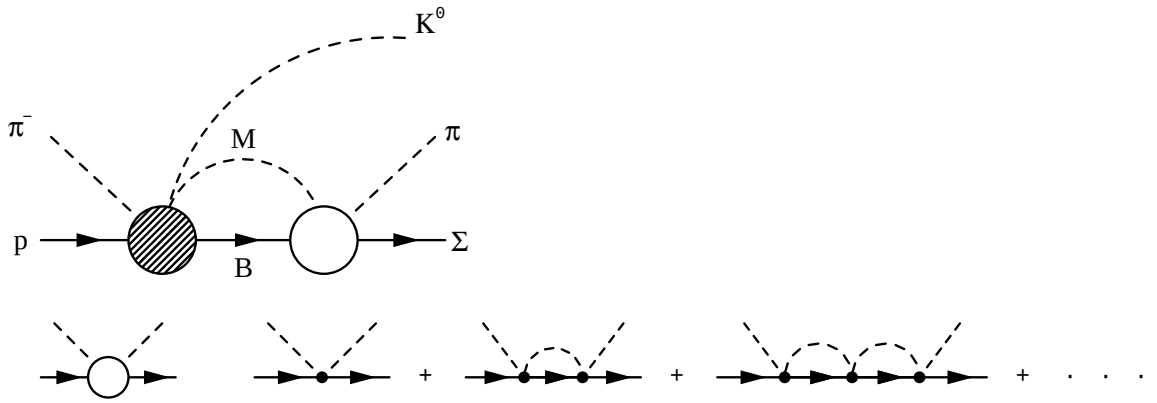

Figure 5.3: Diagrams entering the production of the Λ(1405) in the $\pi^- p \to K^0 MB \to K^0 \pi\Sigma$. In the figure, M and B stand for the meson and baryon of the 10 possible coupled channels. The Λ(1405) resonance is dynamically generated by the final state interaction of M and B (open blob). The initial process (hatched blob) will be given in Fig. 5.4.

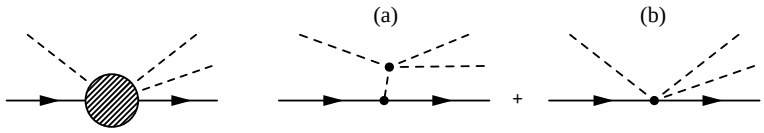

Figure 5.4: Basic terms entering the threshold production of $\pi^- p \to K^0 MB$ in analogy of $\pi N \to \pi\pi N$. (a) : meson pole term, (b) contact term.

Now we describe the formulation for the present reaction. Formally, we can separate the process into two parts as shown in Fig. 5.3. The first one (hatched blob) which involves tree level $\pi^- p \to K^0 MB$ amplitudes, and a second part (open blob) which involves the final state interaction $MB \to \pi\Sigma$, which eventually generates a resonance if kinematical and dynamical conditions allow for it. For the latter one, we produce dynamically the Λ(1405) *via* the final state interaction, which is obtained by solving the Bethe-Salpeter equation in coupled channels in the chiral unitary model. As explained in the previous chapter, the meson-baryon scattering amplitude $t_{\rm ChU}$ is given by

$$t_{\rm ChU} = [1 - VG]^{-1} V,$$

where the interaction kernel V and loop integral G are given in Eqs. (4.2.2) and (4.2.6), respectively. The kernel V obtained from the lowest order chiral Lagrangians of Eq. (5.2.2). The coupled channels appearing in this problem are $K^- p$, $\bar{K}^0 n$, $\pi^0\Lambda$, $\pi^0\Sigma^0$, $\eta\Lambda$, $\eta\Sigma^0$, $\pi^+\Sigma^-$, $\pi^-\Sigma^+$, $K^+\Xi^-$, $K^0\Xi^0$. In the following, the meson-baryon channels are numbered according to this ordering. Concerning the initial process, we extrapolate the result for the $\pi N \to \pi\pi N$ reaction [596]. The hatched blob in Fig. 5.3 can be expressed by the sum of meson pole terms and contact terms as shown in Fig. 5.4.

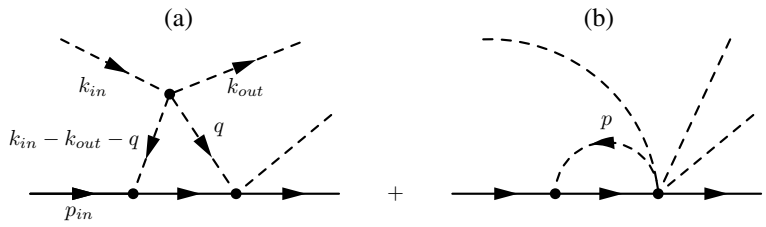

Figure 5.5: One loop functions for $MB \to MMB$.

5.2.2 On-shell factorization

One interesting observation in Ref. [5] is that the V amplitudes can be factorized on-shell (as a function of s) inside the meson-baryon loops appearing in Fig. 5.3. In the present case there is also an on-shell factorization for the initial process $\pi^- p \to K^0 MB$ as we discuss briefly. This process is then followed by the final state interaction, shown by the open blob.

For that purpose, let us consider the one loop diagram of Fig. 5.5 (a). In the following, we first show the factorization of the meson-meson amplitude with the momentum q on-shell, then show the cancellation of the off-shell part of the meson-meson amplitude associated to the momentum $k_{\rm in} - k_{\rm out} - q$. With these arguments, the on-shell factorization of the meson-baryon loops [5] can be applied to the present initial process, and we can calculate the whole amplitude by evaluating the initial process at the tree level, separated from the subsequent meson-baryon loops.

Let us start with showing that the meson-meson amplitude factorizes in Fig. 5.5 (a) with the momentum q on-shell. The s-wave meson-meson amplitudes from the chiral Lagrangians at lowest order have the form [597]

$$t_{MM} = as + \sum_i b_i m_i^2 + \sum_i \beta_i (q_i^2 - m_i^2),$$

where the term with β gives the off-shell extrapolation of the amplitude. If we take just this off-shell part for the meson of momentum q in Fig. 5.5 (a), the loop function reads as

$$\int \frac{d^4q}{(2\pi)^4} (q^2 - m^2) \frac{1}{q^2 - m^2} D_\pi(k_{\rm in} - k_{\rm out} - q) G_N(p_{\rm in} + k_{\rm in} - k_{\rm out} - q) \boldsymbol{\sigma} \cdot (\boldsymbol{k}_{\rm in} - \boldsymbol{k}_{\rm out} - \boldsymbol{q}), \quad (5.2.5)$$

using the non relativistic form $(\boldsymbol{\sigma} \cdot \boldsymbol{p})$ for the MBB vertex, which will be improved later on to account for relativistic corrections. One should note that in Eq. (5.2.5), the off-shell part of the meson-meson amplitude cancels the meson propagator and leads to a contracted diagram of the type of Fig. 5.5 (b). On the other hand, it is interesting to note that genuine diagrams of the type of Fig. 5.5 (b) appear from the consideration of the $BBMMMM$ terms that come from an expansion in the meson fields of the chiral Lagrangian. These terms should be added for consistency. However, by changing $\boldsymbol{q}$ to the $\boldsymbol{p}$ variable of Fig. 5.5 (b) in the loop functions and realizing that the dominant term in the $\gamma^\mu \partial_\mu$ structure of the $BBMMMM$ vertex comes from the $\gamma^0 \partial_0$ component (and hence no three momentum dependence), the loop functions of Fig. 5.5 vanish at this order (corrections coming at order $\mathcal{O}(1/2M)$).

There is also a cancellation of the off-shell part of the meson-meson amplitude for the meson with momentum $k_{\rm in}-k_{\rm out}-q$ in Fig. 5.5 (a). It appears already at tree level, but it comes from an exact cancellation between the off-shell part of the meson pole term and the contact term. This fact justifies the attempt to find out the on-shell $\pi\pi$ scattering amplitude from analysis of the $\pi N \to \pi\pi N$ data omitting the contact term [598], except for the contribution of other terms in the process [596]. This off-shell cancellation found here is important conceptually. In practice, we just calculate the meson pole term with the $p_{\rm ex}$ variable off-shell and add the contact term in each case, and the cancellation takes place automatically.

Next we look into a possible contribution from the p-wave part of the meson-meson amplitude. As anticipated, we are looking at the $\pi^- p \to K^0\pi\Sigma$ reaction close to threshold of the $\bar{K}N$ production in $\pi^- p \to K^0\bar{K}N$. This means that three momenta of the three final particles in the $\pi^- p \to K^0 MB$ are negligible with respect to their energies. Therefore, the on-shell factorization will just pick up the s-wave part of the MM amplitude. One might argue that the p-wave part of the meson-meson amplitude will not be small when taken inside loops. By looking again to the diagram of Fig. 5.5 (a), the p-wave part of the amplitude would lead to a contribution in the loops of the type

$$\int d^4q \boldsymbol{k}_{\rm in}\cdot\boldsymbol{q} D_\pi(k_{\rm in}-k_{\rm out}-q)D(q)G(p_{\rm in}-k_{\rm in}-k_{\rm out}-q)\boldsymbol{\sigma}\cdot(\boldsymbol{k}_{\rm in}-\boldsymbol{k}_{\rm out}-\boldsymbol{q}).$$

Since we know that $|\boldsymbol{k}_{in}| \sim 1500$ MeV/c and the $\boldsymbol{q}$ integral has a cut off of 600 MeV/c [5], $|\boldsymbol{q}/\boldsymbol{k}_{\rm in}|^2$ is a small quantity which would allow one to take a constant propagator for the meson of momentum $k_{\rm in}-k_{\rm out}-q$. Since $\boldsymbol{k}_{\rm out}\sim 0$, the term with $(\boldsymbol{k}_{\rm in}\cdot\boldsymbol{q})(\boldsymbol{\sigma}\cdot\boldsymbol{k}_{\rm in})$ vanishes in the integral, but there remains an integral

$$\int d^4q\,(\boldsymbol{k}_{\rm in}\cdot\boldsymbol{q})(\boldsymbol{\sigma}\cdot\boldsymbol{q})D(q)G_N(p_{\rm in}-k_{\rm in}-k_{\rm out}-q),$$

which should be reasonably smaller than the corresponding term from the meson meson s-wave which is proportional to $\boldsymbol{\sigma}\cdot\boldsymbol{k}_{\rm in}$. Yet, there is more to it. With $\boldsymbol{k}_{\rm in}+\boldsymbol{p}_{\rm in}=0$, and $\boldsymbol{k}_{\rm out}\sim 0$, the argument of G depends on $\boldsymbol{q}^2$ and we are left with an integral of the type

$$\begin{aligned}&\int d^4q q_i q_j D(q)G_N(p_{\rm in}-k_{\rm in}-k_{\rm out}-q)\\ \sim&\frac{1}{3}\delta_{ij}\int d^4q\boldsymbol{q}^2 D(q)G_N(p_{\rm in}-k_{\rm in}-k_{\rm out}-q).\end{aligned}$$

After performing the q^0 integration, we are left with an integral

$$\boldsymbol{\sigma}\cdot\boldsymbol{k}_{\rm in}\int d^3q\frac{1}{2\omega(q)}\frac{\boldsymbol{q}^2}{M_I-\omega(q)-E(q)+i\epsilon}, \tag{5.2.6}$$

with M_I the invariant mass of the MB system and ω, E the meson, baryon energies. The zero in the denominator of Eq. (5.2.6) gets the on-shell condition for a momentum $q_{\rm on}$ and we can write

$$\begin{aligned}\boldsymbol{q}^2&=\omega(q)^2-\omega(q_{\rm on})^2+\boldsymbol{q}_{\rm on}^2,\\ M_I-\omega(q)-E(q)&=\omega(q_{\rm on})-\omega(q)+E(q_{\rm on})-E(q),\end{aligned}$$

By neglecting $E(q_{\rm on}) - E(q)$ which holds in the heavy baryon limit (we are all around neglecting $1/M$ terms), the off-shell part of Eq. (5.2.6) leads to

$$\int d^3q \frac{1}{2\omega(q)} \frac{\omega(q)^2 - \omega(q_{\rm on})^2}{\omega(q_{\rm on}) - \omega(q)} \sim \int d^3q \frac{\omega(q)^2 - \omega(q_{\rm on})^2}{\omega(q_{\rm on})^2 - \omega(q)^2},$$

which is constant in energy. This energy independent term, multiplying the $\boldsymbol{\sigma} \cdot \boldsymbol{k}_{\rm in}$ factor, can be reabsorbed into, for instance, the contact term with the use of renormalized coupling constants, say the physical values of f_π.

5.2.3 Factorized amplitude

With the arguments given above, our approach will require the evaluation of the meson pole and contact terms for the ten coupled channels $\pi^- p \to K^0 M_i B_i$, which are factorized on-shell outside the loop integral. The remaining loop function contains only one meson and one baryon, which is the $G_{MB}(M_I)$ function found out in the chiral unitary model [503]. Hence the whole amplitude for the process $\pi^- p \to K^0 \pi\Sigma$ corresponding to the upper diagrams of Fig. 5.3 is given by

$$-it_{\rm chiral} = \boldsymbol{\sigma} \cdot \boldsymbol{k}_{in} \Big[(a_{\pi\Sigma} + b_{\pi\Sigma}) + \sum_i (a_i + b_i) G_i(M_I) t_{i \to \pi\Sigma}(M_I) \Big], \tag{5.2.7}$$

where i runs for the ten coupled channels, $K^- p$, $\bar{K}^0 n$, $\pi^0\Lambda$, $\pi^0\Sigma^0$, $\eta\Lambda$, $\eta\Sigma^0$, $\pi^+\Sigma^-$, $\pi^-\Sigma^+$, $K^+\Xi^-$, $K^0\Xi^0$ in this order. We denote the invariant mass for $\pi\Sigma$ by M_I, and $t_{i\to\pi\Sigma}$ is the transition T-matrix from the channel i to $\pi\Sigma$ studied in Ref. [503] and a_i, b_i are the on-shell contributions to the $\pi^- p \to K^0 M_i B_i$ tree level amplitude from the meson pole and contact terms, respectively. These are calculated with interactions (5.2.1), (5.2.3), and (5.2.4), which are given by

$$\begin{aligned}
a_1^{(\pi)} =& -\frac{1}{4\sqrt{2}f^3}(D+F) \frac{1}{(m_{K^0} + q^0 - k^0_{\rm in})^2 - \boldsymbol{k}^2_{\rm in} - m^2_{\pi^0}} \\
& \times \Big(m_{K^0}(m_{K^0} - 2k^0_{\rm in}) - (q^0)^2 + 2k^0_{\rm in} q^0 \Big), \\
a_1^{(\eta)} =& -\frac{1}{36\sqrt{2}f^3}(-D+3F) \frac{1}{(m_{K^0} + q^0 - k^0_{\rm in})^2 - \boldsymbol{k}^2_{\rm in} - m^2_{\eta}} \\
& \times \Big(m^2_{K^0} - 4m^2_{\pi^-} + 12 m_{K^0} q^0 + 3(q^0)^2 + 6 m_{K^0} k^0_{\rm in} + 6 q^0 k^0_{\rm in} \Big), \\
b_1 =& \frac{1}{12\sqrt{2}f^3}(D-3F), \\
a_2 =& -\frac{1}{6\sqrt{2}f^3}(D+F) \frac{1}{(m_{K^0} + q^0 - k^0_{\rm in})^2 - \boldsymbol{k}^2_{\rm in} - m^2_{\pi^+}} \\
& \times \Big(3m^2_{K^0} - 2m_{K^0} k^0_{\rm in} + 4 k^0_{\rm in} q^0 + 2 m_{K^0} q^0 - (q^0)^2 \Big), \\
b_2 =& -\frac{1}{12\sqrt{2}f^3}(D+F), \\
a_3 =& -\frac{1}{4\sqrt{6}f^3}(D+3F) \frac{1}{(m_{K^0} + q^0 - k^0_{\rm in})^2 - \boldsymbol{k}^2_{\rm in} - m^2_{K^+}} \\
& \times \Big(m^2_{\pi^-} - (q^0)^2 + 2 m_{K^0} q^0 + 2 m_{K^0} k^0_{\rm in} \Big),
\end{aligned}$$

$$
\begin{aligned}
b_3 =& -\frac{\sqrt{6}}{48f^3}(D+3F),\\
a_4 =& \frac{1}{4\sqrt{2}f^3}(D-F)\frac{1}{(m_{K^0}+q^0-k^0_{\rm in})^2-\boldsymbol{k}^2_{\rm in}-m^2_{K^+}}\\
&\times\Big(m^2_{\pi^-}-(q^0)^2+2m_{K^0}q^0+2m_{K^0}k^0_{\rm in}\Big),\\
b_4 =& \frac{1}{8\sqrt{2}f^3}(D-F),\\
a_5 =& \frac{1}{36\sqrt{2}f^3}(D+3F)\frac{1}{(m_{K^0}+q^0-k^0_{\rm in})^2-\boldsymbol{k}^2_{\rm in}-m^2_{K^+}}\\
&\times\Big(6m_{K^0}k^0_{\rm in}-6m_{K^0}q^0-8m^2_{K^0}-12q^0k^0_{\rm in}+5m^2_{\pi^-}+3(q^0)^2\Big),\\
b_5 =& -\frac{1}{24\sqrt{2}f^3}(D+3F),\\
a_6 =& -\frac{1}{12\sqrt{6}f^3}(D-F)\frac{1}{(m_{K^0}+q^0-k^0_{\rm in})^2-\boldsymbol{k}^2_{\rm in}-m^2_{K^+}}\\
&\times\Big(6m_{K^0}k^0_{\rm in}-6m_{K^0}q^0-8m^2_{K^0}\\
&-12q^0k^0_{\rm in}+5m^2_{\pi^-}+3(q^0)^2\Big),\\
b_6 =& \frac{\sqrt{6}}{48f^3}(D-F),\\
a_7 =& 0,\quad b_7=0,\\
a_8 =& -\frac{1}{6\sqrt{2}f^3}(D-F)\frac{1}{(m_{K^0}+q^0-k^0_{\rm in})^2-\boldsymbol{k}^2_{\rm in}-m^2_{K^0}}\\
&\times\Big(-2m_{K^0}k^0_{\rm in}-2k^0_{\rm in}q^0+3m^2_{\pi^-}-4m_{K^0}q^0-(q^0)^2\Big),\\
b_8 =& \frac{1}{6\sqrt{2}f^3}(D-F),\\
a_9 =& 0,\quad b_9=0,\\
a_{10} =& 0,\quad b_{10}=0,
\end{aligned}
$$

where, we choose the kinematic variables shown in Fig. 5.2, and we have already assumed the three momenta of the final particle $\boldsymbol{k}_{\rm out}$ negligible in all channels. Note that for the meson pole term of channel $1(K^-p)$, both π^0 and η exchange can happen, so that we show both of them. It is worth noting that the channels with null amplitudes, $\pi^+\Sigma^-$, $K^+\Xi^-$, and $K^0\Xi^0$. Focusing on the initial and final baryons, we find that the transition with $\Delta Q=2$ or $\Delta S=2$ becomes zero, since the initial state is π^-p. It is obvious for the meson pole term, since there is no corresponding particle emitted. This is also true for the five-point contact interaction, because the axial current consists of mesons are in **8** representation of SU(3).

For completeness, we also include a recoil factor from the non-relativistic reduction of $\gamma^\mu\gamma_5\partial_\mu$ BBM vertex

$$
F_i=\left(1-\frac{p^{0(i)}_{\rm ex}}{2M_p}\right), \tag{5.2.8}
$$

which is derived in Appendix B.3.1. In addition, we also consider the strong form factor of the BBM vertex for which we take a standard monopole form factor for all vertices

$$F_f(\boldsymbol{p}) = \frac{\Lambda^2 - m_\pi^2}{\Lambda^2 + \boldsymbol{p}^2},$$

with $\Lambda = 800$ MeV. We take the form factor static to avoid the fictitious poles of the covariant $(\Lambda^2 - m^2)/(\Lambda^2 - p^2)$ form. But we have checked that using this latter form only changes the results at the level of less than 5%. Given the cancellation of the off-shell part of the meson pole term with the contact term, which makes the sum of the two terms independent of a possible unitary transformation in the fields, the form factor is applied both in the meson pole and the contact term. This is analogous to what is done with the pion pole and Kroll-Ruderman term in $\gamma N \to \pi N$ to preserve gauge invariance [599].

5.2.4 Results with the chiral amplitudes

We perform the calculations for an initial pion momentum of 1.69 GeV, at which the experiment is done [543]. The $\pi\Sigma$ invariant mass distribution is given by

$$\frac{d\sigma}{dM_I} = \frac{1}{(2\pi)^3}\frac{1}{4s}\frac{M\tilde{M}}{\lambda^{1/2}(s, M^2, m_\pi^2)}\frac{1}{M_I}\lambda^{1/2}(s, M_I^2, m_K^2)\lambda^{1/2}(M_I^2, \tilde{M}^2, m^2)\bar{\Sigma}\Sigma|t|^2, \quad (5.2.9)$$

where M and $\tilde{M}$ are the masses of the nucleon and the baryon of the final state, in this case a Σ, and m the mass of the final meson, in this case a π. A derivation of this formula is given in Appendix A.4.2.

We calculate the invariant mass distribution by taking the average over $\pi^+\Sigma^-$ and $\pi^-\Sigma^+$ channels, which corresponds to what was plotted in Ref. [543]. This combination can eliminate the interference between $I = 0$ and $I = 1$, but the $I = 1$ component still remains in the spectrum. For more detail, we will discuss the isospin decomposition for $\pi\Sigma$ channels in subsection 5.3.3. In Fig. 5.6, we plot the numerical result of the mass spectrum together with the experimental distribution taken from Ref. [543]. We can see that the theoretical distribution peaks around 1420 MeV while the experimental one has the peak around 1400 MeV. The theoretical distribution is also much narrower than experiment. The disagreement between theory and experiment is apparent.

We can easily trace back the origin of the shape of the theoretical distribution. The shape of the obtained distribution shows the feature of the z_2 pole, which couples to $\bar{K}N$ strongly. Indeed, the tree amplitude $\pi^- p \to K^0 M_i B_i$ for the case of $M_i B_i = \bar{K}N$ involve the combinations $3F - D$ and $D + F$, which are large compared to the $D - F$ combination that we find for $M_i B_i \equiv \pi\Sigma$ (we take $F = 0.51$ and $D = 0.75$). Therefore, that the sum of the terms in Eq. (5.2.7) is dominated by the $\bar{K}N$ terms, giving a larger weight to the $t_{\bar{K}N\to\pi\Sigma}$ amplitude than to the $t_{\pi\Sigma\to\pi\Sigma}$ one. As we mentioned, the $\bar{K}N$ states couple strongly to the z_2 pole at higher energy and weakly to the z_1 pole at lower energy. As a consequence, what we see is a distribution which mostly peaks around the resonance found in Ref. [519] at the pole position $z_2 = 1426 - i16$ MeV, with a width of around 30 MeV. The slightly smaller energy of the peak in Fig. 5.6 and larger width reflects the small contribution of the other

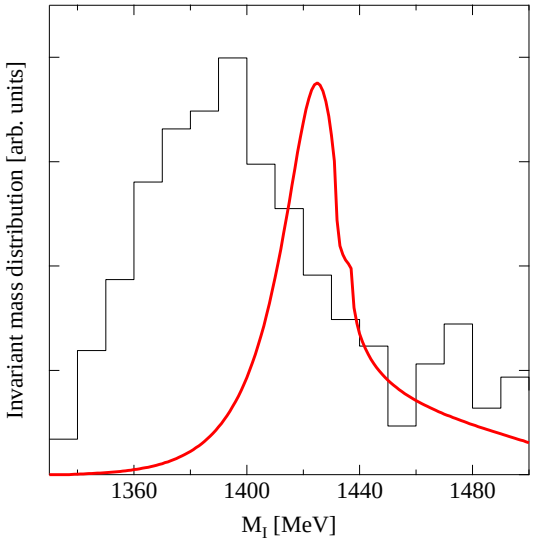

Figure 5.6: Contribution from the meson pole and contact terms (diagrams of Fig. 5.3) to the $\pi\Sigma$ invariant mass obtained averaging $\pi^+\Sigma^-$ and $\pi^-\Sigma^+$. The histogram show the experimental data taken from Ref. [543].

pole $z_1 = 1390 - i66$ MeV. Therefore, we need another mechanism that favors the lower energy pole, in order to reproduce the experimental distribution. Next we investigate this possibility.

5.2.5 The s-channel resonance contribution

Since we have $\sqrt{s} \sim 2$ GeV, one could think of the possibility of having resonance excitation in the πN collision leading to the decay of the resonance in MMB. We would like to have some resonance that can couple to the MMB strongly in s-wave. All $S = 0$ baryon resonances in the region of $1700 \leq \sqrt{s} \leq 2100$ MeV correspond to higher partial waves in the πN collision, except for the $N(1710)$ and the $N(2100)$, which are P_{11} resonances with the same quantum numbers of the nucleon [144]. Out of these two, the $N(1710)$ resonance has a very large branching ratio to $\pi\pi N$ (40-90%), while the one of the $N(2100)$ is unknown, probably small, since the large branching ratio seems to be for $N\eta$ (with large errors). We thus rely upon the $N(1710)$ resonance to provide some contribution to the $\pi^- p \to K^0\pi\Sigma$ process.

With the N^* excitation, the $\pi^- p \to K^0\pi\Sigma$ reaction is given diagrammatically in Fig. 5.7. To calculate this, we need the vertices of N^* coupling to $\pi^- p$ and $K^0 MB$ channels. Let us first consider the $N^* \to K^0 MB$ coupling. Although one can derive different couplings of this resonance to the MMB in an SU(3) scheme (see Ref. [600] for analogy in other P_{11} resonances), the absence of the kinematically allowed $\eta\pi N$ channel in the decay mode of the $N^*(1710)$ strongly suggest a Weinberg-Tomozawa like coupling where this mode is strictly forbidden at the tree level (see C_{ij} coefficients in Appendix D.2). This also has the implicit assumption that the $N^*(1710)$ resonance belongs to an SU(3) octet representation, which is the option adopted in the particle data table [144]. We then assume a coupling of the type

of

$$\mathcal{L}_{N^* \to MMB} = \frac{\tilde{B}}{f^2} \mathrm{Tr}\Big(\bar{B} i\gamma^\mu \big[(\Phi\partial_\mu \Phi - \partial_\mu \Phi\Phi), B^* \big] \Big), \tag{5.2.10}$$

with dimensionless coupling constant $\tilde{B}$. Now $n^*(1710)$ and $p^*(1710)$ would substitute in the B^* matrix as the n and p. This Lagrangian is the same that appears in the s-wave scattering of meson-baryon interaction as we have seen in Eq. (5.2.2). Since we are considering the process with N^* in the initial state for this vertex, we do not write the hermitian conjugate term, which is responsible for the process with N^* in the final state. The Lagrangian of Eq. (5.2.10) leads to the amplitude

$$t_{N^* \to MMB} = -\frac{\tilde{B}}{f^2} C_i (\omega_1 - \omega_2), \tag{5.2.11}$$

where ω_1, ω_2 are the energies of the two mesons and C_i are tabulated in Table 5.1 for the n^* going to pions and in Table 5.2 for n^* going to $K^0 MB$. These can be obtained from the C_{ij} SU(3) coefficients in Appendix D.2, but in this case the ordering of two mesons is important because the amplitude is antisymmetric under the exchange of two mesons. The $\tilde{B}$ coefficient is derived from the partial decay width $n^* \to \pi^+\pi^- n, \pi^-\pi^0 p$, where we have[A)]

$$\Gamma_{\pi\pi N} = \frac{M}{16\pi^3} \int_{\omega_{\min}}^{\omega_{\max}} d\omega \int_{\omega'_{\min}}^{\omega'_{\max}} d\omega' \Theta(1 - a^2) \bar{\Sigma}\Sigma |t|^2, \tag{5.2.12}$$

where $\Theta(x)$ is a step function and

$$a = \frac{(M_R - \omega - \omega')^2 - M^2 - \boldsymbol{k}^2 - (\boldsymbol{k}')^2}{2|\boldsymbol{k}||\boldsymbol{k}'|}, \tag{5.2.13}$$

with k, k' the moduli of the two pion momenta.

$$\begin{aligned} \omega_{\min} &= \omega'_{\min} = m_\pi, \\ \omega_{\max} &= \omega'_{\max} = \frac{M_R^2 - M_p^2 + 2m_\pi M_p}{2M_R}, \end{aligned} \tag{5.2.14}$$

A derivation for these formula can be found in Appendix A.4.2. The amplitude square can be obtained as

$$\bar{\Sigma}\Sigma |t|^2 = 3\frac{\tilde{B}^2}{f^4} (\omega - \omega')^2, \tag{5.2.15}$$

after isospin average.

Similarly, we define the amplitude of $\pi^- p \to n^*$ by (including the isospin factor)

$$-it = \frac{A}{f} \boldsymbol{\sigma} \cdot \boldsymbol{k}_{\mathrm{in}}, \tag{5.2.16}$$

[A)] In the paper [8], we wrote a redundant factor $M_R/\sqrt{s} = 1$, which is removed here.

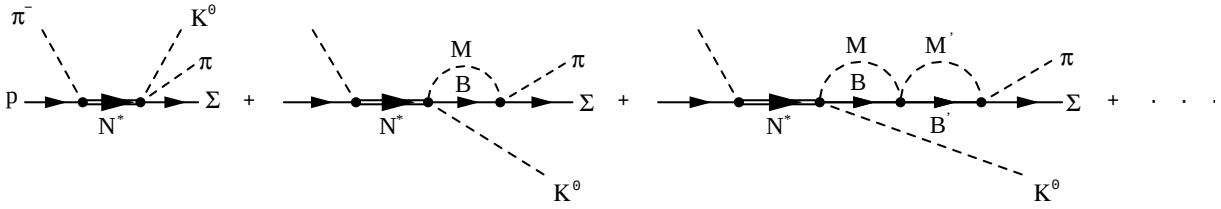

Figure 5.7: Resonant mechanisms for Λ(1405) production in the $\pi^- p \to K^0\pi\Sigma$ reaction.

Table 5.1: The C_i coefficients entering Eq. (5.2.11). The ordering of mesons in this table represents the suffices 1 and 2 in Eq. (5.2.11).

	$\pi^-\pi^0 p$	$\pi^+\pi^- n$	$\pi^0\pi^0 n$
C_i	$-\sqrt{2}$	1	0

with A being the dimensionless coupling constant. The partial decay width is given by

$$\Gamma_{\pi N} = \frac{1}{2\pi}\frac{M}{M_R}\frac{A^2}{f^2}|\boldsymbol{k}_{\rm in}|^3, \tag{5.2.17}$$

whose derivation is explained in Appendix A.4.1. Assuming the middle values of the N^* width ($\Gamma \sim 100$ MeV) and partial decay widths for $\pi\pi N$ and πN channels ($\Gamma_{\pi\pi N} = 65$ MeV and $\Gamma_{\pi N} = 15$ MeV), we find

$$|A| = 0.086, \quad |\tilde{B}| = 0.77. \tag{5.2.18}$$

For later convenience, we refer to this parameter set including $M_R = 1710$ MeV as Set I.

Thus the $N(1710)$ contribution to the $\pi^- p \to K^0\pi\Sigma$ process can be given by

$$\begin{aligned} -it_R =& \frac{A}{f}\boldsymbol{\sigma}\cdot\boldsymbol{k}_{\rm in}\frac{i}{\sqrt{s}-M_R+i\frac{\Gamma}{2}}(-i)\frac{(-)\tilde{B}}{f^2} \\ & \times\left[C_{\pi\Sigma}(\omega_\pi-\omega_{K^0})+\sum_i C_i(\omega_i-\omega_{K^0})G_i(M_I)t_{i\to\pi\Sigma}\right], \end{aligned} \tag{5.2.19}$$

where ω_{K^0} and ω_i are given by their on-shell values,

$$\omega_{K^0} = \frac{s+m_K^2-M_I^2}{2\sqrt{s}}, \quad \omega_i = \frac{M_I^2+m_i^2-M_i^2}{2M_I}, \tag{5.2.20}$$

Table 5.2: The C_i coefficients entering Eq. (5.2.11) with a K^0 in the final state.

	K^-K^0p	$\bar{K}^0K^0n$	$\pi^0K^0\Lambda$	$\pi^0K^0\Sigma^0$	$\eta K^0\Lambda$
C_i	1	2	$-\frac{\sqrt{3}}{2}$	$\frac{1}{2}$	$\frac{3}{2}$
	$\eta K^0\Sigma^0$	$\pi^+K^0\Sigma^-$	$\pi^-K^0\Sigma^+$	$K^+K^0\Xi^-$	$K^0K^0\Xi^0$
C_i	$-\frac{\sqrt{3}}{2}$	1	0	0	0

Table 5.3: Total cross sections for several final states with parameter sets I and II in units of [μb]. Experimental data are taken from Ref. [543].

final state	K^0K^-p	$K^0\bar{K}^0n$	$K^0\pi^0\Lambda$	$K^0\pi^+\Sigma^-$	$K^0\pi^-\Sigma^+$
chiral	2.36	2.84	3.14	3.04	6.78
resonance(I)	0.29	0.28	4.47	6.68	2.24
resonance(II)	0.70	0.67	10.85	16.18	5.43
total(I)	2.82	4.61	1.93	12.00	14.31
total(II)	3.75	5.98	6.02	21.32	20.01
Exp.	2.9	8.3	104.0	25.1	20.2

with m_i, M_i the meson and baryon masses of the particle in the $N^* \to K^0MB$ reaction, and M_I the $\pi\Sigma$ invariant mass. Furthermore, in Eq. (5.2.19) Γ is the total width whose energy dependence is taken into account by using Eqs. (5.2.12) and (5.2.17) for the $\pi\pi N$ and πN channels, respectively, and by considering a $|\boldsymbol{k}_{\rm in}|^3$ dependence for the ηN channel.

5.2.6 Final results

In Fig. 5.8, we show the results that we obtain for the resonant mechanism (dashed curve) with Set I, together with the results from the chiral mechanisms (dotted curve). The calculation was performed at the energy $\sqrt{s} = 2020$ MeV, or equivalently $p_\pi = 1690$ MeV in the laboratory frame. This is the energy at which the experiment we compare with was done [543]. Although the figure is shown in arbitrary units, we have adjusted the relative scale between the experimental and theoretical curves assuming that the integrated experimental mass distribution should coincide with the total cross sections in the $\pi\Sigma$ channels given in Ref. [543]. Theoretical and experimental total cross sections for various channels are shown in Table 5.3. We can see that the strength of the resonant mechanism is smaller than that of the chiral terms, however, the $\pi\Sigma$ distribution created by the resonant mechanism is much broader and peaks around 1390 MeV. It is instructive to see the reason for the shape of the resonant mechanism. We have seen that the $N^* \to NM_1M_2$ vertex takes the form $\tilde{B}(\omega_1 - \omega_2)$. Now for the case of the $K^0\bar{K}N$ channel, the amplitude goes like $\omega_{K^0} - \omega_{\bar{K}}$, but we are at low energies, close to the $K^0\bar{K}N$ threshold production, where the difference of the two kaon energies is close to zero. On the other hand, in the $N^* \to K^0\pi\Sigma$, the difference between the $K^0$and π energies is finite and of the order of 300 MeV in the region that we study. Hence, the $K^0\pi\Sigma$ channel is strongly favored and according to Eq. (5.2.19), the final $\pi\Sigma$ production channel is practically given by $t_{\pi\Sigma\to\pi\Sigma}$. The factors $(\omega_i - \omega_{K^0})$ and $G_i(M_I)$ give extra weight to this amplitude to finally produce a distribution that essentially reflects the lower energy $\Lambda(1405)$ resonance to which the $\pi\Sigma$ channel couples strongly.

Since the relative phase between chiral and resonant mechanism is not determined, we should consider it when we take the coherent sum of the two mechanisms. Here we choose $A \cdot \tilde{B} > 0$, which leads to a mass distribution, given by the solid curve, which still remains to be dominated by the chiral terms and the agreement with the data is not very good.

It is possible to improve the theoretical mass distribution if we play a bit with uncertainties in the resonance mass, the total N^* width and the branching ratios. By assuming $M_R \sim 1740$

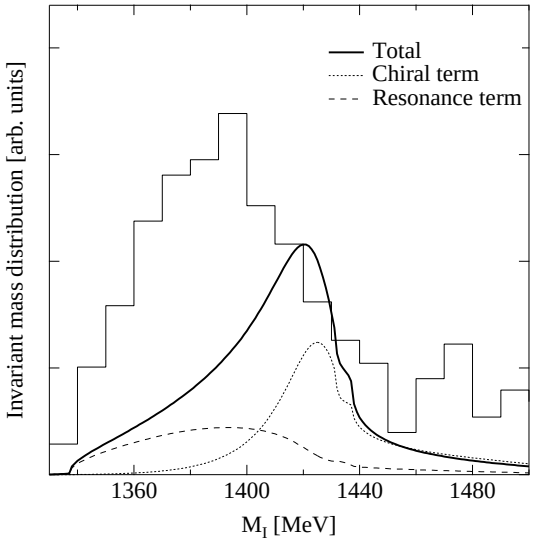

Figure 5.8: Invariant mass distribution of $\pi\Sigma$ obtained by averaging $\pi^+\Sigma^-$ and $\pi^-\Sigma^+$ with parameter Set I. The histogram shows the experimental data taken from Ref. [543]

MeV, $\Gamma = 200$ MeV and $\Gamma_{\pi N} = 40$ MeV and $\Gamma_{\pi\pi N} = 100$ MeV (We refer to this parameter set as Set II) well within the experimental boundaries, we obtain the results of Fig. 5.9 where the agreement with the data becomes acceptable. The increase in the resonant part is mostly due to the increase in the $\pi N N^*(1710)$ coupling constant when using the larger partial width $\Gamma_{\pi N} = 40$. In Table 5.3, we have summarized cross sections of various channels comparing experimental data and theoretical results with the two sets of parameters. Except for the $K^0\pi^0\Lambda$ channel in which $\Sigma(1380)$ resonance, not accounted for in our study, plays a major role, the agreement between theory and experiment is acceptable for Set II. We can also see that the use of Set II not only improves the mass distribution but also the global agreement with the individual cross sections. Note the importance of the interference in the chiral and resonant terms in order to obtain a better agreement between theory and experiment.

5.2.7 Summary for the $\pi^- p \to K^0\pi\Sigma$ reaction

We have developed a model for the $\pi^- p \to K^0\pi\Sigma$ reaction in the region of excitation of the $\Lambda(1405)$ resonance. We have discussed the fact that present theoretical models using chiral dynamics and coupled channel unitarization are all converging to the existence of two poles close to the nominal $\Lambda(1405)$ resonance, which would reflect the singlet pole and one of the $I = 0$ octet poles (although with some mixture). The two resonances appear at different energies and couple very differently to the $\pi\Sigma$ and $\bar{K}N$ channels.

When we try to construct a model for the $\pi^- p \to K^0\pi\Sigma$ in analogy to the low energy chiral model for $\pi N \to \pi\pi N$, we observe that the role of $\bar{K}N$ intermediate state is enhanced, leading to the total amplitude for $\pi^- p \to K^0\pi\Sigma$ mostly sensitive to the $t_{\bar{K}N\to\pi\Sigma}$ amplitude, which is dominated by a narrow resonance peaking around 1420 MeV. The mechanism alone leads to a $\pi\Sigma$ mass distribution in disagreement with the experimental data.

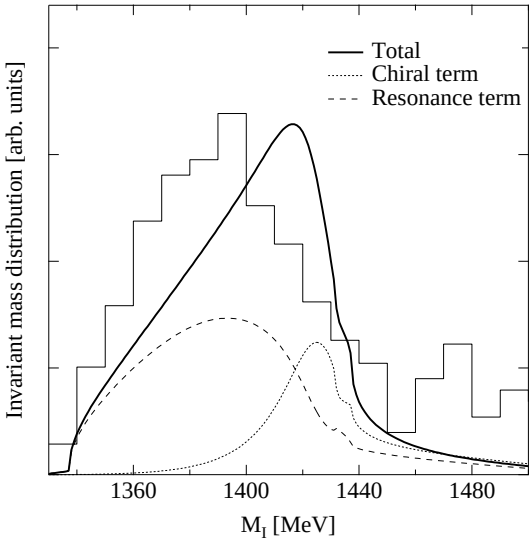

Figure 5.9: Same as in Fig. 5.8 but with Set II.

On the other hand, it is found that there is another mechanism exciting N^* resonances from the $\pi^- p$ entrance channel. Inspection of the partial waves involved in the resonance excitations and the decay modes has singled out a resonance which gives contribution to the process, the $N(1710)$, with the same quantum numbers of the nucleon. The strong decay into $N\pi\pi$ channel together with the absence of the $N\pi\eta$ channel, suggests a coupling of the $N^*(1710)$ resonance to BMM of the Weinberg-Tomozawa type, which we have exploited to see the consequences in the $\pi^- p \to K^0 \pi\Sigma$ reaction. We have observed that this new mechanism has an opposite behavior to the chiral one, and strongly stresses the $\pi\Sigma$ intermediate state instead of the $\bar{K}N$, leading to a production amplitude dominated by the $t_{\pi\Sigma\to\pi\Sigma}$ amplitude. Since this amplitude dominates the wider resonance peaking at around 1390 MeV, we found that the $\pi\Sigma$ mass distribution roughly followed the shape of this resonance and was wide and peaking at an energy below 1400 MeV. The coherent sum of the two mechanism was shown to lead to total cross sections and a mass distribution compatible with the experiment, within the theoretical and experimental uncertainties. Although there is still some deviation from the theoretical prediction, experimental spectrum tells us that the $\pi^- p \to K^0 \pi\Sigma$ reaction is dominated by the lower energy pole of the $\Lambda(1405)$. Investigation of the origin of this small deviation might be interesting in future works.

The present study is telling us that there might be other processes where the reaction mechanism of $\Lambda(1405)$ production filters one or another resonance, hence leading to very different shapes for the $\pi\Sigma$ mass distribution. The $K^- p \to \Lambda(1405)\gamma$ reaction [585] was advocated as one where the narrow higher energy resonance will be populated. In the next section, we will investigate the $\gamma p \to K^* \Lambda(1405) \to K\pi MB$ reaction in order to isolate one of the poles from the other. The findings of the present reaction should stimulate further theoretical and experimental works that help us pin down the existence and properties of these two resonances.

5.3 The $\gamma p \to K\pi MB$ reaction

In the chiral unitary model, one interesting finding is the two-pole structure of the Λ(1405) resonance. In order to understand the hadron dynamics at low energy, it is important to study the nature of the Λ(1405) focusing on whether such two poles really exist in the nominated resonance region.

As was discussed in the previous section, the $\pi^- p \to K^0 MB$ reaction was particularly selective of the z_1 pole in Eq. (5.1.1). Here we propose another reaction $\gamma p \to K^* B^* \to \pi K MB$, which is expected to be useful for the extraction of the z_2 pole. A great advantage of this reaction is the use of a linearly polarized photon beam, which can help to suppress a possible background process. Then the process is dominated by the t-channel K^- exchange, which scatter with the target nucleon, as we will see below. Since the exchanged K^- can be off the mass shell and have the resonant energy for the Λ(1405) together with the target nucleon, it couples to the Λ(1405). Thus we have an amplitude $\bar{K}N \to \pi\Sigma$, which is ideal to the selection of the pole z_2. In the analysis, we introduce the Σ(1385) contribution explicitly, which have not been taken into account in the previous studies. This helps to estimate the contamination of $I = 1$ amplitude to the desired spectrum.

5.3.1 Formulation

Let us consider the mechanisms contributing the $\gamma p \to K^* B^* \to K\pi MB$ reaction with $B^* = \Lambda(1405)$ and Σ(1385). Suppose that we observe the K^* decaying into K and π in the forward direction. In this case, namely the small momentum transfer, the process will be dominated by the t-channel meson exchange as shown in Fig. 5.10, and we can ignore unknown background contributions from, for instance, nucleon resonances in s channel. The exchanged particle can be specified by selecting the polarization vectors of photon and K^*. This is accomplished by the polarized photon beam and measurement of the decay plane of $K\pi$ system from the K^*. If the $K\pi$ system is produced in a plane perpendicular to the photon polarization, the t-channel exchanged particle is dominated by the pseudoscalar kaon and heavier strange mesons contributions should be suppressed due to their larger masses in low momentum transfer region.

We consider the energy region close to the threshold of the $K^*\Lambda(1405)$ production. The exchanged kaon rescatters with a nucleon in isospin $I = 0$ and 1 channels, where the former couples to the Λ(1405), especially to the pole z_2, while the latter does it to the Σ(1385), a p-wave resonance in this energy region. For the $K^- p \to MB$ subprocess, we utilize the s-wave meson-baryon scattering amplitude calculated by the chiral unitary model in Ref. [503]. The chiral interaction generates the Λ(1405) resonance dynamically, producing the poles at Eq. (5.1.1), while the Σ(1385) is not generated because it is a p-wave resonance. In principle, we do not have to care about the Σ(1385) if we can extract the pure $I = 0$ process, which, however, is difficult in actual experiment. Therefore, we introduce the Σ(1385) field explicitly, to see how large the contamination from it to the Λ(1405) spectrum. The $K^- p \to MB$ subprocess is diagrammatically expressed in Fig. 5.11.

Given the above arguments, the scattering amplitude as described in Fig. 5.10 can be

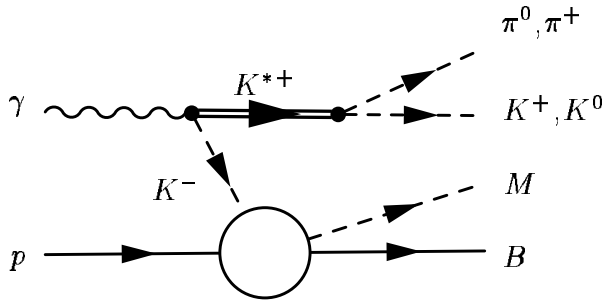

Figure 5.10: Feynman diagram for the $\gamma p \to K\pi MB$ reaction with the K^* production in πK system. We denote M and B for a meson and a baryon among ten coupled channels of $S = -1$ meson-baryon scattering. Here we only take $\pi\Sigma$ and $\pi\Lambda$ channels into account, which are responsible for the study of the $\Lambda(1405)$.

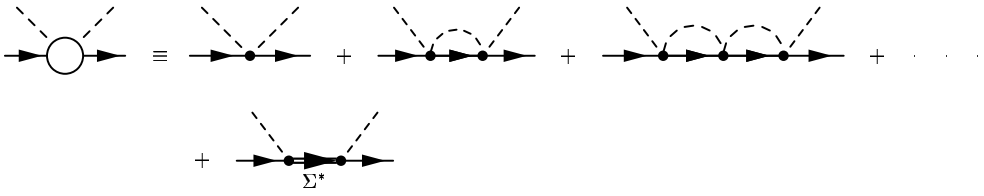

Figure 5.11: Feynman diagram for the $K^- p \to MB$ subprocess. We utilize the scattering amplitude in Ref. [503] with the $\Sigma(1385)$ pole term.

divided into two parts

$$-it = (-it_{\gamma\to K^- K\pi})\frac{i}{p^2_{K^-} - m^2_{K^-}}(-it_{K^- p\to MB}). \tag{5.3.1}$$

The former part $(-it_{\gamma\to K^- K\pi})$, as shown in Fig. 5.12, is derived from the following effective Lagrangians. For the $K^* K\gamma$ coupling [190], we use

$$\mathcal{L}_{K^* K\gamma} = g_{K^* K\gamma}\epsilon^{\mu\nu\alpha\beta}\partial_\mu A_\nu(\partial_\alpha K^{*-}_\beta K^+ + \partial_\alpha \bar{K}^{*0}_\beta K^0) + \text{h.c.}, \tag{5.3.2}$$

where K, K^*_μ, A_μ are the pseudoscalar kaon, vector K^*, photon fields, respectively, and h.c. denotes the hermitian conjugate. The coupling constant is determined from the empirical partial decay width of K^*: $\Gamma_{K^{*\pm}\to K^\pm\gamma} = 0.05$ MeV. The resulting values are $|g_{\gamma K^{*\pm} K^\pm}| = 0.252$ [GeV^{-1}]. We note that the effective Lagrangian (5.3.2) is consistent with a vector meson dominance model [601]. For the decay of the K^*, we utilize the flavor SU(3) Lagrangian [602]

$$\mathcal{L}_{V\Phi\Phi} = -\frac{ig_{V\Phi\Phi}}{\sqrt{2}}\mathrm{Tr}\big(V^\mu[\partial_\mu\Phi, \Phi]\big),$$

with the universal vector meson coupling constant $g_{V\Phi\Phi} = -6.05$ and V_μ being vector meson field;

$$V_\mu = \begin{pmatrix} \frac{1}{\sqrt{2}}\rho^0_\mu + \frac{1}{\sqrt{2}}\omega_\mu & \rho^+_\mu & K^{*+}_\mu \\ \rho^-_\mu & -\frac{1}{\sqrt{2}}\rho^0_\mu + \frac{1}{\sqrt{2}}\omega_\mu & K^{*0}_\mu \\ K^{*-}_\mu & \bar{K}^{*0}_\mu & \phi_\mu \end{pmatrix}.$$

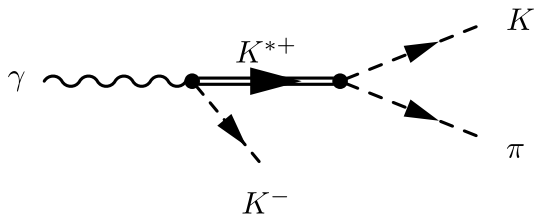

Figure 5.12: Feynman diagram for $\gamma \to K^- K \pi$.

Using the above interaction Lagrangians, the amplitude for the subprocess $\gamma \to K^{*+} K^- \to K^0 \pi^+ K^-$ is given by[B)]

$$-it_{\gamma \to K^- K^0 \pi^+} = \frac{i\sqrt{2} g_{VPP} \epsilon^{\mu\nu\alpha\beta} p_\mu(K^0) p_\nu(\pi^+) k_\alpha(\gamma) \epsilon_\beta(\gamma)}{P_{K^*}^2 - M_{K^*}^2 + i M_{K^*} \Gamma_{K^*}}, \tag{5.3.3}$$

where p and k are the momenta of the particle in parentheses, $P_{K^*} = p(K^0) + p(\pi^+)$, $\epsilon_\mu(\gamma)$ is the polarization vector of photon, and M_{K^*} and Γ_{K^*} are the mass and the total decay width of K^*, for which we include the energy dependence for a virtual K^*, $\Gamma_{K^*} = A p_{CM}^3$, where p_{CM} is the two-body relative momenta of the final state, and $A = 2.05 \times 10^{-6}$ [MeV^{-2}] such that $\Gamma_{K^*} \sim 51$ MeV at the resonance position. Eq. (5.3.3) is instructive to show the correlations between the photon polarization and the K^0 and π^+ momenta. In order to maximize the contribution of the t-channel we select the K^* in the direction of the photon. Then, it is easy to see that the amplitude is proportional to $\sin\phi$ where ϕ is the angle between the plane defined by the K^0 and π^+ momenta and the photon polarization (in the Coulomb gauge, $\epsilon^0 = 0$). Hence, the maximum strength of the amplitude occurs when this plane is perpendicular to the photon polarization.

In addition one needs not to worry about symmetrization in the case when there are two equal charge pions in the final state. In this case the interference term is zero and one can omit the symmetrization and the 1/2 factor in the cross section.

The amplitude ($-it_{K^- p \to MB}$) consists of two parts, as shown in Fig. 5.11

$$-it_{K^- p \to MB}(M_I) = -it_{\rm ChU}(M_I) - it_{\Sigma^*}(M_I), \tag{5.3.4}$$

where $-it_{\rm ChU}$ is the meson-baryon scattering amplitude derived from the chiral unitary model, and $-it_{\Sigma^*}$ is the $\Sigma(1385)$ pole term. We define the invariant mass for $K^- p$ system by $M_I^2 = (p_\gamma + p_N - p_{K^*})^2$. Following the model developed in Ref. [503], the coupled channel amplitude $t_{\rm ChU}$ can be obtained by

$$t_{\rm ChU} = [1 - VG]^{-1} V,$$

where G is the meson-baryon loop function and V is the kernel interaction derived from the Weinberg-Tomozawa term of the chiral Lagrangian (Eqs. (4.2.6) and (4.2.2) in chapter 5).

[B)] For the final state $K^+\pi^0$, the amplitude is reduced by factor $1/\sqrt{2}$, and therefore, the resulting cross section becomes one half. In the rest of this chapter, we show the result for $K^0\pi^+$. However, the final state $K^+\pi^0$ has an advantage that the strangeness can be tagged, which is not possible for the $K^0\pi^+ \to \pi^+\pi^-\pi^+$ mode.

Table 5.4: The c_i coefficients in Eq. (5.3.5).

channel i	K^-p	$\bar{K}^0n$	$\pi^0\Lambda$	$\pi^0\Sigma^0$	$\eta\Lambda$	$\eta\Sigma^0$	$\pi^+\Sigma^-$	$\pi^-\Sigma^+$	$K^+\Xi^-$	$K^0\Xi^0$
c_i	$-\sqrt{\frac{1}{12}}$	$\sqrt{\frac{1}{12}}$	$\sqrt{\frac{1}{4}}$	0	0	$-\sqrt{\frac{1}{4}}$	$-\sqrt{\frac{1}{12}}$	$\sqrt{\frac{1}{12}}$	$\sqrt{\frac{1}{12}}$	$-\sqrt{\frac{1}{12}}$

This amplitude reproduces well the total cross sections for several channels. It also leads to dynamically generated resonances in good agreement with experiment. Since the $\Sigma(1385)$ is not generated in this resummation because it is a p-wave resonance, we introduce it explicitly with its coupling to channel i ($MB \to \Sigma(1385)$) which is deduced from the $\pi N\Delta$ using SU(6) symmetry in [603, 576] and given by

$$-it_{\Sigma^* i} = c_i \frac{12}{5}\frac{g_A}{2f}\boldsymbol{S}^\dagger \cdot \boldsymbol{k}_i, \tag{5.3.5}$$

where $g_A = 1.26$, and we use the meson decay constant $f = 93 \times 1.123$ MeV [503]. This is a nonrelativistic form for the transition between spin 1/2 and 3/2 particles, where $\boldsymbol{S}$ is the spin transition operator defined in Appendix A.1.2[C)], and the coefficients c_i are given in Table 5.4. Note that these couplings reproduce well the observed branching ratio of $\Sigma(1385)$ decay into $\pi\Lambda$ and $\pi\Sigma$. Then we have the amplitude

$$-it_{\Sigma^*}(M_I) = -c_1 c_i \left(\frac{12}{5}\frac{g_A}{2f}\right)^2 \boldsymbol{S}\cdot\boldsymbol{k}_i \boldsymbol{S}^\dagger \cdot \boldsymbol{k}_1 \frac{i}{M_I - M_{\Sigma^*} + i\Gamma_{\Sigma^*}/2} F_f(k_1), \tag{5.3.6}$$

where k_1 and k_i are the momenta of the exchanged K^- and the final meson, and $M_{\Sigma^*} = 1384$ MeV and $\Gamma_{\Sigma^*} = 36$ MeV. We have introduced a strong form factor $F_f(k_1)$ for the vertex $K^-p\Sigma^*$ in order to account for the finite size structure of the baryons. We adopt a covariant monopole type $F_f(q) = (\Lambda^2 - m_K^2)/(\Lambda^2 - q^2)$ with $\Lambda = 1$ GeV. In the present reaction around the region of $\Lambda(1405)$, the effect of the form factor is not very large.

The cross section is then given by the squared amplitude of Eq. (5.3.1) integrated over the four-body phase space. Following the derivation in Appendix A.4.3, we obtain the total cross section

$$\sigma = \frac{2M_pM_B}{s - M_p^2}\int \frac{d^3p_1}{(2\pi)^3}\frac{1}{2\omega_1}\int \frac{d^3p_2}{(2\pi)^3}\frac{1}{2\omega_2}\frac{1}{8\pi}\int_{-1}^{1} d\cos\bar{\theta}\frac{|\tilde{\boldsymbol{p}}_3|}{M_I}\bar{\Sigma}\Sigma|t|^2, \tag{5.3.7}$$

where $p_{1(2)}$ and $\omega_{1(2)}$ are the momenta and energy of the final $K(\pi)$ from K^*[D)]. We define $\tilde{p}_3$ by the relative three momentum of MB in their center of mass frame, and the angle $\bar{\theta}$ denotes the angle between the intermediate K^- and the final M. The integration is performed by the Monte Carlo method.

Before showing the numerical results, here we mention the MB channels decaying from the intermediate baryonic state ($B^* = \Lambda(1405)$ and $\Sigma(1385)$). Below the $\bar{K}N$ threshold, there

[C)] In the paper [11], we defined $\boldsymbol{S}$ as in Ref. [604]. Here we define $\boldsymbol{S}$ as in Ref. [605] to be compatible with other chapters. Accordingly, we change the notation in Eq. (5.3.6).

[D)] In the paper [11], we wrote M_Σ instead of M_B. This is correct for the final states $\pi\Sigma$, but for the $\pi\Lambda$ state, the formula need a modification about $M_\Lambda/M_\Sigma \sim 0.94$. Accordingly, we modify the numerical results including $\pi^0\Lambda$ final state in Figs. 5.13, 5.14, 5.16. Qualitative conclusions remain unchanged.

Table 5.5: Possible decay channels from baryons

Intermediate baryon	Decay channels
$\Lambda(1405)$ $I=0$	$\pi^{\pm}\Sigma^{\mp}$, $\pi^0\Sigma^0$
$\Sigma(1385)$ $I=1$	$\pi^{\pm}\Sigma^{\mp}$, $\pi^0\Lambda$

are four possible MB channels as shown in Table 5.5, two charged and two neutral channels. In the present case, since we have the K^-p channel initially, the $I=2$ component of $\pi\Sigma$ channel is not allowed. As we will explain in subsection 5.3.3, the charged channels ($\pi^{\pm}\Sigma^{\mp}$) are from the decay of both $\Lambda(1405)(I=0)$ and $\Sigma(1385)(I=1)$, while the neutral channels are from either one of the two; $\pi^0\Sigma^0$ is from $\Lambda(1405)$ and $\pi^0\Lambda$ is from $\Sigma(1385)$.

5.3.2 Results

Now we present numerical results for total cross sections. Unless we observe angular distributions, there is not distinction between cross sections of polarized and unpolarized processes. Therefore, our predictions below are compared with the results of both polarized and unpolarized experiments directly. However, from the experimental point of view it is most practical to concentrate in the region where the $K^0\pi^+$ reaction plane is perpendicular to the photon polarization to maximize the weight of the K^* production mechanism and reduce possible backgrounds. In Fig. 5.13, we show the total cross sections $\sigma(\gamma p \to K^*B^* \to K^0\pi^+MB)$ as functions of $\sqrt{s}$ for different MB channels. As seen in the figure, the present mechanism shows up strength at an energy slightly lower than the threshold of $K^*\Lambda(1405)$ since the physical resonances have a finite width and hence a mass distribution. In the total cross section, the isospin one ($I=1$) $MB=\pi^0\Lambda$ channel is the largest in size, coming from the $\Sigma(1385)$ excitation. This might disturb the contribution from $\Lambda(1405)$ of $I=0$, unless the separation of these two isospin channels is done. However, it turns out that the observation of another charged π from the intermediate baryon (either $\Lambda(1405)$ or $\Sigma(1385)$) helps to study the $I=0$ amplitude.

In order to see this, we show in Fig. 5.14 the invariant mass distributions for different decay channels. In the figure the initial photon energy is chosen at $E_\gamma = 2500$ MeV (the threshold for $K^*\Lambda(1405)$ production is about $E_\gamma = 2343$ MeV). Forgetting about the experimental feasibility, the would-be observable in the neutral channel is most helpful in order to distinguish the contributions from $\Lambda(1405)$ and $\Sigma(1385)$, since the $\pi^0\Sigma^0$ channel does not contain the $I=1$ amplitude. As expected, the $\pi^0\Sigma^0$ distribution decaying from $\Lambda(1405)$ (solid curve) has a peak around 1420 MeV which corresponds to the real part of the pole z_2 at higher energy. In contrast, the $\pi^0\Lambda$ distribution (dot-dashed curve) has clearly a peak around 1385 MeV, with a larger value than the $\pi^0\Sigma^0$ distribution. In experiments, the charged states may be observed, which contain both $\Lambda(1405)$ and $\Sigma(1385)$ contributions. Hence, we show the distribution of charged states by the dashed and dash-dot-dotted curves. The shapes of the three $\pi\Sigma$ distributions have a similar tendency as the kaon photoproduction process [584], which has been confirmed in experiments [606]. Note also that the contributions from $\Sigma(1385)$ seem to be small for these channels.

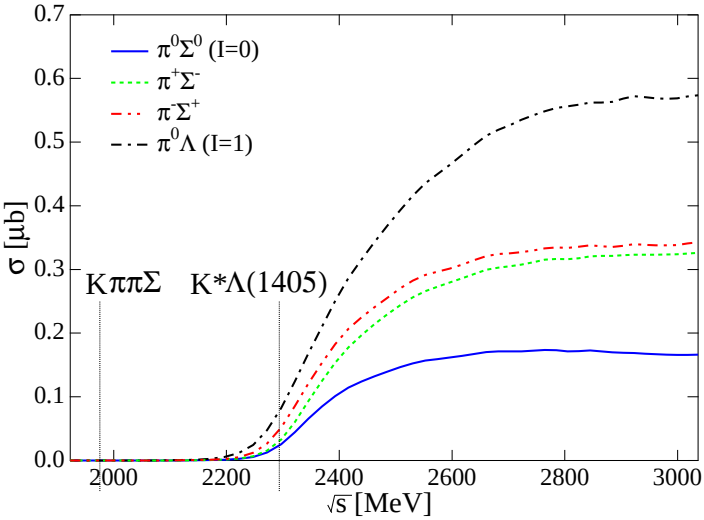

Figure 5.13: Total cross sections of the process $\gamma p \to \pi^+ K^0 MB$ with the final states $\pi^0\Sigma^0$ (Solid), $\pi^+\Sigma^-$ (Dashed), $\pi^-\Sigma^+$ (Dash-dot-dotted), and $\pi^0\Lambda$ (Dash-dotted) in units of [μb]. Solid bars indicate the threshold energy of the channels.

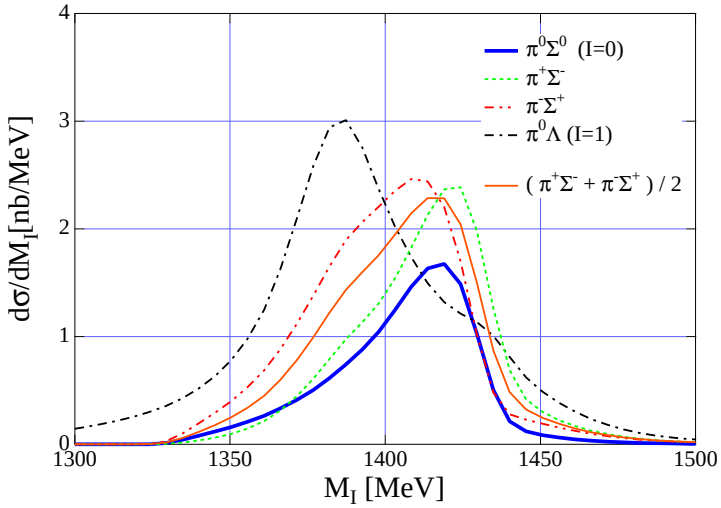

Figure 5.14: Invariant mass distributions of $\pi^0\Sigma^0$ (Thick solid), $\pi^+\Sigma^-$ (Dashed), $\pi^-\Sigma^+$ (Dash-dot-dotted), $\pi^0\Lambda$ (Dash-dotted), and $(\pi^+\Sigma^- + \pi^+\Sigma^-)/2$ (Thin solid) in units of [nb/MeV]. Initial photon energy in Lab. frame is $E_\gamma = 2500$ MeV, slightly above the threshold production of $K^*\Lambda(1405)$, $E_\gamma = 2343$ MeV.

5.3.3 Isospin decomposition for the final states

In order to extract the information of each isospin state, it is worth showing the isospin decomposition of the $\pi\Sigma$ distributions [584]. This would help to estimate the effect of the $\Sigma(1385)$ contribution, which may disturb the desired signal of the $\Lambda(1405)$. The physical $\pi\Sigma$ states are decomposed into isospin states as

$$
\begin{aligned}
|\,\pi^+\Sigma^-\,\rangle &= -\frac{1}{\sqrt{6}}|\,2,0\,\rangle - \frac{1}{\sqrt{2}}|\,1,0\,\rangle - \frac{1}{\sqrt{3}}|\,0,0\,\rangle,\\
|\,\pi^-\Sigma^+\,\rangle &= -\frac{1}{\sqrt{6}}|\,2,0\,\rangle + \frac{1}{\sqrt{2}}|\,1,0\,\rangle - \frac{1}{\sqrt{3}}|\,0,0\,\rangle,\\
|\,\pi^0\Sigma^0\,\rangle &= \sqrt{\frac{2}{3}}|\,2,0\,\rangle - \frac{1}{\sqrt{3}}|\,0,0\,\rangle.
\end{aligned}
$$

In the present reaction, we can neglect the $I = 2$ amplitude, which does not couple to the process initialized by the K^-p state. Then the contribution of the isospin states to the cross sections can be written as

$$
\frac{d\sigma(\pi^\pm\Sigma^\mp)}{dM_I} \propto \frac{1}{3}|T^{(0)}|^2 + \frac{1}{2}|T^{(1)}|^2 \pm \frac{2}{\sqrt{6}}\mathrm{Re}(T^{(0)}T^{(1)*}), \quad \frac{d\sigma(\pi^0\Sigma^0)}{dM_I} \propto \frac{1}{3}|T^{(0)}|^2, \tag{5.3.8}
$$

where $T^{(I)}$ is the amplitude with isospin I for the $\pi\Sigma$ system. Here we neglect the kinematic factors. It is obvious to confirm the decomposition shown in table 5.5. By the construction of the amplitude (5.3.4), $T^{(I)}$ can be decomposed into partial waves as

$$
|T^{(0)}|^2 = |T_s^{(0)}|^2, \quad |T^{(1)}|^2 = |T_s^{(1)}|^2 + |T_p^{(1)}|^2, \tag{5.3.9}
$$

where subscripts s and p denote the partial waves. The spectrum from actual experiment may contain the higher partial wave components, but they would be small because of the presence of resonances ($\Lambda(1405)$ in $T_s^{(0)}$ and $\Sigma(1385)$ in $T_p^{(1)}$). Note that the product of s- and p-wave amplitudes vanishes, since we are looking at the cross sections with the angle variables in MB system being integrated.

Let us first consider the charged $\pi\Sigma$ states. In Eq. (5.3.8), we observe that the difference between $\pi^+\Sigma^-$ and $\pi^-\Sigma^+$ comes from the interference term $\mathrm{Re}(T^{(0)}T^{(1)*})$, and when we take an average of the two distributions this interference term vanishes,

$$
\frac{1}{2}\left(\frac{d\sigma(\pi^+\Sigma^-)}{dM_I} + \frac{d\sigma(\pi^-\Sigma^+)}{dM_I}\right) \propto \frac{1}{3}|T^{(0)}|^2 + \frac{1}{2}|T^{(1)}|^2.
$$

We also show the result for the average of the charged $\pi\Sigma$ channels in Fig. 5.14 (thin solid curve). The feature that the initial K^-p couples dominantly to the second pole of the $\Lambda(1405)$ is well preserved in the mass distribution, although the width of this distribution is slightly larger than that of the pure $I = 0$ resonance because it contains some contribution from the $I = 1$ component. This is a nice feature and suggests that by observing the mass distributions of the charged state from the intermediate baryon, it would be possible to study the nature of the second pole of the $\Lambda(1405)$ resonance.

We can estimate the contribution from the $I = 1$ component to the charged $\pi\Sigma$ states. In Fig. 5.14, it is seen that the average of the charged $\pi\Sigma$ states is always larger than the $\pi^0\Sigma^0$

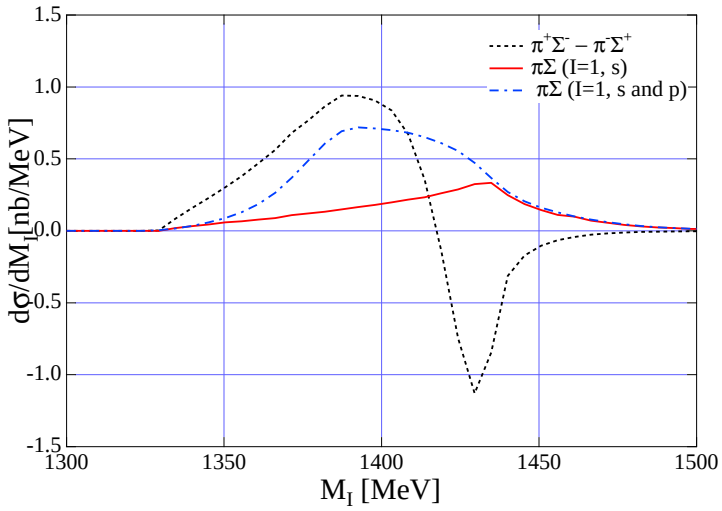

Figure 5.15: Difference of the mass distributions of $\pi^+\Sigma^-$ and $\pi^-\Sigma^+$ (Dashed), $\pi\Sigma(I=1)$ spectrum as in Eq. (5.3.10) (Dash-dotted), and s-wave component of $\pi\Sigma(I=1)$ spectrum, by switching off the $\Sigma(1385)$ contribution theoretically (Solid), in units of [nb/MeV].

result. This is natural because in the difference between the average of charged states and $\pi^0\Sigma^0$ state is given by

$$\frac{1}{2}\left(\frac{d\sigma(\pi^+\Sigma^-)}{dM_I}+\frac{d\sigma(\pi^-\Sigma^+)}{dM_I}\right)-\frac{d\sigma(\pi^0\Sigma^0)}{dM_I}\propto\frac{1}{2}|T^{(1)}|^2=\frac{1}{2}\left(|T_s^{(1)}|^2+|T_p^{(1)}|^2\right), \quad (5.3.10)$$

where the $I=0$ component cancels out, remaining the $I=1$ component, which is positive. Although the $I=1$ component contains the $\Sigma(1385)$ excitation, the contribution to the $\pi\Sigma$ channel is not very large, in the sense that the peak position of the spectrum does not deviate from that of the $I=0$ component (~ 1420 MeV), as we mentioned above.

In Fig. 5.15, we plot the difference (5.3.10) by dash-dotted curve. As seen in the equation, this distribution contains both s- and p-wave components. Indeed, this distribution is not very strong compared with the magnitude of the $I=0$ spectrum shown in Fig. 5.14. Theoretically, in the present framework, we can calculate the pure s-wave $I=1$ by switching off the $\Sigma(1385)$ and making the combination of $\pi\Sigma$ amplitudes (5.3.10), which is plotted by the solid curve in Fig. 5.15. Since the difference between two spectra is the pure contribution from the p-wave component, namely the $\Sigma(1385)$, we can see that its contamination to the $\pi\Sigma$ state is also small. This fact can be understood by the ratio of the couplings $g^2_{\Sigma^*\pi^\pm\Sigma^\mp}/g^2_{\Sigma^*\pi^0\Lambda}=1/3$ (see Table. 5.4) and the phase space factor $(p_{\Sigma^*\pi\Sigma}/p_{\Sigma^*\pi\Lambda})^3\sim 0.24$. This may also justify the treatment in the previous section of the $\pi^- p\to K^0\pi\Sigma$, where we study the average of the charged $\pi\Sigma$ states, without introducing the $\Sigma(1385)$ resonance.

It is also interesting to study the $I=1$ s-wave amplitude in this energy region, since the existence of another pole is discussed [512, 519]. It was shown in Ref. [519] that in the SU(3) decomposition of the meson-baryon states the interaction was attractive in two octet channels in $I=1$ sector, hence it is natural to expect the existence of another s-wave $I=1$ resonance in addition to the $\Sigma(1620)$ already reported in Ref. [503]. Indeed, a pole is found at

$1410 - 40i$ MeV in the model of Ref. [512], which is difficult to detect experimentally, because of the presence of the Σ(1385) resonance. However, the properties of this $I = 1$ pole are very sensitive to the details of the model, since in different models or approximations it appears in different Riemann sheets, but there is still some reflection on the amplitudes in all cases. Therefore, investigation of the $I = 1$ s-wave amplitude would bring further information of resonance properties.

Theoretical $\pi\Sigma(I = 1)$ spectrum for s-wave is shown in Fig. 5.15 (Solid curve) and a small peak is seen as a reflection of the approximate resonant structure predicted in Refs. [512, 519]. In experiments, a naive $I = 1$ combination of the $\pi\Sigma$ state (5.3.10) is contaminated by the Σ(1385) resonance as seen in Fig. 5.15. However, taking into account that the interference term between different partial wave should vanish after we integrate the angular variables, the interference term between $I = 0$ and $I = 1$ contains only the s-wave component;

$$\frac{d\sigma(\pi^+\Sigma^-)}{dM_I} - \frac{d\sigma(\pi^-\Sigma^+)}{dM_I} = \frac{4}{\sqrt{6}}\mathrm{Re}(T_s^{(0)}(T_s^{(1)})^*), \tag{5.3.11}$$

where we assume that the $T^{(0)}$ is dominated by the s-wave component, which is plausible due to the existence of the Λ(1405) resonance. As a guidance for experiments, we plot the quantity (5.3.11) in Fig. 5.15 with the dashed curve. In principle, it is possible to extract $T_s^{(1)}$ from this quantity and the distribution of s-wave $I = 0$ (for instance, from the $\pi^0\Sigma^0$), parametrizing conveniently the $T_s^{(0)}$ amplitude.

Finally we show the results for the sum of all $\pi\Sigma$ and $\pi\Lambda$ channels in Fig. 5.16. This corresponds to the most feasible case in experiment, performing the missing mass analysis with identification of the the three pions decaying from the K^*. The total cross section is about 0.2 μb at the threshold of K^* and Λ(1405). In the mass spectrum as a function of M_I (right panel), we find a two-bump structure reflecting both the Λ(1405) and the Σ(1385). In the actual case, there would be a further contribution from the $\bar{K}N$ channel, raising at around 1430 MeV which we do not include in the calculation. This contribution starts where the mass distribution in Fig. 5.16 has already dropped down and therefore will not blur the shape of the distribution. This is the case in a related reaction studied in Ref. [584]. This figure is also illustrating because it reveals a large strength in the region of 1420 MeV, which makes this shape clearly distinct from the one observed experimentally in the $\pi^- p \to K^0\pi\Sigma$ reaction [543] with a neat peak below 1400 MeV. Hence, this measurement is valuable by itself. Yet, in order to obtain clear signals, one should measure the channels shown in Fig. 5.14. It is interesting to recall that in the chiral model of Ref. [8] it was shown that the $\pi^- p \to K^0\pi\Sigma$ reaction favored the z_1 pole at lower energy.

5.3.4 Summary for the $\gamma p \to K\pi MB$ reaction

In this section, we have proposed a reaction $\gamma p \to K^* B^* \to K\pi MB$ with $B^* = \Lambda(1405)$ and Σ(1385) for the study of the second pole (z_2) possibly existing in the Λ(1405) region. Since this second resonance has been shown to couple more strongly to $\bar{K}N$ than to $\pi\Sigma$ in several chiral models, the present reaction is suitable for the isolation of this pole, where we expect that the t-channel K^- exchange can be maximized by choosing the appropriate experimental conditions. In the $\pi^0\Sigma^0$ spectrum which is purely $I = 0$, the mass distribution shows a peak

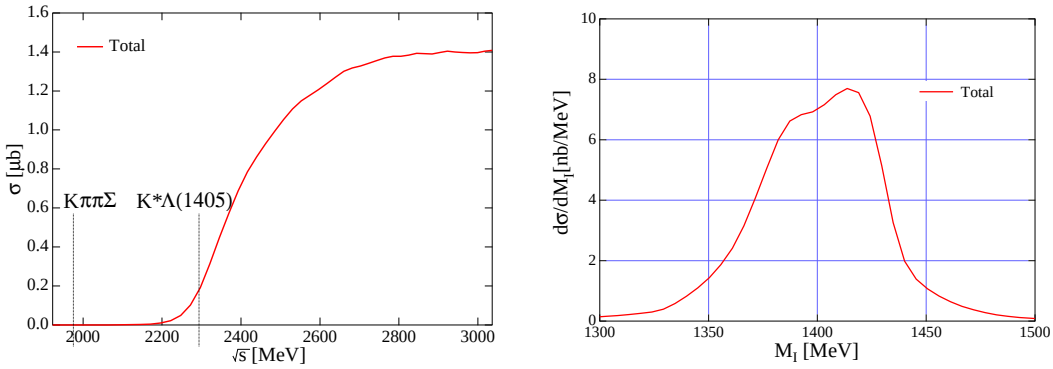

Figure 5.16: Total cross section and invariant mass distribution for the sum of $\pi\Sigma$ and $\pi\Lambda$ channels.

structure pronounced at around 1420 MeV with a relatively narrow width, different from the nominal shape of the $\Lambda(1405)$. The average of the charged $\pi\Sigma$ states, which is more feasible in experiments, still maintains the peak structure around 1420 MeV, although there is a small contaminations from the coupling to $\Sigma(1385)$ states. We also show the possible ways to extract the s-wave $I = 1$ amplitude, in which the existence of another resonance is discussed.

5.4 Summary and later developments

In this chapter, we have investigated the structure of the $\Lambda(1405)$ resonance through the study of the reaction mechanisms. Using the meson-baryon scattering amplitude obtained in the chiral unitary approach, we have provided successful models for the $\pi^- p \to K^0\pi\Sigma$ and $\gamma p \to K\pi MB$ reactions with the $\Lambda(1405)$ excitation in $\pi\Sigma$ and MB states, respectively. In the chiral unitary approach, there are two poles around the $\Lambda(1405)$ energy region. It is found that the $\pi^- p \to K^0\pi\Sigma$ [543] favors the lower energy pole at 1390 MeV (z_1), while the $\gamma p \to K\pi MB$ reaction is dominated by the higher energy pole at 1420 MeV (z_2). The reason for this observation is the difference in the coupling strength of z_1 and z_2 to the meson-baryon channels; z_1 favors $\pi\Sigma$ state and z_2 couples to $\bar{K}N$ strongly. The models developed here clearly shows the different features of the mass spectrum depending on the production reactions. A similar mass distribution to the $\gamma p \to K\pi MB$ reaction was observed in the study of the $K^- p \to \gamma\pi\Sigma$ [585], where the photon is emitted from the initial state and hence the $\Lambda(1405)$ production is also induced by a K^-. Experimental evidence for the existence of such two Λ^* states would provide more information on the nature of the current $\Lambda(1405)$ and thus new clues to understand non-perturbative dynamics of QCD.

The studies done here shows the important role played by the two resonance poles in the production process of the nominal $\Lambda(1405)$ resonance. In section 5.2 ($\pi^- p \to K^0\pi\Sigma$), we have seen how two different mechanisms (chiral and $N(1710)$ terms) filtered each one of the resonance contributions, and then how the coherent sum of the amplitudes from the two mechanisms could describe the data. This exercise has shown the non-triviality of the

Λ(1405) generation, which has not been discussed in all previous theoretical studies. Indeed, one needs to make a careful analysis of each reaction in order to understand the nature of the resonance from the observed shape of the $\pi\Sigma$ mass distribution. This is also true for the study in section 5.3 ($\gamma p \to \pi K M B$), where we examine the effect of the Σ(1385) contribution. Experimental information on several observables in these reactions certainly helps to improve the theoretical understanding on the reaction mechanisms.

After we reported these works, several studies were performed concerning the two-pole structure of the Λ(1405) and recent experimental data. In a similar approach as taken in this chapter, Magas et al., studied the $K^- p \to \pi^0 \Lambda(1405) \to \pi^0\pi^0\Sigma$ reaction [586], motivated by the recent experiment of this process [607]. Indeed, the mass spectrum obtained in Ref. [586] is peaked at the 1420 MeV, which is very different from that in the $\pi^- p \to K^0\pi\Sigma$ reaction [543] (a comparison is done in Fig. 5 in Ref. [586]). In the theoretical study, it is found that the dominant mechanism for this reaction is the emission of the π^0 prior to the $K^- p$ interaction, which leads to a similar mechanism of the interaction of off-shell kaon with nucleon, studied in section 5.3. Hence, the invariant mass spectrum of $\pi^0\Sigma^0$ peaks at 1420 MeV. The model also reproduces well the spectrum and total cross section of the reaction.

There is another experimental developments by DEAR experiment [572], which reports the strong shift and width of the kaonic Hydrogen $1s$ state. This data was examined in Refs. [571, 517], leading to an inconsistency between the new data and previous scattering observables. However, the latest analysis [573] found a scattering amplitude which agrees with both the DEAR experiment and the previous scattering data (see also Refs. [574, 575]). In these studies, the interaction kernel is of $\mathcal{O}(p^2)$, and the two-pole structure, obtained in the leading order calculation, is confirmed.

As future perspective, it will be interesting to study the $\pi^- p \to K^0 M B$ reaction by including the Σ(1385) resonance, as done in section 5.3, since there is still some difference between theory and experiment. From Fig. 5.15, we can see that the inclusion of the Σ(1385) gives more strength in the spectrum at lower energy, but it is not too strong to disturb the peak structure. This will make the agreement of the theoretical distribution to the experimental spectrum better. In Ref. [543], the invariant mass spectrum of the $\pi^0\Lambda$ final state and the angular distribution of the decaying particles are also given. Therefore, comparison of the model prediction with these data will help to determine the reaction dynamics more precisely.

Chapter 6

Magnetic moments of the $N(1535)$ resonance

In this chapter, we calculate the magnetic moments of the $N(1535)$ resonance using the chiral unitary model, where the resonance is dynamically generated in the scatterings of the lowest-lying mesons and baryons. We obtain the magnetic moments of the resonance as $+1.1$ and -0.25 for $p(1535)$ and $n(1535)$, respectively, in units of the nuclear magneton. We discuss the origin of these numbers within the chiral unitary model, then we compare the present results with those of the quark model and the chiral doublet model. The possibility to observe the magnetic moments in experiments is also investigated. This topic is reported in Ref. [13].

6.1 Introduction

The study of the structure of baryon resonances is one of the most important topics in hadron physics, and the recent interest is to understand these properties from the viewpoint of QCD. The baryon resonances, on one side, have been studied by the quark picture, such as the constituent quark model [329, 330, 331]. On the other hand, they are investigated as quasi-bound states in the meson-baryon scattering [506, 507, 508]. Recent progress in chiral physics has brought reconsideration of the meson-baryon picture for the resonance in the contemporary way [4, 5]. Therefore, it is important to clarify the difference and similarity between the two pictures. For this purpose, we study the magnetic moments of the $N(1535)$ resonance, which have a possibility to be observed in experiment.

There are several reasons that the $N(1535)$ resonance is interesting to be studied. For instance, it is known experimentally that the resonance has strong coupling to the ηN state, which is almost an exclusive nature of the resonance. Thanks to this properties, one can easily identify creation of $N(1535)$ in the intermediate state of the reaction by observing the η meson in the final state. On the other hand, there is an interesting scenario when chiral symmetry is restored at finite temperature and density [608, 609, 610]. There is a possibility that positive and negative parity baryons are included in a large chiral multiplet. Such a point of view provides an interesting theoretical approach based on chiral symmetry of QCD, and there $N(1535)$ could play an important role.

The nature of $N(1535)$ has been studied by several theoretical approaches. In an SU(6) quark model, $N(1535)$ state may be described as a three quark state with suitable mixing among the p-wave 70-dimensional representation [329, 330, 331]. Lattice calculations [611, 612, 613, 614, 615, 616, 617] and QCD sum rules [618, 619, 620] are also predicting the resonance masses in a good agreement with experimental data using a three-quark interpolating operator. On the other hand, when having a strong coupling to meson-baryon states, the resonance state must have a significant component of meson-baryon states. Following this line, the resonances have been studied as meson-baryon quasi-bound states in a coupled channel method with unitarized chiral perturbation theory [559, 570, 504, 580]. In this model, the $N(1535)$ resonance is dynamically generated as a $K\Sigma$ quasi-bound state. Generally speaking, both approaches shown above provide a good description of the $N(1535)$ resonance. In such a situation, it is fare to say that our understanding for the resonance nature is not yet complete.

Experimentally, so far, the magnetic moments of Δ^{++}, Δ^{+}, and Ω^{-} have been measured [621, 622, 623, 624]. The measurements were performed through bremsstrahlung processes. For example, the magnetic moments of Δ^{++} have been studied in the reaction $\pi^+ p \to \gamma\pi^+ p$ [621, 623]. Due to the ambiguities of various theoretical models [621, 623, 625, 626], Particle Data Group (PDG) [144] shows the expected value as $\mu_{\Delta^{++}} = 3.7 \sim 7.5\mu_N$, where μ_N is the nucleon magneton. Now for $N(1535)$, a similar process can be used such as $\gamma p \to \gamma\eta p$ [627], where the strong ηN coupling of $N(1535)$ would help to isolate the resonance production from the background.

In this chapter, we compute the magnetic moments of the $N(1535)$ resonance in the chiral unitary model, following the techniques developed in Ref. [588], where they have applied to computation of the magnetic moments of $\Lambda(1405)$ and $\Lambda(1670)$. Recently, the $N(1535)$ resonance magnetic moments were studied also in a constituent quark model [627], and therefore, the present study provides one of alternative descriptions.

This chapter is organized as follows. In section 6.2, We present the formulation to calculate the magnetic moments in the chiral unitary model. The input parameters and numerical results are presented in section 6.3. In section 6.4 we discuss the obtained results from various point of view. In section 6.5, we discuss the possibility to observe the magnetic moments of N^* in experiment and calculate the energy spectra and the angular distributions of the emitted photon in the $\gamma N \to \gamma\eta N$ and $\pi^- p \to \gamma\eta n$ reactions. Section 6.6 is devoted as the summary of the present results.

6.2 Formulation

6.2.1 Definition of resonance magnetic moment

First of all, let us discuss definition of the magnetic moment of a short living resonance state. A model-independent definition of the magnetic moment may be an expectation value of the magnetic moment operator $\hat{\mu}$ by the resonance state: $\mu_R \equiv \langle \Phi^{(\mathrm{in})} | \hat{\mu} | \Phi^{(\mathrm{out})} \rangle$, where the resonance states $|\Phi^{(\mathrm{out}),(\mathrm{in})}\rangle$ are defined as only either outgoing waves or incoming waves

asymptotically [A]. These resonance states cooperatively form a biorthogonal set:

$$\left\langle \Phi^{(\mathrm{in})} \middle| \Phi^{(\mathrm{out})} \right\rangle = 1.$$

This implies that the bra vector $\langle \Phi^{(\mathrm{in})}|$ corresponds as imaginary conjugate of the ket vector $|\Phi^{(\mathrm{out})}\rangle$. These states are eigenvectors of the Hamiltonian with complex eigenvalues $M_R \mp i\Gamma_R/2$ in the generalized Hilbert space, in which the hermitian operator is allowed to have complex eigenvalues. This definition leads us to a complex value of the magnetic moment of the resonance. It is natural, however, that the resonance magnetic moment is expressed by a complex number, since the magnetic moment, in principle, is observed by an energy shift in the presence of a perturbative magnetic field. In the case of the resonance as a shot living particle, the measurement of the energy shift should be uncertain because of its decay in a finite time during the measurement. Consequently, the magnetic moment should be uncertain, since the external magnetic field can be, in principle, adjusted as precise as one desires. Here, following the definition of the expectation value for the resonance state, we define the resonance magnetic moment as

$$\mu_R \equiv \mathrm{Re} \left\langle \Phi^{(\mathrm{in})} \middle| \hat{\mu} \middle| \Phi^{(\mathrm{out})} \right\rangle \ , \tag{6.2.1}$$

and the deviation from the average value $\Delta\mu_R$ is given by

$$(\Delta\mu_R)^2 = - \left(\mathrm{Im} \left\langle \Phi^{(\mathrm{in})} \middle| \hat{\mu} \middle| \Phi^{(\mathrm{out})} \right\rangle \right)^2 \tag{6.2.2}$$

It is important to note that the phase of the resonance magnetic moment can be one of the predictions of this approach, since the resonance is dynamically generated in the meson-baryon scattering driven by the chiral perturbation theory, in which all relative phases between the baryons and mesons are completely fixed by the flavor SU(3) symmetry.

6.2.2 Basic idea

Here we would like to explain briefly our method to calculate the magnetic moments of the $N(1535)$ resonance, which was originally proposed in Ref. [588].

We consider meson-baryon scattering with $I = 1/2$ and $S = 0$ in which the $N(1535)$ resonance is dynamically generated through the non-perturbative resummation of the meson-baryon loop diagrams as shown in Fig. 6.1. The resonance couples to the meson-baryon states in an s-wave due to $N(1535)$ having $J^P = 1/2^-$. With inserting the projection operator $P = |\Phi^{(\mathrm{out})}\rangle\langle\Phi^{(\mathrm{in})}|$ of the resonance state into the scattering amplitude, the resonance contribution is written as

$$T_{ij}^R = \frac{g_i g_j}{\sqrt{s} - M_R + i\Gamma_R/2}, \tag{6.2.3}$$

where M_R and Γ_R are the mass and width of the resonance, $\sqrt{s}$ is the total energy of initial state, and the indexes i, j specify the initial and final meson-baryon states, respectively. This

[A] Here we do not consider relativistic resonance states, which are discussed in Ref. [628].

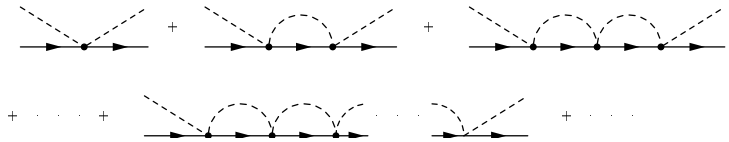

Figure 6.1: Diagrammatic interpretation of non-perturbative resummation in the chiral unitary model.

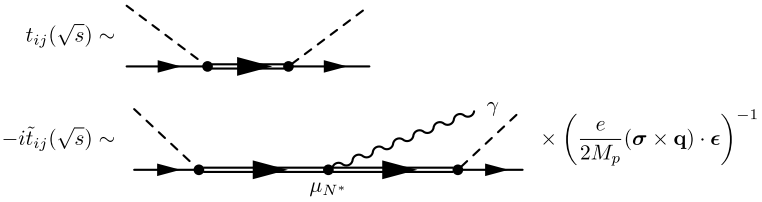

Figure 6.2: Feynman diagrams of the amplitudes $t_{ij}(\sqrt{s})$ and $-i\tilde{t}_{ij}(\sqrt{s})$ around energy region of the resonance. Solid, dashed, wavy and double lines represent baryons, mesons, photon and baryon resonances, respectively. In calculating $-i\tilde{t}_{ij}(\sqrt{s})$, we consider the diagrams which contribute to the magnetic moments, and extract a factor in order to make the coupling of resonance to photon to be magnetic moment in units of the nuclear magneton.

amplitude corresponds to the process shown as the upper diagram in Fig. 6.2. The coupling strengths of the resonance to the meson-baryon states are expressed as $g_i = \langle i|H|\Phi^{(\mathrm{out})}\rangle$ and $g_j = \langle \Phi^{(\mathrm{in})}|H|j\rangle$ with an interaction Hamiltonian H of the resonance with the meson-baryon states. The couplings g_i, g_j are generally complex values. It is worth noting here that g_j appears in Eq. (6.2.3) without taking the complex conjugate in the extended Hilbert space for the hermitian Hamiltonian V.

We also consider a meson-baryon scattering amplitude with a soft photon emission as shown in lower panel of Fig. 6.2. With inserting the projection operator of the resonance twice, the resonance contribution to the magnetic transition is written as

$$T_{ij}^{\gamma R} = \frac{g_i}{\sqrt{s} - M_R + i\Gamma_R/2} \left\langle \Phi^{(-)} \middle| \hat{\mu} \middle| \Phi^{(+)} \right\rangle \frac{g_j}{\sqrt{s} - M_R + i\Gamma_R/2} \left(\frac{e}{2M_p}(\boldsymbol{\sigma} \times \boldsymbol{q}) \cdot \boldsymbol{\epsilon}\right), \tag{6.2.4}$$

with the photon momentum $\boldsymbol{q}$, the photon polarization vector $\boldsymbol{\epsilon}$ and the proton mass M_p, which is used for the unit of nuclear magneton. It is important that, in Eq. (6.2.4), the magnetic moment of the resonance is shown as a residue of the amplitude at the pole of the resonance.

The basic idea to extract the resonance magnetic moment is the followings. At first, we calculate the above two amplitudes within the chiral unitary approach and, then take a ratio of the amplitudes T_{ij}^R and $T_{ij}^{\gamma R}$ after removing the trivial spin factor. Consequently the ratio does not have the coupling constants g_i, g_j, which are irrelevant in the present discussion. As we shall see later, the amplitudes T_{ij}^R and $T_{ij}^{\gamma R}$ can be calculated analytically in the chiral unitary approach. The analytic solution allows us to investigate the structure of the amplitudes in the complex plane, and finally the magnetic moment is calculated as a residue on the top of the resonance pole in the energy complex plane. We also evaluate

the ratio of the amplitudes in the real axis in order to compare the results with experiments directly, since it is very difficult to determine the magnetic moments in the complex plane in the experiment (One could know the analytic structure of the amplitude in principle by extensively detailed observation of the scattering as the determination of the pole position of the resonance.). The detail discussion of the method will come later on.

6.2.3 Chiral unitary model

The chiral unitary model is an extension of the chiral perturbation theory to the resonance energy region by imposing the unitarity condition, and allows us to investigate the properties of the resonances which are expressed in the multiple scattering of hadrons.

As explained in chapter 4, assuming the elastic unitarity and neglect of the crossing symmetry in the N/D method [512, 511], the T-matrix amplitude can be written as

$$t = [1 - VG]^{-1}V, \tag{6.2.5}$$

with the basic interaction V and the meson-baryon loop function G, which are given in the following. This equation provides algebraically the solution to the Bethe-Salpeter equation, which is diagrammatically shown in Fig. 6.1.

The basic meson-baryon interaction V is obtained from the chiral perturbation theory. Now we are interested in the $N(1535)$ resonance with $J^P = 1/2^-$, which will be seen in the s-wave meson-baryon scattering. Hence the basic interaction is given by the Weinberg-Tomozawa term in the chiral Lagrangian and is written in the non-relativistic form as

$$V_{ij} = -\frac{C_{ij}}{4f_i f_j}(2\sqrt{s} - M_i - M_j)\sqrt{\frac{E_i + M_i}{2M_i}}\sqrt{\frac{E_j + M_j}{2M_j}}, \tag{6.2.6}$$

with the channel indices (i, j), the meson decay constant f_i, the baryon mass M_i, the baryon energy E_i and the total energy in the center of mass system $\sqrt{s}$. The coefficients C_{ij} are fixed by chiral symmetry and are given in Tables D.5 and D.6 in Appendix. Note that we write the meson decay constants depending on the channel i, which is different from Eq. (4.2.2) in chapter 4.

The loop-integral function G, which implements the s-channel unitarity associated with the meson-baryon intermediate states, is calculated with the dimensional regularization [503]:

$$\begin{aligned} G_i(\sqrt{s}) =& i\int \frac{d^4q}{(2\pi)^4}\frac{2M_i}{(P-q)^2 - M_i^2}\frac{1}{q^2 - m_i^2} \\ =& \frac{2M_i}{(4\pi)^2}\left\{ a_i(\mu) + \ln\frac{M_i^2}{\mu^2} + \frac{m_i^2 - M_i^2 + s}{2s}\ln\frac{m_i^2}{M_i^2} \right. \\ &+ \frac{\bar{q}_i}{\sqrt{s}}\Big[\ln(s - (M_i^2 - m_i^2) + 2\sqrt{s}\bar{q}_i) + \ln(s + (M_i^2 - m_i^2) + 2\sqrt{s}\bar{q}_i) \\ &\left. - \ln(-s + (M_i^2 - m_i^2) + 2\sqrt{s}\bar{q}_i) - \ln(-s - (M_i^2 - m_i^2) + 2\sqrt{s}\bar{q}_i)\Big]\right\}, \end{aligned} \tag{6.2.7}$$

where m_i is the meson mass in channel i, and its three-momentum $\bar{q}_i$ is defined by

$$\bar{q}_i(\sqrt{s}) = \frac{\sqrt{(s-(M_i-m_i)^2)(s-(M_i+m_i)^2)}}{2\sqrt{s}}.$$

In Eq. (6.2.7), μ and $a_i(\mu)$ are the regularization scale and the subtraction constants, which are not constrained by the unitarity condition nor chiral symmetry [512]. These parameters has been already fitted for $N(1535)$ to provide a good description for scattering observables such as cross sections and phase shifts in Ref. [504].

The advantage of this method is that the amplitude t_{ij} can be calculated in an analytic form as a result of the algebraic equation (6.2.5) and the analytic expression (6.2.7) of the loop function. Therefore we can perform analytic continuation of the amplitude to the complex energy plane in the second Riemann sheet, and there we are allowed to calculate positions and residua of poles, if exist. The poles will have information of the corresponding resonances, which may be free from contaminations of the background effects.

The calculated T-matrix element t_{ij} by Eq.(6.2.5) with Eqs. (6.2.6) and (6.2.7), if the resonance is successfully generated, may be parametrized in the Breit-Wigner form with moderate background in the vicinity of the resonance as

$$t_{ij}(\sqrt{s})\Big|_{\sqrt{s}\sim M_{N^*}} \sim t_{ij}^R(\sqrt{s}) \equiv \frac{g_i g_j}{\sqrt{s}-M_{N^*}+i\Gamma_{N^*}/2} + t_{ij}^{BG} \ , \tag{6.2.8}$$

where M_{N^*} and Γ_{N^*} are the mass and width of the resonance, respectively, and g_i gives the coupling strength of the resonance to the meson-baryon channel i. The background term t_{ij}^{BG} is expected to be slowly varying function of $\sqrt{s}$ in the resonance region. A diagrammatic interpretation of Eq. (6.2.8) is shown in Fig. 6.2 (upper diagram).

In practical calculations, we use two bases for the channels. When we calculate the scattering amplitudes, we adopt the physical basis such as $\pi^- p$ and ηn, because in the following subsections we introduce the electromagnetic interactions, which are not isospin symmetric. While, when we calculate the resonance properties, we use the isospin basis such as $\pi N(I=1/2)$ and $K\Sigma(I=3/2)$, in order to specify the isospin of resonances. The two bases are related each other through the Clebsh-Gordan coefficients.

6.2.4 Electromagnetic interactions in the chiral Lagrangian

In this subsection, we adopt the standard notation of chiral perturbation theory [513, 40, 514]. By gauging the baryon kinetic term in the chiral Lagrangian, we obtain the $BB\gamma$ coupling:

$$\mathcal{L}_{(\gamma)}^B = -e\mathrm{Tr}\left(\bar{B}\gamma^\mu[Q,B]\right)A_\mu \ , \tag{6.2.9}$$

with the quark charge matrix $Q = \mathrm{diag}(2,-1,-1)/3$, and the photon field A_μ, and octet baryon field B. This Lagrangian provides the normal magnetic moments of the ground state baryons.

In addition, there are terms for the anomalous magnetic moments in the effective chiral Lagrangian [629];

$$\mathcal{L}_{(\gamma)}^{MB} = -\frac{i}{4M_p}b_6^F\mathrm{Tr}\left(\bar{B}[S^\mu,S^\nu][F_{\mu\nu}^+,B]\right) - \frac{i}{4M_p}b_6^D\mathrm{Tr}\left(\bar{B}[S^\mu,S^\nu]\{F_{\mu\nu}^+,B\}\right) \quad , \tag{6.2.10}$$

where M_p is the mass of proton, b_6^F and b_6^D are the low energy constants, $F_{\mu\nu}^+ = -e(\xi^\dagger Q F_{\mu\nu}\xi + \xi Q F_{\mu\nu}\xi^\dagger)$ with $\xi = \exp\{i\Phi/\sqrt{2}f\}$ and S^μ is a covariant baryon spin operator. The octet meson and baryon fields Φ and B are given in Appendix B.1.

Expanding the ξ fields, we obtain the magnetic moments of the ground state baryons in terms of b_6^D and b_6^F in the chiral limit, which satisfy the following Coleman-Glashow relations [630];

$$\begin{aligned} &\mu_{\Sigma^+} = \mu_p, \quad 2\mu_\Lambda = \mu_n, \quad \mu_{\Sigma^-} = \mu_{\Xi^-}, \quad \mu_{\Xi^0} = \mu_n, \quad \mu_{\Sigma^-} + \mu_n = -\mu_p, \\ &2\mu_{\Sigma^0\Lambda} = -\sqrt{3}\mu_n, \quad 2\mu_{\Sigma^0} = \mu_{\Sigma^+} + \mu_{\Sigma^-}. \end{aligned} \tag{6.2.11}$$

These relations are independently of the low energy constants.

Recall that the magnetic moments derived from the Lagrangian (6.2.10) are the anomalous magnetic moments, while the normal magnetic moments come from the covariant derivative term (6.2.9). However, the contributions from the normal magnetic moments are exactly the same as the first term of Eq. (6.2.10) except the global factor b_6^F. Indeed the normal magnetic moments just shift the factor b_6^F to $b_6^F + 1$. Therefore we will absorb the normal magnetic moments into b_6^F in the rest of this article. We need to be careful that the values we show are different from the low energy constant b_6^F which appears in chiral perturbation theory.

Fitting the magnetic moments written in terms of b_6^D and b_6^F to data, we find the parameters [629]

$$b_6^D = 2.39, \quad b_6^F = 1.77. \tag{6.2.12}$$

In spite of the use of the only two parameters, the tree level calculation provides good results.

6.2.5 Soft photon emission amplitude

Here we calculate the photon emission amplitude shown in the bottom of Fig. 6.2. Since the baryon resonance is expressed in the multiple scattering of the meson and baryon, the coupling amplitude is obtained by insertion of the elementary photon couplings shown in Fig. 6.3 into the meson-baryon multiple scattering in which the resonance is dynamically generated. Namely we consider the Feynman diagrams shown in Fig. 6.4.

The elementary coupling of the photon to the meson baryon scattering is given in the chiral perturbation theory discussed in the previous section. There are three relevant diagrams for the elementary coupling, as shown in Fig. 6.3. First of all, the diagram (c) does not contribute to the magnetic component of the meson-baryon scattering for the $1/2^-$ resonance, because of the s-wave nature of the meson-baryon coupling. Next we express the contributions from the two terms (a) and (b) as $-i\tilde{t}_{ij}^{(a)}(\sqrt{s})$ and $-i\tilde{t}_{ij}^{(b)}(\sqrt{s})$, respectively. Then, the whole amplitude is given by

$$-i\tilde{t}_{ij}(\sqrt{s}) = \left(-i\tilde{t}_{ij}^{(a)}(\sqrt{s})\right) + \left(-i\tilde{t}_{ij}^{(b)}(\sqrt{s})\right), \tag{6.2.13}$$

In the following, we calculate these two contributions, combining the elementary vertices shown in Fig. 6.3 with the transition amplitude shown in Fig. 6.1.

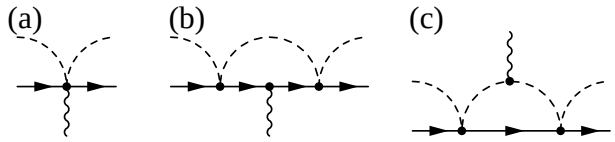

Figure 6.3: Photon coupling diagram in $-i\tilde{t}_{ij}(\sqrt{s})$. We consider that there are meson-baryon loops on the left and right sides of these vertices.

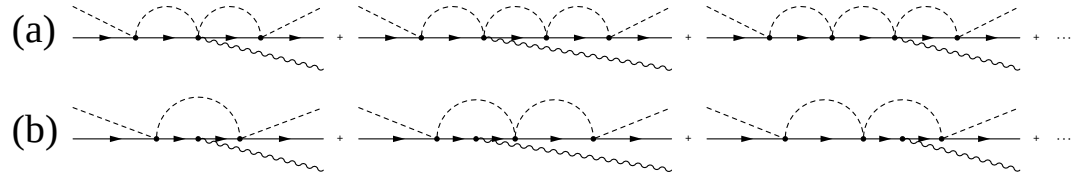

Figure 6.4: Diagrams for the coupling of the photon to the resonance dynamically generated in meson-baryon scattering.

The tree level amplitude of (a) is obtained by expanding the chiral Lagrangian (6.2.10) in terms of the meson field;

$$V_{ij}^{BBMM\gamma} = ie\frac{\boldsymbol{\sigma}\times\mathbf{q}}{2M_p}\cdot\boldsymbol{\epsilon}A_{ij},$$

with

$$A_{ij} = \frac{1}{2f_if_j}[X_{ij}b_6^D + Y_{ij}b_6^F],$$

where the coefficients X_{ij} and Y_{ij} are given in Tables D.15 and D.16 in Appendix. Inserting this tree level amplitude between two meson-baryon scattering amplitudes t_{ij}, we obtain the amplitudes shown in Fig. 6.4 (a);

$$-i\tilde{t}_{ij}^{(a)} = t_{il}G_lA_{lm}G_mt_{mj}, \tag{6.2.14}$$

after removing the spin factor.

The diagram (b) in Fig. 6.3 is calculated by multiplying the magnetic moment of the ground state baryon μ_l and the loop integral with the one-meson and two-baryon propagators $\tilde{G}_l$. Multiplying the meson-baryon scattering amplitude to generate the resonance on both side, we obtain the contribution from the diagram (b):

$$-i\tilde{t}_{ij}^{(b)} = t_{il}\tilde{G}_l\mu_lt_{lj}. \tag{6.2.15}$$

In the soft photon limit, the loop function $\tilde{G}_l$ is obtained by the derivative of the loop integral with the one meson and one baryon propagators in terms of the center of mass energy as

$$\begin{aligned}\tilde{G}_l(\sqrt{s}) =& i\int\frac{d^4q}{(2\pi)^4}\frac{2M_l}{(P-q)^2-M_l^2}\frac{2M_l}{(P-q)^2-M_l^2}\frac{1}{q^2-m_l^2}\\ =& -\frac{\partial}{\partial\sqrt{s}}G_l(\sqrt{s}).\end{aligned} \tag{6.2.16}$$

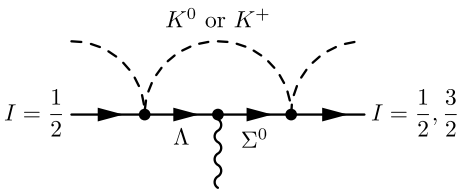

Figure 6.5: Diagrams of off-diagonal components in $\tilde{G}$ including $\Sigma^0\Lambda$ transition in the $S = 0$ channel.

As a consequence of this property, the loop function $\tilde{G}_l$ can be calculated in the analytic form. This enables us to perform the analytic continuation of the amplitude and to search its poles in the complex plane. As we shall see later, the calculation of the magnetic moment in the complex plane is free from the contamination from the non-resonant component.

Since the photon allows the $\Sigma^0\Lambda$ transition in the magnetic coupling, there the different baryons enter to the loop as shown in Fig. 6.5. This implies that the $\tilde{G}$ is no longer a diagonal matrix in terms of the channel. As pointed out in Ref. [588], in the case of the calculation of the magnetic moment of the $\Lambda(1405)$ ($I = 0$), the effects of the $\Sigma^0\Lambda$ transition is negligible, because the transition changes isospin from 0 to 1 and contributes only to the isospin breaking. However, in the present case for the N resonance ($I = 1/2$), the $\Sigma^0\Lambda$ transition occurs among the $K\Sigma^0$ and $K\Lambda$ and both channels have $I = 1/2$, which is the same isospin as the N^* resonance. Therefore, there is no such a suppression of the transition due to the isospin breaking like the $\Lambda(1405)$ case. Indeed, we have checked numerically that the inclusion of the $\Sigma^0\Lambda$ transition provides not a small effect to the amplitude $-i\tilde{t}^{(b)}_{ij}$.

The transition amplitude is calculated by putting the Σ^0 and Λ masses to the propagators in the second line of Eq. (6.2.16). Here we approximate the loop function with the Σ^0 and Λ masses as the average of the loop functions of Σ^0 and Λ, since we want to use their analytic forms:

$$\tilde{G}_{M\Lambda,M\Sigma^0}(\sqrt{s}) = \frac{1}{2}\left(\tilde{G}_{M\Sigma^0}(\sqrt{s}) + \tilde{G}_{M\Lambda}(\sqrt{s})\right), \tag{6.2.17}$$

where M denotes K^+ or K^0 depending on the charge of the N^* resonance we consider, proton or neutron. We have checked that this is good approximation around the energies of $N(1535)$, by seeing the differences among Eq. (6.2.17), and $\tilde{G}$ for the Σ and Λ propagators. The effect of this approximation to the resulting magnetic moment is $\sim 0.5\mu_N$. Since the $N(1535)$ resonance lies far from the thresholds of the $K\Sigma^0$ and $K\Lambda$, there is no significant difference among the values of these functions at energies we consider, although these functions give the different values around the thresholds, where G's are not smooth functions and $\tilde{G}$'s diverge.

Finally, considering the transition effect, we obtain the contribution from the diagram (b) as

$$-i\tilde{t}^{(b)}_{ij} = t_{il}\left[\delta_{lm}\tilde{G}_l\mu_l + \tilde{G}_{lm}\,\mu_{(\Sigma^0\Lambda)}\right]t_{mj}\ , \tag{6.2.18}$$

where $\tilde{G}_{lm}$ has components only in the transition.

In this way, combining Eqs. (6.2.13), (6.2.14), and (6.2.18), we obtain the meson-baryon scattering amplitude with a soft photon emission $-i\tilde{t}$ in the chiral unitary model. Around

the resonance energy region, where the pole contribution becomes dominant, the amplitude $-i\tilde{t}$ can be interpreted as the Breit-Wigner form of resonance:

$$-i\tilde{t}_{ij}(\sqrt{s})\Big|_{\sqrt{s}\sim M_{N^*}} \sim -i\tilde{t}^R_{ij}(\sqrt{s}) \equiv \left(\frac{g_i}{\sqrt{s}-M_{N^*}+i\Gamma_{N^*}/2}+t^{BG}\right) \times \mu_{N^*} \times \left(\frac{g_j}{\sqrt{s}-M_{N^*}+i\Gamma_{N^*}/2}+t^{BG}\right), \tag{6.2.19}$$

where μ_{N^*} is the magnetic moment of the N^* resonance.

6.2.6 Evaluation of the magnetic moments

Here we explain the method to evaluate the magnetic moments of the resonances from the amplitudes t_{ij} and $-i\tilde{t}_{ij}$ obtained in Eqs. (6.2.5) and (6.2.13). The later is given by the combination of Eqs. (6.2.14) and (6.2.18). Around the resonance energy region $\sqrt{s}\sim M_{N^*}$, we can regard these amplitudes as the Breit-Wigner form shown in Eqs. (6.2.8) and (6.2.19), respectively. The basic idea to extract the magnetic moment is to take the ratio of amplitudes t_{ij} and $-i\tilde{t}_{ij}$ in order to single out the magnetic moments by canceling the resonance propagators and the couplings. Technically, there are two methods to calculate the magnetic moment; one is to extract it on the real axis and the other is to evaluate it in the complex plane [588]. We shall see both methods in the followings.

On the real axis, comparing the Eqs. (6.2.8) and (6.2.19) around the resonance energies, we see that the ratio of the photon coupled amplitude $-\tilde{t}^R_{ij}$ to the derivative of t^R_{ij} in terms of the energy gives the magnetic moment of the resonance, if we assume the background terms are neglected;

$$\mu_{N^*}(\sqrt{s}) = \frac{-i\tilde{t}^R_{ij}(\sqrt{s})}{-\frac{\partial}{\partial\sqrt{s}}t^R_{ij}(\sqrt{s})} \sim \left.\frac{-i\tilde{t}_{ij}(\sqrt{s})}{-\frac{\partial}{\partial\sqrt{s}}t_{ij}(\sqrt{s})}\right|_{\sqrt{s}\sim M_{N^*}}, \tag{6.2.20}$$

In order to avoid contaminations of the background effect, we evaluate μ_{N^*} at the resonance energy $\sqrt{s}\sim M_{N^*}$ and choose the suitable external channel which strongly couples to the resonance, as seen below.

The possible error of this approach can be estimated as follows. In the actual cases, since there are background contributions, the denominator of the right hand side of Eq. (6.2.20) is written as

$$\frac{\partial}{\partial\sqrt{s}}t_{ij}(\sqrt{s}) = -\frac{g_i g_j}{(\sqrt{s}-M_{N^*}+i\Gamma_{N^*}/2)^2} + \frac{\partial}{\partial\sqrt{s}}t^{BG}_{ij}.$$

We can safely neglect the last term in this case, since the function t^{BG}_{ij} is assumed to be a slowly varying function of $\sqrt{s}$. However, we have to deal with the numerator carefully, due to absence of derivative unlike the denominator function. Thus the background contribution is estimated as

$$\frac{-i\tilde{t}_{ij}(\sqrt{s})}{-\frac{\partial}{\partial\sqrt{s}}t_{ij}(\sqrt{s})} = \mu_{N^*}(\sqrt{s}) + t^{BG}\frac{\sqrt{s}-z_{N^*}}{g_i} + t^{BG}\frac{\sqrt{s}-z_{N^*}}{g_j} + \left(t^{BG}\right)^2\frac{(\sqrt{s}-z_{N^*})^2}{g_i g_j}, \tag{6.2.21}$$

where $z_{N^*} \equiv M_{N^*} - i\Gamma_{N^*}/2$. Note that the terms other than the first one in Eq. (6.2.21) are not always assumed to be small even around $\sqrt{s} = M_{N^*}$, because $(\sqrt{s} - z_{N^*})$ is not negligible in the case of the large imaginary part of z_{N^*}. Eq. (6.2.21) tells us the criterion to turn down the background contribution, that is, to make g_i larger and $\sqrt{s} - z_{N^*}$ smaller. Therefore, we choose the most effective external channel which strongly couples to the resonance, and evaluate it at energy near the resonance peak. The couplings of the resonance to the meson-baryon channels g_i are calculated as the residua of the scattering amplitude t_{ij} at the pole of the amplitude in the complex plane.

The other method, the calculation in the complex plain, is based on the fact that we obtain the scattering amplitudes analytically, which enable us to perform the analytic continuation of the amplitudes to the complex plane. This is a big advantage of the chiral unitary model, since we can calculate the magnetic moment exactly on the pole and, therefore, the background terms do not give any contributions. The magnetic moment is calculated as the residue of the ratio function:

$$\begin{aligned}\lim_{z\to z_{N^*}} (z - z_R)\frac{-i\tilde{t}_{ij}(z)}{t_{ij}(z)} =& \lim_{z\to z_{N^*}} \left[\frac{\mu_{N^*}(z)}{1 + (z - z_{N^*})t^{BG}/(g_i g_j)} + \mathcal{O}(z - z_{N^*})\right] \\ =& \mu_{N^*}(z_{N^*}).\end{aligned} \tag{6.2.22}$$

Since the position of the pole generated in the unitarization does not depend on the channel, the result (6.2.22) is independent of the channel chosen to calculate the magnetic moments. In the actual calculation we evaluate numerically the position of the pole of the ratio function and calculate its residue at the pole.

Now we have seen the two method to extract the resonance magnetic moment. Each method has its merit and demerit. In the first method, due to the background contaminations the result depends on the choice of the channel and the energy where we evaluate the magnetic moment, which gives the ambiguities of the evaluation. On the other hand, in the second method, we can compute $\mu_{N^*}(z_{N^*})$ without the background contribution and the channel dependence. But the result is conceptual, since experiment cannot directly achieve the complex plane. Hence, we will show the results of both method.

6.3 Numerical results

In this section, we show the results of numerical calculations. First, we present the input parameters and calculate $S = 0$ meson-baryon scattering amplitudes in the chiral unitary model. Next, using the same parameters, we calculate the magnetic moments of the $N(1535)$ resonance. In the following, we denote the two charge states of $N(1535)$ as $n^*(Q = 0)$ and $p^*(Q = 1)$.

6.3.1 The $N(1535)$ resonance in the chiral unitary model

The resonance states are obtained by solving the scattering equation (6.2.5), whose coefficients C_{ij} are shown in Tables D.5 and D.6, while the coefficients X_{ij} and Y_{ij} for the magnetic moments are given in Tables D.15 and D.16. For the mass of the particles m_i and M_i, and

Table 6.1: Coupling strengths of the $N(1535)$ resonance to meson-baryon channels. All the channels have isospin $I = 1/2$.

	$\lvert g_{\pi N}\rvert^2$	$\lvert g_{\eta N}\rvert^2$	$\lvert g_{K\Lambda}\rvert^2$	$\lvert g_{K\Sigma}\rvert^2$
n^*	0.623	2.30	1.93	7.29
p^*	0.619	2.35	1.88	7.37

the magnetic moments of the ground state baryons μ_i, we use the physical values taken from the Particle Data Group (PDG) [144]. The low energy constants b_6^F and b_6^D are given by Eq. (6.2.12). In order to calculate the loop function (6.2.7), we use the regularization scale $\mu = 630$ MeV and the following channel dependent subtraction constants

$$a_{\pi N} = 0.711, \quad a_{\eta N} = -1.09, \quad a_{K\Lambda} = 0.311, \quad a_{K\Sigma} = -4.09. \tag{6.3.1}$$

which are equivalent to the values with $\mu = 1200$ MeV in Ref. [504] because of the relation $a(\mu') = a(\mu) + 2\ln(\mu'/\mu)$. We use the common value for each isospin multiplet. These constants are essential to generate the $N(1535)$ resonance [6, 7]. We adopt the physical meson decay constants,

$$f_\pi = 93 \text{ [MeV]}, \quad f_K = 1.22 \times f_\pi, \quad f_\eta = 1.3 \times f_\pi, \tag{6.3.2}$$

following Ref. [504].

Using these inputs, we calculate the scattering amplitudes (6.2.5), which well describes the S_{11} phase shifts, the scattering amplitudes and the total cross section of $\pi^- p \to \eta n$. In the complex energy plane, we find poles at

$$\begin{aligned} z_{n^*} &= 1536.01 - 37.06i \text{ [MeV]} \quad (Q = 0), \\ z_{p^*} &= 1531.01 - 36.38i \text{ [MeV]} \quad (Q = 1), \end{aligned} \tag{6.3.3}$$

whose real and imaginary parts correspond to the mass M_{N^*} and width $\Gamma_{N^*}/2$, respectively, for the Breit-Wigner parametrization (6.2.8). The width ~ 72 MeV is consistent with the most recent experiments [631, 632] (95 ± 25 MeV), although it is smaller than PDG estimation (150 ± 50 MeV) [144]. Note that before including the electromagnetic interactions, the difference between n^* and p^* comes from the tiny isospin violation due to the particle mass differences.

Their coupling strengths $|g_i|^2$ to the various meson-baryon channels are shown in Table 6.1. From this table, we see that the $K\Sigma$ channel has the largest coupling strength to the $N(1535)$ resonance, which indicates that the resonance is a quasi-bound state of $K\Sigma$, as pointed out in Ref. [559]. We use this channel to calculate the magnetic moment on the real axis. At the energy of the threshold of $N(1535)$, the πN and ηN channels open. Therefore, the decay of the resonance is dominated by ηN channel, which is a characteristic properties of $N(1535)$.

6.3.2 Magnetic moments of the $N(1535)$ resonance

We first show the results obtained in the complex plane, calculating numerically the residues of the ratio function in Eq. (6.2.22) at the poles obtained in Eq. (6.3.3);

$$\begin{aligned}\left\langle n^{*(\mathrm{in})}\right|\hat{\mu}\left|n^{*(\mathrm{out})}\right\rangle &= -0.084 - 0.233i,\\ \left\langle p^{*(\mathrm{in})}\right|\hat{\mu}\left|p^{*(\mathrm{out})}\right\rangle &= 1.120 + 0.170i,\end{aligned} \tag{6.3.4}$$

in units of μ_N. Following the definition (6.2.1) and (6.2.2), we evaluate the magnetic moments and the uncertainties

$$\begin{aligned}\mu_{n^*} &= -0.08 \pm 0.23,\\ \mu_{p^*} &= 1.12 \pm 0.17,\end{aligned} \tag{6.3.5}$$

in units of μ_N. We have checked the channel dependence, and find, as expected, that our magnetic moments do not depend on the choice of the channel of the amplitudes (the deviation is less than 1%), since we can eliminate the non-resonant contributions on the top of the pole.

Next we calculate the magnetic moment $\mu(\sqrt{s})$ on the real axis, where $\mu(\sqrt{s})$ is given by the ratio of the scattering amplitudes $N = -i\tilde{t}_{ij}(\sqrt{s})$ and $D = -\frac{\partial}{\partial\sqrt{s}}t_{ij}(\sqrt{s})$. To avoid the contaminations from the background contribution, we use the external channel which strongly couples to the N^* resonance. In the present case, it is the $K\Sigma$ channel as we have already discussed in the previous section.

In Fig. 6.6, we plot the scattering amplitudes N and D for the $K\Sigma \to K\Sigma$ channel with $I = 1/2$ in the different charge states. Notice that the amplitudes D do not contain the electromagnetic interaction, and therefore, the D amplitudes for $Q = 0$ and $Q = 1$ are the same when isospin violation is neglected. On the other hand, the amplitudes N are different from each other due to the photon couplings. It is worth noting that $N(Q = 0)$ and $N(Q = 1)$ have opposite signs and these signs together with D determines the sign of the magnetic moments. We evaluate the ratio,

$$\mu = \frac{-i\tilde{t}_{ij}(\sqrt{s})}{-\frac{\partial}{\partial\sqrt{s}}t_{ij}(\sqrt{s})}, \tag{6.3.6}$$

whose real and imaginary parts are plotted in the bottom of Fig. 6.6. Finally we determine our value of the magnetic moments of the resonance calculated on the real axis as

$$\begin{aligned}\mu_{n^*} &= [(-0.265 \pm 0.009) + (-0.443 \pm 0.065)i]\mu_N,\\ \mu_{p^*} &= [(1.267 \pm 0.016) + (0.455 \pm 0.014)i]\mu_N,\end{aligned} \tag{6.3.7}$$

with theoretical errors. The way to determine the mean value and errors is explained below.

If there were no background (non-resonant) contributions, for both N and D, the extreme values of the real parts and zero of the imaginary parts (we shall refer to there points as "resonance points") would take place at the same value $\sqrt{s} = M_{N^*}$. In this ideal case, the ratio N/D is a real number. However, in the actual calculations. As shown in Eq. (6.2.21), this imaginary part is considered to be the background contamination. Therefore, we use

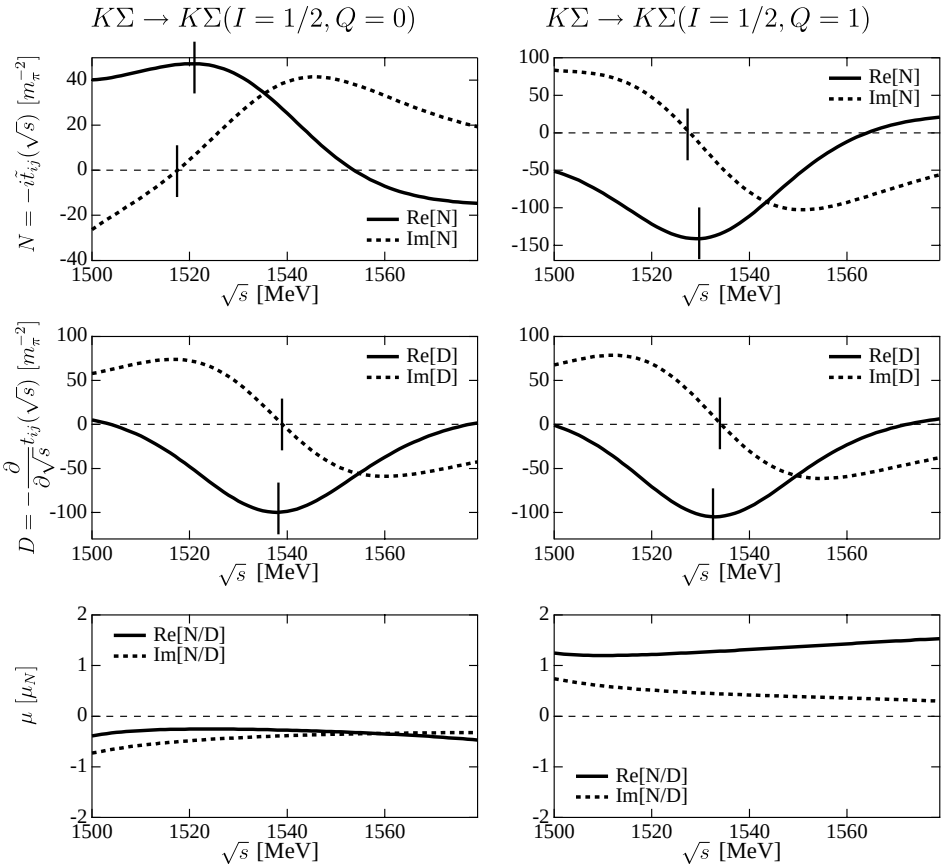

Figure 6.6: Scattering amplitudes and the magnetic moments on the real axis. We plot the real and imaginary parts of the $K\Sigma \to K\Sigma$ amplitudes $N = -i\tilde{t}_{ij}(\sqrt{s})$ and $D = -\frac{\partial}{\partial\sqrt{s}} t_{ij}(\sqrt{s})$, in $Q = 0$ and $Q = 1$. Solid bars represent the position $\sqrt{s} = M_R$, expected by the Breit-Wigner form. The magnetic moments $\mathrm{Re}[N/D]$ and $\mathrm{Im}[N/D]$ are calculated in units of the nuclear magneton.

the real part of the ratio $\mathrm{Re}[N/D]$ as the mean value, and estimate the size of theoretical error as the absolute value of the imaginary part of the ratio $\mathrm{Im}[N/D]$. In addition, the energy corresponding to the resonance points are not completely at the same value and deviate slightly, especially in $Q = 0$. Therefore, we rely upon the resonance points for D, which contains the derivative so expected to have much pure information, and evaluate the magnetic moments at these two points, regarding the deviations from the mean value as theoretical error, too.

The absolute values of Eq. (6.3.7) do not differ very much from the results (6.3.4). This is because we adopt the $K\Sigma$ channel, where $|g_i|^2$ is the largest and the background contribution is expected to be small. When we choose the other channels to evaluate the magnetic moments, the difference from the results (6.3.4) becomes larger, due to the large background effects (second and third lines of Eq. (6.2.21)).

Finally we summarize the results in Table 6.2. Combining the results in the complex plane

Table 6.2: The magnetic moments of the $N(1535)$ resonance in units of the nuclear magneton.

	n^*	p^*
μ (complex plane)	-0.08 ± 0.23	1.12 ± 0.17
μ (real axis)	-0.26 ± 0.44	1.27 ± 0.46

and on the real axis, we show our final result of the magnetic moments as

$$\mu_{n^*(1535)} = -0.25\mu_N, \quad \mu_{p^*(1535)} = 1.1\mu_N, \tag{6.3.8}$$

where we adopt the signs from the results on the real axis, and absolute values from the results in the complex plane. In next section, we discuss these results in detail.

6.4 Discussions

First we discuss the SU(3) relation by comparing the present results with the magnetic moment of $\Lambda(1670)$ obtained in the same framework [588]. Then we decompose the magnetic moment into the various components in order to understand the origin of the obtained values. Then we discuss the magnetic moments in the quark model and chiral doublet model, in comparison with the present results.

6.4.1 The SU(3) relation

In Ref. [588], the magnetic moments of $\Lambda(1670)$ are calculated in the chiral unitary model;

$$\mu_{\Lambda^*(1670)} = -0.29\mu_N. \tag{6.4.1}$$

The $\Lambda(1670)$ and $N(1535)$ have $J^P = 1/2^-$ and similar masses, so that they have been considered to be members of the SU(3) octet. If the SU(3) symmetry is exact, the magnetic moments of the octet should satisfy the Coleman-Glashow relations in Eq. (6.2.11), which tell us that

$$\mu_{n^*} = 2\mu_{\Lambda^*}. \tag{6.4.2}$$

In the present calculation $\mu_{n^*} \sim -0.08\mu_N$, the signs of the magnetic moments are consistent, although the absolute values do not satisfy the relation.

The SU(3) relation is discussed more clearly by looking at the SU(3) decomposition of the resonance states in terms of the coupling strengths g_i. The coupling strengths in the SU(3) basis are obtained by a unitary transformation using SU(3) Clebsh-Gordan coefficients [519]. In Table 6.3, $|g_i|^2$ in SU(3) basis are shown, where we observe that for both $N(1535)$ and $\Lambda(1670)$, octet component are dominant. This fact explains qualitative agreement of the relation between μ_{n^*} and μ_{Λ^*} in the chiral unitary model. Deviation from the relation comes from the large mixture of the singlet component in $\Lambda(1670)$ and SU(3) breaking effects.

Table 6.3: Coupling strengths $|g_i|^2$ of $N(1535)$ and $\Lambda(1670)$ in SU(3) basis. Values for $\Lambda^*(1670)$ are taken from Ref. [519]

representation	**1**	$\mathbf{8}_s$	$\mathbf{8}_a$	**10**	$\overline{\mathbf{10}}$	**27**
$n^*(1535)$	-	5.2	6.2	0.17	-	0.58
$\Lambda^*(1670)$	4.0	2.3	7.3	-	-	0.16

6.4.2 Isospin decomposition

For later discussions, we decompose the magnetic moments in Eq. (6.3.8) into isoscalar (μ_S) and isovector (μ_V) components. These moments are defined by

$$\mu_{\substack{S\\V}} = \frac{1}{2}(\mu_p \pm \mu_n).$$

In units of nuclear magneton $\mu_N = e/2M_N$, these values are

$$\mu_S = 0.52\mu_N, \quad \mu_V = 0.60\mu_N, \tag{6.4.3}$$

The isoscalar magnetic moment of $N(1535)$ is similar to that of the ground state nucleon $N(939)$, but the isovector one is much smaller than that of the nucleon $\mu_V(939) = 2.35\mu_N$.

More quantitatively, it is considered to express these values in units of resonance magneton $\mu_{N^*} \equiv e/2M_{N^*}$ with $M_{N^*} = 1535$ MeV, and extract the anomalous magnetic moments κ in units of μ_{N^*}. The results are

$$\mu_S(1535) = 0.85\mu_{N^*}, \quad \mu_V(1535) = 0.98\mu_{N^*}, \tag{6.4.4}$$

and

$$\kappa_S(1535) = 0.35\mu_{N^*}, \quad \kappa_V(1535) = 0.48\mu_{N^*}.$$

These numbers may be compared with those of the nucleon (in units of nuclear magneton):

$$\kappa_S(939) = -0.06\mu_N, \quad \kappa_V(939) = 1.85\mu_N.$$

Hence the strong isovector dominance as in the $N(939)$ magnetic moments is not realized in $N(1535)$. The origin of the isoscalar component in $N(1535)$ will be discussed below.

6.4.3 Decomposition into various components

In this subsection, we decompose the magnetic moments into various terms in order to understand qualitatively their origins. First we decompose the amplitude into the contributions from the term in Fig. 6.3 (a) (contact vertex) and those from Fig. 6.3 (b) (photon attached to baryon propagator). The total result is a linear combination of the two components as shown in Eq. (6.2.13). In Fig. 6.7, we show the amplitudes corresponding to (a) and (b) terms for $Q = 0$ and $Q = 1$. We see that the contribution from (a) is smaller in magnitude than (b), and that the contributions of (a) and (b) have opposite (same) signs for $Q = 0$ ($Q = 1$).

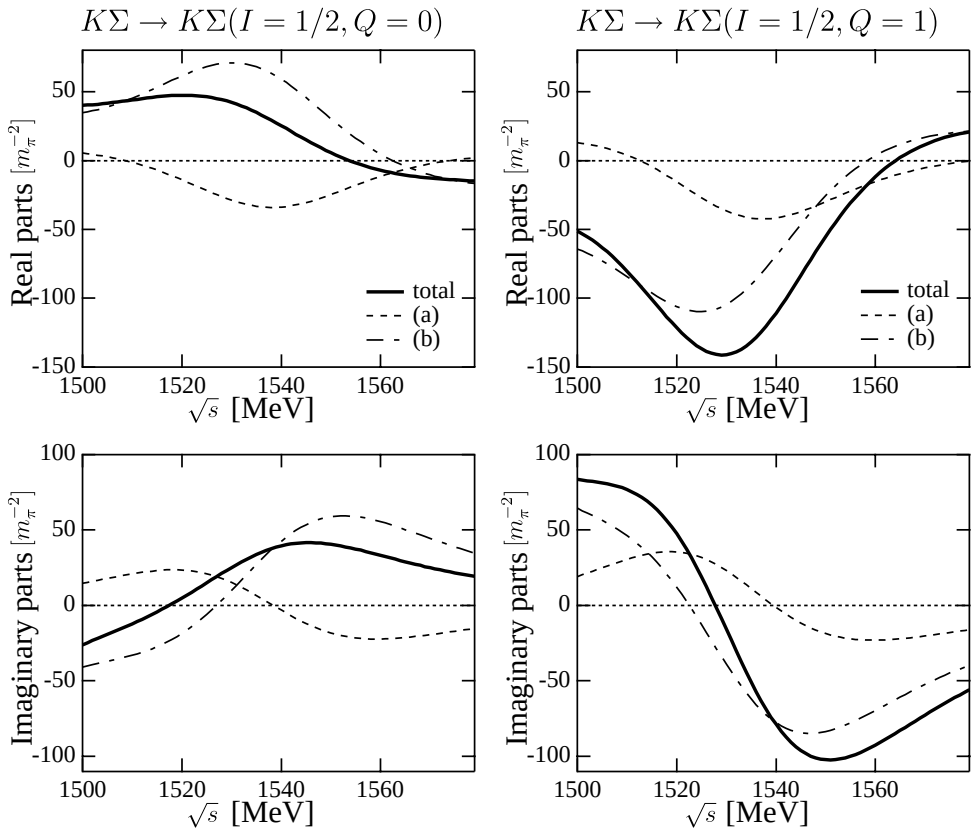

Figure 6.7: Real and imaginary parts of the $K\Sigma \to K\Sigma$ amplitudes $-i\tilde{t}_{ij}^{(a)}$, $-i\tilde{t}_{ij}^{(b)}$ and $-i\tilde{t}_{ij} = -i\tilde{t}_{ij}^{(a)} - i\tilde{t}_{ij}^{(b)}$ (dashed, dash-dotted and solid lines) in $Q = 0$ and $Q = 1$.

Therefore, there is a cancellation between them for $Q = 0$ in the total value, while for $Q = 1$ two terms are added with the same sign. This explains partly smaller magnetic moments of $Q = 0$ than that of $Q = 1$. More quantitatively, the results in the complex plane are given as

$$\begin{aligned} \mu_{n^*}^{(a)} &\sim (0.395 - 0.016i)\mu_N, \quad \mu_{n^*}^{(b)} \sim (-0.479 - 0.217i)\mu_N, \\ \mu_{p^*}^{(a)} &\sim (0.476 - 0.193i)\mu_N, \quad \mu_{p^*}^{(b)} \sim (0.644 + 0.363i)\mu_N, \end{aligned} \tag{6.4.5}$$

where $\mu_{n^*,p^*} = \mu_{n^*,p^*}^{(a)} + \mu_{n^*,p^*}^{(b)}$. As compared with Eq. (6.4.3), these numbers imply that the term $\mu^{(a)}$ is dominated by the isoscalar piece, while the term $\mu^{(b)}$ by the isovector piece. The nonegligible values of $\mu^{(a)}$ is the origin to weaken isovector dominance of the $N(1535)$ magnetic moments.

Let us now consider the the piece $\mu^{(b)}$ and its isovector dominance. As shown in Fig. 6.3 (b), $\mu^{(b)}$ is given by a sum of the diagrams where the photon couples to a ground state baryon. In this case, we can draw a naive picture where the resonance magnetic moment can be written as a sum of the magnetic moments of the ground state baryons weighted by their probabilities in the resonance wave function. In Ref [627], considering $N(1535)$ as a quasi-bound state of $K\Sigma$, they decomposed the $K\Sigma$ isospin state into physical states by the

Clebsh-Gordan coefficients, and evaluate the magnetic moments of the ground state baryon. Here we extend this estimation to sum up all the channels, multiplying $|g_i|^2$ as weight. First, we define the magnetic moments of the isospin states, using the Clebsh-Gordan coefficients and the magnetic moments of the ground states;

$$\begin{aligned}
\mu_{\pi N}(Q=0) &= \frac{1}{3}\mu_n + \frac{2}{3}\mu_p \sim 1.22\mu_N, \\
\mu_{\eta N}(Q=0) &= \mu_n \sim -1.91\mu_N, \\
\mu_{K\Lambda}(Q=0) &= \mu_\Lambda \sim -0.613\mu_N, \\
\mu_{K\Sigma}(Q=0) &= \frac{1}{3}\mu_{\Sigma^0} + \frac{2}{3}\mu_{\Sigma^-} \sim -0.557\mu_N, \\
\mu_{\pi N}(Q=1) &= \frac{2}{3}\mu_n + \frac{1}{3}\mu_p \sim -0.343\mu_N, \\
\mu_{\eta N}(Q=1) &= \mu_p \sim 2.79\mu_N, \\
\mu_{K\Lambda}(Q=1) &= \mu_\Lambda \sim -0.613\mu_N, \\
\mu_{K\Sigma}(Q=1) &= \frac{1}{3}\mu_{\Sigma^0} + \frac{2}{3}\mu_{\Sigma^+} \sim 1.86\mu_N.
\end{aligned} \tag{6.4.6}$$

Multiplying the weight $|g_i|^2$ in Table 6.1, we calculate

$$\mu_{N^*} = \frac{|g_{\pi N}|^2}{\sum_j |g_j|^2}\mu_{\pi N} + \frac{|g_{\eta N}|^2}{\sum_j |g_j|^2}\mu_{\eta N} + \frac{|g_{K\Lambda}|^2}{\sum_j |g_j|^2}\mu_{K\Lambda} + \frac{|g_{K\Sigma}|^2}{\sum_j |g_j|^2}\mu_{K\Sigma} \quad . \tag{6.4.7}$$

The results are

$$\mu_{n^*} \sim -0.74\mu_N, \quad \mu_{p^*} \sim 1.55\mu_N,$$

which are similar values with those obtained in Ref. [627] ($\mu_{n^*} \sim -0.56\mu_N$ and $\mu_{p^*} \sim 1.86\mu_N$), because in Eq. (6.4.7) the $K\Sigma$ component ($|g_{K\Sigma}|^2$) dominates the $N(1535)$ resonance (~ 60 %). Naively, it is expected that this estimation corresponds to the contribution from $-i\tilde{t}_{ij}^{(b)}$, where the magnetic moments of the ground states are summed.

6.4.4 Comparison with quark model

Here we discuss the present results in comparison with the quark model results. The details how to compute the resonance magnetic moments have been presented previously [627], and therefore, here we show some relevant points. In the quark model, the wave function of $N(1535)$ is given as a superposition of two spin ($s = 1/2$ and $3/2$) states in the $l = 1$ 70-dimensional representation of SU(6):

$$|N(1535)\rangle = \cos\theta|s = 1/2\rangle + \sin\theta|s = 3/2\rangle, \tag{6.4.8}$$

where θ is a mixing angle of the two states. Actually, the spin $s = 1/2, 3/2$ states are coupled with the orbital angular momentum $l = 1$ to yield $j = s + l = 1/2$. The magnetic moment operator is a sum of spin and orbital angular momenta of three quarks,

$$\mu = \frac{1}{2m}\sum_{i=1,2,3}\Big(\sigma_3(i) + l_3(i)\Big). \tag{6.4.9}$$

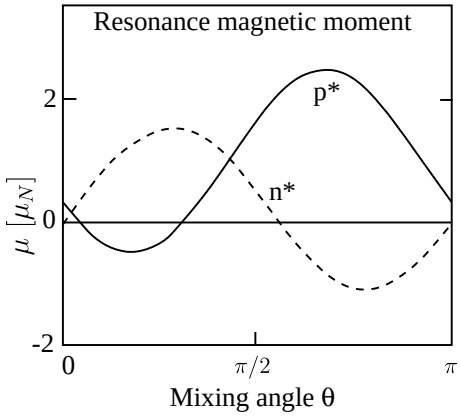

Figure 6.8: Magnetic moments as a function of the mixing angle θ in units of the nuclear magneton.

By taking a matrix element between the quark model state (6.4.8), we obtain the magnetic moment as a function of the mixing angle θ.

The result is presented in Fig. 6.8. As reported in Ref. [627], the mixing angle $\theta \sim 150 \sim -30$ degrees of the Isgur-Karl quark model [329] yields the values

$$\mu_{n^*} = -1.2\mu_N, \quad \mu_{p^*} = 1.9\mu_N. \tag{6.4.10}$$

Although these numbers differ quantitatively from those in the chiral unitary model, they look similar qualitatively. In fact, it is interesting to observe that this happens only in the vicinity of the mixing angle $\theta \sim 150$ degree. The similarity between the predictions in the quark model and the chiral unitary model was also reported for the axial coupling constant of N^*, or equivalently the $\pi N^* N^*$ coupling constant (due to the Goldberger-Treiman relation) [584].

6.4.5 Magnetic moments in the chiral doublet model

In this section, we present yet another description for magnetic moments when the resonance of negative parity is regarded as a chiral partner of the ground state nucleon in linear representations of chiral symmetry. In addition to phenomenological aspects, such a point of view may shed a light on the properties of spontaneous breaking of chiral symmetry. The theoretical scheme for positive and negative parity nucleons has been discussed in detail in Ref. [609, 610], and here we follow the essence of their description. The relevant point is that the chirality structure of the electromagnetic coupling; the vector coupling is of chirality even, while the tensor (anomalous magnetic) coupling is of chirality odd:

$$\begin{aligned}\mathcal{L}_{\gamma NN} =& -e\bar{N}\left(\gamma_\mu Q + i\kappa\frac{\sigma_{\mu\nu}q^\nu}{2M_P}\right)NA^\mu \\ =& -e\left(\bar{N}_l\gamma_\mu Q N_l + \bar{N}_r\gamma_\mu Q N_r\right)A^\mu - ie\left(\bar{N}_l\frac{\sigma_{\mu\nu}q_\nu}{2M_P}\kappa N_r + \bar{N}_r\frac{\sigma_{\mu\nu}q_\nu}{2M_P}\kappa N_l\right)A^\mu,\end{aligned} \tag{6.4.11}$$

with the charge of the nucleons Q and the anomalous magnetic moments $\kappa = \kappa_S + \kappa_V \tau_3$. The proton mass M_p is just used for the unit of the nuclear magneton. The right and left handed components of the nucleon is defined by $N_{r,l} = \frac{1\pm\gamma_5}{2} N$.

In the spirit of the theory of chiral symmetry, the electromagnetic coupling is regarded as a part of the chiral invariant coupling with right and left chiral fields. In Eq. (6.4.11) the vector term preserves chiral symmetry, while the tensor (anomalous) term does not appear so. In order for the latter to be chirally symmetric, it should contain the chiral field $U_5 = \sigma + i\vec{\tau}\cdot\vec{\pi}\gamma_5$. When chiral symmetry is broken spontaneously, σ takes a finite expectation value $\langle\sigma\rangle$, which survives the tensor term.

Another interesting possibility is to construct a chiral invariant tensor term in the mirror model for positive and negative parity nucleons [609, 610], where the basis of the chiral symmetry does not coincides to the physical basis. Denoting the two chiral basis fields as N_1 and N_2, the tensor coupling term takes on the form

$$\mathcal{L}^{\rm mirror}_{\rm tensor} = -\frac{ieq^\nu A^\mu}{2M_P}\left(\bar{N}_1\sigma_{\mu\nu}\gamma_5\kappa N_2 + \bar{N}_2\sigma_{\mu\nu}\gamma_5\kappa N_1\right).$$

This is the lagrangian to the lowest order ($n = 0$) in powers of $\langle\sigma\rangle^n$ and is becoming a dominant term as chiral symmetry is getting restored, $\langle\sigma\rangle \to 0$. Note again that the proton mass M_P here is introduced only for the unit and has nothing to do with the spontaneously generated mass of nucleon in the linear sigma model. In the following discussion, we consider only this leading order term of $\mathcal{O}(\langle\sigma\rangle^0)$, in order to reduce the number of free parameters. Thus we consider the following Lagrangian for the photon-nucleons coupling:

$$\mathcal{L}^{\rm mirror}_{\gamma NN} = -e\left(\bar{N}_1\gamma_\mu Q N_1 + \bar{N}_2\gamma_\mu Q N_2 + \left(\bar{N}_1\Gamma_\mu N_2 + \bar{N}_1\Gamma_\mu N_2\right)\right)A^\mu$$

where we have used the notation $\Gamma_\mu = (ie\kappa/2M_P)\sigma_{\mu\nu}q^\nu$.

As discussed in Ref. [609, 610], the physical nucleon and $N(1535)$ fields are linear combinations of N_1 and N_2;

$$\begin{aligned} N(939) &= \cos\theta N_1 + \gamma_5 \sin\theta N_2, \\ N(1535) &= -\gamma_5 \sin\theta N_1 + \cos\theta N_2 \ , \end{aligned}$$

where θ is a mixing angle. In the physical basis, the coupling term takes on the form ($N_+ \equiv N(939), N_- \equiv N(1535)$):

$$\begin{aligned} \mathcal{L}^{\rm mirror}_{\gamma NN} =& -e\left(\bar{N}_+\gamma_\mu Q N_+ + \bar{N}_-\gamma_\mu Q N_-\right)A^\mu \\ &+ \sin 2\theta(\bar{N}_+\Gamma_\mu N_+ + \bar{N}_-\Gamma_\mu N_-)A^\mu \\ &- \cos 2\theta(\bar{N}_+\Gamma_\mu\gamma_5 N_- + \bar{N}_-\Gamma_\mu\gamma_5 N_+)A^\mu \ . \end{aligned}$$

We find that the anomalous magnetic moments of $N(939)$ and $N(1535)$ are the same in units of nuclear magneton; $\kappa_p = \kappa_{p^*}$, $\kappa_n = \kappa_{n^*}$. In the chiral unitary model, however, this is not the case. It is interesting to see the differences in the two kinds of the "chiral " models [633, 634].

Let us now briefly discuss the transition moments. Note that the transition term has the structure of $E1$ because of the parity. From the pion coupling strength of $N(1535)$ decay, the

mixing angle was estimated as $\theta \sim 6.3$ degree [609, 610, 608]. We can then use the proton and neutron magnetic moments to fix the κ's: $\kappa_S \sin 2\theta = -0.06$ and $\kappa_V \sin 2\theta = 1.85$. Using these numbers, we find for the transition moments: $\mu_{pp^*} = 8.42$ and $\mu_{nn^*} = -8.99$. The isovector dominance in these quantities is consistent with what is known from experiment, but the magnitudes of these numbers are too large as compared with experimental data, $|\mu_{pp^*}| \sim |\mu_{nn^*}| \sim 1$ in units of the nuclear magneton, as extracted from the helicity amplitudes $A^p_{1/2} \sim 95$, $A^n_{1/2} \sim -80$ in units of $10^{-3}\text{GeV}^{-1/2}$ [635, 636]. Phenomenologically the large transition magnetic moment due to the small mixing angle does not agree with date. In other words, the small transition magnetic moment known from experiment prefers to a large mixing angle, which is not consistent with the decay strength of $N(1535)$ to πN. In any event, magnetic moments of the nucleon as well as of its excited state provide useful information of chiral symmetry of baryons.

In summary, we have seen the new possibility for the introduction of the $N(1535)$ anomalous magnetic moments. In this model, the $N(1535)$ is represented as a chiral partner of the nucleon in the linear realization of chiral symmetry. This picture is quite different from the chiral unitary model, which is being discussed here. The chiral doublet model provides $\kappa_N = \kappa_{N^*}$ for the magnetic moments, which is not the case of the chiral unitary model. It is interesting to investigate such a difference of the magnetic moments obtained by the physically distinct models, in order to understand the structure of the $N(1535)$ well.

6.5 Observation of the N^* magnetic moment

In this section, we would like to discuss possibilities of the experimental observations of the N^* magnetic moments. The $N(1535)$ has the special feature that this resonance strongly couples to the ηN system, which is not seen in the other N^* resonances. Thus the η meson in the finial state may be regarded as a probe of $N(1535)$ in the intermediate state. In order to observe the $N(1535)$ magnetic moments, here we would like to calculate cross sections of the following two photon-emission processes; $\gamma N \to \gamma\eta N$ and $\pi^- p \to \gamma\eta n$, and we investigate sensitivity of their cross sections to the value of the magnetic moments of N^*. Such processes that two-boson emission on nucleon target are discussed in Ref. [610, 637] to observe the sign of the $\pi N^* N^*$ coupling. In the present work, we follow their method to calculate the cross sections of the above processes.

In the calculations of the cross sections, we use the Lagrangian formulation for N^*, where the N^* is described as a well-defined field and its propagator is assumed to be the Breit-Wigner form with the mass $M_{N^*} = 1535$ MeV and the width $\Gamma_{N^*} = 150$ MeV. The Lagrangians used in the present calculations are shown in Appendix B.2.

Now we assume the N^* dominance hypothesis in the η-N system near the threshold region, that is, the η meson can couple only to the N and N^* transition, and the other resonances do not couple to the η meson. It is shown in Ref. [610] that this hypothesis reproduces the $N(1535)$ resonance well in the $\pi N \to \eta N$ process. Then the relevant diagrams for these processes are shown in the Fig. 6.9. The diagrams a and b are used only for the pion-induced process. Since we consider the photon-eta production processes in the energies close to the threshold, the final photon and eta meson have small energies and, therefore, the dominant

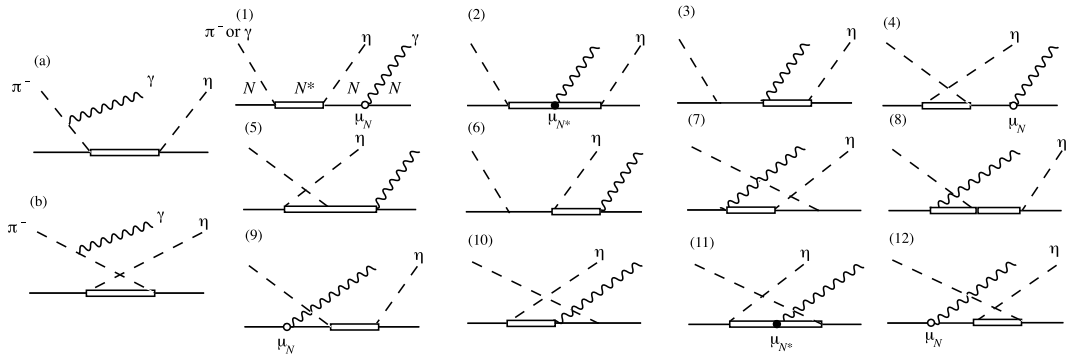

Figure 6.9: The relevant diagrams for the processes $\gamma N \to \gamma\eta N$ and $\pi^- p \to \gamma\eta n$. The diagram 0 is only for the pion induced process. The initial boson is ether photon or pion. The solid and double-solid lines denote N and N^*, respectively. The dotted and wavy lines in the final state are the emitted photon and eta meson, respectively.

contributions come from the diagrams a, 1, 2, 9 as a result of their small energy denominators. The diagram 2 is the one in which the magnetic moment of N^* appears, and we expect that the interference effects of this diagram with the other dominant diagrams is sensitive to the value of the N^* magnetic moments.

The differential cross section of the photon-eta production process is given as

$$d\sigma = \frac{2M_N}{4\sqrt{(p_i \cdot k_i)^2 - M_N^2 m_{IB}^2}} \frac{1}{2}\frac{1}{2} \sum_{\substack{\text{spin} \\ \text{pol.}}} |\mathcal{T}_{fi}|^2 d\Phi \ , \tag{6.5.1}$$

where the summation is taken over the spin of the initial and final nucleons and the polarization of the final (and initial) photon, and the factors in front of the summation are for taking averages of the spin and polarization in the final state. The mass m_{IB} denotes the mass of the initial boson, photon or pion in the present case. The phase space of the three-particle state is given by

$$d\Phi = (2\pi)^4 \delta(p_i + k_i - p_f - k_\gamma - k_\eta) \frac{d^3\vec{k}_\gamma}{(2\pi)^3 2E_\pi} \frac{d^3\vec{k}_\eta}{(2\pi)^3 2E_\eta} \frac{2M_N d^3\vec{p}_f}{(2\pi)^3 2E_f}, \tag{6.5.2}$$

where $k_\gamma = (E_\gamma, \vec{k}_\gamma)$, $k_\eta = (E_\eta, \vec{k}_\eta)$ and $p_f = (E_f, \vec{p}_f)$ are momenta for the finial photon, eta and nucleon, respectively. In the center of mass frame, Eq. (6.5.2) is written as

$$d\Phi = \frac{M_N}{4(2\pi)^5} dE_\gamma dE_f d\alpha d(\cos\beta) d\gamma.$$

Here α, β, γ are the Eular angles, which specify the plane where the three momenta in the final state lie. The normalizations of the state and wave function for nucleon are

$$\bar{u}^{(\alpha)}(p) u^{(\beta)}(p) = \delta^{\alpha\beta}, \quad \langle p | p' \rangle = \frac{E}{M_N} (2\pi)^3 \delta^3(\vec{p} - \vec{p}').$$

In the calculations of the cross sections, we perform the integral over the three-body phase space with the Monte Carlo method. The number of the integration points in the present

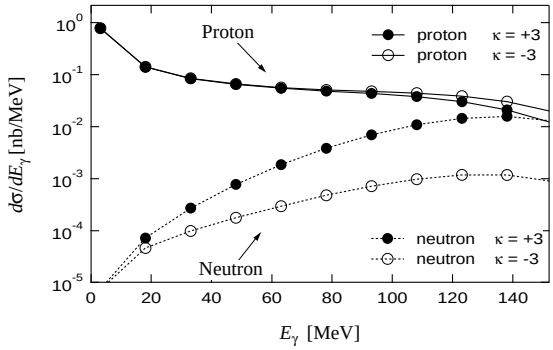

Figure 6.10: Energy spectra of the emitted photon in the photon-induced process. The energy of the initial photon is 1000 MeV. The solid and dotted lines denote the proton and neutron targets, respectively. The anomalous magnetic moments of p^* and n^* are assumed to $+3$ (black circle) or -3 (white circle) in units of nuclear magneton.

calculations are taken larger than 10,000, which may be enough to converge the Monte Carlo integral. The details of the Monte Carlo method for the three-body final state are discussed in Ref. [610, 637].

Shown in Fig. 6.10 are the energy spectra of the emitted photon in the photon-induced processes with the proton and neutron targets; $\gamma N \to \gamma\eta N$. In order to see the sensitivity of the effect of the magnetic couplings of N^* to the cross sections, the anomalous magnetic moments for the nucleon resonances are assumed to be $+3$ or -3 in units of nuclear magneton, although the predicted values by the present work are much smaller.

In the case of the proton target, where we investigate the magnetic moment of p^*, the resonance magnetic moment is not sensitive to the energy spectrum of the emitted photon, as shown in Fig. 6.10. In order to see how large contribution is given by the diagram 2, in which the N^* magnetic moment is involved, we show the energy spectra calculated with each dominant diagram of Fig. 6.9. In Fig. 6.11, it is seen that the energy spectrum for the proton target case is dominated by the contribution from the diagram 9 and that the diagram 2 is less important in these energies. Therefore the $\gamma p \to \gamma\eta p$ is not appropriate process to observe the p^* magnetic moment. The diagram 9 corresponds to the bremsstrahlung of the initial proton. In fact, the bremsstrahlung contribution becomes larger with the faster charged particle and the softer emitted photon. In addition, in the case of the charged particle proton, the electric coupling of the proton to the photon gives larger contributions than the magnetic one at low energies of the emitted photon, since the magnetic coupling linearly depends on the photon momentum and, hence, is suppressed in energies near the threshold.

On the other hand, in the case of the neutron target, the sensitivity of the magnetic moment is seen in the higher energies of the spectra as a result of the interference effects. Here we would have chance to observe the magnetic moment of n^*, although the cross sections are quite small and the all participants in this reaction are neutral particles. As shown in Fig. 6.11, the diagram 9 is less dominant than the proton target case, since there are no electric couplings for the neutron target case. Rather than the amount of the cross section,

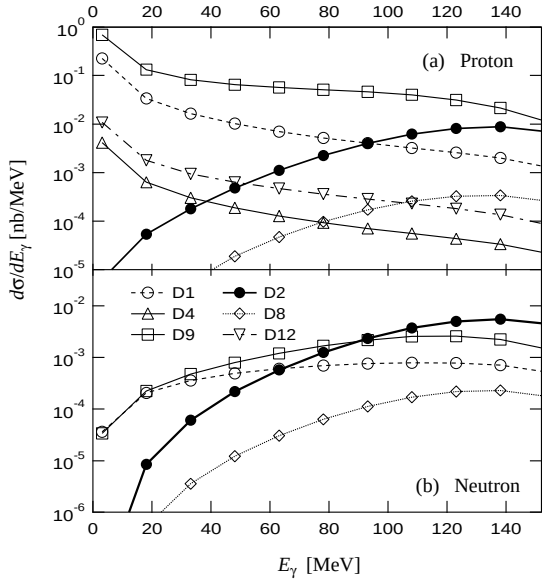

Figure 6.11: Separated contributions for the dominant diagrams to the energy spectra in the photon-induced process with the initial photon energy $E_i = 1000$ MeV. The upper panel (a) is for the proton target case. The lower panel (b) is the same for the neutron target case. The anomalous magnetic moments of p^* and n^* are $+3\mu_N$. The lines with black circles, open circles, triangles, diamonds, squares and down-triangles denote the contributions from the diagrams 1, 2, 4, 8, 9 and 12, respectively.

however, distinct signals of the dependence of the magnetic moments of N^*, such as position of peak, are not seen in the energy spectra of the emitted photon.

Next we calculate the angular distributions of the emitted photon, which is expected to be a better example to see the interference effects. In the calculations of the angular distributions, we perform the integration with respect to the final photon energy from 80 MeV, since we want to see the interference effects of the diagram 2 to the others and the diagram 2 gives dominant contributions at photon energies larger than 80 MeV as seen in Fig. 6.11. Shown in Fig. 6.12 are the calculated angular distributions in terms of the angle θ between the incident and final photons. Here we find the distinct angular dependences in the case of the neutron target, which would be observed. We also plot in Fig. 6.12(b) the angular distributions with the N^* magnetic moments obtained by the chiral unitary model and the quark model. It might be difficult, however, to distinguish these two model in experiment. We show in Fig. 6.13 the separated contributions to the angular distributions to the emitted photon. As seen in the figure, the diagram 2 becomes the dominant diagram in the case of the neutron target, while, in the proton target case, the diagram 9 is still the most dominant diagram.

Finally we discuss the pion-induced process briefly. As discussed before, in the case of neutron, the value of the n^* magnetic moment is sensitive to the cross sections, since the magnetic contributions is relatively enhanced due to the absence of the electric coupling. Thus, we would expect that the $\pi^- p \to \gamma\eta n$ process would be good to observe the mag-

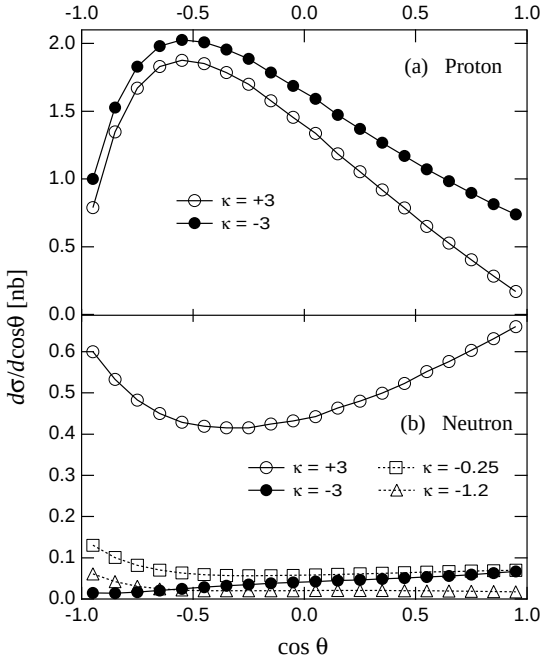

Figure 6.12: Angular distributions of the emitted photon in the photo-induced process with the initial photon energy 1000 MeV. The integration with respect to the emitted energy is performed from 80 MeV to the threshold. The upper panel (a) is for the proton target, and the lower panel (b) is the same for the neutron target. The anomalous magnetic moments of N^* is assumed to $+3$ (open circle) or -3 (black circle) in units of nuclear magneton. In the case of the neutron target, the plots with the N^* magnetic moments obtained in the chiral unitary model ($\mu^{(a)} = -0.25$) and in the quark model ($\mu^{(a)} = -1.2$) cases are shown by the lines with open squares and triangles. respectively.

netic moment of n^*. Unlike our expectation, however, in this case, we conclude that it is very difficult to extract the magnetic moments of N^*, since the diagrams a and 9 are the most dominant contributions to the cross sections, as shown in Fig. 6.14. These diagrams corresponds to the bremsstrahlung of the initial charged particles. Since the initial pion and proton have large momenta to create the eta meson at the final state, they emit the more photon than the slow intermediate n^*.

6.6 Summary

We have calculated the magnetic moments of the $N(1535)$ resonance using the chiral unitary model. We have obtained the magnetic moments of the resonances as $\mu_{n^*(1535)} \sim -0.25\mu_N$ and $\mu_{p^*(1535)} \sim +1.1\mu_N$. Compared with the results of Λ resonances in Ref. [588], the sign of the Coleman-Glashow relations (6.2.11), which comes from the SU(3) symmetry of octet, are satisfied among $\Lambda^*(1670)$ and $n^*(1535)$ in the chiral unitary model. This implies that

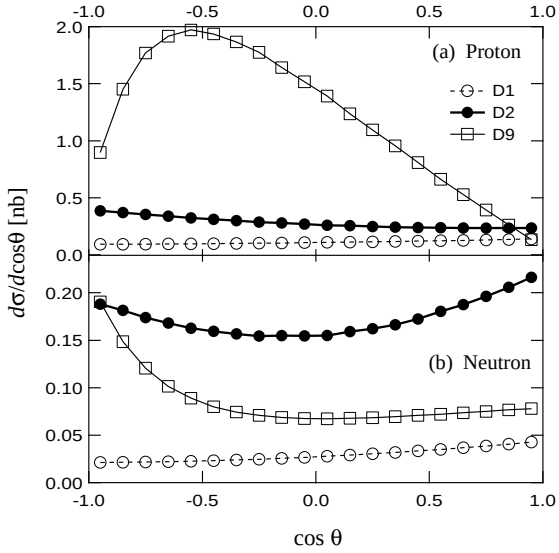

Figure 6.13: Separated contributions of the dominant diagrams to the angular distribution of the emitted photon in the photon-induced process. The integration with respect to the emitted energy is performed from 80 MeV to the threshold. The lines with the open circles, black circles and squares denotes the contributions of the diagrams 1, 2, and 9, respectively.

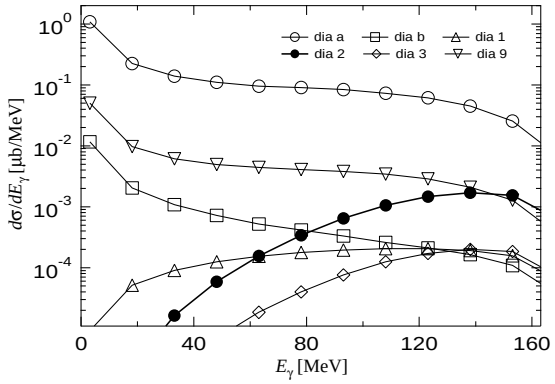

Figure 6.14: Separated contributions of the dominant diagrams to the energy spectrum of the emitted photon in the pion-induced process with the initial pion energy $E_\pi = 1000$ MeV. The lines with the open circles, squares, triangles, black circles, diamonds and down-triangles denote the contributions from the diagram a, b, 1, 2, 3 and 9, respectively.

$1/2^-$ resonances are the member of an SU(3) octet. The present results qualitatively agree with the results of the constituent quark model of Ref. [627]. However, the absolute values of these results are different, so the experimental measurement will bring the information of the structure of the baryon resonances. Finally we have computed reaction cross section in order to observe the resonance magnetic moments; $\gamma N \to \gamma\eta N$, $\pi^- p \to \gamma\eta n$. The difference in the magnetic moments is, however, not very much reflected in the bremsstrahlung processes.

Chapter 7

The coupling of $\bar{K}^*N$ to the $\Lambda(1520)$

We study the coupling of the $\Lambda(1520) \equiv \Lambda^*$ resonance to the $\bar{K}^*$ vector meson and nucleon. This coupling is not directly measured from the resonance decay, but is expected to be important in hyperon production reactions, in particular for the exotic Θ^+ production. We compute the coupling in two different schemes, one in the chiral unitary model where the Λ^* is dominated by the quasi-bound state of mesons and baryons, and the other in the quark model where the resonance is a p-wave excitation in the three valence quarks. Although it is possible to construct both models such that they reproduce the $\bar{K}N$ and $\pi\Sigma$ decays, there is a significant difference between the $\Lambda^*\bar{K}^*N$ couplings in the two models. In the chiral unitary model $|g_{\Lambda^*\bar{K}^*N}| \sim 1.5$, while in the quark model $|g_{\Lambda^*\bar{K}^*N}| \sim 10$. The difference of the results stems from the different structure of the Λ^* in both models, and hence, an experimental determination of this coupling would shed light on the nature of the resonance. This topic is reported in Ref. [14].

7.1 Introduction

In chapter 5, we have seen that the $\Lambda(1405)$ resonance is generated in s-wave $\bar{K}N$ scattering. An interesting feature of such a dynamically generated $\Lambda(1405)$ is that it is a superposition of two poles near the nominal mass region, one of which couples dominantly to the $\bar{K}N$ and the other to $\pi\Sigma$ state.

Recently, another Λ resonance, the $\Lambda(1520) \equiv \Lambda^*$ of $J^P = 3/2^-$, has been investigated in the chiral unitary models. In Refs. [561, 415], the resonance was described as a quasi-bound state of $\pi\Sigma(1385)$ and $K\Xi(1530)$ in s wave. In these studies, the identification of some baryon resonances with s-wave quasi-bound state of an octet meson and a decuplet baryon has been extensively studied. This approach is further extended in particular to the Λ^*, by including the d-wave channels of mesons and ground state baryons [638, 639, 640], leading to a successful description of existing data.

The $\Lambda^*\bar{K}^*N$ coupling is worth being studied. In the experimental data [641] and its analysis for Λ^* photoproduction [642], the important role of $\bar{K}^*$ vector meson was suggested, while a similar behavior was recently explained by means of the photo-K^* contact term [643]. Not much is known for the properties of the interaction with $\bar{K}^*$, which is expected to be

important in associated Λ^* and Θ^+ production from deuteron as observed recently by the LEPS collaboration [207]. As compared to the interactions with a kaon, we must rely much on models for the estimation of the $\bar{K}^*$ interaction, since there is no theoretical framework to introduce it such as chiral symmetry, nor experimental information on the decay of the Λ^* to $\bar{K}^*N$, which is kinematically forbidden.

In this chapter, we investigate exclusively the $\bar{K}^*$ coupling to the Λ^*, where the Λ^* is formed dominantly by the s-wave $\pi\Sigma(1385)$ quasi-bound state, which is supplemented by the $K\Xi(1530)$ state and the d-wave $\bar{K}N$ and $\pi\Sigma$ states. The result is then compared with that of the conventional quark model, where the Λ^* is described as a p-wave excitation of one of the three valence quarks. This comparison should be useful in testing the very different nature of the two descriptions, as we will discuss in detail.

In section 7.2, we describe how the $\Lambda^*\bar{K}^*N$ coupling is computed in the chiral unitary model for Λ^*. Numerical results and discussions are presented in section 7.3, where we compare the result of the chiral unitary model with the quark model predictions. The final section is devoted to summarize the present work.

7.2 Formulation

7.2.1 Structure of the amplitude

We consider an effective interaction Lagrangian [643] given by

$$\mathcal{L}_{\Lambda^*\bar{K}^*N} = \frac{g_{\Lambda^*\bar{K}^*N}}{M_{K^*}}\bar{\Lambda}^*_\mu\gamma_\nu(\partial^\mu K^{*\nu} - \partial^\nu K^{*\mu})N + \text{h.c.}\ , \tag{7.2.1}$$

where M_{K^*} is the mass of the vector K^* meson, h.c. denotes the hermitian conjugate, and $g_{\Lambda^*\bar{K}^*N}$ is the coupling constant. Because $J^P(\Lambda^*) = 3/2^-$, the coupling has two independent components. In terms of multipoles, they are E1 and M2, which are related to the two helicity amplitudes $A_{1/2}$ and $A_{3/2}$. In the E1 amplitude, the orbital angular momentum of the decaying channel of $\bar{K}^*N$ is s wave, while in M2, it is d wave. Here, we investigate the s-wave coupling which is the E1 amplitude in the chiral unitary model. We expect that the s-wave coupling dominates in the small three momentum $|\boldsymbol{k}|$ region, where $\boldsymbol{k}$ is the relative momentum of the (virtual) $\bar{K}^*$ and N. Assuming the interaction region of about 1 fm, the d-wave and hence the M2 component will become important for $|\boldsymbol{k}| > 400$ MeV.

Applying the non-relativistic reduction to Eq. (7.2.1), and picking up the s-wave component, we obtain the transition amplitude of $\bar{K}^*N \to \Lambda^*$ as

$$-it_{\Lambda^*\bar{K}^*N} = g_{\Lambda^*\bar{K}^*N}\boldsymbol{S}^\dagger\cdot\boldsymbol{\epsilon}\ , \tag{7.2.2}$$

Here $\boldsymbol{\epsilon}$ is the polarization vector of the $\bar{K}^*$ and $\boldsymbol{S}$ is the spin transition operator [605], which is defined by $\langle\, 3/2, m+\lambda\,|S^\dagger_\lambda|\,1/2, m\,\rangle = \mathcal{C}(\frac{1}{2}\ 1\ \frac{3}{2}; m, \lambda)$ where λ represents a spherical component ±1 or 0 and $\mathcal{C}(j_1\ j_2\ J; \mu_1, \mu_2)$ denotes the SU(2) Clebsch-Gordan coefficient for $\boldsymbol{J}(\mu_1+\mu_2) = \boldsymbol{j}_1(\mu_1) + \boldsymbol{j}_2(\mu_2)$.

In the chiral unitary model, the Λ^* is generated dynamically in the scattering of the $\pi\Sigma^*$ and $K\Xi^*$ channels in s wave and the $\bar{K}N$ and $\pi\Sigma$ channels in d wave [638, 639]. In order

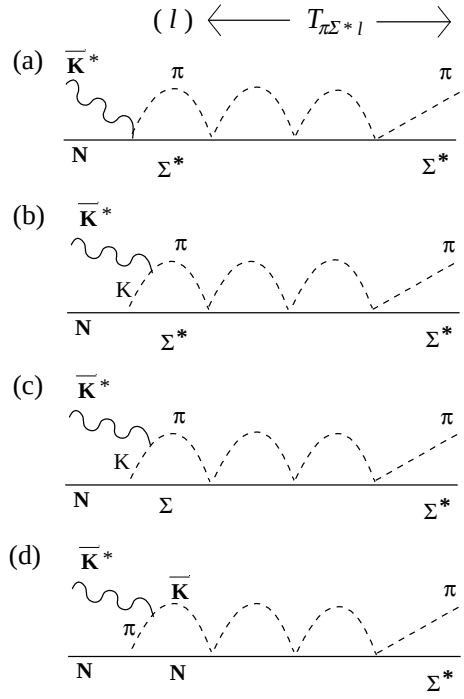

Figure 7.1: Diagrams for the microscopic mechanism of $\bar{K}^*N \to \Lambda^* \to \pi\Sigma^*$ calculated in the chiral unitary model.

to estimate the coupling of the Λ^* resonance to the $\bar{K}^*N$ channel, we follow the microscopic mechanism as illustrated in Fig. 7.1. In this case, the $\bar{K}^*N$ couples to the dynamically generated Λ^*, represented by the amplitude T in the figure, decaying into the $\pi\Sigma^*$ channel. Notice that the $K\Xi^*$ channel does not appear in the first intermediate loop, since there is no direct coupling from $\bar{K}^*N$ to $K\Xi^*$. Schematically, the process $\bar{K}^*N \to \Lambda^* \to \pi\Sigma(1385)$ can be expressed as

$$-it_{\rm ChU} = \sum_l (-iT_{\pi\Sigma^* l}) iG_l (-it_{l\bar{K}^*N}) \ , \tag{7.2.3}$$

where $T_{\pi\Sigma^* l}$ is $l \to \pi\Sigma^*$ amplitude obtained by the chiral unitary model [638, 639], G_l is the loop function of the intermediate state l, and $-it_{l\bar{K}^*N}$ is the amplitude of $\bar{K}^*N \to l$. As shown in Fig. 7.1, there are four types of transition amplitudes for $-it_{l\bar{K}^*N}$ with three different intermediate states $\pi\Sigma^*, \pi\Sigma$, and $\bar{K}N$.

Since we are considering first the s-wave coupling, the amplitude $-it_{l\bar{K}^*N}$ should be written as $-it_{l\bar{K}^*N} = g_{l\bar{K}^*N} \boldsymbol{S}^\dagger \cdot \boldsymbol{\epsilon}$, where $g_{l\bar{K}^*N}$ will be calculated later. We denote the total energy as $\sqrt{s}$, and consider the energy region close to the Λ^* pole $\sqrt{s} \sim M_{\Lambda^*}$ with M_{Λ^*} being the mass of the Λ^* resonance. In this region, the chiral unitary amplitude T_{ij} can be approximated by the Breit-Wigner propagator $T_{ij} \sim g_{\Lambda^* i} g_{\Lambda^* j}/(\sqrt{s} - M_{\Lambda^*})$ with coupling constants $g_{\Lambda^* i}$, where i stands for the channels coupling to Λ^*. Then we have

$$-it_{\rm ChU} \sim -ig_{\Lambda^*\pi\Sigma^*} \frac{i}{\sqrt{s} - M_{\Lambda^*}} \sum_l g_{\Lambda^* l} G_l g_{l\bar{K}^*N} \boldsymbol{S}^\dagger \cdot \boldsymbol{\epsilon} \ . \tag{7.2.4}$$

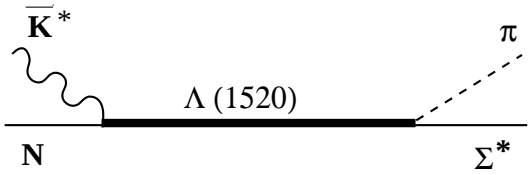

Figure 7.2: Diagram for the resonance dominance model of $\bar{K}^*N \to \Lambda^* \to \pi\Sigma^*$.

On the other hand, with the s-wave coupling Eq. (7.2.2), the resonance model for the amplitude $\bar{K}^*N \to \Lambda^* \to \pi\Sigma(1385)$ can be written as shown in Fig. 7.2,

$$-it_{\rm res} = -ig_{\Lambda^*\pi\Sigma^*}\frac{i}{\sqrt{s}-M_{\Lambda^*}}g_{\Lambda^*\bar{K}^*N}\boldsymbol{S}^\dagger\cdot\boldsymbol{\epsilon}\ ,$$

where $g_{\Lambda^*\bar{K}^*N}$ is the $\Lambda^*\bar{K}^*N$ coupling constant that we are interested in. Hence comparing this amplitude with Eq. (7.2.4), we extract the $\Lambda^*\bar{K}^*N$ coupling as

$$g_{\Lambda^*\bar{K}^*N} = \sum_l g_{\Lambda^* l}G_l g_{l\bar{K}^*N}\ . \tag{7.2.5}$$

In the previous study [639], the coupling constants $g_{\Lambda^* l}$ have been determined as

$$g_{\Lambda^*\pi\Sigma^*} = 0.91\ ,\quad g_{\Lambda^*\pi\Sigma} = -0.45\ ,\quad g_{\Lambda^*\bar{K}N} = -0.54\ , \tag{7.2.6}$$

which well reproduce the partial decay widths of the $\Lambda(1520)$ resonance to these channels. In the following, we evaluate $G_l g_{l\bar{K}^*N}$ by calculating the diagrams in Fig. 7.1 one by one.

7.2.2 Computation of loop diagrams

Let us first consider the diagrams (a) and (b) in Fig. 7.1. The amplitudes for these diagrams $-it^{(a)}$ and $-it^{(b)}$ are related to each other through the gauge condition

$$(-it^{(a)}_\mu - it^{(b)}_\mu)k^\mu = 0\ , \tag{7.2.7}$$

where $-it^{(i)} \equiv -it^{(i)}_\mu\epsilon^\mu$ and k^μ is the momentum of the $\bar{K}^*$. First we consider the diagram (b). Utilizing the interaction Lagrangians given in Appendix, the amplitude of, for instance, $\bar{K}^{*0}n \to \pi^+\Sigma^{*-}$ for the meson pole diagram (b) at tree level is written as

$$-it^{(b)}_{\pi^-\Sigma^{*+}\bar{K}^{*-}n} = \frac{1}{\sqrt{2}}ig\epsilon^\mu(2q_\mu - k_\mu)\frac{i}{(q-k)^2-m_K^2}\frac{1}{\sqrt{3}}\frac{g_A^*}{2f}\boldsymbol{S}^\dagger\cdot(\boldsymbol{q}-\boldsymbol{k})\ . \tag{7.2.8}$$

The momentum valuables in Eq. (7.2.8) are assigned as shown in Fig. 7.3, m_K is the mass of kaon, $g = -6.05$, $g_A^* = (D+F)\times 2.13$, $D+F = 1.26$, $f = f_\pi = 93$ MeV. In order to obtain the corresponding tree level amplitude for the contact diagram (a), $-it^{(a)}_{\pi^-\Sigma^{*+}\bar{K}^{*-}n}$, we first replace ϵ^μ by k^μ in Eq. (7.2.8), set $q^2 = m_\pi^2 = M_K^2$ assuming the SU(3) limit (this manipulation is only for the purpose of determining the contact term) and set $\boldsymbol{q} = \boldsymbol{0}$. Then, the contact term has to be

$$-it^{(a)}_{\pi^-\Sigma^{*+}\bar{K}^{*-}n} = \frac{g}{\sqrt{2}}\frac{g_A^*}{2f}\frac{1}{\sqrt{3}}\boldsymbol{S}^\dagger\cdot\boldsymbol{\epsilon}\ ,$$

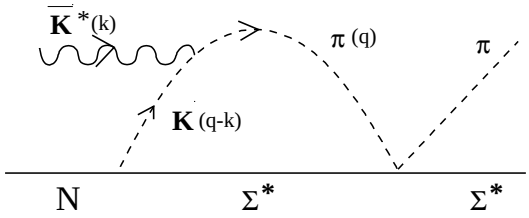

Figure 7.3: Momentum assignment for the diagram (b) in Fig. 7.1.

in order to satisfy Eq. (7.2.7).

We can repeat the same operation for other charge states. Writing the $\bar{K}^*N$ and $\pi\Sigma^*$ states in isospin basis (recalling that $|\, K^{*-}\,\rangle = -|\, 1/2, -1/2\,\rangle$ and $|\, \pi^+\,\rangle = -|\, 1, 1\,\rangle$ in our convention), we find

$$-it^{(a)}_{\pi\Sigma^*\bar{K}^*N} = \frac{g}{2}\frac{g_A^*}{2f}\boldsymbol{S}^\dagger\cdot\boldsymbol{\epsilon}\ , \tag{7.2.9}$$

after projecting over $I = 0$. Inserting Eq. (7.2.9) into Eq. (7.2.3), we can now write

$$-it^{(a)} = (-iT_{\pi\Sigma^*\pi\Sigma^*})iG_{\pi\Sigma^*}g_{\pi\Sigma^*\bar{K}^*N}\boldsymbol{S}^\dagger\cdot\boldsymbol{\epsilon}\ , \tag{7.2.10}$$

where $G_{\pi\Sigma^*}$ is the loop function involving the π and the Σ^*:

$$G_{\pi\Sigma^*}(\sqrt{s}) = i\int\frac{d^4q}{(2\pi)^4}\frac{1}{q^2 - m_\pi^2 + i\epsilon}\frac{1}{\sqrt{s} - q^0 - E_{\Sigma^*} + i\epsilon}\ ,$$

where $E_{\Sigma^*}(\boldsymbol{q}) = \sqrt{M_{\Sigma^*}^2 + \boldsymbol{q}^2}$ and the coupling constant is given by

$$g_{\pi\Sigma^*\bar{K}^*N} = \frac{1}{2}g\frac{g_A^*}{2f}\ . \tag{7.2.11}$$

On the other hand, we can also extract the s-wave component of the meson pole term from Eq. (7.2.8) after projecting over $I = 0$, and we find

$$-it^{(b)}_{l\bar{K}^*N} = g_{\pi\Sigma^*\bar{K}^*N}\frac{2}{3}\frac{\boldsymbol{q}^2}{(q-k)^2 - m_K^2}\boldsymbol{S}^\dagger\cdot\boldsymbol{\epsilon}\ , \tag{7.2.12}$$

where the variable $\boldsymbol{q}$ should be included in the loop function. Therefore, the amplitude for this process can be expressed similarly as in Eq. (7.2.10) but with the meson-baryon loop function $G_{\pi\Sigma^*}$ replaced by the loop function with an additional factor, which is defined by

$$\tilde{G}_{\pi\Sigma^*K}(\sqrt{s}, k) = i\int\frac{d^4q}{(2\pi)^4}\frac{\boldsymbol{q}^2}{(q-k)^2 - m_K^2 + i\epsilon}\frac{1}{q^2 - m_\pi^2 + i\epsilon}\frac{1}{\sqrt{s} - q^0 - E_{\Sigma^*} + i\epsilon}.$$

Finally, combining the contributions from (a) and (b), we obtain

$$-it^{(a)} - it^{(b)} = (-iT_{\pi\Sigma^*\pi\Sigma^*})i\left(G_{\pi\Sigma^*} + \frac{2}{3}\tilde{G}_{\pi\Sigma^*K}\right)g_{\pi\Sigma^*\bar{K}^*N}\boldsymbol{S}^\dagger\cdot\boldsymbol{\epsilon}\ .$$

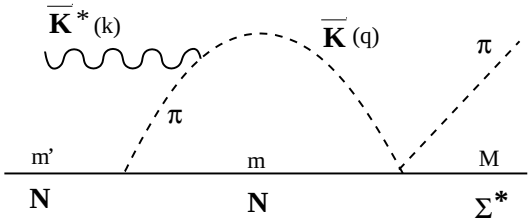

Figure 7.4: Momentum and spin indices assignment for the loop diagram in (d) in Fig. 7.1.

We now evaluate the amplitude for the diagram (c) and (d) in Fig. 7.1. The structure of the first loop can be found from Fig. 7.4. Since we need the d-wave projection of the meson pole term to balance the d-wave $\bar{K}N \to \pi\Sigma^*$ amplitude in the loop, we study the amplitude in some detail. Using the interaction Lagrangians given in the Appendix, the $I = 0$ component of the tree level amplitude for (d), for instance, is given by

$$-it^{(d)}_{\bar{K}N\bar{K}^*N} = -3ig\frac{D+F}{2f}\epsilon^\mu(2q_\mu - k_\mu)\frac{i}{(q-k)^2 - m_\pi^2}\boldsymbol{\sigma}\cdot(\boldsymbol{k}-\boldsymbol{q}) \ .$$

The spin structure takes the form $(\boldsymbol{\epsilon}\cdot\boldsymbol{q})(\boldsymbol{\sigma}\cdot\boldsymbol{q})$, neglecting $\boldsymbol{k}$ which is assumed to be small. Now, the d-wave structure obtained from $\sigma_i q_i \epsilon_j q_j \to \sigma_i\epsilon_j(q_iq_j - \boldsymbol{q}^2\delta_{ij}/3)$ will combine with the d-wave structure coming from the $\bar{K}N \to \pi\Sigma^*$ vertex to produce a scalar quantity after the loop integration is performed. We write

$$\sigma_i\epsilon_j(q_iq_j - \tfrac{1}{3}\boldsymbol{q}^2\delta_{ij}) = A\left[[\sigma\otimes\epsilon]^2_\mu \ Y_2(\hat{q})\right]^0_0 \ , \tag{7.2.13}$$

where A is a constant. This indicates that the two vector operators σ and ϵ combine to produce an operator of rank 2, which couples to the spherical harmonic $Y_2(\hat{q})$ to produce a scalar. The right hand side can be written as

$$A\sum_\mu(-1)^\mu[\sigma\otimes\epsilon]^2_\mu \ Y_{2,-\mu}(\hat{q}) = A\sum_{\mu,\alpha}(-1)^\mu Y_{2,-\mu}(\hat{q}) \ \mathcal{C}(1\ 1\ 2;\alpha,\mu-\alpha)\sigma_\alpha\epsilon_{\mu-\alpha} \ .$$

To find the value of A we take the matrix element of both sides of Eq. (7.2.13) between the states m and m' so that

$$\begin{aligned}&\langle m|\sigma_i\epsilon_j(q_iq_j - \tfrac{1}{3}|\boldsymbol{q}|^2\delta_{ij})|m'\rangle \\ =&A\sum_\mu(-1)^\mu \ Y_{2,-\mu}(\hat{q}) \ \epsilon_{\mu-m+m'}\mathcal{C}(1\ 1\ 2;m-m',\mu-m+m') \ \mathcal{C}(\tfrac{1}{2}\ 1\ \tfrac{1}{2};m',m-m') \ ,\end{aligned} \tag{7.2.14}$$

where we have used $\langle m|\sigma_\alpha|m'\rangle = \sqrt{3}\ \mathcal{C}(\frac{1}{2}\ 1\ \frac{1}{2};m',\alpha)$ with $m = m' + \alpha$. Considering specific values of m and m', we obtain

$$A = \sqrt{\frac{8\pi}{15}}\ \boldsymbol{q}^2 \ . \tag{7.2.15}$$

Following Ref. [638], we now include the $\bar{K}N \to \pi\Sigma^*$ vertex given by

$$-it_{\bar{K}N\to\pi\Sigma^*} = -i\beta_{\bar{K}N}\ \boldsymbol{q}^2\ \mathcal{C}(\tfrac{1}{2}\ 2\ \tfrac{3}{2};m,M-m)Y_{2,m-M}(\hat{q})(-1)^{M-m}\sqrt{4\pi} \ , \tag{7.2.16}$$

so that the total spin structure of the loop shown in Fig. 7.4 is essentially given by

$$J = \sum_m \int \frac{d\Omega_q}{4\pi} \langle m|\sigma_i \epsilon_j (q_i q_j - \tfrac{1}{3}\boldsymbol{q}^2 \delta_{ij})|m'\rangle \; \mathcal{C}(\tfrac{1}{2}\; 2\; \tfrac{3}{2}; m, M-m) Y_{2,m-M}(\hat{q}) (-1)^{M-m} \sqrt{4\pi} \; ,$$

where we perform an average over the angular dependence in the integration over the loop momentum q. Using Eqs. (7.2.14) and (7.2.15) this can be written as

$$\begin{aligned} J =& \sqrt{\frac{2}{3}} \; \boldsymbol{q}^2 \; (-1)^{1-M+m'} \; \epsilon_{m'-M} \\ & \times \sum_m \; \mathcal{C}(\tfrac{1}{2}\; 1\; \tfrac{1}{2}; m', m-m') \; \mathcal{C}(\tfrac{1}{2}\; 2\; \tfrac{3}{2}; m, M-m) \; \mathcal{C}(1\; 2\; 1; m-m', M-m) \; , \end{aligned}$$

where we have used the well known relations

$$\int \; d\Omega_q \; Y_{2,-\mu}(\hat{q}) \; Y_{2,m-M}(\hat{q}) = (-1)^{\mu} \delta_{\mu,m-M} \; ,$$

and

$$\mathcal{C}(1\; 1\; 2; m-m', m'-M) = (-1)^{1-m+m'} \sqrt{\tfrac{5}{3}} \; \mathcal{C}(1\; 2\; 1; m-m', M-m) \; .$$

The product of three Clebsch-Gordan coefficients is then combined into a single one with Racah coefficients, resulting in the identity

$$\begin{aligned} & \sum_m \; \mathcal{C}(\tfrac{1}{2}\; 1\; \tfrac{1}{2}; m', m-m') \; \mathcal{C}(\tfrac{1}{2}\; 2\; \tfrac{3}{2}; m, M-m) \; \mathcal{C}(1\; 2\; 1; m-m', M-m) \\ =& - \sqrt{\tfrac{1}{2}} \; \mathcal{C}(\tfrac{1}{2}\; 1\; \tfrac{3}{2}; m', M-m') \; , \end{aligned}$$

so that, we finally have

$$J = \frac{1}{\sqrt{3}} \; \boldsymbol{q}^2 \; \boldsymbol{S}^{\dagger} \cdot \boldsymbol{\epsilon} \; . \tag{7.2.17}$$

The above relation implies that for practical purposes we can replace in the first vertex $(\boldsymbol{\epsilon} \cdot \boldsymbol{q})(\boldsymbol{\sigma} \cdot \boldsymbol{q})$ by the simple form $\frac{1}{\sqrt{3}} \; \boldsymbol{q}^2 \; \boldsymbol{S}^{\dagger} \cdot \boldsymbol{\epsilon}$ and for the second vertex the factor $\beta_{\bar{K}N} \boldsymbol{q}^2$ and continue with the formalism exactly as in s-wave. Putting everything together, the amplitude for the process shown in Fig. 7.1 (d) can be written as

$$-it^{(d)} = (-iT_{\pi\Sigma^* \bar{K}N}) i \tilde{G}_{\bar{K}N\pi} \; g_{\bar{K}N\bar{K}^* N} \boldsymbol{S}^{\dagger} \cdot \boldsymbol{\epsilon} \; , \tag{7.2.18}$$

which has the same form as Eq. (7.2.11). In the above equation, we have defined

$$g_{\bar{K}N\bar{K}^* N} = \sqrt{3} g \frac{D+F}{2f} \; ,$$

and

$$\begin{aligned} \tilde{G}_{\bar{K}N\pi}(\sqrt{s}, k) =& i \int \frac{d^4 q}{(2\pi)^4} \; \frac{\boldsymbol{q}^2}{(q-k)^2 - m_\pi^2 + i\epsilon} \; \frac{\boldsymbol{q}^2}{q_{\rm on}^2} \\ & \times \frac{1}{q^2 - m_K^2 + i\epsilon} \; \frac{M_N}{E_N} \; \frac{1}{\sqrt{s} - q^0 - E_N + i\epsilon} \; , \end{aligned} \tag{7.2.19}$$

with $q_{\rm on} = \lambda^{1/2}(s, m_N^2, m_K^2)/2\sqrt{s}$. The factor $\boldsymbol{q}^2$ appearing in the vertex of Eq. (7.2.17) is kept in the loop. On the other hand, the amplitudes which we use for $\bar{K}N \to \pi\Sigma^*$ of Eq. (7.2.18) factorize the on shell value $q_{\rm on}^2$. This is the reason for the factor $\frac{\boldsymbol{q}^2}{q_{\rm on}^2}$ in Eq. (7.2.19) since in Eq. (7.2.18) we write explicitly $T_{\pi\Sigma^*\bar{K}N}$.

The amplitude for the process shown in Fig. 7.1 (c) can be evaluated in a similar way as described above. In this case we have

$$-it^{(c)} = (-iT_{\pi\Sigma^*\pi\Sigma}) i\tilde{G}_{\pi\Sigma K} g_{\pi\Sigma\bar{K}^*N} \boldsymbol{S}^\dagger \cdot \boldsymbol{\epsilon} \ ,$$

where

$$g_{\pi\Sigma\bar{K}^*N} = \sqrt{2} g \frac{D-F}{2f} \ ,$$

with $D-F = 0.33$ and $G_{\pi\Sigma K}$ given similarly as in Eq. (7.2.19) with the replacements $\pi \to K$ and $N \to \Sigma$.

Following Eq. (7.2.5), we thus obtain the coupling of the $\Lambda(1520)$ with $\bar{K}^*N$ as

$$\begin{aligned} g_{\Lambda^*\bar{K}^*N}(\sqrt{s}, k) =& g_{\Lambda^*\pi\Sigma^*} \left[G_{\pi\Sigma^*}(\sqrt{s}) + \frac{2}{3}\tilde{G}_{\pi\Sigma^*K}(\sqrt{s}, k) \right] g_{\pi\Sigma^*\bar{K}^*N} \\ &+ g_{\Lambda^*\pi\Sigma}\tilde{G}_{\pi\Sigma K}(\sqrt{s}, k) g_{\pi\Sigma\bar{K}^*N} + g_{\Lambda^*\bar{K}N}\tilde{G}_{\bar{K}N\pi}(\sqrt{s}, k) g_{\bar{K}N\bar{K}^*N} \ . \end{aligned} \tag{7.2.20}$$

7.3 Results and discussions

7.3.1 Chiral unitary model

Before calculating Eq. (7.2.20), let us consider the momentum variables. Since Eq. (7.2.4) is valid close to the pole of the resonance, we choose $\sqrt{s} = 1520$ MeV. For this $\sqrt{s}$, Λ^* cannot decay into $\bar{K}^*(892)$ and $N(940)$. Here we assume that the $\bar{K}^*$ is off the mass shell with the nucleon being on-shell, which would be compatible with the K^* t-channel exchange in Λ^* photoproduction on the nucleon target. Then the energy of the $\bar{K}^*$ can be given by

$$k^0 = \sqrt{s} - E_N(\boldsymbol{k}) = \sqrt{s} - \sqrt{M_N^2 + \boldsymbol{k}^2} \ ,$$

where we are in the center of mass frame. As we have seen, our formulation is consistent with $|\boldsymbol{k}| \sim 0$, where the s-wave interaction is dominant. If $|\boldsymbol{k}| = 0$, we obtain $k^0 = \sqrt{s} - M_N \sim 580$ MeV, which is the maximum energy of the $\bar{K}^*$ when the nucleon is on-shell.

In order to study the finite momentum effect and stability of the result, we vary the momentum $|\boldsymbol{k}|$ from zero to 400 MeV, and plot the real and imaginary parts as well as the absolute value of the $\Lambda^*\bar{K}^*N$ coupling constant in Fig. 7.5. For reference, we also plot the energy k^0 in the lower panel in Fig. 7.5. We observe that the result is stable against the momentum $|\boldsymbol{k}|$ up to ~ 200 MeV, where the s-wave coupling is expected to be dominant. Numerical values are

$$g_{\Lambda^*\bar{K}^*N} \sim 1.53 + 0.41i \ , \quad |g_{\Lambda^*\bar{K}^*N}| \sim 1.58 \ .$$

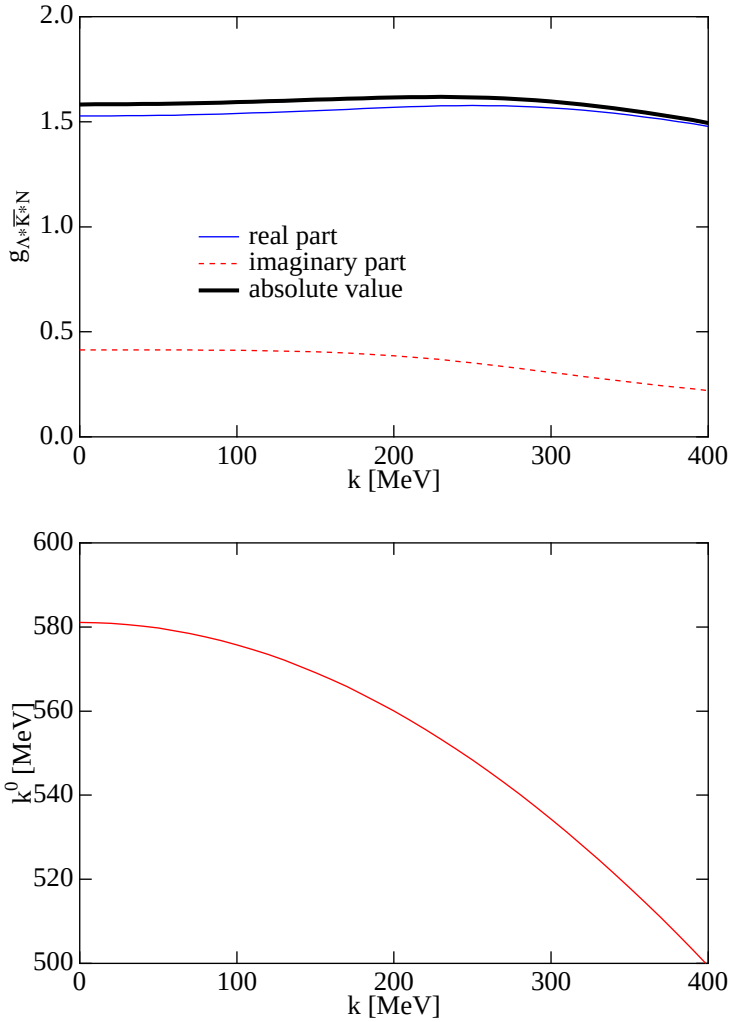

Figure 7.5: Upper : Numerical results for the $\Lambda^*\bar{K}^*N$ coupling constant as a function of K^* momentum $|\boldsymbol{k}|$ in the chiral unitary model. Thick solid line, thin solid line, and dashed line represent absolute value, real part, and imaginary part of the coupling constant, respectively. Lower : Energy of the K^* as a function of $|\boldsymbol{k}|$, assuming the nucleon is on-shell.

The complex phase is the relative one to $g_{\Lambda^*\bar{K}N} = -0.45$ given in Eq. (7.2.6).

Let us look at each component in detail. Substituting the numerical factors, Eq. (7.2.20) can be written as

$$g_{\Lambda^*\bar{K}^*N} \sim -0.042 G_{\pi\Sigma^*} - 0.028 \tilde{G}_{\pi\Sigma^* K} + 0.0068 \tilde{G}_{\pi\Sigma K} + 0.038 \tilde{G}_{\bar{K}N\pi} \ . \tag{7.3.1}$$

Note that the contribution from $\tilde{G}_{\pi\Sigma K}$ is factor 5 smaller than the others, due to the $D-F$ factor.

7.3.2 Quark model

In the quark model, $\Lambda(1520)$ resonance is a p-wave state of 70-dimensional representation of SU(6) [329]. In the spin-flavor group, it is a superposition of ${}^2\mathbf{1}$, ${}^2\mathbf{8}$, and ${}^4\mathbf{8}$. Here we use the notation ${}^{2S+1}D$, where $2S+1$ is the degeneracy of spin states and D denotes a flavor representation. In the standard quark model, Λ^* is dominated by the flavor singlet ${}^2\mathbf{1}$ with some mixture of ${}^2\mathbf{8}$; the spin quartet ${}^4\mathbf{8}$ has only a small fraction.

Such a wave function has been tested for the decay of $\Lambda^* \to \bar{K}N, \pi\Sigma$, and has been proven to work reasonably well [329, 644]. For the decay to the chiral mesons, the matrix elements of the meson-quark interaction can be taken;

$$\mathcal{L}_{mqq} = -ig_{mqq}\bar{q}\gamma_5\Phi q \to \frac{g_{mqq}}{2m_q}\chi^\dagger \boldsymbol{\sigma}\cdot\boldsymbol{\nabla}\Phi\chi \ ,$$

where χ is a two-component spinor, and in the second line the non-relativistic approximation is performed. The SU(3) meson field is defined here by

$$\Phi = \begin{pmatrix} \pi^0 + \frac{\eta}{\sqrt{3}} & \sqrt{2}\pi^+ & \sqrt{2}K^+ \\ \sqrt{2}\pi^- & \pi^0 - \frac{\eta}{\sqrt{3}} & \sqrt{2}K^0 \\ \sqrt{2}K- & \sqrt{2}K^0 & -\frac{2\eta}{\sqrt{3}} \end{pmatrix} .$$

Note that the definition is different from that in the chiral Lagrangians B.1. The meson-quark coupling constant $g_{mqq} \sim 2.6$ is determined from the πNN coupling $g_{\pi NN} \sim 13$, and the constituent quark mass is taken as 330 MeV for all u, d, s quarks for simplicity. The use of a larger mass for m_s will change slightly the SU(6) symmetric wave function such that the excitation of the strange quark will be easier than the excitation of the u, d quarks. But we expect that the following results are not affected too much.

For the $\bar{K}^*$ (vector meson) coupling, we can use the interaction Lagrangian at the quark level

$$\mathcal{L}_{vqq} = g_{vqq}\bar{q}\gamma_\mu V^\mu q \to -\frac{g_{vqq}}{\sqrt{2}m_q}\left\{u^\dagger(i\boldsymbol{\nabla} - i\boldsymbol{\nabla})s + \boldsymbol{\nabla}\times(u^\dagger\boldsymbol{\sigma}s)\right\}\cdot\boldsymbol{\epsilon}(K^{*+}) + \text{h.c.}\,, \quad (7.3.2)$$

where $\boldsymbol{\epsilon}(K^{*+})$ is the polarization vector of the K^{*+}, the quark flavor is indicated explicitly for the $\bar{K}^*$ coupling, and the $g_{vqq} \sim 3$ is determined by the empirical ρNN coupling strength. This Lagrangian of vector type coupling works well for baryon magnetic moments when the $\bar{K}^*$ is replaced by the photon after SU(3) rotation. For the ρNN, however, the tensor coupling is slightly underestimated $g_T/g_V \sim 4$, as compared with the strong tensor coupling $g_T/g_V \sim 6$ [645]. For the present study of qualitative analysis, however, we simply adopt the Lagrangian (7.3.2).

In order to extract the relevant coupling strength, we compute the two transverse helicity amplitudes,

$$a_{3/2} = -\langle\, N(s_z = 1/2), K^*(h = +1)\,|\mathcal{L}_{vqq}|\,\Lambda^*(s_z = 3/2)\,\rangle$$
$$a_{1/2} = -\langle\, N(s_z = -1/2), K^*(h = +1)\,|\mathcal{L}_{vqq}|\,\Lambda^*(s_z = 1/2)\,\rangle\,.$$

Here s_z represents the third component of spin and h the helicity of the photon. In general, for a massive vector meson, there is another type of scalar or longitudinal one, which can be

computed by the time component of the current. For the present purpose, however, the two transverse components are sufficient. They are then related to the multipole amplitudes by

$$E1 = -\frac{1}{2}a_{1/2} - \frac{\sqrt{3}}{2}a_{3/2}\,,$$
$$M2 = \frac{\sqrt{3}}{2}a_{1/2} - \frac{1}{2}a_{3/2}\,.$$

The quark model calculation is rather standard, and so we just show the final result:

$$E1 = -i\frac{3\sqrt{2}\sqrt{\alpha}}{m_q}g_{vqq}\left(1 - \frac{\boldsymbol{k}^2}{6\alpha}\right)e^{-\boldsymbol{k}^2/6\alpha}$$
$$M2 = -i\frac{\sqrt{6}\sqrt{\alpha}}{4m_q}g_{vqq}\frac{\boldsymbol{k}^2}{6\alpha}e^{-\boldsymbol{k}^2/6\alpha}\,,$$

where $\boldsymbol{k}$ is the momentum of K^* and α is a harmonic oscillator parameter of the wave function of the non-relativistic quark model, which is related to the size of the system by

$$\langle r^2\rangle = 3/\alpha\,.$$

The $\Lambda^*\bar{K}^*N$ coupling constant is then related to the $E1$ amplitude by an overall constant

$$g_{\Lambda^*\bar{K}N} = \frac{3}{\sqrt{6}}E1\,. \tag{7.3.3}$$

In the calculation, we consider a mixing of $^2\mathbf{1}$ and $^2\mathbf{8}$ states for $\Lambda(1520)$ as

$$|\,\Lambda(1520)\,\rangle = \cos\theta|\,^2\mathbf{1}\,\rangle + \sin\theta|\,^2\mathbf{8}\,\rangle\,.$$

In the Isgur-Karl model, the mixing angle was obtained $\theta \sim 0.4$ [329]. The result is shown in Fig. 7.6, where the coupling constant $g_{\Lambda^*\bar{K}^*N}$ is shown as a function of K^* three momentum k for different mixing angles θ. The quark model value, in contrast with that of the chiral unitary approach, is of order $g_{\Lambda^*\bar{K}^*N} \sim 10$. In particular, the value increases slightly as the mixing angle increases, which is a consequence of the interference between the two flavor states. The difference between the values of the chiral unitary model and the quark model is large, and it would be interesting to test the coupling by experiments. In reality, the physical resonance state may be a mixture of the two extreme schemes of the chiral unitary and the quark models. The coupling $g_{\Lambda^*\bar{K}^*N}$ could be used to investigate such a hybrid nature of the resonance.

For completeness, we would like to mention the phenomenological analysis of the $g_{\Lambda^*\bar{K}^*N}$ coupling constant. In Ref. [207], the $g_{\Lambda^*\bar{K}^*N}$ is estimated from the Λ^* photoproduction data [641]. They fit the cross section at $E_\gamma = 2.8$-4.8 GeV by a Regge trajectory of K^* exchange, and match the amplitude at $E_\gamma = 2.3$ GeV to the one calculated by the Born terms with the effective Lagrangian approach which includes the $g_{\Lambda^*\bar{K}^*N}$ in the K^* t-channel exchange. The result in the present convention is

$$g_{\Lambda^*\bar{K}^*N} = +7.1 \text{ or } -12.6\,, \tag{7.3.4}$$

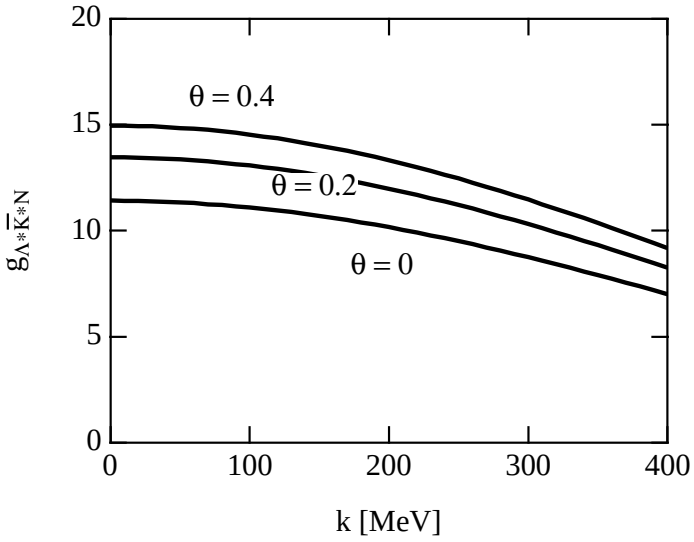

Figure 7.6: Quark model result for the $\Lambda^*\bar{K}^*N$ coupling as a function of K^* momentum k, for different mixing angles θ.

where we denote the relative $\pm$ sign to $g_{\Lambda^*\bar{K}N}$. However, this conclusion depends on the assumption of the Regge trajectory of K^* exchange, and the same data [641] can be equally well reproduced with $g_{\Lambda^*\bar{K}^*N} = 0$ in a different model [643], where the Kroll-Ruderman term plays a dominant role. In order to perform a precise phenomenological analysis, we need further experimental information of the Λ^*.

7.4 Summary and discussions

In this chapter, we have studied the $\Lambda(1520)\bar{K}^*N$ coupling constant. The motivations are twofold; one is to offer a model estimation for the unknown coupling constant which is expected to be important in hyperon production reactions, and the other one is to test different types of models for baryon resonances. In the chiral unitary model the resonances are described as a meson baryon quasi-bound state which may indicate the importance of hadron-like correlations in hadron structure.

Since the coupling constant has not been calculated in the chiral unitary model before, we have shown here a detailed derivation. The resulting coupling constant $g_{\Lambda^*\bar{K}^*N}$ is expressed as a sum over contributions from various channels necessary for the formation of Λ^*. The actual number of the coupling $g_{\Lambda^*\bar{K}^*N}$ turned out to be of order 1-2, which is significantly smaller than the quark model value of order 10.

The difference in the results in two models should be a consequence of the difference of the model setup in various aspects. First, the quark model describes the Λ^* as a three-quark system, while it is five-quark description in the chiral unitary model. Second, in the chiral unitary model, the Λ^* is mainly a member of flavor **8**, while in the quark model it is presumably dominated by the flavor singlet **1**. Third, the wave function of the Λ^* would be

dominated by the s-wave component of $\pi\Sigma(1385)$, while it is a p-wave excitation in the quark model. Such differences in the internal structure should be reflected in the $\Lambda^*\bar{K}^*N$ coupling. If the actual $\Lambda(1520)$ has a mixed structure of the meson-baryon quasi-bound state and the three-quark state, the relevant coupling constant will be an intermediate value.

Since we have no experimental information of the coupling it would be very interesting to have the experimental value. Photoproduction reactions such as $\gamma N \to \Lambda^* K$ and $\gamma N \to \Lambda^* K^*$ may discriminate the coupling constant. In the K production case, comparison between proton target and neutron target will be useful, since the K exchange and contact terms are absent for the neutron target [643]. As a consequence, the t-channel behavior is dominated by the K^* exchange, so that the angular dependence is very sensitive to the strength of the $\Lambda^*\bar{K}^*N$ coupling constant. Hence, the angular dependence of the cross section ratio of proton and neutron will give us the information of the coupling constant of interest. It is also interesting to investigate the $\gamma p \to \Lambda^* K$ and $\gamma p \to \Lambda^* K^*$ reactions with Λ^* going forward, which is naively dominated by the u-channel diagram. When the exchanged particle is the Λ^*, the cross section ratio of the K production and the K^* production provides the ratio of the coupling constants $\Lambda^*\bar{K}N$ and $\Lambda^*\bar{K}^*N$. Information from such experiments as well as theoretical comparison would provide further understanding of the resonance structure.

Part III

Pentaquarks

Chapter 8

Determining the Θ^+ quantum numbers through a kaon-induced reaction

In this chapter, we study the $K^+p \to \pi^+KN$ reaction for the study of the production of the Θ^+ with $J^P = 1/2^{\pm}, 3/2^+$. The KN spectrum in the final state is studied in various kinematical regions. We show that, independently of the quantum numbers of the Θ^+, a resonance signal is always observed with the final kaon in forward direction. In addition, we also show how a combined consideration of the strength at the peak, and the angular dependence of polarization observables can help determine the Θ^+ quantum numbers using the present reaction. This topic is reported in Refs. [17, 18, 19, 20].

8.1 Introduction

A recent experiment by LEPS collaboration at SPring-8 found a clear signal for an $S = +1$ resonance around 1540 MeV [16]. There are more than ten experiments which confirm the existence of the Θ^+, however, the spin and parity of the Θ^+ have not yet been determined experimentally. Theoretically, the parity of Θ^+ is interesting and important. In the naive quark model, all quarks can be put in the lowest $1/2^+$ orbit. Since $\bar{s}$ carries negative parity, the $\Theta(uudd\bar{s})$ in this naive picture would have negative parity, in contrast with the chiral quark soliton model [77], which predicts the positive parity. Therefore, it is strongly desired to present a method to determine the spin and parity experimentally. This is the issue we pursue in this chapter.

The evidences for the existence of the Θ^+ are found in several photoproduction experiments [16, 101]. However, the dynamical mechanisms of photo-induced reactions in the energy region of Θ^+ production are generally very complicated, because of, for instance, the large momentum transfer for the strangeness production. In such a situation, alternative reactions based on known elementary processes are most welcome in order to increase our knowledge of the resonance and help determine properties like spin, isospin and parity. We

present one particularly suited reaction with the process

$$K^+p \to \pi^+\Theta^+ \to \pi^+K^+n \text{ or } \pi^+K^0p. \tag{8.1.1}$$

Characteristic features of this reaction are as follows.

1. This is a hadronic reaction, so that a large cross section is expected compared with the photoproductions.
2. Momentum transfer is smaller than the photoproduction, to which the low energy effective theory can be safely applied.
3. The KN invariant mass can be precisely determined by measuring the π^+ momentum alone.
4. By choosing small momenta of the π^+ in the final state, some of the known non-resonant background contributions can be suppressed, and hence the Θ^+ resonance signal will be more clearly seen.

We calculate this reaction by assuming the Θ^+ is in KN s wave ($J^P = 1/2^-$) or in p wave ($J^P = 1/2^+$ or $3/2^+$) with isospin $I = 0$ or 1. We shall study all these possibilities, but states with higher partial waves and higher isospin are not considered here. Since model calculations of this kind always contains the uncertainties coming from the form factors and unknown coupling constants, quantitative result of cross sections is not adequate to determine the quantum numbers. Therefore, our aim here is to identify observables which differ qualitatively depending on the quantum numbers of the Θ^+.

8.2 Formulation

8.2.1 Kinematics of the reaction

A successful model for the reaction (8.1.1) was considered in Ref. [646] based on the chiral perturbation theory, consisting of the mechanisms depicted in terms of Feynman diagrams in Fig. 8.1. The pion pole term (a) and contact term (b) provide spin flip amplitudes proportional to $\boldsymbol{\sigma}$, derived from the derivative coupling for the (generalized) Yukawa vertices, while the ρ exchange term (c) contains both a spin flip part and a non spin flip part. Having an amplitude proportional to $\boldsymbol{\sigma}$ is important in the present context in order to test the parity of the resonance. Hence, we choose a situation, with the momentum of the final pion $\boldsymbol{p}_{\pi^+}$ small compared to the momentum of the initial kaon, such that the diagram (c), which contains the $\boldsymbol{S}\cdot\boldsymbol{p}_{\pi^+}$ operator can be safely neglected and the terms of Fig. 8.1 (a) and (b) will provide the bulk for this reaction. If there is a resonant state for KN then it will be seen in the final state interaction of this system. This means that in addition to the diagrams (a) and (b) of Fig. 8.1, we shall have the resonant amplitudes shown in Fig. 8.2.

The restriction to have small pion momenta eliminates also other possible resonant contributions like the one in the diagram of Fig. 8.3, which involves the $\boldsymbol{\sigma}\cdot\boldsymbol{p}_{\pi^+}$ coupling. One could in principle have negative parity resonances instead of the intermediate neutron, which

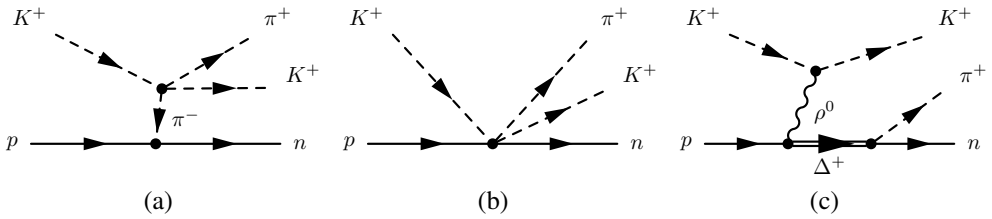

Figure 8.1: Feynman diagrams of the reaction $K^+p \to \pi^+K^+n$ in the model of Ref. [646]. For the $K^+p \to \pi^+K^0p$ reaction, similar diagrams can be obtained by the isospin symmetry. Note that the η exchange exists for the K^0p final state in addition to the π^0 exchange.

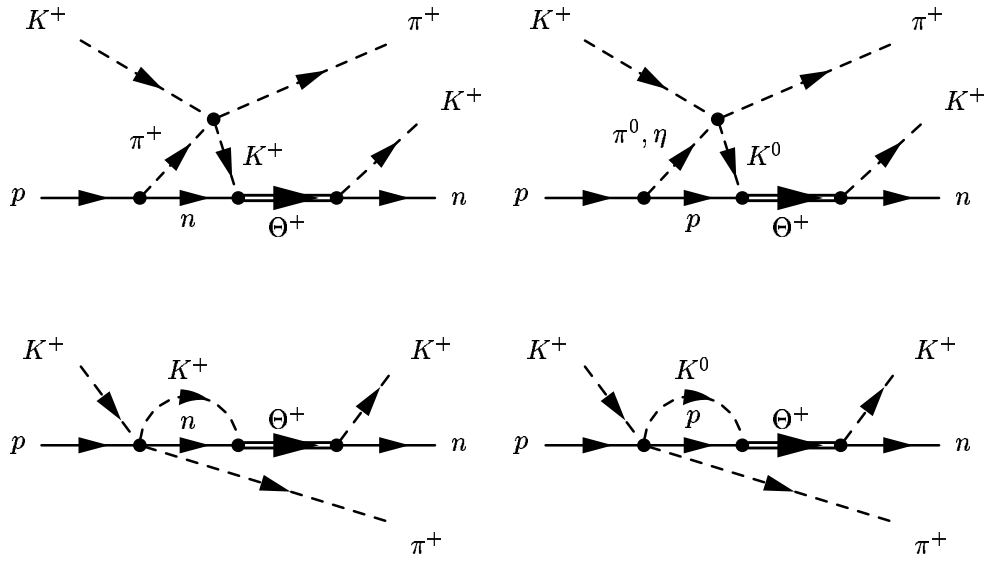

Figure 8.2: Feynman diagrams of the reaction $K^+p \to \pi^+K^+n$ with the Θ^+ resonance. For the $K^+p \to \pi^+K^0p$ reaction, similar diagrams can be obtained by the isospin symmetry.

involve an s-wave πNN^* coupling, but the lightest one would be the $N^*(1535)$ which would be very much off the mass shell, rendering the contribution of the diagram negligible. Note also that the consideration of N^* resonances instead of the intermediate n, p states in Fig 8.2 is not usually done in chiral dynamics calculations since it is accounted for by means of counterterms, or subtraction constants in the loop function which can be equally taken into account by the choice of the cutoff [512]. In summary, we take into account the diagrams (a) and (b) as background contribution in the present calculation. We show the assignment of the kinematic variables in Fig. 8.4, which is summarized in Appendix 8.4.

8.2.2 Background terms

Let us first evaluate the meson pole term (a) and contact term (b) in Fig. 8.1, which are the background contributions to the present reaction. With the meson-meson and meson-baryon interactions derived from the chiral Lagrangians, these diagrams lead to the $K^+n \to \pi^+KN$

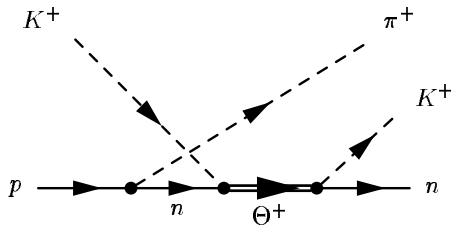

Figure 8.3: Feynman diagrams of the reaction $K^+p \to \pi^+K^+n$ with the Θ^+ resonance and u-channel nucleon pole.

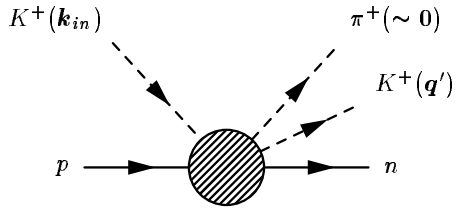

Figure 8.4: Kinematics of the $K^+p \to \pi^+K^+n$ reaction.

amplitudes [646, 647]

$$-it_i = (a_i + b_i \boldsymbol{k}_{in} \cdot \boldsymbol{q}' + c_i)\boldsymbol{\sigma} \cdot \boldsymbol{k}_{in} + (-a_i - b_i \boldsymbol{k}_{in} \cdot \boldsymbol{q}' + d_i)\boldsymbol{\sigma} \cdot \boldsymbol{q}', \tag{8.2.1}$$

where $i = 1, 2$ stands for the final state K^+n, K^0p respectively and k_{in} and q' are the momenta of initial and final kaons. The coefficients a_i and b_i are from meson exchange terms, and c_i and d_i from contact terms. They are given by

$$a_1 = -\frac{1}{3f^2}(m_K^2 - 2m_\pi\omega(q') - \omega(k_{in})\omega(q') - \omega(k_{in})m_\pi) \cdot \frac{\sqrt{2}(D+F)}{2f}\frac{1}{p_{\text{ex}}^2 - m_\pi^2}, \tag{8.2.2}$$

$$a_2 = a_{2,\pi} + a_{2,\eta}, \tag{8.2.3}$$

$$a_{2,\pi} = -\frac{1}{\sqrt{2}f^2}m_\pi(\omega(k_{in}) + \omega(q')) \cdot \frac{D+F}{2f}\frac{1}{p_{\text{ex}}^2 - m_\pi^2}, \tag{8.2.4}$$

$$a_{2,\eta} = \frac{1}{\sqrt{6}f^2}(2\omega(k_{in})\omega(q') + m_\pi\omega(q') - m_\pi\omega(k_{in}) - \frac{2}{3}m_K^2 + \frac{2}{3}m_\pi^2) \cdot \frac{3F-D}{2\sqrt{3}f}\frac{1}{p_{\text{ex}}^2 - m_\eta^2}, \tag{8.2.5}$$

$$b_1 = -\frac{1}{3f^2} \cdot \frac{\sqrt{2}(D+F)}{2f}\frac{1}{p_{\text{ex}}^2 - m_\pi^2}, \tag{8.2.6}$$

$$b_2 = b_{2,\pi} + b_{2,\eta}, \tag{8.2.7}$$

$$b_{2,\pi} = 0\ , \tag{8.2.8}$$

$$b_{2,\eta} = -\frac{1}{\sqrt{6}f^2} \cdot \frac{3F-D}{\sqrt{3}f}\frac{1}{p_{\text{ex}}^2 - m_\eta^2}, \tag{8.2.9}$$

$$c_1 = \frac{\sqrt{2}(D+F)}{12f^3}, \tag{8.2.10}$$

$$c_2 = -\frac{\sqrt{2}D}{12f^3}, \tag{8.2.11}$$

$$d_1 = \frac{\sqrt{2}(D+F)}{24f^3}, \tag{8.2.12}$$

$$d_2 = -\frac{D+3F}{2}\frac{\sqrt{2}}{12f^3}, \tag{8.2.13}$$

where $p_{\rm ex}$ is the momentum of the meson exchanged in the meson pole term and m_X is the mass of meson X, for which we neglect the tiny isospin breaking effect. The three momentum of the final pion is already assumed to be vanish in these formulae.

8.2.3 Resonant terms

Now let us turn to the resonance diagrams of Fig. 8.2 containing a loop integral, which is initiated by the tree diagrams of Figs. 8.1 (a) and (b). We denote the momentum of the intermediate kaon as q, and the amplitudes (8.2.2)-(8.2.13) are incorporated by replacing q' by q. The resonance contributions to the $KN \to KN$ amplitudes are given by

$$\begin{aligned}
t^{(s)}_{K^+n(K^0p)\to K^+n} &= \frac{(\pm)g^2_{K^+n}}{M_I - M_R + i\Gamma/2}, \\
t^{(p,1/2)}_{K^+n(K^0p)\to K^+n} &= \frac{(\pm)\bar{g}^2_{K^+n}(\boldsymbol{\sigma}\cdot\boldsymbol{q}')(\boldsymbol{\sigma}\cdot\boldsymbol{q})}{M_I - M_R + i\Gamma/2}, \\
t^{(p,3/2)}_{K^+n(K^0p)\to K^+n} &= \frac{(\pm)\tilde{g}^2_{K^+n}(\boldsymbol{S}\cdot\boldsymbol{q}')(\boldsymbol{S}^\dagger\cdot\boldsymbol{q})}{M_I - M_R + i\Gamma/2},
\end{aligned} \tag{8.2.14}$$

for s wave, p wave with $J^P = 1/2^+$, and p wave with $3/2^+$, respectively. In these expressions, M_I is the energy of the K^+n system in the center of mass frame, M_R and Γ the mass and width of the resonance (1540 MeV, 20 MeV), and q and q' the momenta of the initial and final kaon, respectively. $\boldsymbol{S}^\dagger$ is the spin transition operator from spin 1/2 to 3/2 states, which is defined in Appendix A.1.2. The signs + and − stand for the $K^0p \to K^+n$ amplitude in the case one has $I = 1$ or $I = 0$ for the Θ^+ resonance. The values of the coupling constants g, $\bar{g}$ and $\tilde{g}$ can be obtained from the Θ^+ width

$$g^2_{K^+n} = \frac{\pi M_R\Gamma}{Mq}, \quad \bar{g}^2_{K^+n} = \frac{\pi M_R\Gamma}{Mq^3}, \quad \tilde{g}^2_{K^+n} = \frac{3\pi M_R\Gamma}{Mq^3}. \tag{8.2.15}$$

Note that the coupling constants for the p-wave resonances have dimension of [mass^{-1}]. A derivation for these relations can be found in Appendix A.4.1.

In the loop diagrams of Fig. 8.2, the momentum of kaon is now an internal variable $\boldsymbol{q}$. In performing the loop integral, the fact that $\boldsymbol{k}_{in}$ is reasonably larger than $\boldsymbol{q}$, allows us to make an angle average of the meson propagator which simplifies the integrals. Furthermore, as shown in Ref. [8] and also found in the meson baryon scattering processes [5], the amplitude $K^+p \to \pi^+K^+n$ factorizes inside the loops with its on-shell value, which means in Eqs. (8.2.2)-(8.2.13) one takes

$$\omega(q) = \frac{M_I^2 + m_K^2 - M_N^2}{2M_I},$$

although they are inside a loop. Note that since we have chosen the π^+ momentum small, the K^+n final state is also approximately in its center of mass frame and we assume this kinematics in the variables.

In what follows, we calculate the $K^+p \to \pi^+K^+n$ reaction, which can easily extrapolate to the π^+K^0p final state by the isospin symmetry. The amplitudes for resonant terms are given by

$$\begin{aligned}
-i\tilde{t}_i^{(s)} =& \frac{g_{K^+n}^2}{M_I - M_R + i\Gamma/2}\left\{G(M_I)(a_i + c_i) - \frac{1}{3}\bar{G}(M_I)b_i\right\}\boldsymbol{\sigma}\cdot\boldsymbol{k}_{in}S_I(i), \\
-i\tilde{t}_i^{(p,1/2)} =& \frac{\bar{g}_{K^+n}^2}{M_I - M_R + i\Gamma/2}\bar{G}(M_I)\left\{\frac{1}{3}b_i\boldsymbol{k}_{in}^2 - a_i + d_i\right\}\boldsymbol{\sigma}\cdot\boldsymbol{q}'S_I(i), \\
-i\tilde{t}_i^{(p,3/2)} =& \frac{\tilde{g}_{K^+n}^2}{M_I - M_R + i\Gamma/2}\bar{G}(M_I)\frac{1}{3}b_i\left\{(\boldsymbol{k}_{in}\cdot\boldsymbol{q}')(\boldsymbol{\sigma}\cdot\boldsymbol{k}_{in}) - \frac{1}{3}\boldsymbol{k}_{in}^2\boldsymbol{\sigma}\cdot\boldsymbol{q}'\right\}S_I(i),
\end{aligned} \tag{8.2.16}$$

for s- and p-wave, and $i = 1, 2$ for K^+n and K^0p intermediate state, respectively. $S_I(i)$ gives the sign for the K^+n and K^0p components in $I = 0$ and 1, namely, $S_0(1) = 1$, $S_1(1) = 1$, $S_0(2) = -1$ and $S_1(2) = 1$. The function $G(M_I)$ and $\tilde{G}(M_I)$ are the loop functions of a meson and a baryon propagator

$$G(M_I) = \int \frac{d^3q}{(2\pi)^3}\frac{1}{2\omega(q)}\frac{M}{E(q)}\frac{1}{M_I - \omega(q) - E(q) + i\epsilon}\ , \tag{8.2.17}$$

$$\tilde{G}(M_I) = \int \frac{d^3q}{(2\pi)^3}\boldsymbol{q}^2\frac{1}{2\omega(q)}\frac{M}{E(q)}\frac{1}{M_I - \omega(q) - E(q) + i\epsilon}\ , \tag{8.2.18}$$

regularized with a three momentum cut off $q_{\max} = 630$ MeV to reproduce the data of $\bar{K}N$ scattering [5].

8.2.4 Formula for the cross section

When taking into account KN scattering through the Θ^+ resonance, as depicted in Fig. 8.2, the $K^+p \to \pi^+K^+n$ amplitude is given by the sum of the background term and the resonant terms,

$$-i\tilde{t} = -it_1 - i\tilde{t}_1 - i\tilde{t}_2. \tag{8.2.19}$$

For completeness, as in the $\Lambda(1405)$ production [8], we include a recoil factor in all terms to account for $\mathcal{O}(p/M)$ relativistic corrections for the $\gamma^\mu\gamma_5\partial_\mu$ BBM vertex, which is given by

$$F_i = \left(1 - \frac{p_{\rm ex}^{0(i)}}{2M_p}\right).$$

In addition, we also consider the strong form factor of the BBM vertex for which we take a standard monopole and static form factor

$$F_f(\boldsymbol{p}) = \frac{\Lambda^2 - m_\pi^2}{\Lambda^2 + \boldsymbol{p}^2},$$

with $\Lambda \sim 900$ MeV. This form factor is applied both to the meson pole and contact terms to preserve the subtle cancellation of off shell terms shown in Ref. [8]. Inside the loops, for the reasons exposed above, the product of the form factor and propagator is replaced by its angle averaged expression which simplifies the formulae. This is implicit in the a_i, b_i coefficients of Eqs. (8.2.16).

We take an initial three momenta of K^+ in the Laboratory frame $k_{\rm in}$(Lab.) = 850 MeV ($\sqrt{s} = 1722$ MeV), which allows us to span K^+n invariant masses up to $M_I = 1580$ MeV, thus covering the peak of the Θ^+, and still is small enough to have negligible π^+ momenta with respect to the one of the incoming K^+. The double differential cross section is given by

$$\frac{d^2\sigma}{dM_I d\cos\theta} = \frac{1}{(2\pi)^3}\frac{1}{8s}\frac{M^2}{\lambda^{1/2}(s, M^2, m_K^2)}\frac{1}{M_I}\lambda^{1/2}(s, M_I^2, m_\pi^2)\lambda^{1/2}(M_I^2, M^2, m_K^2)\bar{\Sigma}\Sigma|t|^2, \tag{8.2.20}$$

where $\cos\theta$ is the angle between $\boldsymbol{k}_{\rm in}$ and $\boldsymbol{q}'$ and $\lambda(x, y, z)$ is the Källen function defined by $\lambda(x, y, z) = x^2 + y^2 + z^2 - 2xy - 2yz - 2zx$. A derivation of this formula is given in Appendix A.4.2. We show below the results for the different options of isospin, spin and parity of the Θ^+.

8.3 Numerical result

8.3.1 Cross sections

In Fig. 8.5, we show the invariant mass distribution $d^2\sigma/dM_I d\cos\theta$ in the K^+ forward direction ($\theta = 0$), for several spin and parity assignments. Here we see that, independently of the quantum numbers of Θ^+, a resonance signal is always observed. The signals for the resonance are quite clear for the case of $I, J^P = 0, 1/2^+$ (these would be the quantum numbers predicted in Ref. [77]) and $I, J^P = 0, 1/2^-$, while in the other cases the signal is weaker and the background more important, particularly for the case of $I, J^P = 1, 1/2^+$. With estimated uncertainties in the theory of the order of 20-30 percent, from the approximations done, the strength of the peak at the resonance could already serve to discriminate among the several possibilities.

It is worth mentioning that the positions of the peak are slightly moved from the input value in the Breit-Wigner propagator ($M_R = 1520$ MeV), while the widths of the peak are generally smeared. There is a tendency that the peak position of an s-wave resonance moves to the lower energy side, whereas the position of a p-wave resonance goes to the higher energy side. These effects are caused by the interference effect between the signal and the background, that we take into account in the present calculation. Although the shifts of the peak position are not very large in this case, the information of the background contribution and understanding of its interference effect are important from the experimental point of view.

We have used a Θ^+ width of 20 MeV, but experimentally it could be smaller since the experimental widths observed are mostly coming from the experimental resolution [134, 135]. It is easy to see how this would change our results. By looking at Eqs. (8.2.16) at the peak of

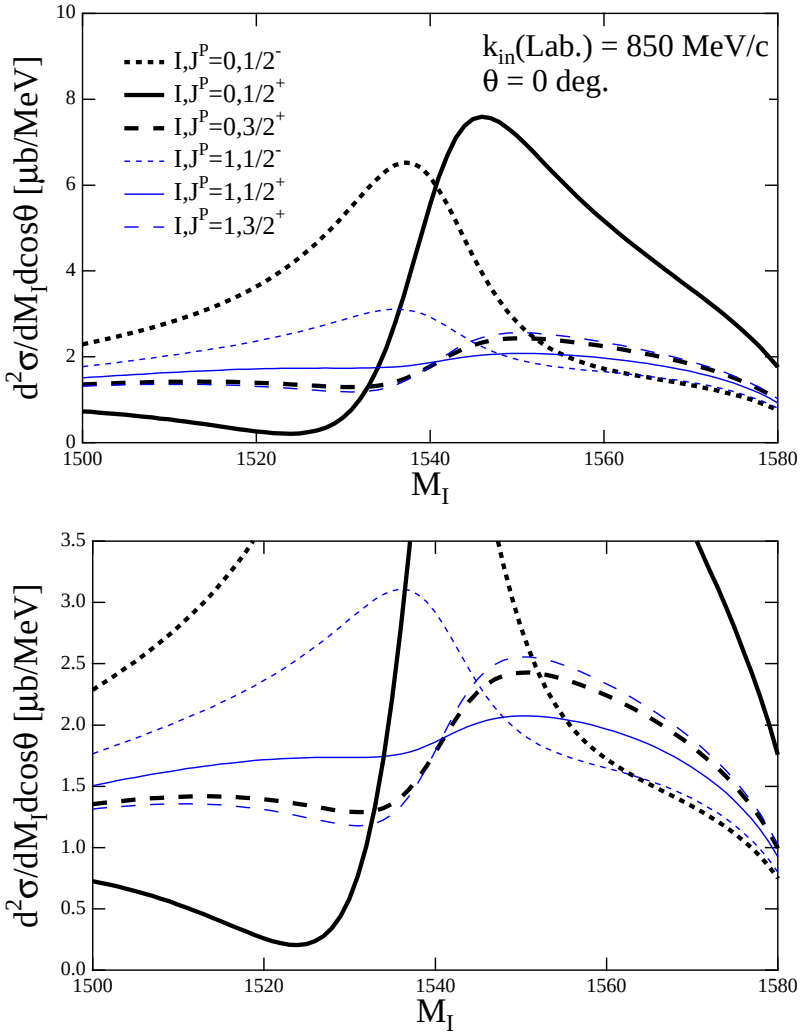

Figure 8.5: The double differential cross sections $d^2\sigma/dM_I d\cos\theta$ with $\theta = 0$ (forward direction) for $I = 0, 1$ and $J^P = 1/2^-, 1/2^+, 3/2^+$. Below, detail of the lower part of the upper figure of the panel.

the resonance distribution and considering the couplings obtained in Eq. (8.2.15) we see that the strength at the peak is independent of Γ. Only the width of the calculated distributions would be smaller for smaller Γ. In Fig. 8.6, we show the spectra with $\Gamma = 10$ MeV and $\Gamma = 1$ MeV.

The angular dependence is shown in Fig. 8.7 for a value of $M_I = 1540$ MeV. What we observe there is that the angular dependence is rather weak in all cases. The background has a weak angular dependence and the resonance signal for this unpolarized cross section has angular dependence only for the case of spin 3/2, where it goes as $(3\cos^2\theta + 1)$, but in this case the resonance contribution is much smaller than the background and this angular dependence is not very visible. The different inflexions of the cross section at $\theta = 0$ are

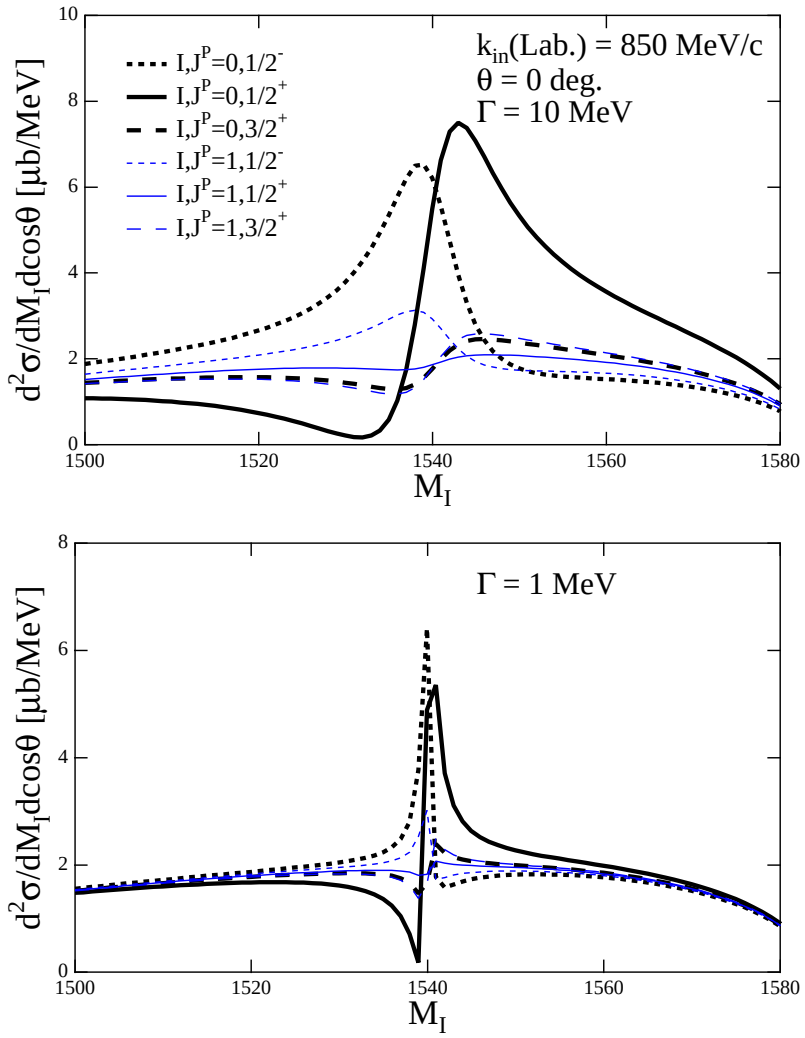

Figure 8.6: The double differential cross sections $d^2\sigma/dM_I d\cos\theta$ with $\theta = 0$ (forward direction) for $I = 0, 1$ and $J^P = 1/2^-, 1/2^+, 3/2^+$ with $\Gamma = 10$ MeV (Upper) and with $\Gamma = 1$ MeV (Lower).

probably too small to be discriminated in an experiment, hence the conclusion is that this unpolarized observable does not shed any further light on the quantum numbers.

8.3.2 Polarization observables

Let us now see what can one learn with resorting to polarization measurements. Eqs. (8.2.16) account for the resonance contribution to the process. The interesting finding there is that if the Θ^+ couples to K^+n in an s wave (hence negative parity) the amplitude goes as $\boldsymbol{\sigma} \cdot \boldsymbol{k}_{in}$, while if it couples in a p-wave it has a term $\boldsymbol{\sigma} \cdot \boldsymbol{q}'$. Hence, a possible polarization test to determine which one of the couplings the resonance chooses is to measure the cross section for initial proton polarization $1/2$ in the direction z ($\boldsymbol{k}_{in}$) and final neutron polarization $-1/2$

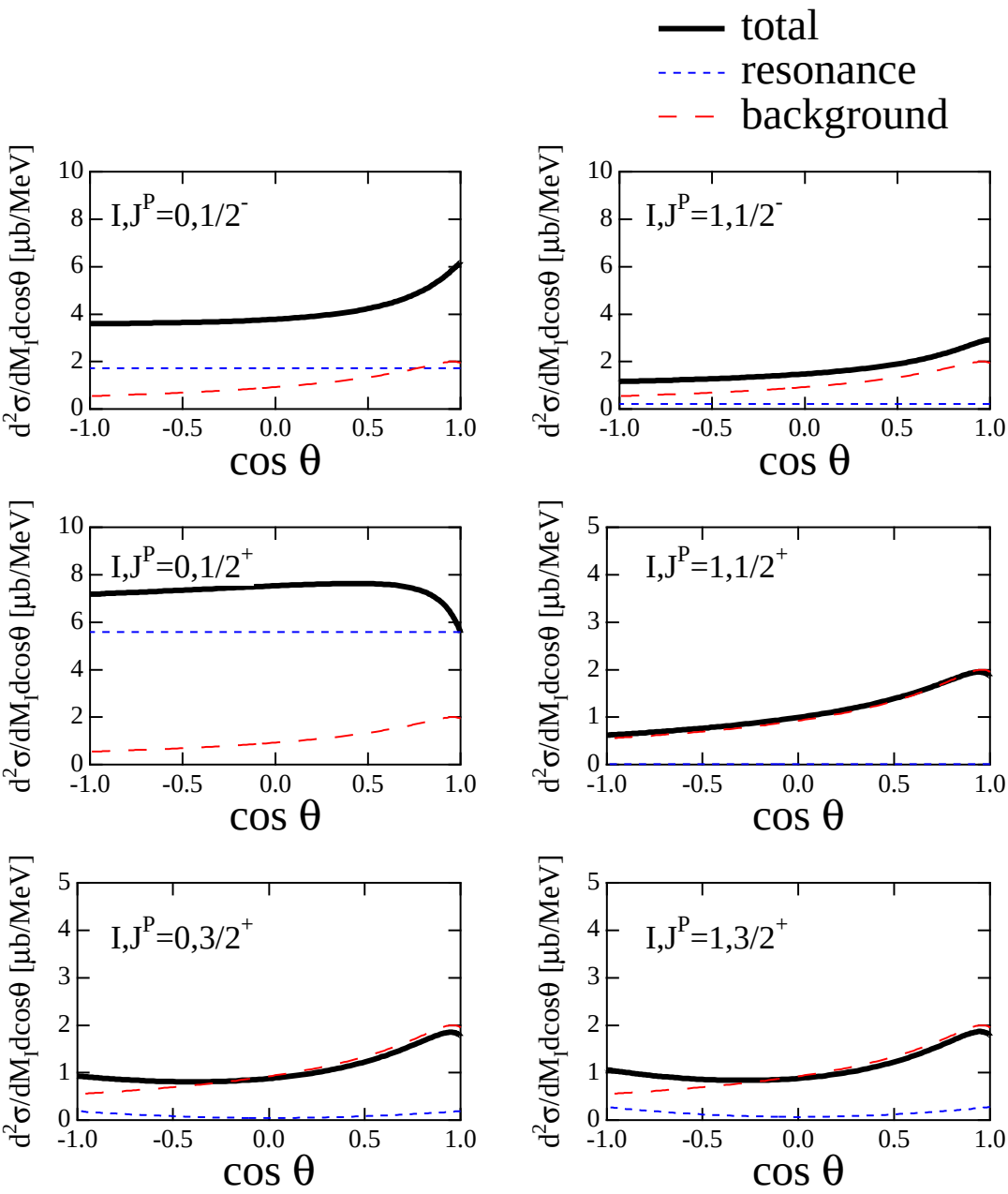

Figure 8.7: Angular dependence of the double differential cross sections $d^2\sigma/dM_I d\cos\theta$ with $M_I = 1540$ MeV at the resonance peak for $I = 0, 1$ and $J^P = 1/2^-, 1/2^+, 3/2^+$.

(the experiment can be equally done with K^0p in the final state, which makes the nucleon detection easier). In this spin flip amplitude $\langle -1/2|t|+1/2\rangle$, the $\boldsymbol{\sigma}\cdot\boldsymbol{k}_{in}$ term vanishes. With this test the resonance signal disappears for the s-wave case, while the $\boldsymbol{\sigma}\cdot\boldsymbol{q}'$ operator of the p-wave case would have a finite matrix element proportional to $q'\sin\theta$. This means, away from the forward direction of the final kaon, the appearance of a resonant peak in the cross section would indicate a p-wave coupling and hence a positive parity resonance.

In Fig. 8.8 we show the results for the polarized cross section measured at 90 degrees as a function of the invariant mass. The two cases with s wave do not show any resonant shape since only the background contributes. All the other cross sections are quite reduced to the point that the only sizeable resonant peak comes from the $I, J^P = 0, 1/2^+$ case. A clear experimental signal of the resonance in this observable would unequivocally indicate the quantum numbers as $I, J^P = 0, 1/2^+$.

Finally, in Fig. 8.9 we show the angular dependence of the polarized cross section for a fixed value of the invariant mass of 1540 MeV. The angular distributions look all of them similar, as a consequence of the weakness or disappearance of the resonance contribution, with a peak around 35 degrees, except for the case of $I, J^P = 0, 1/2^+$, where the peak is found around 80 degrees and has a much larger size than in the other cases.

Since 100% polarization can not be achieved in actual experiments, we have computed cross sections for the case of incomplete polarization. We have then found that for a typical polarization rate of about 80% [A)], the previous results shown in Figs. 6 and 7 do not change much. For instance, as shown in Fig. 8.10, the cross section decreases about 10% for $I, J^P = 0, 1/2^+$. For $I, J^P = 0, 1/2^-$, the peak value at around $M_I \sim 1540$ MeV increases, since there is no resonance contribution for the case of 100% polarization. However, the absolute value is small as compared to the one of $J^P = 1/2^+$. For the totally unpolarized case, the $1/2^+$ cross section reduces to about half of the polarized one, while the $1/2^-$ cross section shows a sizable peak. The tendency for other cross sections such as angular dependence is also similar.

8.4 Summary

In summary, we have shown here an elementary reaction, $K^+p \to \pi^+KN$, where, based on the present knowledge of the Θ^+ resonance, we can make predictions for Θ^+ production cross sections. We see that, independently of the Θ^+ quantum numbers, a resonance signal is always seen in the forward direction of the final kaon. The strength at the peak could serve to discriminate among several cases. Further measurements of a polarized cross section could serve to further eliminate other possibilities. In particular, a strong signal seen at 90 degrees for the polarized cross section would clearly indicate that the quantum numbers of the resonance are those predicted in Ref. [77].

The reaction suggested here can be presumably performed and, in particular, a small change in the set up of the experiment at ITEP used to detect the Θ^+ could be made to perform the reaction. The determination of the quantum numbers of the Θ^+ is an essential

[A)] We define the polarization rate by $(N_+ - N_-)/(N_+ + N_-)$.

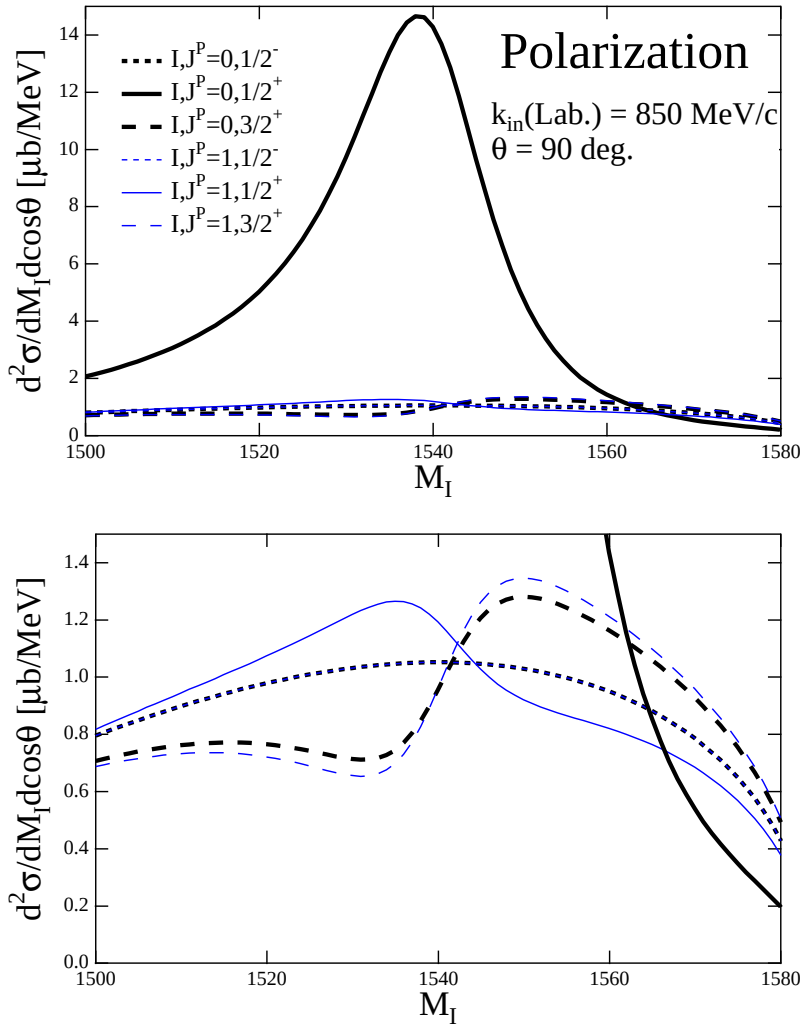

Figure 8.8: The double differential cross sections $d^2\sigma/dM_I d\cos\theta$ with $\theta = 0$ (forward direction) for $I = 0, 1$ and $J^P = 1/2^-, 1/2^+, 3/2^+$. Below, detail of the lower part of the upper figure of the panel. In these figures, thick and thin short-dashed curves ($J^P = 1/2^-$) coincide, since there is only background contribution. In the upper panel, the almost identical results of $J^P = 3/2^+$ drawn by the two long-dashed curves also coincide.

step to further investigate its nature. The implementation of the present reaction would represent a step forward in this direction.

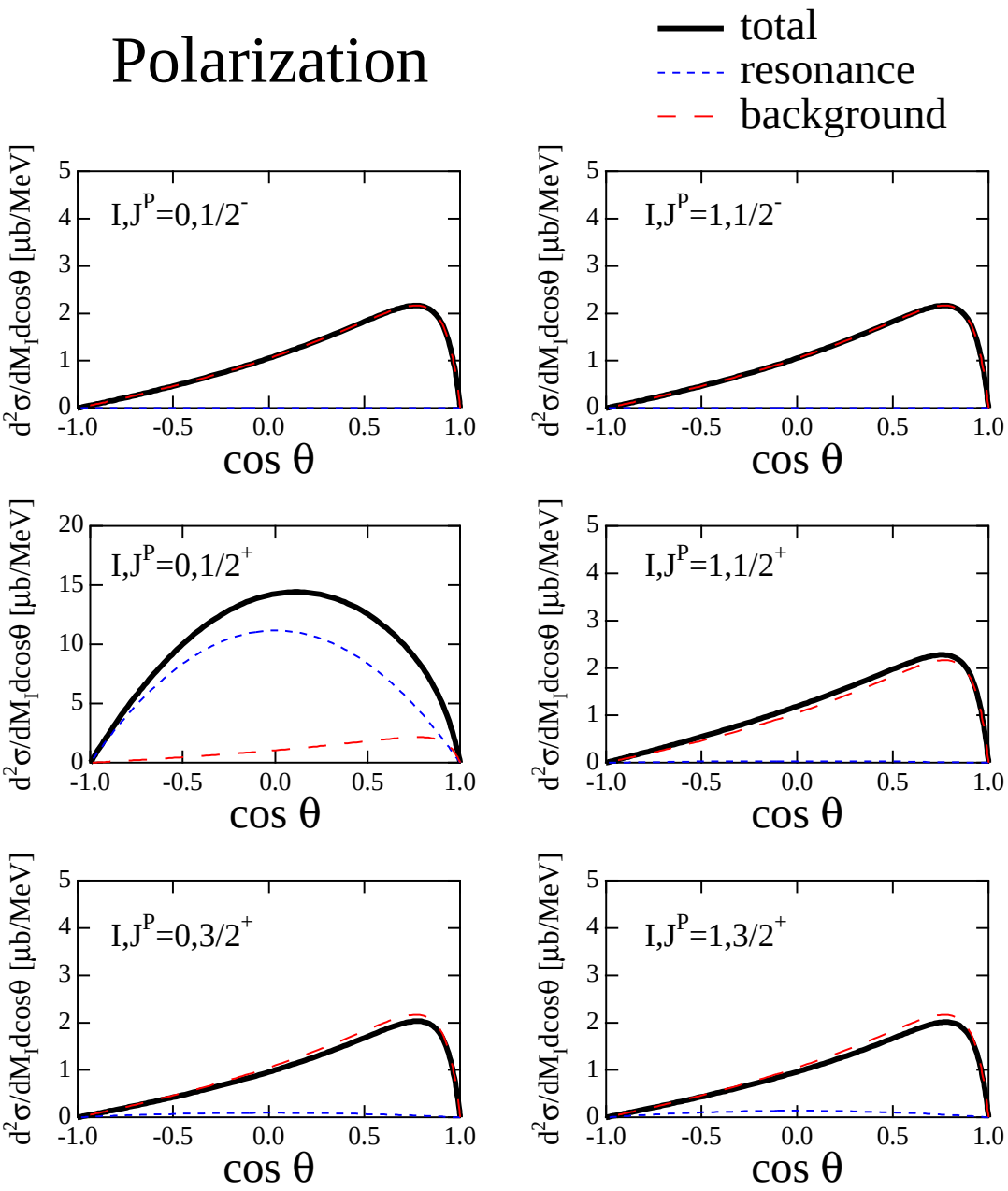

Figure 8.9: Angular dependence of the double differential cross sections of polarized amplitude with $M_I = 1540$ MeV at the resonance peak for $I = 0, 1$ and $J^P = 1/2^-, 1/2^+, 3/2^+$.

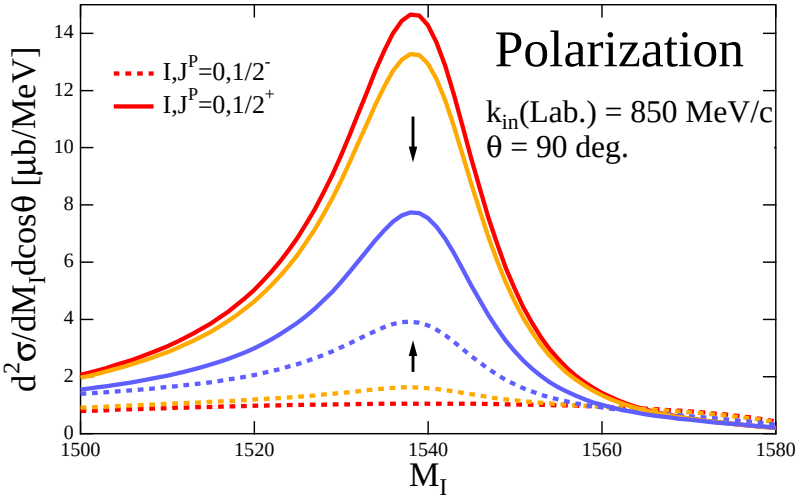

Figure 8.10: Effects of incomplete polarization on the double differential cross sections at $\theta = 90$ degrees. Three solid and dashed curves are for 100%, 80% and 0% (along the direction of an arrow) polarization for $J^P = 1/2^{\pm}$ and $I = 0$.

Chapter 9

Two-meson cloud contribution to the baryon antidecuplet binding

In this chapter, we study the two-meson virtual cloud contribution to the self-energies of the baryons in the SU(3) antidecuplet representation, to which the Θ^+ pentaquark is assumed to belong. This is motivated by the large branching ratio of the $N(1710)$ decay into two pions and one nucleon. We derive effective Lagrangians that describe the $N(1710)$ decay into $N\pi\pi$ with two pions in s and p waves. We find that the two-meson cloud contribution provides attractive self-energies for all members of the antidecuplet. Self-energy contribution to the mass splitting between states with different strangeness which is at least 20% of the empirical one. We also provide predictions for three-body decays of the pentaquark antidecuplet. This topic is reported in Refs. [21, 22, 23].

9.1 Introduction

The Θ^+ has a light mass and a narrow width. These are interesting features, but it is not easy to reproduce in models. For instance, let us consider a resonance in the KN scattering which has these properties. Naively, we expect that the states in lower partial waves should be light, but the width of the states become wide. On the other hand, the width is suppressed for the states in higher partial waves due to the centrifugal barrier, but the mass should be heavy. This is also the same for the quark models; light mass requires the small orbital excitation, whereas the narrow width favors the states with higher spin.

One possible way to solve this problem is the πKN three body bound state conjecture [407, 411]. The energy of the free πKN system is about 1570 MeV, which is only slightly higher than the observed mass of the Θ^+, 1540 MeV. Therefore, an attraction in this channel could make a bound state of the three-body state. In addition, once the bound state is produced, the decay into KN channel should be suppressed, since it requires the absorption of one pion which should be excited in p wave due to the structure of the πNN coupling.

This interesting idea of constructing the Θ^+ as a $K\pi N$ bound state [407, 411] has been examined in some detail [410] employing meson-meson and meson-baryon interactions from chiral Lagrangians. An attraction was found, but not strong enough to bind the system.

Yet, this result leaves one wondering as to what role the two-meson cloud could play in the stability of the state.

In this direction, here we would like to study the two-meson cloud contribution to the masses of baryon antidecuplet, using the effective interactions based on flavor SU(3) symmetry. We introduce the explicit fields for the antidecuplet, and evaluate the self-energies due to the two-meson cloud. Since the contribution of two-meson cloud is of higher order in m_s, this provides another source of mass splitting not contemplated by the Gell-Mann–Okubo (GMO) rule, whose origin is mainly due to the mass difference between the strange and light quarks.

To start with, we assume that the Θ^+ belongs to the antidecuplet representation, and the $N(1710)$ has a large component in the same antidecuplet. Here we implicitly assume $J^P = 1/2^+$ for the Θ^+, which is compatible with the πKN bound state model. This assumption is simple and naive, but still relevant to estimate the two-meson cloud effect to the antidecuplet baryons. It is known that the $N(1710)$ has a relatively large branching ratio into $N\pi\pi$, 40-90% [144], while the ratio into $N\pi$ is small as 10-20%. This fact is consistent with our expectation of the narrow width of the $\Theta \to KN$ and potentially large coupling to the πKN state.

An important experimental input relevant to the present study is the partial decay width into two $N\pi\pi$ modes. The branching ratio decaying into $N\pi\pi$ with the two pions in an s wave is $10 - 40\%$ and into ρN, $5 - 25\%$. Certainly one has to accept a mixing with an octet component for realistic resonances in order, for instance, to explain the $N(1710)$ decay into $\Delta\pi$, which is forbidden for its antidecuplet component [247, 391]. But we do not expect the mixing angle to be close to ideal, as this would imply a stronger ΛK branching ratio than the experimental observed one $5 - 25\%$. The decay pattern of $N(1710)$ and $N(1440)$ also supports the small mixing angle [348, 349]. We will consider a problem of mixing with octet in the next chapter.

In this study, we do not take into account the possible contribution of the one-meson cloud to the antidecuplet binding, which can be easily addressed as a minor correction to our results. The small width of the Θ^+ to KN, in spite of the appreciable phase space available, qualitatively demands that this contribution should be reasonably small; in fact, it has been confirmed quantitatively in Refs. [437, 259, 413]. The self-energy of Θ^+ with a two-meson cloud has been studied in parallel [413] in the context of the medium modification of Θ^+. We here report in full on results for not only the Θ^+ but also other members of the antidecuplet in the vacuum.

This chapter is organized as follows. In section 9.2, we construct various $PBMM$ interactions with the two octet mesons M and one baryon B belonging to octets and with the other baryon P to an antidecuplet. In section 9.3, we compute the contributions of two-meson and one-baryon loops to the mass splittings among the members of antidecuplet baryons. In section 9.4, we present numerical results and discuss the importance of two-meson contributions to the mass splittings and partial decay widths. As we will see, the contributions from the two-meson loops provide sizable contributions to supplement the mass splittings naively expected from the large constituent mass of the strange quark. We will then discuss ranges of interaction strengths of various coupling terms. Section 9.5 is devoted to a summary.

9.2 Construction of effective interaction Lagrangians

9.2.1 Definition of fields

Following a common convention [513, 40, 514], we write the physical meson and baryon fields as follows

$$\phi = \begin{pmatrix} \frac{1}{\sqrt{2}}\pi^0 + \frac{1}{\sqrt{6}}\eta & \pi^+ & K^+ \\ \pi^- & -\frac{1}{\sqrt{2}}\pi^0 + \frac{1}{\sqrt{6}}\eta & K^0 \\ K^- & \bar{K}^0 & -\frac{2}{\sqrt{6}}\eta \end{pmatrix},$$

$$B = \begin{pmatrix} \frac{1}{\sqrt{2}}\Sigma^0 + \frac{1}{\sqrt{6}}\Lambda & \Sigma^+ & p \\ \Sigma^- & -\frac{1}{\sqrt{2}}\Sigma^0 + \frac{1}{\sqrt{6}}\Lambda & n \\ \Xi^- & \Xi^0 & -\frac{2}{\sqrt{6}}\Lambda \end{pmatrix}.$$

The antidecuplet containing the exotic pentaquark states is a tensor P^{ijk} totally symmetric in its three SU(3) indices. The components of P^{ijk} are related to the physical fields by

$$P^{333} = \sqrt{6}\Theta^+_{\overline{\mathbf{10}}}\,,$$
$$P^{133} = \sqrt{2}\,N^0_{\overline{\mathbf{10}}}\,, \qquad P^{233} = -\sqrt{2}\,N^+_{\overline{\mathbf{10}}}\,,$$
$$P^{113} = \sqrt{2}\,\Sigma^-_{\overline{\mathbf{10}}}\,, \qquad P^{123} = -\Sigma^0_{\overline{\mathbf{10}}}\,, \qquad P^{223} = -\sqrt{2}\,\Sigma^+_{\overline{\mathbf{10}}}\,,$$
$$P^{111} = \sqrt{6}\Xi^{--}_{\overline{\mathbf{10}}}\,, \qquad P^{112} = -\sqrt{2}\,\Xi^-_{\overline{\mathbf{10}}}\,, \qquad P^{122} = \sqrt{2}\,\Xi^0_{\overline{\mathbf{10}}}\,, \qquad P^{222} = -\sqrt{6}\Xi^+_{\overline{\mathbf{10}}}\,,$$

where we have adopted the normalization in Ref. [249].

Now we consider the possible interaction Lagrangians, constrained to be SU(3) symmetric. We intend to address the process

$$\mathbf{8}_M + \mathbf{8}_M + \mathbf{8}_B \to \overline{\mathbf{10}}_P,$$

where an octet baryon $\mathbf{8}_B$ and two octet mesons $\mathbf{8}_M$ couple to an antidecuplet baryon $\overline{\mathbf{10}}_P$. To have an SU(3) invariant Lagrangian, we couple first the two $\mathbf{8}_M$ and then combine the resulting irreducible representations with the baryon $\mathbf{8}_B$ to produce a $\overline{\mathbf{10}}_{BMM}$ representation. Irreducible decompositions of the SU(3) algebra give

$$\begin{aligned}
&\mathbf{8}_M \otimes \mathbf{8}_M \otimes \mathbf{8}_B \\
=&(\mathbf{1} \oplus \mathbf{8}^s \oplus \mathbf{8}^a \oplus \mathbf{10} \oplus \overline{\mathbf{10}} \oplus \mathbf{27})_{MM} \otimes \mathbf{8}_B \\
=&\mathbf{8} && \leftarrow \text{from } \mathbf{1}_{MM} \otimes \mathbf{8}_B \\
&\oplus (\mathbf{1} \oplus \mathbf{8} \oplus \mathbf{8} \oplus \mathbf{10} \oplus \overline{\mathbf{10}} \oplus \mathbf{27}) && \leftarrow \text{from } \mathbf{8}^s_{MM} \otimes \mathbf{8}_B \\
&\oplus (\mathbf{1} \oplus \mathbf{8} \oplus \mathbf{8} \oplus \mathbf{10} \oplus \overline{\mathbf{10}} \oplus \mathbf{27}) && \leftarrow \text{from } \mathbf{8}^a_{MM} \otimes \mathbf{8}_B \\
&\oplus (\mathbf{8} \oplus \mathbf{10} \oplus \mathbf{27} \oplus \mathbf{35}) && \leftarrow \text{from } \mathbf{10}_{MM} \otimes \mathbf{8}_B \\
&\oplus (\mathbf{8} \oplus \overline{\mathbf{10}} \oplus \mathbf{27} \oplus \mathbf{35'}) && \leftarrow \text{from } \overline{\mathbf{10}}_{MM} \otimes \mathbf{8}_B \\
&\oplus (\mathbf{8} \oplus \mathbf{10} \oplus \overline{\mathbf{10}} \oplus \mathbf{27} \oplus \mathbf{27} \oplus \mathbf{35} \oplus \mathbf{35''} \oplus \mathbf{64}) && \leftarrow \text{from } \mathbf{27}_{MM} \otimes \mathbf{8}_B.
\end{aligned}$$

Here $\mathbf{8}^s$ and $\mathbf{8}^a$ denote symmetric and antisymmetric combinations of the two-meson fields. Hence we obtain four $\overline{\mathbf{10}}_{BMM}$ representations after recoupling $\mathbf{8}^s_{MM}$, $\mathbf{8}^a_{MM}$, $\mathbf{10}_{MM}$ and $\mathbf{27}_{MM}$ with $\mathbf{8}_B$. In the following, we construct these Lagrangians one by one.

9.2.2 Two-meson 8^s representation

In constructing effective Lagrangians, we follow the principle of using the minimum numbers of derivatives in the fields. This will be released later when we discuss possible structures involving derivatives. To construct $\mathbf{8}^s$ from two $\mathbf{8}_M$, we have in tensor notation

$$D_i{}^j[\mathbf{8}^s_{MM}] = \phi_i{}^a\phi_a{}^j + \phi_i{}^a\phi_a{}^j - \frac{2}{3}\delta_i{}^j\phi_a{}^b\phi_b{}^a = 2\phi_i{}^a\phi_a{}^j - \frac{2}{3}\delta_i{}^j\phi_a{}^b\phi_b{}^a. \tag{9.2.1}$$

We combine this now with an $\mathbf{8}_B$ to give an antidecuplet

$$T^{ijk}[\overline{\mathbf{10}}_{BMM(8s)}] = 2\phi_l{}^a\phi_a{}^i B_m{}^j\epsilon^{lmk} + (i,j,k \text{ symmetrized}).$$

Hence, the interaction Lagrangian becomes

$$\mathcal{L}^{8s} = \frac{g^{8s}}{2f}\bar{P}_{ijk}\epsilon^{lmk}\phi_l{}^a\phi_a{}^i B_m{}^j + \text{h.c.}, \tag{9.2.2}$$

where h.c. denotes the hermitian conjugate terms, in order to take into account the processes in which the antidecuplet is in the initial state. Note also that two ϕ fields have appeared, and we have included a factor $1/2f$ in order to make g^{8s} dimensionless (f is the pion decay constant $f = 93$ MeV).

9.2.3 Two-meson 8^a representation

Next we take the antisymmetric combination of the $\mathbf{8}_M$ and $\mathbf{8}_M$, which for identical meson octets leads to

$$A_i{}^j[\mathbf{8}^a_{MM}] = \phi_i{}^a\phi_a{}^j - \phi_i{}^a\phi_a{}^j = 0.$$

So given the identity of the meson octets, this combination is zero. The simplest way to construct a Lagrangian of this structure is to introduce a derivative in one of the fields, which leads automatically to the vector current consisting of two meson fields. Proceeding as before, we combine this structure with the $\mathbf{8}_B$ to give $\overline{\mathbf{10}}$. Then finally we find

$$\mathcal{L}^{8a} = i\frac{g^{8a}}{4f^2}\bar{P}_{ijk}\epsilon^{lmk}\gamma^\mu(\partial_\mu\phi_l{}^a\phi_a{}^i - \phi_l{}^a\partial_\mu\phi_a{}^i)B_m{}^j + \text{h.c.}, \tag{9.2.3}$$

where g^{8a} is dimensionless. This interaction Lagrangian contains the coupling of the $N(1710)$ with $N\pi\pi$, the two pions in a ρ-meson type correlation. From the experimental branching ratio, we can determine the coupling constant g^{8a}.

9.2.4 Two-meson $\overline{\mathbf{10}}$ representation

To construct the $\overline{\mathbf{10}}$ combination from two mesons, we have now

$$\begin{aligned} T^{ijk}_{MM}[\overline{\mathbf{10}}_{MM}] =& \epsilon^{lmk}\phi_l{}^i\phi_m{}^j + (i,j,k \text{ symmetrized}) \\ =& \epsilon^{lmk}\phi_l{}^i\phi_m{}^j + \epsilon^{lmk}\phi_l{}^j\phi_m{}^i + \epsilon^{lmi}\phi_l{}^j\phi_m{}^k \\ &+ \epsilon^{lmi}\phi_l{}^k\phi_m{}^j + \epsilon^{lmj}\phi_l{}^k\phi_m{}^i + \epsilon^{lmj}\phi_l{}^i\phi_m{}^k \\ =& 0, \end{aligned}$$

which is identically zero for equal meson octets.

9.2.5 Two-meson 27 representation

The expansion for the **27** representation leads to

$$\begin{aligned} H^{jl}_{ik}[\mathbf{27}_{MM}] =& \phi_i{}^j\phi_k{}^l + \phi_i{}^l\phi_k{}^j + \phi_k{}^j\phi_i{}^l + \phi_k{}^l\phi_i{}^j \\ & - \frac{1}{5}\left(\delta_i{}^j D_k{}^l + \delta_i{}^l D_k{}^j + \delta_k{}^j D_i{}^l + \delta_k{}^l D_i{}^j\right) \\ & - \frac{1}{6}\left(\delta_i{}^j\delta_k{}^l\phi_a{}^b\phi_b{}^a + \delta_i{}^l\delta_k{}^j\phi_a{}^b\phi_b{}^a\right), \end{aligned}$$

where $D_i{}^j$ is defined in Eq. (9.2.1). Now the combination of $\mathbf{27}_{MM}$ to $\mathbf{8}_B$ to give the $\overline{\mathbf{10}}$ representation leads to

$$\mathcal{L}^{27} = \frac{g^{27}}{2f}\left[4\bar{P}_{ijk}\epsilon^{lbk}\phi_l{}^i\phi_a{}^j B_b{}^a - \frac{4}{5}\bar{P}_{ijk}\epsilon^{lbk}\phi_l{}^a\phi_a{}^j B_b{}^i\right] + \text{h.c.}, \tag{9.2.4}$$

where the first term gives us a new SU(3) structure, but the second one is equal to $\mathcal{L}^{8s}$ given in Eq. (9.2.2).

To summarize briefly, for the possible SU(3) symmetric couplings of $PBMM$, there are two independent terms with no derivatives, namely Eqs. (9.2.2) and (9.2.4). With one derivative, there are four more terms available, but we will consider only Eq. (9.2.3), which has the structure for the decay of $N(1710) \to N\pi\pi(p\text{-wave})$ as observed experimentally.

9.2.6 Chiral symmetric Lagrangians

In the perturbative chiral Lagrangian approach, one would like to implement chiral symmetry as a derivative expansion. In addition, one of the advantages of chiral Lagrangians is that they relate coupling constants of different processes, in particular, with increasing number of mesons. However, in the present case we cannot take advantage of any of these relations, since the couplings for the present Lagrangians are *a priori* completely arbitrary, and we are only interested in the two-meson problem. Still, in this section we build the lowest-order chiral Lagrangian, with two derivatives. Let us remark that the chiral expansion with baryons is known to converge much more slowly than chiral expansion for mesons, and this lowest-order Lagrangian can only be expected to give a mere qualitative description of the physics. For that reason, to build the Lagrangians of the previous subsections 9.2.2 and 9.2.5 we just relied on flavor SU(3). However, we will check here that the lack of chiral symmetry in those Lagrangians does not have much relevance to the mass splittings and decays we are interested in, since already with the leading-order Lagrangian we get qualitatively the same results. In other words, the relevant symmetry here is SU(3), not chiral symmetry.

To show this, we write a chiral invariant Lagrangian by making the substitution $\phi\cdot\phi \to A_\mu\cdot A^\mu$ in Eq. (9.2.2) such that

$$\mathcal{L}^{\chi} = \frac{g^{\chi}}{2f}\bar{P}_{ijk}\epsilon^{lmk}(A_\mu)_l{}^a(A^\mu)_a{}^i B_m{}^j + \text{h.c.}, \tag{9.2.5}$$

where A_μ is the axial current written in terms of the chiral field ξ [A)]:

$$A_\mu = -\frac{i}{2}\left(\xi^\dagger \partial_\mu \xi - \xi \partial_\mu \xi^\dagger\right),$$

with $\xi = e^{i\phi/\sqrt{2}f}$. It is easy to show that the Eq. (9.2.5) is symmetric under chiral transformation, using the transformation lows in Appendix B.1. To the leading order in meson field, $A_\mu \sim \partial_\mu \phi/\sqrt{2}f$, we find the interaction Lagrangian induced from Eq. (9.2.5) by making the replacement

$$(A_\mu)_l{}^a (A^\mu)_a{}^i \to \frac{1}{2f^2}\partial_\mu \phi_l{}^a \partial^\mu \phi_a{}^i. \tag{9.2.6}$$

Obviously, the SU(3) structure is not affected by this procedure, although the use of Lagrangians involving derivatives will introduce some degree of SU(3) breaking due to the momenta of mesons. Hence, it is useful to verify that this chiral invariant Lagrangian will lead eventually to the same results as those obtained from the Lagrangians without derivatives in the fields. We also perform self-energy calculations using this $\mathbf{8}^s$ chirally symmetric Lagrangian, Eq. (9.2.5).

Notice that the vector current cannot be used for the two-meson coupling of this type, where the baryons in the initial and final states are different. Indeed, the insertion of vector current instead of $A_\mu \cdot A^\mu$ is not invariant under chiral transformation. Vector current can be implemented in the covariant derivative, which originates in the kinetic term of baryons, and hence consists of the same baryon state in the initial and final states. In order to have vector current coupling to two different baryons, we should construct the field strength tensor first, and then combine it with baryon fields. This is however the higher order term in chiral counting.

9.2.7 Explicit SU(3) breaking term

In this subsection, we consider the SU(3) breaking interaction term within the context of chiral Lagrangians. Without using derivatives in the fields, the only possible term is a mass term that violates both SU(3) and chiral symmetry, but in the way demanded by the underlying QCD Lagrangian [513, 40, 514]. The mass term appears through the combination

$$S = \xi \chi \xi + \xi^\dagger \chi \xi^\dagger,$$

with the mass matrix, written in terms of the meson masses,

$$\chi = \begin{pmatrix} m_\pi^2 & & \\ & m_\pi^2 & \\ & & 2m_K^2 - m_\pi^2 \end{pmatrix}.$$

Then it leads to the Lagrangian

$$\mathcal{L}^M = \frac{g^M}{2f}\bar{P}_{ijk}\epsilon^{lmk} S_l{}^i B_m{}^j + \text{h.c.}, \tag{9.2.7}$$

[A)] In the paper [21], we defined the axial current in opposite sign. Here we use the consistent notation with other chapters. The relevant Lagrangian does not affected because of Eq. (9.2.6)

In the expansion of S, we have two meson fields with the structure

$$S^{(2)} = -\frac{1}{2f^2}(2\phi\chi\phi + \phi\phi\chi + \chi\phi\phi).$$

Substituting $S^{(2)}$ for S in Eq. (9.2.7), we obtain the desired mass Lagrangian.

9.3 Self-energies

9.3.1 Two-meson loops

The antidecuplet self-energies deduced from one of the interaction Lagrangians can be obtained by

$$\Sigma_P^{(j)}(p^0) = \sum_{B,m_1,m_2} \left(F^{(j)} C^{(j)}_{P,B,m_1,m_2}\right) I^{(j)}(p^0; B, m_1, m_2) \left(F^{(j)} C^{(j)}_{P,B,m_1,m_2}\right), \tag{9.3.1}$$

where the index j stands for $8s$, $8a$, 27, χ and M for corresponding Lagrangians (9.2.2), (9.2.3), (9.2.4), (9.2.5) and (9.2.7); P denotes the antidecuplet states $P = \Theta_{tenbar}$, $N_{\overline{\mathbf{10}}}$, $\Sigma_{\overline{\mathbf{10}}}$ and $\Xi_{\overline{\mathbf{10}}}$; the argument p^0 is the energy of the antidecuplet baryon; and the factors $F^{(j)}$ are

$$F^{8s} = \frac{g^{8s}}{2f}, \quad F^{8a} = \frac{g^{8a}}{4f^2}, \quad F^{27} = \frac{g^{27}}{2f}, \quad F^{\chi} = \frac{g^{\chi}}{2f}, \quad F^{M} = \frac{g^{M}}{2f}.$$

In Eq. (9.3.1), $C^{(j)}_{P,B,m_1,m_2}$ are SU(3) coefficients that come directly from the Lagrangians when evaluating the different matrix elements. We compile the results in Appendix D.3.1.

The function $I^{(j)}(p^0; B, m_1, m_2)$ of argument p^0 (the energy of the assumed state of the antidecuplet at rest) is the two-loop integral with two mesons and one baryon as shown in Fig. 9.1.

$$\begin{aligned} &I^{(j)}(p^0; B, m_1, m_2) \\ &= -\int \frac{d^4k}{(2\pi)^4} \int \frac{d^4q}{(2\pi)^4} |t^{(j)}|^2 \frac{1}{k^2 - m_1^2 + i\epsilon} \frac{1}{q^2 - m_2^2 + i\epsilon} \frac{M}{E} \frac{1}{p^0 - k^0 - q^0 - E + i\epsilon}, \end{aligned} \tag{9.3.2}$$

where[B)]

$$|t^{(j)}|^2 = 1 \quad \text{for} \quad j = 8s, 27, M, \tag{9.3.3}$$

$$|t^{\chi}|^2 = \frac{(\omega_1\omega_2 - \boldsymbol{k}\cdot\boldsymbol{q})^2}{4f^4}, \tag{9.3.4}$$

$$|t^{8a}|^2 = \frac{1}{2M}\Big\{(E+M)(\omega_1-\omega_2)^2 + 2(|\boldsymbol{k}|^2 - |\boldsymbol{q}|^2)(\omega_1-\omega_2) + (E-M)(\boldsymbol{k}-\boldsymbol{q})^2\Big\}, \tag{9.3.5}$$

$$E = \sqrt{M^2 + (\boldsymbol{k}+\boldsymbol{q})^2}, \quad \omega_1 = \sqrt{m_1^2 + \boldsymbol{k}^2}, \quad \omega_2 = \sqrt{m_2^2 + \boldsymbol{q}^2}.$$

[B)] Here we have neglected the $(E+M)/2M$ factor in Eqs. (9.3.3) and (9.3.4), which will turn out to be small in chapter 11.

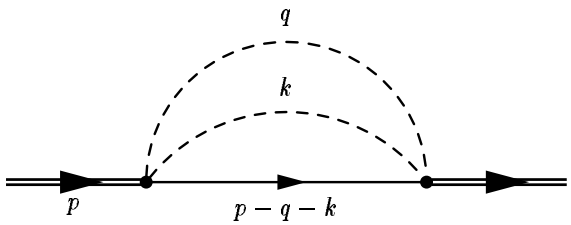

Figure 9.1: Self-energy of baryon antidecuplet caused by two-meson cloud.

In these expressions, M and m_i are the masses of a baryon and mesons, E and ω_i are the energies of a baryon and mesons. A complicated integrand in $|t^{(8a)}|^2$ arises because of the $\bar{u}\gamma^\mu(k-q)_\mu u$ factor when one derivative is included as in Eq. (9.2.3). We neglect the negative-energy intermediate baryon propagator as this is suppressed by a further power of q/M, leading only to a small relativistic correction. The k^0 and q^0 integrations of Eq. (9.3.2) are easily carried out, and we obtain

$$I^{(j)}(p^0;B,m_1,m_2)=\int\frac{d^3k}{(2\pi)^3}\int\frac{d^3q}{(2\pi)^3}|t^{(j)}|^2\frac{1}{2\omega_1}\frac{1}{2\omega_2}\frac{M}{E}\frac{1}{p^0-\omega_1-\omega_2-E+i\epsilon}, \quad (9.3.6)$$

The real part of this integral is divergent. We regularize it with a cutoff Λ in the three momentum on $\boldsymbol{k}$ and $\boldsymbol{q}$, which is a parameter of the calculation and its value must be somewhat larger than the scale of the typical pion momenta. On the other hand, we use low-energy Lagrangians with one or two derivatives at most, and thus the cutoff should not be too large; otherwise, terms with more derivatives could become relevant. In this work we will take Λ in the range 700-800 MeV, roughly the order of magnitude of the cutoff used to regularize the meson-baryon loops in the study of the $\bar{K}N$ interaction [5]. With the $\mathcal{L}^\chi$ of subsection 9.2.6, the cutoff is smaller in order to reproduce analogous results to those with the $8s$ Lagrangian.

The imaginary part of the diagram represents the decay width, in accordance with the optical theorem. The total decay width of a member of the antidecuplet to any BMM states is given by

$$\Gamma_P^{(j)}(p^0)=-2\mathrm{Im}\Sigma_P^{(j)}(p^0),$$

while the partial decay width to a particular channel is given by

$$\Gamma_P^{(j)}(p^0;B,m_1,m_2)=-2\mathrm{Im}\left(F^{(j)}C^{(j)}_{P,B,m_1,m_2}\right)I^{(j)}(p^0;B,m_1,m_2)\left(F^{(j)}C^{(j)}_{P,B,m_1,m_2}\right), \quad (9.3.7)$$

As an example, let us give in detail the contribution from $\mathcal{L}^{8a}$ to the $\Theta_{\overline{\mathbf{10}}}$ self-energy

$$\Sigma^{8a}_\Theta(p^0)=\left(F^{8a}\right)^2[18I^{8a}(p^0;N,K,\pi)+18I^{8a}(p^0;N,K,\eta)],$$

and the contribution from $\mathcal{L}^{8s}$ to the $\Xi_{\overline{\mathbf{10}}}$ self-energy

$$\begin{aligned}\Sigma^{8s}_\Xi(p^0)=\left(F^{8s}\right)^2[&9I^{8s}(p^0;\Sigma,\bar{K},\pi)+I^{8s}(p^0;\Sigma,\bar{K},\eta)\\&+6I^{8s}(p^0;\Xi,\bar{K},K)+4I^{8s}(p^0;\Xi,\pi,\eta)].\end{aligned}$$

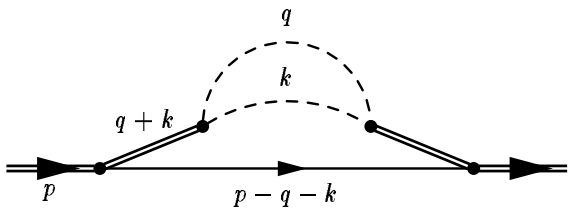

Figure 9.2: Self-energy of baryon antidecuplet caused by two-meson cloud with vector meson propagators.

The expression for all cases can be derived from Tables D.24-D.27 in Appendix D.3.2.

In Eq. (9.3.1), we gave a contribution to the self-energy from one interaction Lagrangian $\mathcal{L}^{(j)}$. For the total self-energy, the sum should be taken over the five interactions ($j = 8s, 8a, 27, \chi$ and M) at each vertex. This means that at each vertex function, we should make the replacement as $(F^{(j)}C^{(j)}_{P,B,m_1,m_2}|t^{(j)}|) \to (|\sum_j F^{(j)}C^{(j)}_{P,B,m_1,m_2}t^{(j)}|)$. We shall, however, not take into account interference between the $8a$ term and the others because of the p-wave nature of the term.

9.3.2 Inclusion of the ρ meson

It is known that $N(1710) \to N\pi\pi(p \text{ wave})$ occurs through the $N\rho$ decay. In order to keep close to the experimental information, we shall also assume that the pair of mesons in the $8a$ case reconstruct a vector meson. Hence, we replace the contact interaction of the $\mathcal{L}^{8a}$ to account for the vector meson propagator (Fig. 9.2) and include the factor

$$\frac{m_v^2}{(q+k)^2 - m_v^2}, \tag{9.3.8}$$

in each $P \to BMM$ vertex. The consideration of these contributions needs extra work on the loop integrals since we introduce new poles. The imaginary part of the integrals (associated to placing on-shell the BMM intermediate states) can be easily accounted for by multiplying the integrand of Eq. (9.3.2) by

$$\left|\frac{m_v^2}{(q+k)^2 - m_v^2 + im_v\Gamma(q+k)}\right|^2, \tag{9.3.9}$$

where $\Gamma(q+k)$ accounts for the width of the vector meson v (ρ or K^* depending on the MM) incorporating the energy dependence through the factor $(P(q+k)/P_{on})^3$ multiplied to the nominal width, with $P(q+k)$ the relative three momentum of the mesons in the decay of the vector meson in the rest frame and $P_{on} = P((M_v, \mathbf{0}))$.

For the real part, one must sort out the poles of the vector meson and the intermediate

BMM state, which is technically implemented by means of the integral

$$\begin{aligned}
&\mathrm{Re}\left[I^{8a}(p^0;B,m_1,m_2)\right]\\
=&-m_v^4\frac{\partial}{\partial(m_v^2)}\mathrm{P.V.}\int\frac{d^4q}{(2\pi)^4}\int\frac{d^4k}{(2\pi)^4}|t^{8a}|^2\frac{1}{k^2-m_1^2+i\epsilon}\frac{1}{q^2-m_2^2+i\epsilon}\\
&\times\frac{1}{(k+q)^2-m_v^2+i\epsilon}\frac{M}{E}\frac{1}{p^0-k^0-q^0-E+i\epsilon},
\end{aligned}$$

where P.V. stands for the principal value. Here, we neglected the width of the vector meson, which does not play much of a role in the off-shell regions of integrations. The k^0 and q^0 integrations can be performed analytically, and one obtains the simple expression

$$\begin{aligned}
&\mathrm{Re}\left[I^{8a}(p^0;B,m_1,m_2)\right]\\
=&m_v^4\frac{\partial}{\partial(m_v^2)}\mathrm{P.V.}\int\frac{d^3k}{(2\pi)^3}\int\frac{d^3q}{(2\pi)^3}|t^{8a}|^2\frac{1}{2\omega_1}\frac{1}{2\omega_2}\frac{1}{\omega_v}\frac{1}{\omega_v+\omega_1+\omega_2}\\
&\times\frac{1}{p_0-\omega_v-E+i\epsilon}\frac{1}{p_0-\omega_1-\omega_2-E+i\epsilon}\frac{M}{E}(\omega_1+\omega_2+\omega_v-p_0+E),
\end{aligned}\tag{9.3.10}$$

where ω_v is the on-shell energy of the vector meson. A derivation of this form can be found in Appendix C.2.2.

9.4 Numerical examples

Next we present some numerical results that illustrate the antidecuplet mass shifts and decay widths to three-body channels. One of the most exciting aspects in the antidecuplet is that the Θ^+ is located about 30 MeV below the $NK\pi$ threshold. Hence, it cannot decay into this or any other BMM channels to which it couples. For the interaction Lagrangians, we obtain the $g^{(j)}$ coefficients from the experimentally allowed decay amplitudes of the $N(1710)$. We give several examples that illustrate the general behavior of the two-meson cloud, common to the Lagrangians described in previous sections.

Before studying each of the Lagrangians, let us recall that the mass splitting of the antidecuplet has a contribution which follows the GMO rule, and it would be originated by the difference of the masses of the constituent quarks and their correlations. To this, we add the splitting coming from the real part of the self-energy due to the meson cloud that we are studying. Thus, the masses of the antidecuplet are approximately given by

$$\begin{aligned}
M_{\Theta_{\overline{\mathbf{10}}}}=&M_0+\mathrm{Re}\Sigma_{\Theta_{\overline{\mathbf{10}}}},\\
M_{N_{\overline{\mathbf{10}}}}=&M_0+\mathrm{Re}\Sigma_{N_{\overline{\mathbf{10}}}}+\Delta,\\
M_{\Sigma_{\overline{\mathbf{10}}}}=&M_0+\mathrm{Re}\Sigma_{\Sigma_{\overline{\mathbf{10}}}}+2\Delta,\\
M_{\Xi_{\overline{\mathbf{10}}}}=&M_0+\mathrm{Re}\Sigma_{\Xi_{\overline{\mathbf{10}}}}+3\Delta,
\end{aligned}\tag{9.4.1}$$

where M_0 is the bare mass of the antidecuplet and Δ is the GMO mass splitting, part of which simply comes from the difference of the constituent quark masses. In the constituent quark model, Δ is related to the difference between the constituent masses of u, d and s

quarks, $3\Delta = \langle m_s - m_{u,d}\rangle_{\rm baryon}$. Certainly, quark correlations can also contribute to the experimental value of Δ.

The difference between the light and strange quark masses has been obtained, for example from hyperfine splittings, in Ref. [648],

$$\langle m_s - m_u\rangle_{\rm meson} = \frac{3(M_{K^*} - M_\rho) + (M_K - M_\pi)}{4} \simeq 180 \text{ MeV}, \tag{9.4.2}$$

whereas for baryons

$$\begin{aligned}\langle m_s - m_u\rangle_{\rm baryon} =& M_\Lambda - M_N \simeq 177 \text{ MeV},\\ \langle m_s - m_u\rangle_{\rm baryon} =& \frac{M_N + M_\Delta}{6}\left(\frac{M_\Delta - M_N}{M_{\Sigma^*} - M_\Sigma} - 1\right) \simeq 190 \text{ MeV}.\end{aligned}$$

But other differences like $M_{K^*} - M_\rho$, $M_\Xi - M_N$ or $M_\Sigma - M_N$ suggest a wider range, from 122 to 190 and 250 MeV, respectively. As we will see, the values of 3Δ needed within this work are of this order of magnitude but somewhat larger, leaving room for extra quark correlations effects.

9.4.1 Antidecuplet mass shift with $\mathcal{L}^{8s}$ and $\mathcal{L}^{8a}$

To fix the couplings of the Lagrangians, we start by taking $\mathcal{L}^{8s}$ and $\mathcal{L}^{8a}$ defined above and adjusting the coupling constants to obtain the partial decay widths of the $N(1710)$ to $N\pi\pi$(s wave, isoscalar) and $N\rho \to N\pi\pi$(p wave, isovector) respectively. These are controlled by the imaginary part of the self-energies (9.3.7), which are finite and independent of the cutoff. The central values in the Particle Data Group (PDG) [144] are

$$\Gamma(N\pi\pi, s \text{ wave}) = 25 \text{ MeV}, \quad \Gamma(N\pi\pi, p \text{ wave}) = 15 \text{ MeV},$$

and the uncertainties (counting those of the branching ratio and the total width) can be a large fraction of these numbers.

A fit to these central values gives us

$$g^{8s} = 1.9, \quad g^{8a} = 0.32. \tag{9.4.3}$$

With these couplings, we calculate the real part of the self-energies for all the antidecuplet. For the bare antidecuplet mass p^0 as input, we take an average value of $p^0 = 1700$ MeV. We also performed a calculation with different values of p^0 and found that the results have the same qualitative trend, but the depth of the binding varies. To estimate the binding, we show the mass shift from the $\mathcal{L}^{8s}$ with respect to p^0 in Fig. 9.3. We see that, independently of the values of p^0, all the self-energies are attractive, and that the interaction is more attractive the larger the strangeness; hence, the $\Theta_{\overline{\mathbf{10}}}$ is always more bound.

In Fig. 9.4 we show the results for the contributions from $\mathcal{L}^{8s}$ and total contributions of $\mathcal{L}^{8a}$ and $\mathcal{L}^{8s}$, with $p^0 = 1700$ MeV and cutoffs 700 and 800 MeV. The numerical values of the mass shifts are displayed in Table 9.1. We see that $\mathcal{L}^{8s}$ provides more binding than $\mathcal{L}^{8a}$ for the same cutoff. The total binding for $\Theta_{\overline{\mathbf{10}}}$ ranges from 90 to about 130 MeV, depending on the cutoff. The splitting between the $\Theta_{\overline{\mathbf{10}}}$ and $\Xi_{\overline{\mathbf{10}}}$ states is about 45 MeV for a cutoff of

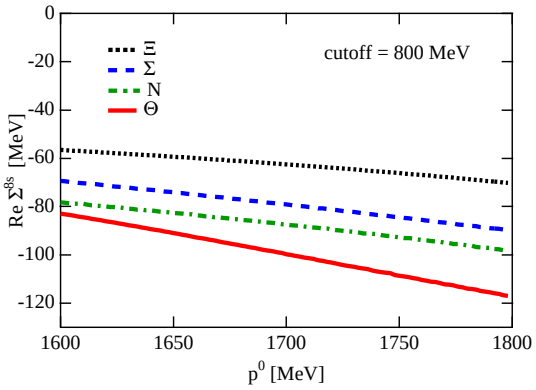

Figure 9.3: Mass shifts of baryon antidecuplet ($\mathrm{Re}\Sigma_P$) due to two-meson cloud from $\mathcal{L}^{8s}$ with cutoff = 800 MeV; p^0 dependence.

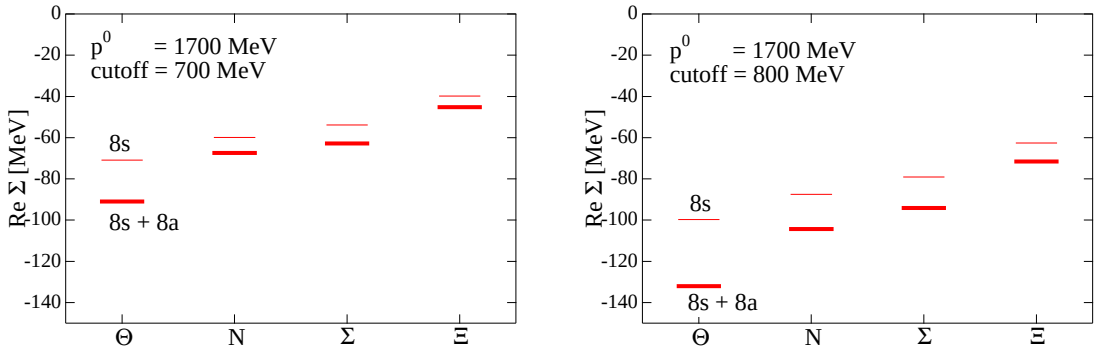

Figure 9.4: Mass shifts of baryon antidecuplet ($\mathrm{Re}\Sigma_P$) due to two-meson cloud with $p^0 = 1700$ MeV at two cutoff values. Thin lines represent the results from contributions from $\mathcal{L}^{8s}$, and thick lines denote the total contribution with $\mathcal{L}^{8s}$ and $\mathcal{L}^{8a}$.

700 MeV and 60 MeV for a cutoff of 800 MeV. Since the experimental splitting is 320 MeV for the $\Theta(1540)$ and $\Xi(1860)$, the splitting provided by the two-meson cloud is on the order of 20% of the experimental one.

We believe these magnitudes to be realistic (and hence one of the reasons to settle for a cutoff) based on the findings of Ref. [410] that the meson-baryon interaction is insufficient to bind the $K\pi N$ system and that one has to increase the interaction by about a factor of 5 to have the three-particle system bound. Indeed, had the nature of the $\Theta(1540)$ been that of the $K\pi N$ system, we would have obtained all the splitting from the two-meson cloud. There is, hence, a qualitative correlation between the moderate amount of the two-meson cloud contribution claimed here and the difficulty to make the stable $K\pi N$ system based alone on the $K\pi N$ dynamics.

Next we present the antidecuplet spectrum generated with the splitting obtained here. We take the cutoff 800 MeV for reference. Inserting $M_{\Theta_{\overline{10}}} = 1540$ MeV and $M_{\Xi_{\overline{10}}} = 1860$ MeV in Eq. (9.4.1), together with our calculated self-energies, we obtain $M_0 = 1670$ MeV and

Table 9.1: Mass shifts of baryon antidecuplet ($\mathrm{Re}\Sigma_P$) due to two-meson cloud with $p^0 = 1700$ MeV and cutoffs 700 and 800 MeV. All values are shown in units of MeV.

	cutoff 700 MeV			cutoff 800 MeV		
	$\mathcal{L}^{8s}$	$\mathcal{L}^{8a}$	total	$\mathcal{L}^{8s}$	$\mathcal{L}^{8a}$	total
$\Theta_{\overline{\mathbf{10}}}$	-71	-20	-91	-100	-32	-132
$N_{\overline{\mathbf{10}}}$	-60	-7	-67	-87	-17	-104
$\Sigma_{\overline{\mathbf{10}}}$	-54	-9	-63	-79	-15	-94
$\Xi_{\overline{\mathbf{10}}}$	-40	-5	-45	-63	-9	-72

$\Delta = 87.5$ MeV, then

$$
\begin{aligned}
M_{\Theta_{\overline{\mathbf{10}}}} &= 1540 \text{ MeV} \quad \text{(input)}, \\
M_{N_{\overline{\mathbf{10}}}} &= 1652 \text{ MeV}, \\
M_{\Sigma_{\overline{\mathbf{10}}}} &= 1749 \text{ MeV}, \\
M_{\Xi_{\overline{\mathbf{10}}}} &= 1860 \text{ MeV} \quad \text{(input)}.
\end{aligned}
$$

The value $3\Delta \sim 260$ MeV is fairly reasonable for our estimate purposes. It would indicate, however, that about 30 MeV of Δ, above the 60 MeV coming from the constituent quark consideration, would come from quark correlations. The large $\Theta_{\overline{\mathbf{10}}}$ binding with respect to that of the $N_{\overline{\mathbf{10}}}$ state is responsible for the new value $M_{N_{\overline{\mathbf{10}}}} = 1652$ MeV, slightly higher than the value we would obtain from an exact GMO rule splitting (1646 MeV), but still far from the 1710 MeV resonance we have assumed for the antidecuplet. As discussed in the introduction, a necessary mixture of an octet representation with the antidecuplet could bring the mass close to that of the $N(1710)$, although the possibility of having a new N^* resonance belonging to the antidecuplet cannot be ruled out [237].

9.4.2 Antidecuplet decay widths from $\mathcal{L}^{8s}$ and $\mathcal{L}^{8a}$

Now we show the partial decay width obtained according to Eq. (9.3.7). As already mentioned, $\Theta(1540)$ has no BMM channel to decay. Among all decay channels, the $N(1710)$ decays broadly into $N\pi\pi$, and it can also decay into $N\pi\eta$. The $\Sigma(1770)$ can decay into $N\bar{K}\pi$, $\Lambda\pi\pi$, and $\Sigma\pi\pi$, and the $\Xi(1860)$ into $\Sigma\bar{K}\pi$ and $\Xi\pi\pi$, because of the threshold energies of BMM channels.

To calculate the decay, since the phase space is essential for the imaginary part, we take the observed masses,

$$
M_{N_{\overline{\mathbf{10}}}} = 1710, \quad M_{\Sigma_{\overline{\mathbf{10}}}} = 1770, \quad M_{\Xi_{\overline{\mathbf{10}}}} = 1860. \tag{9.4.4}
$$

The results are shown in Table 9.2. We can see that the widths are not very large for all channels. Among them, we obtain the partial decay widths of the $\Sigma(1770)$ into $\Sigma\pi\pi$ and $N\bar{K}\pi$. When compared with the experimental data, indeed, the $\Sigma(1770)$ would have a total width into two-meson and baryon of about 24 MeV, which is well within the total width of the $\Sigma(1770)$ of about 70 MeV [144]. As to the $\Xi(1860)$ resonance, we obtain a total width of about 2 MeV, which is certainly compatible with the experimental total width less than

Table 9.2: Partial decay widths for the allowed channels and total width for any BMM channel, at the masses of the antidecuplet members. All values are in MeV.

Decay widths [MeV]	$\Gamma^{(8s)}$	$\Gamma^{(8a)}$	Γ^{tot}_{BMM}
$N(1710) \to N\pi\pi$ (inputs)	25	15	40
$N(1710) \to N\eta\pi$	0.58	-	
$\Sigma(1770) \to N\bar{K}\pi$	4.7	6.0	24
$\Sigma(1770) \to \Sigma\pi\pi$	10	0.62	
$\Sigma(1770) \to \Lambda\pi\pi$	-	2.9	
$\Xi(1860) \to \Sigma\bar{K}\pi$	0.57	0.46	2.1
$\Xi(1860) \to \Xi\pi\pi$	-	1.1	

Table 9.3: Mass shifts of baryon antidecuplet ($\mathrm{Re}\Sigma_P$) due to two-meson cloud with 800 MeV cutoff for $\mathcal{L}^{8s}$ and 525 MeV for $\mathcal{L}^{\chi}$. All values are in MeV.

Mass shifts [MeV]	$\mathcal{L}^{8s}$	$\mathcal{L}^{\chi}$
$\Theta_{\overline{\mathbf{10}}}$	-100	-99
$N_{\overline{\mathbf{10}}}$	-87	-83
$\Sigma_{\overline{\mathbf{10}}}$	-79	-70
$\Xi_{\overline{\mathbf{10}}}$	-63	-57

18 MeV claimed by the NA49 collaboration [145]. Detailed information of the partial decay widths of these resonances to three-body channels will give us more understanding of the $PBMM$ interaction.

9.4.3 Mass shifts and decay widths from $\mathcal{L}^{\chi}$

Here we show the results for the interaction Lagrangian given in subsection 9.2.6, namely the two-meson coupling derived from the chiral symmetric Lagrangian $\mathcal{L}^{\chi}$. We fix the coupling constant g^{χ} from the $N(1710)$ decay to $N\pi\pi$(s wave, isoscalar), and we find $g^{\chi} = 0.218$. Then the antidecuplet mass shifts and decay widths are calculated. However, for the mass shifts, we obtain binding energies that are too large—on the order of several hundreds MeV with cutoffs around 700-800 MeV—because the loop integral is more divergent than the previous $\mathcal{L}^{8s}$ case. To reach some reasonable results, we decrease the cutoff, and find that $\Lambda = 525$ MeV would give mass shifts similar to those of $\mathcal{L}^{8s}$ without derivatives.

We compare the mass shifts of $\mathcal{L}^{\chi}$ with cutoff 525 MeV and $\mathcal{L}^{8s}$ with 800 MeV in Table 9.3. The decay widths obtained from these Lagrangians are given in Table 9.4. As expected from the fact that the $C^{(j)}$ coefficients of two Lagrangians are identical, we obtain almost the same mass shifts for $\mathcal{L}^{\chi}$ and $\mathcal{L}^{8s}$ by properly adjusting the cutoffs. The decay widths are considered to be in fair agreement qualitatively, when considering that the values span two orders of magnitude. Some quantitative differences would come from the SU(3) breaking in the meson momenta appearing in the $\mathcal{L}^{\chi}$ loop, and they are regarded as the uncertainty in our analysis.

Table 9.4: Partial decay widths for the allowed channels with $\mathcal{L}^{8s}$ and $\mathcal{L}^{\chi}$, at the masses of the antidecuplet members. All values are in MeV.

Decay widths [MeV]	$\Gamma^{(8s)}$	$\Gamma^{(\chi)}$
$N(1710) \to N\pi\pi$ (input)	25	25
$N(1710) \to N\eta\pi$	0.58	0.32
$\Sigma(1770) \to N\bar{K}\pi$	4.7	4.5
$\Sigma(1770) \to \Sigma\pi\pi$	10	3.6
$\Xi(1860) \to \Sigma\bar{K}\pi$	0.57	0.40

9.4.4 Effects of $\mathcal{L}^{27}$ and $\mathcal{L}^{M}$

Next we draw our attention to the $\mathcal{L}^{27}$ and $\mathcal{L}^{M}$ Lagrangians, that we have not yet used. First note that it is unrealistic to make these Lagrangians solely responsible for the N(1710) decay width into $N\pi\pi(s$ wave) channel. This would lead to some unphysical results such as very large decay widths of the $\Xi_{\overline{\mathbf{10}}}$ into BMM channels, or a large binding energy of several hundred MeV. Hence, combined with the analyses in the previous section, this fact would justify the approach followed in Ref. [413], where only the $\mathcal{L}^{8s}$ and $\mathcal{L}^{8a}$ terms are taken to study the Θ^{+} self-energies in a nuclear medium. Thus, assuming that one should not have a large contribution from these Lagrangians, we will determine to what extent we can allow the contributions from $\mathcal{L}^{27}$ and $\mathcal{L}^{M}$.

We first pursue a model that mixes $\mathcal{L}^{8s}$ and $\mathcal{L}^{27}$. The coupling constants should be determined such that the decay width of $N_{\overline{\mathbf{10}}} \to N\pi\pi(s\text{-wave})$ is unchanged. According to Table D.21, the $C^{(j)}_{B,m_1,m_2}$ coefficients for $N_{\overline{\mathbf{10}}} \to N\pi\pi$ channels are

$$C^{8s}_{p\pi^0\pi^0} = \frac{1}{\sqrt{2}}, \quad C^{27}_{p\pi^0\pi^0} = -\frac{2\sqrt{2}}{5},$$
$$C^{8s}_{p\pi^+\pi^-} = \sqrt{2}, \quad C^{27}_{p\pi^+\pi^-} = -\frac{4\sqrt{2}}{5}.$$

To see the contribution from each Lagrangian clearly, we set $g^{8s} = g^{27} = 1.88$, and take the combination

$$a\mathcal{L}^{8s} + b\mathcal{L}^{27}, \quad b = -\frac{5}{4}(1-a).$$

In this case,

$$C^{8s+27}_{p\pi^0\pi^0} = \frac{1}{\sqrt{2}}a - \frac{2\sqrt{2}}{5} \times \left(-\frac{5}{4}(1-a)\right) = \frac{1}{\sqrt{2}},$$
$$C^{8s+27}_{p\pi^+\pi^-} = \sqrt{2}a - \frac{4\sqrt{2}}{5} \times \left(-\frac{5}{4}(1-a)\right) = \sqrt{2},$$

and, therefore, we have the same $N(1710) \to N\pi\pi(s$ wave) decay independent of a, but different decays into other channels. With this parametrization, $a = 1$ corresponds to the limit where $\mathcal{L}^{27}$ is switched off, while $a = 0$ relates to the $\mathcal{L}^{27}$ contribution only. We vary

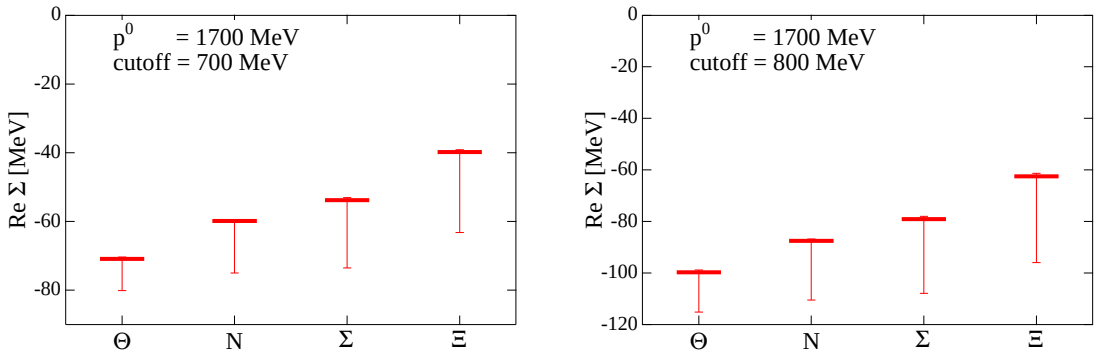

Figure 9.5: Mass shifts of baryon antidecuplet due to two-meson cloud from $\mathcal{L}^{8s}$ and possible $\mathcal{L}^{27}$ contributions with two cutoff values. Horizontal bar: results with $\mathcal{L}^{8s}$ only. Vertical bar: band of values including $\mathcal{L}^{27}$ in the range of the text.

a around 1 and find that for $0.90 < a < 1.06$ the results of the self-energy are acceptable on physical grounds. If we exceed this range, the splitting of the different strangeness states of the antidecuplet spoils agreement with the GMO rule. Taking this range of acceptable values of a into account, we find the results for the binding energies shown in Fig. 9.5. As we see in the figure, $\mathcal{L}^{27}$ tends to contribute to make the binding energy deeper. A possible contribution from $\mathcal{L}^{27}$ would be considered as a theoretical uncertainty in our analysis.

Next we address the $\mathcal{L}^{M}$ term. Once again, as in the $\mathcal{L}^{27}$ case, we set $g^{8s} = g^{M} = 1.88$ and take the combination

$$a\mathcal{L}^{8s} + b\mathcal{L}^{M}, \quad b = \frac{f^2}{m_\pi^2}(1-a), \tag{9.4.5}$$

in order to have the same $N(1710) \to N\pi\pi(s \text{ wave})$. In this case, we also see that the values of $0.76 < a < 1.06$ are acceptable on physical grounds, but larger deviations of a again lead to undesired signs of the splitting between the members of the antidecuplet, as well as to unacceptably large results of the binding energies. Within this interval of coupling constant, the results obtained for the binding energies of the antidecuplet members are given in Fig. 9.6. We observe that $\mathcal{L}^{M}$ also contributes to attractive binding energy, and the splitting of $\Theta_{\overline{\mathbf{10}}}$ and $N_{\overline{\mathbf{10}}}$ becomes large compared with the other splittings.

9.5 Discussion and conclusion

In this chapter we have studied two meson contributions to the self-energies of the antidecuplet baryons based on flavor SU(3) symmetry. We have assumed that the Θ^+ is a $1/2^+$ state with $I = 0$ and that it belongs to an antidecuplet. In addition to these minimal assumptions, we consider that the $N(1710)$ also belongs to this same antidecuplet. The meson cloud mechanism proposed in this chapter leads, in all different cases studied, to the following conclusions:

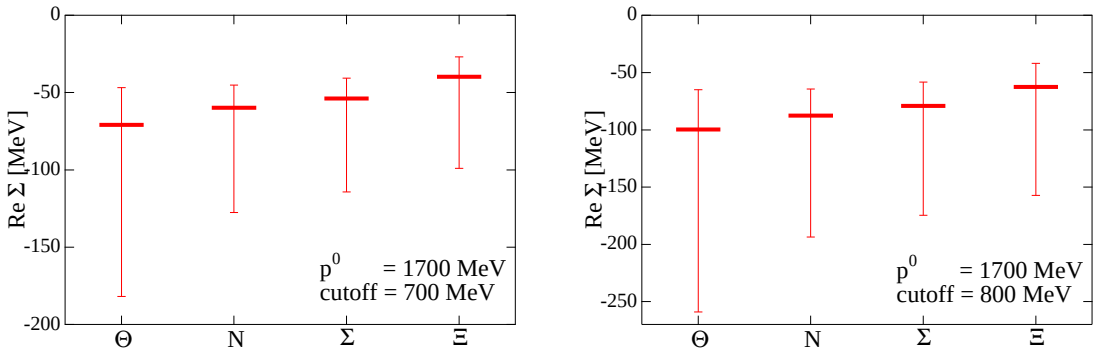

Figure 9.6: Mass shifts of baryon antidecuplet due to two-meson cloud from $\mathcal{L}^{8s}$ and possible $\mathcal{L}^{M}$ contributions with two cutoff values. Horizontal bar: results with $\mathcal{L}^{8s}$ only. Vertical bar: band of values including $\mathcal{L}^{M}$ in the range of the text.

1. The two-meson cloud yields an attractive self-energy for all members of the antidecuplet. The observation of attraction is consistent with the previous attempts to describe the Θ^+ as a $K\pi N$ state [407, 411, 410, 408], although the present study introduce the explicit (kernel) field, which is absent in the previous studies to construct the three-body bound state.

2. It also contributes to the splitting between antidecuplet members, which is only moderately cutoff dependent. The two-meson cloud provides about 20% of the total splitting for reasonable values of the cutoff. The role played by the two-meson cloud is therefore of relevance for a precise understanding of the nature of the Θ^+ and the antidecuplet.

3. The magnitude of 20% is also in agreement quantitatively with the strength of attraction found in the previous study of BMM three-body system [410]. The values of the mass splitting are such that they still leave some room for quark correlation effects after the GMO mass splitting coming from the mass difference between u, d and s constituent quarks is considered. The contribution to the splitting from the meson cloud is of the same order of magnitude as the one provided by these quark correlations.

4. By calculating all the members of SU(3) multiplet, it is found that the non-exotic members such as N and Σ have substantial two-meson cloud component. Since the input of the present study is the $N \to \pi\pi N$ decay, this conclusion may hold when we assign the $N(1710)$ as an octet.

The models we work with in this chapter are rather phenomenological. However, our method, based on symmetry principles, is suited to at least estimating meson cloud effects, which are important for the understanding of pentaquark properties. The main conclusion of this chapter is that the virtual "two-meson cloud" yields an attractive self-energy that provides about 20% of the pentaquark mass splittings. From the experimental point of view, it is clear that the investigation of the decay channels into two mesons and a baryon of the resonances

$N(1710)$, $\Sigma(1770)$, and $\Xi(1860)$ deserves renewed interest. We believe that our study here will become useful when more data are available.

Chapter 10

Phenomenology of spin 3/2 baryons with pentaquarks

In this chapter, using a general framework based on the flavor symmetry, we examine several assignments of spin and parity for the pentaquark Θ^+ state ($J^P = 1/2^\pm, 3/2^\pm$) in connection with known baryon resonances. Assuming that the Θ^+ belongs to an antidecuplet representation which mixes with an octet, we calculate the mass spectra of the flavor partners of the Θ^+ based on the SU(3) symmetry. The decay widths of the Θ^+ and nucleon partners are analyzed for the consistency check of the mixing angle obtained from the masses. It is found that a suitable choice of the mixing angle successfully reproduces the observed masses of $\Theta(1540)$ and $\Xi_{3/2}(1860)$, when their spin and parity are assigned to be $J^P = 3/2^-$, together with other nonexotic resonances of $J^P = 3/2^-$. The decay widths of $\Theta \to KN$, $N(1520) \to \pi N$, and $N(1700) \to \pi N$ are also reproduced simultaneously. This topic is reported in Ref. [24].

10.1 Introduction

In the study of the exotic particles, it is important to consider simultaneously other members with nonexotic flavors in the same SU(3) multiplet which the exotic particles belong to. The identification of the flavor multiplet provides the foundation of the model calculation, for instance, when one tries to construct an effective Lagrangian as in the previous chapters. From the successes of SU(3) flavor symmetry with its breaking in hadron masses and interactions [649], it is naively expected that the exotic states also follows the symmetry relations. In other words, the existence of exotic particles would require the flavor partners, if the flavor SU(3) symmetry plays the same role as in the ordinary three-quark baryons.

To start with, we assume that $\Theta(1540)$ [16] and $\Xi_{3/2}(1860)$ [145] do exist at these energies, despite the controversial situation of experiments[A)]. However, the symmetry relations we derive here are rather general, and can be applied to any exotic states once they are assumed to belong to the same SU(3) representations. Therefore, when any other exotic particles (with the quantum number of Θ^+ or Ξ^{--}) are found experimentally in future, we can immediately

[A)] In this section we refer to the $S = -2$ and $I = 3/2$ exotic state as $\Xi_{3/2}(1860)$ or Ξ^{--}, although the particle is denoted as $\Phi(1860)$ in PDG [144].

apply the formulae to these states.

Concerning the representation that the Θ^+ belongs to, there are several conjectures in model calculations. In the chiral soliton models [77], the Θ^+ and Ξ^{--} belong to the antidecuplet ($\overline{\mathbf{10}}$) representation with spin and parity $J^P = 1/2^+$. An interesting proposal was made by Jaffe and Wilczek [344] in a quark model with diquark correlation. The model is based on the assumption of the strong diquark correlation in hadrons and the representation mixing of an octet ($\mathbf{8}$) with an antidecuplet ($\overline{\mathbf{10}}$). The attractive diquark correlation in the scalar-isoscalar channel leads to again $J^P = 1/2^+$ for the Θ^+. With the ideal mixing of $\mathbf{8}$ and $\overline{\mathbf{10}}$, in which states are classified by the number of strange and anti-strange quarks, $N(1710)$ and $N(1440)$ resonances are well fit into members of the multiplet together with the Θ^+. However, it was pointed out that mixing angles close to the ideal one encountered a problem in the decay pattern of $N(1710) \to \pi N$ and $N(1440) \to \pi N$. Rather, their decays implied a small mixing angle [348, 349, 350]. This is intuitively understood by observing the broad decay width of $N(1440) \to \pi N$ and the narrow widths of $N(1710) \to \pi N$ and $\Theta \to KN$ [347, 348].

At this stage, it is worth noting that the flavor SU(3) symmetry itself does not constrain the spin and parity. Therefore, employing the $\mathbf{8}$-$\overline{\mathbf{10}}$ mixing scenario which is the minimal scheme to include the Θ^+ and Ξ^{--}, here we examine the possibilities to assign other quantum numbers, such as $1/2^-$, $3/2^+$, $3/2^-$, and search for the nucleon partners among the known resonances. Although the formulae are already given previously, they are applied mainly to the $J^P = 1/2^+$ case, and sometimes to the $J^P = 1/2^-$. The spin 3/2 states are rarely examined. This is natural because the lower spin states are expected to be lighter. However, once again, the flavor symmetry is nothing to do with the spin and parity by itself, therefore we investigate the $J^P = 3/2^\pm$ states as well. Indeed, we find a natural solution consistent with both the masses and widths in the $3/2^-$ case. For convenience, properties of relevant resonances are summarized in Appendix E.3.

The present study is based on the flavor SU(3) symmetry, experimental mass spectra and decay widths of the Θ^+, the Ξ^{--} and known baryon resonances. Hence, our analysis presented here is phenomenological, but does not rely upon any specific models. For instance, we do not have to specify the quark contents of the baryons. Although the exotic states require minimally five quarks, nonexotic partners do not have to. Instead, we expect that the resulting properties such as masses and decay rates reflect information from which we hope to learn internal structure of the baryons.

10.2 Analysis with pure antidecuplet

First we briefly discuss the case where the Θ^+ belongs to the pure $\overline{\mathbf{10}}$ without mixing with other representations. In this case, the masses of particles belonging to the $\overline{\mathbf{10}}$ can be determined by the Gell-Mann–Okubo (GMO) mass formula with equal splitting

$$M(\overline{\mathbf{10}}; Y) \equiv \langle\, \overline{\mathbf{10}}; Y \,|\mathcal{H}|\, \overline{\mathbf{10}}; Y \,\rangle = M_{\overline{\mathbf{10}}} - aY, \tag{10.2.1}$$

where Y is the hypercharge of the state, and $\mathcal{H}$ denotes the mass matrix. Note that at this point the spin and parity J^P are not yet specified. The quantum numbers will be assigned

Table 10.1: Summary of subsection 10.2. Masses and Θ^+ decay widths are shown for several assignments of quantum numbers. For $1/2^-$ the masses of Θ and $\Xi_{3/2}$ are the input parameters, while for $1/2^+, 3/2^\pm$, the masses of Θ and N are the input parameters. Values in parenthesis are the predictions, and we show the candidates to be assigned for the states. All values are listed in units of MeV.

J^P	M_Θ	M_N	M_Σ	M_Ξ	Γ_Θ
	1540	[1647]	[1753]	1860	
$1/2^-$		$N(1650)$	$\Sigma(1750)$		$156.1\ ^{+90.8}_{-73.3}$
	1540	1710	[1880]	[2050]	
$1/2^+$			$\Sigma(1880)$	$\Xi(2030)$	$7.2\ ^{+15.3}_{-4.6}$
	1540	1720	[1900]	[2080]	
$3/2^+$			-	-	$10.6\ ^{+7.0}_{-5.0}$
	1540	1700	[1860]	[2020]	
$3/2^-$			-	$\Xi(2030)$	$1.3\ ^{+1.2}_{-0.9}$

as explained below.

In Eq. (10.2.1), there are two parameters, $M_{\overline{\mathbf{10}}}$ and a, which are not determined by the flavor SU(3) symmetry. However, we can estimate the values of these parameters by considering their physical meaning in some models. For instance, in a constituent quark model, $\overline{\mathbf{10}}$ can be minimally expressed as four quarks and one antiquark. Therefore, $M_{\overline{\mathbf{10}}}$ should be larger than the masses of three-quark baryons, such as the lowest-lying octet baryons. In this picture, the mass difference of $\Xi(ssqq\bar{q})$ and $\Theta(qqqq\bar{s})$, namely $3a$, should be the constituent mass difference of the s and the ud quarks, which is about 100-250 MeV [21]. On the other hand, in the chiral quark soliton model, $3a$ is related to the pion nucleon sigma term [316]. In this picture $3a$ can take values in the range of 300-400 MeV, due to the experimental uncertainty of the pion nucleon sigma term $\Sigma_{\pi N}$ =64-79 MeV [236, 284]. Note that in the chiral quark model, spin and parity are assigned as $J^P = 1/2^+$ for the antidecuplet.

Taking into account the above estimation, we test several parameter sets fixed by the experimentally known masses of particles. The results are summarized in Table 10.1. First, we determine the parameters by accommodating $\Theta(1540)$ and $\Xi(1860)$ in the multiplet. In this case we obtain the mass of the N and Σ states at 1647 and 1753 MeV, respectively. Since these values are close to the masses of the $1/2^-$ baryons $N(1650)$ and $\Sigma(1750)$, we expect their spin and parity to be $J^P = 1/2^-$. For $J^P = 1/2^+$, we adopt the $N(1710)$ as the nucleon partner, and predict the Σ and Ξ states. This assignment corresponds to the original assignment of the prediction [77]. For $J^P = 3/2^+$, we pick up $N(1720)$, and for $J^P = 3/2^-$, $N(1700)$. In the three cases of $J^P = 1/2^+, 3/2^\pm$, the exotic Ξ resonance is predicted to be higher than 2 GeV, and the inclusion of $\Xi(1860)$ in the same multiplet seems to be difficult. Furthermore, the Σ states around 1.8-1.9 GeV are not well assigned (either two-star for $J^P = 1/2^+$, or not seen for $J^P = 3/2^\pm$). Therefore, fitting the masses in the pure antidecuplet scheme seems to favor $J^P = 1/2^-$.

Next we study the decay width of the N^* resonances with the above assignments. For the

decay of a resonance R, we define the dimensionless coupling constant g_R by

$$\Gamma_R \equiv g_R^2 F_I \frac{p^{2l+1}}{M_R^{2l}}, \tag{10.2.2}$$

where p is the relative three momentum of the decaying particles in the resonance rest frame, l is the angular momentum of the decaying particles, Γ_R and M_R are the decay width and the mass of the resonance R. F_I is the isospin factor, which takes the value 2 for $\Theta \to KN$ and 3 for $N^* \to \pi N$. This formula contains the correct l dependence, and it can be obtained from the general expression given in Appendix A.4.1. Assuming flavor SU(3) symmetry, a relation between the coupling constants of $\Theta \to KN$ and $N^* \to \pi N$ is given by:

$$g_{\Theta KN} = \sqrt{6} g_{N^*\pi N}. \tag{10.2.3}$$

Here we adopt the definition of the coupling constant in Ref. [248]. Note that this definition is different from Refs. [348, 349], in which $g \equiv \sqrt{g_R^2 F_I}$ is used. With these formulae (10.2.2) and (10.2.3), we calculate the decay width of the Θ^+ from those of $N^* \to \pi N$ of the nucleon partner, which is determined from the mass analysis. Results are also shown in Table 10.1. We quote the errors coming from experimental uncertainties in the total decay widths and branching ratios, taken from the Particle Data Group [144]. It is easily seen that as the partial wave of the two-body final states becomes higher, the decay width of the resonance becomes narrower, due to the effect of the centrifugal barrier. Considering the experimental width of the Θ^+, the results of $J^P = 3/2^-$, $3/2^+$, $1/2^+$ are acceptable, but the result of the $J^P = 1/2^-$ case, which is of the order of hundred MeV, is unrealistic.

In summary, it seems difficult to regard the Θ^+ as a member of the pure antidecuplet $\overline{\mathbf{10}}$ together with known resonances of $J^P = 1/2^\pm, 3/2^\pm$, when we want to explain both their masses and decay widths.

10.3 Analysis with octet-antidecuplet mixing

In this section we consider the representation mixing between $\overline{\mathbf{10}}$ and $\mathbf{8}$. In principle, it is possible to take into account the mixing with multiplets of higher dimension, such as $\mathbf{27}$ and $\mathbf{35}$. However, particles in such higher representations will have heavier masses. Furthermore, the higher representations bring more states with exotic quantum numbers, which are not controlled by the known experimental information. Here we work under the assumption of minimal $\mathbf{8}$-$\overline{\mathbf{10}}$ mixing. Also we do not consider the possible mixing with other octets, such as ground states [351].

The nucleon and Σ states in the $\mathbf{8}$ will mix with the states in the $\overline{\mathbf{10}}$ of the same quantum numbers. Denoting the mixing angles of the N and the Σ as θ_N and θ_Σ, the physical states are represented as

$$\begin{aligned} |\, N_1 \,\rangle &= |\, \mathbf{8}, N \,\rangle \cos\theta_N - |\, \overline{\mathbf{10}}, N \,\rangle \sin\theta_N, \\ |\, N_2 \,\rangle &= |\, \overline{\mathbf{10}}, N \,\rangle \cos\theta_N + |\, \mathbf{8}, N \,\rangle \sin\theta_N, \end{aligned} \tag{10.3.1}$$

and

$$
\begin{aligned}
|\,\Sigma_1\,\rangle &= |\,\mathbf{8},\Sigma\,\rangle\cos\theta_\Sigma - |\,\overline{\mathbf{10}},\Sigma\,\rangle\sin\theta_\Sigma,\\
|\,\Sigma_2\,\rangle &= |\,\overline{\mathbf{10}},\Sigma\,\rangle\cos\theta_\Sigma + |\,\mathbf{8},\Sigma\,\rangle\sin\theta_\Sigma.
\end{aligned}
\tag{10.3.2}
$$

To avoid redundant duplication, the domain of the mixing angles is restricted in $0 \le \theta < \pi/2$, and we will find solutions for N_1 and Σ_1 lighter than N_2 and Σ_2, respectively. The reason for these restrictions is explained in Appendix E.2.

When we construct $\overline{\mathbf{10}}$ and $\mathbf{8}$ from five quarks, the eigenvalues of the strange quark (antiquark) number operator n_s of nucleon states become fractional. In the scenario of the ideal mixing of Jaffe and Wilczek, the physical states are given as

$$
\begin{aligned}
|\,N_1\,\rangle &= \sqrt{\frac{2}{3}}|\,\mathbf{8},N\,\rangle - \sqrt{\frac{1}{3}}|\,\overline{\mathbf{10}},N\,\rangle,\\
|\,N_2\,\rangle &= \sqrt{\frac{2}{3}}|\,\overline{\mathbf{10}},N\,\rangle + \sqrt{\frac{1}{3}}|\,\mathbf{8},N\,\rangle,
\end{aligned}
$$

such that $\langle\, N_1\,|n_s|\,N_1\,\rangle = 0$ and $\langle\, N_2\,|n_s|\,N_2\,\rangle = 2$. In this case, the mixing angle is

$$
\theta_N \sim 35.2^\circ. \tag{10.3.3}
$$

This value will be compared with the angle obtained from the mass spectrum of known resonances. In the Jaffe-Wilczek model [344], $N(1440)$ and $N(1710)$ are assigned to N_1 and N_2, respectively. Notice that the separation of the $s\bar{s}$ component in the ideal mixing is only meaningful for mixing between five-quark states, while the number of quarks in the baryons is arbitrary in the present general framework.

It is worth mentioning that the mixing angle θ_N for $1/2^+$ case is calculated through the dynamical study of constituent quark model [397]. The resulting value is $\theta_N \sim 35.34^\circ$, which is very close to the ideal mixing angle (10.3.3).

10.3.1 Mass spectrum

Let us start with the GMO mass formulae for $\overline{\mathbf{10}}$ and $\mathbf{8}$:

$$
M(\overline{\mathbf{10}};Y) \equiv \langle\, \overline{\mathbf{10}};Y\,|\mathcal{H}|\,\overline{\mathbf{10}};Y\,\rangle = M_{\overline{\mathbf{10}}} - aY, \tag{10.3.4}
$$

$$
M(\mathbf{8};I,Y) \equiv \langle\, \mathbf{8};I,Y\,|\mathcal{H}|\,\mathbf{8};I,Y\,\rangle = M_{\mathbf{8}} - bY + c\left[I(I+1) - \frac{1}{4}Y^2\right], \tag{10.3.5}
$$

where Y and I are the hypercharge and the isospin of the state. Under representation mixing as in Eqs. (10.3.1) and (10.3.2), the two nucleons $(N_{\mathbf{8}}, N_{\overline{\mathbf{10}}})$ and the two sigma states $(\Sigma_{\mathbf{8}}, \Sigma_{\overline{\mathbf{10}}})$ mix, and their mass matrices are given by 2×2 matrices. The diagonal components are given by Eqs. (10.3.4) and (10.3.5), while the off-diagonal elements are given as

$$
\langle\, \mathbf{8},N\,|\mathcal{H}|\,\overline{\mathbf{10}},N\,\rangle = \langle\, \mathbf{8},\Sigma\,|\mathcal{H}|\,\overline{\mathbf{10}},\Sigma\,\rangle \equiv \delta.
$$

The equivalence of the two off-diagonal elements can be verified when the symmetry breaking term is given by λ_8 due to a finite strange quark mass [236].

The physical states $|\,N_i\,\rangle$ and $|\,\Sigma_i\,\rangle$ diagonalize $\mathcal{H}$. Therefore, we have the relations

$$\tan 2\theta_N = \frac{2\delta}{M_{\overline{\mathbf{10}}} - M_{\mathbf{8}} - a + b - \frac{1}{2}c},$$

and

$$\tan 2\theta_\Sigma = \frac{2\delta}{M_{\overline{\mathbf{10}}} - M_{\mathbf{8}} - 2c}.$$

Now we have the mass formulae for the states

$$\begin{aligned}
M_\Theta =& M_{\overline{\mathbf{10}}} - 2a, \\
M_{N_1} =& \left(M_{\mathbf{8}} - b + \frac{1}{2}c\right)\cos^2\theta_N + (M_{\overline{\mathbf{10}}} - a)\sin^2\theta_N \\
& - \delta\sin 2\theta_N, \\
M_{N_2} =& \left(M_{\mathbf{8}} - b + \frac{1}{2}c\right)\sin^2\theta_N + (M_{\overline{\mathbf{10}}} - a)\cos^2\theta_N \\
& + \delta\sin 2\theta_N, \\
M_{\Sigma_1} =& (M_{\mathbf{8}} + 2c)\cos^2\theta_\Sigma + M_{\overline{\mathbf{10}}}\sin^2\theta_\Sigma - \delta\sin 2\theta_\Sigma, \\
M_{\Sigma_2} =& (M_{\mathbf{8}} + 2c)\sin^2\theta_\Sigma + M_{\overline{\mathbf{10}}}\cos^2\theta_\Sigma + \delta\sin 2\theta_\Sigma, \\
M_\Lambda =& M_{\mathbf{8}}, \\
M_{\Xi_8} =& M_{\mathbf{8}} + b + \frac{1}{2}c, \\
M_{\Xi_{\overline{\mathbf{10}}}} =& M_{\overline{\mathbf{10}}} + a.
\end{aligned}$$

We have altogether six parameters $M_{\mathbf{8}}$, $M_{\overline{\mathbf{10}}}$, a, b, c and δ. Eliminating the mixing angles and δ, we obtain a relation independent of the mixing angle [236]

$$2(M_{N_1} + M_{N_2} + M_{\Xi_8}) = M_{\Sigma_1} + M_{\Sigma_2} + 3M_\Lambda + M_\Theta.$$

Let us first examine the case of $J^P = 1/2^+$ [349]. Possible candidates for the partners of the exotic states $\Theta(1540)$ and $\Xi_{\overline{10}}(1860)$ are the following:

$$N(1440),\ N(1710),\ \Lambda(1600),\ \Sigma(1660),\ \Sigma(1880).$$

In order to fix the six parameters, we need to assign six particles as input. Using $\Theta(1540)$, $N_1(1440)$, $N_2(1710)$, $\Lambda(1600)$, $\Sigma_1(1660)$, $\Xi_{\overline{10}}(1860)$, we obtain the parameters as given in Table 10.2. The resulting mass spectrum together with the two predicted masses, $\Sigma_1 = 1894$ MeV and $\Xi_8 = 1797$ MeV, are given in Table 10.3 and also shown in the left panel of Fig. 10.1. In Fig. 10.1, the spectra from experiment and those before the representation mixing are also plotted. For reference, in Table 10.2 and 10.3 we show the parameters and masses of Ref. [349], in which all known resonances including $\Sigma(1660)$ and $\Sigma(1880)$ are used to perform the χ^2 fitting.

As we see in Table 10.3 and Fig. 10.1, even without using the Σ_2 for the fitting, this state appears in the proper position to be assigned as $\Sigma(1880)$. Taking into account the

Table 10.2: Parameters for $1/2^+$ case. All values are listed in MeV except for the mixing angles.

	$M_{\mathbf{8}}$	$M_{\overline{\mathbf{10}}}$	a	b	c	δ	θ_N	θ_Σ
This work	1600	1753.3	106.7	146.7	100.1	114.4	29.0°	50.8°
Ref. [349]	1600	1755	107	144	93	123	29.7°	41.4°

Table 10.3: Mass spectra for $1/2^+$ case. All values are listed in MeV. Values in parenthesis (Σ_2 and $\Xi_{\mathbf{8}}$ of Set 1, Ξ_8 of Ref. [349]) are predictions (those which are not used in the fitting).

	Θ	N_1	N_2	Σ_1	Σ_2	Λ	$\Xi_{\mathbf{8}}$	$\Xi_{\overline{\mathbf{10}}}$
This work	1540	1440	1710	1660	[1894]	1600	[1797]	1860
Ref. [349]	1541	1432	1718	1650	1891	1600	[1791]	1862

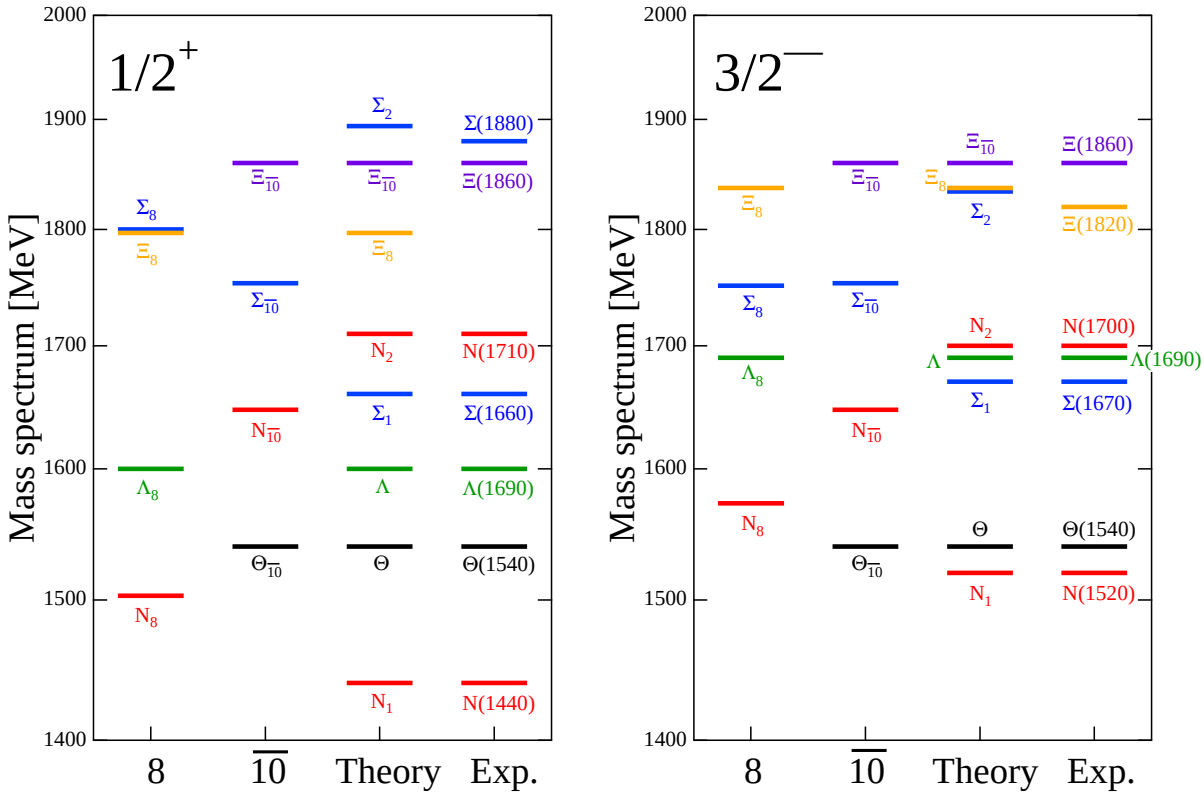

Figure 10.1: Results of mass spectra with representation mixing. Theoretical masses of the octet, antidecuplet, and the one with mixing are compared with the experimental masses. In the left panel, we show the results with $J^P = 1/2^+$, while the results with $J^P = 3/2^-$ (set 1) are presented in the right panel.

experimental uncertainty in the masses, these two parameter sets (the one determined in this work and the one in Ref. [349]) can be regarded as the same one. In both cases, we need a new Ξ state around 1790-1800 MeV, but the overall description of the mass spectrum is acceptable. Note that the mixing angle $\theta_N \sim 30^\circ$ is compatible with the one of the ideal mixing (10.3.3), if we consider the experimental uncertainty of masses [349].

It is interesting to observe that in the spectrum of the octet, as shown in Fig. 10.1, the Ξ_8 and the Σ_8 are almost degenerate, reflecting the large value for the parameter $c \sim 100$ MeV, which is responsible for the splitting of Λ and Σ. For the ground state octet, Eq. (10.3.5) is well satisfied with $b = 139.3$ MeV and $c = 40.2$ MeV [236]. This point will be discussed later.

Now we examine the other cases of J^P. For $J^P = 1/2^-$, as we observed in the previous section, the pure $\overline{\mathbf{10}}$ assignment works well for the mass spectrum, which implies that the mixing with $\mathbf{8}$ is small, as long as we adopt $N(1650)$ and $\Sigma(1750)$ in the multiplet. Then the results of $1/2^-$ with the mixing do not change from the previous results of the pure $\overline{\mathbf{10}}$ assignment, which eventually lead to a broad width of $\Theta^+ \to KN$ of order 100 MeV. Hence, it is not realistic to assign $1/2^-$, even if we consider the representation mixing.

Next we consider the $3/2^+$ case. In this case candidate states are not well established. As we see in Appendix E.3, no state exists for Σ and Ξ, except for two- or one-star resonances. Furthermore, the states are distributed in a wide energy range, and sometimes it is not possible to assign these particles in the $\mathbf{8}$-$\overline{\mathbf{10}}$ representation scheme. For instance, if we choose $N(1720)$, $N(1900)$, $\Lambda(1890)$, $\Sigma(1840)$ and exotic states, no solution is found for the mixing angle. Therefore, at this moment, it is not meaningful to study the $3/2^+$ case unless more states with $3/2^+$ will be observed.

Now we look at the $3/2^-$ case. In contrast to the $3/2^+$ case, there are several well-established resonances. Possible candidates are

$$N(1520),\ N(1700),\ \Lambda(1520),\ \Lambda(1690),\ \Sigma(1670),\ \Sigma(1940),\ \Xi(1820).$$

Following the same procedure as before, we first choose the following four resonances as inputs: $\Theta(1540)$, $N_1(1700)$, $N_2(1520)$, and $\Xi_{3/2}(1860)$. For the remaining two to determine the six parameters, we examine four different choices of Σ and Λ states;

$$\begin{aligned}
&\Sigma(1670) \quad \text{and} \quad \Lambda(1690) \quad \text{(set1)},\\
&\Sigma(1670) \quad \text{and} \quad \Lambda(1520) \quad \text{(set2)},\\
&\Sigma(1940) \quad \text{and} \quad \Lambda(1690) \quad \text{(set3)},\\
&\Sigma(1940) \quad \text{and} \quad \Lambda(1520) \quad \text{(set4)}.
\end{aligned}$$

We have obtained the parameters as given in Table 10.4, and predicted masses of other members are shown in Table 10.5. The masses of $N(1520)$ and $N(1700)$ determine the mixing angle of nucleons $\theta_N \sim 33^\circ$, which is close to the ideal one. In the parameter sets 1 and 2 (sets 3 and 4), the $\Sigma(1670)$ state of a lower mass (the $\Sigma(1940)$ state of a higher mass) is chosen but with different Λ's, $\Lambda(1690)$ and $\Lambda(1520)$. Accordingly, they predict the higher $\Sigma(1834)$ state (the lower $\Sigma(1717)$ state) with the mixing angle $\theta_\Sigma = 44.6^\circ (= 66.2^\circ)$. Interestingly, parameters of set 1 provide $M_{\Xi_8} \sim 1837$ MeV, which is close to the known three-star resonance $\Xi(1820)$ of $J^P = 3/2^-$. Parameters of set 4 predict $M_{\Xi_8} \sim 1659$ MeV,

Table 10.4: Parameters for $3/2^-$ case. All values are listed in MeV except for the mixing angles.

	$M_{\mathbf{8}}$	$M_{\overline{\mathbf{10}}}$	a	b	c	δ	θ_N	θ_Σ
set 1	1690	1753.3	106.7	131.9	30.5	82.2	33.0°	44.6°
set 2	1520	1753.3	106.7	4.4	115.5	82.2	33.0°	44.6°
set 3	1690	1753.3	106.7	170.1	106.9	82.2	33.0°	66.2°
set 4	1520	1753.3	106.7	42.6	191.9	82.2	33.0°	66.2°

Table 10.5: Mass spectra for $3/2^-$ case. All values are listed in MeV. Values in parenthesis are predictions (those which are not used in the fitting).

	Θ	N_1	N_2	Σ_1	Σ_2	Λ	$\Xi_{\mathbf{8}}$	$\Xi_{\overline{\mathbf{10}}}$
set 1	1540	1520	1700	1670	[1834]	1690	[1837]	1860
set 2	1540	1520	1700	1670	[1834]	1520	[1582]	1860
set 3	1540	1520	1700	[1717]	1940	1690	[1914]	1860
set 4	1540	1520	1700	[1717]	1940	1520	[1659]	1860

which is close to another known resonance $\Xi(1690)$. Since the J^P of this state is not known, this fitting scheme predicts J^P of $\Xi(1690)$ to be $3/2^-$. In these two cases, we have obtained acceptable assignments, especially for set 1, although a new Σ state is necessary to complete the multiplet in both cases. The spectrum of set 1 is also shown in Fig. 10.1.

Let us briefly look at the octet and antidecuplet spectra of $1/2^+$ and $3/2^-$ resonances as shown in Fig. 10.1. The antidecuplet spectrum is simple, since the GMO mass formula contains only one parameter which describes the size of the splitting. Contrarily, the octet spectrum contains two parameters which could reflect more information on different internal structure. As mentioned before, in the octet spectrum of $1/2^+$, the mass of Σ_8 is pushed up slightly above Ξ_8, significantly higher than Λ_8. This pattern resembles the octet spectrum which is obtained in the Jaffe-Wilczek model, where baryons are made with two flavor $\bar{\mathbf{3}}$ diquarks and one antiquark. In contrast, the spectrum of the octet of $3/2^-$ resembles the one of the ground state octet; we find the parameters $(b, c) = (131.9, 30.5)$ MeV, which are close to $(b, c) = (139.3, 40.2)$ MeV for the ground states. This is not far from the prediction of an additive quark model of three valence quarks. It would be interesting to investigate further the quark contents from such a different pattern of the mass spectrum.

10.3.2 Decay width

In the previous subsection, mass spectra of the $J^P = 1/2^+$ and $J^P = 3/2^-$ are reasonably well described. Here we study the consistency of the mixing angle obtained from mass spectra and the one obtained from nucleon decay widths for these two cases. Using Eq. (10.2.3), we define a universal coupling constant $g_{\overline{\mathbf{10}}}$ as

$$g_{\Theta KN} = \sqrt{6} g_{N_{\overline{\mathbf{10}}}\pi N} \equiv g_{\overline{\mathbf{10}}}.$$

Table 10.6: Experimental data for the decay of N^* resonances. We denote the total decay width and partial decay width to the πN channel as $\Gamma_{\rm tot}$ and $\Gamma_{\pi N}$, respectively. Values in parenthesis are the central values quoted in PDG [144].

J^P	Resonance	$\Gamma_{\rm tot}$ [MeV]	Fraction ($\Gamma_{\pi N}/\Gamma_{\rm tot}$)
$1/2^+$	$N(1440)$	250-450 (350)	60-70 (65) %
	$N(1710)$	50-250 (100)	10-20 (15) %
$3/2^-$	$N(1520)$	110-135 (120)	50-60 (55) %
	$N(1700)$	50-150 (100)	5-15 (10) %

Table 10.7: Decay width of Θ^+ determined from the nucleon decays and the mixing angle obtained from the mass spectra. Phase 1 corresponds to the same signs of $g_{N_{\mathbf{8}}}$ and $g_{\overline{\mathbf{10}}}$, while phase 2 corresponds to the opposite signs. All values are listed in MeV.

J^P	θ_N	Γ_Θ (Phase 1)	Γ_Θ (Phase 2)
$1/2^+$	29° (Mass)	29.1	103.3
	35.2° (Ideal)	49.3	131.8
$3/2^-$	33° (Mass)	3.1	20.0
	35.2° (Ideal)	3.9	21.3

The coupling constants of the πN decay modes from the $N_{\mathbf{8}}$, N_1, and N_2 are defined as g_{N_8}, g_{N_1}, and g_{N_2}, respectively. The coupling constants of the physical nucleons N_1 and N_2 are

$$g_{N_1} = g_{N_{\mathbf{8}}} \cos\theta_N - \frac{g_{\overline{\mathbf{10}}}}{\sqrt{6}} \sin\theta_N, \tag{10.3.6}$$

$$g_{N_2} = \frac{g_{\overline{\mathbf{10}}}}{\sqrt{6}} \cos\theta_N + g_{N_{\mathbf{8}}} \sin\theta_N, \tag{10.3.7}$$

which are related to the decay widths through Eq. (10.2.2). However, we cannot fix the relative phase between $g_{N_{\mathbf{8}}}$ and $g_{\overline{\mathbf{10}}}$. Hence, there are two possibilities of mixing angles both of which reproduce the same decay widths. In Refs. [349, 350], one mixing angle is determined by neglecting $g_{\overline{\mathbf{10}}}$ in Eqs. (10.3.6) and (10.3.7), which is considered to be small due to the narrow width of Θ^+. Here we include the effect of $g_{\overline{\mathbf{10}}}$ explicitly.

For $J^P = 1/2^+$ and $3/2^-$, we display the decay widths and branching ratios to the πN channel of relevant nucleon resonances in Table 10.6. Using the mixing angle determined from the mass spectrum and experimental information of $N^* \to \pi N$ decays, we obtain the decay width of the Θ^+ as shown in Table 10.7. The widths calculated with the ideal mixing angle are also presented for reference. Among the two values, the former corresponds to the same signs of $g_{N_{\mathbf{8}}}$ and $g_{\overline{\mathbf{10}}}$ (phase 1), while the latter to the opposite signs (phase 2).

For the $1/2^+$ case, the width is about 30 MeV when the mixing angle is determined by the mass spectrum, while about 50 MeV for the ideal mixing angle. Both values exceed the upper bound of the experimentally observed width. In contrast, the case $3/2^-$ predicts much narrower widths of the order of a few MeV both for the two mixing angles, which are compatible with the experimental upper bound of the Θ^+ width.

Alternatively, we can determine θ_N using the experimental decay widths of $\Theta \to KN$, $N_1 \to \pi N$ and $N_2 \to \pi N$. Here we choose the decay width of Θ^+ as 1 MeV. Using the central

values of the decay widths of $N(1440)$ and $N(1710)$ and the experimental uncertainty, we obtain the nucleon mixing angle for the $1/2^+$ case

$$\theta_N = 6^\circ\ {}^{+9^\circ}_{-4^\circ}, \quad \theta_N = 14^\circ\ {}^{+10^\circ}_{-4^\circ}, \tag{10.3.8}$$

where the former corresponds to the phase 1 and the latter to the phase 2. On the other hand, with $N(1520)$ and $N(1700)$, the mixing angle for the $3/2^-$ case is

$$\theta_N = 9^\circ\ {}^{+9^\circ}_{-8^\circ}, \quad \theta_N = 24^\circ\ {}^{+9^\circ}_{-9^\circ}. \tag{10.3.9}$$

For the case of $1/2^+$, the mixing angle of Eq. (10.3.8) may be compared with $\theta_N \sim 30^\circ$, which is determined from the fitting to the masses. If we consider the large uncertainty of the πN decay width of $N(1440)$, the mixing angle (10.3.8) can be 24°, which is not very far from the angle determined by the masses $\theta_N \sim 30^\circ$. On the other hand, for the case of $3/2^-$, the mixing angle (10.3.9) agrees well with the angle determined by the masses $\theta_N \sim 33^\circ$. Considering the agreement of mixing angles and the relatively small uncertainties in the experimental decay widths, the results with the $3/2^-$ case are favorable in the present fitting analysis.

10.4 Summary and discussion

We have studied masses and decay widths of the baryons belonging to the octet (**8**) and antidecuplet ($\overline{\mathbf{10}}$) based on the flavor SU(3) symmetry. As pointed out previously [348, 349, 350], it is confirmed again the inconsistency between the mass spectrum and decay widths of flavor partners in the **8**-$\overline{\mathbf{10}}$ mixing scenario with $J^P = 1/2^+$. However, the assignment of $J^P = 3/2^-$ particles in the mixing scenario well reproduced the mass spectrum as well as the decay widths of $\Theta(1540)$, $N(1520)$, and $N(1700)$. Assignment of $3/2^-$ predicts a new Σ state at around 1840 MeV, and the nucleon mixing angle is close to the one of ideal mixing. The $1/2^-$ assignment is not realistic since the widths are too large for Θ^+. In order to investigate the $3/2^+$ case, better experimental data of the resonances is needed.

The assignment of $J^P = 3/2^-$ for exotic baryons seems reasonable also in a quark model especially when narrow width of the Θ^+ is to be explained [389]. The $(0s)^5$ configuration for the $3/2^-$ Θ^+ is dominated by the K^*N configuration [399], which however cannot be the decay channel, since the total masses of K^* and N is higher than the mass of Θ^+. Hence we expect naturally (in addition to a naive suppression mechanism due to the d-wave KN decay) a strong suppression of the decay of the Θ^+. The possibility of the spin 3/2 for the Θ^+ or its excited states has been discussed not only in quark models [398, 393, 389, 399], but also in the KN potential model [404], the $K\Delta$ resonance model [414], QCD sum rule calculations [474], and lattice QCD [491, 492].

The $3/2^-$ resonances of nonexotic quantum numbers have been also studied in various models of hadrons. A conventional quark model description with a $1p$ excitation of a single quark orbit has been successful qualitatively [329]. Such three-quark states can couple with meson-baryon states which could be a source for the five- (or more-) quark content of the resonance. In the chiral unitary approach, $3/2^-$ states are generated by s-wave scattering

states of an octet meson and a decuplet baryon [561, 414, 415]. By construction, the resulting resonances are largely dominated by five-quark content. These two approaches generate octet baryons which will eventually mix with the antidecuplet partners to generate the physical baryons. In other words, careful investigation of the octet states before mixing will provide further information.

In the present phenomenological study, we have found that $J^P = 3/2^-$ seems to fit the observed data. As we have known, other identifications have been also discussed in the literature, for instance, using large N_c expansion [275, 276, 277]. It is therefore important to determine the quantum numbers of Θ^+ in experiments, not only for the exotic particles but also for the baryon spectroscopy of nonexotic particles. Study of high spin states in phenomenological models and calculations based on QCD are strongly encouraged.

Chapter 11

Two-meson couplings of the Θ^+ and application to reactions

We evaluate two-meson couplings of Θ^+, using experimental information of nucleon resonances decaying into $\pi\pi N$ channels, in which the two pions are in scalar- and vector-type correlations. We examine two assignments of spin and parity of $J^P = 1/2^+$ and $3/2^-$, for which the experimental spectra of known resonances with exotic baryons are properly reproduced by an octet-antidecuplet representation mixing scheme in previous chapter. Using the obtained coupling constants, total cross sections of the reactions $\pi^- p \to K^- \Theta^+$ and $K^+ p \to \pi^+ \Theta^+$ are calculated. Substantial interference of two terms may occur in the reaction processes for the $J^P = 1/2^+$ case, whereas the interference effect is rather small for the $3/2^-$ case. This topic is reported in Ref. [25].

11.1 Introduction

A particularly interesting property that is expected to be characteristic for exotic baryons is their strong coupling to two-meson states in transitions to an ordinary baryon, as studied in chapter 9. Studying two-meson couplings of the exotic baryon Θ^+ is important for several reasons.

First, a heptaquark model has been proposed in the early stage of development to explain a light mass and a narrow decay width [407, 411, 410, 408, 412]. Although a quantitative study—in particular with a model of hadrons where Θ^+ is regarded as a bound state of πKN system—does not work with the present knowledge of hadron interactions, a two-meson contribution to the self-energy of Θ^+ has been shown to be consistent with the expected pattern of the masses of the antidecuplet members [21].

Second, the importance of two-meson coupling has been implied from an empirical observation of the generalized OZI rule [54]. The dominance of connected quark lines favors creation of a $q\bar{q}$ pair in the transition of $\Theta^+(qqqq\bar{q}) \to N(qqq)$, which is naturally associated with couplings to two mesons, whereas couplings to a single meson are suppressed.

Finally, two-meson couplings play important roles in reaction studies. Without two-meson couplings, all the amplitudes for Θ^+ production are proportional to the $\Theta^+ KN$ coupling,

which is fixed by the very small decay width of the Θ^+. However, two-meson couplings are determined from other source as we will see in the following, independently of the $\Theta^+ KN$ coupling. Therefore, even with the extremely narrow width of Θ^+, a sizable cross section can be obtained with two-meson couplings.

In chapter 9 (Ref. [21]), an analysis of the two-meson coupling was performed in the study of the self-energy of the Θ^+, assuming that $J^P = 1/2^+$ with $N(1710)$ in the same antidecuplet ($\overline{\mathbf{10}}$). Since the Θ^+ cannot decay into $K\pi N$ channel, the coupling constants were determined from the N^* decay into the $\pi\pi N$ channel and flavor SU(3) symmetry. Two types of Lagrangians were found to be important for the self-energy of the baryon antidecuplet. It was also shown that the two-meson contribution was indeed dominant over a single-meson contribution. However, the assumption of pure $\overline{\mathbf{10}}$ may not be the case in reality.

This point was clarified in chapter 10 (Ref. [24]), where we studied the phenomenology of flavor partners for the Θ^+. We assigned the masses of experimentally known particles in an octet-antidecuplet mixing scheme, finding good fits for $J^P = 1/2^+$ and $3/2^-$. The decay width of the Θ^+ was also evaluated in the same scheme, and the $J^P = 3/2^-$ case naturally explained the narrow width, in accordance with the quark model estimation [389]. In both J^P cases, we obtained relatively large mixing angles, which implies the importance of the representation mixing.

Hence, combining these two findings, in this chapter, we would like to calculate the two-meson couplings including the representation mixing. First we determine the coupling constants of $N^* \to \pi\pi N$ from the experimental widths and separate the $\overline{\mathbf{10}}$ component from the $\mathbf{8}$ component. Then, by using SU(3) symmetry, the coupling constants of $\Theta K\pi N$ are determined for $J^P = 1/2^+$ and $3/2^-$, including representation mixing of $\mathbf{8}$ and $\overline{\mathbf{10}}$. We focus on the decay channels in which the two pions are correlated in scalar-isoscalar and vector-isovector channels, which are the main decay modes of the resonances and play a dominant role in the Θ^+ self-energy [21].

As an application of the effective Lagrangians, we perform the analysis of the $\pi^- p \to K^- \Theta^+$ and $K^+ p \to \pi^+ \Theta^+$ reactions. These reactions were studied using effective Lagrangian approaches [17, 188, 208, 190]. Experiments for $\pi^- p \to K^- \Theta^+$ have been performed at KEK [650, 131], and a high-resolution experiment for the $K^+ p \to \pi^+ \Theta^+$ reaction is ongoing. We can compare the results with these experiments.

This chapter is organized as follows. In the next section, we show the framework of representation mixing and relevant experimental information of nucleon decay. In section 9.2, the effective interaction Lagrangians for nucleons and for the antidecuplet are introduced for both $J^P = 1/2^+$ and $3/2^-$ cases. The coupling constants are determined in section. 11.4 by considering the decay widths of N^* resonances and the self-energy of the Θ^+. With the effective Lagrangians, the reaction processes $\pi^- p \to K^- \Theta^+$ and $K^+ p \to \pi^+ \Theta^+$ are analyzed in section 3.3. The final section is devoted to a summary.

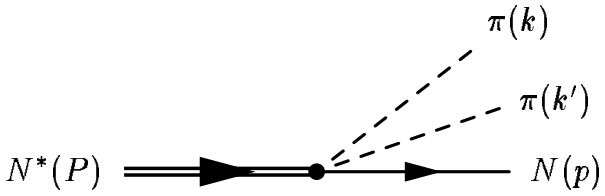

Figure 11.1: Feynman diagram for the three-body decay of the N^* resonance.

11.2 Representation mixing scheme and experimental information

Let us briefly review the representation mixing scheme in the previous chapter [24] and summarize the experimental data for the decays of nucleon resonances. We have performed a phenomenological analysis on the exotic particles using flavor SU(3) symmetry. It is found that the masses of $\Theta(1540)$ and $\Xi_{3/2}(1860)$ are well fitted into an antidecuplet ($\overline{\mathbf{10}}$) representation which mixes with an octet ($\mathbf{8}$), with known baryon resonances of $J^P = 1/2^+$ or $3/2^-$. The $1/2^-$ case gives too large a decay width for the Θ^+, and not enough resonances are well established for $3/2^+$ to complete the analysis. Under the representation mixing, the physical nucleon states are defined as

$$\begin{aligned} |\, N_1 \,\rangle &= |\, \mathbf{8}, N \,\rangle \cos\theta_N - |\, \overline{\mathbf{10}}, N \,\rangle \sin\theta_N, \\ |\, N_2 \,\rangle &= |\, \overline{\mathbf{10}}, N \,\rangle \cos\theta_N + |\, \mathbf{8}, N \,\rangle \sin\theta_N. \end{aligned} \tag{11.2.1}$$

Two states N_1 and N_2 represents $N(1440)$ and $N(1710)$ for the $1/2^+$ case and $N(1520)$ and $N(1700)$ for the $3/2^-$ case. The mixing angles θ_N can be determined by experimental spectra of known resonances as

$$\theta_N = 29^\circ \quad \text{for } J^P = 1/2^+, \quad \theta_N = 33^\circ \quad \text{for } J^P = 3/2^-. \tag{11.2.2}$$

Both angles are close to the ideal mixing $\theta_N \sim 35.2^\circ$, in which the nucleon states are classified by the number of strange quarks (antiquarks). In other words, states are well mixed and the effect of mixing of states is important.

Using these mixing angles and decay widths of nucleon resonances ($\Gamma_{N^* \to \pi N}$), we can calculate the decay width of Θ ($\Gamma_{\Theta \to KN}$) through the SU(3) relation between the coupling constants

$$g_\Theta = \sqrt{6}(g_{N_2} \cos\theta_N - g_{N_1} \sin\theta_N),$$

where g_Θ, g_{N_1}, and g_{N_2} are the coupling constants of Θ and nucleon resonances. With the known coupling constants g_{N_1} and g_{N_2}, we obtained $\Gamma_\Theta \sim 30$ MeV for $J^P = 1/2^+$ and $\Gamma_\Theta \sim 3$ MeV for $J^P = 3/2^-$. Here we extend this approach to three-body decays, as shown in Fig. 11.1.

In Table 11.1, we show the experimental information of the decay pattern of the nucleon resonances $N^* \to \pi\pi N$ taken from the Particle Data Group (PDG) [144]. For convenience, we refer to $\pi\pi(I = 0, s \text{ wave})N$ and $\pi\pi(I = 1, p \text{ wave})N$ modes as "scalar" (s) and "vector"

Table 11.1: Experimental information of two-pion decay of nucleon resonances. "Scalar" represents the mode $\pi\pi(I = 0, s \text{ wave})N$ and "Vector" means $\pi\pi(I = 1, p \text{ wave})N$ mode. Values in parenthesis are averaged over the interval quoted in PDG [144].

J^P	State	$\Gamma_{\rm tot}$ [MeV]	Scalar [%]	Vector [%]
$1/2^+$	$N(1440)$	350	5-10(7.5)	<8
	$N(1710)$	100	10-40(25)	5-25(15)
$3/2^-$	$N(1520)$	120	10-40(25)	15-25(20)
	$N(1700)$	100	< 85-95[A)]	<35

(v), respectively. There is no information for the scalar decay of $N(1700)$. PDG shows only the fraction decaying *via* the $\pi\pi N$ mode (85-95%) and an upper bound for ρN mode (<35%), although several intermediate states including $\pi\pi(I = 0, s \text{ wave})N$ are shown in the table. For the estimation of the coupling constants, we adopt the total branching ratio to $\pi\pi N$ channel as the upper limit of the branch for $\pi\pi(I = 0)N$ state, $BR_{N(1700)\to\pi\pi(I=0)N} < 85\text{-}95\%$.

11.3 Effective interaction Lagrangians

Here we write down the effective Lagrangians that account for the interactions in the present analysis. We need two steps, namely, the extraction of the $\overline{\mathbf{10}}$ component from the $N^* \to \pi\pi N$ decay and the extrapolation of that term to the $\Theta\pi KN$ channel. Lagrangians for nucleons will be used for the former purpose; the Lagrangians for the antidecuplet will tell us the SU(3) relation between channels in the multiplet.

In general, for an $N^* \to \pi\pi N$ vertex with an N^* in octet or antidecuplet representations, there are several structures of interaction Lagrangians that are SU(3) symmetric. However, for octet N^*, information of other channels are not relevant here, because we do not want to study other channels. Therefore, we write down only the $N^*\pi\pi N$ channels, instead of listing all possible Lagrangians.

Using the partial decay widths of the two nucleon resonances $\Gamma_i^{s,v}$, we determine the absolute values of the coupling constants $|g_i^{s,v}|$, where superscripts s and v stand for the scalar- and vector-type correlations of two mesons. From them, we can obtain the antidecuplet and octet components of the $N^*\pi\pi N$ coupling constants as

$$\begin{aligned} g^{s,v}(\overline{\mathbf{10}}) &= -|g_1^{s,v}|\sin\theta_N \pm |g_2^{s,v}|\cos\theta_N, \\ g^{s,v}(\mathbf{8}) &= |g_1^{s,v}|\cos\theta_N \pm |g_2^{s,v}|\sin\theta_N, \end{aligned} \tag{11.3.1}$$

based on Eq. (10.3.1). Since the relative phase of the two coupling constants cannot be determined, the $\pm$ sign appears. Here we use θ_N obtained from the mass spectra as shown in Eqs. (11.2.2). When the coupling constants have ambiguities due to experimental uncertainties, we vary the couplings $g_1^{s,v}$ and $g_2^{s,v}$ within the allowed region and check the minimum and maximum of corresponding values of $g^{s,v}(\overline{\mathbf{10}})$.

11.3.1 Lagrangians for nucleons with $J^P = 1/2^+$

Let us consider the $J^P = 1/2^+$ case. The interaction Lagrangians for nucleons can be written as

$$\mathcal{L}_i^s = \frac{g_i^s}{2\sqrt{2}f}\overline{N}_i^*\boldsymbol{\pi}\cdot\boldsymbol{\pi}N + \text{h.c.} \tag{11.3.2}$$

and

$$\mathcal{L}_i^v = i\frac{g_i^v}{4\sqrt{2}f^2}\overline{N}_i^*(\boldsymbol{\pi}\cdot\overleftrightarrow{\partial}\boldsymbol{\pi})N + \text{h.c.} = i\frac{g_i^v}{4\sqrt{2}f^2}\overline{N}_i^*(\boldsymbol{\pi}\cdot\partial\!\!\!/\boldsymbol{\pi} - \partial\!\!\!/\boldsymbol{\pi}\cdot\boldsymbol{\pi})N + \text{h.c.}, \tag{11.3.3}$$

where $f = 93$ MeV is the pion decay constant, $g_i^{s,v}$ are dimensionless coupling constants, and h.c. stands for the hermitian conjugate. Subscript $i = 1, 2$ denotes the two nucleons $N(1440)$ and $N(1710)$, respectively. The numerical factors are chosen such that the coupling constants $g_i^{s,v}$ should be consistent with the Lagrangians for the antidecuplet, which will be given later. For nucleon, N^*, and pion fields, we adopt the convention

$$N = \begin{pmatrix} p \\ n \end{pmatrix}, \quad N_i^* = \begin{pmatrix} p_i^* \\ n_i^* \end{pmatrix}, \quad \boldsymbol{\pi} = \begin{pmatrix} \pi^0 & \sqrt{2}\pi^+ \\ \sqrt{2}\pi^- & -\pi^0 \end{pmatrix}. \tag{11.3.4}$$

11.3.2 Lagrangians for the antidecuplet with $J^P = 1/2^+$

To relate the coupling constant of the process $N^*\pi\pi N$ to that of $\Theta K\pi N$, we write down the interaction Lagrangian for the antidecuplet. Flavor SU(3) structure of these terms are studied in Ref. [21]. In the present case, for the scalar-type correlation, we have

$$\mathcal{L}_{1/2^+}^s = \frac{g_{1/2^+}^s}{2f}\overline{P}_{ijk}\epsilon^{lmk}\phi_l{}^a\phi_a{}^i B_m{}^j + \text{h.c.}, \tag{11.3.5}$$

whereas for the vector-type correlation, we have

$$\mathcal{L}_{1/2^+}^v = i\frac{g_{1/2^+}^v}{4f^2}\overline{P}_{ijk}\epsilon^{lmk}\gamma^\mu(\partial_\mu\phi_l{}^a\phi_a{}^i - \phi_l{}^a\partial_\mu\phi_a{}^i)B_m{}^j + \text{h.c.} \tag{11.3.6}$$

In Eqs. (11.3.5) and (11.3.6), the coupling constants are for the antidecuplet baryon, which corresponds to Eq. (11.3.1). These Lagrangians correspond to $\mathcal{L}^{8s}$ and $\mathcal{L}^{8a}$ in Ref. [21]. The octet meson (baryon) field ϕ (B) and the antidecuplet baryon field P are defined as

$$\phi = \begin{pmatrix} \frac{1}{\sqrt{2}}\pi^0 + \frac{1}{\sqrt{6}}\eta & \pi^+ & K^+ \\ \pi^- & -\frac{1}{\sqrt{2}}\pi^0 + \frac{1}{\sqrt{6}}\eta & K^0 \\ K^- & \overline{K}^0 & -\frac{2}{\sqrt{6}}\eta \end{pmatrix},$$

$$B = \begin{pmatrix} \frac{1}{\sqrt{2}}\Sigma^0 + \frac{1}{\sqrt{6}}\Lambda & \Sigma^+ & p \\ \Sigma^- & -\frac{1}{\sqrt{2}}\Sigma^0 + \frac{1}{\sqrt{6}}\Lambda & n \\ \Xi^- & \Xi^0 & -\frac{2}{\sqrt{6}}\Lambda \end{pmatrix},$$

$$P^{333} = \sqrt{6}\Theta^+_{\overline{10}}\,,$$
$$P^{133} = \sqrt{2}\,N^0_{\overline{10}}\,, \qquad P^{233} = -\sqrt{2}\,N^+_{\overline{10}}\,,$$
$$P^{113} = \sqrt{2}\,\Sigma^-_{\overline{10}}\,, \qquad P^{123} = -\Sigma^0_{\overline{10}}\,, \qquad P^{223} = -\sqrt{2}\,\Sigma^+_{\overline{10}}\,,$$
$$P^{111} = \sqrt{6}\Xi^{--}_{\overline{10}}\,, \qquad P^{112} = -\sqrt{2}\,\Xi^-_{\overline{10}}\,, \qquad P^{122} = \sqrt{2}\,\Xi^0_{\overline{10}}\,, \qquad P^{222} = -\sqrt{6}\Xi^+_{\overline{10}}\,,$$

Note that the coefficients for $N^*\pi\pi N$ in the expansion of the Lagrangians are the same as Eqs. (11.3.2) and (11.3.3), respectively. This means that the normalization of the coupling constants in both Lagrangians are the same.

There is another Lagrangian for the scalar-type correlation $\mathcal{L}^{27}$ [21]. However, the contribution of this term can be expressed by the following parametrization:

$$a\mathcal{L}^{8s} + b\mathcal{L}^{27}, \quad b = -\tfrac{5}{4}(1-a),$$

with $g^{8s} = g^{27}$. The ratio of $\mathcal{L}^{8s}$ and $\mathcal{L}^{27}$ is controlled by the parameter a, without changing the total coupling constant of $N^*\pi\pi N$. The important point is that this combination of the two Lagrangians also does not change the $\Theta K\pi N$ channel, as we can see in the table in Appendix D.3. Therefore, in the present purpose, it is sufficient to consider the Lagrangians (11.3.5) and (11.3.6).

11.3.3 Lagrangians for nucleons with $J^P = 3/2^-$

We express the spin 3/2 baryons as Rarita-Schwinger fields B^μ [651], whose definition is given in Appendix A.1.2. The effective Lagrangians can be written as

$$\mathcal{L}^s_i = i\frac{g^s_i}{4\sqrt{2}f^2}\overline{N}^{*\mu}_i\partial_\mu(\boldsymbol{\pi}\cdot\boldsymbol{\pi})N + \text{h.c.} = i\frac{g^s_i}{4\sqrt{2}f^2}\overline{N}^{*\mu}_i(\partial_\mu\boldsymbol{\pi}\cdot\boldsymbol{\pi} + \boldsymbol{\pi}\cdot\partial_\mu\boldsymbol{\pi})N + \text{h.c.}$$

and

$$\mathcal{L}^v_i = i\frac{g^v_i}{4\sqrt{2}f^2}\overline{N}^{*\mu}_i(\boldsymbol{\pi}\cdot\overleftrightarrow{\partial_\mu}\boldsymbol{\pi})N + \text{h.c.}$$

Here $i = 1, 2$ denotes the two nucleons $N(1520)$ and $N(1700)$, respectively. Notice that a derivative of meson field is needed for the scalar Lagrangian whose Dirac index is to be contracted with that of Rarita-Schwinger field. Since the flavor structure of these Lagrangians is the same as in Eqs. (11.3.2) and (11.3.3), we will have the same flavor coefficients. The antidecuplet component of the coupling constants can be determined as in Eq. (11.3.1).

11.3.4 Lagrangians for the antidecuplet with $J^P = 3/2^-$

We write the Lagrangians for the antidecuplet as a straightforward extension of those in $1/2^+$ case:

$$\mathcal{L}^s_{3/2^-} = i\frac{g^s_{3/2^-}}{4f^2}\overline{P}^\mu_{ijk}\epsilon^{lmk}\partial_\mu(\phi_l{}^a\phi_a{}^i)B_m{}^j + \text{h.c.}$$

while for the vector type correlation we have

$$\mathcal{L}^v_{3/2^-} = i\frac{g^v_{3/2^-}}{4f^2}\overline{P}^\mu_{ijk}\epsilon^{lmk}(\partial_\mu\phi_l{}^a\phi_a{}^i - \phi_l{}^a\partial_\mu\phi_a{}^i)B_m{}^j + \text{h.c.}$$

Here the flavor structure is the same as in Eq. (11.3.6).

11.4 Evaluation of the coupling constants

To study the coupling constants, let us start with the decay width of a resonance into two mesons and one baryon, which is given by

$$\begin{aligned}\Gamma_{N\pi\pi} =& \int \frac{d^3p}{(2\pi)^3}\frac{M}{E}\int \frac{d^3k}{(2\pi)^3}\frac{1}{2\omega}\int \frac{d^3k'}{(2\pi)^3}\frac{1}{2\omega'}\overline{\Sigma}\Sigma|t(\omega,\omega',\cos\theta)|^2(2\pi)^4\delta^{(4)}(P-p-k-k')\\ =&\frac{M}{16\pi^3}\int_{\omega_{\min}}^{\omega_{\max}} d\omega\int_{\omega'_{\min}}^{\omega'_{\max}} d\omega'\overline{\Sigma}\Sigma|t(\omega,\omega',a)|^2\Theta(1-a^2),\end{aligned}$$

with

$$\begin{aligned}\omega_{\min} =&\omega'_{\min}=m,\quad \omega_{\max}=\omega'_{\max}=\frac{M_R^2-M^2-2Mm}{2M_R},\\ a =&\frac{(M_R-\omega-\omega')^2-M^2-|\boldsymbol{k}|^2-|\boldsymbol{k}'|^2}{2|\boldsymbol{k}||\boldsymbol{k}'|},\end{aligned}$$

where we assign the momentum variables $P=(M_R,\mathbf{0})$, $k=(\omega,\boldsymbol{k})$, $k'=(\omega',\boldsymbol{k}')$, and $p=(E,\boldsymbol{p})$ as in Fig. 11.1; M_R, M, and m are the masses of the resonance, baryon, and mesons, respectively; and θ is the angle between the momenta $\boldsymbol{k}$ and $\boldsymbol{k}'$. The on-shell energies of particles are given by $\omega=\sqrt{m^2+\boldsymbol{k}^2}$, $\omega'=\sqrt{m^2+(\boldsymbol{k}')^2}$, and $E=\sqrt{M^2+\boldsymbol{p}^2}$; Θ denotes the step function; and $\overline{\Sigma}\Sigma$ stands for the spin sum of the fermion states. A derivation can be found in Appendix A.4.2.

In the following, we evaluate the squared amplitude $\overline{\Sigma}\Sigma|t(\omega,\omega',\cos\theta)|^2$ for the $N^*\to\pi\pi N$ decay in the nonrelativistic approximation. For the $1/2^+$ case, from Eq. (11.3.2), the scalar Lagrangian gives the term

$$\overline{\Sigma}\Sigma|t^s_{1/2^+}|^2=3\left(\frac{g^s_{1/2^+}}{2f}\right)^2\frac{E+M}{2M}.$$

Note that we include the normalization factor $(E+M)/2M$ to be consistent with the other amplitude, although the effect of this factor is small (of the order of a few percent) in the results.

For the vector-type coupling, we insert the vector meson propagator to account for the ρ meson correlation [21], as shown in Fig. 11.2. Then the squared amplitude becomes

$$\begin{aligned}\overline{\Sigma}\Sigma|t^v_{1/2^+}|^2 =&6\left(\frac{g^v_{1/2^+}}{4f^2}\right)^2\frac{1}{2M}\Big\{(E+M)(\omega-\omega')^2+2(|\boldsymbol{k}|^2-|\boldsymbol{k}'|^2)(\omega-\omega')\\ &+(E-M)(\boldsymbol{k}-\boldsymbol{k}')^2\Big\}\times\left|\frac{-m_\rho^2}{s'-m_\rho^2+im_\rho\Gamma(s')}\right|^2,\end{aligned}\tag{11.4.1}$$

where m_ρ is the mass of ρ meson, $s'=(k+k')^2$. Furthermore, $\Gamma(s')$ is the energy-dependent width given by

$$\Gamma(s')=\Gamma_\rho\times\left(\frac{p_{\rm cm}(s')}{p_{\rm cm}(m_\rho^2)}\right)^3,$$

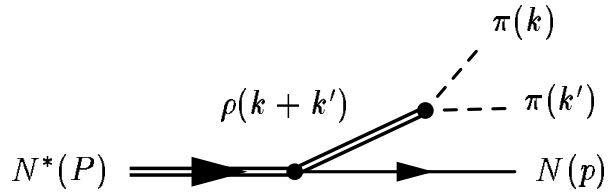

Figure 11.2: Three-body decay of the N^* resonance with insertion of the vector meson propagator.

where the relative three-momentum of the final two particles in the ρ rest frame is given by

$$p_{\rm cm}(s') = \begin{cases} \frac{\lambda^{1/2}(s', m_\pi^2, m_\pi^2)}{2\sqrt{s'}} & \text{for } s' > 4m_\pi^2, \\ 0 & \text{for } s' \leqslant 4m_\pi^2, \end{cases}$$

using the Källen function $\lambda(a, b, c)$. Note that in Eq. (11.4.1) we take the terms up to next to leading order in the nonrelativistic expansion, since the leading order term $(\omega - \omega')$ appears as the difference of two energies, which can be zero.

The squared amplitudes for $J^P = 3/2^-$ can be obtained in a similar way:

$$\overline{\Sigma}\Sigma|t^s_{3/2^-}|^2 = \left(\frac{g^s_{3/2^-}}{4f^2}\right)^2 (\boldsymbol{k} + \boldsymbol{k}')^2 \frac{E+M}{2M},$$
$$\overline{\Sigma}\Sigma|t^v_{3/2^-}|^2 = 2\left(\frac{g^v_{3/2^-}}{4f^2}\right)^2 (\boldsymbol{k} - \boldsymbol{k}')^2 \frac{E+M}{2M} \left|\frac{-m_\rho^2}{s' - m_\rho^2 + i m_\rho \Gamma(s')}\right|^2.$$

11.4.1 Numerical result for the $J^P = 1/2^+$ case

Now we evaluate the coupling constants numerically. Using the averaged values in Table 11.1, we obtain the coupling constants g^s_i and g^v_i for these channels:

$$|g^s_{N(1440)}| = 4.28, \qquad |g^v_{N(1440)}| < 3.68,$$
$$|g^s_{N(1710)}| = 1.84, \qquad |g^v_{N(1710)}| = 0.31. \tag{11.4.2}$$

By substituting them into Eq. (11.3.1) (but suppressing the label $\overline{\mathbf{10}}$ for simplicity), the antidecuplet components are extracted as

$$|g^s_{1/2^+}| = 0.47, \quad 3.68, \tag{11.4.3}$$

where two values correspond to the results with different relative phases between the two coupling constants. For $|g^v_{1/2^+}|$, only the upper bound is given for $N(1440)$; therefore we can not fix the central value.

When we take into account the experimental uncertainties in branching ratio, the antidecuplet components can vary within the following ranges:

$$0 < |g^s_{1/2^+}| < 1.37, \qquad 0 < |g^v_{1/2^+}| < 2.14,$$
$$2.72 < |g^s_{1/2^+}| < 4.42,$$

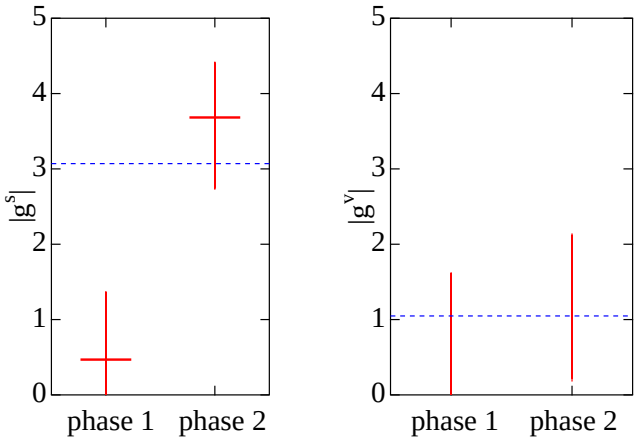

Figure 11.3: Numerical results for the coupling constants with $J^P = 1/2^+$. The two choices of the relative phase between coupling constants are marked as "phase 1" and "phase 2". Allowed regions of the coupling constants are shown by the vertical bar. Horizontal bars represent the results obtained with the averaged values, which are absent for the vector case. Horizontal dashed lines show the upper limits of the coupling constants derived from the self-energy $|\mathrm{Re}\Sigma| < 200$ MeV.

including both cases for the phase. These uncertainties are also shown by the vertical bar in Fig. 11.3, with the horizontal bars being the result with the averaged value in Eq. (11.4.3).

Now let us consider phenomenological implications of this result. In the study of self-energy [21], the coupling constants have been derived by assuming that the Θ^+ belongs to a pure antidecuplet together with $N(1710)$, where we have determined $|g^s_{1/2^+}| = 1.88$ and $|g^v_{1/2^+}| = 0.315$ (essentially the same as values in Eq. (11.4.2) and the values in Eq. (9.4.3) given in chapter 9). In the calculation of the self-energy of Θ^+, the effect of the mixing only changes the coupling constants, by neglecting the small contribution from $\mathcal{L}^{27}$. In this case, the Θ^+ self-energy with the new coupling constants can be written as

$$\Sigma^s_{\Theta^+}(g^s_{1/2^+}) = \Sigma^s_{\Theta^+}(1.88) \times \frac{|g^s_{1/2^+}|^2}{1.88^2}, \tag{11.4.4}$$

$$\Sigma^v_{\Theta^+}(g^v_{1/2^+}) = \Sigma^v_{\Theta^+}(0.315) \times \frac{|g^v_{1/2^+}|^2}{0.315^2}. \tag{11.4.5}$$

The real parts of the self-energy depend on the initial energy and the cutoff value of the loop integral. We have estimated $\mathrm{Re}\Sigma^s_{\Theta^+}(g = 1.88) \sim -75$ MeV and $\mathrm{Re}\Sigma^v_{\Theta^+}(g = 0.315)) \sim -18$ MeV for an initial energy of 1540-1700 MeV and with a cutoff of 700-800 MeV. Using Eqs. (11.4.4) and (11.4.5) with the values of Eq. (11.4.3), we obtain

$$\Sigma^s_{\Theta^+} = -287, \quad -4.7 \text{ MeV}, \qquad\qquad 0 > \Sigma^v_{\Theta^+} > -770 \text{ MeV}.$$

The sum of these values are the contribution to the self-energy of Θ^+ from the two-meson cloud. Naively, we expect that it should be of the order of 100 MeV, at most ∼20% of the

total energy [652, 21]. From this consideration, we adopt the condition that the magnitude of one of the contributions should not exceed 200 MeV: $|\mathrm{Re}\Sigma^v_{\Theta^+}| < 200$.

For the scalar coupling, this condition is satisfied when

$$|g^s_{1/2^+}| < 3.07. \tag{11.4.6}$$

Therefore, we can exclude the choice of "phase 2" in Fig. 11.3. In the same way, the upper limit of $|g^v_{1/2^+}|$ should be imposed as

$$|g^v_{1/2^+}| < 1.05 \tag{11.4.7}$$

to be consistent with the condition $|\mathrm{Re}\Sigma^v_{\Theta^+}| < 200$ MeV. This is compatible with Eq. (11.4.3), although Eq. (11.4.7) gives a more stringent constraint. These upper limits are also shown in Fig. 11.3 by the dashed lines.

11.4.2 Numerical result for the $J^P = 3/2^-$ case

Now we consider the $J^P = 3/2^-$ case. Using the central values in Table 11.1, we obtain the coupling constants g^s_i and g^v_i for these channels:

$$|g^s_{N(1520)}| = 3.56, \qquad |g^v_{N(1520)}| = 1.11,$$
$$|g^s_{N(1700)}| < 2.66, \qquad |g^v_{N(1700)}| < 0.32.$$

In this case, with the same reason as in the vector coupling for the $1/2^+$ case, the central value cannot be determined. Experimental uncertainties allows the antidecuplet components to vary within the following ranges:

$$0 < |g^s_{3/2^-}| < 4.68, \qquad 0.25 < |g^v_{3/2^-}| < 0.94,$$

including both cases for the phase. The result are shown by the vertical bars in Fig. 11.4.

It is worth noting that the region of $|g^v_{3/2^-}|$ does not reach zero, even though the $|g^v_{N(1700)}|$ can be zero. The condition for $g^{s,v}(\overline{\mathbf{10}}) = 0$ leads to

$$\frac{|g^{s,v}_2|}{|g^{s,v}_1|} = \tan\theta_N \sim \begin{cases} 0.55 & \text{for } 1/2^+, \\ 0.65 & \text{for } 3/2^-. \end{cases} \tag{11.4.8}$$

This means that $g^{s,v}(\overline{\mathbf{10}})$ becomes zero only if the condition (11.4.8) is satisfied within the uncertainty of coupling constants.

We can also estimate the magnitude of the self-energy, by substituting the squared amplitudes for $3/2^-$ case in the formulas of the self-energy shown in Ref. [21]. For $|g^s_{3/2^-}| = 4.17$, we estimate the real part of the self-energy as -1518 MeV for an initial energy of 1540-1700 MeV and a cutoff of 700-800 MeV. This huge self-energy for $3/2^-$ case is due to the p-wave nature of the two-meson coupling, namely, the existence of a momentum variable in the loop integral. A similar large self-energy was observed when the self-energy is calculated with the chiral Lagrangian in chapter 9 (subsection 9.4.3). Thus, to have some reasonable values for the self-energy $|\mathrm{Re}\Sigma^s_{\Theta^+}| < 200$ MeV,

$$|g^s_{3/2^-}| < 1.51. \tag{11.4.9}$$

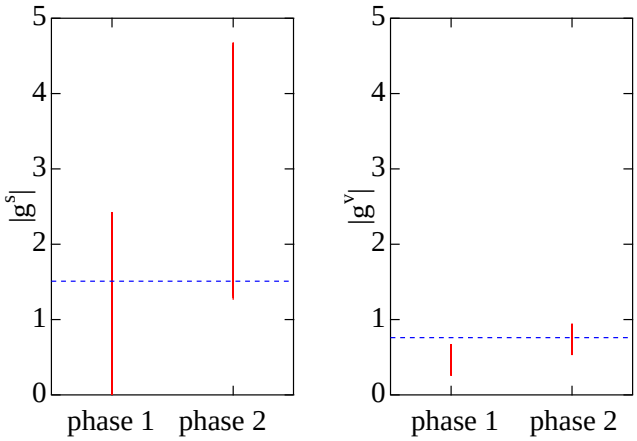

Figure 11.4: Numerical results for the coupling constants with $J^P = 3/2^-$. The two choices of the relative phase between coupling constants are marked as "phase 1" and "phase 2". Allowed regions of the coupling constants are shown by the vertical bar. Horizontal dashed lines show the upper limit of the coupling constants derived from the self-energy $|\mathrm{Re}\Sigma| < 200$ MeV.

In the same way, for the vector term with $|g^v_{3/2^-}| = 0.61$, we estimate the real part of the self-energy as -130 MeV. In this case, the self-energy is suppressed by the vector meson propagator. The use of small number 0.61 for the coupling constant also accounts for the small value of the self-energy. The condition of the self-energy $|\mathrm{Re}\Sigma^v_{\Theta^+}| < 200$ MeV gives the constraints

$$|g^v_{3/2^-}| < 0.76. \tag{11.4.10}$$

Both upper limits (11.4.9) and (11.4.10) are indicated by horizontal dashed lines in Fig. 11.4.

11.5 Analysis of the meson-induced reactions

As an application of effective Lagrangians, we calculate the reaction processes $\pi^- p \to K^- \Theta^+$ and $K^+ p \to \pi^+ \Theta^+$ via tree-level diagrams as shown in Fig. 11.5. These are alternative reactions to, for instance, photo-induced reactions, which are useful for further study of the Θ^+. The amplitudes for these reactions are given by

$$\begin{aligned} -it^s_{1/2^+}(\pi^- p \to K^- \Theta^+) =& -it^s_{1/2^+}(K^+ p \to \pi^+ \Theta^+) \\ =& i\frac{g^s_{1/2^+}}{2f}(-\sqrt{6}) N_{\Theta^+} N_p, \end{aligned} \tag{11.5.1}$$

$$\begin{aligned} -it^v_{1/2^+}(\pi^- p \to K^- \Theta^+) =& it^v_{1/2^+}(K^+ p \to \pi^+ \Theta^+) \\ =& i\frac{g^v_{1/2^+}}{4f^2}(-\sqrt{6})(2\sqrt{s} - M_\Theta - M_p) N_{\Theta^+} N_p F(k-k') \end{aligned} \tag{11.5.2}$$

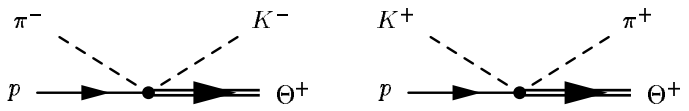

Figure 11.5: Feynman diagrams for the meson-induced reactions for Θ^+ production.

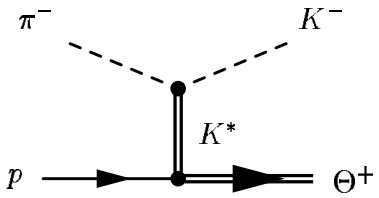

Figure 11.6: Feynman diagram for the meson-induced reaction for Θ^+ production with a vector meson propagator.

for the $1/2^+$ case and by

$$\begin{aligned}
-it^s_{3/2^-}(\pi^- p \to K^- \Theta^+) =& -it^s_{3/2^-}(K^+ p \to \pi^+ \Theta^+) \\
=& i\frac{g^s_{3/2^-}}{4f^2}(-\sqrt{6})(\boldsymbol{k}-\boldsymbol{k}')\cdot \boldsymbol{S}^\dagger N_{\Theta^+} N_p, \\
-it^v_{3/2^-}(\pi^- p \to K^- \Theta^+) =& it^v_{3/2^-}(K^+ p \to \pi^+ \Theta^+) \\
=& -i\frac{g^v_{3/2^-}}{4f^2}(-\sqrt{6})(\boldsymbol{k}+\boldsymbol{k}')\cdot \boldsymbol{S}^\dagger N_{\Theta^+} N_p F(k-k') \qquad (11.5.3)
\end{aligned}$$

for the $3/2^-$ case, where the normalization factor is $N_i = \sqrt{(E_i + M_i)/2M_i}$, $\boldsymbol{S}$ is the spin transition operator defined in Appendix A.1.2[B)], $\sqrt{s}$ is the initial energy, and k and k' are the momenta of the incoming and outgoing mesons, respectively. Here we define the vector meson propagator (Fig. 11.6) as

$$F(k-k') = \frac{-m^2_{K^*}}{(k-k')^2 - m^2_{K^*} + i m_{K^*}\Gamma[(k-k')^2]}, \qquad (11.5.4)$$

which is included in the vector-type amplitude. In the kinematical region in which we are interested, the momentum-dependent decay width of K^*, $\Gamma[(k-k')^2]$ vanishes. Note that the scalar-type amplitude gives the same sign for $\pi^- p \to K^- \Theta^+$ and $K^+ p \to \pi^+ \Theta^+$, whereas the vector one gives opposite signs, reflecting the symmetry under exchange of two meson fields in the effective Lagrangians.

Since the two amplitudes must be summed coherently, the squared amplitudes are given by

$$\begin{aligned}
\overline{\Sigma}\Sigma|t_{1/2^+}|^2 =& \overline{\Sigma}\Sigma|t^s_{1/2^+} \pm t^v_{1/2^+}|^2 \\
=& 6\left(\frac{1}{2f}\right)^2 N^2_{\Theta^+} N^2_p \Big[(g^s_{1/2^+})^2 \pm 2 g^s_{1/2^+} g^v_{1/2^+} \frac{2\sqrt{s} - M_\Theta - M_p}{2f} F(k-k')
\end{aligned}$$

[B)] In the paper [25], we defined $\boldsymbol{S}$ as in Ref. [604]. Here we define $\boldsymbol{S}$ as in Ref. [605] to be compatible with other chapters. Accordingly, we change the notation in Eq. (11.5.3).

$$+ (g^v_{1/2^+})^2 \frac{(2\sqrt{s} - M_\Theta - M_p)^2}{4f^2} F^2(k-k')\Big], \tag{11.5.5}$$

$$\overline{\Sigma}\Sigma|t_{3/2^-}|^2 = 4\left(\frac{1}{4f^2}\right)^2 N^2_{\Theta^+} N_p^2 \Big[(g^s_{3/2^-})^2(\boldsymbol{k}-\boldsymbol{k}')^2 \mp 2 g^s_{3/2^-} g^v_{3/2^-}(|\boldsymbol{k}|^2 - |\boldsymbol{k}'|^2) F(k-k')$$
$$+ (g^v_{3/2^-})^2(\boldsymbol{k}+\boldsymbol{k}')^2 F^2(k-k')\Big], \tag{11.5.6}$$

where $\pm$ and $\mp$ signs denote the $\pi^- p \to K^- \Theta^+$ and $K^+ p \to \pi^+ \Theta^+$ reactions, respectively. Notice that the relative phase between the two coupling constants is important, which affects the interference term of the two amplitudes. To determine the phase, we use the experimental information from $\pi^- p \to K^- \Theta^+$ reaction at KEK [650, 131], where the upper limit of the cross section has been extracted to be a few μb.

The differential cross section for these reactions is given by

$$\frac{d\sigma}{d\cos\theta}(\sqrt{s}, \cos\theta) = \frac{1}{4\pi s}\frac{|\boldsymbol{k}'|}{|\boldsymbol{k}|} M_p M_\Theta \frac{1}{2}\overline{\Sigma}\Sigma |t(\sqrt{s}, \cos\theta)|^2,$$

which is evaluated in the center-of-mass frame. The total cross section can be obtained by integrating Eq. (8.2.20) with respect to $\cos\theta$:

$$\sigma(\sqrt{s}) = \int_{-1}^{1} d\cos\theta \frac{d\sigma}{d\cos\theta}(\sqrt{s}, \cos\theta).$$

11.5.1 Qualitative analysis for $J^P = 1/2^+$ and $3/2^-$

Now let us calculate the cross section using the coupling constants obtained previously. In this section, we focus on the qualitative difference between $J^P = 1/2^+$ and $3/2^-$ cases. A more quantitative estimation of cross sections will be given in later sections.

We first calculate for the $1/2^+$ case, with coupling constants

$$g^s_{1/2^+} = 0.47, \quad g^v_{1/2^+} = 0.47, \tag{11.5.7}$$

where $g^s_{1/2^+}$ is one of the solutions that satisfies the condition (11.4.6). Since the result (11.4.3) spreads over a wide range, we choose $g^v_{1/2^+} = g^s_{1/2^+}$, which is well within the interval (11.4.7) determined from the self-energy. The result is shown in Fig. 11.7, with contributions from s and v terms. Each contribution is calculated by switching off the other term. As we see, the use of the same coupling constant for both terms results in the dominance of the vector term. However, there is a sizable interference effect between s and v terms, although the contribution from the s term itself is small. The two amplitudes interfere constructively for the $\pi^- p \to K^- \Theta^+$ channel, whereas in the $K^+ p \to \pi^+ \Theta^+$ case they destructively interfere.

As already mentioned, the relative phase of the two coupling constants is not determined. If we change the sign,

$$g^s_{1/2^+} = 0.47, \quad g^v_{1/2^+} = -0.47, \tag{11.5.8}$$

then the results change as in Fig. 11.8, where constructive and destructive interference appears in an opposite manner. It is worth noting that the amplitude for $\pi^- p \to K^- \Theta^+$ with

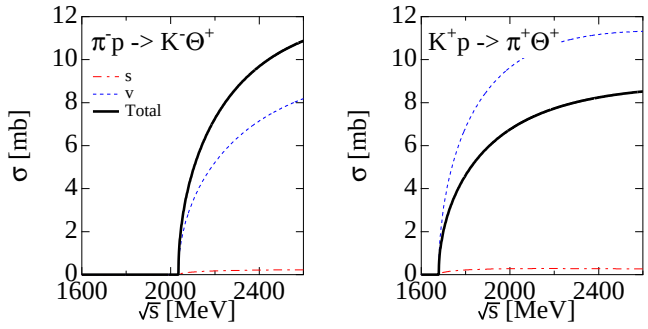

Figure 11.7: Total cross sections for the $J^P = 1/2^+$ case with $g^s = 0.47$ and $g^v = 0.47$. The thick line shows the result with full amplitude. Dash-dotted and dashed lines are the contributions from s and v terms, respectively.

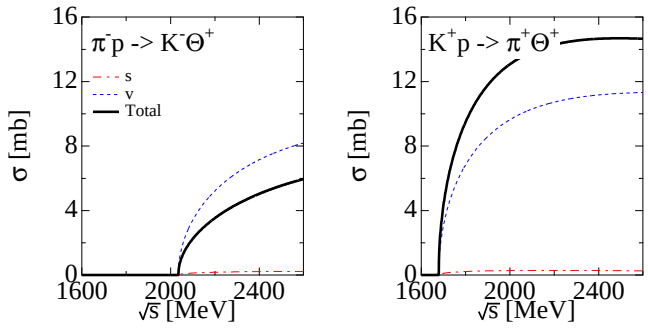

Figure 11.8: Total cross sections for the $J^P = 1/2^+$ case with $g^s = 0.47$ and $g^v = -0.47$. The thick line shows the result with full amplitude. Dash-dotted and dashed lines are the contributions from s and v terms, respectively.

the relative phase of Eq. (11.5.7) and that for $K^+p \to \pi^+\Theta^+$ with Eq. (11.5.8) are the same, as seen in Eq. (11.5.5). The difference only comes from the kinematic factors in cross section (8.2.20).

There is a preliminary result from KEK [650, 131] that the cross section of $\pi^-p \to K^-\Theta^+$ was found to be very small, of the order of a few μb. At this stage, we do not want to calculate the cross section quantitatively, but the experimental result suggests that the relative phase of Eq. (11.5.8) should be plausible, for the small cross section for the $\pi^-p \to K^-\Theta^+$ reaction. In this case, the cross section for $K^+p \to \pi^+\Theta^+$ becomes large.

As a trial, let us search for the set of coupling constants with which the most destructive interference takes place in $\pi^-p \to K^-\Theta^+$, by changing $g^v_{1/2^+}$ within the interval (11.4.7). This means that the difference between cross sections of $\pi^-p \to K^-\Theta^+$ and $K^+p \to \pi^+\Theta^+$ is maximal. Then we find

$$g^s_{1/2^+} = 0.47, \quad g^v_{1/2^+} = -0.08. \tag{11.5.9}$$

The result is shown in Fig. 11.9. A huge difference between $\pi^-p \to K^-\Theta^+$ and $K^+p \to \pi^+\Theta^+$

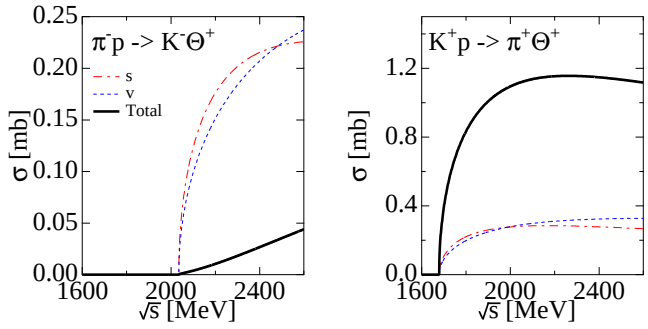

Figure 11.9: Total cross sections for the $J^P = 1/2^+$ case with $g^s = 0.47$ and $g^v = -0.08$, when the most destructive interference for $\pi^- p \to K^- \Theta^+$ takes place. Note that the vertical scale is different in the two panels. The thick line shows the result with full amplitude. Dash-dotted and dashed lines are the contributions from s and v terms, respectively.

can be seen. In this case, we observe the ratio of cross sections

$$\frac{\sigma(K^+ p \to \pi^+ \Theta^+)}{\sigma(\pi^- p \to K^- \Theta^+)} \sim 50. \tag{11.5.10}$$

Here we estimated the cross section σ as the average of the cross section shown in the figures (from threshold to 2.6 GeV). Notice that the ratio of the coupling constants $g^s_{1/2^+}/g^v_{1/2^+} \sim -5.9$ is relevant for the interference effect. It is possible to scale both coupling constants within experimental uncertainties. This does not change the ratio of cross sections, but it does change the absolute values.

Next we examine the case with $J^P = 3/2^-$. Again, we observe constructive and destructive interferences, depending on the relative sign of the two amplitudes. The interference effect is prominent around the energy region close to the threshold but is not very strong in the higher energy region, compared with $1/2^+$ case.

We search for the coupling constants with which the most destructive interference takes place for $\pi^- p \to K^- \Theta^+$. We find that destructive interference is maximized when the ratio of the coupling constants is $g^s_{3/2^-}/g^v_{3/2^-} \sim 0.5$. Taking, for instance, the values

$$g^s_{3/2^-} = 0.2, \quad g^v_{3/2^-} = 0.4, \tag{11.5.11}$$

which are within the experimental bounds given in Sec. 11.4, we obtain the results shown in Fig. 11.10. In contrast to the $J^P = 1/2^+$ case, here the ratio of cross section is not very large:

$$\frac{\sigma(K^+ p \to \pi^+ \Theta^+)}{\sigma(\pi^- p \to K^- \Theta^+)} \sim 3.3. \tag{11.5.12}$$

The high-energy behavior in this case is understood from the p-wave nature of the coupling.

Let us mention the effect of the vector meson propagator. For simplicity, we take the same value for the coupling constants. First, we address the $J^P = 1/2^+$ case. Without introducing the vector meson propagator $F(k - k')$, the magnitude and energy dependence of

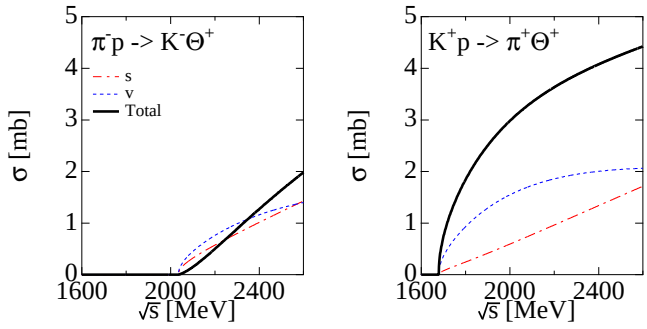

Figure 11.10: Total cross section for the $J^P = 3/2^-$ case with $g^s = 0.2$ and $g^v = 0.4$, when the most destructive interference for $\pi^- p \to K^- \Theta^+$ takes place. The thick line shows the result with full amplitude. Dash-dotted and dashed lines are the contributions from s and v terms, respectively.

the vector term is not similar to the scalar one, reflecting the structure of amplitudes (11.5.1) and (11.5.2). The difference between s and v amplitudes is $(2\sqrt{s} - M_\Theta - M_p)/2f$ with the same coupling constant, which ranges from 3 to 14 in the energy region under consideration. The cross section is proportional to its square, and therefore the vector term becomes the dominant one. The inclusion of the vector meson propagator reduces the cross section of the vector term, especially in the high-energy region. This eventually leads to the similar energy dependence of the two amplitudes t^s and t^v, resulting in a large cancellation between them, as seen in Fig. 11.9, although a factor $g^s_{1/2^+}/g^v_{1/2^+} \sim -5.9$ is still required to make the magnitude the same.

For the $J^P = 3/2^-$ case, without including the vector meson propagator, the scalar and vector contributions to the total cross section [the first and the third terms in Eq. (11.5.6)] become exactly the same, when we take the same coupling constant. Obviously, as seen in Eq. (11.5.6), the difference of the squared amplitudes is the term proportional to $\boldsymbol{k}\cdot\boldsymbol{k}' \propto \cos\theta$, which goes away when the angular integral is performed. This, however, does not lead to complete destructive interference, owing to the second term in Eq. (11.5.6). The vector meson propagator acts in the same way as before, and we obtain somehow a different energy dependence of the s and v results (Fig. 11.10) and a factor $g^s_{3/2^-}/g^v_{3/2^-} \sim 0.5$ to compensate for the reduction of the cross section of the vector term.

11.5.2 Hadronic form factor

Here we consider the reaction mechanism in detail to give a more quantitative result. First we introduce a hadronic form factor at the vertices, which accounts for the energy dependence of the coupling constants. Physically, it is understood as the reflection of the finite size of the hadrons. In practice, however, the introduction of the form factor has some ambiguities in its form and the cutoff parameters [189], which hopefully can be determined from experiment.

In Ref. [190], the $\pi^- p \to K^- \Theta^+$ reaction is studied with a three-dimensional monopole-

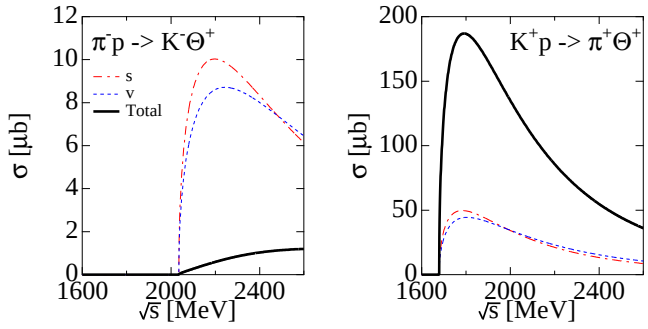

Figure 11.11: Total cross sections for the $J^P = 1/2^+$ case with $g^s = 0.47$ and $g^v = -0.08$, including a hadronic form factor (11.5.13). The thick line shows the result with full amplitude. Dash-dotted and dashed lines are the contributions from s and v terms, respectively.

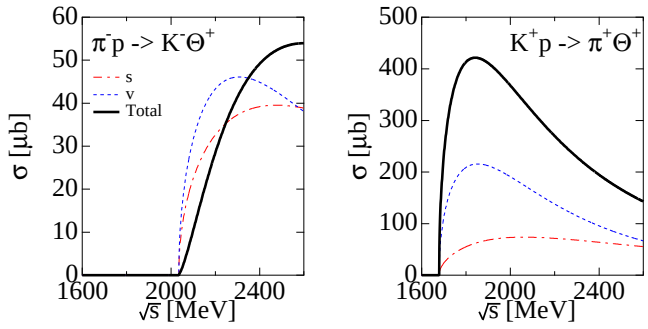

Figure 11.12: Total cross sections for the $J^P = 3/2^-$ case with $g^s = 0.2$ and $g^v = 0.4$, including a hadronic form factor (11.5.13). The thick line shows the result with full amplitude. Dash-dotted and dashed lines are the contributions from s and v terms, respectively.

type form factor

$$F(\sqrt{s}) = \frac{\Lambda^2}{\Lambda^2 + \boldsymbol{q}^2}, \tag{11.5.13}$$

where $\boldsymbol{q}^2 = \lambda(s, M_N^2, m_{\rm in}^2)/4s$ with $m_{\rm in}$ being the mass of the incoming meson and $\Lambda = 0.5$ GeV. Here we adopt this form factor and apply it to the present process. We obtain the results for $J^P = 1/2^+$ in Fig. 11.11 and for $J^P = 3/2^-$ in Fig. 11.12, with the coupling constants given in Eqs. (11.5.9) and (11.5.11). With this form factor, the energy of the $K^+p \to \pi^+\Theta^+$ reaction of the ongoing experiment at KEK ($P_{\rm lab} \sim 1200$ MeV, $\sqrt{s} \sim 1888$ MeV) is close to the maximum value for the cross section.

Notice that the ratio of the cross sections of $\pi^-p \to K^-\Theta^+$ and $K^+p \to \pi^+\Theta^+$ becomes larger than those of Eqs. (11.5.10) and (11.5.12). This is due to the use of the form factor (11.5.13), which contains the mass of the initial meson. It further contributes a factor ~ 2 for the ratio of $\pi^-p \to K^-\Theta^+$ and $K^+p \to \pi^+\Theta^+$.

We observe that the cross section is suppressed down to $\sim 1\mu$b for the $\pi^-p \to K^-\Theta^+$ reaction in the $1/2^+$ case. However, this is also a consequence of our choice of small coupling

constants. Indeed, with these coupling constants, the self-energy of Θ^+ becomes

$$\mathrm{Re}\Sigma_{\Theta^+}^{1/2^+} = \mathrm{Re}\Sigma_{\Theta^+}^{s} + \mathrm{Re}\Sigma_{\Theta^+}^{v} \sim -5.3 - 1.6 = -6.9 \text{ MeV},$$

for $p^0 = 1700$ MeV and a cutoff 750 MeV. This is too small, but as we mentioned before, we can scale these constants without changing the ratio of $K^+p \to \pi^+\Theta^+$ and $\pi^-p \to K^-\Theta^+$. We would like to search for the coupling constants which provide a small cross section for $\pi^-p \to K^-\Theta^+$ reaction compatible with experiment and a moderate amount of self-energy, which guarantee the dominance of the two-meson coupling terms compared with the $KN\Theta^+$ vertex.

In Fig. 11.13, we plot the cross section of $\pi^-p \to K^-\Theta^+$ reaction and the self-energy of Θ^+ by fixing the ratio of coupling constants. The cross section is the value at $\sqrt{s} = 2124$ MeV, which corresponds to the KEK experiment $P_{\rm lab} \sim 1920$ MeV. The horizontal line denotes the factor F, which is defined by

$$g^s_{1/2^+} = F \times 0.47, \quad g^v_{1/2^+} = -F \times 0.08. \tag{11.5.14}$$

We use $F = 1$ for the calculation of Fig. 11.11. Both the cross section and self-energy are proportional to the square of the coupling constant. Using the maximum value of cross section $\sim 4.1\mu$b [C)] estimated by KEK experiment [650, 131], we have

$$\begin{aligned} g^s_{1/2^+} &= 1.59, & g^v_{1/2^+} &= -0.27, \\ \sigma_{\pi^-p\to K^-\Theta^+} &= 4.1\mu\text{b}, & \mathrm{Re}\Sigma_\Theta &= -78 \text{ MeV}. \end{aligned} \tag{11.5.15}$$

Furthermore, if we use the upper limit of the scalar term of the coupling constant, we fix

$$\begin{aligned} g^s_{1/2^+} &= 1.37, & g^v_{1/2^+} &= -0.23, \\ \sigma_{\pi^-p\to K^-\Theta^+} &= 3.2\mu\text{b}, & \mathrm{Re}\Sigma_\Theta &= -58 \text{ MeV}. \end{aligned}$$

However, if we want to obtain $\mathrm{Re}\Sigma_\Theta = -100$ MeV, we have

$$\begin{aligned} g^s_{1/2^+} &= 1.80, & g^v_{1/2^+} &= -0.31, \\ \sigma_{\pi^-p\to K^-\Theta^+} &= 5.0\mu\text{b}, & \mathrm{Re}\Sigma_\Theta &= -100 \text{ MeV}. \end{aligned} \tag{11.5.16}$$

We see that a sizable self-energy is obtained with the coupling constants (11.5.15) and (11.5.16). These results are summarized in Table 11.2.

For the $J^P = 3/2^-$ case, with $g^s_{3/2^-} = 0.2$ and $g^v_{3/2^-} = 0.4$, the self-energy of Θ^+ becomes

$$\mathrm{Re}\Sigma_{\Theta^+}^{3/2^-} = \mathrm{Re}\Sigma_{\Theta^+}^{s} + \mathrm{Re}\Sigma_{\Theta^+}^{v} \sim -4 - 80 = -84 \text{ MeV}.$$

[C)] Here we use the preliminary value 4.1μb reported in Ref. [650], which has been later corrected as 4.3μb [131]. Qualitative conclusions remain unchanged for the upper limit of 4.3 μb. This upper limit is determined by assuming the isotropic decay of $\Theta^+ \to KN$. In our calculation, the angular dependence of the decay is not very large, as shown in the following. Therefore we simply use this value for the estimation of upper limit here.

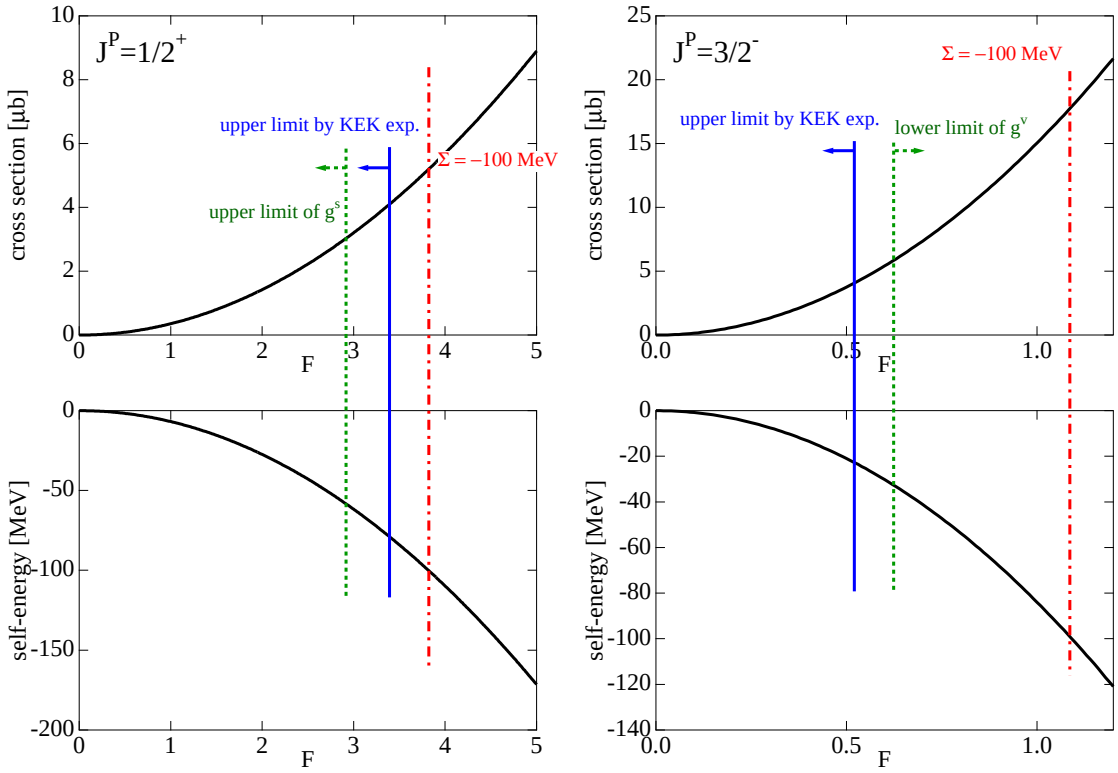

Figure 11.13: The total cross section of $\pi^- p \to K^- \Theta^+$ at $P_{\rm lab} = 1920$ MeV and the real part of the self-energy of Θ^+ as functions of the factor F defined in Eqs. (11.5.14) and (11.5.17) for $J^P = 1/2^+$ (left) and $J^P = 3/2^-$ (right). Solid, dashed and dash-dotted vertical lines show the upper limit of cross section given by the KEK experiment [650, 131], the limit of coupling constant, and the point where $\mathrm{Re}\Sigma = -100$ MeV.

Table 11.2: Summary of the coupling constants, cross sections and self-energies. σ_{π^-} is the total cross section for $\pi^- p \to K^- \Theta^+$ are the values at $P_{\rm lab} = 1920$ MeV; σ_{K^+} is that for $K^+ p \to \pi^+ \Theta^+$, which is the upper limit of the cross section at $P_{\rm lab} = 1200$ MeV.

J^P	g^s	g^v	σ_{π^-} [μb]	σ_{K^+} [μb]	$\mathrm{Re}\Sigma_\Theta$ [MeV]
$1/2^+$	1.59	-0.27	4.1	$<$1928	-78
	1.37	-0.23	3.2	$<$1415	-58
	1.80	-0.31	5.0	$<$2506	-100
$3/2^-$	0.104	0.209	4.1	$<$ 113	-23
	0.125	0.25	5.9	$<$ 162	-32
	0.22	0.44	18	$<$ 502	-100

In Fig. 11.13, we plot the cross section of the $\pi^- p \to K^- \Theta^+$ reaction and the self-energy of Θ^+ by fixing the ratio of coupling constants. The horizontal line denotes the factor F, which is defined by

$$g^s_{1/2^+} = F \times 0.2, \quad g^v_{1/2^+} = F \times 0.4. \tag{11.5.17}$$

Using the maximum value of cross section $\sim 4.1\mu$b estimated by the KEK experiment, we have

$$\begin{aligned} g^s_{3/2^-} &= 0.104, & g^v_{3/2^-} &= 0.209, \\ \sigma_{\pi^- p \to K^- \Theta^+} &= 4.1\mu\text{b}, & \text{Re}\Sigma_\Theta &= -23 \text{ MeV}. \end{aligned}$$

In the region plotted in the figure, the coupling constants do not exceed the upper bounds, but the lower limit of $g^v_{3/2^-}$ appears:

$$\begin{aligned} g^s_{3/2^-} &= 0.125, & g^v_{3/2^-} &= 0.25, \\ \sigma_{\pi^- p \to K^- \Theta^+} &= 5.9\mu\text{b}, & \text{Re}\Sigma_\Theta &= -33 \text{ MeV}. \end{aligned}$$

To make $\text{Re}\Sigma_\Theta = -100$ MeV, we have

$$\begin{aligned} g^s_{3/2^-} &= 0.22, & g^v_{3/2^-} &= 0.44, \\ \sigma_{\pi^- p \to K^- \Theta^+} &= 18\mu\text{b}, & \text{Re}\Sigma_\Theta &= -100 \text{ MeV}. \end{aligned}$$

Finally, we show the angular dependence of the cross sections. In Figs. 11.14 and 11.15, we plot the angler dependence of the differential cross sections at the energy of KEK experiment: $P_{\text{lab}} \sim 1920$ MeV for $\pi^- p \to K^- \Theta^+$ and $P_{\text{lab}} \sim 1200$ MeV for $K^+ p \to \pi^+ \Theta^+$. For the $J^P = 1/2^+$ case, the contribution from the s term has no angular dependence, whereas the v term shows a forward peak, owing to the t-channel exchange of the vector meson propagator. Because of the interference of the two amplitudes, the total result becomes zero at $\cos\theta \sim 0.5$ for the $\pi^- p \to K^- \Theta^+$ reaction. For the $J^P = 3/2^-$ case, the s term varies linearly in $\cos\theta$, leading to a backward peak. The v term shows a forward peak, which is enhanced by the vector meson propagator. Interference of the two amplitude leads to a clear forward peak for both $\pi^- p \to K^- \Theta^+$ and $K^+ p \to \pi^+ \Theta^+$ reactions.

11.5.3 Effect of Born terms

In this subsection, we briefly discuss the possible effect from the Born terms, as shown in Fig. 11.16, which have not been taken into account in the present studies. However, there are reasons that the Born terms are not important in the present reactions. First, the Born terms are proportional to the decay width of Θ^+ and therefore suppressed if the decay width of the Θ^+ is narrow. Second, in the energy region of Θ^+ production, the energy denominator of the exchanged nucleon suppresses the contribution, especially for the s-channel term in the $\pi^- p \to K^- \Theta^+$ reaction. Here we would like to confirm this explicitly.

At the tree level, there are s-, t-, and u-channel diagrams. However, assuming $I = 0$ for Θ^+, there is only a u channel in $K^+ p \to \pi^+ \Theta^+$ (Fig. 11.16, left), whereas there is only an s channel

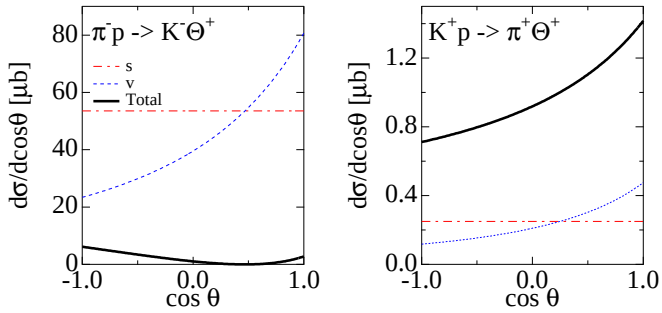

Figure 11.14: Angular dependence of the differential cross section for $\pi^- p \to K^- \Theta^+$ at $P_{\rm lab} \sim 1920$ MeV (left) and for $K^+ p \to \pi^+ \Theta^+$ at $P_{\rm lab} \sim 1200$ MeV (right) for the $J^P = 1/2^+$ case with $g^s = 1.59$ and $g^v = -0.27$, including a hadronic form factor (11.5.13). The thick line shows the result with full amplitude. Dash-dotted and dashed lines are the contributions from s and v terms, respectively.

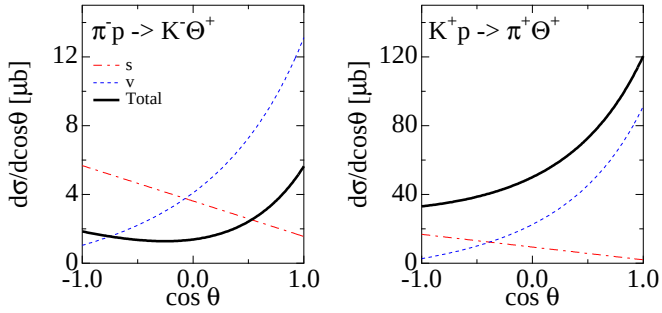

Figure 11.15: Angular dependence of the differential cross section for $\pi^- p \to K^- \Theta^+$ at $P_{\rm lab} \sim 1920$ MeV (left) and for $K^+ p \to \pi^+ \Theta^+$ at $P_{\rm lab} \sim 1200$ MeV (right) for the $J^P = 3/2^-$ case with $g^s = 0.106$ and $g^v = 0.212$, including a hadronic form factor (11.5.13). The thick line shows the result with full amplitude. Dash-dotted and dashed lines are the contributions from s and v terms, respectively.

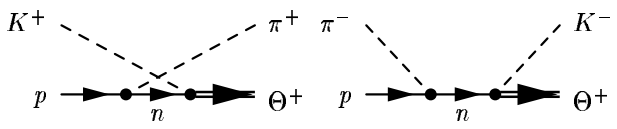

Figure 11.16: Born terms for the reaction: u-channel diagram for $K^+ p \to \pi^+ \Theta^+$ (left); s-channel diagram for $\pi^- p \to K^- \Theta^+$ (right).

in $\pi^- p \to K^- \Theta^+$ (Fig. 11.16, right). For these terms, we need the Yukawa couplings such as $KN\Theta^+$ and πNN couplings. There are two schemes to introduce the Yukawa couplings, namely, pseudoscalar (PS) and pseudovector (PV) schemes. For the construction of the Born amplitude, it is reasonable to rely on chiral symmetry, where the two schemes should provide the same results.

In this case the meson-baryon scattering amplitude should be a quantity of $\mathcal{O}(k)$ or higher, where k is a momentum of mesons. In the PV scheme, since each $KN\Theta$ coupling is of $\mathcal{O}(k)$, the Born amplitude behaves as $\mathcal{O}(k^2)$, consistent with this observation. In contrast, a naive construction of the Born term in the PS scheme leads to an amplitude of $\mathcal{O}(1)$. It is well-known that a scalar exchange term cancel the term of $\mathcal{O}(1)$. However, the interaction of the scalar channel is not well understood. Therefore, we adopt the PV scheme in the following study. Another advantage of the PV scheme is that it can be extended easily to the $J^P = 3/2^-$ case, while it is not so simple in the PS scheme [643]. In this respect, our method differs from the previous study of similar reactions [190, 208], in which the PS scheme was used.

The interaction Lagrangians for $1/2^+$ are

$$\mathcal{L}^{1/2^+}_{KN\Theta} = \frac{g_A^{*,1/2^+}}{2f}\bar{\Theta}^+\gamma_\mu\gamma_5\partial^\mu K N + \text{h.c.},$$
$$\mathcal{L}_{\pi NN} = \frac{g_A}{2f}\bar{N}\gamma_\mu\gamma_5\partial^\mu \boldsymbol{\pi} N.$$

The fields N and $\boldsymbol{\pi}$ are defined in Eq. (11.3.4), and the kaon field is defined as

$$K = \begin{pmatrix} -K^0 & K^+ \end{pmatrix},$$

and the coupling constants are determined as

$$g_A^{*,1/2^+} = 0.0935,$$

which is determined by $\Gamma_{\Theta^+} = 1$ MeV, and we use

$$g_A = 1.25. \tag{11.5.18}$$

The amplitude for $\pi^-(k)p(p) \to K^-(k')\Theta^+(p')$ is given by

$$-it = i\sqrt{2}\frac{g_A^{*,1/2^+} g_A}{4f^2}(\boldsymbol{\sigma}\cdot\boldsymbol{k}')\frac{M}{E}\frac{1}{p_0 + k_0 - E(\boldsymbol{p}+\boldsymbol{k})}(\boldsymbol{\sigma}\cdot\boldsymbol{k}),$$

and for $K^+(k)p(p) \to \pi^+(k')\Theta^+(p')$,

$$-it = i\sqrt{2}\frac{g_A^{*,1/2^+} g_A}{4f^2}(\boldsymbol{\sigma}\cdot\boldsymbol{k})\frac{M}{E}\frac{1}{p_0 - k_0' - E(\boldsymbol{p}-\boldsymbol{k}')}(\boldsymbol{\sigma}\cdot\boldsymbol{k}').$$

In Fig. 11.17 we show the results including Born terms. We can observe that the effect of Born terms is indeed small in both reactions.

For the $J^P = 3/2^-$ case, the interaction Lagrangian can be written as

$$\mathcal{L}^{3/2^-}_{KN\Theta} = \frac{g_A^{*,3/2^-}}{2f}\bar{\Theta}^{+\mu}\gamma_5\partial_\mu K N + \text{h.c.},$$

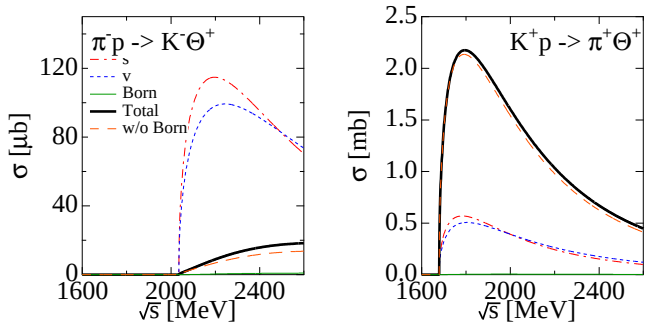

Figure 11.17: Total cross section for the $J^P = 1/2^+$ case with $g^s = 1.59$ and $g^v = -0.27$, including hadronic form factor (11.5.13) and Born terms. The thick line shows the result with full amplitude. Dash-dotted, dashed, and thin lines are the contributions from s, v, and Born terms, respectively. The result without Born terms are shown by the long-dashed lines.

with the same πNN vertex in Eq. (11.5.18). In the nonrelativistic expansion this term yields a d-wave coupling so that the square of momenta appears in the vertex. It reduces the contribution further than the $1/2^+$ case, and therefore, the effect of Born terms for $J^P = 3/2^-$ is also small.

11.6 Summary

In this chapter, we have studied the two-meson couplings of Θ^+ for $J^P = 1/2^+$ and $3/2^-$. The effective interaction Lagrangians for the two-meson couplings were given, and these coupling constants were determined based on the **8-$\overline{\mathbf{10}}$** representation mixing scheme, by using information of the $N^* \to \pi\pi N$ decays. These values were further constrained in order to provide appropriate size of the self-energy of the Θ^+. Finally, we have applied the effective interaction Lagrangians to the meson induced reactions $\pi^- p \to K^- \Theta^+$ and $K^+ p \to \pi^+ \Theta^+$.

(summary for the couplings)

We have found that there was an interference effect between the two amplitudes of the scalar and vector types, which could help to explain the very small cross section for the $\pi^- p \to K^- \Theta^+$ reaction observed at KEK [650, 131]. In this case, reflecting the symmetry under exchange of two amplitudes, large cross sections for $K^+ p \to \pi^+ \Theta^+$ reaction would be obtained as a consequence of the interference. The interference occurs in both $1/2^+$ and $3/2^-$ cases.

In Table 11.2, we have summarized the results obtained in the present analysis. For a given set of coupling constants, the upper bound of the cross sections of the $K^+ p \to \pi^+ \Theta^+$ reactions were estimated by maximizing the interference effect. We observed that large cross sections of the order of millibarns for $K^+ p \to \pi^+ \Theta^+$ was obtained for the $1/2^+$ case, whereas the upper limit of the cross section was not very large for $3/2^-$ case. Therefore, if large cross sections are observed in the $K^+ p \to \pi^+ \Theta^+$ reaction, it would indicate $J^P = 1/2^+$ for the Θ^+.

For completeness, we would like to mention the case where the cross sections for both $\pi^- p \to K^- \Theta^+$ and $K^+ p \to \pi^+ \Theta^+$ reactions are small. If the cross section of $K^+ p \to \pi^+ \Theta^+$

reaction is also small, it is not due to an interference effect, since the interference effect results in relatively large cross sections both for the two reactions. It could be explained by small coupling constants. For the $J^P = 1/2^+$ case, both coupling constants can be zero within the experimental uncertainties. However, for the $3/2^-$ case, there is a lower limit for the $g^v_{3/2^-}$, which means that the lower limit is also imposed for the cross sections. We search for the set of coupling constants that provide the minimum value for the $K^+p \to \pi^+\Theta^+$ cross section, keeping a $\pi^-p \to K^-\Theta^+$ cross section to be less than 4.1μb. We obtain $\sigma_{K^+p\to\pi^+\Theta^+} \sim 58\mu$b with $g^s_{3/2^-} = 0.04$ and $g^v_{3/2^-} = 0.18$. However, one should notice that the small coupling constants do not guarantee the dominance of two-meson coupling, and the Born terms and interference effect may play a role, which is beyond our present scope.

The present analysis provides an extension of effective interactions obtained in Ref. [413] with representation mixing and $J^P = 3/2^-$. It is also interesting to apply the present extension to the study of the medium effect of Θ^+ [413] and the production of Θ^+ hypernuclei [439]. From the experimental point of view, the cross section of $K^+p \to \pi^+\Theta^+$ reaction is of particular importance to the present results. To perform a better analysis for the two-meson coupling, more experimental data for three-body decays of nucleon resonances are strongly desired.

Part IV

Summary

Chapter 12

Summary

In this thesis, we have studied the properties of exotics in meson-baryon dynamics from various points of view. In part II, chiral unitary model was used to investigate baryon resonances which have been considered to contain a large amount of $\bar{q}q$ components, although their quantum numbers can be reproduced by the conventional three-quark picture. In part III, manifestly exotic states such as pentaquarks were studied, mainly based on the flavor SU(3) symmetry and πKN molecule picture for the Θ^+. Here we summarize what we have done and what we have learned.

In chapter 4, we reviewed the formulation of the chiral unitary model in some detail, and demonstrated how the resonances were dynamically generated in meson-baryon scattering. Then we introduced SU(3) breaking effects into the interaction kernel, with the hope that the channel dependence in the subtraction constants would be absorbed into the coefficients in the chiral Lagrangian. However, the effect of the symmetry breaking interaction was so strong that the results were affected very much. Therefore, it was found that the suitable choice of the subtraction constants was essential in the present framework.

The two-pole structure of the $\Lambda(1405)$ resonance was extensively studied together with the reaction dynamics to produce the $\Lambda(1405)$ in chapter 5. In the chiral unitary model, two poles have different coupling strengths to the $\bar{K}N$ and $\pi\Sigma$ channels, which allows us to study this structure in experiments. Indeed, it was found that the $\pi^- p \to K^0\pi\Sigma$ reaction favored the lower energy pole, whereas the $\gamma p \to K^* MB$ reaction was dominated by the higher energy pole, leading to different shapes of the invariant mass distributions in the two reactions. Therefore, we have revealed the possibilities to verify the two-pole structure in experiments, combining the results from both reactions.

In subsequent chapters 6 and 7, we utilized the amplitudes obtained in the chiral unitary model in order to extract various coupling constants of the dynamically generated resonances. Magnetic moments of the $N(1535)$ resonance and coupling constant of the $\Lambda(1520)\bar{K}^*N$ vertex were evaluated. These results were compared with those obtained in a constituent quark model, and we found substantial differences between the results. Since the differences are expected to reflect the internal structure of the resonances (meson-baryon or three-quark), experimental determination of these coupling constants will shed light on the understanding of the properties of the resonances. We have discussed several possibilities to observe the

coupling constants in experiments.

Then we have turned our subject to the pentaquarks. In chapter 8, we studied the Θ^+ production in the $K^+p \to \pi^+KN$ reaction, demonstrating how the observables qualitatively depended on the spin and parity of the Θ^+ for the $J^P = 1/2^\pm$ and $3/2^+$ cases. This was the first theoretical attempt to extract the spin and parity of the Θ^+ in actual experiments. Specifying the polarization of initial and final baryons, it was found possible to extract the information of spin and parity of the Θ^+, although the detection of the spin of the final state baryon in experiments would be difficult.

In chapter 9, we have studied two-meson cloud components in the Θ^+ baryon and flavor partners in an antidecuplet representation. We constructed the effective Lagrangians for two-meson couplings based on flavor SU(3) symmetry, and evaluated the self-energies of the antidecuplet baryons. We found two important structures among several terms, that is, the couplings with two mesons in scalar-isoscalar and vector-isovector channels. With these terms, we observed attractive contributions to the masses of the antidecuplet baryons, which qualitatively agree with the results of the previous attempts to describe the Θ^+ as a πKN bound state. The contributions of the two-meson clouds to the mass splittings of the antidecuplet baryons were found to be about 20%, which was much larger than those of one-meson clouds due to the narrow decay widths of the Θ^+.

In order to determine the flavor representation that the Θ^+ belongs to, we have performed a general analysis of SU(3) symmetry in chapter 10. We assigned the known baryon resonances together with the Θ^+ and the $\Xi_{3/2}$ into the $\mathbf{8}$-$\overline{\mathbf{10}}$ mixing scheme, which was the minimal for the inclusion of the Θ^+. Analyzing the mass formula with symmetry breaking up to linear order in m_s, we obtained reasonable descriptions for the $J^P = 1/2^+$ and $J^P = 3/2^-$ cases. The $J^P = 1/2^+$ case has been studied previously, but we applied the mixing scheme to the $3/2^-$ case for the first time, which was found to be better than the $1/2^+$ case through the analysis of the decay widths.

Since we obtained a successful description of the Θ^+ and baryon resonances in the $\mathbf{8}$-$\overline{\mathbf{10}}$ mixing scheme, we evaluated the two-meson couplings within this scheme in chapter 11. The coupling constants were determined from the nucleon resonances in the multiplet, and also restricted by the self-energy analysis. We then applied the couplings to the meson-induced Θ^+ productions, since the two-meson couplings were expected to be dominant, based on the analysis in chapter 9. We examined production reactions for the Θ^+ with $J^P = 1/2^+$ and $3/2^-$, and found that the interference effects were different in the two cases.

Now we would like to make some remarks based on the above findings.

We have studied several reaction processes for the production of resonances in chapters 5 and 8. A unique point in these studies was that we included not only the resonant terms but also (a part of) background contributions. This is important from the experimental point of view. The background terms always exist in actual experiments, and may disturb the signal of the resonance through the interference with the resonant amplitude. In our studies, since the interference effects were taken into account, we could suggest a way to suppress background contributions, for instance, by choosing suitable kinematical conditions. This may help the experimental studies.

In chapters 8 and 11, we presented the method to determine the spin and parity of the

Θ^+ through the production reactions. We calculated the processes by assuming certain quantum numbers for the Θ^+, and compared the results which differ qualitatively depending on the quantum numbers of the Θ^+. The study in this direction is important for the newly discovered states, but also for the well-established states, since the J^P of the most of known resonances have been assigned by theoretical speculations. For instance, no one knows the J^P of the Ω state experimentally. Therefore, determination of the quantum numbers for several resonances by experimentally available method would be an interesting subject.

In chapters 4 and 9, we observed that the introduction of the SU(3) breaking in the interaction Lagrangians gave strong effects to the observables, which may destroy a good description of the SU(3) symmetric interaction. On the other hand, we have used the physical masses of the particles, which include the SU(3) breaking effects. The symmetry breaking in masses leads to the splitting of the threshold energies of two-body channels, which is important for the dynamics of hadrons. This tells us that we should include the SU(3) breaking in the masses of the particles, while the interaction should be symmetric at the leading order. This observation implicitly justify the approaches with the SU(3) symmetric interaction and with physical masses of hadrons, that we have been taken in chapters 5-8, 10 and 11, at least for the qualitative analysis.

Since the pentaquarks and manifestly exotic particles can provide a firm ground to study the multi-quark physics, it is important to study very the existence (or absence) of exotic particles in QCD. Of course, it is difficult to study QCD directly, but the symmetry principle can help to do it. Symmetries provide restrictions on the masses and interactions and simplify the models in the symmetric limit. The relations under symmetric limit have some relevance in the physical world where the symmetry is not exact, as we can see for instance the low energy theorem of the chiral symmetry. In the same way, scattering theory would be a good tool, since the resonances are observed in the scattering of the hadrons and the scattering theory also restricts the dynamics by, for instance, unitarity, analyticity, crossing symmetry, and so on.

A key issue in this thesis is the study of the multi-quark components, which eventually leads us to the understanding of the quark and hadronic matter. The multi-quark components should exist in various hadrons, since the excited hadrons have been observed in scatterings of ground state hadrons such as meson-meson or meson-baryon scatterings. Indeed, we have shown the importance of the additional $\bar{q}q$ components in excited baryons and pentaquarks in the chiral unitary model (part II) and two-meson cloud contributions (chapter 9). This may indicate the importance of the $\bar{q}q$ correlation in quark dynamics, or the importance of the meson clouds in hadronic description. Of course, the meson cloud complements the description by valence quarks, and reality would be a mixture of them. However, the relative importance of the meson clouds to the valence quarks would depend on the states. It is therefore interesting to study the role of these components in various states, and investigate the internal structure of excited baryons.

Appendix A

Convention and kinematics

A.1 Convention

A.1.1 Dirac spinor

Here we summarize the conventions for Dirac spinor. Our convention is mostly taken from Bjorken and Drell [653, 654]. The metric in Minkowski space is defined by

$$g^{\mu\nu} = \begin{pmatrix} 1 & 0 & 0 & 0 \\ 0 & -1 & 0 & 0 \\ 0 & 0 & -1 & 0 \\ 0 & 0 & 0 & -1 \end{pmatrix},$$

so that the inner product of four vectors $a^\mu = (a_0, \boldsymbol{a})$ and $b^\mu = (b_0, \boldsymbol{b})$ is $a \cdot b = a_\mu b^\mu = a_0 b_0 - \boldsymbol{a} \cdot \boldsymbol{b}$. We utilize the Dirac matrices in Dirac-Pauli representation

$$\gamma^0 = \begin{pmatrix} 1 & 0 \\ 0 & -1 \end{pmatrix}, \quad \gamma^i = \begin{pmatrix} 0 & \sigma^i \\ -\sigma^i & 0 \end{pmatrix}, \quad \gamma^5 = \begin{pmatrix} 0 & 1 \\ 1 & 0 \end{pmatrix},$$

with the Pauli matrices

$$\sigma^1 = \begin{pmatrix} 0 & 1 \\ 1 & 0 \end{pmatrix}, \quad \sigma^2 = \begin{pmatrix} 0 & -i \\ i & 0 \end{pmatrix}, \quad \sigma^3 = \begin{pmatrix} 1 & 0 \\ 0 & -1 \end{pmatrix}.$$

As easily checked, these matrices satisfy

$$\{\gamma^\mu, \gamma^\nu\} = 2g^{\mu\nu}, \quad \{\gamma^\mu, \gamma^5\} = 0, \quad (\gamma^5)^2 = 1, \quad (\gamma^\mu)^\dagger = \gamma^0\gamma^\mu\gamma^0, \quad (\gamma^5)^\dagger = \gamma^5,$$
$$\mathrm{tr}(\sigma^i) = 0, \quad (\sigma^i)^\dagger = \sigma^i, \quad \sigma^i\sigma^j = \delta^{ij} + i\epsilon^{ijk}\sigma^k.$$

With this representation, plane wave solutions for the Dirac equation with positive and negative energies are given by

$$u(p,s) = \sqrt{\frac{E+M}{2M}} \begin{pmatrix} \chi_s \\ \frac{\boldsymbol{\sigma}\cdot\boldsymbol{p}}{E+M}\chi_s \end{pmatrix}, \quad v(p,s) = \sqrt{\frac{E+M}{2M}} \begin{pmatrix} \frac{\boldsymbol{\sigma}\cdot\boldsymbol{p}}{E+M}\chi_{s'} \\ \chi_{s'} \end{pmatrix}, \tag{A.1.1}$$

with M, $p^\mu = (E, \boldsymbol{p})$, and s, s' being the mass, four momentum, and spin indices of the fermion, respectively and $E = \sqrt{M^2 + \boldsymbol{p}^2}$. The two-component spinor χ_s is defined by

$$\chi_{s=+1} = \begin{pmatrix} 1 \\ 0 \end{pmatrix}, \quad \chi_{s=-1} = \begin{pmatrix} 0 \\ 1 \end{pmatrix},$$

and $\chi_{s'} = -i\sigma^2(\chi_s)^*$. The spinor χ_s satisfy the orthonormal and completeness conditions

$$\chi_s^\dagger \chi_r = \delta_{sr}, \quad \sum_s \chi_s \chi_s^\dagger = \begin{pmatrix} 1 & 0 \\ 0 & 1 \end{pmatrix}.$$

Here $s = \pm 1$ stand for the eigenvalues of σ_3, which is the twice of the spin in z direction. The Dirac conjugate of the fermion states is given by

$$\bar{u}(p,s) = u(p,s)^\dagger \gamma_0 = \sqrt{\frac{E+M}{2M}} \begin{pmatrix} \chi_s^\dagger & -\chi_s^\dagger \frac{\boldsymbol{\sigma}\cdot\boldsymbol{p}}{E+M} \end{pmatrix}, \quad \bar{v}(p,s) = v(p,s)^\dagger \gamma_0,$$

and the normalization of spinors is

$$\begin{aligned}
\bar{u}(p,s)u(p,r) &= \frac{E+M}{2M} \chi_s^\dagger \left(1 - \frac{(\boldsymbol{\sigma}\cdot\boldsymbol{p})(\boldsymbol{\sigma}\cdot\boldsymbol{p})}{(E+M)^2}\right) \chi_r \\
&= \frac{E+M}{2M} \frac{(E+M)^2 - (E^2 - M^2)}{(E+M)^2} \chi_s^\dagger \chi_r \\
&= \frac{1}{2M} \frac{2EM + 2M^2}{E+M} \delta_{sr} \\
&= \delta_{sr}, \\
u^\dagger(p,s)u(p,r) &= \frac{E+M}{2M} \frac{(E+M)^2 + (E^2 - M^2)}{(E+M)^2} \chi_s^\dagger \chi_r \\
&= \frac{1}{2M} \frac{2E^2 + 2EM}{E+M} \delta_{sr} \\
&= \frac{2E}{2M} \delta_{sr}, \\
\bar{v}(p,s)v(p,r) &= -\delta_{sr}, \\
v^\dagger(p,s)v(p,r) &= \frac{2E}{2M} \delta_{sr}.
\end{aligned}$$

With this convention, we have

$$\begin{aligned}
\not{p} &= p^0 \gamma^0 - \boldsymbol{p}\cdot\boldsymbol{\gamma} \\
&= \begin{pmatrix} p^0 & -\boldsymbol{\sigma}\cdot\boldsymbol{p} \\ \boldsymbol{\sigma}\cdot\boldsymbol{p} & -p^0 \end{pmatrix}.
\end{aligned}$$

In the fermion rest frame $p = (M, \boldsymbol{0})$, Eq. (A.1.1) reduces into much simpler form as

$$u(p,s) = \begin{pmatrix} \chi_s \\ 0 \end{pmatrix},$$

which gives the leading order contribution for the non-relativistic reduction.

A.1.2 Spin 3/2 fields

We denote the spin 3/2 fields $B^\mu(p,S)$ with momentum p and third component of spin $S = +3/2, +1/2, -1/2$, and $-3/2$ by Rarita-Schwinger field [651], which satisfies the Rarita-Schwinger equations

$$(\not{p} - M_B)B^\mu(p,S) = 0, \quad p_\mu B^\mu(p,S) = \gamma_\mu B^\mu(p,S) = 0.$$

A general form of the solution is obtained by[A)]

$$B^\mu(p,S) = \sum_{r,s} \mathcal{C}(\tfrac{1}{2}\ 1\ \tfrac{3}{2}; \tfrac{s}{2}, \lambda) e^\mu_\lambda(p) u(p,s) \tag{A.1.2}$$

where $S = \lambda + s/2$, $u(p,s)$ is the Dirac spinor of spin 1/2 in Eq. (A.1.1), and $\mathcal{C}(j_1\ j_2\ J; \mu_1, \mu_2)$ denotes the SU(2) Clebsch-Gordan coefficient for $\boldsymbol{J}(\mu_1+\mu_2) = \boldsymbol{j}_1(\mu_1)+\boldsymbol{j}_2(\mu_2)$. In Eq. (A.1.2), $e^\mu_\lambda(p)$ is defined by

$$e^\mu_\lambda(p) = \left(\frac{\hat{\boldsymbol{e}}_\lambda \cdot \boldsymbol{p}}{M}, \hat{\boldsymbol{e}}_\lambda + \frac{\boldsymbol{p}(\hat{\boldsymbol{e}}_\lambda \cdot \boldsymbol{p})}{M(E+M)} \right),$$

which is obtained by boosting the spin 1 vector $e^\mu_\lambda(p)$ in spherical coordinate

$$\hat{\boldsymbol{e}}_{+1} = -\frac{1}{\sqrt{2}}(1,i,0), \quad \hat{\boldsymbol{e}}_0 = (0,0,1), \quad \hat{\boldsymbol{e}}_{-1} = \frac{1}{\sqrt{2}}(1,-i,0).$$

More explicitly, Eq. (A.1.2) can be written as

$$\begin{aligned}
B^\mu(p,+3/2) &= e^\mu_{+1}(p)u(p,+1/2), \\
B^\mu(p,+1/2) &= \sqrt{\frac{2}{3}} e^\mu_0(p)u(p,+1/2) + \sqrt{\frac{1}{3}} e^\mu_{+1}(p)u(p,-1/2), \\
B^\mu(p,-1/2) &= \sqrt{\frac{1}{3}} e^\mu_{-1}(p)u(p,+1/2) + \sqrt{\frac{2}{3}} e^\mu_0(p)u(p,-1/2), \\
B^\mu(p,-3/2) &= e^\mu_{-1}(p)u(p,-1/2),
\end{aligned}$$

In the rest frame $p^\mu = (M, \boldsymbol{0})$, spin 1 vector reduces into $e^\mu_\lambda(M,\boldsymbol{0}) = (0, \hat{\boldsymbol{e}}_\lambda)$, and therefore

$$\begin{aligned}
B^\mu(M,\boldsymbol{0},+3/2) &= (0,\hat{e}_+) \begin{pmatrix} \chi_+ \\ 0 \end{pmatrix}, \\
B^\mu(M,\boldsymbol{0},+1/2) &= (0,\hat{e}_0)\sqrt{\frac{2}{3}} \begin{pmatrix} \chi_+ \\ 0 \end{pmatrix} + (0,\hat{e}_+)\sqrt{\frac{1}{3}} \begin{pmatrix} \chi_- \\ 0 \end{pmatrix}, \\
B^\mu(M,\boldsymbol{0},-1/2) &= (0,\hat{e}_-)\sqrt{\frac{1}{3}} \begin{pmatrix} \chi_+ \\ 0 \end{pmatrix} + (0,\hat{e}_0)\sqrt{\frac{2}{3}} \begin{pmatrix} \chi_- \\ 0 \end{pmatrix}, \\
B^\mu(M,\boldsymbol{0},-3/2) &= (0,\hat{e}_-) \begin{pmatrix} \chi_- \\ 0 \end{pmatrix}.
\end{aligned}$$

[A)] Notice that s is defined by the twice of the third component of the spin.

In this case, it is useful to define the spin transition operator[B)]

$$(\boldsymbol{S}^\dagger)_{S,s} = \sum_\lambda \mathcal{C}(\tfrac{1}{2}\ 1\ \tfrac{3}{2}; \tfrac{s}{2}, \lambda)\hat{\boldsymbol{e}}_\lambda, \quad S = \lambda + \tfrac{s}{2},$$

The operator $(\boldsymbol{S}^\dagger)_{S,s}$ is a three-component spatial vector with two-component Pauli spinor index s on the right, and four-component index S on the left. Then B_μ can be written as

$$B_\mu(M, \boldsymbol{0}, S) = \sum_s (0, (\boldsymbol{S}^\dagger)_{S,s}\chi_s).$$

The spin suffices S and s are usually not written explicitly. By assigning the complete set, we obtain

$$\sum_S S_i|\, S\,\rangle\langle\, S\,|S_j^\dagger = \delta_{ij} - \frac{1}{3}\sigma_i\sigma_j = \frac{2}{3}\delta_{ij} - \frac{i}{3}\epsilon_{ijk}\sigma_k,$$

which is useful for the spin summation explained in next section.

A.2 Spin summation

Here we summarize the issue that appears when we take the square of an amplitude, that we denote $\bar{\Sigma}\Sigma$. Basically, we should take

- average over the degrees of freedom in the initial state and
- sum over the degrees of freedom in the final state.

In this thesis, we are interested in the processes in which at most one baryon is included. Therefore, we sum over the spin of the baryon in the final state s and average over the spin of the baryon in the initial state r. If an amplitude $-it$ does not contain the spin matrices, $\chi_s^\dagger\chi_r$ can be factorized out as $|t|^2 = |\chi_s^\dagger\chi_r|^2|t'|^2$, and then

$$\begin{aligned}\bar{\Sigma}\Sigma|t|^2 =& \frac{1}{2}\sum_s\sum_r |\chi_s^\dagger\chi_r|^2|t'|^2 \\ =& \frac{1}{2}\sum_s\sum_r |\delta_{s,r}|^2|t'|^2 \\ =& |t'|^2.\end{aligned}$$

[B)] Here we follow the definition in Ref. [605], while $\boldsymbol{S}$ and $\boldsymbol{S}^\dagger$ are defined inversely in Ref. [604].

If the Pauli matrices remains in the amplitude, writing $-it = \sigma_i t'_i$, we have

$$\begin{aligned}\bar{\Sigma}\Sigma|t|^2 =&\frac{1}{2}\sum_s\sum_r \chi_r^\dagger \sigma_i^\dagger \chi_s \chi_s^\dagger \sigma_j \chi_r |t_i'^* t'_j| \\ =&\frac{1}{2}\sum_r \chi_r^\dagger \sigma_i \sigma_j \chi_r |t_i'^* t'_j| \\ =&\frac{1}{2}\sum_r \chi_r^\dagger (\delta_{ij} + i\epsilon_{ijk}\sigma_k)\chi_r |t_i'^* t'_j| \\ =&\frac{1}{2} 2\delta_{ij}|t_i'^* t'_j| \\ =&\delta_{ij}|t_i'^* t'_j|.\end{aligned}$$

Next we consider the amplitude including spin transition from 1/2 to 3/2. For the 3/2 state in the initial state, we have ($-it = S_i^\dagger t'_i$)

$$\begin{aligned}\bar{\Sigma}\Sigma|t|^2 =&\frac{1}{2}\sum_r\sum_S \chi_r^\dagger S_i |\, S\,\rangle\langle\, S\,| S_j^\dagger \chi_r |t_i'^* t'_j| \\ =&\frac{1}{2}\sum_r \chi_r^\dagger \left(\frac{2}{3}\delta_{ij} - \frac{i}{3}\epsilon_{ijk}\sigma_k\right)\chi_r |t_i'^* t'_j| \\ =&\frac{1}{2}\frac{2}{3} 2\delta_{ij}|t_i'^* t'_j| \\ =&\frac{2}{3}\delta_{ij}|t_i'^* t'_j|.\end{aligned}$$

When the 3/2 state is in the initial state, the 1/2 factor should be replaced by 1/4, and therefore the result becomes $\frac{1}{3}\delta_{ij}|t_i'^* t'_j|$.

The above argument for spin summation can also be applied to the isospin, when one needs the isospin averaged amplitude. For example, let us consider the decay of $N^* \to \pi N$. Both initial and final states have two isospin state $\pm 1/2$. So the amplitude square should be

$$\begin{aligned}\bar{\Sigma}\Sigma|t|^2 \equiv& \frac{1}{2}\sum_s\sum_r |t_{s\to r}|^2 \\ =& \frac{1}{2}\Big(|t_{n^*\to\pi^0 n}|^2 + |t_{n^*\to\pi^- p}|^2 + |t_{p^*\to\pi^+ n}|^2 + |t_{p^*\to\pi^0 p}|^2\Big) \\ =& |t_{n^*\to\pi^0 n}|^2 + |t_{n^*\to\pi^- p}|^2 \\ =& |t_{p^*\to\pi^+ n}|^2 + |t_{p^*\to\pi^0 p}|^2.\end{aligned}$$

The last two lines are obtained by isospin symmetry. This summed amplitude leads to the decay width of $N^* \to \pi N$, written in the isospin state. This indicate that in practice, we can obtain the isospin averaged amplitude by taking one initial isospin state (since the initial states will be averaged) and all possible decay channels.

A.3 Kinematics

Here we summarize kinematic variables of the reactions. We first consider the kinematics of two-body scattering process, and then study the case with three-body final state, which

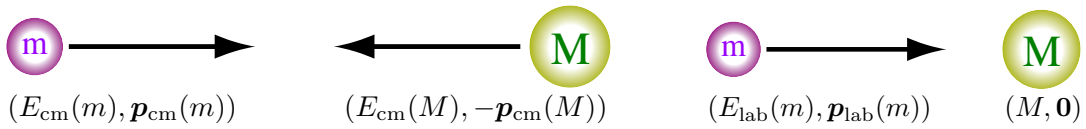

Figure A.1: Kinematics in the center of mass frame (left) and in the laboratory frame (right).

appears in particular calculations in chapters 5 and 8.

A.3.1 Kinematics for two-body process

We consider the energy and momentum of the system with two particles of masses m and M, for a given total energy in the center of mass frame $\sqrt{s}$[C)]. Since the total energy is conserved between the initial and final states, we can apply the formulae to the inelastic channels by replacing the masses of the particles, as long as they are two-body channels.

In the center of mass frame (Fig. A.1, left), energies of particles are given by

$$E_{\rm cm}(M) = \frac{s - m^2 + M^2}{2\sqrt{s}}, \quad E_{\rm cm}(m) = \frac{s - M^2 + m^2}{2\sqrt{s}}, \tag{A.3.1}$$

where $E_{\rm cm}(X)$ is the energy of the particle with mass X. The absolute values of three momenta are given by

$$|\boldsymbol{p}_{\rm cm}(M)| = |\boldsymbol{p}_{\rm cm}(m)| = \frac{\sqrt{(s-(M-m)^2)(s-(M+m)^2)}}{2\sqrt{s}} = \frac{\lambda^{1/2}(s, m^2, M^2)}{2\sqrt{s}}, \tag{A.3.2}$$

with the Källen function defined by

$$\lambda(x, y, z) = x^2 + y^2 + z^2 - 2xy - 2yz - 2zx.$$

These quantities can be easily obtained by the energy-momentum conservation and on-shell condition for the particles. It is obvious to see that $s = [E_{\rm cm}(M) + E_{\rm cm}(m)]^2$.

In the laboratory frame (Fig. A.1, right), where the particle with mass M is the target and that with m is the beam, the energy and momentum of initial particle are given by

$$E_{\rm lab}(m) = \frac{s - m^2 - M^2}{2M}, \quad E_{\rm lab}(M) = M, \tag{A.3.3}$$

and the absolute values of the three momentum of the beam is given by

$$|\boldsymbol{p}_{\rm lab}| = \frac{\lambda^{1/2}(s, m^2, M^2)}{2M} = \sqrt{\left(\frac{s - m^2 - M^2}{2M}\right)^2 - m^2}, \tag{A.3.4}$$

where we observe the relation

$$|\boldsymbol{p}_{cm}| = |\boldsymbol{p}_{\rm lab}|\frac{M}{\sqrt{s}}.$$

[C)] $\sqrt{s}$ is often denoted as $E_{\rm cm}$ or W.

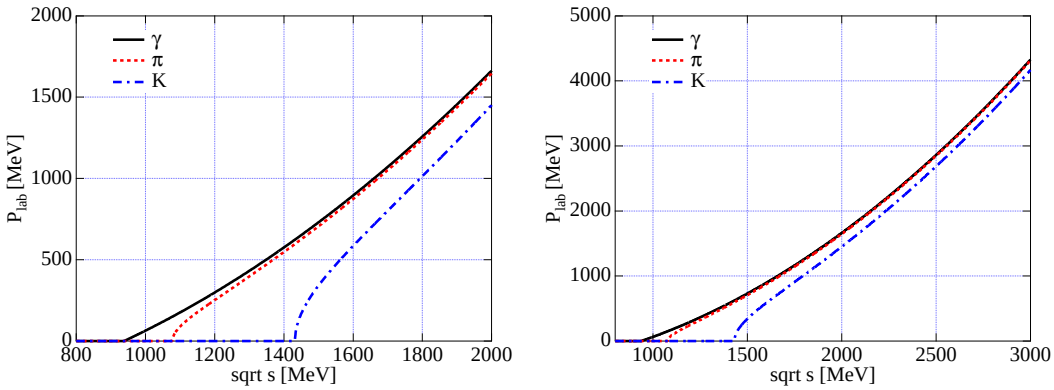

Figure A.2: Three momenta of the beams ($\boldsymbol{p}_{\rm lab}$) as functions of the $\sqrt{s}$ for the γN, πN, and $K(\bar{K})N$ reactions. Left, detail of the lower energy part of the right panel.

Note that this $\boldsymbol{p}_{\rm lab}$ is the three momentum of the initial particle of beam, not for general momentum in laboratory frame. It is easy to confirm that $\sqrt{s}$ can be written in terms of the variables in the laboratory frame $s = [E_{\rm lab}(m) + M]^2 - |\boldsymbol{p}_{\rm lab}|^2$. In Fig. A.2, we plot $|\boldsymbol{p}_{\rm lab}|$ as functions of $\sqrt{s}$ for the γN, πN, and $K(\bar{K})N$ reactions. From Eq. (A.3.4), we obtain

$$\sqrt{s} = \sqrt{2M\sqrt{|\boldsymbol{p}_{\rm lab}|^2 + m^2} + m^2 + M^2},$$

which expresses $\sqrt{s}$ in terms of $|\boldsymbol{p}_{\rm lab}|$.

For a special case of the photon $m = 0$ in the initial state, Eqs. (A.3.1), (A.3.2), (A.3.3), (A.3.4), can be written as

$$E_{\rm cm}(M) = \frac{s + M^2}{2\sqrt{s}}, \quad E_{\rm cm}(0) = |\boldsymbol{p}_{\rm cm}| = \frac{s - M^2}{2\sqrt{s}},$$
$$E_{\rm lab}(0) = |\boldsymbol{p}_{\rm lab}| = \frac{s - M^2}{2M}.$$

A.3.2 Mandelstam variables

In general, a scattering amplitude is expressed by the Mandelstam variables which are Lorentz invariant. For a process shown in Fig. A.3, they are defined by

$$s = (p_1 + p_2)^2 = (k_1 + k_2)^2,$$
$$t = (k_1 - p_1)^2 = (k_2 - p_2)^2,$$
$$u = (k_2 - p_1)^2 = (k_1 - p_2)^2.$$

There is one constraint coming from the four momentum conservation

$$s + t + u = \sum_i m_i,$$

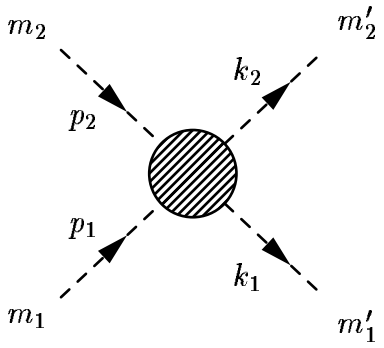

Figure A.3: Two-body scattering process.

hence, the number of independent variables is two. In order to see the angular dependence of these variables, let us evaluate them in the center of mass frame.

$$
\begin{aligned}
s &= (p_1 + p_2)^2 = (E_1 + E_2)^2 = m_1^2 + m_2^2 + 2E_1E_2, \\
t &= (k_1 - p_1)^2 = (m_1')^2 + m_1^2 - 2(E_1E_1' - |\boldsymbol{k}_1||\boldsymbol{k}_1'|\cos\theta), \\
u &= (k_2 - p_1)^2 = (m_2')^2 + m_1^2 - 2(E_2'E_1 + |\boldsymbol{k}_1||\boldsymbol{k}_2'|\cos\theta),
\end{aligned}
$$

where θ is the scattering angle in the center of mass frame. The energies and momenta are expressed in terms of $\sqrt{s}$ as shown in Eqs. (A.3.1) and (A.3.2), so all the mandelstam variables can be expressed in terms of $\sqrt{s}$ and $\cos\theta$.

When all the masses of the particles are the same, t and u can be written as

$$
t = -|\boldsymbol{k}_1|^2(1 - \cos\theta), u = -|\boldsymbol{k}_1|^2(1 + \cos\theta). \tag{A.3.5}
$$

We can see that both $t < 0$ and $u < 0$. It is instructive to not that the amplitudes of the Born diagrams is

$$
t(X) \propto \frac{1}{X - m_{\mathrm{ex}}^2}, \tag{A.3.6}
$$

with X being s, t, or u, and m_{ex} is the mass of the exchanged particle. Putting Eqs. (A.3.5) into Eq. (A.3.6), we observe the following angular dependence:

- s channel is isotropic
- t channel is forward peak
- u channel is backward peak

In practice, this is not everything and the coupling structure also provides the angular dependence.

A.3.3 Kinematics for three-body final state

Here we consider the three-body final state which corresponds to the $\pi^- p \to K^0 MB$ reaction in chapter 5 and the $K^+ p \to \pi^+ KN$ reaction in chapter 8. We assign momentum variables

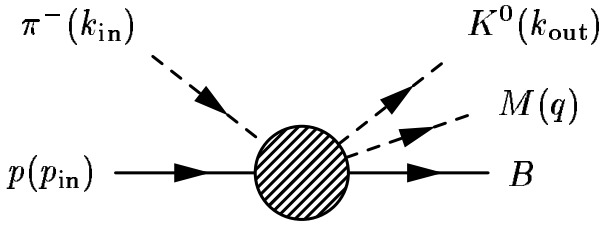

Figure A.4: Kinematics of the $\pi^- p \to K^0 MB$ reaction. For the $K^+ p \to \pi^+ KN$ reaction, we perform the replacements given in Eq. (A.3.7). In both cases, we consider the threshold production of the resonance, then the three momentum $\boldsymbol{k}_{\rm out}$ is assumed to be small.

as shown in Fig. A.4 for the $\pi^- p \to K^0 MB$ reaction. In the following, we consider the $\pi^- p \to K^0 MB$ reaction for simplicity, and one can translate the arguments into the case for the $K^+ p \to \pi^+ KN$ reaction, which is shown in Fig. 8.4, by the following replacements:

$$K^0 \to \pi^+, \quad M(q) \to K(q'), \quad B \to N, \quad \Lambda(1405) \to \Theta^+. \tag{A.3.7}$$

The energy region that we are interested in is around the threshold of K^0 and $\Lambda(1405)$ which is generated in the final state interaction in the MB system. Then the three momentum of K^0 is considered as small, ($\boldsymbol{k}_{\rm out} \sim \boldsymbol{0}$). In the limit of the final K^0 is at rest ($\boldsymbol{k}_{\rm out} = \boldsymbol{0}$), the center of mass system of the initial $\pi^- p$ and the center of mass system of the final MB are the same. We define the total energy of the initial state as $\sqrt{s}$ and the invariant mass of MB as M_I. The momenta of particles are given by

$$k_{\rm in} = (k^0_{\rm in}, \boldsymbol{k}_{\rm in}), \quad p_{\rm in} = (p^0_{\rm in}, -\boldsymbol{k}_{\rm in}), \quad k_{\rm out} = (m_{K^0}, \boldsymbol{0}), \quad q = (q^0, \boldsymbol{q})$$

where

$$|\boldsymbol{k}_{\rm in}| = \frac{\lambda^{1/2}(s, M_p^2, m_{\pi^-}^2)}{2\sqrt{s}}, \quad k^0_{\rm in} = \frac{s - M_p^2 + m_{\pi^-}^2}{2\sqrt{s}}, \quad p^0_{\rm in} = \frac{s - m_{\pi^-}^2 + M_p^2}{2\sqrt{s}},$$
$$|\boldsymbol{q}| = \frac{\lambda^{1/2}(M_I^2, M_B^2, m_M^2)}{2M_I}, \quad q^0 = \frac{M_I^2 - M_M^2 + m_M^2}{2M_I}.$$

For the kinematical factor (phase space), we need to take small $|\boldsymbol{k}_{\rm out}|$ into account, otherwise the M_I is fixed at $M_I = \sqrt{s} - M_{K^0}$. In general, in the center of mass frame of the initial particles,

$$\sqrt{s} = E_{\rm out} + E_{M_I} = \sqrt{m_{K^0}^2 + \boldsymbol{k}_{\rm out}^2} + \sqrt{M_I^2 + \boldsymbol{k}_{\rm out}^2}.$$

The maximum of the M_I is obtained by setting $\boldsymbol{k}_{\rm out} = \boldsymbol{0}$, then

$$M_I = \sqrt{s} - m_{K^0}, \tag{A.3.8}$$

On the other hand, in the center of mass frame of M and B, defining the relative momentum between M and B as $\boldsymbol{p}_{\rm rel}$, the invariant mass of M_I can be written as

$$M_I = \sqrt{m_M^2 + \boldsymbol{p}_{\rm rel}^2} + \sqrt{M_B^2 + \boldsymbol{p}_{\rm rel}^2}.$$

which has a minimum at $\boldsymbol{p}_{\rm rel} = \boldsymbol{0}$, leading to

$$M_I = M_B + m_M. \tag{A.3.9}$$

Hence, from Eqs. (A.3.8) and (A.3.9), kinematically allowed region for M_I is determined as

$$M_B + m_M \leq M_I \leq \sqrt{s} - m_{K^0}.$$

The upper bound corresponds to the K^0 at rest, while the lower bound takes place when the relative momentum of M and B is zero. The maximum of the $\boldsymbol{k}_{\rm out}$ is then obtained as

$$|\boldsymbol{k}_{\rm out}| = \frac{\lambda^{1/2}(s, (m_M + m_B)^2, M_{K^0}^2)}{2\sqrt{s}}.$$

A.4 Phase space, decay width, and cross section

Here we present formulae for cross sections and decay widths, which are used in the text. In general, n-body phase space $d\Pi$ can be written as

$$d\Pi = (2\pi)^4 \delta^{(4)}\left(P - \sum_{i=1}^{n} k_i\right) \prod_{i=1}^{n} \frac{d^3 k_i}{(2\pi)^3} N_i, \tag{A.4.1}$$

where P is the total four momentum, k_i is the momentum of channel i, and

$$N_i = \begin{cases} \dfrac{1}{2\omega_i} & \text{for bosons,} \\ \dfrac{2M_i}{2E_i} & \text{for fermions,} \end{cases}$$

with the conventions given in Appendix A. Here ω_i and E_i are the on-shell energies of the boson and the fermion.

The decay width of a resonance of mass M_R to n-body channel is

$$\Gamma_R = \int d\Pi \; \bar{\Sigma}\Sigma |t|^2, \tag{A.4.2}$$

where $P = (M_R, \boldsymbol{0})$ for the resonance rest frame and spin sum of the squared amplitude $\bar{\Sigma}\Sigma|t|^2$, which is explained in section A.2.

The total cross section with two particles 1 and 2 in the initial state is

$$\sigma = \frac{1}{v_{\rm rel}} N_1 N_2 \int d\Pi \; \bar{\Sigma}\Sigma |t|^2, \tag{A.4.3}$$

where $v_{\rm rel}$ is defined by

$$v_{\rm rel} = \frac{\sqrt{(p_1 \cdot p_2)^2 - m_1^2 m_2^2}}{p_1^0 p_2^0},$$

which coincides with the "relative velocity" $|\boldsymbol{v}_1 - \boldsymbol{v}_2|$ when $\boldsymbol{v}_1$ is parallel to $\boldsymbol{v}_2$. In the center of mass frame, $P^\mu = (\sqrt{s}, \boldsymbol{0})$ and the relative velocity $v_{\rm rel}$ takes the form

$$v_{\rm rel} = \left| \frac{|\boldsymbol{p}_1|}{\omega_1} - \frac{-|\boldsymbol{p}_1|}{\omega_2} \right| = \frac{\omega_2|\boldsymbol{p}_1| + \omega_1|\boldsymbol{p}_1|}{\omega_1\omega_2} = \frac{\sqrt{s}|\boldsymbol{p}_1|}{\omega_1\omega_2}.$$

This gives a simple form for two-boson system;

$$\frac{1}{v_{\rm rel}} N_1 N_2 = \frac{1}{4\sqrt{s}|\boldsymbol{p}_1|} = \frac{1}{2\lambda^{1/2}(s, m_1^2, m_2^2)}. \tag{A.4.4}$$

where we used Eq. (A.3.2). For a fermion, we can multiply $2M$ in the numerator. In the following, we calculate these formulae for specific cases.

A.4.1 Two-body final state

Let us evaluate the phase space for the two-body final state ($n = 2$ for Eq. (A.4.1)) explicitly in the center of mass frame $P^\mu = (\sqrt{s}, \boldsymbol{0})$. As an example, we demonstrate a two-boson system, with masses and momenta being m_i and $k_i^\mu = (\omega_i, \boldsymbol{k}_i)$, $i = 1, 2$. The result is easily extended to the fermion system by replacing $1/2\omega_i$ by $2M_i/2E_i$, *i*.e., multiplying $2M_i$. In the following, we express the variables with proper arguments, and perform integrations for the δ functions implicitly;

$$\begin{aligned}
d\Pi =& \frac{d^3k_1}{(2\pi)^3}\frac{1}{2\omega_1(|\boldsymbol{k}_1|)}\frac{d^3k_2}{(2\pi)^3}\frac{1}{2\omega_2(|\boldsymbol{k}_2|)}(2\pi)^4\delta^{(3)}(-\boldsymbol{k}_1 - \boldsymbol{k}_2)\delta(\sqrt{s} - \omega_1(|\boldsymbol{k}_1|) - \omega_2(|\boldsymbol{k}_2|)) \\
=& \frac{d^3k_1}{(2\pi)^3}\frac{1}{2\omega_1(|\boldsymbol{k}_1|)}\frac{1}{2\omega_2(|\boldsymbol{k}_1|)}(2\pi)\delta(\sqrt{s} - \omega_1(|\boldsymbol{k}_1|) - \omega_2(|\boldsymbol{k}_1|)) \\
=& \frac{1}{(2\pi)^2}d|\boldsymbol{k}_1||\boldsymbol{k}_1|^2 d\Omega \frac{1}{2\omega_1(|\boldsymbol{k}_1|)}\frac{1}{2\omega_2(|\boldsymbol{k}_1|)}\delta(\sqrt{s} - \omega(|\boldsymbol{k}_1|) - \omega(|\boldsymbol{k}_1|)).
\end{aligned}$$

Now we transform the variables $|\boldsymbol{k}_1| \to \omega_1 + \omega_2$[D)];

$$\begin{aligned}
\omega_1 + \omega_2 =& \sqrt{m_1^2 + |\boldsymbol{k}_1|^2} + \sqrt{m_2^2 + |\boldsymbol{k}_1|^2} \\
d(\omega_1 + \omega_2) =& \frac{1}{2}(m_1^2 + |\boldsymbol{k}_1|^2)^{-1/2}2|\boldsymbol{k}_1|d|\boldsymbol{k}_1| + \frac{1}{2}(m_2^2 + |\boldsymbol{k}_1|^2)^{-1/2}2|\boldsymbol{k}_1|d|\boldsymbol{k}_1| \\
=& \left(\frac{1}{\omega_1} + \frac{1}{\omega_2}\right)|\boldsymbol{k}_1|d|\boldsymbol{k}_1| \\
|\boldsymbol{k}_1|d|\boldsymbol{k}_1| =& \left(\frac{1}{\omega_1} + \frac{1}{\omega_2}\right)^{-1} d(\omega_1 + \omega_2) = \frac{\omega_1\omega_2}{\omega_1 + \omega_2} d(\omega_1 + \omega_2),
\end{aligned} \tag{A.4.5}$$

then $d\Pi$ becomes

$$\begin{aligned}
d\Pi =& \frac{1}{4\pi^2} d\Omega d(\omega_1 + \omega_2)\frac{\omega_1\omega_2}{\omega_1 + \omega_2}|\boldsymbol{k}_1(\omega_1 + \omega_2)|\frac{1}{2\omega_1}\frac{1}{2\omega_2}\delta(\sqrt{s} - (\omega_1 + \omega_2)) \\
=& \frac{1}{16\pi^2} d\Omega \frac{|\boldsymbol{k}_1(\sqrt{s})|}{\sqrt{s}} \\
=& \frac{d\Omega}{4\pi}\frac{|\boldsymbol{k}_1(\sqrt{s})|}{4\pi\sqrt{s}}.
\end{aligned} \tag{A.4.6}$$

[D)] For brevity, we denote $dk \equiv d|\boldsymbol{k}|$ in the following.

Following Eqs. (A.4.2) and (A.4.6), the decay width of a resonance with mass M_R is given by

$$\Gamma_R = \int d\Pi\ \bar{\Sigma}\Sigma|t|^2 = \frac{|\boldsymbol{k}_1|}{4\pi M_R}\int \frac{d\Omega}{4\pi}\bar{\Sigma}\Sigma|t|^2. \tag{A.4.7}$$

The cross section for the scattering as shown in Fig. A.3 is given by

$$\begin{aligned}\sigma =&\frac{1}{v_{\rm rel}}\frac{1}{2\omega(p_1)}\frac{1}{2\omega(p_2)}\int d\Pi\ \bar{\Sigma}\Sigma|t|^2\\ =&\frac{1}{4\sqrt{s}|\boldsymbol{p}_1|}\int\frac{d\Omega}{4\pi}\frac{|\boldsymbol{k}_1|}{4\pi\sqrt{s}}\bar{\Sigma}\Sigma|t|^2\\ =&\frac{1}{16\pi s}\frac{|\boldsymbol{k}_1|}{|\boldsymbol{p}_1|}\int\frac{d\Omega}{4\pi}\bar{\Sigma}\Sigma|t|^2,\end{aligned} \tag{A.4.8}$$

where we have used Eqs. (A.4.3), (A.4.4), and (A.4.6).

Let us compare the above results with some cases in the text. Eq. (A.4.8) coincides with Eq. (4.3.1) by multiplying $2m_1 2m_1'$ and performing the angle integration. The decay widths used in chapter 8, can be derived from Eq. (A.4.7). For s- and p-wave Θ^+ resonances, the decay amplitudes can be written as

$$-it = \begin{cases} -ig & \text{for } s \text{ wave},\\ -i\bar{g}(\boldsymbol{\sigma}\cdot\boldsymbol{q}) & \text{for } p \text{ wave and } J=1/2,\\ -i\tilde{g}(\boldsymbol{S}\cdot\boldsymbol{q}) & \text{for } p \text{ wave and } J=3/2,\end{cases}$$

with $g_{\Theta^+\to K^+n}$ being the coupling constant. Since there are two final states K^+n and K^0p, the squared amplitudes are given by

$$\bar{\Sigma}\Sigma|t|^2 = \begin{cases} |-ig|^2\times 2 = 2g^2 & \text{for } s \text{ wave},\\ \delta_{ij}|i\bar{g}q_i(-i\bar{g}q_j)|\times 2 = 2q^2\bar{g}^2 & \text{for } p \text{ wave and } J=1/2,\\ \frac{\delta_{ij}}{3}|i\tilde{g}q_i(-i\tilde{g}q_j)|\times 2 = \frac{2}{3}q^2\tilde{g}^2 & \text{for } p \text{ wave and } J=3/2,\end{cases}$$

where we write the three momentum of the final state as q. Then Eq. (A.4.7) gives the decay widths (with $2M$ for the nucleon in the final state)

$$\Gamma = 2M\frac{q}{4\pi M_R}\int\frac{d\Omega}{4\pi}\bar{\Sigma}\Sigma|t|^2 = \begin{cases}\dfrac{Mq}{\pi M_R}g^2 & \text{for } s \text{ wave},\\ \dfrac{Mq^3}{\pi M_R}\bar{g}^2 & \text{for } p \text{ wave and } J=1/2,\\ \dfrac{Mq^3}{3\pi M_R}\tilde{g}^2 & \text{for } p \text{ wave and } J=3/2.\end{cases}$$

With these formulae, we can verify Eq. (8.2.15) in chapter 8. Eq. (5.2.17) can be reproduced by removing the isospin factor 2 from the result for p wave and $J=1/2$. Defining the amplitude as

$$\bar{\Sigma}\Sigma|t|^2 = F_I g_R^2\frac{n\pi}{M}\frac{p^{2l}}{M_R^{2l-1}},$$

with n being numeric factor (1 for $J = 1/2$ and 3 for $J = 3/2$), we obtain

$$\Gamma_R \equiv g_R^2 F_I \frac{p^{2l+1}}{M_R^{2l}},$$

which corresponds to the formula (10.2.2) in chapter 10.

A.4.2 Three-body final state

In this thesis, we have encountered the calculation for the three-body final state. Let us consider the cases used in our study, namely,

- the decay width of $N^* \to \pi\pi N$ (chapters 5 and 11), and
- the differential cross section for MMB channel in terms of the invariant mass of MB channel (chapters 5 and 8).

We first evaluate the decay width of the process $R \to BMM'$ where R is a resonance with mass M_R, B is a baryon with mass M, and M and M' are mesons with mass m and m', respectively. We assume that the transition amplitude depends on the energies of two mesons and relative angle between them, which is the case for what we used. In the rest frame of the resonance R, we assign the momentum variables as $R(P) \to B(p)M(k)M'(k')$ with $P^\mu = (M_R, \mathbf{0})$, $p^\mu = (E, \boldsymbol{p})$, $k^\mu = (\omega, \boldsymbol{k})$, and $k'^\mu = (\omega', \boldsymbol{k}')$. Following Eqs. (A.4.1) and (A.4.2), the decay width is given by

$$\begin{aligned}
\Gamma_{BMM'} &= \int \frac{d^3p}{(2\pi)^3}\frac{M}{E}\int \frac{d^3k}{(2\pi)^3}\frac{1}{2\omega}\int \frac{d^3k'}{(2\pi)^3}\frac{1}{2\omega'}\bar{\Sigma}\Sigma|t(\omega,\omega',\cos\theta)|^2(2\pi)^4\delta^{(4)}(P-p'-k-k'),\\
&= \int \frac{d^3p}{(2\pi)^3}\frac{M}{E}\delta^{(3)}(-\boldsymbol{p}-\boldsymbol{k}-\boldsymbol{k}')\int \frac{d^3k}{(2\pi)^3}\frac{1}{2\omega}\int \frac{d^3k'}{(2\pi)^3}\frac{1}{2\omega'}\\
&\quad\times \bar{\Sigma}\Sigma|t(\omega,\omega',\cos\theta)|^2(2\pi)^4\delta(M_R-E-\omega-\omega')\\
&= \int \frac{d^3k}{(2\pi)^3}\int \frac{d^3k'}{(2\pi)^3}\frac{M}{E}\frac{1}{2\omega}\frac{1}{2\omega'}\bar{\Sigma}\Sigma|t(\omega,\omega',\cos\theta)|^2(2\pi)\delta(M_R-E-\omega-\omega')
\end{aligned}$$

with the condition $\boldsymbol{p} = -\boldsymbol{k} - \boldsymbol{k}'$. We define $\cos\theta$ by the angle between $\boldsymbol{k}$ and $\boldsymbol{k}'$. Then E can be written as

$$E = \sqrt{M^2 + \boldsymbol{p}^2} = \sqrt{M^2 + \boldsymbol{k}^2 + (\boldsymbol{k}')^2 + 2|\boldsymbol{k}||\boldsymbol{k}'|\cos\theta}.$$

Integrating over the trivial angular variables, we obtain

$$\begin{aligned}
\Gamma_{BMM'} =& \frac{4\pi}{(2\pi)^3}\int \boldsymbol{k}^2 dk \frac{2\pi}{(2\pi)^3}\int (\boldsymbol{k}')^2 dk' \int_{-1}^{1} d\cos\theta \frac{M}{E}\frac{1}{2\omega}\frac{1}{2\omega'}\bar{\Sigma}\Sigma|t(\omega,\omega',\cos\theta)|^2\\
&\times (2\pi)\delta(M_R - \sqrt{M^2 + \boldsymbol{k}^2 + (\boldsymbol{k}')^2 + 2|\boldsymbol{k}||\boldsymbol{k}'|\cos\theta} - \omega - \omega').
\end{aligned}$$

Utilizing the identity

$$\delta[f(x)] = \left|\frac{\partial f(x)}{\partial x}\right|^{-1}_{x=x_0}\delta(x - x_0),$$

which are, in the present case,

$$\begin{aligned} f(\cos\theta) =& M_R - \sqrt{M^2 + \boldsymbol{k}^2 + (\boldsymbol{k}')^2 + 2|\boldsymbol{k}||\boldsymbol{k}'|\cos\theta} - \omega - \omega', \\ \left|\frac{\partial f}{\partial \cos\theta}\right| =& \frac{1}{2}\frac{2|\boldsymbol{k}||\boldsymbol{k}'|}{\sqrt{M^2 + \boldsymbol{k}^2 + (\boldsymbol{k}')^2 + 2|\boldsymbol{k}||\boldsymbol{k}'|\cos\theta}} = \frac{|\boldsymbol{k}||\boldsymbol{k}'|}{E}, \end{aligned}$$

and the singularity point x_0 is given by

$$\begin{aligned} M_R - \omega - \omega' =& \sqrt{M^2 + \boldsymbol{k}^2 + (\boldsymbol{k}')^2 + 2|\boldsymbol{k}||\boldsymbol{k}'|\cos\theta} \\ [M_R - \omega - \omega']^2 =& M^2 + \boldsymbol{k}^2 + (\boldsymbol{k}')^2 + 2|\boldsymbol{k}||\boldsymbol{k}'|\cos\theta \\ \cos\theta =& \frac{(M_R - \omega - \omega')^2 - M^2 - \boldsymbol{k}^2 - (\boldsymbol{k}')^2}{2|\boldsymbol{k}||\boldsymbol{k}'|} \equiv a. \end{aligned} \tag{A.4.9}$$

Hence, we obtain

$$\delta[f(\cos\theta)] = \frac{E}{|\boldsymbol{k}||\boldsymbol{k}'|}\delta(\cos\theta - a),$$

which will be integrated as

$$\int_{-1}^{1} d\cos\theta\ \delta(\cos\theta - a) = \Theta(1-a) - \Theta(-1-a) = \Theta(1-a^2),$$

where $\Theta(x)$ is the step function, 0 for $x < 0$ and 1 for $0 < x$. Thus, we obtain

$$\begin{aligned} \Gamma_{BMM'} =& \frac{4\pi}{(2\pi)^3}\int \boldsymbol{k}^2 dk \frac{2\pi}{(2\pi)^3}\int (\boldsymbol{k}')^2 dk' \frac{M}{E}\frac{1}{2\omega}\frac{1}{2\omega'}(2\pi) \\ & \times \int_{-1}^{1} d\cos\theta \bar{\Sigma}\Sigma |t(\omega,\omega',\cos\theta)|^2 \frac{E}{|\boldsymbol{k}||\boldsymbol{k}'|}\delta(\cos\theta - a) \\ =& \frac{4\pi}{(2\pi)^3}\int \boldsymbol{k}^2 dk \frac{2\pi}{(2\pi)^3}\int (\boldsymbol{k}')^2 dk' \frac{M}{E}\frac{1}{2\omega}\frac{1}{2\omega'}(2\pi)\frac{E}{|\boldsymbol{k}||\boldsymbol{k}'|}|t(\omega,\omega',a)|^2\Theta(1-a^2) \\ =& \frac{M}{16\pi^3}\int |\boldsymbol{k}| dk \int |\boldsymbol{k}'| dk' \frac{1}{\omega}\frac{1}{\omega'}\bar{\Sigma}\Sigma |t(\omega,\omega',a)|^2\Theta(1-a^2) \end{aligned}$$

Now we transform

$$\begin{aligned} \omega &= \sqrt{m^2 + \boldsymbol{k}^2} \\ d\omega &= \frac{1}{2}\frac{2\boldsymbol{k}dk}{\sqrt{m^2 + \boldsymbol{k}^2}} \\ \omega d\omega &= \boldsymbol{k}dk, \qquad \omega' d\omega' = \boldsymbol{k}' dk'. \end{aligned} \tag{A.4.10}$$

Finally we obtain the decay width as

$$\begin{aligned} \Gamma_{BMM'} =& \frac{M}{16\pi^3}\int \omega d\omega \int \omega' d\omega' \frac{1}{\omega}\frac{1}{\omega'}\bar{\Sigma}\Sigma |t(\omega,\omega',a)|^2\Theta(1-a^2) \\ =& \frac{M}{16\pi^3}\int_{\omega_{\min}}^{\omega_{\max}} d\omega \int_{\omega'_{\min}}^{\omega'_{\max}} d\omega' \bar{\Sigma}\Sigma |t(\omega,\omega',a)|^2\Theta(1-a^2). \end{aligned} \tag{A.4.11}$$

The regions of ω and ω' are given by

$$\begin{aligned}
&\omega_{\min} = m, \quad \omega'_{\min} = m', \\
&\omega_{\max} = \frac{M_R^2 + (m')^2 - (M+m')^2}{2M_R}, \quad \omega'_{\max} = \frac{M_R^2 + m^2 - (M+m)^2}{2M_R},
\end{aligned} \tag{A.4.12}$$

where $\omega_{\max}(\omega'_{\max})$ corresponds to the case when $M'(M)$ and B moves together. Eq. (5.2.12) is reproduced by omitting the a dependence in the amplitude. Eq. A.4.11 gives a general expression for the three-body phase space integration. For the specific example with the $N^* \to N\pi\pi$ decay, in which $m = m'$, Eq. (A.4.12) reduces to a simpler form

$$\omega_{\max} = \omega'_{\max} = \frac{M_R^2 - M^2 + 2mM}{2M_R},$$

which, together with Eqs. (A.4.11) and (A.4.9) correspond to Eqs. (5.2.14), (5.2.12), and (5.2.13) in chapter 5, respectively. The formulae are also used in section 11.4 in chapter 11.

Using Eq. (A.4.11), we can obtain the formula for the total cross section for three-body final state with appropriate factors. Here we consider the processes in chapters 5 and 8, in which we need the differential cross section in terms of M_I, the invariant mass of final two-body system. It is possible to differentiate the total cross section numerically, but here we rather calculate it analytically. For convenience, we use the kinematical variables shown in subsection A.3.3. Following Eqs. (A.4.1) and (A.4.3), with notations shown in Fig. A.4, the total cross section is given by

$$\begin{aligned}
\sigma =& \frac{1}{v_{\rm rel}} \frac{1}{2\omega_{\rm in}} \frac{M_p}{E_p} \int d\Pi \bar{\Sigma}\Sigma |t|^2 \\
=& \frac{M_p}{\lambda^{1/2}(s, M_p^2, m_\pi^2)} \int \frac{d^3k_{\rm out}}{(2\pi)^3} \frac{1}{2\omega_{\rm out}} \int \frac{d^3q}{(2\pi)^3} \frac{1}{2\omega_m} \int \frac{d^3p'}{(2\pi)^3} \frac{M_B}{E_B} \\
& \times (2\pi)^4 \delta^{(4)}(P - k_{\rm out} - q - p') \bar{\Sigma}\Sigma |t|^2 \\
=& \frac{M_p}{\lambda^{1/2}(s, M_p^2, m_\pi^2)} \int \frac{d^3k_{\rm out}}{(2\pi)^3} \frac{1}{2\omega_{\rm out}} \int \frac{d^3q}{(2\pi)^3} \frac{1}{2\omega_m} \frac{M_B}{E_B} (2\pi) \delta(\sqrt{s} - \omega_{\rm out} - \omega_m - E_B) \bar{\Sigma}\Sigma |t|^2
\end{aligned}$$

We transform one of the integration variables into M_I, which can be expressed as $M_I^2 = s + m_K^2 - 2\sqrt{s}\omega_{\rm out}$. This leads to

$$2M_I dM_I = 2\sqrt{s} d\omega_{\rm out}$$

Using this and Eq. (A.4.10) ($\omega d\omega = |\boldsymbol{k}| dk$), we have

$$\begin{aligned}
\sigma =& \frac{M_p}{\lambda^{1/2}(s, M_p^2, m_\pi^2)} \int d\Omega \int \frac{dk_{\rm out}}{(2\pi)^3} |\boldsymbol{k}_{\rm out}|^2 \frac{1}{2\omega_{\rm out}} \\
& \times \int \frac{d^3q}{(2\pi)^3} \frac{1}{2\omega_m} \frac{M_B}{E_B} (2\pi) \delta(\sqrt{s} - \omega_{\rm out} - \omega_m - E_B) \bar{\Sigma}\Sigma |t|^2 \\
=& \frac{M_p}{\lambda^{1/2}(s, M_p^2, m_\pi^2)} \frac{4\pi}{(2\pi)^3} \int d\omega_{\rm out} |\boldsymbol{k}_{\rm out}| \omega_{\rm out} \frac{1}{2\omega_{\rm out}}
\end{aligned}$$

$$
\begin{aligned}
&\times \int \frac{d^3q}{(2\pi)^3}\frac{1}{2\omega_m}\frac{M_B}{E_B}(2\pi)\delta(\sqrt{s}-\omega_{\rm out}-\omega_m-E_B)\bar{\Sigma}\Sigma|t|^2 \\
=&\frac{M_p}{\lambda^{1/2}(s,M_p^2,m_\pi^2)}\frac{1}{2\pi^2}\int dM_I\frac{M_I}{\sqrt{s}}|\boldsymbol{k}_{\rm out}|\frac{1}{2} \\
&\times \int \frac{d^3q}{(2\pi)^3}\frac{1}{2\omega_m}\frac{M_B}{E_B}(2\pi)\delta(M_I-\omega_m-E_B)\bar{\Sigma}\Sigma|t|^2 \\
=&\frac{M_p}{\lambda^{1/2}(s,M_p^2,m_\pi^2)}\frac{1}{2\pi}\int dM_I\frac{M_I}{\sqrt{s}}|\boldsymbol{k}_{\rm out}|\int \frac{d^3q}{(2\pi)^3}\frac{1}{2\omega_m}\frac{M_B}{E_B}\delta(M_I-\omega_m-E_B)\bar{\Sigma}\Sigma|t|^2.
\end{aligned}
$$

Now we use a similar transformation as in Eq. (A.4.5), then

$$
dq=\frac{E_B\omega_m}{E_B+\omega_m}d(E_B+\omega_m),
$$

which leads to

$$
\begin{aligned}
\sigma =&\frac{M_p}{\lambda^{1/2}(s,M_p^2,m_\pi^2)}\frac{1}{2\pi}\int dM_I\frac{M_I}{\sqrt{s}}|\boldsymbol{k}_{\rm out}| \\
&\times \int d\Omega\frac{1}{(2\pi)^3}\int d(E_B+\omega_m)\frac{E_B\omega_m}{E_B+\omega_m}|\boldsymbol{q}|\frac{1}{2\omega_m}\frac{M_B}{E_B}\delta(M_I-\omega_m-E_B)\bar{\Sigma}\Sigma|t|^2 \\
=&\frac{M_p}{\lambda^{1/2}(s,M_p^2,m_\pi^2)}\frac{1}{2\pi}\int dM_I\frac{M_I}{\sqrt{s}}|\boldsymbol{k}_{\rm out}||\boldsymbol{q}|\int d\Omega\frac{1}{(2\pi)^3}\frac{1}{M_I}\frac{1}{2}M_B\bar{\Sigma}\Sigma|t|^2 \\
=&\frac{1}{(2\pi)^3}\frac{M_pM_B}{\lambda^{1/2}(s,M_p^2,m_\pi^2)}\int dM_I\frac{|\boldsymbol{k}_{\rm out}||\boldsymbol{q}|}{\sqrt{s}}\int\frac{d\Omega}{4\pi}\bar{\Sigma}\Sigma|t|^2 \\
=&\frac{1}{(2\pi)^3}\frac{M_pM_B}{\lambda^{1/2}(s,M_p^2,m_\pi^2)}\int dM_I\frac{1}{\sqrt{s}}\frac{\lambda^{1/2}(s,M_I^2,m_{K^0}^2)}{2\sqrt{s}}\frac{\lambda^{1/2}(M_I^2,M_B^2,m_M^2)}{2M_I}\int\frac{d\Omega}{4\pi}\bar{\Sigma}\Sigma|t|^2 \\
=&\frac{1}{(2\pi)^3}\frac{1}{4s}\frac{M_pM_B}{\lambda^{1/2}(s,M_p^2,m_\pi^2)}\int dM_I\frac{1}{M_I}\lambda^{1/2}(s,M_I^2,m_{K^0}^2)\lambda^{1/2}(M_I^2,M_B^2,m_M^2)\int\frac{d\Omega}{4\pi}\bar{\Sigma}\Sigma|t|^2
\end{aligned}
$$

Hence, the differential cross section in terms of M_I is written as

$$
\frac{d\sigma}{dM_I}=\frac{1}{(2\pi)^3}\frac{1}{4s}\frac{M_pM_B}{\lambda^{1/2}(s,M_p^2,m_\pi^2)}\frac{1}{M_I}\lambda^{1/2}(s,M_I^2,m_{K^0}^2)\lambda^{1/2}(M_I^2,M_B^2,m_M^2)\bar{\Sigma}\Sigma|t|^2 \quad \text{(A.4.13)}
$$

when the amplitude does not have the angular dependence. This corresponds to Eq. (5.2.9) in chapter 5. When the amplitude contain the $\cos\theta$ dependence as in chapter 8, we have

$$
\frac{d^2\sigma}{dM_Id\cos\theta}=\frac{1}{(2\pi)^3}\frac{1}{8s}\frac{M^2}{\lambda^{1/2}(s,M^2,m_K^2)}\frac{1}{M_I}\lambda^{1/2}(s,M_I^2,m_\pi^2)\lambda^{1/2}(M_I^2,M^2,m_K^2)\bar{\Sigma}\Sigma|t|^2, \quad \text{(A.4.14)}
$$

with the suitable replacements (A.3.7). This corresponds to Eq. (8.2.20) in chapter 8.

A.4.3 Four-body final state

Here we show the cross section for the $\gamma p\to\pi^+K^0MB$ reaction studied in chapter 5. We assign momentum variables as $\gamma p\to K^0(p_1)\pi^+(p_2)M(p_3)B(p_4)$. According to Eqs. (A.4.1)

and (A.4.3), the total cross section for this process is given by

$$\begin{aligned}
\sigma =& \frac{1}{v_{\rm rel}} \frac{1}{2\omega_\gamma} \frac{2M_p}{2E_p} \int d\Pi \bar{\Sigma}\Sigma |t|^2 \\
=& \frac{M_p}{\lambda^{1/2}(s, M_p^2, 0)} \int \frac{d^3p_1}{(2\pi)^3} \frac{1}{2\omega_1} \int \frac{d^3p_2}{(2\pi)^3} \frac{1}{2\omega_2} \int \frac{d^3p_3}{(2\pi)^3} \frac{1}{2\omega_3} \int \frac{d^3p_4}{(2\pi)^3} \frac{2M_B}{2E_B} \\
& \times (2\pi)^4 \delta^{(4)}(P - p_1 - p_2 - p_3 - p_4) \bar{\Sigma}\Sigma |t|^2 \\
=& \frac{2M_p M_B}{s - M_p^2} \int \frac{d^3p_1}{(2\pi)^3} \frac{1}{2\omega_1} \int \frac{d^3p_2}{(2\pi)^3} \frac{1}{2\omega_2} \int \frac{d^3p_3}{(2\pi)^3} \frac{1}{2\omega_3} \int \frac{d^3p_4}{(2\pi)^3} \frac{1}{2E_B} \\
& \times (2\pi)^4 \delta^{(4)}(P - p_1 - p_2 - p_3 - p_4) \bar{\Sigma}\Sigma |t|^2 .
\end{aligned}$$

Since the phase space is Lorentz invariant, we evaluate the last two integrations and the δ function in the center of mass frame of the MB system. Defining $M_I = (P - p_1 - p_2)^2$, we obtain

$$\begin{aligned}
& \int \frac{d^3\tilde{p}_3}{(2\pi)^3} \frac{1}{2\tilde{\omega}_3} \int \frac{d^3\tilde{p}_4}{(2\pi)^3} \frac{1}{2\tilde{E}_B} (2\pi)^4 \delta^{(4)}(P - p_1 - p_2 - \tilde{p}_3 - \tilde{p}_4) \bar{\Sigma}\Sigma |t|^2 \\
=& \int \frac{d^3\tilde{p}_3}{(2\pi)^3} \frac{1}{2\tilde{\omega}_3} \frac{1}{2\tilde{E}_B} (2\pi) \delta(M_I - \tilde{\omega}_3 - \tilde{E}_B) \bar{\Sigma}\Sigma |t|^2 \\
=& \frac{1}{(2\pi)^3} 2\pi \int_{-1}^{1} d\cos\bar{\theta} \int \tilde{\boldsymbol{p}}_3^2 d\tilde{p}_3 \frac{1}{2\tilde{\omega}_3} \frac{1}{2\tilde{E}_B} (2\pi) \delta(M_I - \tilde{\omega}_3 - \tilde{E}_B) \bar{\Sigma}\Sigma |t|^2 \\
=& \frac{1}{2\pi} \frac{1}{4} \int_{-1}^{1} d\cos\bar{\theta} \int |\tilde{\boldsymbol{p}}_3| \frac{d(\tilde{\omega}_3 + \tilde{E}_B)}{\tilde{\omega}_3 + \tilde{E}_B} \delta(M_I - \tilde{\omega}_3 - \tilde{E}_B) \bar{\Sigma}\Sigma |t|^2 \\
=& \frac{1}{8\pi} \int_{-1}^{1} d\cos\bar{\theta} \frac{|\tilde{\boldsymbol{p}}_3|}{M_I} \bar{\Sigma}\Sigma |t|^2 ,
\end{aligned}$$

where we use $|\tilde{\boldsymbol{p}}_3| d\tilde{p}_3 = \tilde{\omega}_3 \tilde{E}_B d(\tilde{\omega}_3 + \tilde{E}_B)/(\tilde{\omega}_3 + \tilde{E}_B)$ and $\bar{\theta}$ is the angle between the intermediate K^- and the final M, to account for the Σ^* intermediate state. Finally we have

$$\sigma = \frac{2M_p M_B}{s - M_p^2} \int \frac{d^3p_1}{(2\pi)^3} \frac{1}{2\omega_1} \int \frac{d^3p_2}{(2\pi)^3} \frac{1}{2\omega_2} \frac{1}{8\pi} \int_{-1}^{1} d\cos\bar{\theta} \frac{|\tilde{\boldsymbol{p}}_3|}{M_I} \bar{\Sigma}\Sigma |t|^2 ,$$

which corresponds to Eq. (5.3.7) in chapter 5. It is also possible to derive the differential cross section in terms of M_I analytically as done in the previous subsection, but in practice we adopt the Monte-Carlo method to integrate the cross section, and calculate the differential cross section numerically.

Appendix B

Effective Lagrangians

In this chapter, we present the effective Lagrangians that have been used in this thesis. First we show the Lagrangians in chiral perturbation theory, and then display the other effective Lagrangians used in the calculation of the reaction processes. We also demonstrate the nonrelativistic reduction of the amplitudes which have been often used in this thesis.

B.1 Chiral Lagrangians

Here we summarize the Lagrangians of flavor SU(3) chiral perturbation theory. We follow mainly the notation given in Ref. [48], but for the chiral transformation we use a common notation [3, 41, 42, 565, 40, 513, 514].

B.1.1 Definition of the fields

Chiral perturbation theory is constructed based on the nonlinear realization of the chiral symmetry group $\mathrm{SU}(3)_L \times \mathrm{SU}(3)_R$, which spontaneously breaks down into the vector subgroup $\mathrm{SU}(3)_V$. The octet pseudoscalar mesons are identified as the Nambu-Goldstone bosons associated with the spontaneous breaking of chiral symmetry. Their fields are defined in the SU(3) matrix form as

$$\Phi = \begin{pmatrix} \frac{1}{\sqrt{2}}\pi^0 + \frac{1}{\sqrt{6}}\eta & \pi^+ & K^+ \\ \pi^- & -\frac{1}{\sqrt{2}}\pi^0 + \frac{1}{\sqrt{6}}\eta & K^0 \\ K^- & \bar{K}^0 & -\frac{2}{\sqrt{6}}\eta \end{pmatrix},$$

and the chiral fields U and ξ are defined by

$$U(\Phi) = \exp\left\{\frac{i\sqrt{2}\Phi}{f}\right\}, \quad \xi(\Phi) = \exp\left\{\frac{i\Phi}{\sqrt{2}f}\right\}, \quad U(\Phi) = \xi^2(\Phi), \tag{B.1.1}$$

where f is a quantity of mass dimension, and will be identified with the meson decay constant.

Explicit SU(3) breaking quark mass term and electromagnetic and weak interactions are introduced by the external fields v_μ, a_μ, s and p as in section 2.4. We define the scalar χ and

left and right currents l_μ and r_μ as

$$\chi = 2B_0(s+ip), \quad l_\mu = v_\mu - a_\mu, \quad r_\mu = v_\mu + a_\mu, \tag{B.1.2}$$

where B_0 is a coefficient and will be defined when we introduce the symmetry breaking mass term in the Lagrangian. Associated with these external currents, the covariant derivative for the chiral field is defined by [A)]

$$D_\mu U = \partial_\mu U - ir_\mu U + iUl_\mu, \quad D_\mu U^\dagger = \partial_\mu U^\dagger + iU^\dagger r_\mu - il_\mu U^\dagger. \tag{B.1.3}$$

The field strength tensors are defined by

$$R^{\mu\nu} = \partial^\mu r^\nu - \partial^\nu r^\mu - i[r^\mu, r^\nu], \quad L^{\mu\nu} = \partial^\mu l^\nu - \partial^\nu l^\mu - i[l^\mu, l^\nu].$$

These will be used to construct the Lagrangians for meson system.

For later convenience to introduce matter fields, here we define the scalar (σ) and pseudoscalar (ρ) quantities by

$$\sigma = \xi\chi^\dagger\xi + \xi^\dagger\chi\xi^\dagger, \quad \rho = \xi\chi^\dagger\xi - \xi^\dagger\chi\xi^\dagger. \tag{B.1.4}$$

We also introduce the vector (V_μ) and axial vector (A_μ) currents

$$V_\mu = -\frac{i}{2}(\xi^\dagger\partial_\mu\xi + \xi\partial_\mu\xi^\dagger) - \frac{1}{2}(\xi^\dagger r_\mu\xi + \xi l_\mu\xi^\dagger), \tag{B.1.5}$$

$$A_\mu = -\frac{i}{2}(\xi^\dagger\partial_\mu\xi - \xi\partial_\mu\xi^\dagger) - \frac{1}{2}(\xi^\dagger r_\mu\xi - \xi l_\mu\xi^\dagger), \tag{B.1.6}$$

and the field strength tensors

$$F_R^{\mu\nu} = \xi^\dagger R^{\mu\nu}\xi, \quad F_L^{\mu\nu} = \xi L^{\mu\nu}\xi^\dagger. \tag{B.1.7}$$

It is useful to present the expansion of the chiral fields and currents:

$$\begin{aligned}
U(\Phi) =& 1 + \frac{i\sqrt{2}}{f}\Phi - \frac{1}{f^2}\Phi^2 - i\frac{\sqrt{2}\Phi^3}{3f^3} + \frac{\Phi^4}{6f^4} + \cdots, \\
U^\dagger(\Phi) =& 1 - \frac{i\sqrt{2}}{f}\Phi - \frac{1}{f^2}\Phi^2 + i\frac{\sqrt{2}\Phi^3}{3f^3} + \frac{\Phi^4}{6f^4} + \cdots, \\
\xi(\Phi) =& 1 + i\frac{\Phi}{\sqrt{2}f} - \frac{\Phi^2}{4f^2} - i\frac{\Phi^3}{12\sqrt{2}f^3} + \frac{\Phi^4}{96f^4} + \cdots, \\
\xi^\dagger(\Phi) =& 1 - i\frac{\Phi}{\sqrt{2}f} - \frac{\Phi^2}{4f^2} + i\frac{\Phi^3}{12\sqrt{2}f^3} + \frac{\Phi^4}{96f^4} + \cdots.
\end{aligned}$$

Using these, the vector and axial vector currents made from mesons are expressed as

$$\begin{aligned}
V_\mu =& -\frac{i}{4f^2}(\Phi\partial_\mu\Phi - \partial_\mu\Phi\cdot\Phi) + \cdots, \\
A_\mu =& \frac{\partial_\mu\Phi}{\sqrt{2}f} - \frac{1}{12\sqrt{2}f^3}\left(\partial_\mu\Phi(\Phi^2) - 2\Phi\partial_\mu\Phi(\Phi) + \Phi^2\partial_\mu\Phi\right) + \cdots.
\end{aligned}$$

[A)] Here we adopt the convention in Refs. [40, 513, 514], because of the chiral transformation defined in the next subsection.

Correspondence to the notations in Refs. [565, 40, 513, 514] can be expressed by the present conventions as

$$u = \xi, \quad \Gamma_\mu = iV_\mu, \quad u_\mu = \Delta_\mu = -2A_\mu.$$

The other hadrons than the pseudoscalar bosons are introduced as matter fields. The fields of the octet baryons are defined as

$$B = \begin{pmatrix} \frac{1}{\sqrt{2}}\Sigma^0 + \frac{1}{\sqrt{6}}\Lambda & \Sigma^+ & p \\ \Sigma^- & -\frac{1}{\sqrt{2}}\Sigma^0 + \frac{1}{\sqrt{6}}\Lambda & n \\ \Xi^- & \Xi^0 & -\frac{2}{\sqrt{6}}\Lambda \end{pmatrix},$$

and the antidecuplet baryons are expressed in the totally symmetric tensor P^{ijk} as

$$\begin{gathered} P^{333} = \sqrt{6}\Theta^+_{\mathbf{\overline{10}}}\,, \\ P^{133} = \sqrt{2}\,N^0_{\mathbf{\overline{10}}}\,, \qquad P^{233} = -\sqrt{2}\,N^+_{\mathbf{\overline{10}}}\,, \\ P^{113} = \sqrt{2}\,\Sigma^-_{\mathbf{\overline{10}}}\,, \qquad P^{123} = -\Sigma^0_{\mathbf{\overline{10}}}\,, \qquad P^{223} = -\sqrt{2}\,\Sigma^+_{\mathbf{\overline{10}}}\,, \\ P^{111} = \sqrt{6}\Xi^{--}_{\mathbf{\overline{10}}}\,, \qquad P^{112} = -\sqrt{2}\,\Xi^-_{\mathbf{\overline{10}}}\,, \qquad P^{122} = \sqrt{2}\,\Xi^0_{\mathbf{\overline{10}}}\,, \qquad P^{222} = -\sqrt{6}\Xi^+_{\mathbf{\overline{10}}}\,, \end{gathered}$$

where we have adopted the normalization in Ref. [249], which is different from those used in Refs. [259, 256, 258] by a sign and/or a factor. The covariant derivative for the octet baryon fields can be defined as

$$\mathcal{D}_\mu B = \partial_\mu B + i[V_\mu, B]. \tag{B.1.8}$$

B.1.2 Chiral transformation

In order to construct chiral Lagrangians, we combine the above fields to be invariant under chiral transformations. The Lagrangians are classified in terms of the number of derivatives acting on the meson fields, according to the chiral order counting rule. In the following, we denote the chiral Lagrangians as

$$\mathcal{L}_n^{X(i)},$$

where n is the chiral order, i denotes the number of mesons, if necessary, and $X = M$, B, or P labels the Lagrangians for mesons, mesons and baryons, or those including antidecuplet.

Under a chiral transformation $g \in \mathrm{SU}(3)_L \times \mathrm{SU}(3)_R$, chiral fields U and ξ in Eq. (B.1.1) transform as

$$\begin{aligned} &U \xrightarrow{g} RUL^\dagger, \quad U^\dagger \xrightarrow{g} LU^\dagger R^\dagger, \\ &\xi \xrightarrow{g} R\xi h^\dagger = h\xi L^\dagger, \quad \xi^\dagger \xrightarrow{g} L\xi^\dagger h^\dagger = h\xi^\dagger R^\dagger, \end{aligned}$$

where $L \in \mathrm{SU}(3)_L$, $R \in \mathrm{SU}(3)_R$, and $h(\Phi, g) \in \mathrm{SU}(3)_V$.

The transformation low for the external fields in Eq. (B.1.2) are given by

$$\chi \xrightarrow{g} R\chi L^\dagger, \quad l_\mu \xrightarrow{g} Ll_\mu L^\dagger + iL\partial_\mu L^\dagger, \quad r_\mu \xrightarrow{g} Rr_\mu R^\dagger + iR\partial_\mu R^\dagger.$$

It is easy to confirm that the covariant derivative of the chiral field in Eq. (B.1.3) transforms as in the same way with the original chiral field as

$$D_\mu U \xrightarrow{g} R D_\mu U L^\dagger, \quad D_\mu U^\dagger \xrightarrow{g} L D_\mu U R^\dagger,$$

The transformation lows for the quantities defined in Eqs. (B.1.4), (B.1.6), and (B.1.7) are

$$O \xrightarrow{g} h O h^\dagger \quad \text{for } O = \sigma, \rho, A_\mu, F_R^{\mu\nu}, F_L^{\mu\nu}.$$

and that for the vector current is given by

$$V_\mu \xrightarrow{g} h V_\mu h^\dagger - i h \partial_\mu h^\dagger.$$

Using these external fields, we can introduce terms of explicit chiral symmetry breaking and of photon coupling, by choosing

$$s = \mathbf{m}, \quad l_\mu = r_\mu = eQA_\mu,$$

where A_μ is the photon field and e is the unit electric charge and

$$\mathbf{m} = \begin{pmatrix} m_u & & \\ & m_d & \\ & & m_s \end{pmatrix} \quad Q = \frac{1}{3}\begin{pmatrix} 2 & & \\ & -1 & \\ & & -1 \end{pmatrix}. \tag{B.1.9}$$

The transformation lows for the matter fields follows the representation in $\mathrm{SU}(3)_V$. For instance, baryon octet field B transform as

$$B \xrightarrow{g} h B h^\dagger, \quad \bar{B} \xrightarrow{g} h \bar{B} h^\dagger,$$

and the antidecuplet field P^{ijk} transforms as

$$P^{ijk} \xrightarrow{g} h^i{}_a h^j{}_b h^k{}_c P^{abc}.$$

B.1.3 Meson system

For the meson system, the lowest order Lagrangian consists of terms with two derivatives on the U field which is of order $\mathcal{O}(p^2)$ and is uniquely given by [3, 41, 42]

$$\mathcal{L}_2^M = \frac{f^2}{4}\mathrm{Tr}(D_\mu U^\dagger D^\mu U + U^\dagger \chi + \chi^\dagger U),$$

where f is the meson decay constant. Expanding the chiral field, we obtain the kinetic terms and mass terms for mesons in the $\mathcal{L}_2^{M(2)}$ where two meson fields are included:

$$\mathcal{L}_2^{M(2)} = \frac{1}{2}\mathrm{Tr}(\partial_\mu \Phi \partial^\mu \Phi) - B_0 \mathrm{Tr}\left(\boldsymbol{m}\Phi^2\right),$$

where the meson kinetic term and mass term appear. The terms including four meson fields are responsible for meson-meson interactions

$$\mathcal{L}_2^{M(4)} = \frac{1}{12f^2}\mathrm{Tr}\left((\Phi\partial_\mu\Phi - \partial_\mu\Phi\Phi)^2\right) - \frac{B_0}{6f^2}\mathrm{Tr}\left(\boldsymbol{m}\Phi^4\right),$$

which are used in the calculation in chapters 5 and 8. Lagrangians for the next to leading order are given by

$$\begin{aligned}\mathcal{L}_4^M =& L_1\left[\mathrm{Tr}(D_\mu U^\dagger D^\mu U)\right]^2 + L_2\mathrm{Tr}(D_\mu U^\dagger D_\nu U)\mathrm{Tr}(D^\mu U^\dagger D^\nu U)\\ &+ L_3\mathrm{Tr}(D_\mu U^\dagger D^\mu U D_\nu U^\dagger D^\nu U) + L_4\mathrm{Tr}(D_\mu U^\dagger D^\mu U)\mathrm{Tr}(U^\dagger\chi + \chi^\dagger U)\\ &+ L_5\mathrm{Tr}\left[(D_\mu U^\dagger D^\mu U)(U^\dagger\chi + \chi^\dagger U)\right] + L_6\left[\mathrm{Tr}(U^\dagger\chi + \chi^\dagger U)\right]^2\\ &+ L_7\left[\mathrm{Tr}(U^\dagger\chi - \chi^\dagger U)\right]^2 + L_8\mathrm{Tr}(\chi^\dagger U\chi^\dagger U + U^\dagger\chi U^\dagger\chi)\\ &- iL_9\mathrm{Tr}(R_{\mu\nu}D^\mu U D^\nu U^\dagger + L_{\mu\nu}D^\mu U^\dagger D^\nu U) + L_{10}\mathrm{Tr}(U^\dagger R_{\mu\nu}U L_{\mu\nu})\\ &+ H_1\mathrm{Tr}(R_{\mu\nu}R^{\mu\nu} + L_{\mu\nu}L^{\mu\nu}) + H_2\mathrm{Tr}(\chi^\dagger\chi)\end{aligned}$$

with the low energy constants L_i (i = 1-10) and H_i (i = 1, 2).

B.1.4 Meson-baryon system

The chiral Lagrangian for baryons in the lowest-order of the chiral expansion is given by [48]

$$\mathcal{L}_1^B = \mathrm{Tr}\Big(\bar{B}(i\not{D} - M_0)B - D(\bar{B}\gamma^\mu\gamma_5\{A_\mu, B\}) - F(\bar{B}\gamma^\mu\gamma_5[A_\mu, B])\Big).$$

Here M_0 is the common mass of the baryon octet in the chiral limit, D and F are coupling constants, $F = 0.51,\ D = 0.75$.

Expanding the chiral fields in the vector current, the covariant derivative term provides the Lagrangian with two mesons

$$\mathcal{L}_1^{B(2)} = \mathcal{L}_{WT} = \mathrm{Tr}\Big(\bar{B}i\gamma^\mu\frac{1}{4f^2}\big[(\Phi\partial_\mu\Phi - \partial_\mu\Phi\Phi), B\big]\Big),$$

which gives the Weinberg-Tomozawa interaction. Substituting photon field as in Eq. (B.1.9), we obtain the baryon-photon coupling term

$$\mathcal{L}_1^{B(0)} = -e\mathrm{Tr}\Big(\bar{B}\gamma^\mu\big[Q, B\big]\Big)A_\mu,$$

which was used in Eq. (6.2.9) in chapter 6. The meson-baryon Yukawa interaction can be derived from the axial vector coupling terms

$$\mathcal{L}_1^{B(1)} = \mathcal{L}_{\mathrm{Yukawa}} = -\frac{1}{\sqrt{2}f}\mathrm{Tr}\left(D(\bar{B}\gamma^\mu\gamma_5\{\partial_\mu\Phi, B\}) + F(\bar{B}\gamma^\mu\gamma_5[\partial_\mu\Phi, B])\right), \tag{B.1.10}$$

and the same terms provides three meson-two baryon contact interaction as

$$\begin{aligned}\mathcal{L}_1^{B(3)} =& \frac{1}{12\sqrt{2}f^3}\mathrm{Tr}\Big(D(\bar{B}\gamma^\mu\gamma_5\{(\partial_\mu\Phi(\Phi^2) - 2\Phi\partial_\mu\Phi(\Phi) + \Phi^2\partial_\mu\Phi), B\})\\ &+ F(\bar{B}\gamma^\mu\gamma_5[(\partial_\mu\Phi(\Phi^2) - 2\Phi\partial_\mu\Phi(\Phi) + \Phi^2\partial_\mu\Phi), B])\Big).\end{aligned}$$

These terms have been used in section 5.2.

In the next to leading order, we have several terms. Following the convention in Ref. [44], the SU(3) breaking terms are given by

$$\mathcal{L}^B_{2(SB)} = b_0 \mathrm{Tr}(\bar{B}B)\mathrm{Tr}(\sigma) + b_d \mathrm{Tr}\big(\bar{B}\{\sigma, B\}\big) + b_f \mathrm{Tr}\big(\bar{B}[\sigma, B]\big). \tag{B.1.11}$$

The definition of the low energy constants are the same with that adopted in Ref. [514]. In chapter 4, we denote these terms as

$$\begin{aligned}\mathcal{L}^B_{2(SB)} \equiv \mathcal{L}_{SB} = &-\frac{Z_0}{2}\mathrm{Tr}\Big(d_m \bar{B}\{\xi \boldsymbol{m}\xi + \xi^\dagger \boldsymbol{m}\xi^\dagger, B\} + f_m \bar{B}[\xi \boldsymbol{m}\xi + \xi^\dagger \boldsymbol{m}\xi^\dagger, B]\Big) \\ &- \frac{Z_1}{2}\mathrm{Tr}(\bar{B}B)\mathrm{Tr}(\boldsymbol{m}U + U^\dagger \boldsymbol{m}).\end{aligned} \tag{B.1.12}$$

with $d_m + f_m = 1$. The constants Z_0, Z_1, d_m, and f_m are related with those in Eq. (B.1.11) as

$$2B_0 b_0 = -\frac{Z_1}{2}, \quad 2B_0 b_d = -\frac{Z_0}{2} d_m, \quad 2B_0 b_f = -\frac{Z_0}{2} d_f.$$

In the expansion of the chiral fields in Eq. (B.1.12), we obtain the mass splitting contribution to the baryons, which leads to the Gell-Mann–Okubo mass formula for the octet baryons. The meson-baryon interaction Lagrangian with SU(3) breaking is obtained by picking up the terms with two meson fields;

$$\begin{aligned}\mathcal{L}^{B(2)}_2 = \mathcal{L}^{(2)}_{SB} = &\frac{Z_0}{4f^2}\mathrm{Tr}\Big(d_m \bar{B}\big\{(2\Phi \boldsymbol{m}\Phi + \Phi^2 \boldsymbol{m} + \boldsymbol{m}\Phi^2), B\big\} \\ &+ f_m \bar{B}\big[(2\Phi \boldsymbol{m}\Phi + \Phi^2 \boldsymbol{m} + \boldsymbol{m}\Phi^2), B\big]\Big) + \frac{Z_1}{f^2}\mathrm{Tr}(\bar{B}B)\mathrm{Tr}(\boldsymbol{m}\Phi^2).\end{aligned}$$

These terms have been used in chapter 4.

Couplings to photons are derived from the terms

$$\mathcal{L}^B_{(\gamma)} = \frac{b^D_6}{8M_p}\mathrm{Tr}\big(\bar{B}\sigma^{\mu\nu}\{F^+_{\mu\nu}, B\}\big) + \frac{b^F_6}{8M_p}\mathrm{Tr}\big(\bar{B}\sigma^{\mu\nu}[F^+_{\mu\nu}, B]\big), \tag{B.1.13}$$

with

$$F^{\mu\nu}_+ = F^{\mu\nu}_L + F^{\mu\nu}_R, \quad \sigma^{\mu\nu} = \frac{i}{2}[\gamma^\mu, \gamma^\nu].$$

In the heavy baryon chiral perturbation theory, these terms are expressed as

$$\mathcal{L}^B_{(\gamma)} = -\frac{i}{4M_p} b^D_6 \mathrm{Tr}\big(\bar{B}[S^\mu, S^\nu]\{F^+_{\mu\nu}, B\}\big) - \frac{i}{4M_p} b^F_6 \mathrm{Tr}\big(\bar{B}[S^\mu, S^\nu][F^+_{\mu\nu}, B]\big), \tag{B.1.14}$$

with the replacement $\sigma^{\mu\nu} \to 2\epsilon^{\mu\nu\alpha\beta} v_\alpha S_\beta = -2i[S^\mu, S^\nu]$ given in Ref. [45]. We have used this form in chapter 6.

B.2 Other effective Lagrangians and interactions

In this section, we present effective interaction Lagrangians used in the calculation in this thesis.

B.2.1 $N(1535)$ production

Here we show the interaction Lagrangians used in section 3.2 to calculate the cross sections of the $\gamma N \to \gamma\eta N$ and $\pi N \to \gamma\eta N$ processes through the N^* intermediate state. Here N^* denotes the $N(1535)$ resonance, which has the negative parity.

For the $\eta N N^*$ vertex, we take the scalar coupling:

$$\mathcal{L}_{\eta N N^*} = g_\eta \bar{N} N^* \eta + \text{h.c.},$$

where the coupling constant $g_\eta \simeq 2.0$ is determined so as to reproduce the partial decay width $\Gamma_{N^* \to \eta N} \simeq 75$ MeV [144] at tree level.

The transition vertex of N to N^* with one photon is given by

$$\mathcal{L}_{\gamma N N^*} = \frac{e}{4M_N} \mu_N^{(T)} \bar{N} i\gamma_5 \sigma^{\mu\nu} F_{\mu\nu} N + \text{h.c.}$$

Here we assume the isovector dominance on the transition magnetic moments $\mu_N^{(T)}$, and their values are given by $\mu_p^{(T)} = -\mu_n^{(T)} = 0.68$ in units of nuclear magneton, which correspond to $\kappa_V^* \equiv 2M_N \mu_N^{(T)}/(M_N + M_N^*) = 0.9$ determined from analyses of eta photoproduction [636].

The γNN and $\gamma N^* N^*$ vertices have two parts, which are so-called the Dirac term and the Pauli term:

$$\begin{aligned}
\mathcal{L}_{\gamma NN} &= -eQ\bar{N}\gamma_\mu A^\mu N + \frac{e}{4M_N}\kappa_N \bar{N}\sigma^{\mu\nu}F_{\mu\nu}N, \\
\mathcal{L}_{\gamma N^* N^*} &= -eQ\bar{N}^*\gamma_\mu A^\mu N^* + \frac{e}{4M_N}\kappa_{N^*} \bar{N}^*\sigma^{\mu\nu}F_{\mu\nu}N^*.
\end{aligned}$$

The anomalous magnetic moments of the ground state nucleons κ_N are used the experimental value $\kappa_p = 1.79284739$ and $\kappa_n = -1.9130428$ in units of nuclear magneton [144], while the anomalous magnetic moments of N^* are assumed to be ± 3 to see sensitivity of their values to the cross sections.

For the calculations of the pion-induced process, we use the following Lagrangians. The $\pi N N^*$ vertex has the scalar type coupling, which given by

$$\mathcal{L}_{\pi N N^*} = g_{\pi N N^*} \bar{N} \vec{\tau} \cdot \vec{\pi} N^* + \text{h.c.}$$

with the coupling constant $g_{\pi N N^*} \simeq 0.7$, which is determined so as to reproduce the partial decay width $\Gamma_{N^* \to \pi N} \simeq 75$ MeV [144] at tree level. The diagonal vertices πNN and $\pi N^* N^*$ are assumed to be here the pseudo scalar couplings:

$$\mathcal{L}_{\pi NN} = g_{\pi NN} \bar{N}\gamma_5 \vec{\tau} \cdot \vec{\pi} N, \quad \mathcal{L}_{\pi N^* N^*} = g_{\pi N^* N^*} \bar{N}^* \gamma_5 \vec{\tau} \cdot \vec{\pi} N^*,$$

Here we use the empirical value of the πNN coupling $g_{\pi NN} \simeq 13$. For the $\pi N^* N^*$ coupling, we assume $g_{\pi N^* N^*} \simeq +13$, although the sign of this coupling is important for the properties of N^*. The value of the $\pi N^* N^*$ coupling is absolutely insensitive to the final results, since this coupling appears in the less dominant diagrams. In this formulation, we do not include the Kroll-Ruderman type diagram, since we use the scalar type coupling for the $\pi N N^*$ vertex and it already contains the partial contribution of the Kroll-Ruderman type vertex. The pion-photon coupling is given by

$$\mathcal{L}_{\gamma\pi\pi} = ie(\partial_\mu \pi^-)^\dagger \pi^- A^\mu - ie\pi^{-\dagger}(\partial_\mu \pi^-) A^\mu.$$

B.2.2 $\Lambda^* \bar{K}^* N$ coupling

Here we summarize the chiral Lagrangians which are used in the present analysis. The coupling of vector meson and pseudoscalar mesons is given by

$$\mathcal{L}_1 = -i\frac{g}{\sqrt{2}}\mathrm{Tr}(V^\mu[\partial_\mu\Phi, \Phi]) \ , \tag{B.2.1}$$

with $g = -6.05$ and the vector meson field is given by

$$V_\mu = \begin{pmatrix} \frac{1}{\sqrt{2}}\rho^0_\mu + \frac{1}{\sqrt{2}}\omega_\mu & \rho^+_\mu & K^{*+}_\mu \\ \rho^-_\mu & -\frac{1}{\sqrt{2}}\rho^0_\mu + \frac{1}{\sqrt{2}}\omega_\mu & K^{*0}_\mu \\ K^{*-}_\mu & \bar{K}^{*0}_\mu & \phi_\mu \end{pmatrix},$$

Yukawa coupling of the ground state baryon is given in Eq. (B.1.10) by

$$\mathcal{L}_2 = -\frac{1}{\sqrt{2}f}\mathrm{Tr}\left(D(\bar{B}\gamma^\mu\gamma_5\{\partial_\mu\Phi, B\}) + F(\bar{B}\gamma^\mu\gamma_5[\partial_\mu\Phi, B])\right),$$

with standard notations given in Refs. [513, 40, 514]. The coupling constants are such that $D + F = 1.26$ and $D - F = 0.33$. With these Lagrangians, we obtain the amplitudes for the t-channel meson exchange processes $\bar{K}^*(k) + \pi(q-k) \to \bar{K}(q)$ and $N \to \pi(q-k) + N$

$$\begin{aligned} -it_1 &= -i\alpha\frac{g}{2}(2q-k)_\mu\epsilon^\mu, \\ -it_2 &= \left(\beta\frac{D+F}{2f} + \gamma\frac{D-F}{2f}\right)\boldsymbol{\sigma}\cdot(\boldsymbol{q}-\boldsymbol{k}), \end{aligned}$$

with suitable SU(3) coefficients α, β and γ. The Yukawa coupling of $\Sigma^* \to M_i(q-k) + B_i$ is similarly given by

$$-it_3 = c_i\frac{12}{5}\frac{g^*_A}{2f}\boldsymbol{S}\cdot(\boldsymbol{q}-\boldsymbol{k}) \ .$$

with $g^*_A = (D+F)\times 2.13$. The numerical factor comes from the relation $f_{\pi N\Delta} = 2.13 f_{\pi NN}$. SU(3) coefficients c_i are tabulated in Refs. [576, 11].

B.3 Nonrelativistic reduction of amplitudes

In practical calculations, we have performed the nonrelativistic reduction for the amplitudes, since we are interested in the phenomena in low energy regions, where the nonrelativistic approximation works sufficiently well. We demonstrate the derivation of various amplitudes used in this thesis. Typically, we only take into account the leading order term, but we include the higher order correction for some specific cases.

B.3.1 Yukawa interaction

Let us consider the nonrelativistic reduction of the Yukawa interaction of the process $B(p) \to B'(p') + M(k)$

$$\mathcal{L} = \frac{g_A}{2f}\bar{B}'\not{\partial}M\gamma_5 B,$$

where $p = k + p'$ and $g_A/2f$ is the coupling constant. In this case, the amplitude can be written by

$$-it = -\frac{g_A}{2f}\bar{u}(p')\not{k}\gamma_5 u(p),$$

with the positive energy spinor. Expanding this equation, we obtain

$$\begin{aligned}
-it =& -\frac{g_A}{2f}\sqrt{\frac{E'+M'}{2M'}}\begin{pmatrix}\chi_r^\dagger & -\chi_r^\dagger\frac{\boldsymbol{\sigma}\cdot\boldsymbol{p}'}{E'+M'}\end{pmatrix}\begin{pmatrix}\omega & -\boldsymbol{\sigma}\cdot\boldsymbol{k}\\ \boldsymbol{\sigma}\cdot\boldsymbol{k} & -\omega\end{pmatrix}\begin{pmatrix}0 & 1\\ 1 & 0\end{pmatrix}\sqrt{\frac{E+M}{2M}}\begin{pmatrix}\chi_s\\ \frac{\boldsymbol{\sigma}\cdot\boldsymbol{p}}{E+M}\chi_s\end{pmatrix}\\
=& -\frac{g_A}{2f}\chi_r^\dagger\left[-\boldsymbol{\sigma}\cdot\boldsymbol{k}+\omega\left(\frac{\boldsymbol{\sigma}\cdot\boldsymbol{p}'}{E'+M'}+\frac{\boldsymbol{\sigma}\cdot\boldsymbol{p}}{E+M}\right)-\frac{\boldsymbol{\sigma}\cdot\boldsymbol{p}'}{E'+M'}\boldsymbol{\sigma}\cdot\boldsymbol{k}\frac{\boldsymbol{\sigma}\cdot\boldsymbol{p}}{E+M}\right]\chi_s\\
&\times\sqrt{\frac{E'+M'}{2M'}}\sqrt{\frac{E+M}{2M}},
\end{aligned}$$

where E, E', and ω are the on-shell energies of B, B', and M, respectively. In the nonrelativistic limit $\boldsymbol{p}\sim\boldsymbol{p}'\sim\boldsymbol{0}$, we obtain

$$-it \sim \frac{g_A}{2f}\chi_r^\dagger\,\boldsymbol{\sigma}\cdot\boldsymbol{k}\,\chi_s.$$

Taking into account that $\boldsymbol{p}=\boldsymbol{p}'+\boldsymbol{k}$, we can add a correction for the case $\boldsymbol{p}'\sim\boldsymbol{0}$,

$$\begin{aligned}
-it &\sim \frac{g_A}{2f}\chi_r^\dagger\,\boldsymbol{\sigma}\cdot\boldsymbol{k}\,F\chi_s,\\
F &= 1-\frac{\omega}{2M},
\end{aligned}$$

where F is called as the recoil correction, which is used in Eq. (5.2.8) in chapter 5.

B.3.2 Weinberg-Tomozawa interaction

Next we consider the Weinberg-Tomozawa type interaction of the process $B(p)+M(k)\to B'(p')+M'(k')$. The interaction Lagrangian is given by

$$\mathcal{L} = i\frac{C}{4f^2}\overline{B}'M'\overleftrightarrow{\partial}MB, \tag{B.3.1}$$

where $p+k=p'+k'$ and $C/4f^2$ is the coupling constant. Then Eq. (B.3.1) gives the amplitude as

$$-it = i\frac{C}{4f^2}\overline{u}(p')(\not{k}+\not{k}')u(p).$$

Expanding this, we obtain

$$\begin{aligned}
-it =& i\frac{C}{4f^2}\sqrt{\frac{E'+M'}{2M'}}\begin{pmatrix}\chi_r^\dagger & -\chi_r^\dagger\frac{\boldsymbol{\sigma}\cdot\boldsymbol{p}'}{E'+M'}\end{pmatrix}\begin{pmatrix}\omega+\omega' & -\boldsymbol{\sigma}\cdot(\boldsymbol{k}+\boldsymbol{k}')\\ \boldsymbol{\sigma}\cdot(\boldsymbol{k}+\boldsymbol{k}') & -\omega-\omega'\end{pmatrix}\sqrt{\frac{E+M}{2M}}\begin{pmatrix}\chi_s\\ \frac{\boldsymbol{\sigma}\cdot\boldsymbol{p}}{E+M}\chi_s\end{pmatrix}\\
=& i\frac{C}{4f^2}\sqrt{\frac{E'+M'}{2M'}}\sqrt{\frac{E+M}{2M}}\chi_r^\dagger\Bigg((\omega+\omega')-\boldsymbol{\sigma}\cdot(\boldsymbol{k}+\boldsymbol{k}')\frac{\boldsymbol{\sigma}\cdot\boldsymbol{p}}{E+M}\\
&-\frac{\boldsymbol{\sigma}\cdot\boldsymbol{p}'}{E'+M'}\boldsymbol{\sigma}\cdot(\boldsymbol{k}+\boldsymbol{k}')+\frac{\boldsymbol{\sigma}\cdot\boldsymbol{p}'}{E'+M'}(\omega+\omega')\frac{\boldsymbol{\sigma}\cdot\boldsymbol{p}}{E+M}\Bigg)\chi_s,
\end{aligned}\tag{B.3.2}$$

where E, E', ω, and ω' are the on-shell energies of B, B', M, and M' respectively. In the center of mass frame $P^\mu = p^\mu + k^\mu = (p')^\mu + (k')^\mu = (\sqrt{s}, \mathbf{0})$, $\boldsymbol{k} = -\boldsymbol{p}$, and $\boldsymbol{k}' = -\boldsymbol{p}'$, we have

$$-it = i\frac{C}{4f^2}\chi_r^\dagger \left((2\sqrt{s} - M - M') + \boldsymbol{\sigma}\cdot\boldsymbol{k}'\boldsymbol{\sigma}\cdot\boldsymbol{k}\frac{2\sqrt{s}+M+M'}{(E'+M')(E+M)} \right) \chi_s \sqrt{\frac{E'+M'}{2M'}}\sqrt{\frac{E+M}{2M}}.$$

We find the leading order term as used in Eq. (4.2.2) in chapter 4, where t is written as V.

For the decay process of $R(p) \to B'(p') + M(k) + M'(k')$, we can use the above expressions by replacing $k \to -k$. In the resonance rest frame $p^\mu = (p')^\mu + k^\mu + (k')^\mu = (M, \mathbf{0})$, $\boldsymbol{p}' = -\boldsymbol{k}' - \boldsymbol{k}$. Eq. (B.3.2) leads to

$$-it = i\frac{C}{4f^2}\sqrt{\frac{E'+M'}{2M'}}\chi_r^\dagger \left(-(\omega - \omega') - \frac{\boldsymbol{\sigma}\cdot(\boldsymbol{k}+\boldsymbol{k}')}{E'+M'}\boldsymbol{\sigma}\cdot(\boldsymbol{k}-\boldsymbol{k}') \right) \chi_s.$$

The leading order term gives the amplitude in Eq. (5.2.11), while the second term provides the relativistic corrections used in Eqs. (9.3.5) and (11.4.1).

Appendix C

Loop integrals

Here we summarize the calculation of loop integrals which are used in this thesis. Since we are interested in the low energy phenomena, we have performed the non-relativistic reduction for baryons. In contrast, bosons in loop integrals are usually the pseudoscalar mesons, which originate in the NG bosons of the spontaneous chiral symmetry breaking, and have small masses. Therefore, we use the relativistic propagator for bosons. To perform the reduction, we decompose the propagator of a baryon with mass M into positive and negative energy components by using the identity

$$\frac{1}{\not{q} - M + i\epsilon} = \frac{M}{E(\boldsymbol{q})} \left(\frac{\sum_s u(\boldsymbol{q}, s)\bar{u}(\boldsymbol{q}, s)}{q^0 - E(\boldsymbol{q}) + i\epsilon} + \frac{\sum_s v(-\boldsymbol{q}, s)\bar{v}(-\boldsymbol{q}, s)}{q^0 + E(\boldsymbol{q}) - i\epsilon} \right),$$

where the normalization of spinor is given in Eq. (A.1.1) and $E(\boldsymbol{q}) = \sqrt{M^2 + \boldsymbol{q}^2}$. Taking into account the positive energy part, we obtain

$$\frac{1}{\not{q} - M + i\epsilon} \sim \frac{M}{E} \frac{1}{q^0 - E + i\epsilon},$$

which gives the leading order contribution in the non-relativistic expansion and is consistent with the treatment of the amplitude in Appendix B.3. This approximation becomes exact in the heavy baryon limit, $M \to \infty$. In the following, we evaluate the integrations by three-momentum cutoff scheme. For the meson-baryon one-loop integral, we show the relation of the cutoff scheme with the analytic form obtained by dimensional regularization. Analytic continuation to the complex energy plane is also explained. We then show the calculations for one-loop integrals with two meson propagators and two-loop integrals.

C.1 One-loop functions

C.1.1 Meson-baryon loop function on the real axis

We calculate a one-loop function including a meson with mass m and a baryon with mass M, which is diagrammatically depicted in Fig. C.1. In the center of mass frame, total four momentum is $P = (\sqrt{s}, \boldsymbol{0})$, and the loop integral is given by

$$G(\sqrt{s}) = i \int \frac{d^4q}{(2\pi)^4} \frac{1}{q^2 - m^2 + i\epsilon} \frac{M}{E} \frac{1}{\sqrt{s} - q_0 - E + i\epsilon}.$$

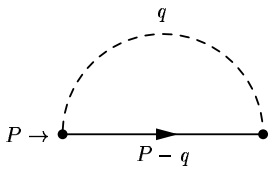

Figure C.1: Diagrammatic representation for the one-loop of a meson and a baryon. Dashed and solid lines represent the meson and the baryon respectively.

Here we assume that the vertices at the both ends of the loop are essentially constant. When it has a momentum dependence, we should perform d^3q integration including the vertices. We define on-shell energies of the meson and the baryon are given by $\omega(\boldsymbol{q}) = \sqrt{m^2 + \boldsymbol{q}^2}$ and $E(\boldsymbol{q}) = \sqrt{M^2 + \boldsymbol{q}^2}$. This integral diverges quadratically, therefore we regularize it by a cutoff in three-momentum. We first integrate the zeroth component q_0 analytically;

$$\begin{aligned}
G(\sqrt{s}) =& i \int \frac{d^4q}{(2\pi)^4} \frac{1}{q^2 - m^2 + i\epsilon} \frac{M}{E} \frac{1}{\sqrt{s} - q_0 - E + i\epsilon} \\
=& i \int \frac{d^3q}{(2\pi)^4} \frac{M}{E} \int dq_0 \frac{1}{(q_0)^2 - \boldsymbol{q}^2 - m^2 + i\epsilon} \frac{-1}{q_0 - (\sqrt{s} - E) - i\epsilon} \\
=& i \int \frac{d^3q}{(2\pi)^4} \frac{M}{E} \int dq_0 \frac{1}{(q_0)^2 - \omega^2 + i\epsilon} \frac{-1}{q_0 - (\sqrt{s} - E) - i\epsilon} \\
=& i \int \frac{d^3q}{(2\pi)^4} \frac{M}{E} \int dq_0 \frac{1}{(q_0)^2 - (\omega - i\epsilon)^2} \frac{-1}{q_0 - (\sqrt{s} - E) - i\epsilon} \\
=& i \int \frac{d^3q}{(2\pi)^4} \frac{M}{E} \int dq_0 \frac{1}{q_0 - \omega + i\epsilon} \frac{1}{q_0 + \omega - i\epsilon} \frac{-1}{q_0 - (\sqrt{s} - E) - i\epsilon},
\end{aligned}$$

where poles in the complex q_0 plane locate at

$$z_1 = \omega - i\epsilon, \quad z_2 = -\omega + i\epsilon, \quad z_3 = \sqrt{s} - E + i\epsilon.$$

We close the integration contour downward, picking up the residues of the poles in the lower half-plane, in this case z_1, and then

$$\begin{aligned}
G(\sqrt{s}) =& (-2\pi i) i \int \frac{d^3q}{(2\pi)^4} \frac{M}{E} \frac{1}{2\omega} \frac{-1}{\omega - (\sqrt{s} - E) - i\epsilon} \\
=& \int \frac{d^3q}{(2\pi)^3} \frac{M}{E} \frac{1}{2\omega} \frac{1}{\sqrt{s} - \omega - E + i\epsilon} \\
=& \frac{M}{(2\pi)^3} \int d\Omega \int_0^{q_{\max}} dq \boldsymbol{q}^2 \frac{1}{E} \frac{1}{2\omega} \frac{1}{\sqrt{s} - \omega - E + i\epsilon} \\
=& \frac{M}{4\pi^2} \int_0^{q_{\max}} dq \frac{\boldsymbol{q}^2}{E} \frac{1}{\omega} \frac{1}{\sqrt{s} - \omega - E + i\epsilon},
\end{aligned}$$

where we denote $dq \equiv d|\boldsymbol{q}|$ for brevity.

It is instructive to divide $G(\sqrt{s})$ into real and imaginary parts. Using

$$\lim_{\epsilon \to +0} \frac{1}{x - a \pm i\epsilon} = \text{P.V.} \frac{1}{x - a} \mp i\pi\delta(x - a),$$

where P.V. stands for the principle value of the integral, we obtain

$$\mathrm{Re}[G(\sqrt{s})] = \frac{M}{4\pi^2}\mathrm{P.V.}\int_0^{q_{\max}} dq \frac{\boldsymbol{q}^2}{E}\frac{1}{\omega}\frac{1}{\sqrt{s}-\omega-E}, \tag{C.1.1}$$

and

$$\begin{aligned}
\mathrm{Im}[G(\sqrt{s})] &= -\frac{M}{4\pi}\int_0^{q_{\max}} dq \frac{\boldsymbol{q}^2}{E}\frac{1}{\omega}\delta(\sqrt{s}-\omega-E) \\
&= -\frac{M}{4\pi}\int_0^{q_{\max}} d(\omega+E)\frac{\boldsymbol{q}}{E+\omega}\delta(\sqrt{s}-\omega-E) \\
&= \begin{cases} -\dfrac{M|\boldsymbol{q}|}{4\pi\sqrt{s}} = -\dfrac{\rho}{2} & \text{for} \quad \sqrt{s} > \omega+E \geq \sqrt{s_+} \quad \text{(above threshold)}, \\ 0 & \text{for} \quad \sqrt{s} \leq \omega+E \leq \sqrt{s_+} \quad \text{(below threshold)}, \end{cases}
\end{aligned} \tag{C.1.2}$$

where $\rho = \int d\Pi$ is the two-body phase space of meson-baryon system and we define the threshold energy $\sqrt{s_+} = m + M$. It is important that the imaginary part is determined only by the value of $\sqrt{s}$ and does not depend on the cutoff value.

Eq. (C.1.1) can be calculated numerically, but it is not adequate to perform the analytic continuation to the complex energy plane. To do that, we utilize another loop function

$$G'(\sqrt{s}) = i\int \frac{d^4q}{(2\pi)^4}\frac{1}{q^2-m^2+i\epsilon}\frac{2M}{(P-q)^2-M^2+i\epsilon},$$

with $P = (\sqrt{s}, \boldsymbol{0})$. This function provides exactly the same imaginary part as Eq. (C.1.2), as can be seen by, for instance, the Cutkosky rule. The $G'(\sqrt{s})$ function also has an advantage that it can be calculated analytically. Adopting the dimensional regularization scheme, finite part of this integral is given by

$$\begin{aligned}
G'(\sqrt{s}) = \frac{2M}{(4\pi)^2}\Bigg\{ & a(\mu) + \ln\frac{M^2}{\mu^2} + \frac{m^2-M^2+s}{2s}\ln\frac{m^2}{M^2} \\
& + \frac{\bar{q}}{\sqrt{s}}\Big[\ln(s-(M^2-m^2)+2\sqrt{s}\bar{q}) + \ln(s+(M^2-m^2)+2\sqrt{s}\bar{q}) \\
& - \ln(-s+(M^2-m^2)+2\sqrt{s}\bar{q}) - \ln(-s-(M^2-m^2)+2\sqrt{s}\bar{q})\Big]\Bigg\},
\end{aligned}$$

where μ is the regularization scale, $a(\mu)$ is the subtraction constant. Notice that the result depends on a single parameter μ, since the change of μ can be absorbed into the change of $a(\mu)$ through the relation $a(\mu') = a(\mu) + 2\ln(\mu'/\mu)$. Here $\bar{q}$ is defined by

$$\bar{q}(\sqrt{s}) = \frac{\lambda^{1/2}(s, M^2, m^2)}{2\sqrt{s}},$$

with the Källen function $\lambda(x,y,z) = x^2+y^2+z^2-2xy-2yz-2zx$. Above the threshold, $\bar{q}$ corresponds to the magnitude of the three momentum $|\boldsymbol{q}|$ in the center of mass frame, but

it is also defined below the threshold, where it becomes pure imaginary. In order to extract the imaginary part of $G'(\sqrt{s})$, we rewrite the resulting function as

$$\begin{aligned} G'(\sqrt{s}) =& \frac{2M}{16\pi^2}\Big\{a(\mu) + \ln\frac{M^2}{\mu^2} + \frac{m^2 - M^2 + s}{2s}\ln\frac{m^2}{M^2} \\ &+ \frac{\lambda^{1/2}}{2s}[\ln(A) + \ln(B) - \ln(C) - \ln(D)]\Big\}, \end{aligned} \tag{C.1.3}$$

where we abbreviate $\lambda^{1/2} \equiv \lambda^{1/2}(s, M^2, m^2)$ and define

$$\begin{aligned} &A = s - (M^2 - m^2) + \lambda^{1/2}, \quad B = s + (M^2 - m^2) + \lambda^{1/2}, \\ &C = -s + (M^2 - m^2) + \lambda^{1/2}, \quad D = -s - (M^2 - m^2) + \lambda^{1/2}. \end{aligned}$$

The terms in the first line of Eq. (C.1.3) are always real for real values of $\sqrt{s}$, and therefore the imaginary part of the loop function comes from the second line. Below the threshold, $\lambda^{1/2}$ is pure imaginary, so that A, B, C, and D are all complex numbers. Then we see that $[\ln(A) + \ln(B) - \ln(C) - \ln(D)]$ becomes pure imaginary[A)], while $\lambda^{1/2}$ is also pure imaginary. Hence, no imaginary part appears in $G'(\sqrt{s})$ below the threshold;

$$\mathrm{Im}[G'(\sqrt{s})] = 0 \quad \text{for} \quad \sqrt{s} \le \sqrt{s_+} \tag{C.1.4}$$

On the other hand, above the threshold, $\lambda^{1/2}$ is real, so that A, B, C, and D are real numbers. The real logarithmic function is defined in the region $0 \le x < \infty$, while $\log(x) = \log(-x) + i\pi$ if x is negative. When $\sqrt{s} > \sqrt{s_+}$, we see that

$$A > 0, \quad B > 0, \quad C < 0, \quad D < 0.$$

Then

$$\begin{aligned} G'(\sqrt{s}) =& \frac{2M}{16\pi^2}\Big\{a(\mu) + \ln\frac{M^2}{\mu^2} + \frac{m^2 - M^2 + s}{2s}\ln\frac{m^2}{M^2} \\ &+ \frac{\lambda^{1/2}}{2s}[\ln(A) + \ln(B) - \ln(-C) - \ln(-D) - 2\pi i]\Big\}, \quad \text{for} \quad \sqrt{s} > \sqrt{s_+}, \end{aligned} \tag{C.1.5}$$

In this expression, $\lambda^{1/2}$ and all logarithmic function are real, so we extract the imaginary part of the G' function as

$$\mathrm{Im}[G'(\sqrt{s})] = -\frac{M\lambda^{1/2}(s, M^2, m^2)}{8s\pi} = -\frac{\rho(\sqrt{s})}{2} \quad \text{for} \quad \sqrt{s} > \sqrt{s_+}. \tag{C.1.6}$$

Combining Eqs. (C.1.2), (C.1.4), and (C.1.6), we verify that

$$\mathrm{Im}[G(\sqrt{s})] = \mathrm{Im}[G'(\sqrt{s})].$$

The real part of the integrals $G(\sqrt{s})$ and $G'(\sqrt{s})$ depend on the scale parameter (cutoff $q_{\max}$ and $a(\mu)$). As done in Ref. [503], we compare the real part of the loop function in two scheme numerically. In Fig. C.2, we plot the real and imaginary parts of the loop integral G

[A)] We define $\log(z)$ on the first Riemann sheet, namely, we restrict the argument of z within $0 \le \theta < 2\pi$

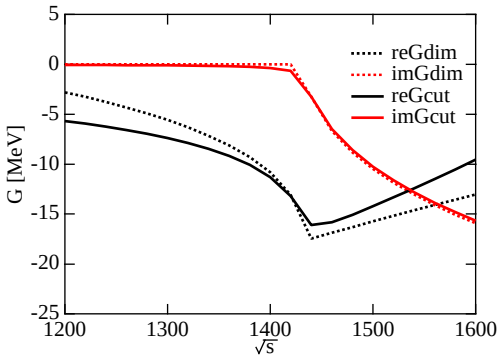

Figure C.2: Comparison of the loop functions $G(\sqrt{s})$ and $G'(\sqrt{s})$ for $\bar{K}N$ channel. The $G(\sqrt{s})$ is calculated by the three momentum cutoff with $q_{\max} = 630$ MeV, while $G'(\sqrt{s})$ is regularized by the dimensional regularization with $a(630\text{ MeV}) = -1.84$.

and G' with $q_{\max} = 630$ MeV and $a(630\text{ MeV}) = -1.84$ for $\bar{K}N$ channel. Qualitatively, two functions agree with each other in this energy region. The parameter $a(630\text{ MeV}) = -1.84$ was obtained in Ref. [503] by fitting these two functions around the $\bar{K}N$ threshold. Similar values around $a = -2$ are found for other channels of $S = -1$. This observation agrees with the analytical comparison performed in Ref. [512], where they found that $a(630\text{ MeV}) = -2$ corresponds to $q_{\max} = 630$ MeV.

In short summary, we evaluate the loop functions $G(\sqrt{s})$ and $G'(\sqrt{s})$ with three momentum cutoff scheme and dimensional regularization, respectively. It is shown that the two functions provide the same imaginary part[B)], and the real parts can be matched by choosing the scale parameters appropriately. On one hand, the three momentum cutoff scheme is useful to consider the physical meaning of the cutoff value (the maximum of the three momentum in the intermediate state), while the subtraction constant in the dimensional regularization is not related to physics directly. On the other hand, the loop function can be calculated analytically in the dimensional regularization, whereas the integration of the three momentum cutoff scheme should be performed numerically. Therefore, we can utilize both the methods complementary, depending on the situations.

C.1.2 Meson-baryon loop function in the complex plane

Here we compute the loop function numerically in the complex plane, showing how the structure in the second Riemann sheet influences the scattering amplitude on the real axis. In this subsection, we utilize $G'(\sqrt{s})$ in Eq. (C.1.3), and refer to it as G for convenience. When we deal with multi-valued functions, several Riemann sheets appear. The definition of the Riemann sheets and branches can be found in Appendix E.1. For the scattering we are considering, $\bar{q}(\sqrt{s})$ is the double-valued function of $\sqrt{s}$ because of the square root of the Källen function, and we need two Riemann sheets. According to the result of the chiral

[B)] Small deviation in Fig. C.2 is due to the numerical error.

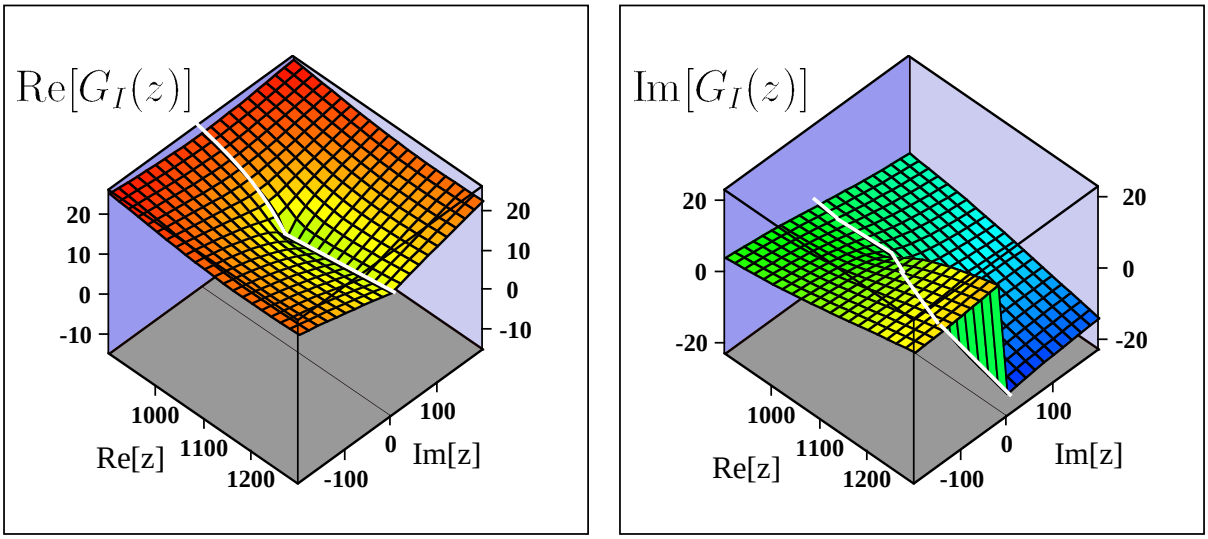

Figure C.3: Real and imaginary parts of the $G_I(z)$ function. Here we plot the loop function of the πN channel. White line in the figure denotes the values on the scattering line (real axis).

unitary model (4.2.7), the relation between the T-matrix and the G function is given by

$$T^{-1} = V^{-1} - G. \tag{C.1.7}$$

Now V is a tree vertex, so that it is always real. Using the unitarity condition (4.2.3) and Eq. (C.1.7), we find

$$2\mathrm{Im}G(\sqrt{s}) = -\rho(\sqrt{s}) \quad \text{for} \quad \sqrt{s} > \sqrt{s^+}. \tag{C.1.8}$$

This relation is consistent with the result (C.1.2). Since the inverse of the T-matrix amplitude has the same branch cut as G, we investigate G instead of the T-matrix. We perform analytic continuation of $G(\sqrt{s})$ to the whole complex energy plane $\sqrt{s} \to z$. In Fig. C.3, real and imaginary parts of $G(z)$ for the πN channel on the first Riemann sheet are shown, where we see the discontinuity of the imaginary part.

As we mentioned, the origin of this discontinuity lies in the square root of the $\bar{q}$ in $\rho(\sqrt{s})$. In the complex z plane, $\rho(z)$ is a double-valued function with the cut along the real axis $(\sqrt{s^+}, +\infty)$;

$$\rho(\sqrt{s} + i0) = -\rho(\sqrt{s} - i0), \quad \text{for} \quad \sqrt{s} > \sqrt{s^+}, \tag{C.1.9}$$

Therefore the discontinuity of the loop function G and relation between branches of G on the first and second Riemann sheets are given as

$$\begin{aligned} G_I(\sqrt{s} + i0) &= G_I(\sqrt{s} - i0) - i\rho(\sqrt{s} + i0) \\ G_{II}(\sqrt{s} + i0) &= G_I(\sqrt{s} - i0) \end{aligned}, \quad \text{for} \quad \sqrt{s} > \sqrt{s^+}, \tag{C.1.10}$$

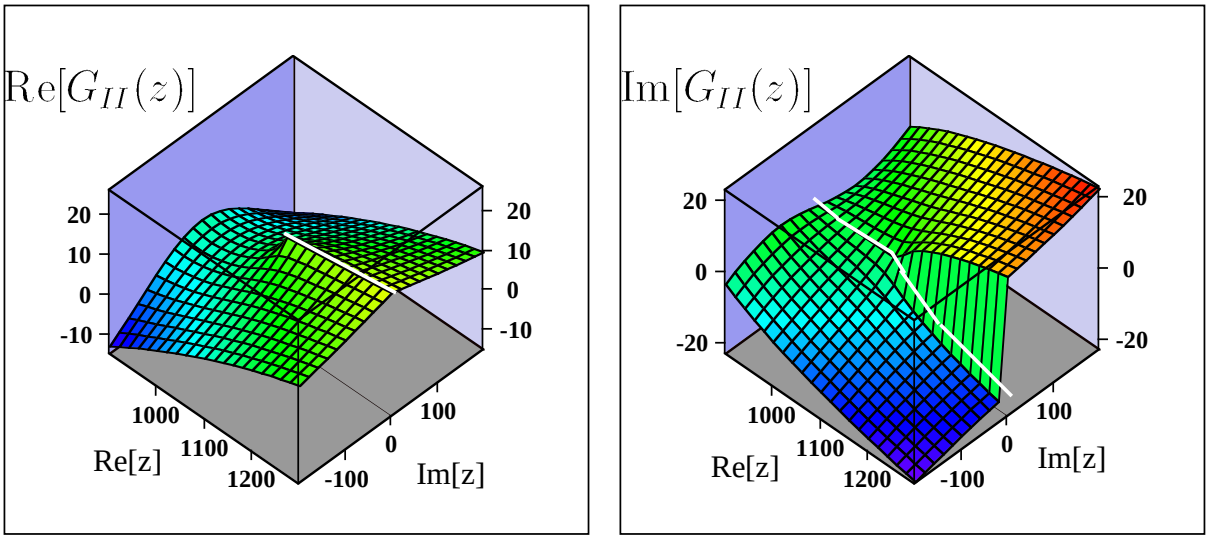

Figure C.4: Real and imaginary parts of the $G_{II}(z)$ function. Here we plot the loop function of the πN channel. White line in the figure denotes the values on the scattering line (real axis).

where $G_I(z)$ and $G_{II}(z)$ represent the first and second branches, respectively. Using Eq. (C.1.10), we obtain the expression of the second branch

$$G_{II}(z) = G_I(z) + i\rho(z). \tag{C.1.11}$$

In Fig. C.4, the real and imaginary parts of the G_{II} function for the πN channel, where we again see the discontinuity of the imaginary part. From Eqs. (C.1.5) and (C.1.11), the explicit form of the function $G_{II}(z)$ is given as

$$\begin{aligned} G_{II}(z) =& \frac{2M}{16\pi^2}\Big\{a(\mu) + \ln\frac{M^2}{\mu^2} + \frac{m^2 - M^2 + z^2}{2z^2}\ln\frac{m^2}{M^2} \\ &+ \frac{\lambda^{1/2}(z)}{2z^2}\left[\ln(A) + \ln(B) - \ln(-C) - \ln(-D) + 2\pi i\right]\Big\}, \end{aligned}$$

for $\mathrm{Re}[z] > \sqrt{s_+}$.

In practical calculations to find poles, we use the most relevant branches for amplitude on the real axis. The white lines in Figs. C.3 and C.4 indicates the corresponding values. From these lines, we see that

- below the threshold, the first branch contains the scattering line.
- above the threshold and $\mathrm{Im}z > 0$, the first branch is connected with the scattering line.
- above the threshold and $\mathrm{Im}z < 0$, the second branch is connected with the scattering line.

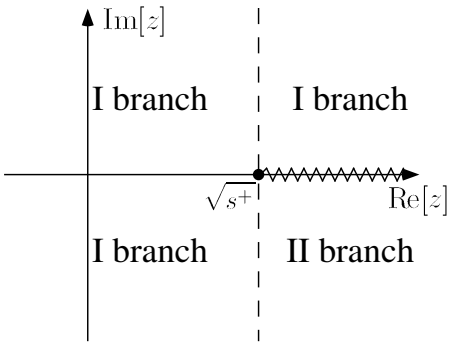

Figure C.5: Diagrammatic expression of the definition of G_{pole}.

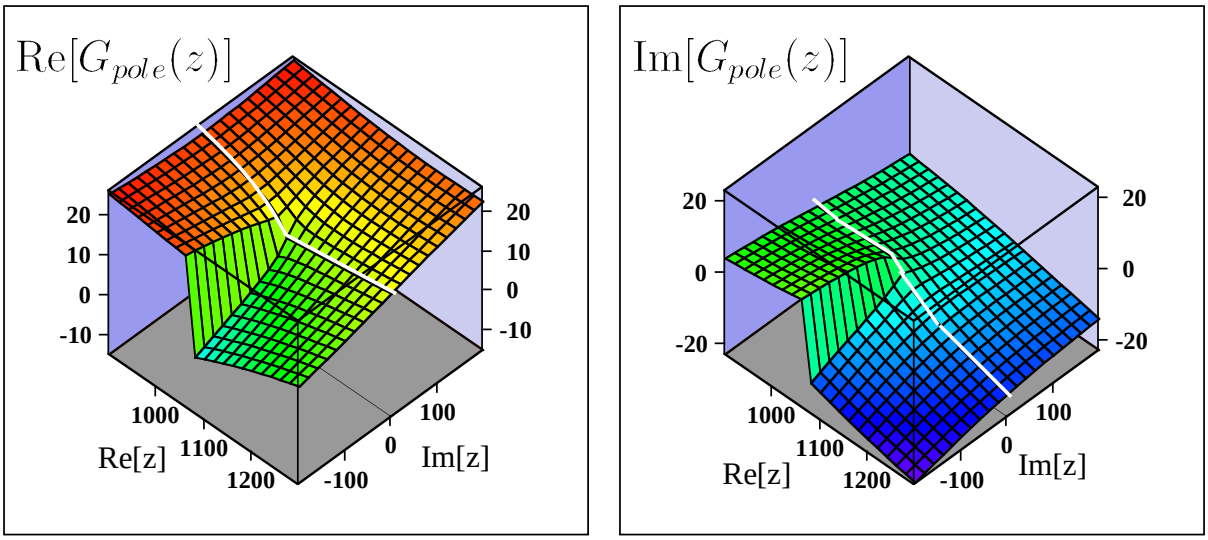

Figure C.6: Real and imaginary parts of the $G_{pole}(z)$ function. Here we plot the loop function of the πN channel. White line in the figure denotes the values on the scattering line (real axis).

For this purpose, we define the function $G_{pole}(z)$ as

$$G_{pole}(z) = \begin{cases} G_I(z) & \text{for} \quad \mathrm{Re}[z] \leq \sqrt{s^+} \\ G_I(z) & \text{for} \quad \mathrm{Re}[z] > \sqrt{s^+} \quad \text{and} \quad \mathrm{Im}[z] > 0\,. \\ G_{II}(z) & \text{for} \quad \mathrm{Re}[z] > \sqrt{s^+} \quad \text{and} \quad \mathrm{Im}[z] < 0 \end{cases}$$

The function G_{pole} is shown schematically in Fig. C.5 and is plotted in Fig. C.6, where we see that the scattering line is included in the sheet. In this way we search poles in the branch which is the closest to the scattering line, namely which includes the scattering line.

Finally we consider the third branch, which is defined as

$$G_{III}(\sqrt{s} + i0) \equiv G_{II}(\sqrt{s} - i0), \quad \text{for} \quad \sqrt{s} > \sqrt{s^+}.$$

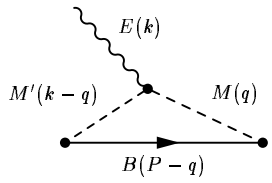

Figure C.7: Diagrammatic representation fo the one-loop for two mesons M, M' and one baryon B with one external current E. Dashed and solid lines represent the mesons and the baryon respectively.

However, using Eqs. (C.1.9) and (C.1.10), if we go through the unitarity cut once again,

$$\begin{aligned} G_{III}(\sqrt{s}+i0) &= G_I(\sqrt{s}-i0)+i\rho(\sqrt{s}-i0) \\ &= G_I(\sqrt{s}+i0)+i\rho(\sqrt{s}+i0)+i\rho(\sqrt{s}-i0) \\ &= G_I(\sqrt{s}+i0)-i\rho(\sqrt{s}-i0)+i\rho(\sqrt{s}-i0) \\ &= G_I(\sqrt{s}+i0), \end{aligned}$$

we back to the first branch. This means that there are only two Riemann sheets. Note that this result is expected from the fact that $\lambda^{1/2}(\sqrt{s})$ is double-valued function (C.1.9).

C.1.3 A one-loop function for two mesons and one baryon

Let us now consider the one-loop integral including two mesons with masses m and m', one baryon with mass M, and one external current with momentum k^μ. Using kinematical variables shown in Fig. C.7, in the frame with $P^\mu = (\sqrt{s}, \mathbf{0})$, the loop function is given by

$$G(\sqrt{s}, k^\mu) = i\int \frac{d^4q}{(2\pi)^4} \frac{1}{(q-k)^2-(m')^2+i\epsilon} \frac{1}{q^2-m^2+i\epsilon} \frac{M}{E} \frac{1}{\sqrt{s}-q^0-E+i\epsilon},$$

with on-shell energies of particles are written as

$$\omega = \sqrt{m^2+\boldsymbol{q}^2}, \quad \omega' = \sqrt{(m')^2+\boldsymbol{q}^2+\boldsymbol{k}^2-2|\boldsymbol{q}||\boldsymbol{k}|\cos\theta}, \quad E = \sqrt{M^2+\boldsymbol{q}^2},$$

where θ is the angle between $\boldsymbol{k}$ and $\boldsymbol{q}$. With these values, the integrand can be written as

$$\begin{aligned} G(\sqrt{s}, k^\mu) =& i\int \frac{d^4q}{(2\pi)^4} \frac{1}{(q^0-k^0)^2-(\omega')^2+i\epsilon} \frac{1}{(q^0)^2-\omega^2+i\epsilon} \frac{M}{E} \frac{1}{\sqrt{s}-q^0-E+i\epsilon} \\ =& i\int \frac{d^4q}{(2\pi)^4} \frac{1}{q^0-k^0-\omega'+i\epsilon} \frac{1}{q^0-k^0+\omega'-i\epsilon} \\ & \times \frac{1}{q^0-\omega+i\epsilon} \frac{1}{q^0+\omega-i\epsilon} \frac{M}{E} \frac{1}{\sqrt{s}-q^0-E+i\epsilon}. \end{aligned}$$

In the lower half plane, we find two poles at $q^0 = k^0+\omega'-i\epsilon$ and $q^0 = \omega-i\epsilon$. In this case, when we take the residue of each one of the poles, we will have a "fallacious pole", which

contains $+i\epsilon - i\epsilon$, and hence, not well defined. In this case,

$$
\begin{aligned}
&G(\sqrt{s}, k^\mu) \\
=& -2\pi i i \int \frac{d^3q}{(2\pi)^4} \frac{M}{E} \\
&\times \Big[\frac{1}{k^0 + \omega' - k^0 + \omega' - i\epsilon} \frac{1}{k^0 + \omega' - \omega \pm i\epsilon} \frac{1}{k^0 + \omega' + \omega - i\epsilon} \frac{1}{P^0 - k^0 - \omega' - E + i\epsilon} \\
&+ \frac{1}{\omega - k^0 - \omega' \pm i\epsilon} \frac{1}{\omega - k^0 + \omega' - i\epsilon} \frac{1}{\omega + \omega - i\epsilon} \frac{1}{P^0 - \omega - E + i\epsilon} \Big]
\end{aligned}
$$

we have the fallacious pole at $k^0 + \omega' - \omega \pm i\epsilon$, where we conventionally denote the imaginary part as $\pm i\epsilon$. Since the initial integral is well-defined, the appearance of this pole is only superficial one, and we will have the same factor in the numerator. Indeed, we obtain

$$
\begin{aligned}
&G(\sqrt{s}, k^\mu) \\
=& \int \frac{d^3q}{(2\pi)^3} \frac{M}{E} \Big[\frac{1}{2\omega'} \frac{1}{k^0 + \omega' - \omega \pm i\epsilon} \frac{1}{k^0 + \omega' + \omega} \frac{1}{P^0 - k^0 - \omega' - E + i\epsilon} \\
&+ \frac{1}{\omega - k^0 - \omega' \pm i\epsilon} \frac{1}{\omega - k^0 + \omega' - i\epsilon} \frac{1}{2\omega} \frac{1}{P^0 - \omega - E + i\epsilon} \Big] \\
=& \int \frac{d^3q}{(2\pi)^3} \frac{M}{E} \Big[\frac{1}{2\omega'} \frac{1}{k^0 + \omega' - \omega \pm i\epsilon} \frac{1}{k^0 + \omega' + \omega} \frac{1}{P^0 - k^0 - \omega' - E + i\epsilon} \\
&+ \frac{1}{k^0 - \omega + \omega' \pm i\epsilon} \frac{1}{k^0 - \omega - \omega' + i\epsilon} \frac{1}{2\omega} \frac{1}{P^0 - \omega - E + i\epsilon} \Big] \\
=& \int \frac{d^3q}{(2\pi)^3} \frac{M}{E} \frac{1}{2} \frac{1}{k^0 + \omega' - \omega \pm i\epsilon} \Big[\frac{1}{\omega'} \frac{1}{k^0 + \omega' + \omega} \frac{1}{P^0 - k^0 - \omega' - E + i\epsilon} \\
&+ \frac{1}{k^0 - \omega - \omega' + i\epsilon} \frac{1}{\omega} \frac{1}{P^0 - \omega - E + i\epsilon} \Big] \\
=& \int \frac{d^3q}{(2\pi)^3} \frac{M}{E} \frac{1}{2} \frac{1}{k^0 + \omega' - \omega \pm i\epsilon} \Big[\frac{1}{\omega'} \frac{1}{k^0 + \omega' + \omega} \frac{1}{P^0 - k^0 - \omega' - E + i\epsilon} \\
&\times \frac{1}{k^0 - \omega - \omega' + i\epsilon} \frac{1}{\omega} \frac{1}{P^0 - \omega - E + i\epsilon} \Big] \\
&\times [\omega(k^0 - \omega - \omega')(P^0 - \omega - E) + \omega'(k^0 + \omega' + \omega)(P^0 - k^0 - \omega' - E)] \\
=& -\int \frac{d^3q}{(2\pi)^3} \frac{M}{E} \\
&\times \frac{1}{2} \Big[\frac{1}{\omega'} \frac{1}{k^0 + \omega' + \omega} \frac{1}{P^0 - k^0 - \omega' - E + i\epsilon} \frac{1}{k^0 - \omega - \omega' + i\epsilon} \frac{1}{\omega} \frac{1}{P^0 - \omega - E + i\epsilon} \Big] \\
&\times [(\omega + \omega')^2 + (E - P^0)(\omega + \omega') + \omega' k^0] \\
=& -\int \frac{d^3q}{(2\pi)^3} \frac{1}{\omega'} \frac{1}{\omega} \frac{1}{2} \frac{1}{k^0 + \omega' + \omega} \frac{1}{k^0 - \omega' - \omega + i\epsilon} \\
&\times \frac{M}{E} \frac{1}{P^0 - \omega - E + i\epsilon} \frac{1}{P^0 - k^0 - \omega' - E + i\epsilon} \left[(\omega + \omega')^2 + (\omega + \omega')(E - P^0) + \omega' k^0 \right] \\
=& -\frac{1}{4\pi^2} \int_{-1}^{1} d\cos\theta \int_0^{q_{\max}} dq q^2 \frac{1}{\omega'} \frac{1}{\omega} \frac{1}{2} \frac{1}{k^0 + \omega' + \omega} \frac{1}{k^0 - \omega' - \omega + i\epsilon} \\
&\times \frac{M}{E} \frac{1}{P^0 - \omega - E + i\epsilon} \frac{1}{P^0 - k^0 - \omega' - E + i\epsilon} \left[(\omega + \omega')^2 + (\omega + \omega')(E - P^0) + \omega' k^0 \right]
\end{aligned}
$$

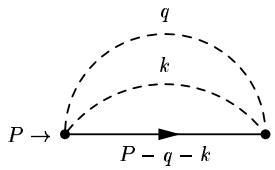

Figure C.8: Diagrammatic representation fo the two-loop for two mesons and one baryon. Dashed and solid lines represent the mesons and the baryon respectively.

This result was used to calculate the integrals in chapter 7, with appropriate factors in the numerator.

C.2 Two-loop functions

C.2.1 A two-loop function for two mesons and one baryon

Let us now consider a two-loop function with two meson propagators and one baryon propagator. The masses of the mesons and the baryon are given by m_1, m_2, and M. We assign momentum variables as shown in Fig. C.8. In the center of mass frame $P = (\sqrt{s}, \mathbf{0})$, the loop function is given by

$$G(\sqrt{s}) = -\int \frac{d^4q}{(2\pi)^4} \int \frac{d^4k}{(2\pi)^4} \frac{1}{k^2 - m_1^2 + i\epsilon} \frac{1}{q^2 - m_2^2 + i\epsilon} \frac{M}{E} \frac{1}{\sqrt{s} - k_0 - q_0 - E + i\epsilon}$$

with on-shell energies of particles are written as

$$\omega_1 = \sqrt{m_1^2 + \boldsymbol{k}^2}, \quad \omega_2 = \sqrt{m_2^2 + \boldsymbol{q}^2}, \quad E = \sqrt{M^2 + \boldsymbol{k}^2 + \boldsymbol{q}^2 + 2|\boldsymbol{k}||\boldsymbol{q}|\cos\theta},$$

where θ is the angle between $\boldsymbol{k}$ and $\boldsymbol{q}$. With these values, we calculate the function:

$$\begin{aligned} G(\sqrt{s}) =& -\int \frac{d^4q}{(2\pi)^4} \int \frac{d^4k}{(2\pi)^4} \frac{1}{k^2 - m_1^2 + i\epsilon} \frac{1}{q^2 - m_2^2 + i\epsilon} \frac{M}{E} \frac{1}{\sqrt{s} - k_0 - q_0 - E + i\epsilon} \\ =& -i \int \frac{d^4q}{(2\pi)^4} \int \frac{d^3k}{(2\pi)^3} \frac{M}{E} \frac{1}{2\omega_1} \frac{1}{q^2 - m_2^2 + i\epsilon} \frac{1}{\sqrt{s} - \omega_1 - q_0 - E + i\epsilon} \\ =& \int \frac{d^3q}{(2\pi)^3} \int \frac{d^3k}{(2\pi)^3} \frac{M}{E} \frac{1}{2\omega_1} \frac{1}{2\omega_2} \frac{1}{\sqrt{s} - \omega_1 - \omega_2 - E + i\epsilon}. \end{aligned}$$

This form corresponds to Eq. (9.3.6) in chapter 9. In practical calculation, we can perform angular integrals

$$\begin{aligned} G(\sqrt{s}) =& \frac{M}{4(2\pi)^6} \int d\Omega_1 \int_0^{q_{\max}} dq \boldsymbol{q}^2 \int d\Omega_2 \int_0^{k_{\max}} dk \boldsymbol{k}^2 \frac{1}{E} \frac{1}{\omega_1} \frac{1}{\omega_2} \frac{1}{\sqrt{s} - \omega_1 - \omega_2 - E + i\epsilon} \\ =& \frac{M}{4(2\pi)^6} \int d\Omega_1 \int_0^{q_{\max}} dq \boldsymbol{q}^2 \int d\Omega_2 \int_0^{k_{\max}} dk \boldsymbol{k}^2 \frac{1}{E} \frac{1}{\omega_1} \frac{1}{\omega_2} \frac{1}{\sqrt{s} - \omega_1 - \omega_2 - E + i\epsilon} \\ =& \frac{M}{2(2\pi)^4} \int_{-1}^{1} d\cos\theta \int_0^{q_{\max}} dq \int_0^{k_{\max}} dk \frac{\boldsymbol{q}^2 \boldsymbol{k}^2}{E} \frac{1}{\omega_1} \frac{1}{\omega_2} \frac{1}{\sqrt{s} - \omega_1 - \omega_2 - E + i\epsilon}, \end{aligned}$$

where we left the integration of the $\cos\theta$ since E depends on it.

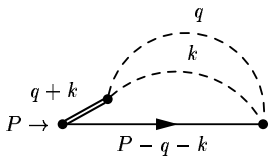

Figure C.9: Diagrammatic representation fo the two-loop for two mesons and one baryon with an extra propagator of vector meson. Dashed and solid lines represent the mesons and the baryon respectively.

C.2.2 A two-loop function for two mesons and one baryon with extra propagators

Next we consider the two-loop function studied in the previous subsection with one extra propagator of vector meson, which is shown in Fig. C.9. The masses of the mesons, the baryon, and the vector meson are given by m_1, m_2, M, and m_v. We assign momentum variables as shown in Fig. C.9. As explained in subsection 9.3.2, the imaginary part can be obtained by multiplying a factor in the loop function (9.3.6). For the real part, in the center of mass frame $P = (\sqrt{s}, \mathbf{0})$, we evaluate the loop function

$$\begin{aligned} G(\sqrt{s}) = &- \int \frac{d^4q}{(2\pi)^4} \int \frac{d^4k}{(2\pi)^4} \frac{1}{k^2 - m_1^2 + i\epsilon} \frac{1}{q^2 - m^2 + i\epsilon} \\ &\times \frac{m_v^2}{(k+q)^2 - m_v^2 + i\epsilon} \frac{M}{E} \frac{1}{\sqrt{s} - k_0 - q_0 - E + i\epsilon} \end{aligned} \tag{C.2.1}$$

with on-shell energies of particles are written as

$$\begin{aligned} &\omega_1 = \sqrt{m_1^2 + \boldsymbol{k}^2}, \quad \omega_2 = \sqrt{m_2^2 + \boldsymbol{q}^2}, \\ &E = \sqrt{M^2 + \boldsymbol{k}^2 + \boldsymbol{q}^2 + 2|\boldsymbol{k}||\boldsymbol{q}|\cos\theta}, \quad \omega_v = \sqrt{m_v^2 + \boldsymbol{k}^2 + \boldsymbol{q}^2 + 2|\boldsymbol{k}||\boldsymbol{q}|\cos\theta}, \end{aligned}$$

where θ is the angle between $\boldsymbol{k}$ and $\boldsymbol{q}$. In order to have two extra propagators as in subsection 9.3.2, we differentiate the factor $1/((k+q)^2 - m_v^2 + i\epsilon)$ in Eq. (C.2.1) with respect to m_v^2.

For later convenience, we transform the variable q_0 as

$$k_0 + q_0 = Q_0, \quad dq_0 = dQ_0$$

then calculate the integration

$$\begin{aligned} G(\sqrt{s}) = &- \int \frac{d^3q dQ_0}{(2\pi)^4} \int \frac{d^3k}{(2\pi)^4} \int dk_0 \frac{1}{k_0^2 - \omega_1^2 + i\epsilon} \frac{1}{(Q_0 - k_0)^2 - \omega_2^2 + i\epsilon} \\ &\times \frac{m_v^2}{Q_0^2 - \omega_v^2 + i\epsilon} \frac{M}{E} \frac{1}{\sqrt{s} - Q_0 - E + i\epsilon} \\ = &- \int \frac{d^3q dQ_0}{(2\pi)^4} \int \frac{d^3k}{(2\pi)^4} \int dk_0 \frac{1}{k_0^2 - (\omega_1 - i\epsilon)^2} \frac{1}{(k_0 - Q_0)^2 - (\omega_2 - i\epsilon)^2} \\ &\times \frac{m_v^2}{Q_0^2 - \omega_v^2 + i\epsilon} \frac{M}{E} \frac{1}{\sqrt{s} - Q_0 - E + i\epsilon} \end{aligned}$$

$$
\begin{aligned}
&= -\int \frac{d^3qdQ_0}{(2\pi)^4}\int \frac{d^3k}{(2\pi)^4}\frac{m_v^2}{Q_0^2-\omega_v^2+i\epsilon}\frac{M}{E}\frac{1}{\sqrt{s}-Q_0-E+i\epsilon}\\
&\quad\times\int dk_0 \frac{1}{k_0-\omega_1+i\epsilon}\frac{1}{k_0+\omega_1-i\epsilon}\frac{1}{k_0-Q_0-\omega_2+i\epsilon}\frac{1}{k_0-Q_0+\omega_2-i\epsilon}.
\end{aligned}
$$

In the lower half of the k_0 plane, we find poles at

$$
k_0=\omega_1-i\epsilon,\quad Q_0+\omega_2-i\epsilon
$$

In this case, we again have the fallacious pole. Cancelling the fallacious pole at $Q_0-\omega_1+\omega_2$, we next search for the poles in Q_0 plane;

$$
\begin{aligned}
&= -\int \frac{d^3qdQ_0}{(2\pi)^4}\int \frac{d^3k}{(2\pi)^4}\frac{m_v^2}{Q_0^2-\omega_v^2+i\epsilon}\frac{M}{E}\frac{1}{\sqrt{s}-Q_0-E+i\epsilon}\\
&\quad\times(-2\pi i)\left\{\frac{1}{\omega_1+\omega_1-i\epsilon}\frac{1}{\omega_1-Q_0-\omega_2\pm i\epsilon}\frac{1}{\omega_1-Q_0+\omega_2-i\epsilon}\right.\\
&\quad\left.+\frac{1}{Q_0+\omega_2-\omega_1\pm i\epsilon}\frac{1}{Q_0+\omega_2+\omega_1-i\epsilon}\frac{1}{Q_0+\omega_2-Q_0+\omega_2-i\epsilon}\right\}\\
&=i\int \frac{d^3qdQ_0}{(2\pi)^4}\int \frac{d^3k}{(2\pi)^3}\frac{m_v^2}{Q_0^2-\omega_v^2+i\epsilon}\frac{M}{E}\frac{1}{\sqrt{s}-Q_0-E+i\epsilon}\\
&\quad\times\left\{\frac{1}{\omega_1+\omega_1-i\epsilon}\frac{1}{\omega_1-Q_0-\omega_2\pm i\epsilon}\frac{1}{\omega_1-Q_0+\omega_2-i\epsilon}\right.\\
&\quad\left.+\frac{1}{Q_0+\omega_2-\omega_1\pm i\epsilon}\frac{1}{Q_0+\omega_2+\omega_1-i\epsilon}\frac{1}{Q_0+\omega_2-Q_0+\omega_2-i\epsilon}\right\}\\
&=i\int \frac{d^3qdQ_0}{(2\pi)^4}\int \frac{d^3k}{(2\pi)^3}\frac{m_v^2}{Q_0^2-\omega_v^2+i\epsilon}\frac{M}{E}\frac{1}{\sqrt{s}-Q_0-E+i\epsilon}\\
&\quad\times\left\{\frac{1}{2\omega_1}\frac{1}{\omega_1-Q_0-\omega_2\pm i\epsilon}\frac{1}{\omega_1-Q_0+\omega_2-i\epsilon}+\frac{1}{Q_0+\omega_2-\omega_1\pm i\epsilon}\frac{1}{Q_0+\omega_2+\omega_1-i\epsilon}\frac{1}{2\omega_2}\right\}\\
&=i\int \frac{d^3qdQ_0}{(2\pi)^4}\int \frac{d^3k}{(2\pi)^3}\frac{m_v^2}{Q_0^2-\omega_v^2+i\epsilon}\frac{M}{E}\frac{1}{\sqrt{s}-Q_0-E+i\epsilon}\\
&\quad\times\left\{\frac{1}{2}\frac{1}{Q_0-\omega_1+\omega_2\pm i\epsilon}\frac{1}{\omega_1}\frac{1}{Q_0-\omega_1-\omega_2+i\epsilon}+\frac{1}{2}\frac{1}{Q_0-\omega_1+\omega_2\pm i\epsilon}\frac{1}{Q_0+\omega_2+\omega_1-i\epsilon}\frac{1}{\omega_2}\right\}\\
&=i\int \frac{d^3qdQ_0}{(2\pi)^4}\int \frac{d^3k}{(2\pi)^3}\frac{m_v^2}{Q_0^2-\omega_v^2+i\epsilon}\frac{M}{E}\frac{1}{\sqrt{s}-Q_0-E+i\epsilon}\\
&\quad\times\frac{1}{2}\frac{1}{Q_0-\omega_1+\omega_2\pm i\epsilon}\left\{\frac{1}{\omega_1}\frac{1}{Q_0-\omega_1-\omega_2+i\epsilon}+\frac{1}{Q_0+\omega_2+\omega_1-i\epsilon}\frac{1}{\omega_2}\right\}\\
&=i\int \frac{d^3qdQ_0}{(2\pi)^4}\int \frac{d^3k}{(2\pi)^3}\frac{m_v^2}{Q_0^2-\omega_v^2+i\epsilon}\frac{M}{E}\frac{1}{\sqrt{s}-Q_0-E+i\epsilon}\\
&\quad\times\frac{1}{2}\frac{1}{Q_0-\omega_1+\omega_2\pm i\epsilon}\frac{1}{\omega_1}\frac{1}{\omega_2}\frac{1}{Q_0-\omega_1-\omega_2+i\epsilon}\frac{1}{Q_0+\omega_2+\omega_1-i\epsilon}\\
&\quad\times\{\omega_1(Q_0-\omega_1-\omega_2+i\epsilon)+\omega_2(Q_0+\omega_2+\omega_1-i\epsilon)\}
\end{aligned}
$$

$$
\begin{aligned}
=& i\int\frac{d^3qdQ_0}{(2\pi)^4}\int\frac{d^3k}{(2\pi)^3}\frac{m_v^2}{Q_0^2-\omega_v^2+i\epsilon}\frac{M}{E}\frac{1}{\sqrt{s}-Q_0-E+i\epsilon}\\
&\times\frac{1}{2}\frac{1}{\omega_1}\frac{1}{\omega_2}\frac{1}{Q_0-\omega_1+\omega_2\pm i\epsilon}\frac{1}{Q_0-\omega_1-\omega_2+i\epsilon}\frac{1}{Q_0+\omega_2+\omega_1-i\epsilon}\\
&\times\{\omega_1Q_0-\omega_1^2-\omega_1\omega_2+\omega_2Q_0+\omega_2^2+\omega_2\omega_1\pm i\epsilon\}\\
=& i\int\frac{d^3qdQ_0}{(2\pi)^4}\int\frac{d^3k}{(2\pi)^3}\frac{m_v^2}{Q_0^2-\omega_v^2+i\epsilon}\frac{M}{E}\frac{1}{\sqrt{s}-Q_0-E+i\epsilon}\\
&\times\frac{1}{2}\frac{1}{\omega_1}\frac{1}{\omega_2}\frac{1}{Q_0-\omega_1+\omega_2\pm i\epsilon}\frac{1}{Q_0-\omega_1-\omega_2+i\epsilon}\frac{1}{Q_0+\omega_2+\omega_1-i\epsilon}\\
&\times\{(\omega_1+\omega_2)Q_0+(\omega_2-\omega_1)(\omega_2+\omega_1)\pm i\epsilon\}\\
=& i\int\frac{d^3qdQ_0}{(2\pi)^4}\int\frac{d^3k}{(2\pi)^3}\frac{m_v^2}{Q_0^2-\omega_v^2+i\epsilon}\frac{M}{E}\frac{1}{\sqrt{s}-Q_0-E+i\epsilon}\\
&\times\frac{1}{2}\frac{1}{\omega_1}\frac{1}{\omega_2}\frac{1}{Q_0-\omega_1+\omega_2\pm i\epsilon}\frac{1}{Q_0-\omega_1-\omega_2+i\epsilon}\frac{1}{Q_0+\omega_2+\omega_1-i\epsilon}\\
&\times(\omega_2-\omega_1+Q_0\pm i\epsilon)(\omega_2+\omega_1)\\
=& i\int\frac{d^3qdQ_0}{(2\pi)^4}\int\frac{d^3k}{(2\pi)^3}\frac{m_v^2}{Q_0^2-\omega_v^2+i\epsilon}\frac{M}{E}\frac{1}{\sqrt{s}-Q_0-E+i\epsilon}\\
&\times\frac{1}{2}\frac{\omega_1+\omega_2}{\omega_1\omega_2}\frac{1}{Q_0-\omega_1-\omega_2+i\epsilon}\frac{1}{Q_0+\omega_2+\omega_1-i\epsilon}\\
=& i\int\frac{d^3q}{(2\pi)^4}\int\frac{d^3k}{(2\pi)^3}\frac{1}{2}\frac{\omega_1+\omega_2}{\omega_1\omega_2}\frac{Mm_v^2}{E}\\
&\times\int dQ_0\frac{1}{Q_0-\omega_v+i\epsilon}\frac{1}{Q_0+\omega_v-i\epsilon}\frac{-1}{Q_0-\sqrt{s}+E-i\epsilon}\frac{1}{Q_0-\omega_1-\omega_2+i\epsilon}\frac{1}{Q_0+\omega_2+\omega_1-i\epsilon}\\
=& i\int\frac{d^3q}{(2\pi)^4}\int\frac{d^3k}{(2\pi)^3}\frac{1}{2}\frac{\omega_1+\omega_2}{\omega_1\omega_2}\frac{Mm_v^2}{E}\\
&\times\int dQ_0\frac{1}{Q_0-\omega_v+i\epsilon}\frac{1}{Q_0+\omega_v-i\epsilon}\frac{-1}{Q_0-\sqrt{s}+E-i\epsilon}\frac{1}{Q_0-\omega_1-\omega_2+i\epsilon}\frac{1}{Q_0+\omega_2+\omega_1-i\epsilon},
\end{aligned}
$$

and found at

$$
Q_0=\omega_v-i\epsilon,\quad \omega_1+\omega_2-i\epsilon
$$

Picking up these poles, and cancelling another fallacious pole at $\omega_v-\omega_1-\omega_2$, we finally arrive at

$$
\begin{aligned}
=&-i\int\frac{d^3q}{(2\pi)^4}\int\frac{d^3k}{(2\pi)^3}\frac{1}{2}\frac{\omega_1+\omega_2}{\omega_1\omega_2}\frac{Mm_v^2}{E}\\
&\times(-2\pi i)\left\{\frac{1}{\omega_v+\omega_v-i\epsilon}\frac{1}{\omega_v-\sqrt{s}+E-i\epsilon}\frac{1}{\omega_v-\omega_1-\omega_2\pm i\epsilon}\frac{1}{\omega_v+\omega_2+\omega_1-i\epsilon}\right.\\
&\left.+\frac{1}{\omega_1+\omega_2-\omega_v\pm i\epsilon}\frac{1}{\omega_1+\omega_2+\omega_v-i\epsilon}\frac{1}{\omega_1+\omega_2-\sqrt{s}+E-i\epsilon}\frac{1}{\omega_1+\omega_2+\omega_2+\omega_1-i\epsilon}\right\}
\end{aligned}
$$

$$
\begin{aligned}
=&-\int\frac{d^3q}{(2\pi)^3}\int\frac{d^3k}{(2\pi)^3}\frac{1}{2}\frac{\omega_1+\omega_2}{\omega_1\omega_2}\frac{Mm_v^2}{E}\\
&\times\left\{\frac{1}{2}\frac{1}{\omega_v-\omega_1-\omega_2\pm i\epsilon}\frac{1}{\omega_v+\omega_1+\omega_2-i\epsilon}\frac{1}{\omega_v}\frac{1}{\omega_v-\sqrt{s}+E-i\epsilon}\right.\\
&\left.-\frac{1}{2}\frac{1}{\omega_v-\omega_1-\omega_2\pm i\epsilon}\frac{1}{\omega_v+\omega_1+\omega_2-i\epsilon}\frac{1}{\omega_1+\omega_2-\sqrt{s}+E-i\epsilon}\frac{1}{\omega_1+\omega_2}\right\}\\
=&-\int\frac{d^3q}{(2\pi)^3}\int\frac{d^3k}{(2\pi)^3}\frac{1}{2}\frac{\omega_1+\omega_2}{\omega_1\omega_2}\frac{Mm_v^2}{E}\frac{1}{2}\frac{1}{\omega_v-\omega_1-\omega_2\pm i\epsilon}\frac{1}{\omega_v+\omega_1+\omega_2-i\epsilon}\\
&\times\left\{\frac{1}{\omega_v}\frac{1}{\omega_v-\sqrt{s}+E-i\epsilon}-\frac{1}{\omega_1+\omega_2-\sqrt{s}+E-i\epsilon}\frac{1}{\omega_1+\omega_2}\right\}\\
=&-\int\frac{d^3q}{(2\pi)^3}\int\frac{d^3k}{(2\pi)^3}\frac{1}{2}\frac{\omega_1+\omega_2}{\omega_1\omega_2}\frac{Mm_v^2}{E}\frac{1}{2}\frac{1}{\omega_v-\omega_1-\omega_2\pm i\epsilon}\frac{1}{\omega_v+\omega_1+\omega_2-i\epsilon}\\
&\times\frac{(\omega_1+\omega_2)(\omega_1+\omega_2-\sqrt{s}+E-i\epsilon)-\omega_v(\omega_v-\sqrt{s}+E-i\epsilon)}{\omega_v(\omega_v-\sqrt{s}+E-i\epsilon)(\omega_1+\omega_2-\sqrt{s}+E-i\epsilon)(\omega_1+\omega_2)}\\
=&-\int\frac{d^3q}{(2\pi)^3}\int\frac{d^3k}{(2\pi)^3}\frac{1}{2}\frac{\omega_1+\omega_2}{\omega_1\omega_2}\frac{Mm_v^2}{E}\frac{1}{2}\frac{1}{\omega_v-\omega_1-\omega_2\pm i\epsilon}\frac{1}{\omega_v+\omega_1+\omega_2-i\epsilon}\\
&\times\frac{(\omega_1+\omega_2)^2+(\omega_1+\omega_2)(-\sqrt{s}+E)-\omega_v^2-\omega_v(-\sqrt{s}+E)\pm i\epsilon}{\omega_v(\omega_v-\sqrt{s}+E-i\epsilon)(\omega_1+\omega_2-\sqrt{s}+E-i\epsilon)(\omega_1+\omega_2)}\\
=&-\int\frac{d^3q}{(2\pi)^3}\int\frac{d^3k}{(2\pi)^3}\frac{1}{2}\frac{\omega_1+\omega_2}{\omega_1\omega_2}\frac{Mm_v^2}{E}\frac{1}{2}\frac{1}{\omega_v-\omega_1-\omega_2\pm i\epsilon}\frac{1}{\omega_v+\omega_1+\omega_2-i\epsilon}\\
&\times\frac{(\omega_1+\omega_2+\omega_v)(\omega_1+\omega_2-\omega_v)+(\omega_1+\omega_2-\omega_v)(-\sqrt{s}+E)\pm i\epsilon}{\omega_v(\omega_v-\sqrt{s}+E-i\epsilon)(\omega_1+\omega_2-\sqrt{s}+E-i\epsilon)(\omega_1+\omega_2)}\\
=&-\int\frac{d^3q}{(2\pi)^3}\int\frac{d^3k}{(2\pi)^3}\frac{1}{2}\frac{\omega_1+\omega_2}{\omega_1\omega_2}\frac{Mm_v^2}{E}\frac{1}{2}\frac{1}{\omega_v-\omega_1-\omega_2\pm i\epsilon}\frac{1}{\omega_v+\omega_1+\omega_2-i\epsilon}\\
&\times\frac{(\omega_1+\omega_2+\omega_v-\sqrt{s}+E)(\omega_1+\omega_2-\omega_v\pm i\epsilon)}{\omega_v(\omega_v-\sqrt{s}+E-i\epsilon)(\omega_1+\omega_2-\sqrt{s}+E-i\epsilon)(\omega_1+\omega_2)}\\
=&\frac{1}{4}\int\frac{d^3q}{(2\pi)^3}\int\frac{d^3k}{(2\pi)^3}\frac{1}{\omega_1\omega_2\omega_v}\frac{1}{\omega_v+\omega_1+\omega_2}\frac{Mm_v^2}{E}\\
&\times\frac{(\omega_1+\omega_2+\omega_v-\sqrt{s}+E)}{(\sqrt{s}-\omega_v-E+i\epsilon)(\sqrt{s}-\omega_1-\omega_2-E+i\epsilon)},
\end{aligned}
$$

which corresponds to Eq. (9.3.10) by differentiating in terms of m_v^2 and taking the principle value.

Appendix D

Flavor SU(3) coefficients

In this chapter we summarize the flavor SU(3) coefficients used in this thesis. First we classify the meson-baryon channels in particle and isospin bases, and then show the explicit forms of the flavor coefficients. Coefficients for the interaction including antidecuplet is then displayed.

D.1 Classification of meson-baryon channels

Here we classify meson-baryon channels in terms of the conserved quantum numbers. There are 64 meson-baryon channels when we consider scatterings of octet mesons and octet baryons. They are coupled within the sectors in which the channels have the same flavor quantum number.

D.1.1 Conservation of quantum numbers

Since we are considering the strong interaction, there are conserved quantum numbers. The channels of the meson-baryon scatterings are specified by two quantum numbers, the hypercharge Y and the third component of isospin I_3, or equivalently the strangeness S and the electric charge Q, through the Gell-Mann–Nakano–Nishijima relation [655, 656]

$$Q = T_3 + \frac{Y}{2}, \quad S = Y - B,$$

where the baryon number $B = 1$ for the meson-baryon scatterings. In Table D.1, all channels of octet mesons and octet baryons are classified in terms of quantum numbers. The channels with the same quantum numbers can couple each other.

D.1.2 Basis transformation

In Table D.1, we show the meson-baryon channels in particle basis. It is also useful to express them in isospin basis using the SU(2) Clebsch-Gordan coefficients. We define particle basis

Table D.1: Channels of meson-baryon scatterings in particle basis.

Y	S	I_3	Q	channels
-2	-3	1	0	$\bar{K}^0\Xi^0$
		0	-1	$K^-\Xi^0,\ \bar{K}^0\Xi^-$
		-1	-2	$K^-\Xi^-$
-1	-2	$\frac{3}{2}$	1	$\pi^+\Xi^0,\ \bar{K}^0\Sigma^+$
		$\frac{1}{2}$	0	$\pi^0\Xi^0,\ \pi^+\Xi^-,\ \eta\Xi^0,\ \bar{K}^0\Lambda,\ \bar{K}^0\Sigma^0,\ K^-\Sigma^+$
		$-\frac{1}{2}$	-1	$\pi^0\Xi^-,\ \pi^-\Xi^0,\ \eta\Xi^-,\ K^-\Lambda,\ K^-\Sigma^0,\ \bar{K}^0\Sigma^-$
		$-\frac{3}{2}$	-2	$\pi^-\Xi^-,\ K^-\Sigma^-$
0	-1	2	2	$\pi^+\Sigma^+$
		1	1	$\bar{K}^0p,\ \pi^0\Sigma^+,\ \pi^+\Sigma^0,\ \pi^+\Lambda,\ \eta\Sigma^+,\ K^+\Xi^0$
		0	0	$K^-p,\ \bar{K}^0n,\ \pi^0\Lambda,\ \pi^0\Sigma^0,\ \eta\Lambda,\ \eta\Sigma^0,\ \pi^+\Sigma^-,\ \pi^-\Sigma^+,\ K^+\Xi^-,\ K^0\Xi^0$
		-1	-1	$K^-n,\ \pi^0\Sigma^-,\ \pi^-\Sigma^0,\ \pi^-\Lambda,\ \eta\Sigma^-,\ K^0\Xi^-$
		-2	-2	$\pi^-\Sigma^-$
1	0	$\frac{3}{2}$	2	$\pi^+p,\ K^+\Sigma^+$
		$\frac{1}{2}$	1	$\pi^0p,\ \pi^+n,\ \eta p,\ K^+\Lambda,\ K^+\Sigma^0,\ K^0\Sigma^+$
		$-\frac{1}{2}$	0	$\pi^0n,\ \pi^-p,\ \eta n,\ K^0\Lambda,\ K^0\Sigma^0,\ K^+\Sigma^-$
		$-\frac{3}{2}$	-1	$\pi^-n,\ K^0\Sigma^-$
2	1	1	2	K^+p
		0	1	$K^+n,\ K^0p$
		-1	0	K^0n

(P) and isospin basis (I) as

$$(P) \equiv \begin{pmatrix} \text{channel 1 in particle basis} \\ \text{channel 2 in particle basis} \\ \cdot \\ \cdot \\ \cdot \\ \cdot \\ \cdot \end{pmatrix}, \quad (I) \equiv \begin{pmatrix} \text{channel 1 with } I_1 \text{ in isospin basis} \\ \text{channel 2 with } I_1 \text{ in isospin basis} \\ \cdot \\ \text{channel 1 with } I_2 \text{ in isospin basis} \\ \text{channel 2 with } I_2 \text{ in isospin basis} \\ \cdot \\ \cdot \end{pmatrix}.$$

where I_i means each values of total isospin I. The numbers of the channels in (P) and (I) are the same. In Table D.2 the channels in isospin basis are shown.

Now we define the transformation matrix (Ω) between the particle basis and the isospin basis as

$$(I) \equiv (\Omega) \cdot (P), \quad (P) = (\Omega)^{-1} \cdot (I).$$

The components of Ω is determined by the SU(2) Clebsch-Gordan coefficients and suitable phase conventions of the fields. Mathematically, this is a transformation between bases of finite dimension complex vector space, therefore, it is expressed by a unitary matrix in order to conserve the norm of basis;

$$\Omega^{-1} = \Omega^\dagger.$$

Table D.2: Channels of meson-baryon scatterings in isospin basis. The number in the bracket denotes the total isospin I.

Y	S	channels
-2	-3	$\bar{K}\Xi(1)$
		$\bar{K}\Xi(0)$, $\bar{K}\Xi(1)$
		$\bar{K}\Xi(1)$
-1	-2	$\pi\Xi(3/2)$, $\bar{K}\Sigma(3/2)$
		$\pi\Xi(1/2)$, $\eta\Xi(1/2)$, $\bar{K}\Lambda(1/2)$, $\bar{K}\Sigma(1/2)$, $\pi\Xi(3/2)$, $\bar{K}\Sigma(3/2)$
		$\pi\Xi(1/2)$, $\eta\Xi(1/2)$, $\bar{K}\Lambda(1/2)$, $\bar{K}\Sigma(1/2)$, $\pi\Xi(3/2)$, $\bar{K}\Sigma(3/2)$
		$\pi\Xi(3/2)$, $\bar{K}\Sigma(3/2)$
0	-1	$\pi\Sigma(2)$
		$\bar{K}N(1)$, $\pi\Sigma(1)$, $\pi\Lambda(1)$, $\eta\Sigma(1)$, $K\Xi(1)$, $\pi\Sigma(2)$
		$\bar{K}N(0)$, $\pi\Sigma(0)$, $\eta\Lambda(0)$, $K\Xi(0)$, $\bar{K}N(1)$, $\pi\Sigma(1)$, $\pi\Lambda(1)$, $\eta\Sigma(1)$, $K\Xi(1)$, $\pi\Sigma(2)$
		$\bar{K}N(1)$, $\pi\Sigma(1)$, $\pi\Lambda(1)$, $\eta\Sigma(1)$, $K\Xi(1)$, $\pi\Sigma(2)$
		$\pi\Sigma(2)$
1	0	$\pi N(3/2)$, $K\Sigma(3/2)$
		$\pi N(1/2)$, $\eta N(1/2)$, $K\Lambda(1/2)$, $K\Sigma(1/2)$, $\pi N(3/2)$, $K\Sigma(3/2)$
		$\pi N(1/2)$, $\eta N(1/2)$, $K\Lambda(1/2)$, $K\Sigma(1/2)$, $\pi N(3/2)$, $K\Sigma(3/2)$
		$\pi N(3/2)$, $K\Sigma(3/2)$
2	1	$KN(1)$
		$KN(0)$, $KN(1)$
		$KN(1)$

In practice, since the all elements of Ω are Clebsch-Gordan coefficients and hence the real numbers, so that it becomes an orthogonal matrix $\Omega^{-1} = \Omega^t$, where the superscript ^{t} denotes transpose of matrices.

Relation between a matrix M (for example, C_{ij} coefficients or the T-matrix) in (P) basis and (I) basis is

$$(I)^t \cdot M^I \cdot (I) = (P)^t \cdot M^P \cdot (P) = (I)^t \cdot (\Omega) \cdot M^P \cdot (\Omega)^{-1} \cdot (I).$$

So we have relations

$$M^I = (\Omega) \cdot M^P \cdot (\Omega)^{-1} \quad M^P = (\Omega)^{-1} \cdot M^I \cdot (\Omega).$$

In this way we can change basis for any matrices. The form of these basis and Ω are given explicitly as follows. For instance, for $S = -1, T_3 = 0$ channel,

$$(P)^t \equiv \begin{pmatrix} K^- p & \bar{K}^0 n & \pi^0\Lambda & \pi^0\Sigma^0 & \eta\Lambda & \eta\Sigma^0 & \pi^+\Sigma^- & \pi^-\Sigma^+ & K^+\Xi^- & K^0\Xi^0 \end{pmatrix}$$
$$(I)^t \equiv \begin{pmatrix} \bar{K}N(0) & \pi\Sigma(0) & \eta\Lambda(0) & K\Xi(0) & \bar{K}N(1) & \pi\Sigma(1) & \pi\Lambda(1) & \eta\Sigma(1) & K\Xi(1) & \pi\Sigma(2) \end{pmatrix}$$

$$(\Omega) = \begin{pmatrix} \sqrt{\frac{1}{2}} & \sqrt{\frac{1}{2}} & 0 & 0 & 0 & 0 & 0 & 0 & 0 & 0 \\ 0 & 0 & 0 & -\sqrt{\frac{1}{3}} & 0 & 0 & -\sqrt{\frac{1}{3}} & -\sqrt{\frac{1}{3}} & 0 & 0 \\ 0 & 0 & 0 & 0 & 1 & 0 & 0 & 0 & 0 & 0 \\ 0 & 0 & 0 & 0 & 0 & 0 & 0 & 0 & -\sqrt{\frac{1}{2}} & -\sqrt{\frac{1}{2}} \\ -\sqrt{\frac{1}{2}} & \sqrt{\frac{1}{2}} & 0 & 0 & 0 & 0 & 0 & 0 & 0 & 0 \\ 0 & 0 & 0 & 0 & 0 & 0 & -\sqrt{\frac{1}{2}} & \sqrt{\frac{1}{2}} & 0 & 0 \\ 0 & 0 & 1 & 0 & 0 & 0 & 0 & 0 & 0 & 0 \\ 0 & 0 & 0 & 0 & 0 & 1 & 0 & 0 & 0 & 0 \\ 0 & 0 & 0 & 0 & 0 & 0 & 0 & 0 & -\sqrt{\frac{1}{2}} & \sqrt{\frac{1}{2}} \\ 0 & 0 & 0 & \frac{2}{\sqrt{6}} & 0 & 0 & -\sqrt{\frac{1}{6}} & -\sqrt{\frac{1}{6}} & 0 & 0 \end{pmatrix}$$

and for the $S = 0, T_3 = -1/2$ channel,

$$(P)^t \equiv \begin{pmatrix} \pi^0 n & \pi^- p & \eta n & K^0\Lambda & K^0\Sigma^0 & K^+\Sigma^- \end{pmatrix}$$
$$(I)^t \equiv \begin{pmatrix} \pi N(1/2) & \eta N(1/2) & K\Lambda(1/2) & K\Sigma(1/2) & \pi N(3/2) & K\Sigma(3/2) \end{pmatrix}$$
$$(\Omega) = \begin{pmatrix} \sqrt{\frac{1}{3}} & -\sqrt{\frac{2}{3}} & 0 & 0 & 0 & 0 \\ 0 & 0 & 1 & 0 & 0 & 0 \\ 0 & 0 & 0 & 1 & 0 & 0 \\ 0 & 0 & 0 & 0 & \sqrt{\frac{1}{3}} & -\sqrt{\frac{2}{3}} \\ \sqrt{\frac{3}{2}} & \sqrt{\frac{1}{3}} & 0 & 0 & 0 & 0 \\ 0 & 0 & 0 & 0 & \sqrt{\frac{3}{2}} & \sqrt{\frac{1}{3}} \end{pmatrix}$$

As in the same way, the transformation to the SU(3) basis can be obtained, using the SU(3) Clebsch-Gordan coefficients [649].

D.2 Coefficients for meson-baryon interactions

We summarize the coefficients of meson-baryon vertex obtained from the Lagrangian of the chiral perturbation theory. Here we show the coefficients of the Weinberg-Tomozawa (WT) terms, flavor SU(3) breaking terms and the photon coupling terms. Tables of specific channels which we have used in this thesis are presented.

D.2.1 Lagrangians and amplitudes

The interaction Lagrangians corresponding to the meson-baryon scattering are given by

$$\begin{aligned} \mathcal{L}_{WT} =& \frac{1}{4f^2}\mathrm{Tr}\Big(\bar{B}i\gamma^\mu\left[(\Phi\partial_\mu\Phi - \partial_\mu\Phi\Phi), B\right]\Big) \ , \\ \mathcal{L}^{(2)}_{SB} =& \frac{Z_0}{4f^2}\mathrm{Tr}\Big(d_m\bar{B}\big\{(2\Phi\mathbf{m}\Phi + \Phi^2\mathbf{m} + \mathbf{m}\Phi^2), B\big\} + f_m\bar{B}\big[(2\Phi\mathbf{m}\Phi + \Phi^2\mathbf{m} + \mathbf{m}\Phi^2), B\big]\Big) \\ &+ \frac{Z_1}{f^2}\mathrm{Tr}(\bar{B}B)\mathrm{Tr}(\mathbf{m}\Phi^2) \ , \end{aligned}$$

Table D.3: $D_i^{Z_1}$ coefficients.

meson	π	$K, \bar{K}$	η
$D_i^{Z_1}$	$2\hat{m}$	$\hat{m}+m_s$	$\frac{2}{3}(\hat{m}+2m_s)$

$$\mathcal{L}_{(\gamma)}^{MB} = -\frac{i}{4M_P} b_6^F \mathrm{Tr}\left(\bar{B}[S^\mu, S^\nu][F_{\mu\nu}^+, B]\right) - \frac{i}{4M_P} b_6^D \mathrm{Tr}\left(\bar{B}[S^\mu, S^\nu]\{F_{\mu\nu}^+, B\}\right).$$

From these terms, the amplitude at tree level are given by

$$\begin{aligned}
V_{ij}^{(WT)} =& -\frac{C_{ij}}{4f^2}(2\sqrt{s} - M_i - M_j)\sqrt{\frac{E_i+M_i}{2M_i}}\sqrt{\frac{E_j+M_j}{2M_j}}, \\
V_{ij}^{(SB)} =& -\frac{1}{f^2}\Big[Z_0\Big((A_{ij}^d d_m + A_{ij}^f f_m)\hat{m} + (B_{ij}^d d_m + B_{ij}^f f_m)m_s\Big) + Z_1\delta_{ij}D_i^{Z_1}\Big] \\
& \times \sqrt{\frac{E_i+M_i}{2M_i}}\sqrt{\frac{E_j+M_j}{2M_j}}, \\
V_{ij}^{MMBB\gamma} =& ie\frac{\boldsymbol{\sigma}\times\mathbf{q}}{2M_p}\cdot\boldsymbol{\epsilon}\frac{1}{2f^2}[X_{ij}b_6^D + Y_{ij}b_6^F].
\end{aligned} \tag{D.2.1}$$

where we have applied the nonrelativistic reduction to the amplitudes. The coefficients C, A, B, D, X and Y are the numbers in matrix form and the indices (i, j) denote the channels of the meson-baryon scatterings as shown in Table D.1.

The coefficient $D_i^{Z_1}$ is specified only by the meson in channel i independently of baryons, because $\mathrm{Tr}(\bar{B}B)$ in the last term of Eq. (D.2.1) gives a common contribution to all baryons. Also, there is no off-diagonal component when the isospin symmetry is assumed. The explicit form of $D_i^{Z_1}$ is shown in Table D.3.

The values of the coefficients C (WT interactions) are shown in the following tables;

- Table D.4 ($S = 0$ Isospin basis)
- Table D.5 ($S = 0, Q = 0$)
- Table D.6 ($S = 0, Q = 1$)
- Table D.7 ($S = -1$ Isospin basis)
- Table D.8 ($S = 0, Q = 0$).

The values of the coefficients A and B (flavor $SU(3)$ breaking interactions) are shown in the following tables;

- Tables D.9 and D.10 ($S = 0, Q = 0$)
- Tables D.11,D.12, D.13 and D.14 ($S = -1, Q = 0$).

The values of the coefficients X and Y (photon coupling interactions) are shown in the following tables;

Table D.4: $C_{ij}(S=0)$ in isospin basis.

$S=0$		$I=\frac{1}{2}$				$I=\frac{3}{2}$	
		πN	ηN	$K\Lambda$	$K\Sigma$	πN	$K\Sigma$
$I=\frac{1}{2}$	πN	2	0	$\frac{3}{2}$	$\frac{1}{2}$		
	ηN		0	$-\frac{3}{2}$	$\frac{3}{2}$		
	$K\Lambda$			0	0		
	$K\Sigma$				2		
$I=\frac{3}{2}$	πN					-1	-1
	$K\Sigma$						-1

Table D.5: $C_{ij}(S=0,Q=0)$ in particle basis.

	$\pi^0 n$	$\pi^- p$	ηn	$K^0\Lambda$	$K^0\Sigma^0$	$K^+\Sigma^-$
$\pi^0 n$	0	$-\sqrt{2}$	0	$\frac{\sqrt{3}}{2}$	$-\frac{1}{2}$	$-\frac{1}{\sqrt{2}}$
$\pi^- p$		1	0	$-\sqrt{\frac{3}{2}}$	$-\frac{1}{\sqrt{2}}$	0
ηn			0	$-\frac{3}{2}$	$\frac{\sqrt{3}}{2}$	$-\sqrt{\frac{3}{2}}$
$K^0\Lambda$				0	0	0
$K^0\Sigma^0$					0	$-\sqrt{2}$
$K^+\Sigma^-$						1

Table D.6: $C_{ij}(S=0,Q=1)$ in particle basis.

	$\pi^0 p$	$\pi^+ n$	ηp	$K^+\Lambda$	$K^+\Sigma^0$	$K^0\Sigma^+$
$\pi^0 p$	0	$\sqrt{2}$	0	$-\frac{\sqrt{3}}{2}$	$-\frac{1}{2}$	$\frac{1}{\sqrt{2}}$
$\pi^+ n$		1	0	$-\sqrt{\frac{3}{2}}$	$\frac{1}{\sqrt{2}}$	0
ηp			0	$-\frac{3}{2}$	$-\frac{\sqrt{3}}{2}$	$-\sqrt{\frac{3}{2}}$
$K^+\Lambda$				0	0	0
$K^+\Sigma^0$					0	$\sqrt{2}$
$K^0\Sigma^+$						1

- Table D.15 ($S=0,Q=0$)
- Table D.16 ($S=0,Q=1$)
- Tables D.17 and D.18 ($S=-1,Q=0$).

D.2.2 Relations among coefficients

There are two symmetry relations among coefficients. Using these relations, we can derive the coefficients which are not shown explicitly in the tables.

First, the channels, which have the same strangeness S and different charge Q, are related

Table D.7: $C_{ij}(S=-1)$ in Isospin basis.

$S=-1$		$I=0$				$I=1$					$I=2$
		$\bar{K}N$	$\pi\Sigma$	$\eta\Lambda$	$K\Xi$	$\bar{K}N$	$\pi\Sigma$	$\pi\Lambda$	$\eta\Sigma$	$K\Xi$	$\pi\Sigma$
$I=0$	$\bar{K}N$	3	$-\sqrt{\frac{3}{2}}$	$\frac{3}{\sqrt{2}}$	0						
	$\pi\Sigma$		4	0	$\sqrt{\frac{3}{2}}$						
	$\eta\Lambda$			0	$-\frac{3}{\sqrt{2}}$						
	$K\Xi$				3						
$I=1$	$\bar{K}N$					1	-1	$-\sqrt{\frac{3}{2}}$	$-\sqrt{\frac{3}{2}}$	0	
	$\pi\Sigma$						2	0	0	1	
	$\pi\Lambda$							0	0	$-\sqrt{\frac{3}{2}}$	
	$\eta\Sigma$								0	$-\sqrt{\frac{3}{2}}$	
	$K\Xi$									1	
$I=2$	$\pi\Sigma$										-2

Table D.8: $C_{ij}(S=-1,Q=0)$ in particle basis.

	K^-p	$\bar{K}^0n$	$\pi^0\Lambda$	$\pi^0\Sigma^0$	$\eta\Lambda$	$\eta\Sigma^0$	$\pi^+\Sigma^-$	$\pi^-\Sigma^+$	$K^+\Xi^-$	$K^0\Xi^0$
K^-p	2	1	$\frac{\sqrt{3}}{2}$	$\frac{1}{2}$	$\frac{3}{2}$	$\frac{\sqrt{3}}{2}$	0	1	0	0
$\bar{K}^0n$		2	$-\frac{\sqrt{3}}{2}$	$\frac{1}{2}$	$\frac{3}{2}$	$-\frac{\sqrt{3}}{2}$	1	0	0	0
$\pi^0\Lambda$			0	0	0	0	0	0	$\frac{\sqrt{3}}{2}$	$-\frac{\sqrt{3}}{2}$
$\pi^0\Sigma^0$				0	0	0	2	2	$\frac{1}{2}$	$\frac{1}{2}$
$\eta\Lambda$					0	0	0	0	$\frac{3}{2}$	$\frac{3}{2}$
$\eta\Sigma^0$						0	0	0	$\frac{\sqrt{3}}{2}$	$-\frac{\sqrt{3}}{2}$
$\pi^+\Sigma^-$							2	0	1	0
$\pi^-\Sigma^+$								2	0	1
$K^+\Xi^-$									2	1
$K^0\Xi^0$										2

through the $SU(2)$ Clebsch-Gordan coefficients due to the isospin symmetry. This relation is valid for the WT interactions and the $SU(3)$ breaking interactions because they do not break the isospin symmetry. This is the relation among the channels in the block separated by the horizontal lines in Table D.1.

Second, the coefficients of the sector (Y, I_3) are related with those of $(-Y, -I_3)$. Let us consider the channels (i, j) and (i', j') in the sectors (Y, I_3) and $(-Y, -I_3)$, respectively, as shown in Table D.19. Then the coefficients of the sector $(-Y, -I_3)$ are given by

$$\begin{aligned}
&C_{i'j'}(-Y,-I_3) = C_{ij}(Y,I_3), \\
&A^d_{i'j'}(-Y,-I_3) = A^d_{ij}(Y,I_3), \quad A^f_{i'j'}(-Y,-I_3) = -A^f_{ij}(Y,I_3), \\
&B^d_{i'j'}(-Y,-I_3) = B^d_{ij}(Y,I_3), \quad B^f_{i'j'}(-Y,-I_3) = -B^f_{ij}(Y,I_3), \\
&X_{i'j'}(-Y,-I_3) = X_{ij}(Y,I_3), \quad Y_{i'j'}(-Y,-I_3) = -Y_{ij}(Y,I_3).
\end{aligned} \tag{D.2.2}$$

Table D.9: A^d_{ij} and $A^f_{ij}(S=0,Q=0)$.

	A^d_{ij}						A^f_{ij}					
	$\pi^0 n$	$\pi^- p$	ηn	$K^0\Lambda$	$K^0\Sigma^0$	$K^+\Sigma^-$	$\pi^0 n$	$\pi^- p$	ηn	$K^0\Lambda$	$K^0\Sigma^0$	$K^+\Sigma^-$
$\pi^0 n$	1	0	$-\frac{1}{\sqrt{3}}$	$\frac{\sqrt{3}}{8}$	$\frac{3}{8}$	$\frac{3}{4\sqrt{2}}$	1	0	$-\frac{1}{\sqrt{3}}$	$\frac{3\sqrt{3}}{8}$	$-\frac{3}{8}$	$-\frac{3}{4\sqrt{2}}$
$\pi^- p$		1	$\sqrt{\frac{2}{3}}$	$-\frac{\sqrt{6}}{8}$	$\frac{3}{4\sqrt{2}}$	0		1	$\sqrt{\frac{2}{3}}$	$-\frac{3\sqrt{6}}{8}$	$-\frac{3}{4\sqrt{2}}$	0
ηn			$\frac{1}{3}$	$-\frac{1}{24}$	$-\frac{1}{8\sqrt{3}}$	$\frac{1}{4\sqrt{6}}$			$\frac{1}{3}$	$-\frac{1}{8}$	$\frac{1}{8\sqrt{3}}$	$-\frac{1}{4\sqrt{6}}$
$K^0\Lambda$				$\frac{5}{6}$	$-\frac{1}{2\sqrt{3}}$	$\frac{1}{\sqrt{6}}$				0	0	0
$K^0\Sigma^0$					$\frac{1}{2}$	0					0	$\frac{1}{\sqrt{2}}$
$K^+\Sigma^-$						$\frac{1}{2}$						$-\frac{1}{2}$

Table D.10: B^d_{ij} and $B^f_{ij}(S=0,Q=0)$.

	B^d_{ij}						B^f_{ij}					
	$\pi^0 n$	$\pi^- p$	ηn	$K^0\Lambda$	$K^0\Sigma^0$	$K^+\Sigma^-$	$\pi^0 n$	$\pi^- p$	ηn	$K^0\Lambda$	$K^0\Sigma^0$	$K^+\Sigma^-$
$\pi^0 n$	0	0	0	$\frac{1}{8\sqrt{3}}$	$\frac{1}{8}$	$\frac{1}{4\sqrt{2}}$	0	0	0	$\frac{\sqrt{3}}{8}$	$-\frac{1}{8}$	$-\frac{1}{4\sqrt{2}}$
$\pi^- p$		0	0	$-\frac{1}{4\sqrt{6}}$	$\frac{1}{4\sqrt{2}}$	0		0	0	$-\frac{\sqrt{6}}{8}$	$-\frac{1}{4\sqrt{2}}$	0
ηn			$\frac{4}{3}$	$\frac{5}{24}$	$\frac{5}{8\sqrt{3}}$	$-\frac{5}{4\sqrt{6}}$			$-\frac{4}{3}$	$\frac{5}{8}$	$-\frac{5}{8\sqrt{3}}$	$\frac{5}{4\sqrt{6}}$
$K^0\Lambda$				$\frac{5}{6}$	$-\frac{1}{2\sqrt{3}}$	$\frac{1}{\sqrt{6}}$				0	0	0
$K^0\Sigma^0$					$\frac{1}{2}$	0					0	$\frac{1}{\sqrt{2}}$
$K^+\Sigma^-$						$\frac{1}{2}$						$-\frac{1}{2}$

Table D.11: $A^d_{ij}(S=-1,Q=0)$.

	$K^- p$	$\bar{K}^0 n$	$\pi^0\Lambda$	$\pi^0\Sigma^0$	$\eta\Lambda$	$\eta\Sigma^0$	$\pi^+\Sigma^-$	$\pi^-\Sigma^+$	$K^+\Xi^-$	$K^0\Xi^0$
$K^- p$	1	$\frac{1}{2}$	$-\frac{\sqrt{3}}{8}$	$\frac{3}{8}$	$-\frac{1}{24}$	$\frac{1}{8\sqrt{3}}$	0	$\frac{3}{4}$	0	0
$\bar{K}^0 n$		1	$\frac{\sqrt{3}}{8}$	$\frac{3}{8}$	$-\frac{1}{24}$	$-\frac{1}{8\sqrt{3}}$	$\frac{3}{4}$	0	0	0
$\pi^0\Lambda$			$\frac{2}{3}$	0	0	$\frac{2}{3}$	0	0	$-\frac{\sqrt{3}}{8}$	$\frac{\sqrt{3}}{8}$
$\pi^0\Sigma^0$				2	$\frac{2}{3}$	0	0	0	$\frac{3}{8}$	$\frac{3}{8}$
$\eta\Lambda$					$\frac{2}{9}$	0	$\frac{2}{3}$	$\frac{2}{3}$	$-\frac{1}{24}$	$-\frac{1}{24}$
$\eta\Sigma^0$						$\frac{2}{3}$	0	0	$\frac{1}{8\sqrt{3}}$	$-\frac{1}{8\sqrt{3}}$
$\pi^+\Sigma^-$							2	0	$\frac{3}{4}$	0
$\pi^-\Sigma^+$								2	0	$\frac{3}{4}$
$K^+\Xi^-$									1	$\frac{1}{2}$
$K^0\Xi^0$										1

Table D.12: $A^f_{ij}(S=-1, Q=0)$.

	K^-p	$\bar{K}^0n$	$\pi^0\Lambda$	$\pi^0\Sigma^0$	$\eta\Lambda$	$\eta\Sigma^0$	$\pi^+\Sigma^-$	$\pi^-\Sigma^+$	$K^+\Xi^-$	$K^0\Xi^0$
K^-p	0	$\frac{1}{2}$	$-\frac{3\sqrt{3}}{8}$	$-\frac{3}{8}$	$-\frac{1}{8}$	$-\frac{1}{8\sqrt{3}}$	0	$-\frac{3}{4}$	0	0
$\bar{K}^0n$		0	$\frac{3\sqrt{3}}{8}$	$-\frac{3}{8}$	$-\frac{1}{8}$	$\frac{1}{8\sqrt{3}}$	$-\frac{3}{4}$	0	0	0
$\pi^0\Lambda$			0	0	0	0	0	0	$\frac{3\sqrt{3}}{8}$	$-\frac{3\sqrt{3}}{8}$
$\pi^0\Sigma^0$				0	0	0	0	0	$\frac{3}{8}$	$\frac{3}{8}$
$\eta\Lambda$					0	0	0	0	$\frac{1}{8}$	$\frac{1}{8}$
$\eta\Sigma^0$						0	$\frac{2}{\sqrt{3}}$	$-\frac{2}{\sqrt{3}}$	$\frac{1}{8\sqrt{3}}$	$-\frac{1}{8\sqrt{3}}$
$\pi^+\Sigma^-$							0	0	$\frac{3}{4}$	0
$\pi^-\Sigma^+$								0	0	$\frac{3}{4}$
$K^+\Xi^-$									0	$-\frac{1}{2}$
$K^0\Xi^0$										0

Table D.13: $B^d_{ij}(S=-1, Q=0)$.

	K^-p	$\bar{K}^0n$	$\pi^0\Lambda$	$\pi^0\Sigma^0$	$\eta\Lambda$	$\eta\Sigma^0$	$\pi^+\Sigma^-$	$\pi^-\Sigma^+$	$K^+\Xi^-$	$K^0\Xi^0$
K^-p	1	$\frac{1}{2}$	$-\frac{1}{8\sqrt{3}}$	$\frac{1}{8}$	$\frac{5}{24}$	$-\frac{5}{8\sqrt{3}}$	0	$\frac{1}{4}$	0	0
$\bar{K}^0n$		1	$\frac{1}{8\sqrt{3}}$	$\frac{1}{8}$	$\frac{5}{24}$	$\frac{5}{8\sqrt{3}}$	$\frac{1}{4}$	0	0	0
$\pi^0\Lambda$			0	0	0	0	0	0	$-\frac{1}{8\sqrt{3}}$	$\frac{1}{8\sqrt{3}}$
$\pi^0\Sigma^0$				0	0	0	0	0	$\frac{1}{8}$	$\frac{1}{8}$
$\eta\Lambda$					$\frac{16}{9}$	0	0	0	$\frac{5}{24}$	$\frac{5}{24}$
$\eta\Sigma^0$						0	0	0	$-\frac{5}{8\sqrt{3}}$	$\frac{5}{8\sqrt{3}}$
$\pi^+\Sigma^-$							0	0	$\frac{1}{4}$	0
$\pi^-\Sigma^+$								0	0	$\frac{1}{4}$
$K^+\Xi^-$									1	$\frac{1}{2}$
$K^0\Xi^0$										1

Table D.14: $B^f_{ij}(S=-1, Q=0)$.

	K^-p	$\bar{K}^0n$	$\pi^0\Lambda$	$\pi^0\Sigma^0$	$\eta\Lambda$	$\eta\Sigma^0$	$\pi^+\Sigma^-$	$\pi^-\Sigma^+$	$K^+\Xi^-$	$K^0\Xi^0$
K^-p	0	$\frac{1}{2}$	$-\frac{\sqrt{3}}{8}$	$-\frac{1}{8}$	$\frac{5}{8}$	$\frac{5}{8\sqrt{3}}$	0	$-\frac{1}{4}$	0	0
$\bar{K}^0n$		0	$\frac{\sqrt{3}}{8}$	$-\frac{1}{8}$	$\frac{5}{8}$	$-\frac{5}{8\sqrt{3}}$	$-\frac{1}{4}$	0	0	0
$\pi^0\Lambda$			0	0	0	0	0	0	$\frac{\sqrt{3}}{8}$	$-\frac{\sqrt{3}}{8}$
$\pi^0\Sigma^0$				0	0	0	0	0	$\frac{1}{8}$	$\frac{1}{8}$
$\eta\Lambda$					0	0	0	0	$-\frac{5}{8}$	$-\frac{5}{8}$
$\eta\Sigma^0$						0	0	0	$-\frac{5}{8\sqrt{3}}$	$\frac{5}{8\sqrt{3}}$
$\pi^+\Sigma^-$							0	0	$\frac{1}{4}$	0
$\pi^-\Sigma^+$								0	0	$\frac{1}{4}$
$K^+\Xi^-$									0	$-\frac{1}{2}$
$K^0\Xi^0$										0

Table D.15: $X_{ij}, Y_{ij}(S=0, Q=0)$.

	X_{ij}						Y_{ij}					
	$\pi^0 n$	$\pi^- p$	ηn	$K^0\Lambda$	$K^0\Sigma^0$	$K^+\Sigma^-$	$\pi^0 n$	$\pi^- p$	ηn	$K^0\Lambda$	$K^0\Sigma^0$	$K^+\Sigma^-$
$\pi^0 n$	0	$\frac{1}{\sqrt{2}}$	0	0	0	$\frac{1}{2\sqrt{2}}$	0	$\frac{1}{\sqrt{2}}$	0	0	0	$-\frac{1}{2\sqrt{2}}$
$\pi^- p$		-1	0	$\frac{1}{2\sqrt{6}}$	$-\frac{1}{2\sqrt{2}}$	0		-1	0	$\frac{\sqrt{6}}{4}$	$\frac{1}{2\sqrt{2}}$	0
ηn			0	0	0	$\frac{\sqrt{6}}{4}$			0	0	0	$-\frac{\sqrt{6}}{4}$
$K^0\Lambda$				0	0	$-\frac{1}{\sqrt{6}}$				0	0	0
$K^0\Sigma^0$					0	0					0	$-\frac{1}{\sqrt{2}}$
$K^+\Sigma^-$						-1						1

Table D.16: $X_{ij}, Y_{ij}(S=0, Q=1)$.

	X_{ij}						Y_{ij}					
	$\pi^0 p$	$\pi^+ n$	ηp	$K^+\Lambda$	$K^+\Sigma^0$	$K^0\Sigma^+$	$\pi^0 p$	$\pi^+ n$	ηp	$K^+\Lambda$	$K^+\Sigma^0$	$K^0\Sigma^+$
$\pi^0 p$	0	$\frac{1}{\sqrt{2}}$	0	$-\frac{1}{4\sqrt{3}}$	$\frac{1}{4}$	0	0	$\frac{1}{\sqrt{2}}$	0	$-\frac{\sqrt{3}}{4}$	$-\frac{1}{4}$	0
$\pi^+ n$		1	0	$-\frac{1}{\sqrt{6}}$	$-\frac{1}{\sqrt{2}}$	0		1	0	$-\sqrt{\frac{3}{2}}$	$\frac{1}{\sqrt{2}}$	0
ηp			0	$-\frac{1}{4}$	$\frac{\sqrt{3}}{4}$	0			0	$-\frac{3}{4}$	$-\frac{\sqrt{3}}{4}$	0
$K^+\Lambda$				1	$-\frac{1}{\sqrt{3}}$	$-\frac{1}{\sqrt{6}}$				0	0	0
$K^+\Sigma^0$					-1	0					0	$\frac{1}{\sqrt{2}}$
$K^0\Sigma^+$						0						0

Table D.17: $X_{ij}(S=-1, Q=0)$.

	$K^- p$	$\bar{K}^0 n$	$\pi^0\Lambda$	$\pi^0\Sigma^0$	$\eta\Lambda$	$\eta\Sigma^0$	$\pi^+\Sigma^-$	$\pi^-\Sigma^+$	$K^+\Xi^-$	$K^0\Xi^0$
$K^- p$	0	$-\frac{1}{2}$	$-\frac{1}{4\sqrt{3}}$	$\frac{1}{4}$	$-\frac{1}{4}$	$\frac{3}{4\sqrt{3}}$	0	1	0	0
$\bar{K}^0 n$		0	0	0	0	0	$-\frac{1}{2}$	0	0	0
$\pi^0\Lambda$			0	0	0	0	$\frac{1}{\sqrt{3}}$	$\frac{1}{\sqrt{3}}$	$-\frac{1}{4\sqrt{3}}$	0
$\pi^0\Sigma^0$				0	0	0	0	0	$\frac{1}{4}$	0
$\eta\Lambda$					0	0	0	0	$-\frac{1}{4}$	0
$\eta\Sigma^0$						0	0	0	$\frac{3}{4\sqrt{3}}$	0
$\pi^+\Sigma^-$							0	0	1	0
$\pi^-\Sigma^+$								0	0	$-\frac{1}{2}$
$K^+\Xi^-$									0	$-\frac{1}{2}$
$K^0\Xi^0$										0

Table D.18: $Y_{ij}(S=-1,Q=0)$.

	K^-p	$\bar{K}^0n$	$\pi^0\Lambda$	$\pi^0\Sigma^0$	$\eta\Lambda$	$\eta\Sigma^0$	$\pi^+\Sigma^-$	$\pi^-\Sigma^+$	$K^+\Xi^-$	$K^0\Xi^0$
K^-p	-2	$-\frac{1}{2}$	$-\frac{3}{4\sqrt{3}}$	$-\frac{1}{4}$	$-\frac{3}{4}$	$-\frac{3}{4\sqrt{3}}$	0	-1	0	0
$\bar{K}^0n$		0	0	0	0	0	$\frac{1}{2}$	0	0	0
$\pi^0\Lambda$			0	0	0	0	0	0	$\frac{3}{4\sqrt{3}}$	0
$\pi^0\Sigma^0$				0	0	0	1	-1	$\frac{1}{4}$	0
$\eta\Lambda$					0	0	0	0	$\frac{3}{4}$	0
$\eta\Sigma^0$						0	0	0	$\frac{3}{4\sqrt{3}}$	0
$\pi^+\Sigma^-$							2	0	1	0
$\pi^-\Sigma^+$								-2	0	$-\frac{1}{2}$
$K^+\Xi^-$									2	$\frac{1}{2}$
$K^0\Xi^0$										0

Table D.19: Quantum numbers of channels i, j, i' and j'

channel	hypercharge			third component of isospin		
	meson	baryon	total	meson	baryon	total
i	y_i	$Y-y_i$	Y	i_{3i}	I_3-i_{3i}	I_3
j	y_j	$Y-y_j$	Y	i_{3j}	I_3-i_{3j}	I_3
i'	$-y_i$	$-Y+y_i$	$-Y$	$-i_{3i}$	$-I_3+i_{3i}$	$-I_3$
j'	$-y_j$	$-Y+y_j$	$-Y$	$-i_{3j}$	$-I_3+i_{3j}$	$-I_3$

Also, using the relation (D.2.2), the coefficients of the sector $(S=-2,Q=0)$ are obtained from the tables of the sector $(S=0,Q=0)$. For example, if we specify (i,j) to be $(\pi^0 n, K^0\Lambda)$, the corresponding (i',j') is $(\pi^0\Xi^0, \bar{K}^0\Lambda)$. The coefficients for (i',j') are obtained by $A^d_{i'j'} = \sqrt{3}/8$, $A^f_{i'j'} = -3\sqrt{3}/8$, $B^d_{i'j'} = 1/(8\sqrt{3})$ and $B^f_{i'j'} = -\sqrt{3}/8$.

D.3 Coefficients for interactions including antidecuplet

Now we consider the system including antidecuplet baryons used in chapter 9. First we present the flavor coefficients in the particle basis, and then show the weight factors used in the self-energy calculations.

D.3.1 Flavor coefficients for $PBMM$ vertices

This appendix contains the flavor coefficients for the tree-level vertices in the four interaction Lagrangians, which are given by

$$\mathcal{L}^{8s} = \frac{g^{8s}}{2f}\bar{P}_{ijk}\epsilon^{lmk}\phi_l{}^a\phi_a{}^i B_m{}^j + \text{h.c.},$$

$$\mathcal{L}^{8a} = i\frac{g^{8a}}{4f^2}\bar{P}_{ijk}\epsilon^{lmk}\gamma^\mu(\partial_\mu\phi_l{}^a\phi_a{}^i - \phi_l{}^a\partial_\mu\phi_a{}^i)B_m{}^j + \text{h.c.},$$

Table D.20: The $C^{(j)}_{B,m_1,m_2}$ flavor coefficients for the vertex with $\Theta^+_{\overline{10}}$, octet baryons, and two octet mesons.

P	BMM	$8s$	$8a$	27	M
$\Theta^+_{\overline{10}}$	$pK^+\pi^-$	$-\sqrt{6}$	$-\sqrt{6}$	$\frac{4\sqrt{6}}{5}$	$-\sqrt{6}\frac{m_K^2+m_\pi^2}{2f^2}$
	$pK^0\pi^0$	$\sqrt{3}$	$\sqrt{3}$	$-\frac{4\sqrt{3}}{5}$	$\sqrt{3}\frac{m_K^2+m_\pi^2}{2f^2}$
	$pK^0\eta$	1	-3	$\frac{36}{5}$	$\frac{5m_K^2-3m_\pi^2}{2f^2}$
	$nK^+\pi^0$	$\sqrt{3}$	$\sqrt{3}$	$-\frac{4\sqrt{3}}{5}$	$\sqrt{3}\frac{m_K^2+m_\pi^2}{2f^2}$
	$nK^+\eta$	-1	3	$-\frac{36}{5}$	$-\frac{5m_K^2-3m_\pi^2}{2f^2}$
	$nK^0\pi^+$	$\sqrt{6}$	$\sqrt{6}$	$-\frac{4\sqrt{6}}{5}$	$\sqrt{6}\frac{m_K^2+m_\pi^2}{2f^2}$
	$\Sigma^+K^0K^0$	-	-	$-4\sqrt{6}$	-
	$\Sigma^0K^0K^+$	-	-	$-8\sqrt{3}$	-
	$\Sigma^-K^+K^+$	-	-	$4\sqrt{6}$	-

$$\mathcal{L}^{27} =\frac{g^{27}}{2f}\left[4\bar{P}_{ijk}\epsilon^{lbk}\phi_l{}^i\phi_a{}^jB_b{}^a-\frac{4}{5}\bar{P}_{ijk}\epsilon^{lbk}\phi_l{}^a\phi_a{}^jB_b{}^i\right]+\text{h.c.},$$
$$\mathcal{L}^{M} =\frac{g^{M}}{2f}\bar{P}_{ijk}\epsilon^{lmk}\left[-\frac{1}{2f^2}(2\phi M\phi+\phi\phi M+M\phi\phi)\right]_l{}^iB_m{}^j+\text{h.c.}.$$

These Lagrangians provide the tree-level amplitude

$$\left(F^{(j)}C^{(j)}_{P,B,m_1,m_2}\right)|t^{(j)}|^2\left(F^{(j)}C^{(j)}_{P,B,m_1,m_2}\right),$$

with

$$|t^{(j)}|^2 =1\quad\text{for}\quad j=8s,27,M,$$
$$|t^{\chi}|^2 =\frac{(\omega_1\omega_2-\boldsymbol{k}\cdot\boldsymbol{q})^2}{4f^4},$$
$$|t^{8a}|^2 =\frac{1}{2M}\Big\{(E+M)(\omega_1-\omega_2)^2+2(|\boldsymbol{k}|^2-|\boldsymbol{q}|^2)(\omega_1-\omega_2)+(E-M)(\boldsymbol{k}-\boldsymbol{q})^2\Big\},$$

and factors are given by

$$F^{8s}=\frac{g^{8s}}{2f},\quad F^{8a}=\frac{g^{8a}}{4f^2},\quad F^{27}=\frac{g^{27}}{2f},\quad F^{\chi}=\frac{g^{\chi}}{2f},\quad F^{M}=\frac{g^{M}}{2f}.$$

Note that the coefficients for $\mathcal{L}^{\chi}$ is the same as those for $\mathcal{L}^{8s}$. The coefficients $C^{(j)}_{P,B,m_1,m_2}$ for $\Theta_{\overline{10}}$, $N_{\overline{10}}$, $\Sigma_{\overline{10}}$, and $\Xi_{\overline{10}}$ are shown in Tables D.20, D.21, D.22,and D.23, respectively.

D.3.2 Self-energy formulae

Below are the formulae for calculating the self-energies as described in Eq. (9.3.1). In the isospin symmetric limit,

$$\Sigma^{(j)}_P=\left(F^{(j)}\right)^2\sum_\alpha I^{(j)}(\alpha)D^{(j)}_{P,\alpha},$$

Table D.21: The $C^{(j)}_{B,m_1,m_2}$ flavor coefficients for the vertex with $N^+_{\overline{10}}$, octet baryons, and two octet mesons. Coefficients for $N^0_{\overline{10}}$ are obtained by using isospin symmetry.

P	BMM	$8s$	$8a$	27	M
$N^+_{\overline{10}}$	pK^+K^-	$-\sqrt{2}$	$-\sqrt{2}$	$\frac{4\sqrt{2}}{5}$	$-\sqrt{2}\frac{m_K^2}{f^2}$
	$pK^0\bar{K}^0$	-	$-2\sqrt{2}$	$4\sqrt{2}$	-
	$p\pi^0\pi^0$	$\frac{1}{\sqrt{2}}$	-	$-\frac{2\sqrt{2}}{5}$	$\frac{1}{\sqrt{2}}\frac{m_\pi^2}{f^2}$
	$p\pi^+\pi^-$	$\sqrt{2}$	$\sqrt{2}$	$-\frac{4\sqrt{2}}{5}$	$\sqrt{2}\frac{m_\pi^2}{f^2}$
	$p\eta\eta$	$-\frac{1}{\sqrt{2}}$	-	$-\frac{18\sqrt{2}}{5}$	$-\frac{1}{\sqrt{2}}\frac{8m_K^2-5m_\pi^2}{3f^2}$
	$p\eta\pi^0$	$-\sqrt{\frac{2}{3}}$	-	$\frac{8\sqrt{6}}{5}$	$-\sqrt{\frac{2}{3}}\frac{m_\pi^2}{f^2}$
	$n\bar{K}^0K^+$	$-\sqrt{2}$	$-\sqrt{2}$	$-\frac{16\sqrt{2}}{5}$	$-\sqrt{2}\frac{m_K^2}{f^2}$
	$n\pi^+\eta$	$-\frac{2}{\sqrt{3}}$	-	$\frac{16\sqrt{3}}{5}$	$-\frac{2}{\sqrt{3}}\frac{m_\pi^2}{f^2}$
	$n\pi^+\pi^0$	-	-2	-	-
	$\Lambda K^+\pi^0$	$-\sqrt{\frac{3}{2}}$	$-\sqrt{\frac{3}{2}}$	$\frac{2\sqrt{6}}{5}$	$-\sqrt{\frac{3}{2}}\frac{m_K^2+m_\pi^2}{2f^2}$
	$\Lambda K^+\eta$	$\frac{1}{\sqrt{2}}$	$-\frac{3}{\sqrt{2}}$	$\frac{18\sqrt{2}}{5}$	$\frac{1}{\sqrt{2}}\frac{5m_K^2-3m_\pi^2}{2f^2}$
	$\Lambda K^0\pi^+$	$-\sqrt{3}$	$-\sqrt{3}$	$\frac{4\sqrt{3}}{5}$	$-\sqrt{3}\frac{m_K^2+m_\pi^2}{2f^2}$
	$\Sigma^+K^+\pi^-$	$\sqrt{2}$	$\sqrt{2}$	$-\frac{4\sqrt{2}}{5}$	$\sqrt{2}\frac{m_K^2+m_\pi^2}{2f^2}$
	$\Sigma^+K^0\eta$	$-\frac{1}{\sqrt{3}}$	$\sqrt{3}$	$\frac{28\sqrt{3}}{5}$	$-\frac{1}{\sqrt{3}}\frac{5m_K^2-3m_\pi^2}{2f^2}$
	$\Sigma^+K^0\pi^0$	-1	-1	$-\frac{36}{5}$	$-\frac{m_K^2+m_\pi^2}{2f^2}$
	$\Sigma^0K^+\pi^0$	$\frac{1}{\sqrt{2}}$	$\frac{1}{\sqrt{2}}$	$-\frac{22\sqrt{2}}{5}$	$\frac{1}{\sqrt{2}}\frac{m_K^2+m_\pi^2}{2f^2}$
	$\Sigma^0K^0\pi^+$	1	1	$\frac{36}{5}$	$\frac{m_K^2+m_\pi^2}{2f^2}$
	$\Sigma^0K^+\eta$	$-\frac{1}{\sqrt{6}}$	$\sqrt{\frac{3}{2}}$	$\frac{14\sqrt{6}}{5}$	$-\frac{1}{\sqrt{6}}\frac{5m_K^2-3m_\pi^2}{2f^2}$
	$\Sigma^-K^+\pi^+$	-	-	$-8\sqrt{2}$	-
	$\Xi^-K^+K^+$	-	-	$4\sqrt{2}$	-
	$\Xi^0K^+K^0$	-	-	$4\sqrt{2}$	-

with α being the BMM channel in the isospin basis, such as $NK\pi$, $NK\eta$, etc., and $D^{(j)}$ are expressed as the sum of the $(C^{(j)})^2$. In Table D.24-D.27, we show the $D^{(j)}$ coefficients. For the 27 and M cases, following the procedure in Sec. 9.4.4, we set $g^{8s} = g^{27} = g^M = 1.88$ and take

$$a\mathcal{L}^{8s} + b\mathcal{L}^{27}, \quad b = -\frac{5}{4}(1-a)$$

and

$$a\mathcal{L}^{8s} + b\mathcal{L}^{M}, \quad b = \frac{f^2}{m_\pi^2}(1-a),$$

Table D.22: The $C^{(j)}_{B,m_1,m_2}$ flavor coefficients for the vertex with $\Sigma^+_{\overline{10}}$, octet baryons, and two octet mesons. Coefficients for $\Sigma^0_{\overline{10}}$ and $\Sigma^-_{\overline{10}}$ are obtained by using isospin symmetry.

P	BMM	$8s$	$8a$	27	M
$\Sigma^+_{\overline{10}}$	$p\pi^+K^-$	$-\sqrt{2}$	$-\sqrt{2}$	$\frac{4\sqrt{2}}{5}$	$-\sqrt{2}\frac{m_K^2+m_\pi^2}{2f^2}$
	$p\pi^0\bar{K}^0$	1	1	$-\frac{24}{5}$	$\frac{m_K^2+m_\pi^2}{2f^2}$
	$p\bar{K}^0\eta$	$\frac{1}{\sqrt{3}}$	$\sqrt{3}$	$\frac{32\sqrt{3}}{5}$	$\frac{1}{\sqrt{3}}\frac{5m_K^2-3m_\pi^2}{2f^2}$
	$n\bar{K}^0\pi^+$	-	-	$-4\sqrt{2}$	-
	$\Lambda\bar{K}^0K^+$	$-\sqrt{3}$	$-\sqrt{3}$	$-\frac{16\sqrt{3}}{5}$	$-\sqrt{3}\frac{m_K^2}{f^2}$
	$\Lambda\pi^+\eta$	$-\sqrt{2}$	-	$\frac{24\sqrt{2}}{5}$	$-\sqrt{2}\frac{m_\pi^2}{f^2}$
	$\Lambda\pi^+\pi^0$	-	$-\sqrt{6}$	-	-
	$\Sigma^+K^+K^-$	$-\sqrt{2}$	$-\sqrt{2}$	$\frac{4\sqrt{2}}{5}$	$-\sqrt{2}\frac{m_K^2}{f^2}$
	$\Sigma^+\pi^+\pi^-$	$\sqrt{2}$	$\sqrt{2}$	$-\frac{4\sqrt{2}}{5}$	$\sqrt{2}\frac{m_\pi^2}{f^2}$
	$\Sigma^+\eta\eta$	$-\frac{1}{\sqrt{2}}$	-	$\frac{12\sqrt{2}}{5}$	$-\frac{1}{\sqrt{2}}\frac{8m_K^2-5m_\pi^2}{3f^2}$
	$\Sigma^+\eta\pi^0$	$-\sqrt{\frac{2}{3}}$	-	$-\frac{12\sqrt{6}}{5}$	$-\sqrt{\frac{2}{3}}\frac{m_\pi^2}{f^2}$
	$\Sigma^+\pi^0\pi^0$	$\frac{1}{\sqrt{2}}$	-	$\frac{8\sqrt{2}}{5}$	$\frac{1}{\sqrt{2}}\frac{m_\pi^2}{f^2}$
	$\Sigma^+K^0\bar{K}^0$	-	$-2\sqrt{2}$	$-4\sqrt{2}$	-
	$\Sigma^0\bar{K}^0K^+$	1	1	$-\frac{24}{5}$	$\frac{m_K^2}{f^2}$
	$\Sigma^0\eta\pi^+$	$\sqrt{\frac{2}{3}}$	-	$\frac{12\sqrt{6}}{5}$	$\sqrt{\frac{2}{3}}\frac{m_\pi^2}{f^2}$
	$\Sigma^0\pi^+\pi^0$	-	$\sqrt{2}$	$-4\sqrt{2}$	-
	$\Sigma^-\pi^+\pi^+$	-	-	$-4\sqrt{2}$	-
	$\Xi^0K^+\pi^0$	1	1	$-\frac{24}{5}$	$\frac{m_K^2+m_\pi^2}{2f^2}$
	$\Xi^0K^0\pi^+$	$\sqrt{2}$	$\sqrt{2}$	$\frac{16\sqrt{2}}{5}$	$\sqrt{2}\frac{m_K^2+m_\pi^2}{2f^2}$
	$\Xi^0K^+\eta$	$-\frac{1}{\sqrt{3}}$	$-\sqrt{3}$	$\frac{8\sqrt{3}}{5}$	$-\frac{1}{\sqrt{3}}\frac{5m_K^2-3m_\pi^2}{2f^2}$
	$\Xi^-K^+\pi^+$	-	-	$8\sqrt{2}$	-

In these cases, D^j are defined as

$$\Sigma_P^{(j)} = \left(F^{(8s)}\right)^2 \sum_\alpha I^{(j)}(\alpha) D^{(j)}_{P,\alpha},$$

for $(j) = 8s+27, 8s+M$. One can easily check that when $a=1$, $b=0$, $D^{(j)}_{P,\alpha}$ for $(j) = 8s+27, 8s+M$ becomes $D^{(8s)}_{P,\alpha}$.

Table D.23: The $C^{(j)}_{B,m_1,m_2}$ flavor coefficients for the vertex with $\Xi^+_{\overline{10}}$, octet baryons, and two octet mesons. Coefficients for $\Xi^0_{\overline{10}}$, $\Xi^-_{\overline{10}}$ and $\Xi^{--}_{\overline{10}}$ are obtained by using isospin symmetry.

P	BMM	$8s$	$8a$	27	M
$\Xi^+_{\overline{10}}$	$\Sigma^+\pi^+K^-$	$-\sqrt{6}$	$-\sqrt{6}$	$\frac{4\sqrt{6}}{5}$	$-\sqrt{6}\frac{m_K^2+m_\pi^2}{2f^2}$
	$\Sigma^+\pi^0\bar{K}^0$	$\sqrt{3}$	$\sqrt{3}$	$\frac{16\sqrt{3}}{5}$	$\sqrt{3}\frac{m_K^2+m_\pi^2}{2f^2}$
	$\Sigma^+\bar{K}^0\eta$	1	3	$-\frac{24}{5}$	$\frac{5m_K^2-3m_\pi^2}{2f^2}$
	$\Sigma^0\bar{K}^0\pi^+$	-	-	$-4\sqrt{3}$	-
	$\Lambda\bar{K}^0\pi^+$	-	-	-12	-
	$p\bar{K}^0\bar{K}^0$	-	-	$-4\sqrt{6}$	-
	$\Xi^0\bar{K}^0K^+$	$\sqrt{6}$	$\sqrt{6}$	$-\frac{4\sqrt{6}}{5}$	$\sqrt{6}\frac{m_K^2}{f^2}$
	$\Xi^0\eta\pi^+$	2	-	$\frac{12}{5}$	$2\frac{m_\pi^2}{f^2}$
	$\Xi^0\pi^+\pi^0$	-	$2\sqrt{3}$	$-4\sqrt{3}$	-
	$\Xi^-\pi^+\pi^+$	-	-	$4\sqrt{6}$	-

Table D.24: The $D^{(j)}_\alpha$ coefficients for the $\Theta_{\overline{10}}$ self-energies.

P	α	$8s$	$8a$	$8s+27$	$8s+M$
$\Theta_{\overline{10}}$	$NK\pi$	18	18	18	$18(a+\frac{m_K^2+m_\pi^2}{2f^2}b)^2$
	$NK\eta$	2	18	$2(a+\frac{36}{5}b)^2$	$2(a+\frac{5m_K^2-3m_\pi^2}{2f^2}b)^2$
	$\Sigma K\pi$	-	-	$576b^2$	-

Table D.25: The $D^{(j)}_\alpha$ coefficients for the $N_{\overline{10}}$ self-energies.

P	α	$8s$	$8a$	$8s+27$	$8s+M$
$N_{\overline{10}}$	$NK\bar{K}$	4	12	$2+2(a+\frac{16}{5}b)^2-32b^2$	$4(a+\frac{m_K^2}{f^2}b)^2$
	$N\pi\pi$	3	6	3	$3(a+\frac{m_\pi^2}{f^2}b)^2$
	$N\pi\eta$	2	-	$2(-a+\frac{24}{5}b)^2$	$2(a+\frac{m_\pi^2}{f^2}b)^2$
	$N\eta\eta$	1	-	$(a+\frac{36}{5})^2$	$(a+\frac{8m_K^2-5m_\pi^2}{3f^2}b)^2$
	$\Lambda K\pi$	$\frac{9}{2}$	$\frac{9}{2}$	$\frac{9}{2}$	$\frac{9}{2}(a+\frac{m_K^2+m_\pi^2}{2f^2}b)^2$
	$\Lambda K\eta$	$\frac{1}{2}$	$\frac{9}{2}$	$\frac{1}{2}(a+\frac{36}{5})^2$	$\frac{1}{2}(a+\frac{5m_K^2-3m_\pi^2}{2f^2}b)^2$
	$\Sigma K\pi$	$\frac{9}{2}$	$\frac{9}{2}$	$2+2(a+\frac{36}{5}b)^2$ $+\frac{1}{2}(a-\frac{44}{5})^2+128b^2$	$(a+\frac{m_K^2+m_\pi^2}{2f^2}b)^2$
	$\Sigma K\eta$	$\frac{1}{2}$	$\frac{9}{2}$	$\frac{1}{2}(-a+\frac{84}{5})^2$	$\frac{1}{2}(a+\frac{5m_K^2-3m_\pi^2}{2f^2}b)^2$
	$\Xi K K$	-	-	$96b^2$	-

Table D.26: The $D_\alpha^{(j)}$ coefficients for the $\Sigma_{\overline{10}}$ self-energies.

P	α	$8s$	$8a$	$8s+27$	$8s+M$
$\Sigma_{\overline{10}}$	$N\bar{K}\pi$	3	3	$2+(a-\frac{24}{5}b)^2+32b^2$	$3(a+\frac{m_K^2+m_\pi^2}{2f^2}b)^2$
	$N\bar{K}\eta$	$\frac{1}{3}$	3	$\frac{1}{3}(a+\frac{96}{5}b)^2$	$\frac{1}{3}(a+\frac{5m_K^2-3m_\pi^2}{2f^2})^2$
	$\Lambda K\bar{K}$	3	3	$3(a+\frac{16}{5}b)^2$	$3(a+\frac{m_K^2}{f^2}b)^2$
	$\Lambda\pi\eta$	2	-	$2(a-\frac{24}{5}b)^2$	$2(a+\frac{m_\pi^2}{f^2}b)^2$
	$\Lambda\pi\pi$	-	6	-	-
	$\Sigma K\bar{K}$	3	11	$2+(a-\frac{24}{5}b)^2+32b^2$	$3(a+\frac{m_K^2}{f^2}b)^2$
	$\Sigma\pi\pi$	3	4	$2+(a+\frac{16}{5})^2+96b^2$	$(a+\frac{m_\pi^2}{f^2}b)^2$
	$\Sigma\pi\eta$	$\frac{4}{3}$	-	$\frac{4}{3}(a+\frac{36}{5})^2$	$\frac{4}{3}(a+\frac{m_\pi^2}{f^2}b)^2$
	$\Sigma\eta\eta$	1	-	$(a-\frac{24}{5}b)^2$	$(a+\frac{8m_K^2-5m_\pi^2}{3f^2}b)^2$
	$\Xi K\pi$	3	3	$2(a+\frac{16}{5})^2$ $+(a-\frac{24}{5})^2+128b^2$	$3(a+\frac{m_K^2+m_\pi^2}{2f^2}b)^2$
	$\Xi K\eta$	$\frac{1}{3}$	3	$\frac{1}{3}(a-\frac{24}{5}b)^2$	$\frac{1}{3}(a+\frac{5m_K^2-3m_\pi^2}{2f^2}b)^2$

Table D.27: The $D_\alpha^{(j)}$ coefficients for the $\Xi_{\overline{10}}$ self-energies.

P	α	$8s$	$8a$	$8s+27$	$8s+M$
$\Xi_{\overline{10}}$	$\Sigma\bar{K}\pi$	9	9	$6+3(a+\frac{16}{5}b)^2+48b^2$	$9(a+\frac{m_K^2+m_\pi^2}{2f^2}b)^2$
	$\Sigma\bar{K}\eta$	1	9	$(a-\frac{24}{3}b)^2$	$(a+\frac{5m_K^2-3m_\pi^2}{2f^2}b)^2$
	$\Xi K\bar{K}$	6	6	6	$6(a+\frac{m_K^2}{f^2}b)^2$
	$\Xi\pi\eta$	4	-	$4(a+\frac{6}{5}b)^2$	$4(a+\frac{m_\pi^2}{f^2}b)^2$
	$\Xi\pi\pi$	-	12	$240b^2$	-
	$\Lambda\bar{K}\pi$	-	-	$144b^2$	-
	$N\bar{K}\bar{K}$	-	-	$192b^2$	-

Appendix E

Miscellaneous notes

E.1 Riemann sheets and branches

Let us recall the definition of the "Riemann sheets" and "branches", when we consider a multi-valued function $w = f(z)$. In order to avoid multi-valueness, we put a branch cut on the z plane. Then we connect usual z plane, which is defined in the region $0 \leq \theta < 2\pi$, to another "Riemann sheet", which is defined in the region $2\pi \leq \theta < 4\pi$. The former region is called as the first Riemann sheet, while the latter as the second Riemann sheet. The higher Riemann sheets are also defined in the same way. Although we usually do not distinguish the difference between z_1 and $z_2 = z_1 e^{2\pi i}$, the points z_1 on the first Riemann sheet and $z_2 = z_1 e^{2\pi i}$ on the second Riemann sheet are mapped to the different points $w_1 = f(z_1)$ and $w_2 = f(z_2 = z_1 e^{2\pi i})$, respectively. We call these w_1 and w_2 planes as "branches". We show this schematically in Fig. E.1. In this way we extend z plane into several Riemann sheets, and the function $w = f(z)$ is uniquely defined on each Riemann sheet.

E.2 Mixing angle

By looking at the mass formulae given in subsection 10.3.1, the masses of mixed states can be written, in general, by

$$M_1(\theta) = A\cos^2\theta + B\sin^2\theta - \frac{(B-A)}{2}\tan 2\theta \sin 2\theta,$$
$$M_2(\theta) = A\sin^2\theta + B\cos^2\theta + \frac{(B-A)}{2}\tan 2\theta \sin 2\theta.$$

These functions obey the following relations

$$M_i(\theta) = M_i(\theta + \pi), \quad \text{for } i = 1, 2 \tag{E.2.1}$$
$$M_i(\theta) = M_i(\pi - \theta), \quad \text{for } i = 1, 2 \tag{E.2.2}$$
$$M_1(\theta) = M_2(\pi/2 - \theta), \quad M_2(\theta) = M_1(\pi/2 - \theta). \tag{E.2.3}$$

Equation (E.2.1) shows that $M_1(\theta)$ and $M_2(\theta)$ are periodic functions with period π, while Eq. (E.2.2) shows that there is a reflection symmetry of $0 \leq \theta \leq \pi/2$ and $\pi/2 \leq \theta \leq \pi$. In

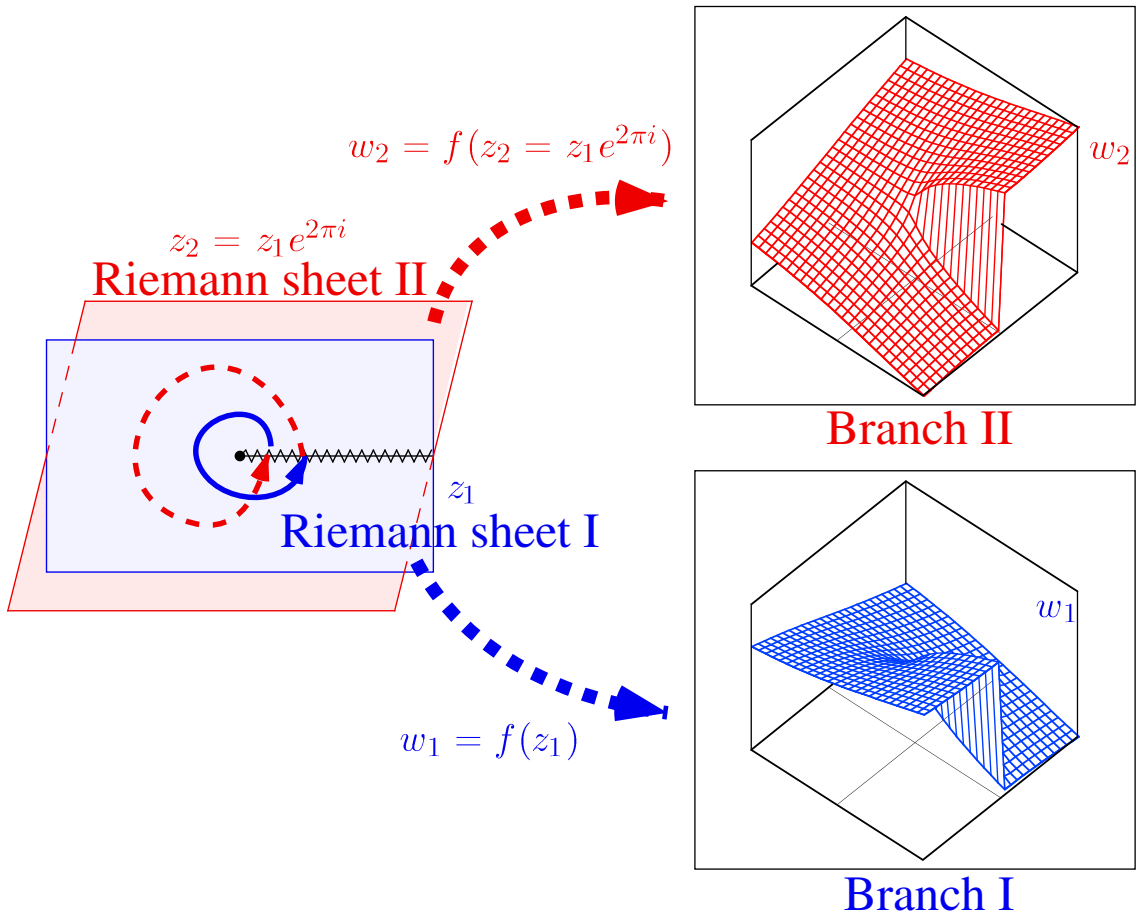

Figure E.1: Riemann sheets and branches. The points z_1 and $z_2 = z_1 e^{2\pi i}$ are mapped to the different points $w_1 = f(z_1)$ and $w_2 = f(z_2)$

order to make a one to one correspondence between θ and the masses, the domain of θ should be $0 \leq \theta < \pi/2$. In addition, there is a discrete symmetry under the interchange $\theta \leftrightarrow \pi/2 - \theta$ and $M_1 \leftrightarrow M_2$, due to Eq. (E.2.3). Fixing the assignment of M_1 and M_2 to the physical states, the mixing angle can be determined without duplication.

E.3 Experimental information

Let us tabulate the masses of the particles, which will be useful to estimate the threshold of meson-baryon channels. In the followings, all the values are taken from PDG [144]. The masses of the ground state octet baryons are given by

$$M_N = 939 \text{ MeV}, \quad M_\Lambda = 1116 \text{ MeV}, \quad M_\Sigma = 1193 \text{ MeV}, \quad M_\Xi = 1318 \text{ MeV},$$

where we have averaged over the isospin states. The masses of the lowest lying decuplet baryons are given by

$$M_\Delta = 1232 \text{ MeV}, \quad M_{\Sigma_{\mathbf{10}}} = 1385 \text{ MeV}, \quad M_{\Xi_{\mathbf{10}}} = 1535 \text{ MeV}, \quad M_\Omega = 1672 \text{ MeV}.$$

The masses of the lowest lying pseudoscalar octet mesons are given by

$$M_\pi = 138 \text{ MeV}, \quad M_K = 496 \text{ MeV}, \quad M_\eta = 548 \text{ MeV}.$$

The masses of the lowest lying vector nonet mesons are given by

$$M_\rho = 776 \text{ MeV}, \quad M_\omega = 783 \text{ MeV}, \quad M_{K^*} = 894 \text{ MeV}, \quad M_\phi = 1019 \text{ MeV}.$$

In PDG [144], the masses and widths of Θ^+ and Ξ^{--} are given as

$$M_{\Theta^+} = 1539.2 \pm 1.6 \text{ MeV}, \quad \Gamma_{\Theta^+} = 0.9 \pm 0.3 \text{ MeV}.$$
$$M_{\Xi^{--}} = 1862 \pm 2 \text{ MeV}, \quad \Gamma_{\Xi^{--}} < 18 \text{ MeV}.$$

In Tables E.1, E.2, and E.3, we summarize the resonances with several spins and parities. Note that the $\Sigma(1385)$, the $\Xi(1530)$, and the $\Delta(1232)$ are not listed because they are assigned in the decuplet.

Table E.1: Strangeness $S = 0$ resonances listed in PDG [144]. The $\Delta(1232)$ is not shown because it is assigned in the lowest lying decuplet. We denote stars following the definition in PDG, except for three- or four-star resonances which are well established.

R	$J^P(L_{2I,2J})$	States
N^*	$1/2^-(S_{11})$	N(1535), N(1650), N(2090)*
	$1/2^+(P_{11})$	N(1440), N(1710), N(2100)*
	$3/2^+(P_{13})$	N(1720), N(1900)**
	$3/2^-(D_{13})$	N(1520), N(1700), N(2080)**
	$5/2^-(D_{15})$	N(1675), N(2200)**
	$5/2^+(F_{15})$	N(1680), N(2000)**
	$7/2^+(F_{17})$	N(1990)**
	$7/2^-(G_{17})$	N(2190)
	$9/2^-(G_{19})$	N(2250)
	$9/2^+(H_{19})$	N(2220)
	$11/2^-(I_{1,11})$	N(2600)
	$13/2^+(K_{1,13})$	N(2700)**
Δ^*	$1/2^-(S_{31})$	$\Delta(1620)$, $\Delta(1900)^{**}$, $\Delta(2150)^*$
	$1/2^+(P_{31})$	$\Delta(1750)^*$, $\Delta(1910)$
	$3/2^+(P_{33})$	$\Delta(1600)$, $\Delta(1920)$
	$3/2^-(D_{33})$	$\Delta(1700)$, $\Delta(1940)^*$
	$5/2^-(D_{35})$	$\Delta(1930)$, $\Delta(2350)^*$
	$5/2^+(F_{35})$	$\Delta(1905)$, $\Delta(2000)^{**}$
	$7/2^+(F_{37})$	$\Delta(1950)$, $\Delta(2390)^*$
	$7/2^-(G_{37})$	$\Delta(2200)^*$
	$9/2^-(G_{39})$	$\Delta(2400)^{**}$
	$9/2^+(H_{39})$	$\Delta(2300)^{**}$
	$11/2^+(H_{3,11})$	$\Delta(2420)$
	$13/2^-(I_{3,13})$	$\Delta(2750)^{**}$
	$15/2^+(K_{3,15})$	$\Delta(2950)^{**}$

Table E.2: Strangeness $S = -1$ resonances listed in PDG [144]. The $\Sigma(1385)$ is not shown because it is assigned in the decuplet with the $\Delta(1232)$. We denote stars following the definition in PDG, except for three- or four-star resonances which are well established.

R	$J^P(L_{I,2J})$	States
Λ^*	$1/2^-(S_{01})$	$\Lambda(1405)$, $\Lambda(1670)$, $\Lambda(1800)$
	$1/2^+(P_{01})$	$\Lambda(1600)$, $\Lambda(1810)$
	$3/2^+(P_{03})$	$\Lambda(1890)$
	$3/2^-(D_{03})$	$\Lambda(1520)$, $\Lambda(1690)$, $\Lambda(2325)^*$
	$5/2^-(D_{05})$	$\Lambda(1830)$
	$5/2^+(F_{05})$	$\Lambda(1820)$, $\Lambda(2110)$
	$7/2^+(F_{07})$	$\Lambda(2020)^*$
	$7/2^-(G_{07})$	$\Lambda(2100)$
	$9/2^+(H_{09})$	$\Lambda(2350)$
	unknown	$\Lambda(2000)^*$, $\Lambda(2585)^{**}$
Σ^*	$1/2^-(S_{11})$	$\Sigma(1620)^{**}$, $\Sigma(1750)$, $\Sigma(2000)^*$
	$1/2^+(P_{11})$	$\Sigma(1660)$, $\Sigma(1770)^*$, $\Sigma(1880)^{**}$
	$3/2^+(P_{13})$	$\Sigma(1840)^*$, $\Sigma(2080)^{**}$
	$3/2^-(D_{13})$	$\Sigma(1580)^{**}$, $\Sigma(1670)$, $\Sigma(1940)$
	$5/2^-(D_{15})$	$\Sigma(1775)$
	$5/2^+(F_{15})$	$\Sigma(1915)$, $\Sigma(2070)^*$
	$7/2^+(F_{17})$	$\Sigma(2030)$
	$7/2^-(G_{17})$	$\Sigma(2100)^*$
	unknown	$\Sigma(1480)^*$, $\Sigma(1560)^{**}$, $\Sigma(1690)^{**}$, $\Sigma(2250)$, $\Sigma(2455)^{**}$, $\Sigma(2620)^{**}$, $\Sigma(3000)^{**}$, $\Sigma(3170)^{**}$

Table E.3: Strangeness $S \geq -2$ resonances listed in PDG [144]. The $\Xi(1530)$ and $\Omega(1672)$ are not shown because they are assigned in the decuplet with the $\Delta(1232)$. We denote stars following the definition in PDG, except for three- or four-star resonances which are well established.

R	$J^P(L_{2I,2J})$	States
Ξ^*	$3/2^-(D_{13})$	$\Xi(1820)$
	unknown	$\Xi(1620)^*$, $\Xi(1690)$, $\Xi(1950)$, $\Xi(2030)$, $\Xi(2120)^*$, $\Xi(2250)^{**}$, $\Xi(2370)^{**}$, $\Xi(2500)^*$
Ω^*	unknown	$\Omega(2250)$, $\Omega(2380)^{**}$, $\Omega(2470)^{**}$

Bibliography

[1] A. Hosaka and H. Toki, *Quarks, baryons and chiral symmetry* (World Scientific, Singapore, 2001).

[2] S. Weinberg, Physica **A96**, 327 (1979).

[3] J. Gasser and H. Leutwyler, Nucl. Phys. **B250**, 465 (1985).

[4] N. Kaiser, P. B. Siegel, and W. Weise, Nucl. Phys. **A594**, 325 (1995), nucl-th/9505043.

[5] E. Oset and A. Ramos, Nucl. Phys. **A635**, 99 (1998), nucl-th/9711022.

[6] T. Hyodo, S. I. Nam, D. Jido, and A. Hosaka, Phys. Rev. **C68**, 018201 (2003), nucl-th/0212026.

[7] T. Hyodo, S. I. Nam, D. Jido, and A. Hosaka, Prog. Theor. Phys. **112**, 73 (2004), nucl-th/0305011.

[8] T. Hyodo, A. Hosaka, E. Oset, A. Ramos, and M. J. Vicente Vacas, Phys. Rev. **C68**, 065203 (2003), nucl-th/0307005.

[9] T. Hyodo, A. Hosaka, M. J. Vicente Vacas, E. Oset, and A. Ramos, Prepared for Workshop on Strangeness Nuclear Physics at J- PARC, Tsukuba, Japan, 29-31 Jul 2003.

[10] A. Ramos, C. Bennhold, A. Hosaka, T. Hyodo, D. Jido, U. G. Meissner, J. A. Oller, E. Oset, and M. J. Vicente Vacas, (2005), nucl-th/0502053, Prepared for Workshop on physics of excited nucleons Nstar2004, Grenoble, March 2004, World Scientific, page 228-238.

[11] T. Hyodo, A. Hosaka, M. J. Vicente Vacas, and E. Oset, Phys. Lett. **B593**, 75 (2004), nucl-th/0401051.

[12] T. Hyodo, A. Hosaka, M. J. Vicente Vacas, and E. Oset, (2004), nucl-th/0404031, Prepared for YITP Workshop on Multi-quark Hadrons: Four, Five and More? (YITP-W-03-21), Kyoto, Japan, 17-19 Feb 2004.

[13] T. Hyodo, S. I. Nam, D. Jido, and A. Hosaka, (2003), nucl-th/0305023.

[14] T. Hyodo, S. Sarkar, A. Hosaka, and E. Oset, (2006), hep-ph/0601026.

[15] LEPS, T. Nakano, Nucl. Phys. **A721**, 112c (2003).

[16] LEPS, T. Nakano *et al.*, Phys. Rev. Lett. **91**, 012002 (2003), hep-ex/0301020.

[17] T. Hyodo, A. Hosaka, and E. Oset, Phys. Lett. **B579**, 290 (2004), nucl-th/0307105.

[18] E. Oset, T. Hyodo, and A. Hosaka, (2003), nucl-th/0312014, Prepared for 8th International Conference on Hypernuclear and Strange Particle Physics (HYP 2003), Newport News, Virginia, 14-18 Oct 2003.

[19] E. Oset, T. Hyodo, A. Hosaka, F. J. Llanes-Estrada, V. Mateu, S. Sarkar, and M. J. Vicente Vacas, (2004), hep-ph/0405239, Prepared for Workshop on physics of excited nucleons Nstar2004, Grenoble, March 2004, World Scientific, page 71-81.

[20] T. Hyodo, A. Hosaka, E. Oset, and M. J. Vicente Vacas, (2004), nucl-th/0410013, Prepared for International Workshop on PENTAQUARK04, Spring-8, Hyogo, Japan, 20-23 Jul 2004. Published in Nishiharima 2004, Pentaquark, 202-205.

[21] A. Hosaka, T. Hyodo, F. J. Llanes-Estrada, E. Oset, J. R. Peláez, and M. J. Vicente Vacas, Phys. Rev. **C71**, 045205 (2005), hep-ph/0411311.

[22] E. Oset, S. Sarkar, M. J. Vicente Vacas, V. Mateu, T. Hyodo, A. Hosaka, and F. J. Llanes-Estrada, (2004), nucl-th/0410071, Prepared for International Workshop on PENTAQUARK04, Spring-8, Hyogo, Japan, 20-23 Jul 2004. Published in Nishiharima 2004, Pentaquark, 398-405.

[23] T. Hyodo, A. Hosaka, F. J. Llanes-Estrada, E. Oset, J. R. Peláez, and M. J. Vicente Vacas, Nucl. Phys. **A755**, 395 (2005), hep-ph/0501116.

[24] T. Hyodo and A. Hosaka, Phys. Rev. **D71**, 054017 (2005), hep-ph/0502093.

[25] T. Hyodo and A. Hosaka, Phys. Rev. **C72**, 055202 (2005), hep-ph/0509104.

[26] D. J. Gross and F. Wilczek, Phys. Rev. Lett. **30**, 1343 (1973).

[27] H. D. Politzer, Phys. Rev. Lett. **30**, 1346 (1973).

[28] Y. Nambu, Phys. Rev. Lett. **4**, 380 (1960).

[29] J. Goldstone, Nuovo Cim. **19**, 154 (1961).

[30] J. Goldstone, A. Salam, and S. Weinberg, Phys. Rev. **127**, 965 (1962).

[31] B. W. Lee, *Chiral dynamics* (Gordon and Breach science publishers, New York, 1972).

[32] S. Weinberg, *The Quantum theory of fields* volume 2: Modern applications (Cambridge University Press, London, 1996).

[33] M. L. Goldberger and S. B. Treiman, Phys. Rev. **111**, 354 (1958).

[34] G. 't Hooft, Phys. Rept. **142**, 357 (1986).

[35] M. Gell-Mann, Cal. Tech. Synchrotron Laboratory Report CTSL **20**, unpublished (1961).

[36] M. Gell-Mann and Y. Ne'eman, *The Eightfold Way* (Benjamin, New York, 1964).

[37] Y. Ne'eman, Nucl. Phys. **26**, 222 (1961).

[38] S. R. Coleman, J. Wess, and B. Zumino, Phys. Rev. **177**, 2239 (1969).

[39] C. G. Callan, S. R. Coleman, J. Wess, and B. Zumino, Phys. Rev. **177**, 2247 (1969).

[40] A. Pich, Rept. Prog. Phys. **58**, 563 (1995), hep-ph/9502366.

[41] J. Gasser and H. Leutwyler, Nucl. Phys. **B250**, 517 (1985).

[42] J. Gasser and H. Leutwyler, Nucl. Phys. **B250**, 539 (1985).

[43] M. Gell-Mann, R. J. Oakes, and B. Renner, Phys. Rev. **175**, 2195 (1968).

[44] A. Krause, Helv. Phys. Acta **63**, 3 (1990).

[45] E. Jenkins and A. V. Manohar, Phys. Lett. **B255**, 558 (1991).

[46] E. Jenkins and A. V. Manohar, Phys. Lett. **B259**, 353 (1991).

[47] E. Jenkins, Nucl. Phys. **B368**, 190 (1992).

[48] J. F. Donoghue, E. Golowich, and B. R. Holstein, *Dynamics of the standard model* (Cambridge University Press, London, 1992).

[49] B. K. Jennings and K. Maltman, Phys. Rev. **D69**, 094020 (2004), hep-ph/0308286.

[50] D. Diakonov, (2004), hep-ph/0406043.

[51] M. Oka, Prog. Theor. Phys. **112**, 1 (2004), hep-ph/0406211.

[52] R. L. Jaffe, Phys. Rept. **409**, 1 (2005), hep-ph/0409065.

[53] K. H. Hicks, Prog. Part. Nucl. Phys. **55**, 647 (2005), hep-ex/0504027.

[54] D. P. Roy, J. Phys. **G30**, R113 (2004), hep-ph/0311207.

[55] F. Stancu, Int. J. Mod. Phys. **A20**, 209 (2005), hep-ph/0408042.

[56] R. A. Arndt and L. D. Roper, Phys. Rev. **D31**, 2230 (1985).

[57] J. S. Hyslop, R. A. Arndt, L. D. Roper, and R. L. Workman, Phys. Rev. **D46**, 961 (1992).

[58] H. G. Fischer and S. Wenig, Eur. Phys. J. **C37**, 133 (2004), hep-ex/0401014.

[59] E791, E. M. Aitala *et al.*, Phys. Rev. Lett. **81**, 44 (1998), hep-ex/9709013.

[60] E791, E. M. Aitala *et al.*, Phys. Lett. **B448**, 303 (1999).

[61] D. P. Roy and M. Suzuki, Phys. Lett. **B28**, 558 (1969).

[62] E. Golowich, Phys. Rev. **D4**, 262 (1971).

[63] R. L. Jaffe, SLAC Report No. SLAC-PUB-1774 (1976).

[64] H. Hogaasen and P. Sorba, Nucl. Phys. **B145**, 119 (1978).

[65] D. Strottman, Phys. Rev. **D20**, 748 (1979).

[66] M. Gell-Mann, Phys. Lett. **8**, 214 (1964).

[67] C. Gignoux, B. Silvestre-Brac, and J. M. Richard, Phys. Lett. **B193**, 323 (1987).

[68] H. J. Lipkin, Phys. Lett. **B195**, 484 (1987).

[69] H. J. Lipkin, Nucl. Phys. **A625**, 207 (1997), hep-ph/9804218.

[70] F. Stancu, Phys. Rev. **D58**, 111501 (1998), hep-ph/9803442.

[71] C. Helminen and D. O. Riska, Nucl. Phys. **A699**, 624 (2002), nucl-th/0011071.

[72] A. V. Manohar, Nucl. Phys. **B248**, 19 (1984).

[73] M. Chemtob, Nucl. Phys. **B256**, 600 (1985).

[74] M. Karliner and M. P. Mattis, Phys. Rev. **D34**, 1991 (1986).

[75] M. Praszalowicz, talk at Workshop on Skyrmions and Anomalies, M. Jezabek and M. Praszalowicz editors, World Scientific 1987, page 112. .

[76] M. Praszalowicz, Phys. Lett. **B575**, 234 (2003), hep-ph/0308114.

[77] D. Diakonov, V. Petrov, and M. V. Polyakov, Z. Phys. **A359**, 305 (1997), hep-ph/9703373.

[78] D. O. Riska and N. N. Scoccola, Phys. Lett. **B299**, 338 (1993).

[79] H. Weigel, Eur. Phys. J. **A2**, 391 (1998), hep-ph/9804260.

[80] H. Weigel, AIP Conf. Proc. **549**, 271 (2002), hep-ph/0006191.

[81] M. V. Polyakov, A. Sibirtsev, K. Tsushima, W. Cassing, and K. Goeke, Eur. Phys. J. **A9**, 115 (2000), nucl-th/9909048.

[82] H.-Y. Gao and B.-Q. Ma, Mod. Phys. Lett. **A14**, 2313 (1999), hep-ph/0305294.

[83] Y. Ohashi, (2004), hep-ex/0402005.

[84] T. Nakano and K. Hicks, Mod. Phys. Lett. **A19**, 645 (2004).

[85] T. Nakano, Nucl. Phys. **A738**, 182 (2004).

[86] K. Hicks, Int. J. Mod. Phys. **A20**, 219 (2005), hep-ph/0408001.

[87] K. H. Hicks, Acta Phys. Polon. **B35**, 3039 (2004).

[88] LEPS, T. Hotta, Acta Phys. Polon. **B36**, 2173 (2005).

[89] DIANA, V. V. Barmin *et al.*, Phys. Atom. Nucl. **66**, 1715 (2003), hep-ex/0304040.

[90] A. Sibirtsev, J. Haidenbauer, S. Krewald, and U.-G. Meissner, Eur. Phys. J. **A23**, 491 (2005), nucl-th/0407011.

[91] CLAS, S. Stepanyan *et al.*, Phys. Rev. Lett. **91**, 252001 (2003), hep-ex/0307018.

[92] R. A. Schumacher, (2003), nucl-ex/0309006.

[93] CLAS, V. Kubarovsky and S. Stepanyan, AIP Conf. Proc. **698**, 543 (2004), hep-ex/0307088.

[94] E. S. Smith, Braz. J. Phys. **34**, 910 (2004), nucl-ex/0310007.

[95] CLAS, V. D. Burkert, R. De Vita, and S. Niccolai, (2004), nucl-ex/0408019.

[96] K. H. Hicks, (2005), hep-ex/0510067.

[97] SAPHIR, J. Barth *et al.*, Phys. Lett. **B572**, 127 (2003), hep-ex/0307083.

[98] the CLAS, M. Battaglieri *et al.*, (2005), hep-ex/0510061.

[99] A. E. Asratyan, A. G. Dolgolenko, and M. A. Kubantsev, Phys. Atom. Nucl. **67**, 682 (2004), hep-ex/0309042.

[100] A. E. Asratian, A. G. Dolgolenko, and M. A. Kubantsev, Nucl. Phys. Proc. Suppl. **142**, 79 (2005).

[101] CLAS, V. Kubarovsky *et al.*, Phys. Rev. Lett. **92**, 032001 (2004), hep-ex/0311046.

[102] CLAS, V. Kubarovsky and P. Stoler, Nucl. Phys. Proc. Suppl. **142**, 356 (2005), hep-ex/0409025.

[103] CLAS, P. Rossi, Nucl. Phys. **A752**, 111 (2005), hep-ex/0409057.

[104] H. Gao and W. Xu, (2004), nucl-ex/0411013.

[105] CLAS, V. D. Burkert, Int. J. Mod. Phys. **A20**, 1531 (2005), nucl-ex/0412033.

[106] D. S. Carman, Eur. Phys. J. **A24S1**, 15 (2005), hep-ex/0412074.

[107] CLAS, P. Rossi, Nucl. Phys. **A755**, 371 (2005).

[108] HERMES, A. Airapetian *et al.*, Phys. Lett. **B585**, 213 (2004), hep-ex/0312044.

[109] the HERMES, W. Lorenzon, (2004), hep-ex/0411027.

[110] HERMES, A. Airapetian, Nucl. Phys. **A755**, 379 (2005).

[111] HERMES, A. Airapetian, Acta Phys. Polon. **B36**, 2213 (2005).

[112] SVD, A. Aleev *et al.*, Phys. Atom. Nucl. **68**, 974 (2005), hep-ex/0401024.

[113] A. Kubarovsky and V. Popov, (2005), hep-ex/0510006.

[114] SVD, A. Aleev *et al.*, (2005), hep-ex/0509033.

[115] COSY-TOF, M. Abdel-Bary *et al.*, Phys. Lett. **B595**, 127 (2004), hep-ex/0403011.

[116] COSY-TOF, W. Eyrich, Acta Phys. Polon. **B36**, 2189 (2005).

[117] P. Z. Aslanyan, V. N. Emelyanenko, and G. G. Rikhkvitzkaya, Nucl. Phys. **A755**, 375 (2005), hep-ex/0403044.

[118] P. Z. Aslanyan, (2005), hep-ex/0507105.

[119] ZEUS, S. Chekanov *et al.*, Phys. Lett. **B591**, 7 (2004), hep-ex/0403051.

[120] ZEUS, S. V. Chekanov, (2004), hep-ex/0404007.

[121] ZEUS, S. Chekanov, (2004), hep-ex/0405013.

[122] ZEUS, M. Barbi, (2004), hep-ex/0407006.

[123] S. Chekanov, M. Dasgupta, and D. Milstead, (2004), hep-ph/0409284.

[124] the ZEUS, U. Karshon, (2004), hep-ex/0410029.

[125] ZEUS, M. Vazquez, Acta Phys. Slov. **55**, 109 (2005), hep-ex/0411045.

[126] D. Ozerov, (2005), hep-ex/0502018.

[127] H1, HERMES and ZEUS, K. Daum, Nucl. Phys. Proc. Suppl. **142**, 378 (2005).

[128] S. Schmidt, (2005), hep-ex/0506021.

[129] E. Gallo, (2005), hep-ex/0507022.

[130] ZEUS, R. Yoshida, Acta Phys. Polon. **B36**, 2201 (2005).

[131] K. Miwa, (2006), nucl-ex/0601032.

[132] NA49, K. Kadija, Acta Phys. Polon. **B36**, 2239 (2005).

[133] L. Camilleri, Nucl. Phys. Proc. Suppl. **143**, 129 (2005).

[134] S. Nussinov, (2003), hep-ph/0307357.

[135] R. A. Arndt, I. I. Strakovsky, and R. L. Workman, Phys. Rev. **C68**, 042201 (2003), nucl-th/0308012.

[136] R. A. Arndt, I. I. Strakovsky, and R. L. Workman, Nucl. Phys. **A754**, 261 (2005), nucl-th/0311030.

[137] J. Haidenbauer and G. Krein, Phys. Rev. **C68**, 052201 (2003), hep-ph/0309243.

[138] A. Sibirtsev, J. Haidenbauer, S. Krewald, and U.-G. Meissner, Phys. Lett. **B599**, 230 (2004), hep-ph/0405099.

[139] R. N. Cahn and G. H. Trilling, Phys. Rev. **D69**, 011501 (2004), hep-ph/0311245.

[140] R. L. Workman, R. A. Arndt, I. I. Strakovsky, D. M. Manley, and J. Tulpan, Phys. Rev. **C70**, 028201 (2004), nucl-th/0404061.

[141] R. L. Workman, R. A. Arndt, I. I. Strakovsky, D. M. Manley, and J. Tulpan, (2004), nucl-th/0410110.

[142] W. R. Gibbs, Phys. Rev. **C70**, 045208 (2004), nucl-th/0405024.

[143] A. Casher and S. Nussinov, Phys. Lett. **B578**, 124 (2004), hep-ph/0309208.

[144] Particle Data Group, S. Eidelman *et al.*, Phys. Lett. **B592**, 1 (2004).

[145] NA49, C. Alt *et al.*, Phys. Rev. Lett. **92**, 042003 (2004), hep-ex/0310014.

[146] NA49, K. Kadija, J. Phys. **G30**, S1359 (2004).

[147] M. I. Adamovich *et al.*, Phys. Rev. **C70**, 022201 (2004).

[148] HERA-B, I. Abt *et al.*, Phys. Rev. Lett. **93**, 212003 (2004), hep-ex/0408048.

[149] ALEPH, S. Schael *et al.*, Phys. Lett. **B599**, 1 (2004).

[150] CDF, D. O. Litvintsev, Nucl. Phys. Proc. Suppl. **142**, 374 (2005), hep-ex/0410024.

[151] FOCUS, K. Stenson, Int. J. Mod. Phys. **A20**, 3745 (2005), hep-ex/0412021.

[152] HERMES, A. Airapetian *et al.*, Phys. Rev. **D71**, 032004 (2005), hep-ex/0412027.

[153] ZEUS, S. Chekanov *et al.*, Phys. Lett. **B610**, 212 (2005), hep-ex/0501069.

[154] BABAR, B. Aubert, (2005), hep-ex/0502004.

[155] COMPASS, E. S. Ageev *et al.*, Eur. Phys. J. **C41**, 469 (2005), hep-ex/0503033.

[156] E690, D. C. Christian *et al.*, Phys. Rev. Lett. **95**, 152001 (2005), hep-ex/0507056.

[157] H1, A. Aktas *et al.*, Phys. Lett. **B588**, 17 (2004), hep-ex/0403017.

[158] H1, K. Lipka, (2004), hep-ex/0405051.

[159] C. Risler, Acta Phys. Polon. **B36**, 2283 (2005), hep-ex/0506077.

[160] ZEUS, S. Chekanov *et al.*, Eur. Phys. J. **C38**, 29 (2004), hep-ex/0409033.

[161] FOCUS, J. M. Link *et al.*, Phys. Lett. **B622**, 229 (2005), hep-ex/0506013.

[162] T. Berger-Hryn'ova, (2005), hep-ex/0510044.

[163] CLAS, H. G. Juengst, Nucl. Phys. **A754**, 265 (2005), nucl-ex/0312019.

[164] BABAR, B. Aubert *et al.*, Phys. Rev. **D72**, 051101 (2005), hep-ex/0507012.

[165] H. Z. Huang, (2005), nucl-ex/0509037.

[166] BES, J. Z. Bai *et al.*, Phys. Rev. **D70**, 012004 (2004), hep-ex/0402012.

[167] PHENIX, C. Pinkenburg, J. Phys. **G30**, S1201 (2004), nucl-ex/0404001.

[168] SPHINX, Y. M. Antipov *et al.*, Eur. Phys. J. **A21**, 455 (2004), hep-ex/0407026.

[169] M. J. Longo *et al.*, (2004), hep-ex/0410027.

[170] J. Napolitano, J. Cummings, and M. Witkowski, (2004), hep-ex/0412031.

[171] Belle, K. Abe *et al.*, (2005), hep-ex/0507014.

[172] WA89 and COMPASS, M. Zavertyaev, Nucl. Phys. **A755**, 387 (2005).

[173] WA89, M. I. Adamovich *et al.*, Phys. Rev. **C72**, 055201 (2005), hep-ex/0510013.

[174] M. Karliner and H. J. Lipkin, Phys. Lett. **B597**, 309 (2004), hep-ph/0405002.

[175] Y. I. Azimov and I. I. Strakovsky, Phys. Rev. **C70**, 035210 (2004), hep-ph/0406312.

[176] A. I. Titov, A. Hosaka, S. Date, and Y. Ohashi, Phys. Rev. **C70**, 042202 (2004), nucl-th/0408001.

[177] S. Nussinov, (2004), hep-ph/0408082.

[178] S. Chekanov, Eur. Phys. J. **C44**, 367 (2005), hep-ph/0502098.

[179] Q. Zhao and F. E. Close, J. Phys. **G31**, L1 (2005), hep-ph/0404075.

[180] S.-I. Nam, A. Hosaka, and H.-C. Kim, (2005), hep-ph/0505134.

[181] M. Karliner and H. J. Lipkin, (2005), hep-ph/0506084.

[182] A. R. Dzierba, D. Krop, M. Swat, S. Teige, and A. P. Szczepaniak, Phys. Rev. **D69**, 051901 (2004), hep-ph/0311125.

[183] M. Zavertyaev, (2003), hep-ph/0311250.

[184] M. Zavertyaev, (2005), hep-ex/0501028.

[185] K. Hicks, V. Burkert, A. E. Kudryavtsev, I. I. Strakovsky, and S. Stepanyan, (2004), hep-ph/0411265.

[186] A. R. Dzierba, D. Krop, M. Swat, S. Teige, and A. P. Szczepaniak, Phys. Rev. **D71**, 098502 (2005).

[187] D. V. Bugg, Phys. Lett. **B598**, 8 (2004), hep-ph/0406293.

[188] W. Liu and C. M. Ko, Phys. Rev. **C68**, 045203 (2003), nucl-th/0308034.

[189] S. I. Nam, A. Hosaka, and H. C. Kim, Phys. Lett. **B579**, 43 (2004), hep-ph/0308313.

[190] Y.-s. Oh, H.-c. Kim, and S. H. Lee, Phys. Rev. **D69**, 014009 (2004), hep-ph/0310019.

[191] W. Liu and C. M. Ko, Nucl. Phys. **A741**, 215 (2004), nucl-th/0309023.

[192] B.-G. Yu, T.-K. Choi, and C.-R. Ji, Phys. Rev. **C70**, 045205 (2004), nucl-th/0312075.

[193] W. Roberts, Phys. Rev. **C70**, 065201 (2004), nucl-th/0408034.

[194] Y. Oh, K. Nakayama, and T. S. H. Lee, Phys. Rept. **423**, 49 (2006), hep-ph/0412363.

[195] T. Mart, Phys. Rev. **C71**, 022202 (2005), nucl-th/0412096.

[196] H. Kwee, M. Guidal, M. V. Polyakov, and M. Vanderhaeghen, Phys. Rev. **D72**, 054012 (2005), hep-ph/0507180.

[197] Q. Zhao, Phys. Rev. **D69**, 053009 (2004), hep-ph/0310350.

[198] K. Nakayama and K. Tsushima, Phys. Lett. **B583**, 269 (2004), hep-ph/0311112.

[199] Q. Zhao and J. S. Al-Khalili, Phys. Lett. **B585**, 91 (2004), hep-ph/0312348.

[200] M. P. Rekalo and E. Tomasi-Gustafsson, J. Phys. **G30**, 1459 (2004), hep-ph/0401050.

[201] K. Nakayama and W. G. Love, Phys. Rev. **C70**, 012201 (2004), hep-ph/0404011.

[202] A. I. Titov, H. Ejiri, H. Haberzettl, and K. Nakayama, Phys. Rev. **C71**, 035203 (2005), nucl-th/0410098.

[203] W. Liu, C. M. Ko, and V. Kubarovsky, Phys. Rev. **C69**, 025202 (2004), nucl-th/0310087.

[204] Y.-s. Oh, H.-c. Kim, and S. H. Lee, Nucl. Phys. **A745**, 129 (2004), hep-ph/0312229.

[205] S.-I. Nam, A. Hosaka, and H.-C. Kim, (2005), hep-ph/0508210.

[206] V. Guzey, Phys. Rev. **C69**, 065203 (2004), hep-ph/0402060.

[207] A. I. Titov, B. Kampfer, S. Date, and Y. Ohashi, Phys. Rev. **C72**, 035206 (2005), nucl-th/0506072.

[208] Y. Oh, H. Kim, and S. H. Lee, Phys. Rev. **D69**, 074016 (2004), hep-ph/0311054.

[209] A. I. Titov and B. Kampfer, Phys. Rev. **C71**, 062201 (2005), nucl-th/0504073.

[210] S. I. Nam, A. Hosaka, and H. C. Kim, Phys. Rev. **D70**, 114027 (2004), hep-ph/0402138.

[211] A. W. Thomas, K. Hicks, and A. Hosaka, Prog. Theor. Phys. **111**, 291 (2004), hep-ph/0312083.

[212] C. Hanhart *et al.*, Phys. Lett. **B590**, 39 (2004), hep-ph/0312236.

[213] Y. N. Uzikov, Phys. Lett. **B595**, 277 (2004), hep-ph/0401150.

[214] M. P. Rekalo and E. Tomasi-Gustafsson, Phys. Lett. **B591**, 225 (2004), hep-ph/0401162.

[215] M. P. Rekalo and E. Tomasi-Gustafsson, Eur. Phys. J. **A22**, 119 (2004), hep-ph/0402277.

[216] S. I. Nam, A. Hosaka, and H. C. Kim, Phys. Lett. **B602**, 180 (2004), hep-ph/0401074.

[217] C. Hanhart, J. Haidenbauer, K. Nakayama, and U. G. Meissner, Phys. Lett. **B606**, 67 (2005), hep-ph/0407107.

[218] H. W. Barz and M. Zetenyi, Phys. Rev. **C71**, 065207 (2005), nucl-th/0411006.

[219] J. Randrup, Phys. Rev. **C68**, 031903 (2003), nucl-th/0307042.

[220] L. W. Chen, V. Greco, C. M. Ko, S. H. Lee, and W. Liu, Phys. Lett. **B601**, 34 (2004), nucl-th/0308006.

[221] F. Becattini, M. Gazdzicki, A. Keranen, J. Manninen, and R. Stock, Phys. Rev. **C69**, 024905 (2004), hep-ph/0310049.

[222] J. Letessier, G. Torrieri, S. Steinke, and J. Rafelski, Phys. Rev. **C68**, 061901 (2003), hep-ph/0310188.

[223] M. Bleicher, F. M. Liu, J. Aichelin, T. Pierog, and K. Werner, Phys. Lett. **B595**, 288 (2004), hep-ph/0401049.

[224] F. M. Liu, H. Stoecker, and K. Werner, Phys. Lett. **B597**, 333 (2004), hep-ph/0404156.

[225] F.-l. Shao, Q.-b. Xie, and Q. Wang, Phys. Rev. **C71**, 044903 (2005), nucl-th/0409018.

[226] S. Scherer, J. Phys. **G31**, S1199 (2005), hep-ph/0411296.

[227] J. L. Rosner, Phys. Rev. **D69**, 094014 (2004), hep-ph/0312269.

[228] S. Armstrong, B. Mellado, and S. L. Wu, J. Phys. **G30**, 1801 (2004), hep-ph/0312344.

[229] T. E. Browder, I. R. Klebanov, and D. R. Marlow, Phys. Lett. **B587**, 62 (2004), hep-ph/0401115.

[230] K. Cheung, Phys. Lett. **B595**, 283 (2004), hep-ph/0405281.

[231] M. Karliner and B. R. Webber, JHEP **12**, 045 (2004), hep-ph/0409121.

[232] N. G. Kelkar, M. Nowakowski, and K. P. Khemchandani, J. Phys. **G29**, 1001 (2003), hep-ph/0307134.

[233] N. G. Kelkar, M. Nowakowski, and K. P. Khemchandani, Mod. Phys. Lett. **A19**, 2001 (2004), nucl-th/0405008.

[234] M. Diehl, B. Pire, and L. Szymanowski, Phys. Lett. **B584**, 58 (2004), hep-ph/0312125.

[235] M. P. Rekalo and E. Tomasi-Gustafsson, Phys. Lett. **B599**, 247 (2004), hep-ph/0405027.

[236] D. Diakonov and V. Petrov, Phys. Rev. **D69**, 094011 (2004), hep-ph/0310212.

[237] R. A. Arndt, Y. I. Azimov, M. V. Polyakov, I. I. Strakovsky, and R. L. Workman, Phys. Rev. **C69**, 035208 (2004), nucl-th/0312126.

[238] S. Ceci, A. Svarc, and B. Zauner, (2004), nucl-th/0406055.

[239] W. Liu and C. M. Ko, Phys. Rev. **C69**, 045204 (2004), nucl-th/0312119.

[240] S.-I. Nam, A. Hosaka, and H.-C. Kim, (2004), hep-ph/0405227.

[241] D. L. Borisyuk, A. P. Kobushkin, and Y. V. Kutafin, (2004), hep-ph/0408201.

[242] B. Levchenko, (2004), hep-ph/0401122.

[243] M. Karliner and H. J. Lipkin, Phys. Lett. **B616**, 191 (2005), hep-ph/0501189.

[244] F. E. Close and Q. Zhao, Phys. Lett. **B590**, 176 (2004), hep-ph/0403159.

[245] V. Y. Grishina, L. A. Kondratyuk, W. Cassing, M. Mirazita, and P. Rossi, Eur. Phys. J. **A25**, 141 (2005), nucl-th/0506053.

[246] X. Chen, Y.-j. Mao, and B.-Q. Ma, Mod. Phys. Lett. **A19**, 2289 (2004), hep-ph/0307381.

[247] Y.-s. Oh, H. c. Kim, and S. H. Lee, Phys. Rev. **D69**, 094009 (2004), hep-ph/0310117.

[248] S. H. Lee, H. Kim, and Y.-s. Oh, J. Korean Phys. Soc. **46**, 774 (2005), hep-ph/0402135.

[249] Y.-s. Oh and H.-c. Kim, Phys. Rev. **D70**, 094022 (2004), hep-ph/0405010.

[250] S. Golbeck and M. Savrov, (2004), hep-ph/0406060.

[251] B. Grinstein and M. A. Savrov, (2004), hep-ph/0408346.

[252] R. W. Gothe and S. Nussinov, (2003), hep-ph/0308230.

[253] R. Jaffe and F. Wilczek, Phys. Rev. **D69**, 114017 (2004), hep-ph/0312369.

[254] T. Mehen and C. Schat, Phys. Lett. **B588**, 67 (2004), hep-ph/0401107.

[255] X.-G. He and X.-Q. Li, Phys. Rev. **D70**, 034030 (2004), hep-ph/0403191.

[256] P. Ko, J. Lee, T. Lee, and J.-h. Park, Phys. Lett. **B611**, 87 (2005), hep-ph/0312147.

[257] X.-G. He, T. Li, X.-Q. Li, and C. C. Lih, Phys. Rev. **D71**, 014006 (2005), hep-ph/0409006.

[258] Y. R. Liu *et al.*, Phys. Rev. **D70**, 094045 (2004), hep-ph/0404123.

[259] V. Mohta, Phys. Rev. **D70**, 114022 (2004), hep-ph/0406233.

[260] V. Mohta, (2004), hep-ph/0411247.

[261] M. A. Nowak, M. Praszalowicz, M. Sadzikowski, and J. Wasiluk, Phys. Rev. **D70**, 031503 (2004), hep-ph/0403184.

[262] S. R. Beane, Phys. Rev. **D70**, 114010 (2004), hep-ph/0408066.

[263] B. L. Ioffe and A. G. Oganesian, JETP Lett. **80**, 386 (2004), hep-ph/0408152.

[264] D. Melikhov and B. Stech, Phys. Lett. **B608**, 59 (2005), hep-ph/0409015.

[265] G. 't Hooft, Nucl. Phys. **B72**, 461 (1974).

[266] E. Witten, Nucl. Phys. **B160**, 57 (1979).

[267] J.-L. Gervais and B. Sakita, Phys. Rev. Lett. **52**, 87 (1984).

[268] R. F. Dashen and A. V. Manohar, Phys. Lett. **B315**, 425 (1993), hep-ph/9307241.

[269] E. Jenkins, Phys. Lett. **B315**, 431 (1993), hep-ph/9307243.

[270] T. D. Cohen and R. F. Lebed, Phys. Lett. **B578**, 150 (2004), hep-ph/0309150.

[271] N. Itzhaki, I. R. Klebanov, P. Ouyang, and L. Rastelli, Nucl. Phys. **B684**, 264 (2004), hep-ph/0309305.

[272] E. Jenkins and A. V. Manohar, Phys. Rev. Lett. **93**, 022001 (2004), hep-ph/0401190.

[273] E. Jenkins and A. V. Manohar, Phys. Rev. **D70**, 034023 (2004), hep-ph/0402150.

[274] R. F. Dashen, E. Jenkins, and A. V. Manohar, Phys. Rev. **D51**, 3697 (1995), hep-ph/9411234.

[275] E. Jenkins and A. V. Manohar, JHEP **06**, 039 (2004), hep-ph/0402024.

[276] M. E. Wessling, Phys. Lett. **B603**, 152 (2004), hep-ph/0408263.

[277] D. Pirjol and C. Schat, Phys. Rev. **D71**, 036004 (2005), hep-ph/0408293.

[278] T. D. Cohen, P. M. Hohler, and R. F. Lebed, Phys. Rev. **D72**, 074010 (2005), hep-ph/0508199.

[279] T. H. R. Skyrme, Nucl. Phys. **31**, 556 (1962).

[280] G. S. Adkins, C. R. Nappi, and E. Witten, Nucl. Phys. **B228**, 552 (1983).

[281] E. Witten, Nucl. Phys. **B223**, 433 (1983).

[282] E. Guadagnini, Nucl. Phys. **B236**, 35 (1984).

[283] A. Blotz *et al.*, Nucl. Phys. **A555**, 765 (1993).

[284] J. R. Ellis, M. Karliner, and M. Praszalowicz, JHEP **05**, 002 (2004), hep-ph/0401127.

[285] T. D. Cohen, Phys. Lett. **B581**, 175 (2004), hep-ph/0309111.

[286] T. D. Cohen, Phys. Rev. **D70**, 014011 (2004).

[287] D. Diakonov and V. Petrov, Phys. Rev. **D69**, 056002 (2004), hep-ph/0309203.

[288] J. Callan, Curtis G. and I. R. Klebanov, Nucl. Phys. **B262**, 365 (1985).

[289] B.-Y. Park, M. Rho, and D.-P. Min, Phys. Rev. **D70**, 114026 (2004), hep-ph/0405246.

[290] P. V. Pobylitsa, Phys. Rev. **D69**, 074030 (2004), hep-ph/0310221.

[291] A. Cherman, T. D. Cohen, and A. Nellore, Phys. Rev. **D70**, 096003 (2004), hep-ph/0408209.

[292] A. Cherman, T. D. Cohen, T. R. Dulaney, and E. M. Lynch, Phys. Rev. **D72**, 094015 (2005), hep-ph/0509129.

[293] H. Walliser and H. Weigel, (2005), hep-ph/0510055.

[294] T. D. Cohen, (2005), hep-ph/0511174.

[295] H. Walliser and H. Weigel, (2005), hep-ph/0511297.

[296] M. Praszalowicz, Phys. Lett. **B583**, 96 (2004), hep-ph/0311230.

[297] R. L. Jaffe, Eur. Phys. J. **C35**, 221 (2004), hep-ph/0401187.

[298] D. Diakonov, V. Petrov, and M. Polyakov, (2004), hep-ph/0404212.

[299] R. L. Jaffe, (2004), hep-ph/0405268.

[300] D. Diakonov and V. Petrov, Annalen Phys. **13**, 637 (2004), hep-ph/0409362.

[301] D. Diakonov and V. Petrov, Phys. Rev. **D72**, 074009 (2005), hep-ph/0505201.

[302] G. Duplancic and J. Trampetic, Phys. Rev. **D69**, 117501 (2004), hep-ph/0402027.

[303] G. Duplancic, H. Pasagic, and J. Trampetic, Phys. Rev. **D70**, 077504 (2004), hep-ph/0404193.

[304] G. Duplancic, H. Pasagic, and J. Trampetic, JHEP **07**, 027 (2004), hep-ph/0405029.

[305] B. Wu and B.-Q. Ma, Phys. Rev. **D70**, 034025 (2004), hep-ph/0402244.

[306] R. Casalbuoni and G. Nardulli, Phys. Lett. **B602**, 205 (2004), hep-ph/0406030.

[307] H. K. Lee and H. Y. Park, Phys. Rev. **D70**, 074033 (2004), hep-ph/0406051.

[308] K. Harada, Y. Mitsunari, and N.-a. Yamashita, Prog. Theor. Phys. **113**, 1315 (2005), hep-ph/0410145.

[309] H. Walliser and V. B. Kopeliovich, J. Exp. Theor. Phys. **97**, 433 (2003), hep-ph/0304058.

[310] B. Wu and B.-Q. Ma, Phys. Rev. **D69**, 077501 (2004), hep-ph/0312041.

[311] B. Wu and B.-Q. Ma, Phys. Lett. **B586**, 62 (2004), hep-ph/0312326.

[312] B. Wu and B.-Q. Ma, Phys. Rev. **D70**, 094042 (2004), hep-ph/0408121.

[313] B. Wu and B.-Q. Ma, Phys. Rev. **D70**, 097503 (2004), hep-ph/0311331.

[314] D. Borisyuk, M. Faber, and A. Kobushkin, (2003), hep-ph/0307370.

[315] D. Borisyuk, M. Faber, and A. Kobushkin, Ukr. J. Phys. **49**, 944 (2004), hep-ph/0312213.

[316] P. Schweitzer, Eur. Phys. J. **A22**, 89 (2004), hep-ph/0312376.

[317] M. Praszalowicz, Acta Phys. Polon. **B35**, 1625 (2004), hep-ph/0402038.

[318] M.-L. Yan and X.-H. Meng, Commun. Theor. Phys. **24**, 435 (1995), hep-ph/0402072.

[319] H. Weigel, Eur. Phys. J. **A21**, 133 (2004), hep-ph/0404173.

[320] V. B. Kopeliovich and A. M. Shunderuk, J. Exp. Theor. Phys. **100**, 929 (2005), nucl-th/0409010.

[321] J. R. Ellis and Y. Frishman, JHEP **08**, 081 (2005), hep-ph/0502193.

[322] M. V. Polyakov and A. Rathke, Eur. Phys. J. **A18**, 691 (2003), hep-ph/0303138.

[323] H.-C. Kim and M. Praszalowicz, Phys. Lett. **B585**, 99 (2004), hep-ph/0308242.

[324] G.-S. Yang, H.-C. Kim, M. Praszalowicz, and K. Goeke, Phys. Rev. **D70**, 114002 (2004), hep-ph/0410042.

[325] H.-C. Kim, M. Polyakov, M. Praszalowicz, G.-S. Yang, and K. Goeke, Phys. Rev. **D71**, 094023 (2005), hep-ph/0503237.

[326] SELEX, V. V. Molchanov *et al.*, Phys. Lett. **B590**, 161 (2004), hep-ex/0402026.

[327] GRAAL, V. Kuznetsov, (2004), hep-ex/0409032.

[328] A. De Rujula, H. Georgi, and S. L. Glashow, Phys. Rev. **D12**, 147 (1975).

[329] N. Isgur and G. Karl, Phys. Rev. **D18**, 4187 (1978).

[330] L. Y. Glozman and D. O. Riska, Phys. Rept. **268**, 263 (1996), hep-ph/9505422.

[331] S. Capstick and W. Roberts, Prog. Part. Nucl. Phys. **45**, S241 (2000), nucl-th/0008028.

[332] F. Stancu and D. O. Riska, Phys. Lett. **B575**, 242 (2003), hep-ph/0307010.

[333] C. E. Carlson, C. D. Carone, H. J. Kwee, and V. Nazaryan, Phys. Lett. **B573**, 101 (2003), hep-ph/0307396.

[334] C. E. Carlson, C. D. Carone, H. J. Kwee, and V. Nazaryan, Phys. Lett. **B579**, 52 (2004), hep-ph/0310038.

[335] F. Huang, Z. Y. Zhang, Y. W. Yu, and B. S. Zou, Phys. Lett. **B586**, 69 (2004), hep-ph/0310040.

[336] D. Zhang, F. Huang, Z. Y. Zhang, and Y. W. Yu, Nucl. Phys. **A756**, 215 (2005), nucl-th/0506041.

[337] F. Huang, Z. Y. Zhang, and Y. W. Yu, Phys. Rev. **C70**, 044004 (2004), nucl-th/0406046.

[338] F. Huang and Z. Y. Zhang, Phys. Rev. **C70**, 064004 (2004), nucl-th/0409029.

[339] K. Maltman, Phys. Lett. **B604**, 175 (2004), hep-ph/0408145.

[340] T. Shinozaki, M. Oka, and S. Takeuchi, Phys. Rev. **D71**, 074025 (2005), hep-ph/0409103.

[341] G. 't Hooft, Phys. Rev. **D14**, 3432 (1976).

[342] T. Shinozaki, M. Oka, and S. Takeuchi, (2005), hep-ph/0510001.

[343] V. Dmitrasinovic, Phys. Rev. **D71**, 094003 (2005).

[344] R. L. Jaffe and F. Wilczek, Phys. Rev. Lett. **91**, 232003 (2003), hep-ph/0307341.

[345] M. Karliner and H. J. Lipkin, Phys. Lett. **B575**, 249 (2003), hep-ph/0402260.

[346] E. Shuryak and I. Zahed, Phys. Lett. **B589**, 21 (2004), hep-ph/0310270.

[347] L. Y. Glozman, Phys. Rev. Lett. **92**, 239101 (2004), hep-ph/0309092.

[348] T. D. Cohen, Phys. Rev. **D70**, 074023 (2004), hep-ph/0402056.

[349] S. Pakvasa and M. Suzuki, Phys. Rev. **D70**, 036002 (2004), hep-ph/0402079.

[350] M. Praszalowicz, Annalen Phys. **13**, 709 (2004), hep-ph/0410086.

[351] V. Guzey and M. V. Polyakov, (2005), hep-ph/0501010.

[352] S. Nussinov, Phys. Rev. **D69**, 116001 (2004), hep-ph/0403028.

[353] A. Zhang *et al.*, High Energy Phys. Nucl. Phys. **29**, 250 (2005), hep-ph/0403210.

[354] G. C. Rossi and G. Veneziano, Phys. Lett. **B597**, 338 (2004), hep-ph/0404262.

[355] R. Ramachandran, Pramana **65**, 381 (2005), hep-ph/0411103.

[356] M. Karliner and H. J. Lipkin, (2003), hep-ph/0307243.

[357] M. Karliner and H. J. Lipkin, (2003), hep-ph/0307343.

[358] K. Cheung, Phys. Rev. **D69**, 094029 (2004), hep-ph/0308176.

[359] N. I. Kochelev, H. J. Lee, and V. Vento, Phys. Lett. **B594**, 87 (2004), hep-ph/0404065.

[360] H. Hogaasen and P. Sorba, Mod. Phys. Lett. **A19**, 2403 (2004), hep-ph/0406078.

[361] P. Jimenez Delgado, Few Body Syst. **37**, 215 (2005), hep-ph/0409128.

[362] H.-J. Lee, N. I. Kochelev, and V. Vento, Phys. Lett. **B610**, 50 (2005), hep-ph/0412127.

[363] H. Li, C. M. Shakin, and X. Li, Phys. Rev. **C71**, 068203 (2005), hep-ph/0503145.

[364] H. Li, C. M. Shakin, and X. Li, (2005), hep-ph/0504125.

[365] H. Li, C. M. Shakin, and X. Li, (2005), nucl-th/0506062.

[366] C. Semay, F. Brau, and B. Silvestre-Brac, Phys. Rev. Lett. **94**, 062001 (2005), hep-ph/0408225.

[367] D. K. Hong, Y. J. Sohn, and I. Zahed, Phys. Lett. **B596**, 191 (2004), hep-ph/0403205.

[368] D. K. Hong, (2004), hep-ph/0412132.

[369] I. W. Stewart, M. E. Wessling, and M. B. Wise, Phys. Lett. **B590**, 185 (2004), hep-ph/0402076.

[370] R. S. Kaushal, D. Parashar, and A. K. Sisodiya, Phys. Lett. **B600**, 215 (2004).

[371] S.-L. Zhu, Phys. Rev. **C70**, 045201 (2004), hep-ph/0405149.

[372] M. Karliner and H. J. Lipkin, Phys. Lett. **B612**, 197 (2005), hep-ph/0411136.

[373] T. Burns, F. E. Close, and J. J. Dudek, Phys. Rev. **D71**, 014017 (2005), hep-ph/0411160.

[374] Y. Kanada-En'yo, O. Morimatsu, and T. Nishikawa, Phys. Rev. **D71**, 094005 (2005), hep-ph/0502042.

[375] S. Capstick, P. R. Page, and W. Roberts, Phys. Lett. **B570**, 185 (2003), hep-ph/0307019.

[376] P. R. Page, AIP Conf. Proc. **717**, 436 (2004), hep-ph/0310200.

[377] A. Hosaka, Phys. Lett. **B571**, 55 (2003), hep-ph/0307232.

[378] A. Hosaka and H. Toki, Phys. Rept. **277**, 65 (1996).

[379] Y. R. Liu, P. Z. Huang, W. Z. Deng, X. L. Chen, and S.-L. Zhu, Phys. Rev. **C69**, 035205 (2004), hep-ph/0312074.

[380] W. W. Li *et al.*, High Energy Phys. Nucl. Phys. **28**, 918 (2004), hep-ph/0312362.

[381] P. Z. Huang, Y. R. Liu, W. Z. Deng, X. L. Chen, and S.-L. Zhu, Phys. Rev. **D70**, 034003 (2004), hep-ph/0401191.

[382] L. Y. Glozman, Phys. Lett. **B575**, 18 (2003), hep-ph/0308232.

[383] R. Bijker, M. M. Giannini, and E. Santopinto, Eur. Phys. J. **A22**, 319 (2004), hep-ph/0310281.

[384] R. Bijker, M. M. Giannini, and E. Santopinto, Phys. Lett. **B595**, 260 (2004), hep-ph/0403029.

[385] T. Inoue, V. E. Lyubovitskij, T. Gutsche, and A. Faessler, Prog. Theor. Phys. **113**, 801 (2005), hep-ph/0408057.

[386] J. J. Dudek and F. E. Close, Phys. Lett. **B583**, 278 (2004), hep-ph/0311258.

[387] C. E. Carlson, C. D. Carone, H. J. Kwee, and V. Nazaryan, Phys. Rev. **D70**, 037501 (2004), hep-ph/0312325.

[388] D. Melikhov, S. Simula, and B. Stech, Phys. Lett. **B594**, 265 (2004), hep-ph/0405037.

[389] A. Hosaka, M. Oka, and T. Shinozaki, Phys. Rev. **D71**, 074021 (2005), hep-ph/0409102.

[390] F. Buccella and P. Sorba, Mod. Phys. Lett. **A19**, 1547 (2004), hep-ph/0401083.

[391] F. E. Close and J. J. Dudek, Phys. Lett. **B586**, 75 (2004), hep-ph/0401192.

[392] M. Karliner and H. J. Lipkin, Phys. Lett. **B594**, 273 (2004), hep-ph/0402008.

[393] T. Inoue, V. E. Lyubovitskij, T. Gutsche, and A. Faessler, Int. J. Mod. Phys. **E14**, 995 (2005), hep-ph/0407305.

[394] Y. Maezawa, T. Maruyama, N. Itagaki, and T. Hatsuda, Acta Phys. Hung. **A22**, 61 (2005), hep-ph/0408056.

[395] J.-l. Ping, D. Qing, F. Wang, and T. Goldman, Phys. Lett. **B602**, 197 (2004), hep-ph/0408176.

[396] B. S. Zou and D. O. Riska, Phys. Rev. Lett. **95**, 072001 (2005), hep-ph/0502225.

[397] F. Stancu, Phys. Lett. **B595**, 269 (2004), hep-ph/0402044.

[398] Y. Kanada-Enyo, O. Morimatsu, and T. Nishikawa, Phys. Rev. **C71**, 045202 (2005), hep-ph/0404144.

[399] S. Takeuchi and K. Shimizu, Phys. Rev. **C71**, 062202 (2005), hep-ph/0410286.

[400] S. Takeuchi and K. Shimizu, (2004), hep-ph/0411016.

[401] E. Hiyama, M. Kamimura, A. Hosaka, H. Toki, and M. Yahiro, (2005), hep-ph/0507105.

[402] M. W. Paris, Phys. Rev. Lett. **95**, 202002 (2005), nucl-th/0507061.

[403] H. Matsumura and Y. Suzuki, (2006), nucl-th/0601011.

[404] D. E. Kahana and S. H. Kahana, Phys. Rev. **D69**, 117502 (2004), hep-ph/0310026.

[405] R. L. Jaffe and A. Jain, Phys. Rev. **D71**, 034012 (2005), hep-ph/0408046.

[406] X.-G. He, X.-Q. Li, X. Liu, and X.-Q. Zeng, Eur. Phys. J. **C44**, 419 (2005), hep-ph/0502236.

[407] P. Bicudo and G. M. Marques, Phys. Rev. **D69**, 011503 (2004), hep-ph/0308073.

[408] P. Bicudo, Phys. Rev. **D70**, 111504 (2004), hep-ph/0403146.

[409] P. Bicudo, Phys. Rev. **D71**, 011501 (2005), hep-ph/0403295.

[410] F. J. Llanes-Estrada, E. Oset, and V. Mateu, Phys. Rev. **C69**, 055203 (2004), nucl-th/0311020.

[411] T. Kishimoto and T. Sato, (2003), hep-ex/0312003.

[412] F. Huang, Z. Y. Zhang, and Y. W. Yu, Phys. Rev. **C72**, 065208 (2005), hep-ph/0411222.

[413] D. Cabrera, Q. B. Li, V. K. Magas, E. Oset, and M. J. Vicente Vacas, Phys. Lett. **B608**, 231 (2005), nucl-th/0407007.

[414] S. Sarkar, E. Oset, and M. J. Vicente Vacas, Eur. Phys. J. **A24**, 287 (2005), nucl-th/0404023.

[415] S. Sarkar, E. Oset, and M. J. Vicente Vacas, Nucl. Phys. **A750**, 294 (2005), nucl-th/0407025.

[416] F. Huang and Z. Y. Zhang, Phys. Rev. **C72**, 068201 (2005), nucl-th/0511057.

[417] C. Garcia-Recio, J. Nieves, and L. L. Salcedo, (2005), hep-ph/0505233.

[418] J. Hofmann and M. F. M. Lutz, Nucl. Phys. **A763**, 90 (2005), hep-ph/0507071.

[419] I. M. Narodetskii, Y. A. Simonov, M. A. Trusov, and A. I. Veselov, Phys. Lett. **B578**, 318 (2004), hep-ph/0310118.

[420] C. Semay and B. Silvestre-Brac, Eur. Phys. J. **A22**, 1 (2004).

[421] I. M. Narodetskii, C. Semay, B. Silvestre-Brac, and Y. A. Simonov, Nucl. Phys. Proc. Suppl. **142**, 383 (2005), hep-ph/0409304.

[422] M. Bando, T. Kugo, A. Sugamoto, and S. Terunuma, Prog. Theor. Phys. **112**, 325 (2004), hep-ph/0405259.

[423] H. Suganuma, H. Ichie, F. Okiharu, and T. T. Takahashi, (2004), hep-ph/0412271.

[424] B. V. Martemyanov, C. Fuchs, A. Faessler, and M. I. Krivoruchenko, Phys. Rev. **D71**, 017502 (2005), hep-ph/0502021.

[425] N. Auerbach and V. Zelevinsky, Phys. Lett. **B590**, 45 (2004), nucl-th/0310029.

[426] M. Karliner and H. J. Lipkin, Phys. Lett. **B586**, 303 (2004), hep-ph/0401072.

[427] S. M. Gerasyuta and V. I. Kochkin, Phys. Rev. **D71**, 076009 (2005), hep-ph/0310227.

[428] S. M. Gerasyuta and V. I. Kochkin, Phys. Rev. **D72**, 016002 (2005), hep-ph/0504254.

[429] S. M. Gerasyuta and V. I. Kochkin, Mod. Phys. Lett. **A20**, 1813 (2005), hep-ph/0501267.

[430] H.-q. Zheng, Int. J. Mod. Phys. **A20**, 1981 (2005), hep-ph/0411025.

[431] A. K. Leibovich, Z. Ligeti, I. W. Stewart, and M. B. Wise, Phys. Lett. **B586**, 337 (2004), hep-ph/0312319.

[432] X.-C. Song and S.-L. Zhu, Mod. Phys. Lett. **A19**, 2791 (2004), hep-ph/0403093.

[433] H.-Y. Cheng, C.-K. Chua, and C.-W. Hwang, Phys. Rev. **D70**, 034007 (2004), hep-ph/0403232.

[434] H.-Y. Cheng and C.-K. Chua, JHEP **11**, 072 (2004), hep-ph/0406036.

[435] M. Nunez V. *et al.*, (2004), nucl-th/0405053.

[436] M. Nunez V. *et al.*, Phys. Rev. **C70**, 025201 (2004), nucl-th/0405052.

[437] H.-C. Kim, C.-H. Lee, and H.-J. Lee, J. Korean Phys. Soc. **46**, 393 (2005), hep-ph/0402141.

[438] G. A. Miller, Phys. Rev. **C70**, 022202 (2004), nucl-th/0402099.

[439] H. Nagahiro, S. Hirenzaki, E. Oset, and M. J. Vicente Vacas, Phys. Lett. **B620**, 125 (2005), nucl-th/0408002.

[440] D. E. Lanskoy, (2004), nucl-th/0411004.

[441] X. H. Zhong, Y. H. Tan, L. Li, and P. Z. Ning, Phys. Rev. **C71**, 015206 (2005), nucl-th/0408046.

[442] P. G. Reinhard, Rept. Prog. Phys. **52**, 439 (1989).

[443] X.-H. Zhong and P.-Z. Ning, (2005), nucl-th/0501064.

[444] F. S. Navarra, M. Nielsen, and K. Tsushima, Phys. Lett. **B606**, 335 (2005), nucl-th/0408072.

[445] T. D. Cohen, R. J. Furnstahl, D. K. Griegel, and X.-m. Jin, Prog. Part. Nucl. Phys. **35**, 221 (1995), hep-ph/9503315.

[446] J. Sugiyama, T. Doi, and M. Oka, Phys. Lett. **B581**, 167 (2004), hep-ph/0309271.

[447] X.-u. Huang, X.-w. Hao, and P.-f. Zhuang, Phys. Lett. **B607**, 78 (2005), nucl-th/0409001.

[448] H. Shen and H. Toki, Phys. Rev. **C71**, 065208 (2005), nucl-th/0410072.

[449] H. Shen and H. Toki, Phys. Rev. **C61**, 045205 (2000), nucl-th/9911046.

[450] H. Shen and H. Toki, Nucl. Phys. **A707**, 469 (2002), nucl-th/0104072.

[451] A. Gal and E. Friedman, Phys. Rev. Lett. **94**, 072301 (2005), nucl-th/0411052.

[452] A. Gal and E. Friedman, (2005), nucl-th/0511033.

[453] L. Tolos, D. Cabrera, A. Ramos, and A. Polls, Phys. Lett. **B632**, 219 (2006), hep-ph/0503009.

[454] C. Samanta, P. R. Chowdhury, and D. N. Basu, (2005), nucl-th/0504085.

[455] C. Y. Ryu, C. H. Hyun, J. Y. Lee, and S. W. Hong, Phys. Rev. **C72**, 045206 (2005), nucl-th/0506052.

[456] P. K. Panda, C. Providencia, and D. P. Menezes, Phys. Rev. **C72**, 058201 (2005), nucl-th/0508007.

[457] M. A. Shifman, A. I. Vainshtein, and V. I. Zakharov, Nucl. Phys. **B147**, 385 (1979).

[458] M. A. Shifman, A. I. Vainshtein, and V. I. Zakharov, Nucl. Phys. **B147**, 448 (1979).

[459] L. J. Reinders, H. Rubinstein, and S. Yazaki, Phys. Rept. **127**, 1 (1985).

[460] B. L. Ioffe, Nucl. Phys. **B188**, 317 (1981).

[461] Y. Chung, H. G. Dosch, M. Kremer, and D. Schall, Phys. Lett. **B102**, 175 (1981).

[462] Y. Chung, H. G. Dosch, M. Kremer, and D. Schall, Nucl. Phys. **B197**, 55 (1982).

[463] S.-L. Zhu, Phys. Rev. Lett. **91**, 232002 (2003), hep-ph/0307345.

[464] R. D. Matheus, F. S. Navarra, M. Nielsen, R. Rodrigues da Silva, and S. H. Lee, Phys. Lett. **B578**, 323 (2004), hep-ph/0309001.

[465] M. Eidemuller, Phys. Lett. **B597**, 314 (2004), hep-ph/0404126.

[466] Y. Kondo, O. Morimatsu, and T. Nishikawa, Phys. Lett. **B611**, 93 (2005), hep-ph/0404285.

[467] S. H. Lee, H. Kim, and Y. Kwon, Phys. Lett. **B609**, 252 (2005), hep-ph/0411104.

[468] Y. Kwon, A. Hosaka, and S. H. Lee, (2005), hep-ph/0505040.

[469] R. D. Matheus and S. Narison, (2004), hep-ph/0412063.

[470] H. Kim, S. H. Lee, and Y.-s. Oh, Phys. Lett. **B595**, 293 (2004), hep-ph/0404170.

[471] Y. Sarac, H. Kim, and S. H. Lee, (2005), hep-ph/0510304.

[472] R. D. Matheus, F. S. Navarra, M. Nielsen, and R. R. da Silva, Phys. Lett. **B602**, 185 (2004), hep-ph/0406246.

[473] T. Nishikawa, Y. Kanada-En'yo, O. Morimatsu, and Y. Kondo, Phys. Rev. **D71**, 016001 (2005), hep-ph/0410394.

[474] T. Nishikawa, Y. Kanada-En'yo, O. Morimatsu, and Y. Kondo, Phys. Rev. **D71**, 076004 (2005), hep-ph/0411224.

[475] W. Wei, P. Z. Huang, H. X. Chen, and S.-L. Zhu, JHEP **07**, 015 (2005), hep-ph/0503166.

[476] H.-J. Lee, N. I. Kochelev, and V. Vento, Phys. Rev. **D73**, 014010 (2006), hep-ph/0506250.

[477] P.-Z. Huang, W.-Z. Deng, X.-L. Chen, and S.-L. Zhu, Phys. Rev. **D69**, 074004 (2004), hep-ph/0311108.

[478] Z.-G. Wang, W.-M. Yang, and S.-L. Wan, J. Phys. **G31**, 703 (2005), hep-ph/0501278.

[479] Z.-G. Wang, S.-L. Wan, and W.-M. Yang, Eur. Phys. J. **C45**, 201 (2006), hep-ph/0503007.

[480] M. Eidemuller, F. S. Navarra, M. Nielsen, and R. Rodrigues da Silva, Phys. Rev. **D72**, 034003 (2005), hep-ph/0503193.

[481] Z.-G. Wang, W.-M. Yang, and S.-L. Wan, Phys. Rev. **D72**, 034012 (2005), hep-ph/0504151.

[482] K. G. Wilson, Phys. Rev. **D10**, 2445 (1974).

[483] R. Gupta, (1997), hep-lat/9807028.

[484] F. Csikor, Z. Fodor, S. D. Katz, and T. G. Kovacs, JHEP **11**, 070 (2003), hep-lat/0309090.

[485] S. Sasaki, Phys. Rev. Lett. **93**, 152001 (2004), hep-lat/0310014.

[486] T.-W. Chiu and T.-H. Hsieh, Phys. Rev. **D72**, 034505 (2005), hep-ph/0403020.

[487] N. Mathur *et al.*, Phys. Rev. **D70**, 074508 (2004), hep-ph/0406196.

[488] N. Ishii *et al.*, Phys. Rev. **D71**, 034001 (2005), hep-lat/0408030.

[489] B. G. Lasscock *et al.*, Phys. Rev. **D72**, 014502 (2005), hep-lat/0503008.

[490] T. T. Takahashi, T. Umeda, T. Onogi, and T. Kunihiro, Phys. Rev. **D71**, 114509 (2005), hep-lat/0503019.

[491] B. G. Lasscock *et al.*, Phys. Rev. **D72**, 074507 (2005), hep-lat/0504015.

[492] N. Ishii, T. Doi, Y. Nemoto, M. Oka, and H. Suganuma, Phys. Rev. **D72**, 074503 (2005), hep-lat/0506022.

[493] A. W. Thomas and R. D. Young, (2005), hep-ph/0510293.

[494] F. Csikor, Z. Fodor, S. D. Katz, T. G. Kovacs, and B. C. Toth, (2005), hep-lat/0503012.

[495] C. Alexandrou and A. Tsapalis, Phys. Rev. **D73**, 014507 (2006), hep-lat/0503013.

[496] K. Holland and K. J. Juge, (2005), hep-lat/0504007.

[497] O. Jahn, J. W. Negele, and D. Sigaev, PoS **LAT2005**, 069 (2005), hep-lat/0509102.

[498] D. Hierl, C. Hagen, and A. Schaefer, PoS **LAT2005**, 026 (2005), hep-lat/0509109.

[499] F. Okiharu, H. Suganuma, and T. T. Takahashi, Phys. Rev. Lett. **94**, 192001 (2005), hep-lat/0407001.

[500] C. Alexandrou and G. Koutsou, Phys. Rev. **D71**, 014504 (2005), hep-lat/0407005.

[501] E. E. Salpeter and H. A. Bethe, Phys. Rev. **84**, 1232 (1951).

[502] N. Nakanishi, Prog. Theor. Phys. Suppl. **43**, 1 (1969).

[503] E. Oset, A. Ramos, and C. Bennhold, Phys. Lett. **B527**, 99 (2002), nucl-th/0109006.

[504] T. Inoue, E. Oset, and M. J. Vicente Vacas, Phys. Rev. **C65**, 035204 (2002), hep-ph/0110333.

[505] A. Ramos, E. Oset, and C. Bennhold, Phys. Rev. Lett. **89**, 252001 (2002), nucl-th/0204044.

[506] R. H. Dalitz and S. F. Tuan, Annals Phys. **10**, 307 (1960).

[507] R. H. Dalitz, T. C. Wong, and G. Rajasekaran, Phys. Rev. **153**, 1617 (1967).

[508] M. Jones, R. H. Dalitz, and R. R. Horgan, Nucl. Phys. **B129**, 45 (1977).

[509] J. H. W. Wyld, Phys. Rev. **155**, 1649 (1967).

[510] G. F. Chew and S. Mandelstam, Phys. Rev. **119**, 467 (1960).

[511] U.-G. Meissner and J. A. Oller, Nucl. Phys. **A673**, 311 (2000), nucl-th/9912026.

[512] J. A. Oller and U. G. Meissner, Phys. Lett. **B500**, 263 (2001), hep-ph/0011146.

[513] G. Ecker, Prog. Part. Nucl. Phys. **35**, 1 (1995), hep-ph/9501357.

[514] V. Bernard, N. Kaiser, and U.-G. Meissner, Int. J. Mod. Phys. **E4**, 193 (1995), hep-ph/9501384.

[515] S. Weinberg, Phys. Rev. Lett. **17**, 616 (1966).

[516] Y. Tomozawa, Nuovo Cim. **46A**, 707 (1966).

[517] B. Borasoy, R. Nissler, and W. Weise, Eur. Phys. J. **A25**, 79 (2005), hep-ph/0505239.

[518] C. Bennhold and H. Tanabe, Nucl. Phys. **A530**, 625 (1991).

[519] D. Jido, J. A. Oller, E. Oset, A. Ramos, and U. G. Meissner, Nucl. Phys. **A725**, 181 (2003), nucl-th/0303062.

[520] R. J. Nowak *et al.*, Nucl. Phys. **B139**, 61 (1978).

[521] D. N. Tovee *et al.*, Nucl. Phys. **B33**, 493 (1971).

[522] T. S. Mast *et al.*, Phys. Rev. **D14**, 13 (1976).

[523] J. Ciborowski *et al.*, J. Phys. **G8**, 13 (1982).

[524] R. O. Bangerter *et al.*, Phys. Rev. **D23**, 1484 (1981).

[525] T. S. Mast *et al.*, Phys. Rev. **D11**, 3078 (1975).

[526] M. Sakitt *et al.*, Phys. Rev. **139**, B719 (1965).

[527] M. B. Watson, M. Ferro-Luzzi, and R. D. Tripp, Phys. Rev. **131**, 2248 (1963).

[528] J. K. Kim, Phys. Rev. Lett. **14**, 29 (1965).

[529] M. Ferro-Luzzi, R. D. Tripp, and M. B. Watson, Phys. Rev. Lett. **8**, 28 (1962).

[530] M. Csejthey-Barth *et al.*, Phys. Lett. **16**, 89 (1965).

[531] J. Paul Nordin, Phys. Rev. **123**, 2168 (1961).

[532] W. Kittel, G. Ptter, and I. Wacek, Phys. Lett. **21**, 349 (1966).

[533] H. Going, Nuovo Cim. **16**, 848 (1960).

[534] Rutherford-London, G. P. Gopal *et al.*, Nucl. Phys. **B119**, 362 (1977).

[535] R. J. Hemingway, Nucl. Phys. **B253**, 742 (1985).

[536] C. Garcia-Recio, M. F. M. Lutz, and J. Nieves, Phys. Lett. **B582**, 49 (2004), nucl-th/0305100.

[537] M. Batinic, I. Slaus, A. Svarc, and B. M. K. Nefkens, Phys. Rev. **C51**, 2310 (1995), nucl-th/9501011.

[538] J. C. Hart *et al.*, Nucl. Phys. **B166**, 73 (1980).

[539] D. H. Saxon *et al.*, Nucl. Phys. **B162**, 522 (1980).

[540] R. D. Baker *et al.*, Nucl. Phys. **B145**, 402 (1978).

[541] R. D. Baker *et al.*, Nucl. Phys. **B141**, 29 (1978).

[542] B. Nelson *et al.*, Phys. Rev. Lett. **31**, 901 (1973).

[543] D. W. Thomas, A. Engler, H. E. Fisk, and R. W. Kraemer, Nucl. Phys. **B56**, 15 (1973).

[544] J. J. Jones *et al.*, Phys. Rev. Lett. **26**, 860 (1971).

[545] T. O. Binford *et al.*, Phys. Rev. **183**, 1134 (1969).

[546] O. Van Dyck *et al.*, Phys. Rev. Lett. **23**, 50 (1969).

[547] T. M. Knasel *et al.*, Phys. Rev. **D11**, 1 (1975).

[548] R. L. Crolius *et al.*, Phys. Rev. **155**, 1455 (1967).

[549] J. Keren, Phys. Rev. **133**, B457 (1963).

[550] L. L. Yoder, C. T. Coffin, D. I. Meyer, and K. M. Terwilliger, Phys. Rev. **132**, 1778 (1963).

[551] L. B. Leipuner and R. K. Adair, Phys. Rev. **109**, 1358 (1958).

[552] L. Bertanza *et al.*, Phys. Rev. Lett. **8**, 332 (1962).

[553] F. S. Crawford *et al.*, Phys. Rev. Lett. **3**, 394 (1959).

[554] R. T. V. de Walle, C. L. A. Pols, D. J. Schotanus, H. J. G. M. Tiecke, and D. Z. Toet, Nuovo Cim. **A53**, 745 (1968).

[555] O. Goussu *et al.*, Nuovo Cim. **42A**, 606 (1966).

[556] F. Eisler *et al.*, Nuovo Cim. **10**, 468 (1958).

[557] C. of Nuclear Study, http://gwdac.phys.gwu.edu (2000).

[558] S. Mandelstam, Phys. Rev. **112**, 1344 (1958).

[559] N. Kaiser, P. B. Siegel, and W. Weise, Phys. Lett. **B362**, 23 (1995), nucl-th/9507036.

[560] N. Kaiser, T. Waas, and W. Weise, Nucl. Phys. **A612**, 297 (1997), hep-ph/9607459.

[561] E. E. Kolomeitsev and M. F. M. Lutz, Phys. Lett. **B585**, 243 (2004), nucl-th/0305101.

[562] M. Gell-Mann, Phys. Rev. **125**, 1067 (1962).

[563] S. Okubo, Prog. Theor. Phys. **27**, 949 (1962).

[564] J. Gasser, H. Leutwyler, and M. E. Sainio, Phys. Lett. **B253**, 252 (1991).

[565] U. G. Meissner, Rept. Prog. Phys. **56**, 903 (1993), hep-ph/9302247.

[566] M. Frink, U.-G. Meissner, and I. Scheller, Eur. Phys. J. **A24**, 395 (2005), hep-lat/0501024.

[567] V. Bernard, N. Kaiser, and U. G. Meissner, Phys. Lett. **B309**, 421 (1993), hep-ph/9304275.

[568] V. Bernard, N. Kaiser, and U. G. Meissner, Phys. Rev. **C52**, 2185 (1995), hep-ph/9506204.

[569] G. Ecker, J. Gasser, A. Pich, and E. de Rafael, Nucl. Phys. **B321**, 311 (1989).

[570] M. F. M. Lutz and E. E. Kolomeitsev, Nucl. Phys. **A700**, 193 (2002), nucl-th/0105042.

[571] B. Borasoy, R. Nissler, and W. Weise, Phys. Rev. Lett. **94**, 213401 (2005), hep-ph/0410305.

[572] DEAR, G. Beer *et al.*, Phys. Rev. Lett. **94**, 212302 (2005).

[573] J. A. Oller, J. Prades, and M. Verbeni, Phys. Rev. Lett. **95**, 172502 (2005), hep-ph/0508081.

[574] B. Borasoy, R. Nissler, and W. Weise, (2005), hep-ph/0512279.

[575] J. A. Oller, J. Prades, and M. Verbeni, (2006), hep-ph/0601109.

[576] D. Jido, E. Oset, and A. Ramos, Phys. Rev. **C66**, 055203 (2002), nucl-th/0208010.

[577] S. I. Nam, H. C. Kim, T. Hyodo, D. Jido, and A. Hosaka, J. Korean Phys. soc. **45**, 1466 (2004), hep-ph/0309017.

[578] M. F. M. Lutz and E. E. Kolomeitsev, (2000), nucl-th/0004021.

[579] M. F. M. Lutz and E. E. Kolomeitsev, Found. Phys. **31**, 1671 (2001), nucl-th/0105068.

[580] J. Nieves and E. Ruiz Arriola, Phys. Rev. **D64**, 116008 (2001), hep-ph/0104307.

[581] C. Garcia-Recio, J. Nieves, E. Ruiz Arriola, and M. J. Vicente Vacas, Phys. Rev. **D67**, 076009 (2003), hep-ph/0210311.

[582] M. F. M. Lutz and E. E. Kolomeitsev, Nucl. Phys. **A730**, 110 (2004), hep-ph/0307233.

[583] M. F. M. Lutz and M. Soyeur, Nucl. Phys. **A748**, 499 (2005), nucl-th/0407115.

[584] J. C. Nacher, E. Oset, H. Toki, and A. Ramos, Phys. Lett. **B455**, 55 (1999), nucl-th/9812055.

[585] J. C. Nacher, E. Oset, H. Toki, and A. Ramos, Phys. Lett. **B461**, 299 (1999), nucl-th/9902071.

[586] V. K. Magas, E. Oset, and A. Ramos, Phys. Rev. Lett. **95**, 052301 (2005), hep-ph/0503043.

[587] J. C. Nacher *et al.*, Nucl. Phys. **A678**, 187 (2000), nucl-th/9906018.

[588] D. Jido, A. Hosaka, J. C. Nacher, E. Oset, and A. Ramos, Phys. Rev. **C66**, 025203 (2002), hep-ph/0203248.

[589] B. Borasoy, P. C. Bruns, U. G. Meissner, and R. Nissler, (2005), hep-ph/0508307.

[590] T. Waas, N. Kaiser, and W. Weise, Phys. Lett. **B365**, 12 (1996).

[591] T. Waas and W. Weise, Nucl. Phys. **A625**, 287 (1997).

[592] A. Ramos and E. Oset, Nucl. Phys. **A671**, 481 (2000), nucl-th/9906016.

[593] R. H. Dalitz and S. F. Tuan, Phys. Rev. Lett. **2**, 425 (1959).

[594] M. H. Alston *et al.*, Phys. Rev. Lett. **6**, 698 (1961).

[595] J. Fink, P. J., G. He, R. H. Landau, and J. W. Schnick, Phys. Rev. **C41**, 2720 (1990).

[596] E. Oset and M. J. Vicente-Vacas, Nucl. Phys. **A446**, 584 (1985).

[597] J. A. Oller and E. Oset, Nucl. Phys. **A620**, 438 (1997), hep-ph/9702314.

[598] J. B. Lange *et al.*, Phys. Rev. **C61**, 025201 (2000).

[599] R. C. Carrasco and E. Oset, Nucl. Phys. **A536**, 445 (1992).

[600] E. Oset and M. J. Vicente Vacas, Nucl. Phys. **A678**, 424 (2000), nucl-th/0004030.

[601] A. Bramon, A. Grau, and G. Pancheri, Phys. Lett. **B283**, 416 (1992).

[602] J. E. Palomar and E. Oset, Nucl. Phys. **A716**, 169 (2003), nucl-th/0208013.

[603] E. Oset and A. Ramos, Nucl. Phys. **A679**, 616 (2001), nucl-th/0005046.

[604] G. E. Brown and W. Weise, Phys. Rept. **22**, 279 (1975).

[605] T. E. O. Ericson and W. Weise, *Pions and Nuclei* (Clarendon press, Oxford, UK, 1988).

[606] LEPS, J. K. Ahn, Nucl. Phys. **A721**, 715 (2003).

[607] Crystall Ball, S. Prakhov *et al.*, Phys. Rev. **C70**, 034605 (2004).

[608] C. DeTar and T. Kunihiro, Phys. Rev. **D39**, 2805 (1989).

[609] D. Jido, Y. Nemoto, M. Oka, and A. Hosaka, Nucl. Phys. **A671**, 471 (2000), hep-ph/9805306.

[610] D. Jido, M. Oka, and A. Hosaka, Prog. Theor. Phys. **106**, 873 (2001), hep-ph/0110005.

[611] F. X. Lee and D. B. Leinweber, Nucl. Phys. Proc. Suppl. **73**, 258 (1999), hep-lat/9809095.

[612] UKQCD, D. G. Richards, Nucl. Phys. Proc. Suppl. **94**, 269 (2001), hep-lat/0011025.

[613] W. Melnitchouk *et al.*, Phys. Rev. **D67**, 114506 (2003), hep-lat/0202022.

[614] QCDSF, M. Gockeler *et al.*, Phys. Lett. **B532**, 63 (2002), hep-lat/0106022.

[615] S. Sasaki, T. Blum, and S. Ohta, Phys. Rev. **D65**, 074503 (2002), hep-lat/0102010.

[616] N. Mathur *et al.*, Phys. Lett. **B605**, 137 (2005), hep-ph/0306199.

[617] Y. Nemoto, N. Nakajima, H. Matsufuru, and H. Suganuma, Phys. Rev. **D68**, 094505 (2003), hep-lat/0302013.

[618] D. Jido, N. Kodama, and M. Oka, Phys. Rev. **D54**, 4532 (1996), hep-ph/9604280.

[619] D. Jido, M. Oka, and A. Hosaka, Phys. Rev. Lett. **80**, 448 (1998), hep-ph/9707307.

[620] D. Jido and M. Oka, (1996), hep-ph/9611322.

[621] B. M. K. Nefkens *et al.*, Phys. Rev. **D18**, 3911 (1978).

[622] H. T. Diehl *et al.*, Phys. Rev. Lett. **67**, 804 (1991).

[623] A. Bosshard *et al.*, Phys. Rev. **D44**, 1962 (1991).

[624] M. Kotulla *et al.*, Phys. Rev. Lett. **89**, 272001 (2002), nucl-ex/0210040.

[625] G. Lopez Castro and A. Mariano, Phys. Lett. **B517**, 339 (2001), nucl-th/0006031.

[626] G. Lopez Castro and A. Mariano, Nucl. Phys. **A697**, 440 (2002), nucl-th/0010045.

[627] W.-T. Chiang, S. N. Yang, M. Vanderhaeghen, and D. Drechsel, Nucl. Phys. **A723**, 205 (2003), nucl-th/0211061.

[628] W. Blum and H. Saller, Eur. Phys. J. **C28**, 279 (2003).

[629] U.-G. Meissner and S. Steininger, Nucl. Phys. **B499**, 349 (1997), hep-ph/9701260.

[630] S. R. Coleman and S. L. Glashow, Phys. Rev. Lett. **6**, 423 (1961).

[631] BES, B. S. Zou, X. B. Ji, and H. X. Yang, PiN Newslett. **16**, 174 (2002), hep-ph/0110264.

[632] BES, B.-s. Zou, (2002), hep-ex/0210028.

[633] D. Jido, H. Nagahiro, and S. Hirenzaki, Phys. Rev. **C66**, 045202 (2002), nucl-th/0206043.

[634] H. Nagahiro, D. Jido, and S. Hirenzaki, Phys. Rev. **C68**, 035205 (2003), nucl-th/0304068.

[635] N. C. Mukhopadhyay, J. F. Zhang, and M. Benmerrouche, Phys. Lett. **B364**, 1 (1995), hep-ph/9510307.

[636] M. Benmerrouche, N. C. Mukhopadhyay, and J. F. Zhang, Phys. Rev. **D51**, 3237 (1995), hep-ph/9412248.

[637] D. Jido, M. Oka, and A. Hosaka, Prog. Theor. Phys. **106**, 823 (2001), hep-ph/0007127.

[638] S. Sarkar, E. Oset, and M. J. Vicente Vacas, Phys. Rev. **C72**, 015206 (2005), hep-ph/0503066.

[639] L. Roca, S. Sarkar, V. K. Magas, and E. Oset, submitted to Phys. Rev. C. .

[640] S. Sarkar, L. Roca, E. Oset, V. K. Magas, and M. J. V. Vacas, (2005), nucl-th/0511062.

[641] D. P. Barber *et al.*, Zeit. Phys. **C7**, 17 (1980).

[642] A. Sibirtsev, J. Haidenbauer, S. Krewald, U.-G. Meissner, and A. W. Thomas, (2005), hep-ph/0509145.

[643] S.-I. Nam, A. Hosaka, and H.-C. Kim, Phys. Rev. **71**, 114012 (2005), hep-ph/0503149.

[644] A. J. G. Hey, P. J. Litchfield, and R. J. Cashmore, Nucl. Phys. **B95**, 516 (1975).

[645] R. Machleidt, K. Holinde, and C. Elster, Phys. Rept. **149**, 1 (1987).

[646] E. Oset and M. J. Vicente Vacas, Phys. Lett. **B386**, 39 (1996).

[647] U.-G. Meissner, E. Oset, and A. Pich, Phys. Lett. **B353**, 161 (1995), nucl-th/9503011.

[648] Y. Zeldovich and A. Sakharov, Yad. Fiz. **4**, 395; Sov. J. Nucl. Phys. **4** (1967) 283. H. Lipkin, hep (1966).

[649] J. J. de Swart, Rev. Mod. Phys. **35**, 916 (1963).

[650] K. Imai, Talk given at Exotic Hadrons workshop, May 27, 2005; http://www.hepl.phys.nara-wu.ac.jp/exohad05/files/exohad05_imai.pdf, K. Miwa, private communication. .

[651] W. Rarita and J. S. Schwinger, Phys. Rev. **60**, 61 (1941).

[652] S. Theberge, A. W. Thomas, and G. A. Miller, Phys. Rev. **D22**, 2838 (1980).

[653] J. D. Bjorken and S. D. Drell, *Relativistic quantum mechanics* (McGraw-Hill, New York, 1964).

[654] J. D. Bjorken and S. D. Drell, *Relativistic quantum fields* (McGraw-Hill, New York, 1965).

[655] M. Gell-Mann, Phys. Rev. **92**, 833 (1954).

[656] T. Nakano and K. Nishijima, Prog. Theor. Phys. **10**, 581 (1954).